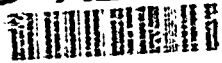


AD-A247 934



AGARD-CP-502

1

AGARD-CP-502

# AGARD

ADVISORY GROUP FOR AEROSPACE RESEARCH & DEVELOPMENT  
7 RUE ANCELLE 92200 NEUILLY SUR SEINE FRANCE

AGARD CONFERENCE PROCEEDINGS 502

## Remote Sensing of the Propagation Environment (La Télédétection du Milieu de Propagation)

DTIC  
ELECTE  
MAR 25 1992  
S D

This document has been approved  
for public release and sale; its  
distribution is unlimited.

*Papers presented at the Electromagnetic Wave Propagation Panel  
Symposium, held in Çeşme, Turkey, 30th September—4th October 1991.*



NORTH ATLANTIC TREATY ORGANIZATION

92-07505



92

008

Published February 1992

Distribution and Availability on Back Cover

40th  
Anniversary  
Year

**Best  
Available  
Copy**

AGARD-CP-502

# AGARD

ADVISORY GROUP FOR AEROSPACE RESEARCH & DEVELOPMENT

7 RUE ANCELLE 92200 NEUILLY SUR SEINE FRANCE

AGARD CONFERENCE PROCEEDINGS 502

## Remote Sensing of the Propagation Environment

(La Télédétection du Milieu de Propagation)

Papers presented at the Electromagnetic Wave Propagation Panel  
Symposium, held in Çeşme, Turkey, 30th September—4th October 1991.



North Atlantic Treaty Organization  
*Organisation du Traité de l'Atlantique Nord*

## The Mission of AGARD

According to its Charter, the mission of AGARD is to bring together the leading personalities of the NATO nations in the fields of science and technology relating to aerospace for the following purposes:

- Recommending effective ways for the member nations to use their research and development capabilities for the common benefit of the NATO community;
- Providing scientific and technical advice and assistance to the Military Committee in the field of aerospace research and development (with particular regard to its military application);
- Continuously stimulating advances in the aerospace sciences relevant to strengthening the common defence posture;
- Improving the co-operation among member nations in aerospace research and development;
- Exchange of scientific and technical information;
- Providing assistance to member nations for the purpose of increasing their scientific and technical potential;
- Rendering scientific and technical assistance, as requested, to other NATO bodies and to member nations in connection with research and development problems in the aerospace field.

The highest authority within AGARD is the National Delegates Board consisting of officially appointed senior representatives from each member nation. The mission of AGARD is carried out through the Panels which are composed of experts appointed by the National Delegates, the Consultant and Exchange Programme and the Aerospace Applications Studies Programme. The results of AGARD work are reported to the member nations and the NATO Authorities through the AGARD series of publications of which this is one.

Participation in AGARD activities is by invitation only and is normally limited to citizens of the NATO nations.

The content of this publication has been reproduced directly from material supplied by AGARD or the authors.

Published February 1992

Copyright © AGARD 1992  
All Rights Reserved

ISBN 92-835-0654-5



Printed by Specialised Printing Services Limited  
40 Chigwell Lane, Loughton, Essex IG10 3TZ

## Theme

Increasing complexity and sophistication of modern military sensor and weapon systems require a more accurate and timely description of the propagation environment for the entire electromagnetic spectrum (from extremely low frequencies through the ultraviolet band). Active and passive remote sensing techniques, deployed from the ground, from airborne platforms and, very importantly, from satellites offer the greatest potential for producing the desired information in a timely manner. For example, high resolution ionospheric sounders can provide temporal and spatial structure variations which are critical to performance of HF over-the-horizon radars, and modern geolocation techniques; lidars have the potential of providing continuous atmospheric profiles of temperature, humidity, winds and extinction; radars may be able to sense refractivity profiles directly and, in combination with acoustic sounders, give information presently obtained by radiosondes. Assessment of propagation under horizontally inhomogeneous conditions necessitates real time information of atmospheric structure of the region of interest. Only satellite remote sensors are capable of measuring the propagation environment over a wide area in a short time span. The data may be sensed directly using active or passive remote sensing techniques or be inferred through interpretation of optically or infrared sensed imagery. In the above areas, new and promising remote sensing technologies are emerging. Some of the techniques (especially satellite imagery) may produce large amounts of data which need special handling and processing schemes to be useful in an operational environment. In addition, some sensing techniques rely on complicated physical processes which necessitates complex profile inversion techniques.

### Topics Covered

- 1 — ionospheric and magnetospheric sensing
- 2 — sensing of temperature, humidity, liquid water, wind profiles
- 3 — sensing of tropospheric refractivity
- 4 — molecular and aerosol extinction
- 5 — surface parameter (see surface temperature, roughness)
- 6 — profile inversion techniques
- 7 — data handling and processing techniques



Accession For	
NTIS CRA&	<input checked="" type="checkbox"/>
DTIC TAB	<input type="checkbox"/>
Unannounced	<input type="checkbox"/>
Justification	
By	
Distribution/	
Availability Codes	
Dist	Avail and/or Special
A-1	

## Thème

La sophistication et la complexité de plus en plus grandes des réseaux de capteurs militaires et des systèmes d'armes modernes nécessitent une description actualisée et plus précise du milieu de propagation pour tout le spectre électromagnétique (allant des très basses fréquences jusqu'à l'ultraviolet). Les techniques de télédétection actives et passives mises en oeuvre soit du sol, soit à partir de plateformes aériennes, soit, et surtout, à partir de satellites, offrent les meilleures possibilités d'obtenir les informations demandées en temps voulu.

A titre d'exemple, les sondes ionosphériques à haute résolution sont capables de transmettre les variations de la structure spatio-temporelle qui régissent les performances des radars transhorizon HF et qui permettent l'emploi des techniques modernes de géolocalisation; les lidars offrent la possibilité de fournir en permanence des profils atmosphériques de température, d'humidité, d'anémométrie et d'extinction et les radars pourraient détecter directement les profils de réfraction et fournir, en association avec les sondes acoustiques, les informations obtenues actuellement au moyen des radiosondes.

L'évaluation de la propagation dans des conditions de couches d'atmosphère hétérogènes passe par l'obtention de données temps réel sur la structure atmosphérique de la zone considérée. Seuls les télédéTECTEURS sur satellite sont capables de sonder le milieu de propagation sur un large domaine dans un intervalle de temps très court.

Les informations peuvent être captées soit directement au moyen des techniques de télédétection actives et passives, soit déduites par interprétation, soit captées optiquement ou par imagerie infra-rouge. Des nouvelles techniques prometteuses de télédétection commencent à apparaître dans ces domaines. Certaines de ces techniques (l'imagerie par satellite en particulier) produiront de grandes quantités de données qui nécessiteront des systèmes de manipulation et de traitement adaptés pour permettre leur utilisation en environnement opérationnel. En outre, certaines techniques de télédétection sont tributaires de procédés manuels compliqués, ce qui implique des techniques d'inversion de profil complexes.

### Sujets

- 1 — la détection ionosphérique et magnétosphérique
- 2 — la détection de la température, de l'humidité, de l'eau liquide, des profils du vent
- 3 — la détection de la réfraction troposphérique
- 4 — l'extinction moléculaire et aérosoï
- 5 — les paramètres surfaciques (température, état de la surface de la mer)
- 6 — les techniques d'inversion de profil
- 7 — les techniques de manipulation et de traitement des données

# Electromagnetic Wave Propagation Panel

**Chairman:** Dr J.H. Richter  
Head, Ocean and Atmospheric  
Sciences Division, Code 54  
Naval Ocean Systems Center  
San Diego, CA 92152-5000  
United States

**Deputy Chairman:** Dr D.H. Höhn, apl. Prof.  
FGAN-FfO  
Forschungsinstitut für  
Optik  
Schloss Kressbach  
W-7400 Tübingen  
Germany

## TECHNICAL PROGRAMME COMMITTEE

### CO-CHAIRMEN

Mr F. Christophe  
Département Micro-Ondes  
ONERA-CERT Toulouse  
BP 4025  
2, Avenue E. Belin  
31055 Toulouse Cedex  
France

Dr J.H. Richter  
Head, Ocean and Atmospheric  
Sciences Division, Code 54  
Naval Ocean Systems Center  
San Diego, CA 92152-5000  
United States

### MEMBERS

Prof. P. Broche  
LSEET  
639, Boulevard des Armaris  
83100 Toulon  
France

Dr S.F. Clifford  
Director, Wave Propagation Laboratory  
NOAA/ERL/WPL - R/E/WP  
325 Broadway  
Boulder, CO 80303  
United States

Ir J. Rogge  
Koninklijke Militaire Academie  
Kasteelplein 10  
4811 XC Breda  
The Netherlands

Prof. K.C. Yeh  
Department of Electrical and Computer  
Engineering  
University of Illinois  
1406 W. Green Street  
Urbana, IL 61801-2991  
United States

Dr P.S. Cannon  
Applied Ionospheric Physics  
Flight Management Department  
Building P 161  
Defence Research Agency  
Farnborough  
Hants GU14 6TD  
United Kingdom

Prof. D.T. Gjessing  
Royal Norwegian Council for Scientific  
and Ind. Research  
Environmental Surveillance  
Technology Programme  
PO Box 25  
2007 Kjeller  
Norway

Dr C. Werner  
Institut für Optoelektronik  
Abteilung Lasertechnik  
DLR  
8031 Oberpfaffenhofen  
Germany

### PANEL EXECUTIVE

**Mail from Europe:**  
AGARD-OTAN  
Attn: EPP Executive  
7, rue Ancelle  
92200 Neuilly sur Seine  
France

**Mail from US and Canada:**  
AGARD-NATO  
Attn: EPP Executive  
Unit 21551  
APO AE 09777

Tel: 33(1) 47 38 57 68  
Telex: 610176 (France)  
Telefax: 33(1) 47 38 57 99

## Preface

Advances in propagation modeling, signal processing and computer technology demand a better spatial and temporal description of the propagation environment. For example, efficient and accurate models have been developed for calculating tropospheric radio propagation under horizontally varying refractivity conditions. What does not exist are adequate modeling or measurement techniques which characterize the temporal and spatial variability of the refractivity field. The only hope to obtain the needed measurements is through remote sensing techniques. The need for new and improved remote sensing techniques applies equally to ionospheric propagation and to visible and infrared radiation calculations.

Accordingly, the Symposium addressed remote sensing techniques for tropospheric and ionospheric parameters affecting propagation. It was organized into seven sessions; two dealing with tropospheric refractivity, two with sensing ionospheric parameters, one addressing sensing of aerosols, one covering sensing of wind, temperature, liquid water and humidity, and a final session on measurement, inversion and processing techniques. A total of 37 papers were presented. The Symposium provided an excellent review of various remote sensing techniques and ideas for new directions. It was a scientifically stimulating and rewarding experience.

Gratefully acknowledged are the cooperation and assistance received by the Symposium co-chairman, Mr F. Christophe and the members of the technical program committee: Prof. P. Broche, Dr P. Cannon, Dr S. Clifford, Prof. D. Gjessing, Ir J. Rogge, Dr C. Werner and Prof. K.C. Yeh. The EPP Executive, LTC R. Cariglia and The EPP Secretary Mr Jean-Philippe Prouteau deserve special thanks for their excellent planning and execution of the Symposium and their help in preparing the proceedings.

Major credit for this very successful and stimulating Symposium goes to the Turkish hosts who provided superb local arrangements. Professor C. Toker and his staff facilitated both an excellent scientific information exchange and many unforgettable opportunities for direct sensing of the beautiful and fascinating local environment.

Juergen H. Richter  
Co-Chairman and Editor

# Contents

	Page
Theme	iii
Theme	iv
Electromagnetic Wave Propagation Panel and Technical Programme Committee	v
Preface	vi
	Reference
<b>SESSION I — TROPOSPHERIC REFRACTIVITY (A)</b>	
Session Chairman: Dr H.J. Albrecht, GE	
Remote Sensing of Refractivity Structure by Direct Radio Measurements at UHF by H.V. Hitney	1
Sensing Propagation Events and Fade Statistics at C-Band for Two Over-Water, Line-of-Sight Propagation Paths over a One Year Period by J. Goldhirsh, G.D. Dockery and B.H. Musiani	2
Remote Sensing of the Evaporation Duct Using an X-Band Radar by K.D. Anderson	3
Propagation Transhorizon en Atmosphère Marine — Modélisation et Nouveaux Résultats Expérimentaux (Over the Horizon Propagation in a Marine Environment — Modelling and Recent Experimental Results) par J. Claverie et Y. Hurtaud	4
<b>SESSION II — TROPOSPHERIC REFRACTIVITY (B)</b>	
Session Chairman: Ir J. Rogge, NE	
Etude Théorique de la Caractérisation Radioélectrique du Conduit d'Evaporation (A Theoretical Study of a Radiowave Characterization Method of the Evaporation Duct) par N. Douchin, S. Bolioli, F. Christophe et P. Combes	5
Radio Refractivity Profiles Deduced from Aerosol Lidar Measurements by H.G. Hughes, M.R. Paulson and J.H. Richter	6
Use of Mesoscale Models for Refractivity Forecasting by M.F. Levy and K.H. Craig	7
Refractive Assessments from Satellite Observations by J. Rosenthal and R. Helvey	8
A "Virtual Sensor" for Evaporation Ducts — The Impact of Data Uncertainties by J. Cook	9
<b>SESSION III — IONOSPHERIC SENSING (A)</b>	
Session Chairman: Prof. K.C. Yeh, US	
ROSE — A High Resolution, Amplitude Coded, High Frequency Oblique Ionosonde by P.C. Arthur, A.H. Dickson and P.S. Cannon	10

	<b>Reference</b>
<b>The New Portable Digisonde for Vertical and Oblique Sounding</b> by B.W. Reinisch, D.M. Haines and W.S. Kuklinski	<b>11</b>
<b>Sensing the Ionospheric Reflection Channel with a Sounder</b> by K.C. Yeh and H. Soicher	<b>12</b>
<b>Adaptive Remote Sensing of the Ionosphere to Minimise Spectral Intrusion</b> by M. Gallagher and M. Darnell	<b>13</b>
<b>A Review of Various Techniques for Computerized Tomographic Imaging of the Ionosphere</b> by T.D. Raymund	<b>14</b>
<b>Mapping Electron Content and Electron Density in the Sub-Auroral Ionosphere</b> by I.K. Walker, S.E. Pryse, C.D. Russell, D.L. Rice and L. Kersley	<b>15</b>

#### **SESSION IV – IONOSPHERIC SENSING (B)**

Session Chairman: Dr P.S. Cannon, UK

<b>Ionosphere and Troposphere Seen through a Radio Interferometer</b> by T.A.Th. Spoelstra	<b>16</b>
<b>Radio Interferometric Techniques for Investigating Field-Aligned Ionospheric Plasma Irregularities</b> by F. Sürücü and E. Kudeki	<b>17</b>
<b>Active Remote Sensing of the Ionosphere and the Earth Surface Irregularities</b> by E. Bahar	<b>18</b>
<b>Sensing of ELF Signatures Arising from Space Vehicle Disturbances of the Ionosphere</b> by J.Y. Dea, W. Van Bise, E.A. Rauscher and W.-M. Boerner	<b>19</b>
<b>Sensing of Seismo-Electromagnetic Earthquake Precursor Radiation Signatures along Southern California Fault Zones: Evidence of Long Distance Precursor ULF Signals Observed before a Moderate Southern California Earthquake Episode</b> by J.Y. Dea, C.I. Richman and W.-M. Boerner	<b>20</b>

Paper 21 withdrawn

#### **SESSION V – AEROSOL SENSING**

Session Chairman: Dr C. Werner, GE

<b>Remote Sensing of Aerosol Extinction Using Single-ended Lidars</b> by J.H. Richter, H.G. Hughes and M.R. Paulson	<b>22</b>
<b>Probing of the Atmosphere with Lidar</b> by G.J. Kunz	<b>23</b>
<b>Lidar Remote Sensing Techniques for Developing and Evaluating Atmospheric Aerosol Models</b> by D.R. Jensen, H.G. Hughes and M.R. Paulson	<b>24</b>
Paper 25 withdrawn	
<b>Far-Infrared Characterization of Horizontal Path Image Degradation</b> by W.R. Watkins	<b>26</b>

#### **SESSION VI – SENSING OF WIND, TEMPERATURE, LIQUID WATER AND HUMIDITY**

Session Chairman: Dr S.F. Clifford, US

<b>Compact Laser Doppler Anemometer</b> by Ch. Werner, M. Klier, H. Herrmann, E. Biselli and R. Häring	<b>27</b>
---	-----------

	Reference
<b>Remote Sensing of the Atmosphere by Multi-Channel Radiometers</b> by F. Davarian	28
<b>Optical Refraction in the Atmospheric Surface Layer</b> by J.B. Gillespie and D.H. Tofsted	29
<b>Inverting Radiometric Measurements with a Neural Network</b> by E.M. Measure, Y.P. Yee, J.M. Balding and W.R. Watkins	30
<b>Clear-Air Wind Profilers as Cloud Monitors and Hydrometeor Identifiers</b> by E.E. Gossard, S.Y. Matrosov, R.G. Strauch and D.C. Welsh	31
<b>Meteorological Measurement Techniques for Atmospheric Propagation Studies</b> by D. Thomson	32†

**SESSION VII — MEASUREMENT, INVERSION AND PROCESSING TECHNIQUES**  
Session Chairman: Dr W.A. Flood, US

Paper 33 withdrawn

<b>Digital Channel Sounder for Remote Sensing of Scatterers in Mobile Radio Environment</b> by R.W. Lorenz and G. Kadel	34
<b>Basic Equations of Radar Polarimetry and Solutions for the Sensing of Propagation Path Polarization State Changes</b> by W.-M. Boerner, W.L. Yan, A.-Q. Xi and Y. Yamaguchi	35
<b>Adaptive Communications Polarimetry: Sensing of Propagation Path Changes and Adaptation to Optimal Performance in Cellular Communications</b> by Y. Yamaguchi, H.J. Eom and W.-M. Boerner	36
<b>Analysis Algorithms for Processing Ultraviolet Fluorescence Data</b> by J.B. Gillespie, D.L. Rosen, Y.P. Yee and R. Gonzales	37
<b>Recently Implemented Weather Radar Data Processing Technique for Rain-Cell Modelling and Ground Clutter Detection</b> by Y. Korbay and L. Ligthart	38
<b>Calibration Technique for the CNET HF Backscatter Radar</b> by N. Ruelle, F. Gauthier, J.Y. Le Saout, L. Bertel and V. Baltazart	39
<b>Attractor-Based Interpretation of Measurements Made with Radar and Acoustic Remote Sensing Systems</b> by D. Thomson	40†
<b>List of Participants</b>	LP

---

† Not available at the time of printing.

# Remote Sensing of Refractivity Structure by Direct Radio Measurements at UHF

Herbert V. Nitney  
Ocean and Atmospheric Sciences Division  
Naval Ocean Systems Center  
San Diego, CA 92152-5000 USA

## 1. SUMMARY

A method is presented that allows the base of a trapping layer to be determined directly from observations of signal strength on a UHF path in the southern California coastal area. The method uses long-term statistics of trapping layer thickness and refractivity gradient in the area. These statistics are used to compute radio signal strength as a function of the base height of the trapping layer using the Naval Ocean Systems Center Radio Physical Optics (RPO) model. The radio path selected is an over-water 148 km path with transmitter and receiver both located 30 m above sea level. The RPO results are used to infer the trapping layer base height directly from observations of received signal strength. This method has been applied to a 40-day period of continuous signal strength recordings during which the trapping layer base height was known to vary considerably from near zero to about 1000 meters. Inferred base height versus time is compared to direct meteorological measurements of the base of the temperature inversion in the area of the measurements.

## 2. INTRODUCTION

During 1944 and 1945, the U.S. Navy Radio and Sound Laboratory (a predecessor of the

Naval Ocean Systems Center) performed a radio transmission experiment along the coast of southern California [1, 2]. Transmitters 30 meters above sea level at 52, 100, and 547 MHz were placed at San Pedro (near Los Angeles) and receivers 30 meters above sea level were placed at Point Loma in the city of San Diego. The transmission path was 148 km in length and was entirely over water. Signal levels relative to free space were recorded continuously for long periods of time and meteorological soundings were made using radiosondes in San Diego, shipboard balloon-tethered wired sondes near midpath, and airplane sensors along and near the transmission path. Figure 1 shows radio data for the three frequencies and base of the temperature inversion observed during 40 days from late August to early October 1944.

Figure 1 shows a striking negative correlation between the base of the temperature inversion and the received signal strength, particularly at the highest frequency of 547 MHz. Apparently the height of the trapping layer that is usually associated with a temperature inversion is an important, if not dominant, factor in controlling radio propagation on this over-the-horizon path. Figure 1 also indicates the meteorological situation was reasonably homogeneous in range during the time period studied, since

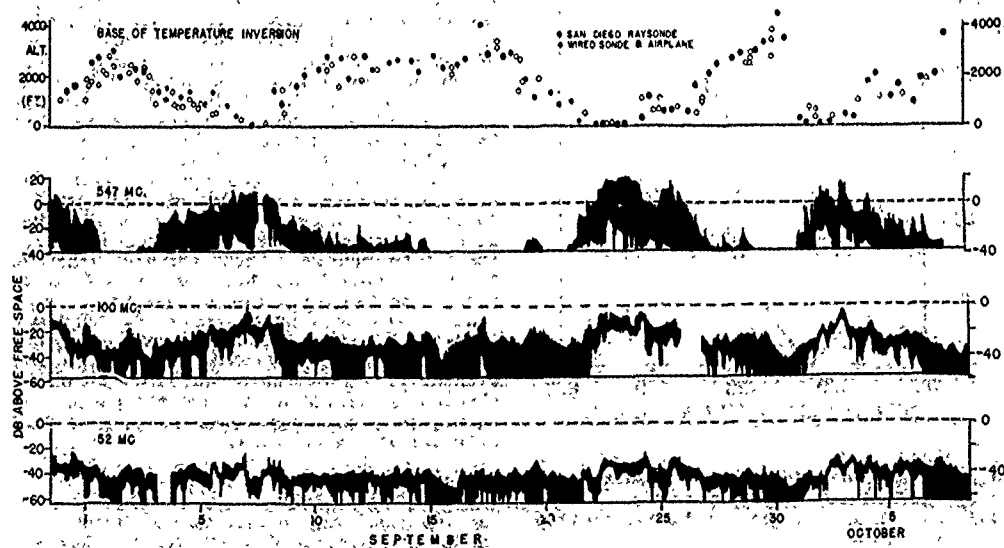


Figure 1. Observed base of temperature inversion and received signal levels at 547, 100, and 52 MHz versus time for the 1944 San Pedro to Point Loma experiment. Path length was 148 km and transmitter and receiver heights were 30 m.

the base heights measured in San Diego, shown by the solid dots, are approximately equal to the base heights measured at other locations along or near the propagation path, shown by the open dots. These two characteristics of the data set suggest using a propagation model to infer the base height. This model assumes horizontal homogeneity and a simple tri-linear modified refractivity profile, in which all characteristics except trapping-layer base height are derived from historical values for the southern California area. If observed signal level could be used to infer the base height, then this technique would be the first step in developing a remote sensing capability for refractivity structure based on direct radio measurements.

### 3. REFRACTIVITY STATISTICS

Modified refractivity versus altitude profiles derived from 261 radiosonde measurements taken at the Naval Ocean Systems Center on Point Loma were analyzed. The radiosondes were taken in the years 1969 through 1976 and cover all months of the year. Nearly all of the soundings were taken during the daytime. Modified refractivity in M units and altitude in meters were calculated for each radiosonde from the observed pressure, temperature, and relative humidity. Each profile was plotted on a graphics terminal where a trained operator determined the best-fit tri-linear profile using a pointing device and a "trial and error" technique. The tri-linear profile fit was evaluated only by the operator's eye, and hence the following statistics are based on subjective data. Figure 2 is an example of one of the 261 measured soundings, shown by the solid trace, and the corresponding tri-linear profile, shown by the dashed lines. This example is neither the best nor the worst fit of the entire set. Indeed, many of the measured profiles are so close to a tri-linear profile, that the original and fit profiles could not be distinguished when plotted together.

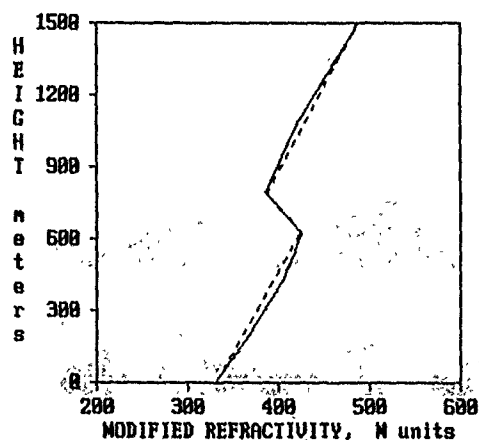


Figure 2. Sample radiosonde-derived refractivity profile for Point Loma on 14 AUG 74: 2233Z (solid) and fitted tri-linear profile (dashed).

Of the entire set of 261 profiles, the median thickness of the middle layer is approximately 130 meters, and the median modified refractivity difference across the middle layer is about 30 M units, which means a trapping layer with a strength of 30 M units. The mean gradient of the lowest layer is 0.125 M-units per meter (M/m) and the mean gradient of the highest layer is 0.116 M/m. Based on these statistics, five sets of tri-linear profiles were constructed for the propagation analysis described in this paper. Each profile contained a trapping layer with a strength,  $\delta M$ , in M units and a thickness,  $\delta z$ , in meters. The first set used the medians,  $\delta M = 30$  and  $\delta z = 130$ . The next two sets varied  $\delta M$  arbitrarily by 10 M units on either side of the median, i.e.  $\delta M = 20$  and  $\delta M = 40$ , leaving  $\delta z = 130$ . The last two sets varied  $\delta z$  arbitrarily by 30 meters on either side of the median, i.e.  $\delta z = 100$  and  $\delta z = 160$ , leaving  $\delta M = 30$ . For all sets, the refractivity gradients of the lowest and highest layers were set to the mean values of 0.125 and 0.116 M/m, respectively. Since only gradients of refractivity are important to propagation effects, a surface value of 330 M units was arbitrarily assumed for all profiles. Each set consisted of 15 profiles with the base of the trapping layer varying from 0 to 1400 meters in 100 meter steps. Note that for a base height of 0, there is no layer below the trapping layer, and the profile is actually bi-linear instead of tri-linear.

### 4. PROPAGATION MODEL

The propagation model used in this study was developed by the author and is known as the Radio Physical Optics (RPO) model. RPO is a hybrid model that combines full amplitude and phase ray optics (RO) models with a split-step parabolic equation (PE) model. RO models are used for elevation angles above a limiting value that is usually a fraction of one degree. The actual limiting value depends on the profile. In the RO model, the complete effects of focusing or defocusing by refractive effects of the profile and the relative phase effects resulting from the integrated optical path length are considered. Below the RO limiting angle, a PE model based on the methods of Tappert [3] and incorporating many of the techniques described by Dockery [4] is used. Two of the significant features of the PE model in RPO are the use of real-valued sine Fast Fourier Transforms (FFTs) and variable FFT sizes up to a maximum of only 1024 points. RPO is a true hybrid model that uses the complementary strengths of both the RO and PE methods to construct a fast yet accurate composite model. In tests comparing RPO to pure PE methods for high altitude 3 GHz applications, RPO has proven to be from 25 to 100 times faster than the pure PE models with no loss of accuracy. RPO can also accommodate wide antenna patterns, including omni-directional antenna patterns, with no impact on the speed of computation. Although it is not needed for the purpose of this paper, RPO can model range-dependent refractivity conditions.

### 5. RESULTS

The RPO model was applied to each profile in the 5 sets described above for the 547 MHz

case of the experiment. Figures 3 and 4 illustrate the propagation loss contours computed by RPO on a height versus range display for two sample profiles, and Figure 5 shows the propagation loss plotted versus height at the receiver location for these two cases. No information could be found on the polarization or type of antennas used in the 1944 experiment, so horizontal polarization and an omni-directional antenna were assumed. The propagation loss (equivalent to path loss for an omni-directional antenna) is defined as the decibel ratio of

transmitted to received power not including any effects of antenna gain. Thus the effects of the actual antenna on all the RPO results would only be noticed at the higher elevation angles, and not for the receiver at a height of 30 m and a range of 148 km. The profiles used for figures 3 through 5 assumed the median values of  $\delta M = 30$  and  $\delta z = 130$ . Figure 3 shows the results for a base height of 200 m and Figure 4 shows the results for a base height of 600 m. Figure 5 shows results for both the 200 m and 600 m base heights along with a dashed free-space

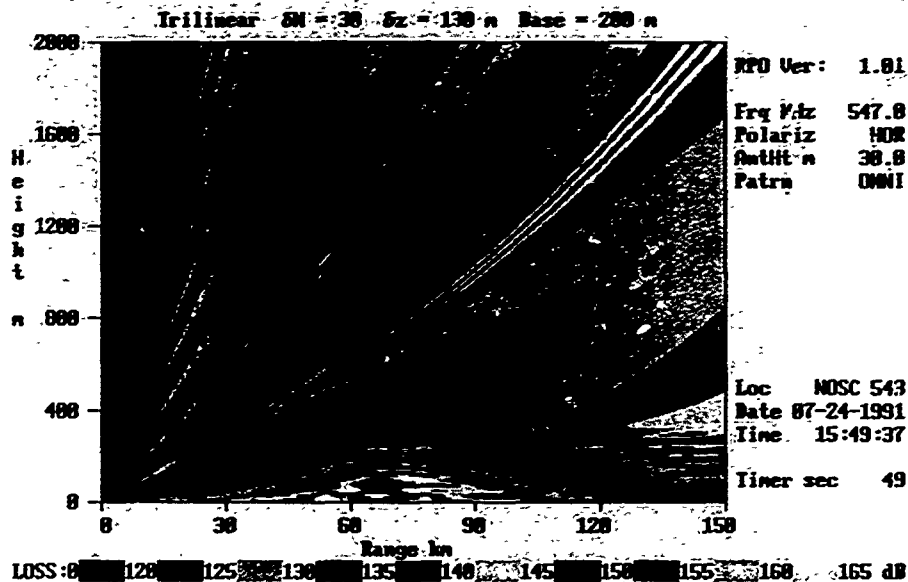


Figure 3. RPO coverage display for 547-MHz and a trapping layer strength of 30 M units and thickness of 130 m with a base height of 200 m.

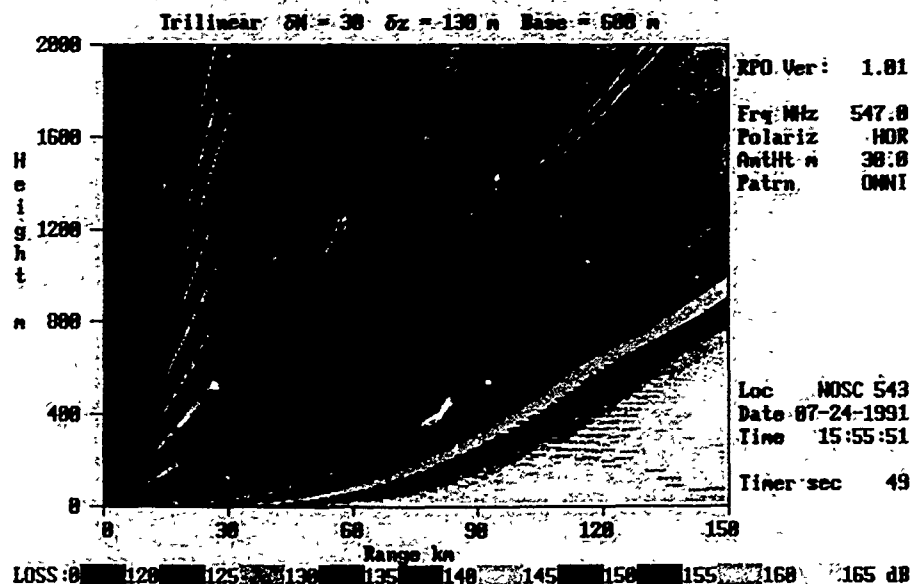


Figure 4. RPO coverage display for 547-MHz and a trapping layer strength of 30 M units and thickness of 130 m with a base height of 600 m.

path loss reference line at 130.6 dB. At the receiver height of 30 m, Figure 5 indicates a loss value of 120 dB, or 11 dB above free space, for the 200 m base height, and a loss value of 156 dB, or 25 dB below free space, for the 600 m base height. Note these calculations are roughly in line with the measured results presented in Figure 1.

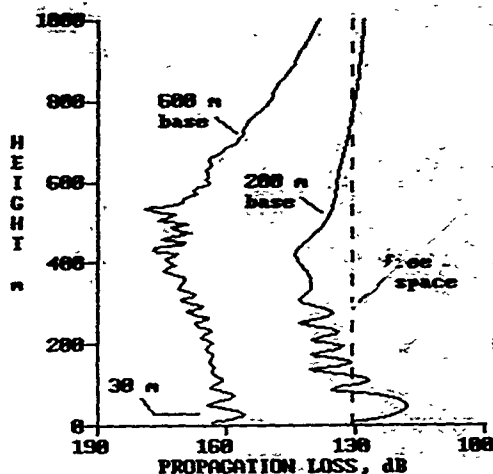


Figure 5. RPO propagation loss versus height at 148 km for the cases shown in Figures 3 and 4. The dashed line is a free-space reference.

The RPO results for all of the 5 profile sets are summarized in Figure 6, which plots propagation factor in dB versus the base of the trapping layer in meters. Propagation factor is the received signal relative to free space. Since the experimental data were limited to 40 dB below free space, Figure 6 was limited to -50 dB, which precluded any results for base heights in excess of 1000 meters. Results for each set are plotted using a unique symbol defined in the figure. The line in Figure 6 is an approximate fit through all the data giving a preference to the median data set indicated by the solid circles. Although there is substantial variation between the various data sets for most base heights, it is apparent that base height is the dominant factor controlling propagation.

The received signal and temperature inversion base height data from Figure 1 were digitized using a graphics tablet so the data could be processed on a personal computer. Figure 7 is a plot of the observed propagation factor at 547 MHz and the corresponding observed base heights versus time. The solid line in the upper portion of Figure 7 is the base height inferred from the radio data using the straight-line fit indicated in Figure 6. Only the highest propagation factor at each time point was used to infer the base height, even though both the highest and lowest observed propagation factors are shown in Figure 7.

#### 6. DISCUSSION

The inferred base height compares quite well to the observed base heights in Figure 7 for

heights up to 800 m. The limit on the observed propagation factor of -40 dB at 547 MHz limited the method in this case to base heights below 800 meters. Since the 100 MHz data shown in Figure 1 were recorded to -60 dB, it was hoped that applying the same method to these data would allow higher base heights to be inferred. The method was applied to the 100 MHz data and higher base heights were inferred. However, the correlation of inferred and observed base heights and the overall scatter of results was much worse at 100 MHz than at 547 MHz. The sensitivity of received signal to the refractivity structure seems to increase substantially with higher frequencies, as is apparent from Figure 1. A better method of inferring higher base heights would appear to be a more sensitive radio receiver at the higher frequencies that would allow a greater dynamic range of received signals to be recorded. No attempt was made to model the 52 MHz case also shown in Figure 1.

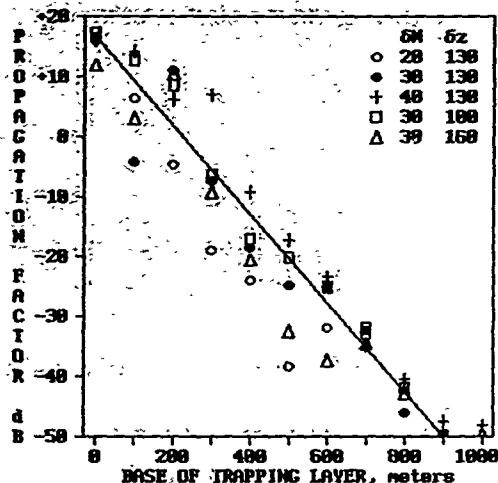


Figure 6. Propagation factor at 547 MHz versus base of trapping layer for the 5 tri-linear profile sets studied. Solid line is a fit to all data.

The good results shown in Figure 7 indicate that either the refractive conditions over the path were reasonably homogeneous, or the method described is not very sensitive to range-dependent effects. It is believed the conditions were homogeneous most of the time because of the similar base heights measured in San Diego and along and near the path by the wired sonde and the airplane. Also, reference [1] contains a few cases of vertical refractivity profiles measured along the propagation path, and these profiles indicate homogeneous conditions. The extent to which this method could be applied to non-homogeneous conditions or expanded to give more information about the trapping layer strength or thickness is not known, but it is certainly a technique that deserves some further investigation. Toward this end, an experiment is being planned that will use transmitters at Point Loma and San Nicolas Island and receivers at the Pacific Missile Test Center in Point Mugu to simultaneously sense conditions on two nearly orthogonal paths of 230 and 100 km length.

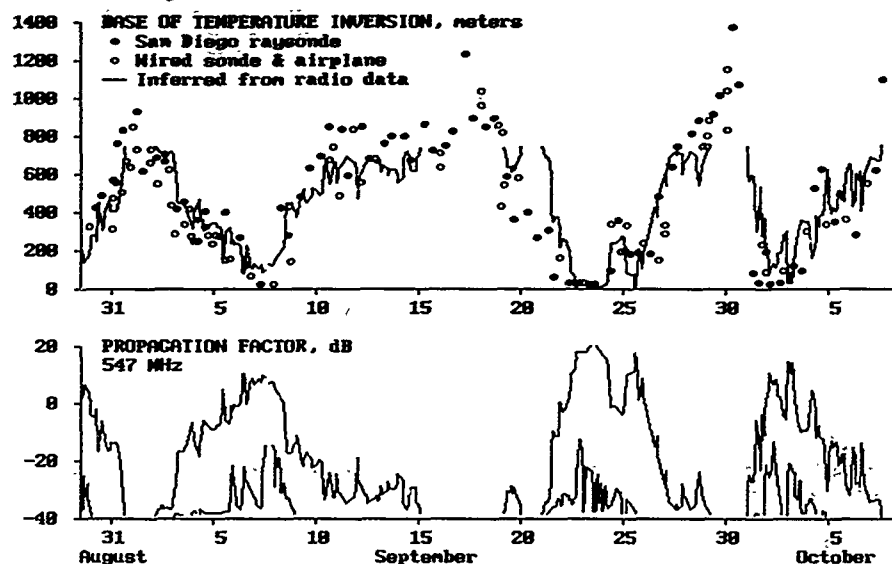


Figure 7. Observed and inferred base of temperature inversion and observed propagation factor at 547 MHz versus time.

#### 7. CONCLUSION

A method has been described to infer trapping layer base height directly from UHF radio measurements. This method has been demonstrated to work well for one 40-day period in southern California. Although several aspects of the technique should be investigated further, the method shows promise as a means to remotely sense refractivity structure.

#### A KNOWLEDGEMENT

This work was supported by the Office of Naval Technology.

#### REFERENCES

- [1] Anderson, L.J., et al., "Atmospheric Refraction - A Preliminary Quantitative Investigation", NRSL Report No. WP-17, Dec 1944.
- [2] Kerr, Donald E., "Propagation of Short Radio Waves", New York, McGraw-Hill Book Company, Inc., 1951, pp 328-335.
- [3] Tappert, Fred D., "The Parabolic Approximation Method", in "Wave Propagation and Underwater Acoustics", J.B. Keller and J.S. Papadakis, Eds., New York, Springer-Verlag, 1977, pp 224-285.
- [4] Dockery, G. Daniel, "Modeling Electromagnetic Wave Propagation in the Troposphere Using the Parabolic Equation", IEEE Trans. Antennas & Propagation, 36, 10, Oct 1988, pp 1464-1470.

# DISCUSSION

## **H. ALBRECHT**

*Do you plan any future activity to prove the validity of your results for other environmental conditions displaying a more disturbed troposphere, such as the North Sea?*

## **AUTHOR'S REPLY**

*We have no specific plans at this time to investigate areas other than southern California using this technique.*

## **K. CRAIG**

*Continuing the previous question, can you quantify the goodness of fit of the tri-linear model to your data, both in the vertical and also in the assumption of horizontal homogeneity? In this case study, the fit certainly appears to be excellent.*

## **AUTHOR'S REPLY**

*I cannot quantify the "goodness of fit", however the majority of the 261 profiles studied were visually a very good fit to the tri-linear model. We do have some statistics that show the assumption of horizontal homogeneity is a good one about 85% of the time.*

## SENSING PROPAGATION EVENTS AND FADE STATISTICS AT C-BAND FOR TWO OVER-WATER, LINE-OF-SIGHT PROPAGATION PATHS OVER A ONE YEAR PERIOD

Julius Goldhirsh

G. Daniel Dockery

Bert H. Musiani

The Johns Hopkins University

Applied Physics Laboratory

Laurel, Maryland, 20723-6099, USA

### 1. SUMMARY

We examine signal fading statistics over a year period corresponding to two over-water, line-of-sight, propagation links in the mid-Atlantic coast of the United States. These links are comprised of a transmitter on a tower at Parramore Island, Virginia operating at 4.7 GHz sending simultaneous cw signals to two receiver systems located on a lighthouse and a lookout tower on Assateague Beach, Virginia at distances of 44 km and 39 km, respectively. The receiving sites are separated by approximately 5 km. Cumulative fade distributions corresponding to yearly, monthly, and diurnal time scales were derived. The yearly distributions showed fades in excess of 49 and 54 dB during approximately 7.7 hours of the year for the lighthouse and lookout tower links, respectively. Fade duration statistics corresponding to sustained attenuation events were also derived. These events, which were arbitrarily defined as having fades relative to free space powers in excess of 20 dB for durations of two hours or more, are believed to be generally due to subrefraction. Analysis of synoptic weather conditions and nearby rawinsonde data during two sustained deep fading periods showed atmospheric conditions consistent with extreme subrefraction, where the refractivity-height profile had a positive lapse rate. The efficacy of employing the links as indicators of real time conditions of atmospheric propagation (e.g., ducting, superrefraction, or quiescent) was also demonstrated by a telephone call-up procedure which enabled displays of time-series of the fading at remote locations to be generated.

### 2. INTRODUCTION

Propagation measurements and modeling for the same over-the-water links examined here were characterized by Goldhirsh and Dockery (Ref 1). The previous results were derived from measurements obtained during a focused five day experimental period in August 1989. The results described here cover the year period June 1, 1989 through May 31, 1990, over which both links operated almost continuously.

The long term objectives of this experiment are: [1] to establish a multi-year data base of fade statistics, from which are derived cumulative fade distributions pertaining to yearly, monthly, and diurnal time scales, [2] to determine fade duration statistics, [3] to establish space diversity criteria pertaining to the nearby sites, and [4] to better understand the physics of propagation by injecting direct refractivity profile measurements into propagation models and comparing the calculated and measured signal levels. In this paper, we describe results pertaining to the above objectives over the one year period.

Long term measurements, of the type described here, should provide designers of over-water, line-of-sight communications systems with statistical data from which to generate realistic fade margins. Simultaneous measurements and comparisons of the fading as measured by the two nearby receiver systems also enable the sensing of the "variability" of the refractivity environment and the efficacy of communications using "space diversity" techniques.

Direct measurements of signal fading for such links represent a means to sense the "integrated effects" of the refractivity environment. For example, the systems described here have been used as a "real time" indicators by the authors to assess whether ducting and/or extreme subrefracting conditions exist. Both effects may produce severe degradation of the received signals.

### 3.0 EXPERIMENTAL DETAILS

#### 3.1 Experimental Geometry and Electrical Parameters

The experimental geometry is described by the map in Figure 1, the vertical profile in Figure 2, and the parameter listing in Table 1. The propagation related parameters are summarized in Table 2. A single transmitter located atop a tower at Parramore Island (PI) radiates cw signals at 4.7 GHz simultaneously to two receiving sites on Assateague Island; one on a lighthouse (44.1 km), and the other on a lookout-tower (39.0 km). The corresponding propagation paths are hereafter referred to as the "Lighthouse" (LH) and the "Lookout Tower" (LT) links, respectively. The receiver sites are separated from one another by 5.5 km. The heights of PI, LH, and LT are 36.9 m, 45.5 m, and 13.7 m, respectively. The heights of the line-of-sight rays above the reflections points for the LH and LT links are respectively 12.5 m and 1.4 m (Figure 2), and the corresponding "standard atmosphere" smooth earth diffraction losses for these links are 2 dB and 13.4 dB, respectively.

#### 3.2 Data Acquisition

The received transmissions at each site are sampled at a rate of 2 Hz, digitized and recorded in PC memory. These data are subsequently stored in hourly files on magnetic disk. Also stored on the magnetic disk are the receiver calibrations which are executed twice per day (12 hours apart). The calibrations are implemented automatically by injecting a stable signal through the receiver input via a series of attenuators in 2 dB increments (70 dB range) and recording the digital outputs. The calibrations were found to be highly repeatable to within 0.5 dB between the 12 hour time increments. At

four minute intervals, the transmitter power is radiated via code to both receiver systems and are independently stored on magnetic disk. In this way, we achieve a constant independent monitoring of the "health" of the transmitter at both sites. These power levels were also stored in hourly files and found to be extremely stable (0.1 dB rms). Sites LH and LT suffered from 11.5% and 13.3% downtime over the year, respectively. These were caused by equipment failure, down-loading of data, and time lost during calibrations.

#### 4.0 TIME-SERIES DATA AND CUMULATIVE DISTRIBUTIONS

Examples of time-series fade events for the LH and LT links are plotted in Figure 3. The vertical scales represents the fades relative to the estimated free space powers (no earth), where positive and negative values correspond to signal reduction and enhancement, respectively. The abscissa is the local time of day. Since each pixel in these figures represents approximately 2.25 minutes, the fade values are plotted within a vertical band comprising this time interval. Time series levels of the types shown in Figure 3 were obtained for each operational day of the year and the fade statistics described here were derived employing developed software which sampled each of the fade values at 0.5 seconds intervals.

The fading event depicted in Figure 3 has been previously characterized by refractivity measurements and modeling calculations, and has been shown to be caused by dynamically changing modal interference patterns (Ref 1).

#### 5. YEARLY CUMULATIVE FADE DISTRIBUTIONS

In Figure 4 are plotted the yearly cumulative fade distributions for both the LH and LT links. The ordinate represents the percentage of operating time the fades exceeded the abscissa values, where the abscissa represents the fade relative to the free space power (in dB). The total operating times are noted in the figures and, represent 88.5% and 86.7% of the total year for the LH and LT links, respectively. It is interesting to note that the "median" fade levels are 0.1 dB and 3.8 dB for the LH and LT links. As mentioned, standard propagation conditions (e.g., effective radius =  $4/3$  earth) result in diffraction losses of 2 and 13.4 dB for the LH and LT links. Hence, the median conditions show signal enhancements of 2 dB and 9.6 dB relative to the "standard" propagation levels for these links suggesting that superrefractive conditions more frequently dominated. It is also worthy to note that the distributions tend to "bulge" at the larger fade levels (e.g., greater than 10 dB). This is due to sustained deep fade events which dominate the statistics at the larger attenuations. These types of events are described in Section 8.

#### 6. MONTHLY FADE DISTRIBUTIONS

##### 6.1 Lighthouse Link

In Figure 5 are plotted the monthly cumulative fade distributions for the Lighthouse link. The ordinate represents the percentage of the operational time during the month in which the abscissa value of the fade is exceeded. The monthly operational times are listed in the accompanying legends. The monthly downtimes ranged from approximately 3% of the month (April) to 30% (June) with the average monthly downtime being approximately 11%. We note seven contiguous months stand out as showing excessive fades at percentages of 1% and smaller. These months correspond to December through June, with February being the "worst

month" (highest fades). Five contiguous months are also noted as showing minimal fades; namely, the months July through November, with September being the "best month" (lowest fades). These months correlate with periods over which the ocean water is colder (December through June) and warmer (July through November). The months also correlate well with the incidence of the sustained deep fade events described in Section 8.

##### 6.2 Lookout Tower Link

Figure 6 shows the monthly cumulative fade distributions for the Lookout Tower link. The monthly downtimes for this site ranged from 4% (May) to 27% (June); with the average monthly downtime being 12.4%. Since the line-of-sight path for this link is closer to the earth's surface than it is for the Lighthouse case, comparatively greater earth diffraction losses are expected for the LT case during subrefractive conditions. We note that the groupings of months as noted for the LH case which exhibit higher and lower fades are the same for the LT link.

##### 6.3 Dependence on Season

In Table 3 are listed the monthly and yearly fades exceeded for percentages of 50%, 10%, 1%, and 0.1%. We note that the median fades for the LH link range between +1.4 dB (June) and -1.4 dB (July); and for LT between 0.5 dB (July) and 7.7 dB (December). The 1% fades range between 12.1 dB (September) and 47.2 dB (February) for the LH path, and 13.1 dB (April) and 52.6 dB (January) for the LT link. In Figures 7 and 8 are shown LH and LT plots of the fade levels relative to free space powers versus months of the year for both the 50% (median) and 1% levels. The maximum differences between the highest and lowest monthly fades over the year at the 1% level are noted. (Figure 8) to be approximately 35 dB for the LH and 40 dB for the LT links. A clear indication is also noted from these figures of the cyclic monthly dependence as described above.

#### 7. DIURNAL VARIATIONS

##### 7.1 Yearly Distributions

The fade levels were culled into four six hour time slots namely, 00:00-06:00, 06:00-12:00, 12:00-18:00, and 18:00-24:00. These time intervals are denoted as periods 1, 2, 3, and 4, respectively. Shown plotted in Figures 9 and 10 are the yearly cumulative distributions for each of these periods for the LH and LT links. The vertical scale represents the percentage of operating time during these individual periods over the year in which the fades exceeded the abscissa value. It is apparent from these figures that no significant diurnal dependence is noted.

##### 7.2 Monthly Dependence

The plots shown in Figures 11 (LH case) and 12 (LT case) were constructed by culling the fade levels in a similar fashion as described in Section 6.1 but over individual monthly periods. The vertical scale in these figures represent the fade levels relative to free space which are exceeded 1% of the time for the entire month corresponding to the given period of the day as indicated by the abscissa. Each of the curves in this figure represents a different month. We note that although considerable variability in fade exists for the different periods of the individual months, no consistent diurnal variation pattern is evident.

## 8. SUSTAINED DEEP FADES

Many of the events during the seven contiguous months (December through June) are believed to be due to severe "subrefractive" events in which the received signals experienced "sustained deep fades," (hereafter referred to as SDF). These are (arbitrarily) defined here as events in which the fades relative to the free space power are in excess of 20 dB over a period of two hours or more. Many of these events are believed caused by synoptic weather conditions in which the refractivity increases with altitude up to such heights that the transmitted rays bend concave upwards away from the direction of the receiving antennas, resulting in a dramatic reduction in received power.

### 8.1 Meteorological Conditions

The meteorological conditions that produced the the subrefractive conditions which, in turn, caused the SDF events in June 1989 and March 1990 were investigated by Meyer (Refs 2, 3). These events are depicted in the time-series fades in Figure 13 for June 20-21 1989 and Figure 14 for March 15-17 1990. The June case depicts SDF events with durations of approximately 5 hours on June 21 for the LH link. For the LT link, 4.5 h and 13 h events are noted on June 20 and June 21, respectively. During the period March 15-17, 1990 (Figure 14), SDF events occurred for approximately 48 and 63 hours for the LH and LT links. Meyer found from weather reports, that during the June and March periods there was an advection of moist warm air over the cooler water and land. This created an increase of the temperature lapse rate and at the same time an increase of the saturation water vapor pressure with altitude. Such conditions caused an increase of the vapor pressure with altitude which, in turn, resulted in a increase of the refractivity. During both days, fog and haze were prominent features of these meteorological effects.

Examining morning rawinsonde data on 07:00 EST on June 21 1989 and March 16 1990 at Wallops Island (coastal region located approximately 13 km from links center), a refractivity slope of +23 N units/km was noted up to an altitude of approximately 130 m for the June case, and +43 N units/km up to an altitude of 185 m for the March case. These positive refractivity lapse rates are indicative of extreme subrefractive conditions which should be even more pronounced over the colder water.

For completeness, we show in Figures 15 and 16 two other significant time series of SDF events during periods in December-January (1989-90) and February (1990), respectively. The December-January events (Figure 15) showed maximum durations of 19 and 20.5 hours for the LH and LT links, respectively. The February events showed maximum durations of 31 and 35.5 hours for the LH and LT links.

### 8.2 Fade Duration Statistics

Density distributions of fade-durations for SDF events were determined for both the LH and LT links over the year period and are plotted in Figure 17. The vertical scale represent the number of events within two hour fade duration bins between 2-4 h, 4-6 h, 6-8 h, etc. There were a total of 29 and 61 distinct events for the LH and LT links, respectively. In Figure 18 are plotted the longest duration events versus the month of the year for each of the months in which the SDF events occurred. We note that the durations for the LT path always exceeded those for the LH link with the longest duration fades being 47.5 and 63.25 hours (March 1990).

An interesting point is that for every SDF event which existed for the LH link, one simultaneously occurred for the LT link which was longer in duration. In other words, the SDF events for the LT link always flanked those for the LH case. Of course, there were many SDF events which occurred for the LT link and not the LH path. The above results are likely due to enhanced diffraction which affects the LT link more significantly than the LH path during severe subrefraction events. In fact, SDF could alternately have been defined relative to the "standard atmosphere powers" which include diffraction fades of 2 dB and 13 dB for the LH and LT, respectively, instead of relative to their "free space powers." This would have partially compensated for the larger and more sustained fading (relative to free space power) experienced by the LT link vis a vis the LH path during severe subrefractive events.

## 9. CALCULATIONS EMPLOYING MODELS AND REFRACTIVITIES

### 9.1 Propagation Model

Propagation calculations using hypothetical and measured refractivity profiles with large negative lapse rates of the refractivity (ducting condition) did not predict the severe fading calculated employing positive lapse rates (highly subrefractive). The model used is based on an approximation to the scalar Helmholtz wave equation which was solved using a numerical technique called the Fourier split-step algorithm. A theoretical description is given by Dockery (Ref 4), and Kuttler and Dockery (Ref 5), and the performance of the method is described by Dockery and Konstanzer (Ref 6). The inputs to the model are the two-dimensional refractivity structure and the electrical parameters of the radiating system, and its output is the power density field relative to free space power levels in the great circle plane containing the propagation paths.

### 9.2 Model Calculations for Extreme Subrefraction

Measurements of the refractivity environment along the LH and LT links were executed during one week in August 1989 within the experimental period. The refractivity levels were calculated from measurements of pressure, temperature, and humidity employing probes on a helicopter, where the specific procedures are described by Rowland and Babin (Ref 7), and the modeling results are given by Goldhirsh and Dockery (Ref 1). No strong subrefractive conditions or SDF events were observed during this period. Refractivity measurements in the vicinity of the PL-LH link were, however, made over water on November 16, 1988 (before the experimental period) when a strong subrefractive condition was present. The profile is given in Figure 19 and shows an increase of the refractivity with altitude up to about 75 m with an approximate height gradient of +180 N units per km. As a simulation example, this profile was assumed uniform along the LH propagation path and was injected into the above described propagation model. The resultant calculated fade profile at the LH distance is shown in Figure 20. We note that fades between 30-60 dB result in the height interval below 120 m, where fades approaching 60 dB may occur at the LH height (45.5 m); consistent with levels frequently observed during SDF events (Figures 13 - 16). The calculated fade levels in Figure 20 were noted to be significantly larger than the modeled fades caused by ducting events as given by Goldhirsh and Dockery (Ref 1). As another basis of comparison, we also show in Figure 20 the relative fading for the

case of a standard atmosphere (dashed curve), which corresponds to a refractivity gradient of approximately  $-39$  N units per km (Ref 9). We note an approximate 2 dB fade exists (earth diffraction) at the height of LH for this case.

#### 10. REAL TIME LINK CAPABILITIES

Capabilities have been developed for both receiving sites whereby they can be "called up" via the telephone system and calibrated receiver data may be passed in "real time" to a PC at the remote calling location. The transferred data are displayed on a monitor and the power levels (relative to free space power) are simultaneously printed out with any time scale desired. Typical displays span 0.5 hours with a two second running average of the data plotted at 0.5 second intervals. This capability is used routinely and has enabled a convenient check on the "health" of the system at any time of the day. It also provides a means to "sense" in real time the condition of propagation; namely, quiescent, super-refracting, subrefracting, or ducting. It also provides a real time measure of the inhomogeneity of atmospheric conditions since both sites may be simultaneously accessed (via different telephone lines).

#### 11. SUMMARY AND CONCLUSIONS

This experiment offers a unique data base of fade statistics for an over-water, line-of-sight geometry at 4.7 GHz which is particularly suitable for the Mid-Atlantic coastal regions of the United States. It is not known whether these statistics may be applied to other over-water regions. Analysis of the synoptic meteorology, calculations using measured refractivity profiles in a propagation model, and examination of case histories of time series of fades suggest that under similar atmospheric conditions and terminal geometries, the same propagation effects may exist over deep water, although the frequency of occurrence is unknown. The results covering one year of this investigation may be summarized as follows:

##### Yearly Fade Distributions

(1) The yearly median fade levels (relative to free space power) were 0.1 dB and 3.8 dB for the LH and LT links, respectively (Figure 4 and Table 3). When compared with "standard" diffractions of 2 dB and 13 dB, this result is indicative that "superrefractive conditions" predominated. The approximate 9 dB enhancement over standard conditions for the LT case was probably caused by persistent evaporation duct conditions as characterized during the "focused" experimental period in August 1989 (Ref 1).

(2) At 0.1% of the yearly operating time ( $\approx 7.6$  hours), the fades exceeded 49 dB and 54 dB for the LH and LT links, respectively. The yearly LT fades consistently exceeded LH over percentage ranges down to 0.1% of the year. The maximum difference was 10 dB at approximately 2% of the time (Figure 4). This result is consistent with the expected enhanced diffraction by the LT link relative to LH based on their relative geometries.

(3) Both the LH and LT distributions were skewed towards the larger fades at percentages smaller than 1%. This was due to sustained deep fading events (SDF) which are fades in excess of 20 dB which last two hours or more and are generally believed to be due to severe subrefractive conditions.

##### Monthly Fade Distributions

(1) The monthly median fades varied between +1.4 dB (June) and -1.4 dB (July) for LH; and between 0.5 dB (July) and 7.7 dB (December) for LT (Table 3).

(2) Considerable monthly variability in the fade distributions existed at the smaller percentages for both the LH and LT links (Figure 5 and 6 and Table 3). For example, the

0.1% fades ranged between 18.8 dB (September) and 54.2 dB (February) for LH and 16.8 dB (September) and 57.6 dB (February) for LT. (3) Both receiver locations showed five contiguous months (July - November) with minimal fades and the remaining seven month period with the largest fades (Figures 5 and 6 and Table 3). The weaker fades occurred during the summer and fall and the larger ones during the winter and spring.

(4) The distributions for the winter and spring months appear skewed in the direction of the higher fades due to significant SDF events (Figures 5 and 6).

##### Diurnal Variations

An examination of the fade distributions during four contiguous six hour time slots (0-6, 6-12, 12-18, and 18-24) showed no diurnal variations in fades for either the yearly (Figures 9 and 10) or monthly (Figures 11 and 12) time scales.

##### Sustained Deep Fades

(1) SDF events are believed to be generally caused by severe subrefractive conditions along the paths where the refractivity exhibits a positive lapse rate.

(2) Analysis of synoptic meteorological conditions and rawinsonde data during two distinct periods in which SDF events existed confirmed the condition of warm, moist air over colder ground and water giving rise to positive lapse rates of refractivity with altitude up to 130 m and 185 m from the surface.

(3) In a simulation example, a measured refractivity profile which exhibited a strong positive lapse rate was injected into a parabolic propagation model. The resultant fade-height profile at the LH location showed fades in the range 30 dB to 60 dB, consistent with high fading SDF events. Although the refractivity profile was measured outside the experimental period, it was obtained over water in the vicinity of the propagation paths indicating that refractivity profiles with large lapse rates are possible.

(4) Whenever a SDF event existed at the LH site, one also existed at the LT site. The SDF events at LT were consistently longer than those at LH (Figure 18). This result is consistent with the relative geometry of LT and LH such that significantly more diffraction is expected at LT (the lower height site) than at LH.

(5) There were 29 and 61 distinct events for the LH and LT links, respectively. The larger number of events at LT is consistent with the relative geometry and the enhanced diffraction losses during subrefraction propagation for LT.

(6) March exhibited the longest duration SDF event which lasted for 47.5 and 63.25 hours for the LH and LT links, respectively (Figures 14 and 18).

#### 12. ACKNOWLEDGEMENTS

The authors are grateful to Adam E. Bulharowski for the hardware design of the receiver and transmitter systems. Many thanks to James H. Meyer for his meteorological input to this paper. The authors are particularly grateful to John Rowland and Robert Miller for their assistance in the development of the data acquisition system and associated software. We enthusiastically thank Charles Etheridge for the development of the "real time" remote sensing capabilities and for his maintenance of the transmitter, receiver, and data acquisition systems. Last, but certainly not least, the authors are grateful to Norman E. Gebro who was the permanent APL liaison and assisted in directing operations from the NASA Goddard Space Facility at Wallops Island, Virginia. This work was supported under Navy Contract N00039-89-C-0001.

## 13. REFERENCES

1. Goldhirsh, J., and Dockery, G.D., "Propagation Measurements and Modeling at C Band for Over-the-Water, Line-of-Sight Propagation Links in the Mid-Atlantic Coast", *Radio Science*, 26, 3, May-June 1991, pp 671-690.
2. Meyer, J. H., "An Overview of the Weather and Reconstruction of Atmospheric Refractivity Profiles for the Over-Water DDS Fade Margin Experiment's Propagation Path off Wallops Island, Virginia During Fog Conditions, June 1988", *APL/JHU Technical Memorandum* STE-90-014, 13 March 1990.
3. Meyer, J. H., "Deep and Long Duration Fades Experienced by the Over-Water DDS Fade Margin Experimental Propagation Path off the Coast of Wallops Island, Virginia During the Week of 11 - 17 March 1990 and the Associated Meteorological and Propagation Conditions", *APL/JHU Technical Memorandum* STE-90-021, 9 April 1990.
4. Dockery, G. D., "Modeling Electromagnetic Wave Propagation in the Troposphere Using the Parabolic Equation", *IEEE Trans. Ant. Prop.*, 36, 10, 1988 pp 1464-1470.
5. Kuttler, J. R. and Dockery, G. D., "Theoretical Description of the Parabolic Approximation/Fourier Split-Step Method of Representing Electromagnetic Propagation in the Troposphere", *Radio Science*, 26, 2, March-April 1991, pp 381-393.
6. Dockery, G. D., and Konstanzer, G. C., "Recent Advances in Prediction of Tropospheric Propagation Using the Parabolic Equation", *APL/JHU Technical Digest*, 8, 4, 1987, pp 404-412.
7. Rowland, J. R., and Babin, S. M., "Fine-Scale Measurements of Microwave Refractivity Profiles with Helicopter and Low-Cost Rocket Probes", *APL/JHU Technical Digest*, 8, 4, 1987, pp 413-417.
8. Livingston, D. C., "The Physics of Microwave Propagation", Prentice Hall, NJ, USA, 1970. (Microwave and Field Series, Nathan Marcuvitz, Editor).
9. Bean, B. R., and Dutton, E. J., *Radio Meteorology*, Dover Publications, Inc., New York, USA, 1968.

Table 1: Geometric Parameters for the Lighthouse and Lookout Tower links (respectively).

Parameter	Value
Latitudes of PI, LH, LT	37°34'23", 37°54'42", 37°51'48"
Longitudes of PI, LH, LT	75°37'04", 75°21'24", 75°22'06"
Azimuth (CW Rel. to N: PI-LT), (deg)	34.1
Azimuth (CW Rel. to N: PI-LH), (deg)	31.3
Antenna Heights (PI, LH, LT), (m)	36.9, 45.5, 13.8
Link Distances (km)	44.1, 39.0
Distance Between LH and LT (km)	5.5
Reflection Point Distances from PI (km)	20.6, 24.5
Heights of Direct Ray Above Refl. Pt., (m)	12.5, 1.4

Table 2: Propagation Parameters for PI-LH and PI-LT Links (respectively) Assuming a 4/3 Earth Radius

Parameter	Value
Antenna Transmit Power at PI (dBm)	37.8
Gain of Transmit Antenna (dB)	25.0
Gains of Receiver Antennas (dB)	25.6
Nominal Gaseous Attenuations (dB)	0.26, 0.23
Trans. Ant. Gain Reduction in Dir. of PI-LT (dB)	2.5
Estimated Free Space Powers (dBm)	-50.7, -52.0
Diffraction Losses for Standard Propagation (dB)	2.0, 13.4
Standard Powers Received (dBm)	-52.7, -65.4
Multipath Grazing Angles (deg)	.0325, .0045
Reflection Coef. Magnitudes	1.0, 1.0
Reflection Coef. Phases (deg)	180, 180
Multipath Length Differences (deg)	39.6, 0.6

Table 3: Fades Exceeded for the Indicated Percentages Pertaining to the LH and LT Links for Different Months and Entire Year.

%	1989							1990					89-90
	J	J	A	S	O	N	D	J	F	M	A	M	
50 (LH)	1.4	-1.4	-1.0	-0.9	0.2	-0.3	1.2	0.3	1.3	1.3	0.6	0.2	0.1
50 (LT)	4.2	0.5	1.7	2.5	2.9	3.5	7.7	3.3	5.7	6.4	3.2	4.1	3.8
10 (LH)	20.2	4.7	3.3	3.6	7.3	8.2	5.4	18.4	26.9	16.4	7.1	10.9	9.3
10 (LT)	31.9	9.0	9.3	9.9	12.9	19.6	11.9	34.7	33.4	32.4	14.8	19.4	16.3
1.0 (LH)	39.4	14.6	14.1	12.1	17.3	16.0	37.7	42.6	47.2	44.0	23.1	30.0	37.2
1.0 (LT)	46.4	18.6	13.1	13.1	21.1	26.1	42.6	52.6	49.4	49.0	38.8	41.4	44.8
0.1 (LH)	49.4	23.9	22.7	18.8	25.4	26.6	50.7	51.4	54.2	51.3	39.8	42.1	49.4
0.1 (LT)	54.2	34.3	19.1	16.8	27.7	32.4	52.2	>60	57.6	54.2	50.1	52.4	54.1

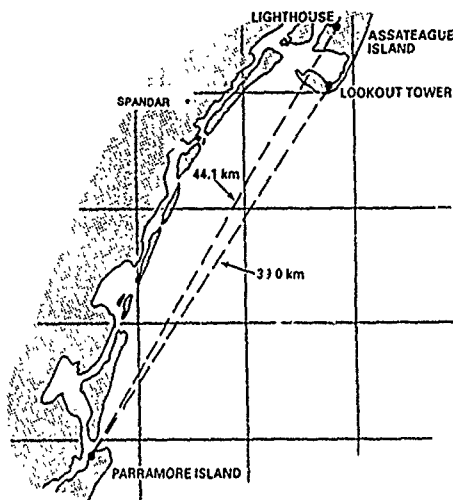


Figure 1: Map of Mid-Atlantic coast region of the United States depicting the location of the transmitter site at Parramore Island (PI) and the Lookout Tower (LT) and Lighthouse (LH) receiver sites at Assateague Island. The distance between grids is 10 km and the coordinate locations are given in Table 1.

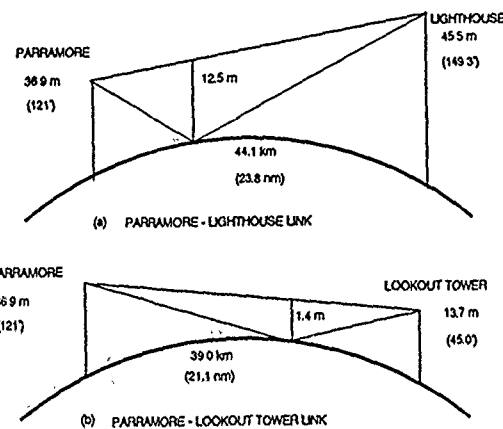


Figure 2: Vertical plane geometries for the Lighthouse and Lookout Tower links depicting terminal heights, line of sight rays, and reflection point geometry assuming "standard refraction."

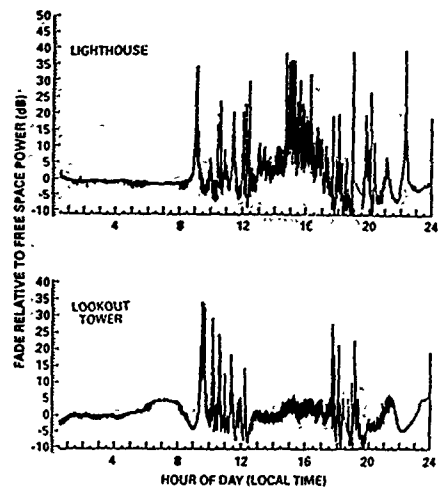


Figure 3: Time-series fade data for the Lighthouse and Lookout Tower links during August 22, 1989

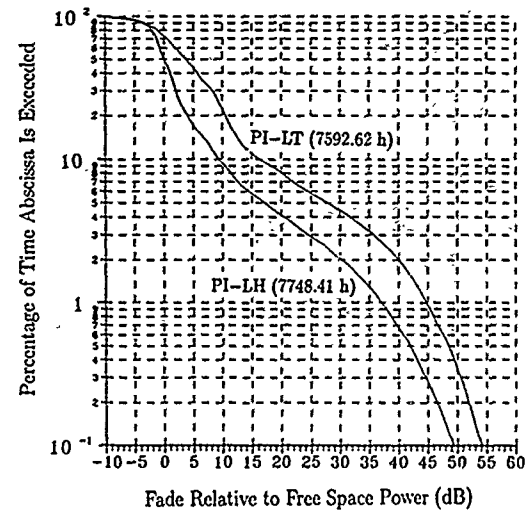


Figure 4: Cumulative fade distributions for the Parramore Island-Lighthouse and Parramore Island-Lookout Tower links over the year period June 1, 1989 through May 31, 1990.

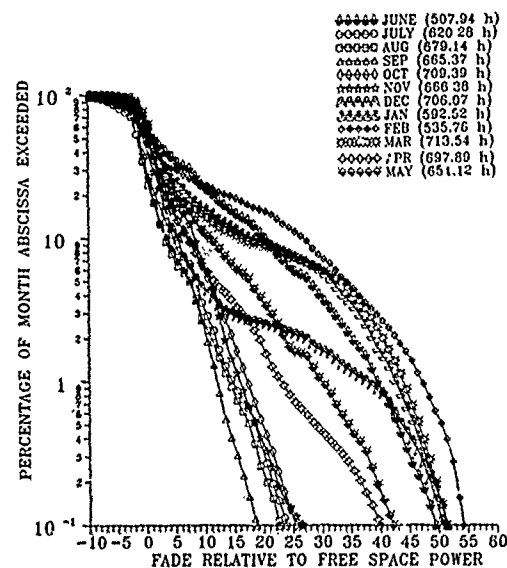


Figure 5: Monthly cumulative fade distributions for the Parramore Island-Lighthouse link for the year period June 1, 1989 through May 31, 1990. The monthly operating times are noted in the indicated legend.

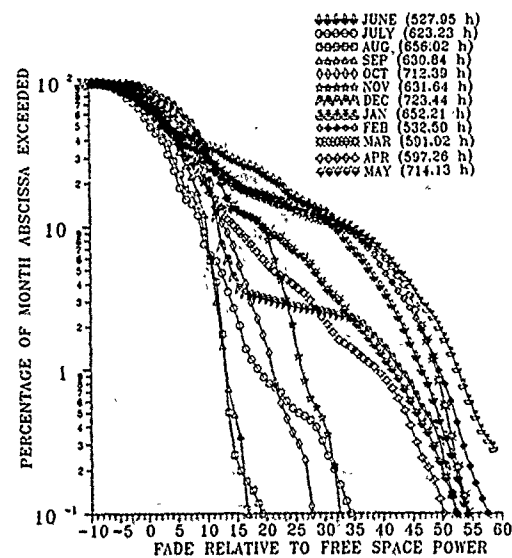


Figure 6: Monthly cumulative fade distributions for the Parramore Island-Lighthouse link for the year period June 1, 1989 through May 31, 1990.

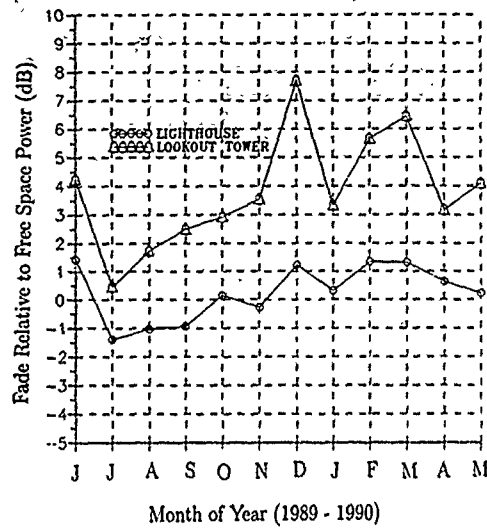


Figure 7: Fifty percentile fade levels for different months of the year for the LH and LT links.

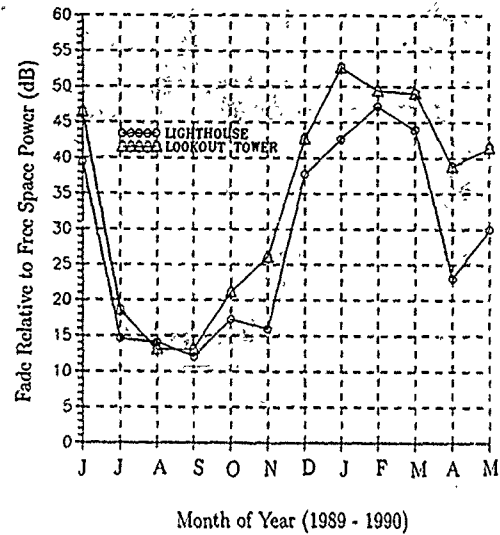


Figure 8: One percentile fade levels for different months of the year for the LH and LT links.

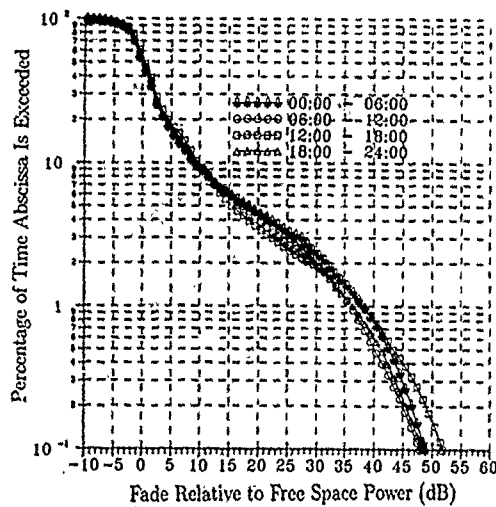


Figure 9: Cumulative fade distributions for the Lighthouse Link for four contiguous six hour time slots corresponding to the period June 1, 1989 through May 31, 1990.

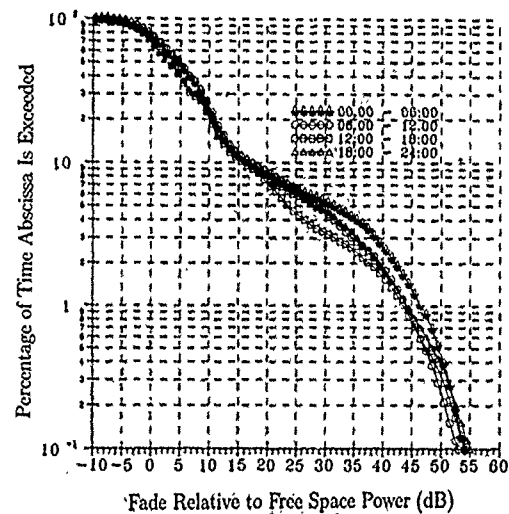


Figure 10: Cumulative fade distributions for the Lookout Tower link for four contiguous six hour time slots corresponding to the period June 1, 1989 through May 31, 1990.

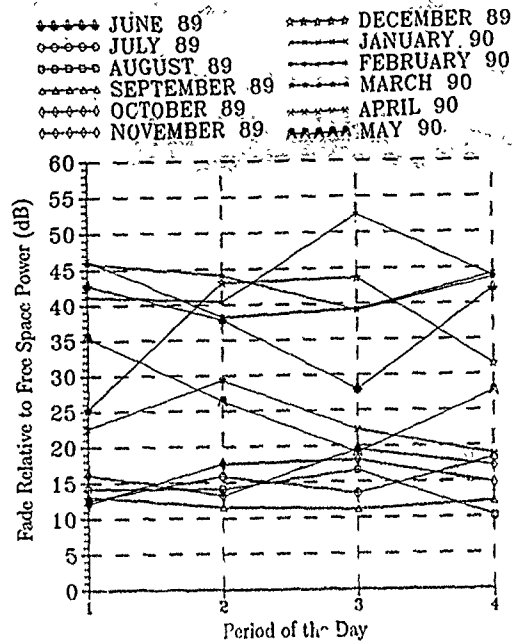


Figure 11: One percentile fades versus period of day for each month of the year for the Lighthouse link

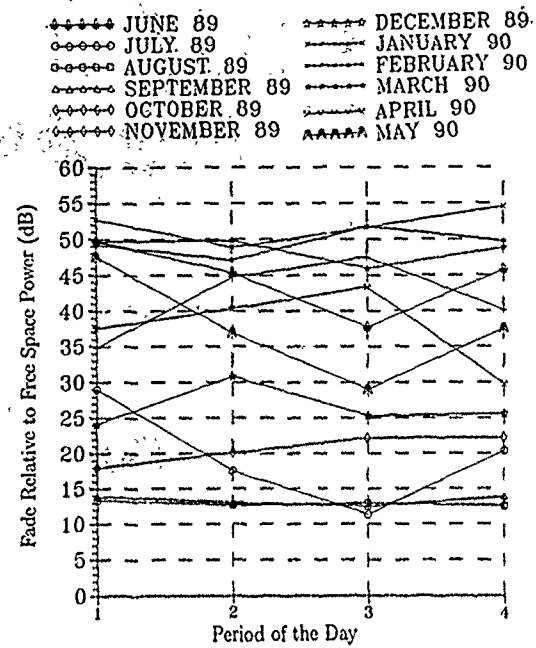


Figure 12: One percentile fades versus period of day for each month of the year for the Lookout Tower link

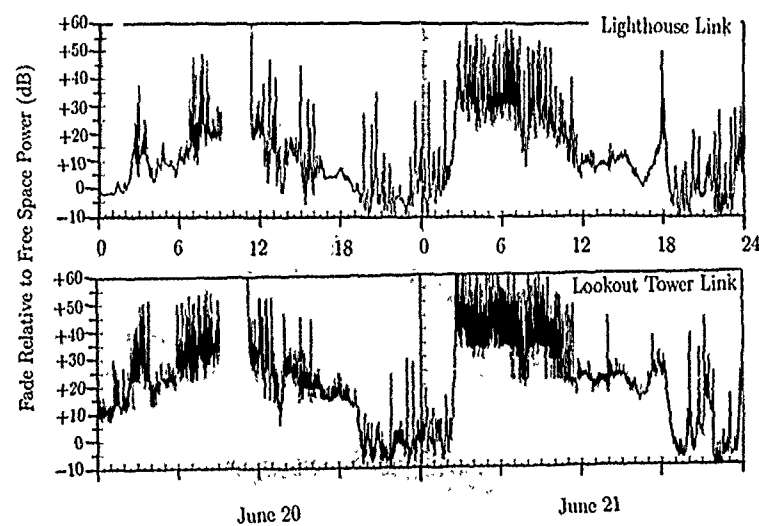


Figure 13: Sustained deep fade events occurring during the period June 20 - 21, 1989 for the Lighthouse and Lookout Tower Links

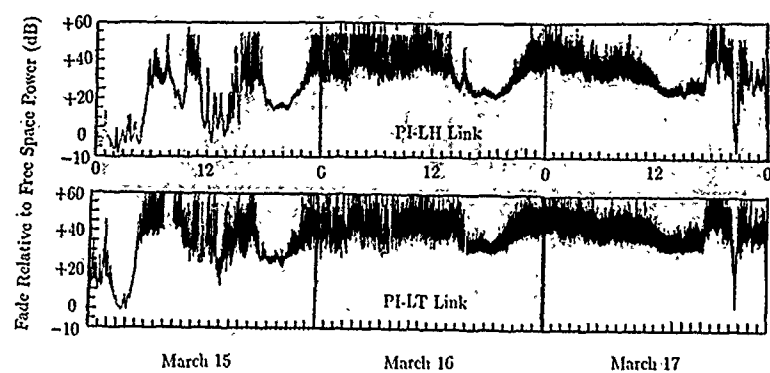


Figure 14: Sustained deep fade events occurring during the period March 15 - 17, 1990 for the Lighthouse and Lookout Tower Links

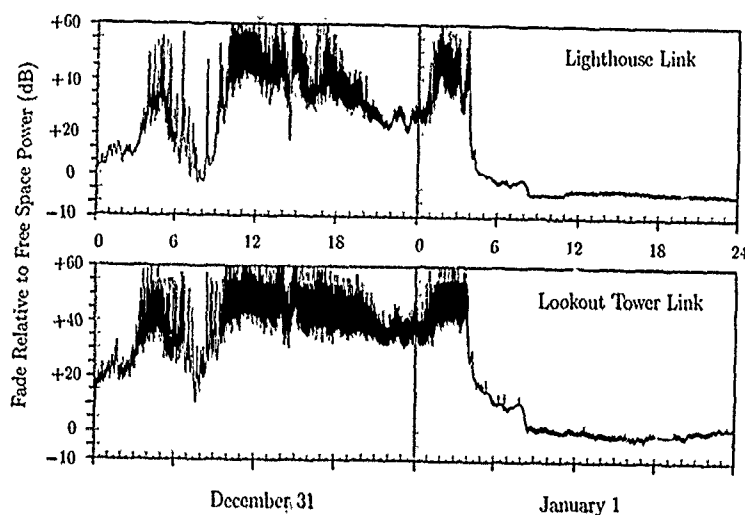


Figure 15: Sustained deep fade events occurring during the period December 31, 1989 - January 1, 1990 for the Lighthouse and Lookout Tower Links

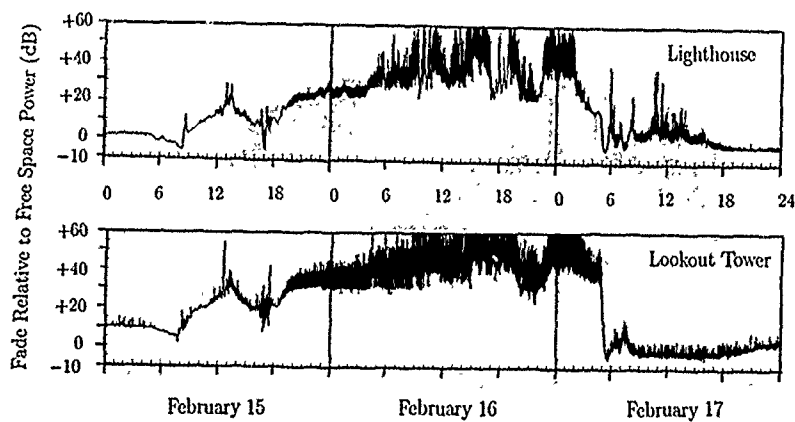


Figure 16: Sustained deep fade events occurring during the period February 15 - 17, 1990 for the Lighthouse and Lookout Tower Links

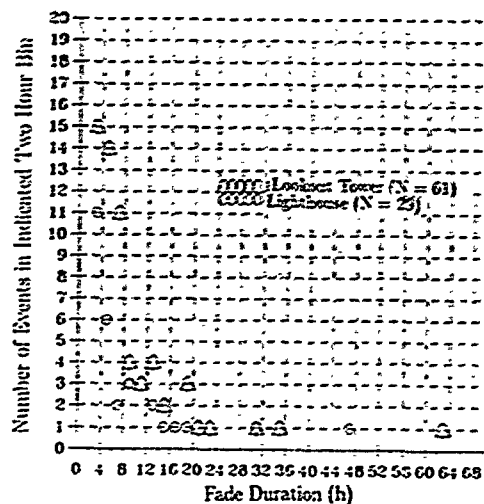


Figure 17: Histogram of number of SDF events having fade durations in given bins. Bins are defined by duration intervals 2-4 h, 4-6 h, 8-6 h, etc.

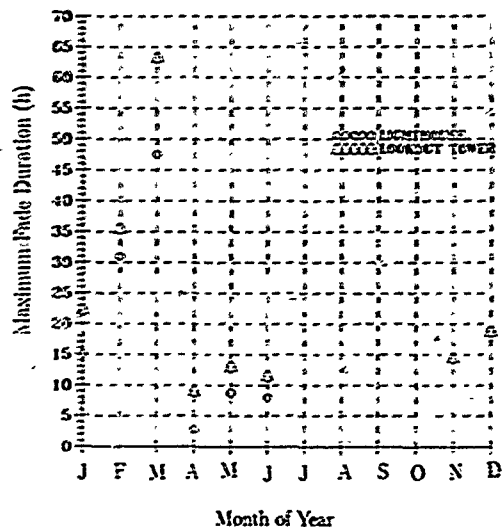


Figure 18: Maximum fade durations for the Lighthouse and Lookout Tower Links versus month of year.

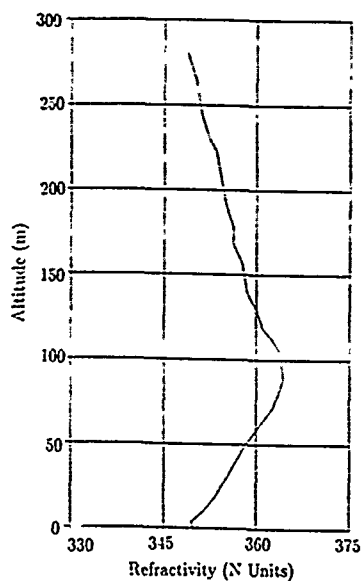


Figure 19: Refractivity profile measured over the water on November 16, 1988 (11:18-11:21 local time) in the vicinity of the propagation links resulting in extreme subrefractive propagation conditions.

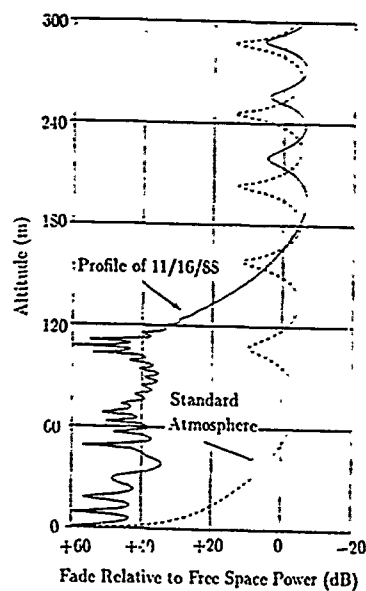


Figure 20: Modeled fade relative to free space power for subrefracting profile of Figure 19.

## DISCUSSION

### J. RICHTER

*In a line-of-sight propagation link you may have signal enhancements and fades for either sub- or super-refraction. A specific correlation to either of these conditions based on signal level changes is difficult.*

### AUTHOR'S REPLY

*During the week of August 12, 1989, refractivity profiles were measured along the propagation path. It was observed that refractivity profiles were such that both surface and elevated ducts existed. [See paper by Goldhirsh and Dockery, Radio Science, May-June 1991, pp 671-690]. The fade time series measurements during this week showed both signal fading and enhancement. We did not see fades which exceeded 20 dB for periods of two hours or more. These sustained deep fades were however observed on June 21, 1989 and March 16, 1990. The Lighthouse link showed 5 hour duration fading of greater than 20 dB for June and 47 hours for March 1991. Both of these long term fades did correlate exactly with positive refractive index slopes measured at the NASA Wallops Flight Facility, Wallops Island, Virginia which is a coastal location near the links. These long duration fades also correlated very well with weather reports showing a temperature inversion and the advection of moist warm air at altitude over cold water. Such conditions may give rise to an increase of the refractive index with altitude consistent with the rawinsonde measurements.*

### B. REINISCH

*You referred twice, first on your second slide and then in your third to the last slide, to "real-time sensing of the environment". I am puzzled, since the "sensing" is always done when it is done, i.e., in real time.*

### AUTHOR'S REPLY

*I should have said "real time sensing of the environment at remote locations". Through telephone call-up procedures we transferred the fade-versus-time series measurements to remote locations. We are able to display the fade-versus-time on a PC and at the same time obtain a simultaneous hard copy. Hence, if we wish to sense the propagation environment at the mid-Atlantic coast links at a remote location such as in Turkey, we may do so through telephone call-up procedures. We have used such procedures for a number of propagation field tests in the vicinity of Wallops Island, Virginia.*

### R. BENSON

*In the ionosphere and magnetosphere, wave ducting refers to propagation along field-aligned electron density irregularities. Ducted propagation, depending on wave mode, occurs in either field-aligned enhancements or depletions in electron density. Please explain what you mean by wave ducting in the present work.*

### AUTHOR'S REPLY

*A simple surface duct may occur when the refractivity close to the earth is such that  $dn/dh < -157$  N-Units per kilometer. Rays launched horizontally will bend concave downward, reflect from the earth, bend concave downwards after reflection and reach the height of launch pointing horizontally. This cycle will repeat itself in the direction of the receiver. Such a ray is "trapped" and said to be in a "surface duct".*

### D. THOMSON

*It is likely that the air-water temperature difference along with depth of the refractive index inversion are the critical factors in determining the fading depth and variability. Do you attempt to reconstruct this information, e.g., using data which might be available from Wallops Island or did you attempt to conditionally sample your database on the basis of the air-sea temperature difference?*

### AUTHOR'S REPLY

*Air-sea temperature differences were not routinely measured except during the week of August 21, 1989. These measurements were used to calculate evaporation duct properties which were combined with helicopter measurements of the refractivity structure to give modeled fade structures. The events we are talking about occurred when the water was cold and moist warm air advected over it. This causes a temperature inversion and at the same time moisture at altitude. On June 21, 1989 and March 16, 1990, temperature inversions were in fact observed along with measured positive increases of refractivity with altitude (+ 23 N-Units/km for June 21 up to 130m and + 43 N-Units/km for March 16 up to 185m). Although these slopes were measured at nearby coastal locations at Wallops Island Virginia they are expected to be even larger over the colder water. Such refractive slopes give rise to severe subrefraction and strong fading. Both of these weather related conditions lasted a few days.*

## REMOTE SENSING OF THE EVAPORATION DUCT USING AN X-BAND RADAR

Kenneth D. Anderson  
Ocean and Atmospheric Sciences Division  
Naval Ocean Systems Center  
San Diego, CA 92152-5000 USA

### SUMMARY

Results from a unique analytical and measurement effort to assess low-altitude, short-range radar detection capabilities in an evaporation ducting environment are presented. Although the measurement effort is ongoing, current results for unstable conditions validate propagation model predictions of reduced radar detection ranges within the radio horizon. In addition, discrepancies between measured and predicted radar data demand a close examination of both meteorological data and surface layer theory. At ranges near and beyond the horizon, radar detection capabilities crucially depend both on the surface layer refractivity profile and on the refractivity profile determined from upper-air observations. An empirical model to merge the surface layer with the mixed layer is discussed. Other discrepancies, which are thought to be caused either by inadequate surface layer modeling (perhaps the moisture stability function) or by inadequate surface layer meteorological measurements, suggest the need for an improved surface layer model.

Remote sensing of the evaporation duct by radar measurements is not a viable tactical tool. However, the combination of direct surface and upper-air meteorological measurements with remotely sensed radar measurements and with advanced numerical modeling capabilities does provide valuable insight for a better understanding of the atmospheric surface layer and its effects on low-altitude short-range radar detection.

### 1. INTRODUCTION

In recent years, instances have been noted where maximum radar detection ranges of low-altitude targets over the ocean is less than expected. These instances of reduced detection ranges are associated with surface-based atmospheric ducting, particularly with evaporation ducting. Effects from these ducts are normally considered to be a long-range phenomena, but an analysis by Dockery of Johns Hopkins University Applied Physics Laboratory (JHU/APL) clearly shows reduced detection capabilities for common duct heights, frequencies, and ranges. In addition to the well-known signal enhancement at ranges near and beyond the radio horizon, his modeling indicates that the evaporation duct affects radar detection of small-sized, low-altitude targets within the horizon in two ways: First, it can shift the location of the last optical interference null several kilometers in range, which can cause nondetection at ranges where detection is expected. Second, it can substantially decrease signal levels near the last optical interference peak, which may explain the instances of greatly reduced detection ranges.

An ongoing analytical and measurement effort to assess low-altitude, short-range propagation effects at X-band has validated Dockery's modeling. The propagation model used in this analysis is an atmospheric surface layer model [1,2] and a radio propagation model known as Radio-Physical Optics (RPO) [3]. All three features predicted by the model (enhanced signal beyond the horizon, range shifted null locations, and reduced signal at the last interference peak) have been observed in a carefully controlled radar experiment. Although the essential features are observed in the radar data, discrepancies between the predicted and measured data warrant a closer examination of the meteorological measurements and surface

layer theory. New techniques for describing the evaporation ducting environment are discussed. These techniques reduce the discrepancies between the predicted and measured radar data, and they provide valuable insight into the problems associated with measurement of surface meteorological conditions.

### 2. MEASUREMENT PROGRAM

A measurement program to validate the predicted propagation effects was started in June of 1989. To represent typical shipboard radars, an X-band radar, operating at a frequency of 9.415 GHz, was placed on a site at the Naval Ocean Systems Center (NOSC) 23.5 m above mean sea level (msl). At this site (called the F35 site) azimuths from 180 to 340 degrees provide an unobstructed view of the ocean. Winds are generally from the northwest, which implies that the local conditions are representative of the sea and not the land. Air temperature, relative humidity, wind speed, and direction sensors are mounted approximately 22 m above msl. Sea surface temperature is monitored with two infrared temperature transducers pointed toward the surface at zenith angles of approximately 60 and 75 degrees. The infrared spots are in the surf zone and are not considered representative of the sea temperature at ranges beyond 1 km or so; their primary purpose is to check the consistency of other data. A small boat has been specially adapted to carry two lightweight corner reflectors of 30 dBsm cross-section, one facing aft and one facing forward. Both are mounted 4.9 m above the surface of the ocean. Horizontal and vertical beamwidths of the corner reflectors are approximately 40 degrees, which allows considerable motion of the boat without affecting the cross-section seen by the radar. Temperature, humidity, wind speed, and direction sensors are mounted on the boat 2.5 m above the surface. Two temperature probes are mounted at the stern of the boat to monitor sea temperature. All meteorological sensors are monitored by computers that sample the data every 10 seconds and calculate an average value for every minute. Upper-air conditions are measured using Vaisala radiosondes launched either from the boat or from the shore site (F35). Data from the radiosondes are recorded on computer.

In a typical measurement, the boat is positioned 2 to 3 km seaward from the radar, where the crew makes a measurement of the surface meteorological conditions with a set of sensors independent of those monitored by the computer. The crew may also launch a radiosonde for upper-air analysis. After these measurements are complete, the boat proceeds on a radial from the radar in a seaward direction to a range of about 25 km. During this run, communication between radar site personnel and boat crew is maintained either on a VHF or on a UHF link to provide course corrections. So far, little or no course correction has been needed. At the maximum range, the crew makes another measurement of the meteorological conditions. For its inbound run, the boat returns on a radial to the starting point. If interesting results or measurement problems arise from the first two runs, the boat may repeat both the outbound and the inbound run, making any additional surface or upper-air measurements. At the F35 site on shore, additional surface meteorological measurements are made by hand every half hour or so, depending on conditions.

### 3. MEASUREMENT RESULTS

The first trial runs were made on 3 October 1990 and, after minor adjustments to the hardware and software, the first data were taken on 11 October 1990. A total of 37 runs (a run is either an inbound or an outbound movement of the boat) have been made so far on 12 separate days. Of these 12 days or cases, 4 are during thermally stable atmospheric conditions in which surface trapping layers, caused by air mass subsidence or advection, dominate the propagation. To limit the scope of this paper, only unstable cases are considered. For the eight unstable cases, Table 1 lists the median wind direction, wind speed, air temperature, sea temperature, and relative humidity, measured both at the F35 site and at the boat. In addition, the table lists the median modified refractivity ( $M$ ) gradient in the lowest layer, which is determined from upper-air observations. Also listed are the duct height and the gradient form of the Monin and Obukhov scaling length ( $\ell$ ). Both quantities are calculated for the F35 and for the boat meteorology. A third duct height is listed that is the result of a surface layer model, which will be explained later.

For the first four cases listed in Table 1, agreement between the propagation model results and the measured data is remarkably good when the surface layer refractivity profile is generated from the F35 site meteorological measurements using the theory developed by Jeske [1,2]. For example, Figure 1 shows the one-way propagation loss (the ratio of transmitted to received power) measured from the radar to a corner reflector as the boat made two runs on 11 October 1990. The solid line labeled "Std" corresponds to the propagation loss expected in a standard atmosphere, where the modified refractivity increases with increasing height at a constant rate of 118 M/km. The dashed line represents the propagation loss expected in free space. A comparison of the radar data to the standard atmosphere prediction shows that the last optical interference null is shifted a kilometer or so outward in range, and signal strength at the last optical peak (at about 10 km) is reduced by about 3 dB. These data were measured over 51 minutes (1041 to 1132 local time). Bulk measurements at the F35 site during the same time show wind speed of 6.2 knots, air temperature of 19.35 C, relative humidity of 88%, and a sea temperature of 19.95 C, which are used to generate the  $M$  profile [2]. The third curve on Figure 1 is the propagation loss calculated for this  $M$  profile. The agreement between the prediction and the measurements is excellent out to a range of 12 km; the measured null shift and signal reduction are nearly identical to the model results. Beyond 12 km, however, the predicted rate of signal falloff is less than measured. At 18 km, the predicted loss underestimates observed loss (overestimates signal strength) by about 3 dB.

#### 3.1 Ranges Beyond the Last Optical Peak

If the refractivity profile is calculated from the surface layer model for altitudes to 150 m, RPO predictions for the first four cases listed in Table 1 agree with the observed radar data for ranges about half way to the horizon (the horizon is approximately 29 km). At ranges near and beyond the horizon, RPO predictions underestimate the observed loss. For these ranges, the signal strength is dependent on both the surface layer and the upper-air  $M$  profiles.

Figure 2 shows the surface layer  $M$  profile and the measured upper-air  $M$  profile for 13 February 1991. At an altitude of about 45 m, the surface layer profile coincides with the upper-air profile, which suggests that the surface and upper-air measurements are consistent. However,  $L'$  from the median bulk measurements is between -2.7 and -4.9 m, so the mixed layer should therefore dominate at altitudes just above a few meters. For all eight cases, better comparisons to the measured radar data at ranges beyond the last optical peak are found when the surface layer height is limited to the duct height and the mixing layer represented by the upper-air measurements. For the first four cases, the stability length, as measured at the F35 site, is less than the duct height, so limiting the surface layer to the duct height is justifiable. For the last four cases, the stability length is comparable to the duct height, so again,

placing the mixed layer at the duct height appears to be reasonable. The term "limited surface layer" will be used to refer to the model where the surface layer is empirically limited in vertical extent to the altitude of the duct height.

Figure 3 compares the radar data taken on 13 February to RPO results predicted using both the limited surface layer and the unlimited surface layer model. For the unlimited surface layer, the predicted loss curve is close to the measured data for ranges less than about 12 km; Beyond this range, the loss gradient is clearly different from the observed. For the limited surface layer, the predicted loss curve is a better match to the radar data. This technique of limiting the surface layer to the duct height is empirical and may need refinement. However, this limited surface layer model is consistent with the assumption that theory is applicable only to altitudes much less than the base of the inversion. It is believed that a better model can be developed as more radar and meteorological data are acquired. However, the comparisons to measured data illustrate the crucial role both of the surface layer and of the upper-air meteorological characteristics in propagation modeling.

#### 3.2 Ranges Less Than the Last Peak

Results of propagation modeling for the last four cases listed in Table 1 do not agree with the measured radar data for ranges less than and near the last optical peak. The stability length,  $L'$ , at the F35 site, is greater than the duct height, which implies that the surface layer extends to at least the duct height. Figure 4 shows the radar data from 20 November 1990. The curve labeled "F-Profile" is the calculated loss using the meteorology at F35. The curve labeled "B-Profile" is the calculated loss using the meteorology from the boat. Both predictions differ from the measured data for ranges less than about 14 km and both incorporate the limited surface layer model. However, for ranges in excess of 14 km, the F35 profile overestimates the loss by only 3 dB or so. It is apparent that the surface layer should be lower in altitude so the RPO predictions match the radar data at ranges less than 14 km.

The consistency of the meteorological data, shown in Figure 5, gives no indication of strong range dependency for ranges less than 14 km. One technique, termed "K-Profile", reduces the surface layer height using the same meteorological data and surface layer theory. The K-Profile procedure is (1) calculate the temperature profile between the boat and F35 (horizontal homogeneity is implied) using  $L'$  as measured on the boat, and (2) calculate the  $M$  profile with the supposition that it follows the temperature profile by assuming that the relative humidity is constant in the surface layer. Postulating that the relative humidity is constant appears reasonable because the median relative humidities measured both at the boat and at the F35 site (for all eight cases) are within 5% of each other, which is within the bounds of measurement error. The duct heights with the heading of K-Profile in Table 1 are calculated using constant humidity in the surface layer.

In Figure 4, the loss curve labeled "K-Profile" is the result of assuming constant relative humidity in the surface layer. This curve is a good approximation to the measured data for ranges less than 18 km, but the rate of signal falloff at longer ranges overestimates the observed. At shorter ranges, comparisons to observed data are qualitatively better when the K-Profile technique is applied to the last four cases listed in Table 1. For the 30 January 1991 case, the K-Profile and the Jeske formalism generate comparable results. However, for the first three cases in Table 1, the Jeske formalism yields a better comparison to measured radar data.

Although the K-Profile model does improve the comparisons of predicted to observed radar data in at least half of the cases, the assumptions are nettlesome. One of the least understood aspects of surface layer modeling is the shape of the moisture profile (stability function). Although stability functions for temperature and wind speed have been studied by numerous investigators [4] and are well known, data describing the moisture profile over the sea are not readily available. Typical-

ly, the moisture stability function is assumed to follow either the heat or the momentum function. In the Jeske formalism, moisture is assumed to follow the momentum. Additional comparisons to radar data were made using a modified Jeske formalism where moisture follows heat, but these comparisons showed no significant improvement in matching the radar data. A surface layer model following the formalism described by Liu, Katsaros, and Businger (LKB model) [5], was used to create  $M$  profiles for input to RPO. In the LKB model,  $L'$  is comparable to the  $L'$  calculated using the Jeske formalism.  $M$  profiles using both moisture following heat and moisture following momentum generated comparisons (to radar data) similar to those generated by the Jeske formalism. Another propagation model, Craig and Levy's PCPEM [6,7], which uses a surface layer model developed by Battaglia [8], was used to develop a set of comparisons to the radar data. Median meteorological values for several cases in Table 1 were used as inputs to PCPEM and the resulting loss curves are nearly identical to the loss curves obtained using the Jeske model with RPO. Clearly, additional radar and meteorological studies are needed to resolve the modeling discrepancies, particularly in conditions of low wind speed and low humidity as well as in conditions of high wind speed and high humidity.

### 3.3 Horizontal Homogeneity

One of the assumptions necessary for the K-Profile surface layer model is horizontal homogeneity, which is a subject of intense debate and is critical to the practical application of an operational propagation model. The radar data examined here (on the scale of tens of kilometers) appears to be homogeneous. Over periods of approximately one to two hours, as illustrated by Figures 1, 4, and 5, the consistency between the outbound and inbound radar measurements is remarkable, which suggests at least temporal, if not spatial, homogeneity. For seven of the eight cases, the outbound run and the inbound run overlay each other to within 5 dB of propagation loss--the exception is the data taken on 20 November 1990 for which only one run is valid (equipment problems do not allow the use of the other runs on this day.) The greatest difference between runs was observed on 30 January 1991, shown in Figure 6. The meteorology for this case (Figure 7) clearly shows large fluctuations in both wind speed and humidity. However, as shown in Figure 6, RPO loss curves derived from both the Jeske and from the K-Profile surface models (using the median meteorological data at F35) respectively agree with the observed radar data. Even though the meteorology may fluctuate, indicating atmospheric inhomogeneity, the aggregate radio data do not, which lends credence to the assumption of homogeneity in the propagation of radio frequency signals.

To further strengthen the case for homogeneity in the propagation of radio frequency signals, data measured by JHU/APL [9,10] on 9 October 1986 at Wallops Island, Virginia, are reproduced in Figure 8. In this experiment, a beacon was mounted in an aircraft and tracked by a 5.6 GHz radar located 27 m above msl. The aircraft was flown over water towards the radar at a constant altitude of 31 m. The first run was made between 0835 and 0850 local time and the last run was made between 1105 and 1121 local time--approximately 3 hours separation in time, yet the 5.6 GHz radio data are remarkably consistent. The enhanced signal, indicative of surface ducting, is preserved over this time interval for ranges beyond about 37 km (20 nmi on the plot). Only minor differences between the two runs are observed at ranges less than 27 km (15 nmi). This radio data clearly shows both horizontal and temporal homogeneity in the larger sense--a surface duct at 0835 is still a surface duct 3 hours later. A standard atmosphere curve and two prediction curves (based on the observed meteorology) are supplied by JHU/APL. A fifth curve was calculated by NOSC using the Engineer's Refractive Effects Prediction System (EREPS) [11] program with a duct height determined from a climatology of ducting [12,13] for the month of October in the Wallops Island area. Both JHU/APL predictions and the EREPS prediction reasonably match the observed data. The ability to use climatological data and achieve this good agreement suggests that temporal and

horizontal homogeneity for radio propagation purposes may be the rule and not the exception.

### 4. CONCLUSIONS

The evaporation duct significantly affects X-band radar detection capabilities of low-altitude targets at all ranges. Within the horizon, the duct may shift the location of the last interference null several kilometers in range, which may cause nondetection at ranges where detection is expected and detection at ranges where detection is not expected. In addition, the evaporation duct may reduce the signal strength at ranges near the last interference peak so that detection of low-altitude targets may not be possible until the target is much closer. These effects have been observed in a carefully controlled radar experiment.

At ranges beyond the last optical peak, the radar signal strength depends both on the surface layer and on the mixed layer. To accurately model propagation in this region, knowledge of both surface layer and upper-air meteorology is required. An empirical model to merge the surface layer with the mixed layer has been developed. However, additional studies and measurements are needed to refine this model.

A new surface layer model has been developed to account for discrepancies between the observed radar data and the propagation model. However, it does not explain all discrepancies and even fails where classical surface layer theory is successful. Further studies of the surface layer, particularly the moisture profile, are needed to develop a reliable propagation model.

Horizontal homogeneity has been examined from a radio point of view. In eight days of measurements, with wind speeds from 3 to 10 knots, horizontal homogeneity in the radio data, not necessarily in the meteorology, appears to dominate. Range dependency in the signals, although not fully explored, seems to be a minor effect because the predictions derived from the meteorology at a single site account for a substantial portion of the observations.

Remote sensing of the environment using an X-band radar in conjunction with modern numerical modeling capabilities has proven to be a valuable tool in the understanding and utilization of tropospheric propagation.

### ACKNOWLEDGEMENT

This work was supported by the Office of Naval Technology.

### REFERENCES

1. Jeske, H., "State and Limits of Prediction Methods of Radar Wave Propagation Conditions Over Sea," Modern Topics in Microwave Propagation and Air-Sea Interaction, A. Zanca, ed., Reidel Pub., 1973.
2. Paulus, R.A., "Specification for Environmental Measurements to Assess Radar Sensors," Naval Ocean Systems Center (NOSC) Tech. Doc. 1685, November 1989.
3. Hitney, H.V., "Remote sensing of refractivity structure by direct radio measurements at UHF," 49th AGARD-EPP Symposium, 30 Sep.-04 Oct. 1991, Paper 1.
4. Panofsky, H.A., and J.A. Dutton, "Atmospheric Turbulence," John Wiley & Sons, NY, 1983.
5. Liu, W.T., and T.V. Blanc, "The Liu, Katsaros, and Businger (1979) Bulk Atmospheric Flux Computational Iteration Program in FORTRAN and BASIC," Naval

- Research Laboratory (NRL) Memorandum Rep. 5291; May 8, 1984.
- 6. -, "PCPEM User Guide," Signal Science Limited, 19 Curtis Avenue, Abingdon, OX14 3TT, UK.
- 7. Craig, K.H., and M.F. Levy, "A Forecasting System Using the Parabolic Equation - Application to Surface-to-Air Propagation in the Presence of Elevated Layers," AGARD CP 453, 15-19 May 1989, Paper 18.
- 8. Battaglia, M.R., "Modelling the Radar Evaporative Duct," RAN Research Laboratory, Tech Note No. 3/85, 1985.
- 9. Dockery, G.D., "Description and Validation of the Electromagnetic Parabolic Equation Propagation Model (EMPE)," The Johns Hopkins University/Applied Physics Laboratory, FS-87-152, September 1987.
- 10. Dockery, G.D., and E.R. Thews, "The Parabolic Equation Approach to Predicting Tropospheric Effects in Operational Environments," AGARD CP 453, 15-19 May 1989, Paper 20.
- 11. Patterson, W.L., et al, "Engineer's Refractive Effects Prediction System (EREPS) Revision 2.0," NOSC Tech. Doc. 1342, Revision 2.0, February 1990.
- 12. Patterson, W.L., "Historical Electromagnetic Propagation Condition Database Description," NOSC Tech. Doc. 1149, May 1987.
- 13. Anderson, K.D., "Worldwide Distributions of Shipboard Surface Meteorological Observations for EM Propagation Analysis," NOSC Tech. Doc. 1150, September 1987.

	11 Oct 1990	13 Feb 1991	30 Apr 1991	30 Jan 1991	20 Nov 1990	6 Mar 1991	11 Mar 1991	14 Mar 1991
Wind Dir (deg)	172.	334.	210.	333.	285.	303.	318.	302
Speed (knt) F35 Boat	4.5 3.3	3.9 2.8	4.9 4.4	4.5 4.6	8.4 9.4	7.4 8.7	9.9 10.0	6.9 9.1
Air Temp (C) F35 Boat	19.5 20.4	12.9 14.0	15.0 16.0	14.2 15.3	16.9 17.9	14.4 15.7	13.2 14.3	13.1 14.5
Sea Temp (C) Boat	21.0	15.5	17.4	15.5	18.0	15.4	15.4	15.1
RelHumid (%) F35 Boat	84. 82.	87. 82.	82. 78.	61. 61.	72. 69.	68. 63.	59. 61.	58. 57.
Upper-air M Grad. (M/km)	127.	133.	128.	161.	115.	124.	128.	128.
F35 Duct Height(m)	7.4	5.0	6.8	9.8	11.9	11.1	13.0	11.3
F35 L' (m)	-6.7	-2.7	-4.8	-7.6	-33.0	-27.5	-22.2	-11.8
Boat Duct Height(m)	8.5	5.7	7.8	14.5	18.5	40+	14.5	14.5
Boat L' (m)	-17.2	-4.9	-8.5	-64.3	-584.7	+177.8	-53.6	-45.4
K-Profile Duct Ht (m)	9.1	7.8	7.7	5.9	7.6	7.7	5.3	6.3

**Table 1.** Surface and upper-air meteorology for the eight cases where the atmosphere was thermally unstable.

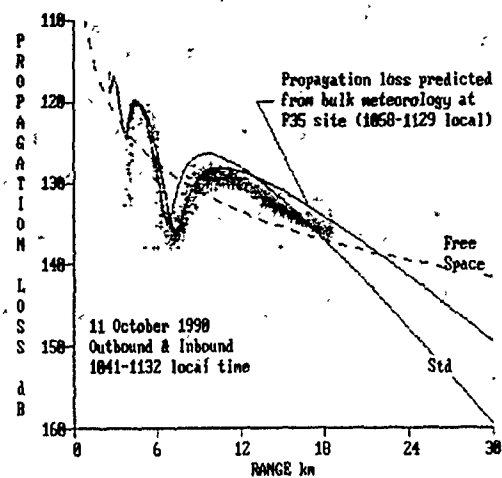


Figure 1. Radar measurements (Grey crosses) made on 11 October 1990. The curve labeled "Std" corresponds to the expected propagation loss in a normal or standard atmosphere (4/3 earth). Propagation loss predicted from the bulk meteorology at the F35 site reasonably matches the measurements out to a range of 12 km.

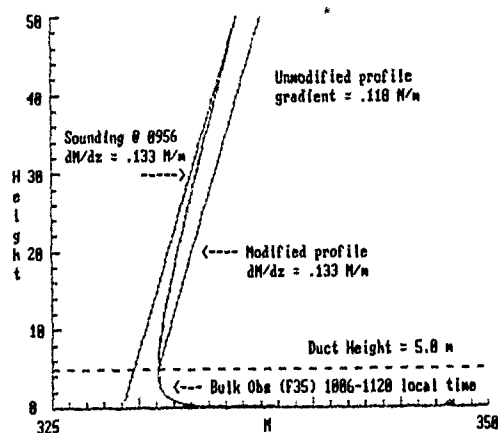


Figure 2. Modified refractivity profiles for 13 February 1991. The evaporation duct profile is calculated using the Jeske formalism from the bulk measurements made at the F35 site.

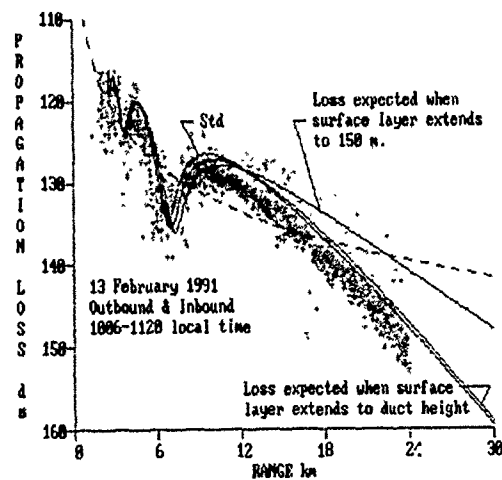


Figure 3. Radar measurements (Grey crosses) made on 13 February 1991 compared to predicted propagation loss for a standard atmosphere, the unmodified Jeske profile from Figure 2, and the modified (surface layer limited to 5 m) Jeske profile from Figure 2.

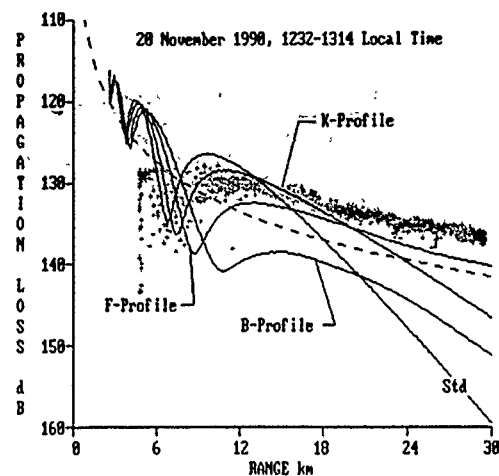


Figure 4: Radar measurements (Grey crosses) made on 20 November 1990 compared to predictions for (1) a standard atmosphere; (2) limited surface layer profiles calculated from bulk measurements at both F35 ("F-Profile") and the boat ("B-Profile"); and (3) the K-Profile technique.

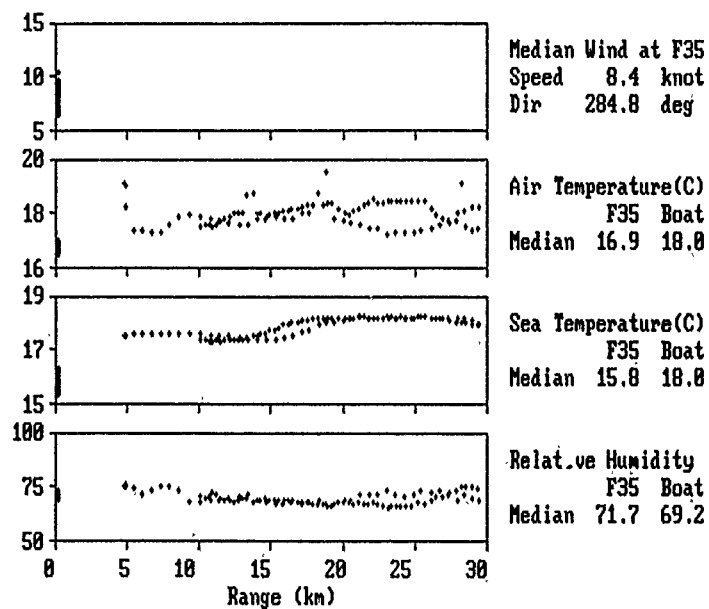


Figure 5: Surface meteorology measured on 20 November 1990 between 1124 to 1314 local time. Crosses indicate one-minute average of data. Median value at both F35 and boat are listed on the right side of the plot.

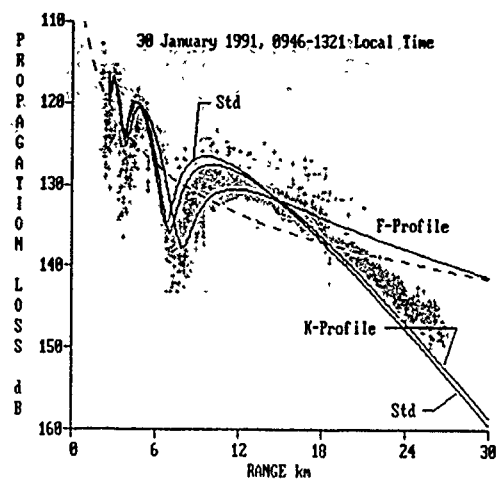


Figure 6. Radar measurements (Grey crosses) made on 30 January 1991 compared to predictions for (1) a standard atmosphere; (2) a limited surface layer profile calculated from bulk measurements at F35; and (3) the K-Profile technique.

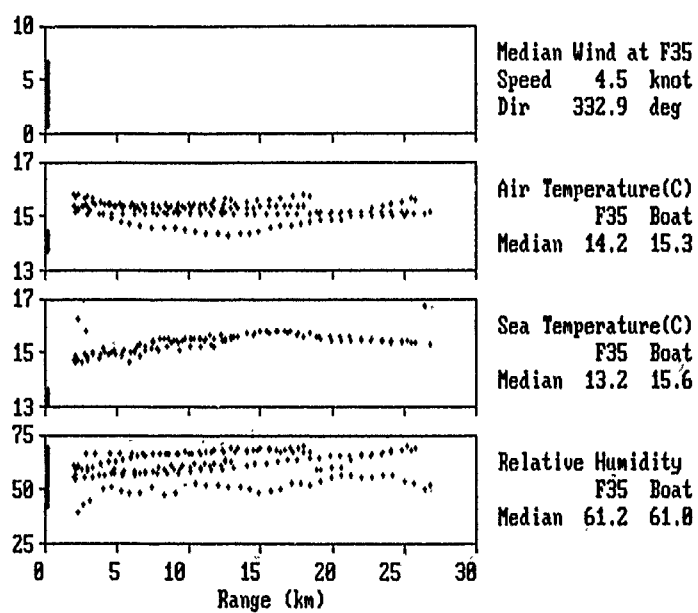


Figure 7. Surface meteorology measured on 30 January 1991 between 0946 to 1332 local time. Crosses indicate one-minute average of data. Median value at both F35 and boat are listed on the right side of the plot.

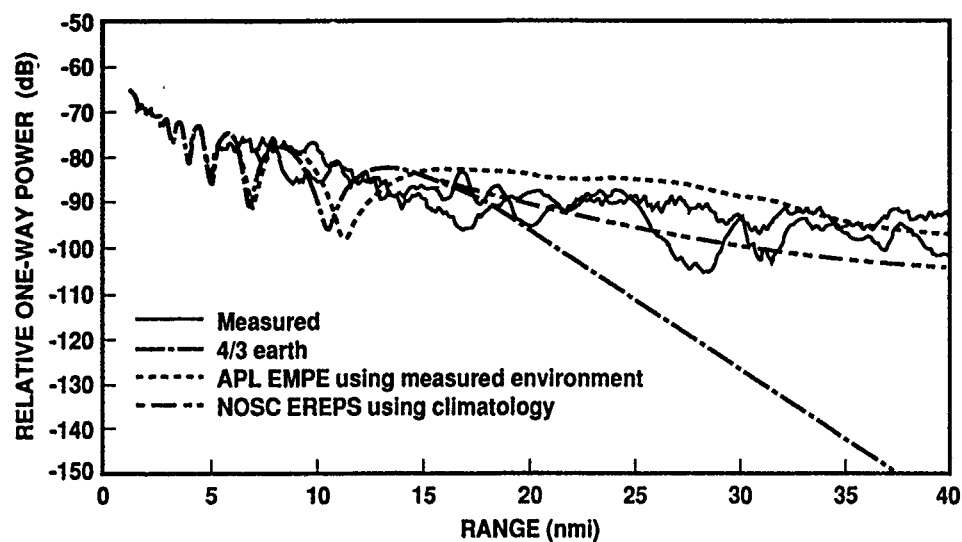


Figure 8. Measurements from the JHU/APL Wallops Island experiment of 9 October 1986, 0835 to 1121 local time. Radar frequency is 5650 MHz, radar height is 26.7 m, target height is 31 m.

#### DISCUSSION

##### **J. GOLDBIRSH**

*On the East Coast we do generally see horizontal inhomogeneity of the refractivity structure when ducting does exist. This horizontal inhomogeneity was verified by radar measurements where we examined the clutter maps of PPIs. We also verified the inhomogeneity by in situ measurements using helicopters. The difference between what you see and what we see is probably due to East Coast versus West Coast atmospheric conditions.*

##### **AUTHOR'S REPLY**

*Yes, that is correct. On the East Coast, you are influenced by continental air moving from west to east. On the West Coast, the winds are generally from the ocean, which tends to give homogeneity.*

## PROPAGATION TRANSHORIZON EN ATMOSPHERE MARINE MODELISATION ET NOUVEAUX RESULTATS EXPERIMENTAUX

Jacques CLAVERIE et Yvonick HURTAUD

Division ASRE

CENTRE D'ELECTRONIQUE DE L'ARMEMENT

35170 BRUZ

FRANCE

### RESUME :

*Dans le cadre des travaux entrepris par le sous-groupe Propagation de l'AC 243/RSG8/com. III, deux importantes campagnes de mesures ont été menées au voisinage des côtes françaises : en Atlantique (région de LORIENT), à l'automne 1989, et en Méditerranée (région de TOULON), durant l'été 1990. Ces campagnes concernent des liaisons transhorizon au dessus de la mer, en incidence rasante, aux longueurs d'ondes centimétriques et millimétriques (de 3 à 94 GHz). Afin de caractériser finement la Couche Limite de Surface Océanique, des mesures météorologiques ont été entreprises à l'aide de stations automatiques, d'une bouée placée à proximité de la ligne de visée et de radiosondes suspendues à un ballon.*

*L'ensemble des données recueillies permet la mise au point et la validation d'un programme de calcul global de propagation en atmosphère marine. Ce programme est construit à partir d'un modèle de propagation, s'appuyant sur la méthode de l'équation parabolique et d'un modèle d'environnement, développé en se basant sur une méthode de type "Bulk". L'analyse statistique des données expérimentales conclut à la bonne qualité d'ensemble des modélisations utilisées. L'intérêt d'une approche multifréquentielle est aussi clairement démontré. Cependant, la comparaison temporelle entre les pertes de propagation prédites et mesurées s'avère plus délicate. Une amélioration sensible passe par la prise en compte, tant au niveau des mesures effectuées que des modèles d'environnement, de situations atmosphériques complexes et, notamment, des inhomogénéités spatiales.*

### I. INTRODUCTION

L'amélioration constante des systèmes d'armes exige une connaissance approfondie du milieu de propagation. Dans le cadre des liaisons transhorizon en ondes centimétriques et millimétriques au ras de la mer, cette connaissance s'est fortement développée depuis une vingtaine d'années ([1], [2], [3], [4]). Le canal de propagation est principalement caractérisé par l'existence quasi-permanente d'un conduit d'évaporation, dont la hauteur peut varier de quelques mètres à quelques dizaines de mètres. Les modélisations de ce canal de propagation permettent essentiellement, à l'heure actuelle, de calculer la hauteur du conduit d'évaporation

à partir des paramètres météorologiques classiques relevés à quelques mètres de hauteur. Parallèlement, des modèles de propagation ont été développés en suivant différentes techniques de résolution des équations de propagation : solution modale, méthode dite "de l'équation parabolique", optique géométrique.

Afin de valider ces modélisations, deux campagnes de mesures ont été entreprises par le sous-groupe Propagation de l'AC 243/RSG 8/commission III. La première expérimentation a eu lieu pendant l'automne 1989 sur la côte atlantique française, près de la ville de LORIENT. La seconde s'est déroulée durant l'été 1990 sur la côte méditerranéenne française, à proximité de la ville de TOULON. Les résultats recueillis constituent une base de données remarquable, tant par les moyens radioélectriques et météorologiques mis en oeuvre, que par la diversité des conditions de propagation rencontrées.

L'ensemble des mesures effectuées, au cours de ces deux campagnes, sera décrit dans la partie II. La partie III précisera les modèles utilisés pour analyser les résultats expérimentaux, en insistant sur l'étude du milieu de propagation. Une nouvelle méthode, de type "bulk", permettant le calcul du profil d'indice de réfraction, sera présentée, ainsi qu'une détermination de la hauteur du conduit d'évaporation à partir des données de propagation. Une première étude statistique, visant à valider les différents modèles, à partir des données de la campagne de LORIENT, fera l'objet de la partie IV, alors que dans la partie V, deux cas particuliers issus de la campagne de TOULON seront détaillés. On remarquera que la modélisation du conduit d'évaporation, aussi fidèle soit-elle, n'est pas toujours suffisante pour caractériser de façon satisfaisante les mécanismes réels de la propagation.

### II. DESCRIPTION DES EXPERIMENTATIONS

Deux campagnes de propagation ont eu lieu en France depuis 1989. La première d'entre elles s'est déroulée du 13 Septembre au 13 Décembre 1989 sur la côte sud de la Bretagne, entre la presqu'île de Gâvres et la presqu'île de Quiberon. Des liaisons fonctionnant à 3, 10,5, 16, 35, 36 et 94 GHz ont été mises en oeuvre sur une distance de 27,7 km. Leurs caractéristiques géométriques et radioélectriques sont données dans le tableau n° 2.1. Les récepteurs étaient placés juste derrière l'horizon radioélectrique. L'absorption atmosphé-

rique sur le trajet de propagation, très faible à 3 GHz, cause une atténuation moyenne d'environ 15 dB à 94 GHz.

Avec des caractéristiques radioélectriques similaires, mais afin d'obtenir des conditions de propagation se rapprochant de celles des mers chaudes, une seconde campagne de mesures a eu lieu sur la côte méditerranéenne, entre la ville de Hyères et l'île du Levant. Les liaisons étudiées, d'une distance de 23.1 km sont décrites dans le tableau n° 2.2.

Les mesures de propagation ont été effectuées par l'intermédiaire des tensions de C.A.G échantillonnées, puis numérisées à la cadence de 0.1 Hz. Les pertes de propagation ont ensuite été déduites en utilisant les courbes d'étalonnage des systèmes. Un moyennage a enfin été effectué sur 10 minutes afin de former une base de données de propagation compatible avec celle des données météorologiques.

Durant chacune des deux campagnes, un certain nombre de moyens météorologiques ont été utilisés : deux stations météorologiques, une à chaque extrémité de la liaison, et une bouée météorologique, mouillée à proximité de la ligne de propagation. La bouée mesurait, toutes les 10 minutes, l'ensemble des paramètres permettant de calculer la structure verticale de la couche limite de surface océanique (paramètres "bulk"), soit : la température de l'air, l'humidité relative, la pression atmosphérique, les vitesse et direction du vent, à une altitude de 4.5 m (LORIENT) ou 3.4 m (TOULON), ainsi que la température de l'eau à une profondeur d'environ 30 cm.

Afin de caractériser plus finement le canal de propagation, des mesures en mer ont été entreprises durant la campagne de TOULON, les 17 Juillet et 23 Août, au matin, par l'intermédiaire de sondes ventilées DIGIDROP conçues par la météorologie nationale et fabriquées par la société LEREL. La sonde DIGIDROP mesure la température et l'humidité de l'air ainsi que la pression atmosphérique. Elle est munie d'un aspirateur qui assure sa ventilation interne ainsi qu'un flux d'air de 2 à 3 m/s.

#### Mesure du 17 Juillet

Trois sondes ont été placées respectivement à 1.5 m, 10 m et 25 m au-dessus de la mer. Ces sondes étaient supportées par un ballon tracté par une vedette. Les mesures ont eu lieu près de la bouée météorologique, moteur de la vedette coupé. Chacune des mesures a duré environ 10 minutes. Afin de s'affranchir des fluctuations rapides, les données de température, humidité et pression ont fait l'objet d'un traitement donnant accès à la valeur moyenne, aux valeurs extrêmes et à l'écart-type. Les conditions météorologiques étaient celles d'un temps calme et brumeux (tableau n° 2.3). Ces conditions sont restées quasiment identiques tout le long de la matinée.

#### Mesure du 23 Août

A cause de la présence d'un vent supérieur à 5 m/s

persistant durant toute la journée, l'expérience du 17 Juillet n'a pu être reproduite. Les trois sondes ont alors été redispuestas sur la vedette de la façon suivante :

- la sonde la plus basse est restée à son emplacement précédent, fixée au bout d'une perche de 1.5 m au-dessus de la mer.

- la deuxième sonde a été fixée sur le mât principal de la vedette, à une altitude de 4.9 m.

- enfin, la troisième sonde a été fixée au haut d'une perche à l'avant du bateau, à une altitude de 5.05 m.

Les conditions météorologiques de cette journée sont également indiquées dans le tableau n° 2.3. Au cours de l'expérimentation, la température et l'humidité de l'air évolueront faiblement sous l'action du rayonnement solaire tandis que le vent d'Est ne diminuera pas de façon significative.

### III. MOYENS D'ANALYSE

Dans un contexte opérationnel (radar embarqué sur navire, par exemple), la prédiction en temps réel des conditions de propagation peut s'appuyer sur la mesure in-situ des paramètres météorologiques "bulk". De ceux-ci on déduit, dans un premier temps, les caractéristiques du conduit d'évaporation, puis, dans un second temps, les pertes de propagation dans la configuration employée (fréquence émise, hauteurs d'aériens...). Si les modèles de propagation existants permettent la prise en compte de situations de plus en plus complexes, tout en étant adaptés à un fonctionnement sur micro-ordinateur, la connaissance de la structure atmosphérique est beaucoup plus imprécise car elle repose sur des hypothèses simplificatrices et sur des formulations semi-empiriques dont l'universalité reste à démontrer.

#### 3.1 Calcul des pertes de propagation

Par analogie avec la propagation dans un guide d'onde, la propagation atmosphérique en présence de conduit d'évaporation, peut être traitée par la théorie modale. Aux longueurs d'onde centimétriques, plusieurs modes se superposent. Aux fréquences inférieures à 20 GHz, on peut ne considérer que le premier mode, ce qui réduit considérablement le temps de calcul. Cette dernière configuration correspond au logiciel EREPS développé par le Naval Ocean System Center (USA) dans les années 70 ([5]). EREPS prend en compte l'absorption atmosphérique, la réflexion sur la mer et utilise la hauteur du conduit d'évaporation pour déterminer les pertes de propagation en supposant une atmosphère horizontalement homogène. Son emploi permet d'analyser les données des campagnes de LORIENT et TOULON aux fréquences les plus basses.

Plus récemment, les méthodes basées sur la résolution de "l'équation parabolique" ont suscité un regain d'intérêt, en partie explicable par les performances sans cesse accrues des micro-ordinateurs. A ce jour, une réalisation intéressante est disponible avec le logi-

ciel PCPEM développé par LEVY et CRAIG ([6]) du Rutherford Appleton Laboratory (Grande-Bretagne). Fonctionnant pour des fréquences comprises entre 30 MHz et 1000 GHz et tenant compte de l'absorption atmosphérique ainsi que de la réflexion sur la mer, PCPEM utilise le profil vertical d'indice de réfraction pour calculer les pertes de propagation. Il autorise de plus la modélisation de structures atmosphériques complexes, incluant notamment des inhomogénéités horizontales.

### 3.2 Calcul de la structure atmosphérique

Basés sur la théorie de MONIN-OBUKHOV appliquée à la Couche Limite de Surface Océanique et sur des formules semi-empiriques issues de différents travaux en météorologie, plusieurs modèles de conduit ont déjà été élaborés. Ces modèles, comme EVAP du NOSC ([7]), déterminent essentiellement la hauteur du conduit d'évaporation et ne sont valides que pour les altitudes inférieures à 40 m, ce qui est généralement suffisant pour caractériser la propagation au voisinage de l'interface air-mer. Cependant ils peuvent, à notre avis, être critiqués sur deux points.

Tout d'abord, ils ne calculent pas le profil vertical d'indice de réfraction, nécessaire à l'exécution de PCPEM (comme nous le verrons plus bas, cette difficulté peut être en partie contournée). Or, lors de la campagne de LORIENT, de longues périodes, pendant lesquelles le niveau des signaux reçus était nettement inférieur au niveau de diffraction, ont été enregistrées. Ces événements s'expliquent a priori par le phénomène d'infraréfraction. Prédire l'absence de conduit durant ces périodes est insuffisant pour conclure; il faut impérativement connaître le profil vertical d'indice de réfraction.

De plus, la modélisation des situations atmosphériques stables (température de l'air supérieure à la température de l'eau), qui se traduisent parfois par des conduits d'évaporation relativement élevés, n'a été que partiellement traitée. Certes, en plein océan, il est admis que les situations stables sont peu probables. Il en va tout autrement lorsque l'influence côtière n'est plus négligeable.

Un nouveau modèle de conduit a été développé au CELAR, en s'inspirant des méthodes de type "bulk" ([8]). Les points essentiels du calcul sont exposés dans l'annexe A et, par la suite, nous ferons référence à la méthode "Bulk-CELAR". Cette méthode permet de calculer les profils verticaux de température, d'humidité, de vent et d'indice de réfraction jusqu'à une altitude de 40 m, ainsi que la hauteur du conduit d'évaporation. Ces profils peuvent constituer directement les entrées du logiciel PCPEM. A titre d'exemple, lors de la campagne de LORIENT, le 21 septembre, on a enregistré ponctuellement des pertes de propagation supérieures à 190 dB à la fréquence de 10.5 GHz. Durant cet événement, la hauteur du conduit d'évaporation était nulle, entraînant des pertes calcu-

lées de 167 dB seulement. Cette valeur de 167 dB diffère du niveau de diffraction mentionné dans le tableau n° 2.1, tout simplement à cause de l'influence de la hauteur de marée. Les profils issus de la méthode Bulk-CELAR conduisent à un gradient moyen d'indice de réfraction de 195 M/km, caractéristique d'une situation d'infraréfraction. Les pertes de propagation déduites de ces profils coïncident alors bien avec les observations.

En l'absence d'infraréfraction, une démarche simplificatrice consiste à ne calculer que la hauteur de conduit et à supposer un profil d'indice de réfraction log-linéaire:

$$M(z) = M(0) + 0,125 \cdot (z - z_c) \ln((z + z_0)/z_0) \quad (1)$$

avec:  $M(z)$ : indice de réfraction modifié (unité M) à l'altitude  $z$  (m)

$z_c$ : hauteur du conduit d'évaporation (m)

$z_0$ : longueur de rugosité égale à  $1,5 \cdot 10^{-4}$  m.

Dans ces conditions le calcul des pertes de propagation ne dépend que de la hauteur du conduit d'évaporation, si on fixe par ailleurs la pression atmosphérique, la température de l'air, l'humidité relative et la vitesse du vent à des valeurs arbitraires (dans la pratique les mêmes que celles figurant dans les tableaux n° 2.1 et n° 2.2). Cela revient à supposer qu'indépendamment des conditions réellement observées, la rugosité de la mer et l'absorption atmosphérique pour chaque fréquence sont des constantes: cela risque de fausser sensiblement la valeur des pertes calculées aux fréquences les plus élevées.

Pour l'interprétation des campagnes de LORIENT et TOULON, la modélisation du conduit d'évaporation par la méthode Bulk-CELAR s'appuie sur les données de bouée. Pour des atmosphères instables, la précision des capteurs météorologiques entraîne une incertitude de quelques % sur la hauteur de conduit calculée. Par contre, en situation atmosphérique stable, et notamment pour des hauteurs de conduit relativement élevées (supérieures à 15 m), cette incertitude peut dépasser 50%. Le fait que les conduits d'évaporation élevés influencent surtout la propagation des fréquences étudiées les plus basses, les prédictions à ces fréquences sont très sensibles à la qualité de la mesure des paramètres "bulk".

Dans l'hypothèse précédemment développée où les pertes de propagation ne dépendent que de la hauteur du conduit d'évaporation, la figure n° 3.1 donne, pour la campagne de TOULON, les variations des pertes à 3 GHz, calculées par PCPEM, en fonction de la hauteur de conduit. Compte tenu de sa monotonie et de sa régularité, cette courbe peut facilement être inversée. Un ajustement polynomial simple permet alors de déterminer une relation donnant la hauteur de conduit connaissant les pertes de propagation à 3 GHz. Pour la campagne de LORIENT, l'existence du phénomène de marée complique la mise en oeuvre mais une relation similaire a été élaborée. L'intérêt de cette opération est

double.

Tout d'abord, les hauteurs de conduit prédites par les différents modèles météorologiques peuvent être comparées à celles déduites des pertes de propagation mesurées à 3 GHz, en gardant à l'esprit que ces dernières résultent d'hypothèses de calcul bien particulières. Un exemple de comparaison, extrait de la campagne de LORIENT pour la journée du 27 septembre, est représenté sur la figure n° 3.2. En situation instable, les modèles météorologiques, Bulk-CELAR ou EVAP, aboutissent à des hauteurs de conduit voisines mais supérieures aux valeurs issues du 3 GHz. Cependant, ceci étant confirmé par d'autres analyses, Bulk-CELAR donne des résultats plus proches de la réalité. Entre 9h et 19h, l'atmosphère est stable et les mesures à 3 GHz conduisent à l'existence d'un conduit assez élevé en milieu d'après-midi. La méthode Bulk-CELAR, contrairement à EVAP, modélise elle-aussi un conduit relativement élevé. L'estimation de sa hauteur est, comme nous l'avons déjà dit, assez imprécise, en raison des incertitudes de mesures qui, à elles-seules, suffisent à expliquer l'écart observé avec les hauteurs déduites du 3 GHz.

Par ailleurs, parmi les fréquences étudiées, la propagation à 3 GHz est la plus sensible aux conduits en altitude ou aux conduits de surface non modélisés par Bulk-CELAR. Le calcul des pertes de propagation pour toutes les fréquences, à partir des données à 3 GHz, permet, en cas d'écart important avec les valeurs réellement mesurées, de diagnostiquer l'existence de ces phénomènes particuliers (voir la partie V).

Dans la suite de l'étude, les calculs de pertes de propagation ont été effectués en supposant une atmosphère horizontalement homogène. Cette hypothèse sera également discutée dans la partie V.

#### IV. STATISTIQUES DE PROPAGATION SUR LA CAMPAGNE DE LORIENT

##### 4.1 Mesures à 3, 10.5 et 36 GHz

Les courbes de probabilités cumulées des pertes de propagation à 3, 10.5 et 36 GHz mesurées durant une période de 76 jours entre 20 Septembre et le 13 décembre sont présentées sur la figure n° 4.1. A partir de cette figure et en tenant compte des tableaux n° 2.1 et 2.2, on détermine facilement les pourcentages de temps où les pertes de propagation sont inférieures à celles correspondant à l'espace libre, atténuation atmosphérique comprise. Ces pourcentages sont respectivement de 2.5%, 28% et 30% pour les liaisons fonctionnant à 3, 10.5 et 36 GHz. A 10.5 GHz (respectivement 36 GHz), le niveau d'espace libre est atteint pour des hauteurs de conduit dépassant environ 8 m (respectivement 5 m). Ces conduits, relativement bas, sont les plus fréquents en Atlantique Nord. En revanche, à 3 GHz, le niveau d'espace libre est atteint pour les hauteurs de conduits supérieures à 20 m. Lors la campagne de LORIENT, les conduits élevés, dus

généralement à la forte évaporation par beau temps, et les conduits de surface liés aux mouvements des masses d'air n'ont été mis en évidence que durant 2 à 3 % du temps. Cependant, leurs présences peuvent se traduire, à 3 GHz, par des pertes de propagation inférieures de 10 dB par rapport au niveau d'espace libre. Cette surélévation du signal est moins prononcée aux autres fréquences. Mais, globalement, la structure de la couche limite de surface rencontrée durant l'expérimentation a favorisé la propagation à 10.5 GHz et à 36 GHz comparativement à celle à 3 GHz.

Par ailleurs, la durée pendant laquelle les pertes de propagation sont supérieures à celles du niveau de diffraction représente respectivement environ 18%, 10% et 8% du temps total de l'expérimentation, aux fréquences de 3, 10.5 et 36 GHz. Ces fortes pertes s'expliquent par les deux phénomènes suivants :

##### - l'infraréfraction

Les profils d'indice de réfraction modifié, calculés à partir des données météorologiques relevées par la bouée, présentent un gradient supérieur à 157 M/km. La modélisation des événements d'infraréfraction n'est pas toujours aussi satisfaisante que dans l'exemple mentionné dans le paragraphe 3.2. En effet, ces événements sont caractérisés par de fortes valeurs de l'humidité relative (> 90 %) pour lesquelles la fiabilité du capteur de bouée est discutable. De plus, ils interviennent pour des situations atmosphériques très stables, débordant du strict cadre de validité des équations à la base de la méthode Bulk-CELAR.

L'effet de l'infraréfraction sur les liaisons étudiées est surtout sensible aux fréquences les plus basses.

##### - l'effet des hydrométéores

La présence de brouillards ou de chutes de pluie rend la couche limite de surface homogène: l'existence de conduits d'évaporation est alors peu probable et le niveau de signal reçu, hors atténuation par les hydrométéores, est proche de celui correspondant à la diffraction.

Si l'effet de la pluie est toujours très faible à 3 GHz, il peut devenir non négligeable à 10 GHz (0.2 dB/km pour une intensité de pluie de 10 mm/h). A 36 GHz, sur la distance considérée, il est toujours significatif (0.2 dB/km pour une pluie de 1 mm/h, 1.5 dB/km à 10 mm/h). Les brumes épaisses, présentes sur de grandes étendues, atténuent aussi fortement les signaux émis aux longueurs d'onde millimétriques (0.15 dB/km à 36 GHz, pour un brouillard d'advection où la visibilité est de 200 m).

##### 4.2 Comparaison statistique entre la mesure et la modélisation

###### 4.2.1 modélisation à partir des données météorologiques

Les probabilités cumulées des pertes de propagation

mesurées et modélisées sont données aux fréquences de 3, 10.5 et 36 GHz sur les figures n° 4.2 à 4.4. Elles sont relatives à l'ensemble de la période de fonctionnement nominal de l'expérimentation (du 20 Septembre au 13 Novembre). Les périodes de pluie, de faible visibilité et d'infraréfraction n'ont pas été considérées dans cette analyse. Elles peuvent faire l'objet d'un traitement particulier.

On constate que la modélisation Bulk-CELAR+PCPEM, en termes de probabilités cumulées, rend compte de façon satisfaisante des mesures effectuées. A la fréquence de 3 GHz, les deux courbes sont quasiment identiques sauf pour les pertes les plus faibles où la stratification des couches au-dessus du conduit d'évaporation intervient. A 10.5 GHz, l'écart entre les courbes n'excède pas 3 dB. A 36 GHz, il devient plus important pour les fortes pertes (10 dB). On peut tenter d'expliquer cet écart en remarquant la forte variation des pertes de propagation pour les faibles hauteurs de conduits. En effet, pour un certain nombre d'événements associés à des conditions météorologiques particulières (vent faible, forte humidité), les paramètres "bulk" fournis par la bouée peuvent être erronés ou non représentatifs de la liaison. Ces données conduisent alors à une sous-estimation de la hauteur du conduit et à une surestimation des pertes de propagation.

#### 4.2.2 Modélisation à partir des données de propagation à 3 GHz

Suivant la méthode exposée au paragraphe 3.2, la hauteur du conduit d'évaporation peut être déduite des pertes de propagation à 3 GHz. Cette valeur permet alors de calculer les pertes de propagation à d'autres fréquences. Ce type de travail a été effectué à 10.5 GHz et à 36 GHz. Les courbes de probabilité cumulée des pertes de propagation mesurées et déduites sont présentées sur les figures n° 4.5 et 4.6. Comme précédemment, les périodes de pluie, de faible visibilité et d'infraréfraction ont été retirées des statistiques. A la fréquence de 10.5 GHz, les courbes s'écartent au maximum de 6 dB. A la fréquence de 36 GHz, les écarts sont plus significatifs pour les fortes atténuations. En tout état de cause, il est intéressant de remarquer que ces interpolations fréquentielles donnent, en termes de probabilités cumulées, des résultats équivalents ou même meilleurs que ceux que l'on a en utilisant les données relevées par la bouée.

### **V. ETUDE DE CAS**

#### **5.1 Introduction**

La modélisation temporelle des pertes de propagation; et a fortiori, leur prédiction est difficile à effectuer puisque l'ensemble des phénomènes météorologiques intervenant sur le trajet doivent être pris en compte : inhomogénéités, déplacement des masses d'air, stratifi-

cation verticale et présence éventuelle de discontinuités de la température et de l'humidité, présence de pluie ou de brouillard. L'analyse des événements de propagation permet d'apprécier l'écart entre la modélisation et la mesure. Elle suggère les voies d'amélioration à apporter, soit aux modèles de propagation, soit à leurs données d'entrée. Deux journées relatives à la campagne de propagation de TOULON 1990 ont été analysées. Elles correspondent aux périodes pendant lesquelles des mesures de profils en mer ont été effectuées.

#### **5.2 Examen de la journée du 17 Juillet**

##### 5.2.1 profils d'indice

Les profils de température, humidité, vitesse du vent et coïndice de réfraction d'une part calculés à partir des capteurs de la bouée placés à 3.4 m et d'autre part mesurés par l'intermédiaire des 3 sondes soutenues par le ballon ont été reportés en figure n° 5.1.

Les incertitudes de mesure sont également représentées. Elles s'appuient sur la précision des capteurs et conduisent au tracé d'un profil minimum et d'un profil maximum pour chacun des paramètres. Ces deux profils sont déduits d'un traitement où l'on a fait simultanément varier :

- la différence de température entre l'air et l'eau ( $\pm 0.2^\circ\text{C}$ )
- l'humidité relative ( $\pm 3\%$ )
- la vitesse du vent ( $\pm 0.2 \text{ m/s}$ )

De la même façon, les points de mesures ont été encadrés par les valeurs minimales et maximales déduites de l'étude de chaque relevé.

La température de l'air sur la bouée est inférieure d'environ  $1^\circ\text{C}$  à celle de la mer. La période traitée correspond à une situation atmosphérique instable. Les variations des paramètres sont peu importantes. L'humidité augmente faiblement (moins de 1% sur 23.5 m). La température présente un profil plus prononcé et sa valeur relevée à 1.5 m est proche de celle de l'eau. Le profil du coïndice s'inscrit dans le domaine d'incertitude lié à la précision des capteurs. La hauteur de conduit déduite des données de la sonde placée à 10 m est proche de celle calculée à partir des paramètres relevés par la bouée (environ 5 m).

##### 5.2.2 étude des pertes de propagation

Durant toute cette journée, l'atmosphère était en situation instable et les hauteurs de conduit calculées par la méthode Bulk-CELAR sont restées assez faibles, oscillant entre 3 et 10 m. La figure n° 5.3 permet la comparaison entre les pertes de propagation calculées et mesurées, à la fréquence de 16 GHz. On constate que la modélisation Bulk-CELAR+PCPEM est constamment supérieure, d'environ 20 dB, aux mesures, alors que les résultats déduits des pertes de propagation à 3 GHz en sont relativement proches. Si on effectue les

mêmes comparaisons aux fréquences de 3 et 10.5 GHz, les conclusions sont similaires : on observe un écart systématique de 5 dB à 3 GHz et de 10 dB à 10.5 GHz. Or, les données de bouée ainsi que les hauteurs de conduit calculées par la méthode Bulk-CELAR ont été validées par l'ensemble des mesures de profils verticaux décrites précédemment. On note d'ailleurs (Cf figure n° 5.3) que les variations relatives des signaux prédits et mesurés sont tout à fait identiques. De plus, les comparaisons à 36 GHz, montrées sur la figure n° 5.4 sont satisfaisantes; il n'y a pas d'écart systématique entre les valeurs moyennes des signaux mesurés et prédits. Par contre, l'utilisation des pertes de propagation à 3 GHz conduit à des valeurs sans rapport perceptible avec la réalité.

Une interprétation de cet ensemble de résultats apparemment contradictoires peut toutefois être avancée. La valeur élevée des pertes de propagation (supérieures au niveau de diffraction) observées à 3, 10.5 et 16 GHz, en début et fin de journée, ainsi que la forte humidité de l'air peuvent laisser supposer l'existence de situations d'infraréfraction. Par ailleurs, le vent faible au niveau de la bouée et quasiment nul près des côtes accreditte l'hypothèse d'une liaison horizontalement inhomogène. Il est donc légitime de supposer un canal de propagation ayant la structure suivante : près des côtes, aux extrémités de la liaison, absence de conduit voire situation de légère infraréfraction; au milieu de la liaison, existence d'un conduit d'évaporation assez bas et bien caractérisé par les données de bouée. La simulation par PCPEM d'une telle configuration permet aux pertes calculées à 3, 10.5 et 16 GHz de se rapprocher des niveaux mesurés, sans pour autant affecter sensiblement les valeurs prédites à 36 GHz. Seuls des moyens d'observation météorologiques supplémentaires auraient permis de vérifier ces hypothèses.

Il est intéressant de noter que pour les deux jours précédant le 17 Juillet, les conditions météorologiques, d'une part, et les comparaisons entre mesures et modèles, d'autre part, présentent des caractéristiques similaires à celles que nous venons d'analyser.

### 5.3 Examen de la journée du 23 Août

#### 5.3.1 profils d'indice

Le profil d'indice a été acquis seulement pour deux altitudes car la présence d'un vent supérieur à 5 m/s ne permettait pas de sortir le ballon.

L'écart de température entre l'air et l'eau légèrement négatif en début d'expérience devient positif par la suite. L'état de la Couche Limite de Surface Océanique est proche de la neutralité. La décroissance de l'humidité (5% sur 3.5m) est liée à la présence du vent. Le profil d'indice (figure n° 5.2) est marqué par une forte variation sur les 5 premiers mètres. La hauteur du conduit calculé à partir des capteurs de la bouée est d'environ une vingtaine de mètres. Les profils obtenus

diffèrent de ceux du 17 Juillet.

#### 5.3.2 étude des pertes de propagation

Des fluctuations importantes de pertes de propagation sont observées durant la journée, spécialement aux basses fréquences entre 0-4 h et 19-23 h durant la nuit (à la fréquence de 3 GHz, 20 dB en moins d'une demi-heure, vers 1 h, 20 dB en moins d'une heure vers 22 h). La modélisation Bulk-CELAR utilisant les données de bouée ne rend pas compte d'un tel comportement (figure n° 5.5). En revanche, les hauteurs du conduit déduit des données de propagation à 3 GHz par la méthode exposée au paragraphe 3.2 sont largement plus élevées que celles calculées à partir des paramètres relevés par la bouée. Enfin, ces périodes sont caractérisées par une brise de terre liée à la circulation des masses d'air par temps chaud sur le littoral. Cette circulation d'air peut entraîner la formation d'un conduit de surface qui vient se superposer au conduit d'évaporation. La présence d'un tel profil sur la liaison permet de rendre compte de la variation des pertes de propagation mesurées. Il favorise en effet la propagation dans le domaine centimétrique sans augmenter de façon significative celle dans le domaine millimétrique.

A partir d'environ 7 h, il s'instaure un vent de secteur Est sensiblement plus humide qui tend à rendre plus homogène le profil vertical de l'indice, sans toutefois supprimer entièrement le conduit de surface. En effet, durant cette période s'étendant jusqu'à 18 h, les pertes calculées à 3 GHz sont sensiblement inférieures à celles mesurées (entre 4 et 11 dB). En revanche, les écarts entre la mesure et le modèle à 10, 16 et 36 GHz (figure n° 5.6) sont en moyenne plus faibles. Ces écarts faibles ainsi que les mesures de profils effectuées à l'aide des sondes ventilées tendent à valider la modélisation du profil d'indice dans le conduit d'évaporation par la méthode Bulk-CELAR + PCPEM.

### VI. CONCLUSION

En s'appuyant sur l'importante base de données de propagation et de météorologie recueillie durant deux campagnes successives, la validation globale d'un modèle de propagation (PCPEM) associé à un modèle de calcul de la partie basse de la couche limite de surface (BULK-CELAR) a été effectuée. Cette validation s'est opérée en utilisant deux voies de comparaison entre les pertes de propagation mesurées et modélisées :

- la comparaison statistique est satisfaisante si les conditions de propagation se rapprochent de celles présentes en pleine mer, comme cela fut le cas pour la campagne de LORIENT. L'extension fréquentielle à partir des pertes mesurées à 3 GHz a été entreprise avec succès. Elle permet d'apprécier de façon précise les conditions de propagation dans une bande de fréquences très large (de 3 à 36 GHz);
- la comparaison temporelle montre en revanche que la condition d'homogénéité horizontale prise fré-

quemment dans les modélisations n'est pas systématiquement vérifiée. Cette modélisation est d'autant plus difficile que la liaison se place à proximité de la côte. En effet, les diverses circulations de masse d'air, d'origine advective ou convective, donnent naissance à des conduits de surface qui influent fortement sur la propagation aux longueurs d'ondes centimétriques. Par ailleurs, la présence de la côte rend le conduit d'évaporation inhomogène quand les écarts thermiques et hygrométriques sont importants entre la terre et la mer.

Si la méthode de l'équation parabolique répond bien à la résolution du problème de la propagation centimétrique et millimétrique au-dessus de la mer, il demeure donc la difficulté de modéliser le canal de propagation du point de vue météorologique.

Dans la partie basse de ce canal, la modélisation du conduit d'évaporation à partir des paramètres collectés à l'interface air-mer s'avère délicate quand la température de l'air est supérieure à celle de l'eau (cas stables). Pour ces situations, courantes près des côtes, la méthode BULK-CELAR propose une nouvelle approche.

Au-dessus d'une quarantaine de mètres d'altitude, le profil vertical de l'indice n'est plus exclusivement lié aux conditions présentes à la surface de la mer. Sa connaissance passe alors par la mise en oeuvre de moyens lourds (radiosondages, réfractomètres embarqués...) et par l'étude fine de la situation météorologique.

#### ANNEXE A : LA METHODE BULK-CELAR

Aux fréquences radioélectriques, le coïndice de réfraction de l'air,  $N$ , est fonction de la pression atmosphérique  $p$  (en HPa), de la température  $T$  (en K) et de la pression partielle de vapeur d'eau  $e$  (en HPa):

$$N = 77.6(p/T + 4810.e/T^2) \quad (A-1)$$

Il existe un conduit de guidage des ondes radioélectriques lorsque  $dN/dz < -157 \text{ N/km}$  ou  $dM/dz < 0$ , où la variable  $z$  représente l'altitude et  $M$ , le coïndice de réfraction modifié, défini par :  $M = N + 0.157z$ . Au voisinage de l'interface air-mer, la forte décroissance de l'humidité sur les premiers mètres d'altitude suffit, à elle-seule, à expliquer l'existence d'un conduit de guidage, appelé conduit d'évaporation. La hauteur de conduit,  $z_c$ , est solution de l'équation :

$$dM/dz = 0. \quad (A-2)$$

Dans la basse troposphère, on admet que la pression atmosphérique décroît linéairement en fonction de l'altitude avec une pente de  $-0.12 \text{ HPa/m}$ . Le profil vertical d'indice de réfraction pourra donc être calculé si on connaît les profils verticaux de température et d'humidité (l'humidité de l'air est quantifiée par diffé-

rents paramètres, entre autres :  $e$ , définie ci-dessus,  $q$ , l'humidité spécifique et  $H$ , l'humidité relative).

En supposant l'atmosphère horizontalement homogène, on ne modélise que les échanges verticaux et, dans la Couche Limite de Surface, dont l'épaisseur n'excède pas une quarantaine de mètres, la théorie de MONIN-OBUKHOV conduit aux équations suivantes, où  $k = 0.4$  est la constante de Von Karman :

$$du/dz = (u_* / kz) \cdot \Phi_m(z/L) \quad (A-3)$$

$$d\Theta/dz = (\Theta_* / kz) \cdot \Phi_h(z/L) \quad (A-4)$$

$$dq/dz = (q_* / kz) \cdot \Phi_h(z/L) \quad (A-5)$$

$u$  désigne la vitesse du vent et n'intervient pas directement dans le calcul de l'indice  $N$ , mais (A-3) est nécessaire à la résolution du problème.  $\Theta$  représente la température potentielle ( $\Theta = T + \Gamma z$  où  $\Gamma = 9.86 \cdot 10^{-3} \text{ K/m}$ ).  $u_*$ ,  $\Theta_*$  et  $q_*$  sont des paramètres d'échelle et  $L$ , la longueur de MONIN-OBUKHOV, est un indicateur de stabilité ( $L < 0$  pour une atmosphère instable et  $L > 0$  pour une atmosphère stable).  $\Phi_m$  et  $\Phi_h$  sont des fonctions universelles pour lesquelles de nombreuses formulations semi-empiriques existent. La méthode Bulk-CELAR utilise :

- pour les cas instables, les fonctions données par DYER et HICKS ([9])

$$\begin{aligned} \Phi_m(z/L) &= (1 - 16z/L)^{1/4} \\ \Phi_h(z/L) &= (1 - 16z/L)^{1/2} \end{aligned} \quad (A-6)$$

- pour les cas stables, les fonctions proposées par KONDO ([10])

$$\Phi_m(z/L) = \Phi_h(z/L) = 1 + (6z/L)/(1 + z/L) \quad (A-7)$$

La longueur de MONIN-OBUKHOV est déterminée en utilisant le nombre de Richardson de gradients  $R_i$ , fonction de l'altitude  $z$ . Il peut être mis sous la forme :

$$R_i(z) = (z/L) \cdot \Phi_h(z/L) / \Phi_m^2(z/L) \quad (A-8)$$

Les expressions utilisées de  $\Phi_m$  et  $\Phi_h$  permettent, aussi bien pour les cas instables que pour les cas stables, le calcul de  $L$  à partir de la valeur de  $R_i$  à une altitude  $z_1$ . Cette dernière valeur n'est pas accessible directement mais s'obtient assez simplement par une méthode itérative, connaissant le nombre de Richardson "bulk",  $R_{ib}$ , à la même altitude  $z_1$ . (La définition de  $R_i$  fait intervenir les gradients verticaux de  $u$  et de  $\Theta$ . Le nombre de Richardson "bulk" est défini en remplaçant ces gradients par les variations des paramètres entre l'altitude nulle et  $z_1$  qui, en pratique, correspond à l'altitude des capteurs.  $R_{ib}$  se déduit donc simplement de la mesure des paramètres "bulk").

$L$  étant déterminée, l'intégration analytique des équations (A-3), (A-4) et (A-5), c'est à dire le calcul des profils verticaux de vent, de température et d'humidité, est possible. Le domaine d'intégration commence à l'altitude  $z_0$  pour (A-3) et à l'altitude  $z_{0t}$

pour (A-4) et (A-5). Les grandeurs  $z_0$  et  $z_{0s}$  appelées longueurs de rugosité et généralement très faibles ( $< 1$  cm), correspondent aux altitudes où les variables météorologiques  $u$ ,  $\theta$  et  $q$  cessent d'être égales aux valeurs imposées par l'interface air-mer (vent nul, température de l'air égale à la température de l'eau, humidité relative de 100 %). Elles dépendent essentiellement de la vitesse du vent à quelques mètres d'altitude et sont calculées à partir des résultats publiés par KONDO. Quant aux paramètres d'échelle,  $u_s$ ,  $\theta_s$  et  $q_s$ , ils sont déterminés à partir des valeurs de  $u$ ,  $\theta$  et  $q$  à l'altitude  $z_1$ .

Le profil vertical d'indice de réfraction est ensuite déduit des profils verticaux de température et d'humidité, par la relation (A-1). Par ailleurs, la hauteur du conduit d'évaporation est obtenue par la résolution analytique, moyennant quelques approximations au premier ordre, de l'équation (A-2).

#### BIBLIOGRAPHIE

- [1] ROTHERAM, S., "Radiowave Propagation in the Evaporation Duct", Marconi Rev., vol 37, 1974, pp 18-40.
- [2] PAULUS, R.A., "Practical Application of an Evaporation Duct Model", Radio Sci., vol 20, n°4, July-Aug. 1985, pp 887-896.
- [3] ANDERSON, K.D., "94 GHz Propagation in the Evaporation Duct", IEEE TRANS. A.P., vol 38, n°5, May 1990, pp 746-753.
- [4] HITNEY, H.V. and VIETH, R., "Statistical Assessment of Evaporation Duct Propagation", IEEE TRANS. A.P., vol 38, n°6, June 1990, pp 794-799.
- [5] HITNEY, H.V. and RICHTER, J.H., "Integrated Refractive Effects Prediction System", Nav. Eng. J., 88(2), 1976, pp 257-262.
- [6] LEVY, M.F. and CRAIG, K.H., "Millimeter Wave Propagation in the Evaporation Duct", 45th AGARD EPP Symposium, Copenhagen, October 1989, paper 26.
- [7] PAULUS, R.A., "Specification for Evaporation Duct Height Calculations", NOSC Techn. Doc. 1596, July 1989.
- [8] CLAVERIE, J., "Détermination des Profils Météorologiques dans le Conduit d'Evaporation", CELAR/ASRE Note Technique 16437, Octobre 1990.
- [9] DYER, A.J. and HICKS, B.B., "Flux-Gradient Relationships in the Constant Flux Layer", Quart. J. Roy. Meteor. Soc., 96, 1970, pp 715-721.
- [10] KONDO, J., "Air-Sea Bulk Transfer Coefficients in Diabatic Conditions", Bound. Layer Meteor., 9, 1975, pp 91-112.

#### REMERCIEMENTS

Les auteurs remercient le Service Technique des Télécommunications et des Equipements aéronautiques (STTE) qui a financé la contribution française des expérimentations. Ils expriment leur gratitude aux membres du sous-groupe Propagation de l'AC 243/RSG 8/COM. III pour les échanges fructueux de données et d'informations.

**TABLEAU N° 2.1**  
**CAMPAGNE DE LORIENT**

118 M/km - 1013 HPa - 15°C - 75 % - 7 m/s  
longueur de la liaison : 27.7 km

F (Ghz)	He (m)	Hr (m)	Fsl (dB)	Diff (dB)	H (km)	A (dB/km)
3	8.36	10.41	131	154	25.0	0.01
5.6	8.36	10.41	136	159	25.2	0.01
10.5	8.35	10.50	142	162	25.2	0.02
16	8.35	10.40	145	166	25.2	0.04
35	8.23	10.26	152	176	25.0	0.12
36	8.74	8.40	152	178	24.2	0.12
94	9.25	11.29	161	187	26.4	0.54

**TABLEAU N° 2.2**  
**CAMPAGNE DE TOULON**

118 M/km - 1020 HPa - 20°C - 75 % - 7 m/s  
Longueur de la liaison : 23.1 km

F (Ghz)	He (m)	Hr (m)	Fsl (dB)	Diff (dB)	H (km)	A (dB/km)
3	3.88	5.88	129	159	18.1	0.01
5.6	3.88	5.88	135	163	18.1	0.01
10.5	3.86	5.97	140	167	18.2	0.02
16	3.87	5.87	144	171	18.1	0.05
35	3.74	5.74	151	183	17.8	0.16
36	2.80	11.05	151	176	20.5	0.16
94	4.76	6.76	159	193	19.7	0.73

He(m) : hauteur de l'antenne d'émission par rapport au niveau moyen de la mer

Hr(m) : hauteur de l'antenne de réception par rapport au niveau moyen de la mer

fsl(dB) : pertes d'espace libre

diff(dB) : pertes correspondant au niveau de diffraction (absorption atmosphérique incluse)

H(km) : horizon radioélectrique

A(dB/km) : absorption atmosphérique

TABLEAU N° 23  
CONDITIONS METEOROLOGIQUES MOYENNES  
RELEVÉES LES 17 JUILLET ET 23 AOUT

PARAMETRES	17 JUILLET	23 AOUT
Température de l'air	21°C	25°C
Humidité relative	85%	65%
Pression	1019 HPa	1022 HPa
Vitesse du vent	1-3 m/s	5 m/s
Direction du vent	secteur SUD	secteur EST
Visibilité	6 km	> 15 km
Nébulosité	7/8	0/8

TOULON 90 fréquence : 03 GHz

Pertes de propagation calculées par PCPEM  
en fonction de la hauteur de conduit

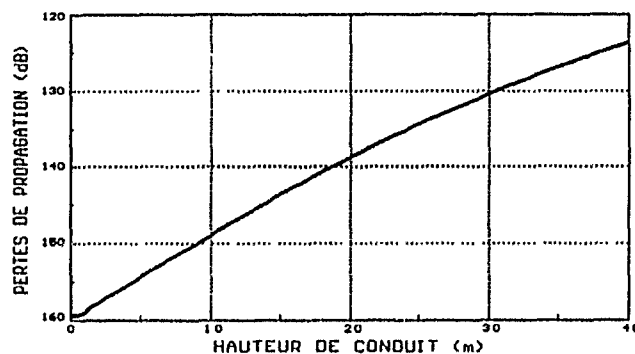


Figure n° 3.1

LORIENT 89 le 27/09

CALCUL DES HAUTEURS DE CONDUIT

Modèle Bulk-CELAR

Modèle EVAP (NOSC)

Données à 3 GHz

atmosphère instable

atmosphère stable

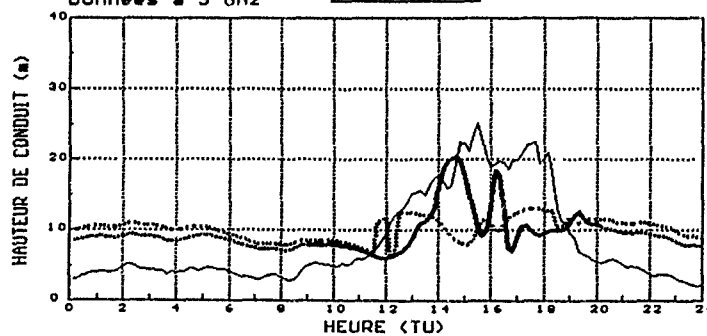


Figure n° 3.2

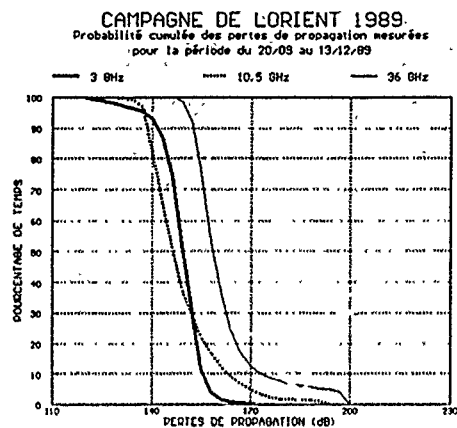


Figure n° 4.1

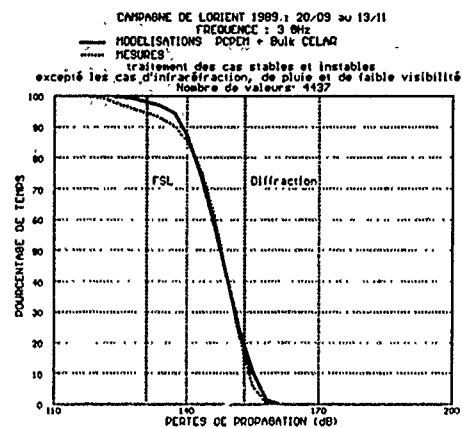


Figure n° 4.2

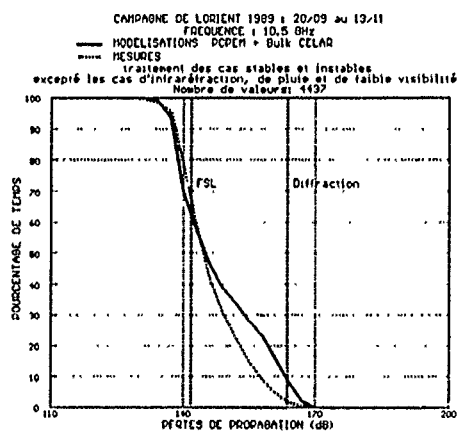


Figure n° 4.3

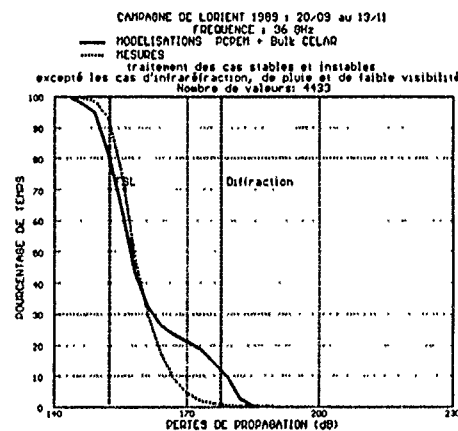


Figure n° 4.4

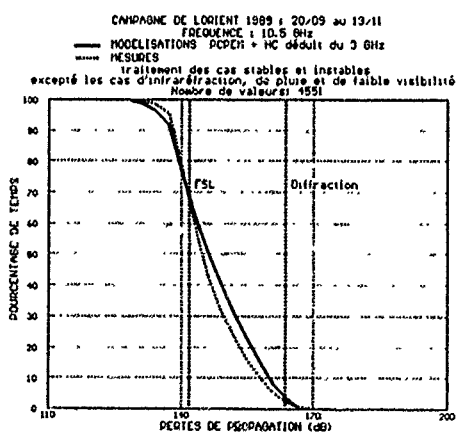


Figure n° 4.5

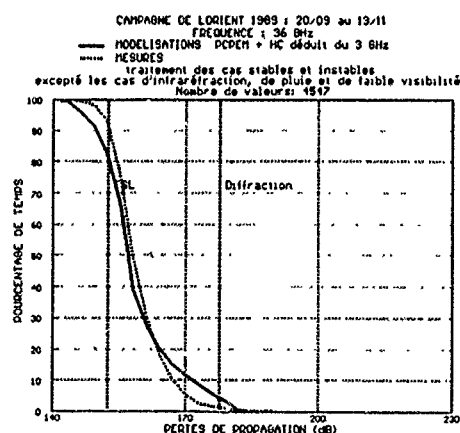


Figure n° 4.6

# PROFILS VERTICAUX le 17/07/90 exp. n° 2

Données de bouée : Tair=21.4°C  
Tner=22.6°C  
Hrel= 84%  
Vent= 2.2m/s

mesure avec bouée à 3.4 m : +  
mesure avec sondes vent. : \*

Hauteur de conduit= 5.1m  
(ou 4.3m ou 5.9m)

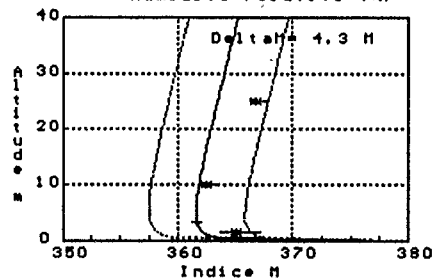
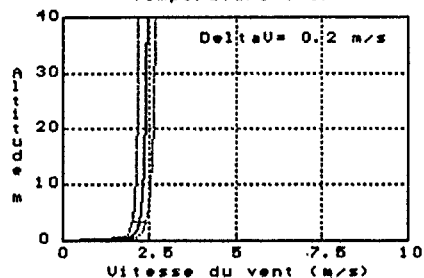
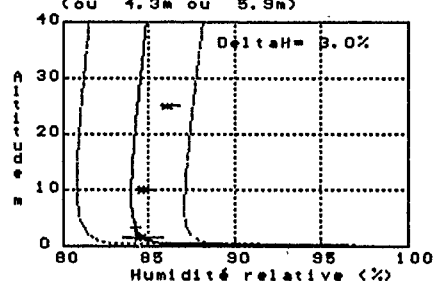
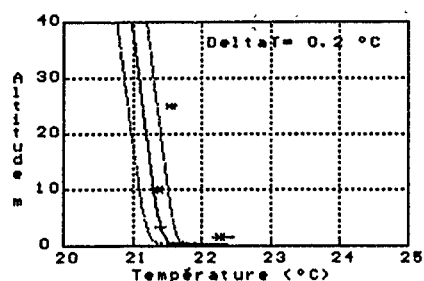


Figure n° 5.1

# PROFILS VERTICAUX le 23/08/90 exp. n° 5

Données de bouée : Tair=24.8°C  
Tner=24.3°C  
Hrel= 67%  
Vent= 5.3m/s

mesure avec bouée à 3.4 m : +  
mesure avec sondes vent. : \*

Hauteur de conduit=18.5m  
(ou 16.2m ou 21.2m)

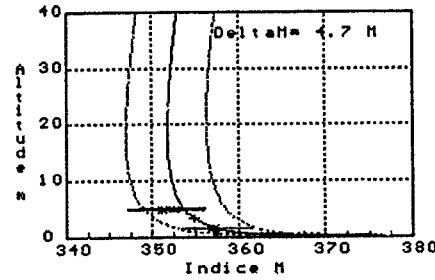
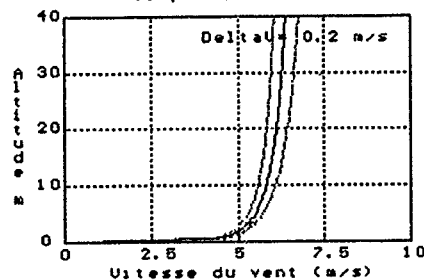
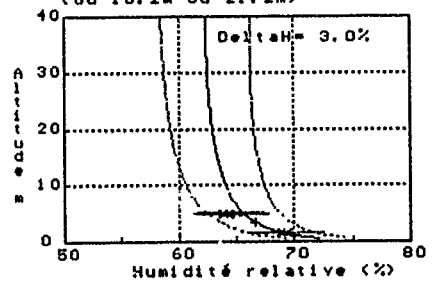
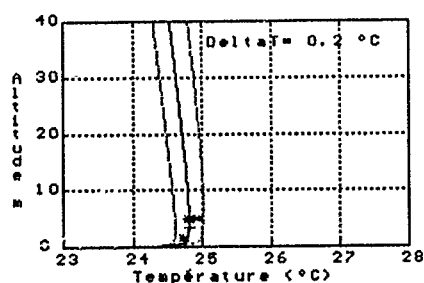


Figure n° 5.2

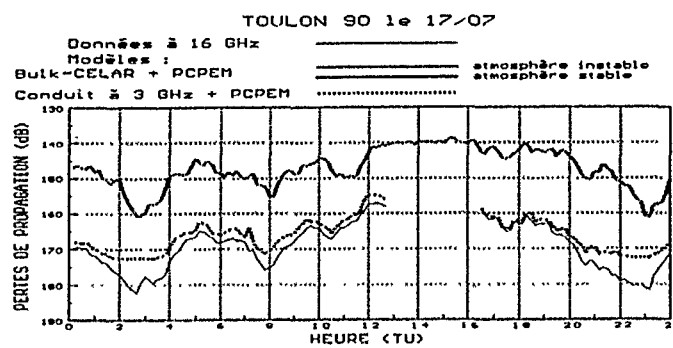


Figure n° 5.3

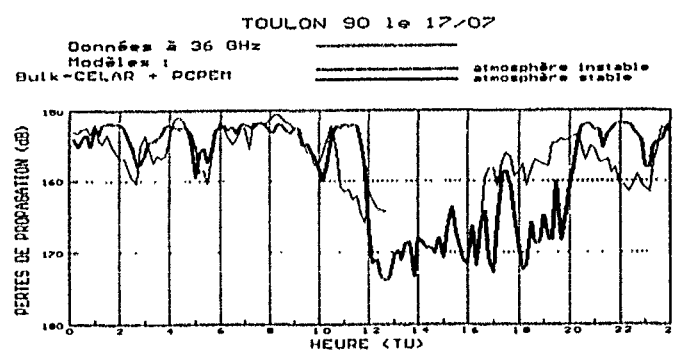


Figure n° 5.4

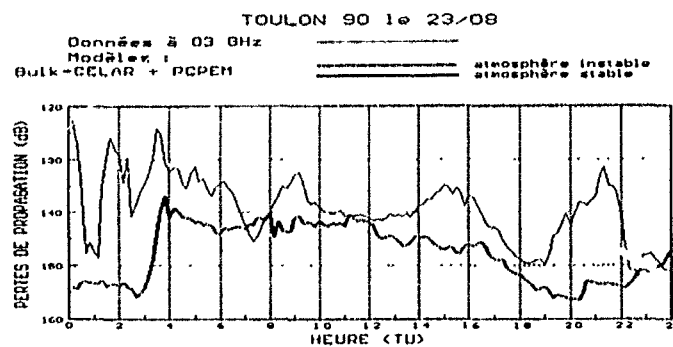


Figure n° 5.5

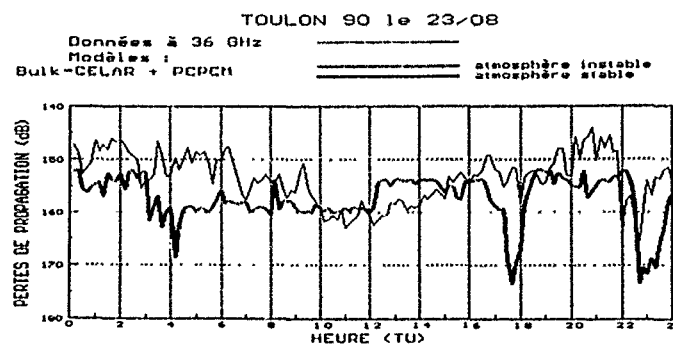


Figure n° 5.6

## DISCUSSION

### C. GOUTELARD

Vous constatez sur la liaison effectuée à Toulon les effets d'inhomogénéité. Un orateur précédent a signalé au contraire une homogénéité remarquable sur la liaison qu'il a étudié. Pouvez-vous commenter cette différence apparente? *You say that you noted inhomogeneity effects on the link in Toulon. On the contrary, a previous speaker found remarkable homogeneity on the link he designed. How do you explain this apparent difference?*

### AUTHOR'S REPLY

C'est du fait de la proximité immédiate de la côte et de la période de mesure (été) que les liaisons mises en oeuvre à Toulon peuvent présenter de fortes inhomogénéités. C'est en particulier le cas par temps calme et ensoleillé où les vents locaux sont générés par le phénomène de brise côtière. En bordure d'océan atlantique, les vents ont, durant un fort pourcentage du temps un régime bien établi et cela contribue de fait à homogénéiser les liaisons. *The links set up at Toulon showed such marked inhomogeneity effects because of the immediate proximity of the coast and the season during which the measurement was carried out (summer). This is particularly the case in calm, sunny weather, when local winds are generated by the phenomenon of coastal breeze. For a high percentage of the time, the winds around the edge of the Atlantic ocean are steady, which helps make the links homogeneous.*

### C. GOUTELARD

Ne pensez-vous pas que la gamme de mesures n'est pas la raison - d'ailleurs nécessaire - de mise en évidence des inhomogénéités qui demeurent invisibles dans des mesures trop rudimentaires? *Don't you think that the measurement range is the necessary reason, that inhomogeneities show up which are not observed in other, more rudimentary measurements?*

### AUTHOR'S REPLY

J'ai présenté de deux façons distinctes le résultat des analyses: une forme statistique, moyennant l'ensemble des événements rencontrés et une forme temporelle, mettant en évidence les incidents de propagation. Grâce à l'utilisation simultanée de plusieurs canaux (centimétriques et millimétriques), la probabilité de mettre en évidence des situations d'inhomogénéité augmente. On le voit nettement le 17 juillet où les écarts mesure-modélisation diffèrent fortement selon la fréquence.

*I have presented the results of the analyses in two separate ways: one in statistical form, averaging all the events which occurred and the other in temporal form, showing the propagation incidents. Thanks to the simultaneous use of several channels (centimetre and millimetre) the probability of detecting inhomogeneity situations increases. We can see this quite clearly on 17 July, where measurement/modelling deviation differs considerably depending on frequency.*

### K. ANDERSON

Vos Lorient measurements are similar to my measurements in San Diego, which indicate that the atmosphere is horizontally homogeneous. The Toulon measurements seem to be similar to APL's experience. In San Diego, we generally have onshore winds. At APL, they generally have winds from the land. Can you comment?

### AUTHOR'S REPLY

En effet, l'homogénéité des liaisons est certainement liée à la situation géographique de la liaison. Lorsque celle-ci s'effectue sur un site où les vents dominants viennent de l'océan, les conditions d'homogénéité ont plus de chance de se voir vérifier. En revanche lorsque les vents dominants sont d'origine locale, les inhomogénéités peuvent être fortes.

Je précise toutefois que je n'ai présenté que deux exemples particuliers de la campagne de Toulon. En effet il existe aussi durant cette campagne des vents forts avec une direction bien établie. Il faut donc attendre l'analyse complète des résultats pour pouvoir apprécier l'effet des inhomogénéités sur les statistiques globales.

*I agree, homogeneity is certainly tied to the geographical situation of the link. When it is established on a site where the prevailing winds are from the ocean there is more likelihood of homogeneous conditions. Where the prevailing winds are of local origin, however, there may be a strong inhomogeneity.*

*I would however stress that I only presented two specific examples from the Toulon project. In fact, strong winds from a well established direction were encountered during the measurement period, so we must wait for a complete analysis of all the results in order to assess the effects of inhomogeneities on the overall statistics.*

ETUDE THEORIQUE DE LA CARACTERISATION  
RADIOELECTRIQUE DU CONDUIT  
D'EVAPORATION.

N. DOUCHIN , S. BOLIOLI , F. CHRISTOPHE

O.N.E.R.A./C.E.R.T.  
 2, Av. Ed. Belin B.P. 4025  
 31055 TOULOUSE Cedex

P. COMBES

Université Paul Sabatier de TOULOUSE.

**Abstract** - The aim in this study is to consider the possibility to identify the evaporation duct parameters from a fluctuations analysis of a near the horizon satellite-ship path. The latter is split in two different parts and reciprocity is applied. Thus we get two different field distributions on a connecting interface which has to be suitable for a good calculation of the coupling between both of them.

Then, the model is used with the intention of evaluating the fluctuations of the received signal due to the movement of the satellite and their sensitivity to the parameters of the propagation medium: sea roughness, height and strength of the evaporation duct, presence of horizontal gradients in the refractive index distribution. Obviously, sensitivity to these parameters is examined for several values of the frequency.

## 1. INTRODUCTION

Le conduit d'évaporation désigne la couche limite presque toujours présente à la surface des océans, dans laquelle la teneur en vapeur d'eau est forte, du fait de l'évaporation, mais décroît rapidement avec l'altitude. Aussi, si sa hauteur  $h_d$  dépend des conditions météorologiques du moment, elle n'excède que très rarement 30 mètres.

Néanmoins, le conduit d'évaporation peut engendrer un allongement important de la portée basse altitude des systèmes électromagnétiques embarqués sur les navires, mais également une modification sensible de leur diagramme de rayonnement. C'est pourquoi la connaissance précise, à tout instant, de ses caractéristiques est essentielle pour une bonne utilisation de ces moyens embarqués.

Si les effets du conduit d'évaporation sur une liaison point à point, au voisinage de la surface de la mer, sont bien connus, il n'y est fait que très rarement allusion dans l'analyse d'une liaison satellite-navire. Pourtant, si l'angle de site de celle-ci est très faible, typiquement inférieur au degré, l'influence du conduit sur les fluctuations du signal reçu sur le navire peut être non négligeable.

L'étude consiste alors à modéliser et à analyser ces fluctuations temporelles, dans le but d'examiner si il existe une dépendance entre celles-ci et les caractéristiques du conduit d'évaporation. La procédure de caractérisation proposée ne nécessite pas d'apport logistique supplémentaire car les liaisons entre satellites à défilement et navires existent déjà ou sont amenées à se développer considérablement. En cela, elle se distingue des méthodes qui, reposant sur la mesure de paramètres météorologiques et l'emploi d'un modèle de couche limite atmosphérique, se heurtent à l'incertitude des mesures et aux lacunes des modèles dans les cas d'atmosphère stable ( $T_{air} > T_{mer}$ ). En outre, celles-ci supposent implicitement que la couche limite est stratifiée horizontalement, ce qui n'est pas le cas a priori de la méthode étudiée ici.

Une étude basée sur le même principe de base, mais exclusivement expérimentale, a été menée au N.O.S.C. il y a quelques années [1]. Notre but est d'y apporter des critiques et éventuellement des améliorations, au plan théorique.

## 2. METHODOLOGIE DE CALCUL DE LA PROPAGATION

### 2.1 Modèle utilisé

Bien que le domaine d'influence du conduit d'évaporation sur le profil d'indice de réfraction ait une hauteur égale à 5 ou 10 fois  $h_d$ , seule l'extrémité inférieure de la liaison satellite-navire en subit les effets. De plus, il est irréaliste, du point de vue temps de calcul, de vouloir modéliser la liaison avec le même maillage, dans son intégralité. C'est pourquoi, il est nécessaire de découper le trajet de propagation en deux parties.

Entre l'émission à partir du satellite et le sommet du domaine d'influence du conduit d'évaporation, les effets ionosphériques, l'absorption et la scintillation sont négligés, essentiellement en raison de l'intervalle de fréquences retenu [1,0GHz, 18,0GHz]. Si, en outre, il est admis que le front d'onde issu du satellite n'est pas déformé par la réfraction à grande échelle, cette première partie du trajet est calculée en espace libre et l'onde incidente est supposée plane comme si le satellite était à l'infini.

Dans la seconde partie de la liaison, entre l'interface de raccordement interposée de manière implicite et le navire, les effets dus aux gradients horizontal et vertical de l'indice de réfraction prédominent. Nous prenons en compte également la rugosité de la mer due au vent quasi permanent en milieu marin.

## 2.2 Les bases physiques et théoriques

Si la propagation entre le satellite et l'interface fictive se calcule aisément par l'optique géométrique, la présence du conduit d'évaporation nécessite le recours aux équations de Maxwell en milieu inhomogène pour le calcul de la seconde partie du trajet. Alors, l'équation de propagation est donnée par:

$$(\nabla^2 E + k_0^2 E) + \text{grad}\left(\frac{1}{\epsilon} E \cdot \text{grad} \epsilon\right) = 0 \quad (1)$$

Pour des distances à l'émetteur courtes, il est avantageux d'utiliser le modèle de Terre plane. Par ailleurs, l'hypothèse d'invariance du milieu par rapport à un axe vertical passant par l'émetteur rend le problème bidimensionnel, pour lequel le système de coordonnées cylindriques  $(h, s)$  est utilisé:

-  $h$  : hauteur par rapport à la surface de la mer.

-  $s$  : abscisse curviligne le long de la Terre.

A partir de (1), il vient alors une équation aux dérivées partielles de type elliptique délicate à résoudre numériquement. C'est pourquoi, le champ est divisé par la solution de l'équation d'Helmoltz en espace libre, bidimensionnelle, pour donner le potentiel de Bremmer  $U$  dont les variations sont lentes; d'où la disparition du terme "d'ellipticité" dans (1). Enfin, pour des distances à la source supérieures à  $100 \lambda$ , un terme supplémentaire disparaît de l'équation aux dérivées partielles et il ne reste que:

$$\frac{\partial^2 U}{\partial h^2} + 2jk_0 \frac{\partial U}{\partial s} + k_0^2 (m^2(h, s) - 1) U = 0 \quad (2)$$

Cette nouvelle équation est du type parabolique. Ainsi, sa résolution entièrement numérique est plus aisée.

L'hypothèse principale qui permet d'obtenir (2) est la suivante:

$$\left| \frac{\partial^2 U}{\partial s^2} \right| \ll 2k_0 \left| \frac{\partial U}{\partial s} \right| \quad (3)$$

V.A. FOCK (2) a démontré que (3) est vérifiée pour une propagation à l'intérieur d'un cône de demi-angle au sommet inférieur à  $20^\circ$ ; c'est donc, en quelque sorte, une hypothèse large de paraxialité.

## 2.3 Les conditions aux limites

A la limite supérieure du domaine, la condition aux limites est une condition de rayonnement à l'infini (condition de Sommerfeld) :

$$\lim \left( \frac{\partial U}{\partial r} + jk_0 U \right) = 0 \quad (4)$$

A la limite de la mer, la condition la plus générale s'écrit:

$$\left( \frac{\partial U}{\partial h} \right)_{h=0} + \alpha(U)_{h=0} = 0 \quad (5)$$

La valeur de  $\alpha$  dépend de la polarisation utilisée:

$$\text{avec } \alpha_h = jk_0 \sqrt{\epsilon_s} \quad \text{et} \quad \alpha_v = \frac{jk_0}{\sqrt{\epsilon_s}} \quad (6)$$

-  $\epsilon_s$  désigne la permittivité complexe de l'eau de mer.

(6) n'est en fait qu'une approximation valable si  $|\epsilon_s| \gg 1$  ce qui est bien le cas de l'eau de mer aux fréquences étudiées.

Dans le cas d'une mer parfaitement conductrice, (5) donne une condition simplifiée pour les deux cas fondamentaux de polarisation rectiligne car  $|\epsilon_s| \rightarrow +\infty$  :

$$(U)_{h=0} = 0 \text{ en polar. H, } \left( \frac{\partial U}{\partial h} \right)_{h=0} = 0 \text{ en polar. V} \quad (7)$$

### 3. RESOLUTION NUMERIQUE DE L'EQUATION PARABOLIQUE

#### 3.1 Choix de la méthode de résolution

Essentiellement pour sa stabilité et pour son exigence moins forte en temps de calcul, la méthode "Split-Step Fourier" [3] est retenue. Elle fait appel à la transformation de Fourier directe et inverse, obtenues numériquement par F.F.T., et conduit à l'écriture d'une relation récurrente qui permet de calculer la solution à l'abscisse  $s+\delta s$  à partir de la solution à l'abscisse  $s$  :

$$U(h, s+\delta s) = e^{\frac{j k_0 \delta s^2 (k_0^2(h, s) - 1)}{2}} \text{T.F.} \left[ e^{-j \frac{\delta s^2}{k_0^2 \sqrt{k_0^2 - 1}}} \text{T.F.}[U(h, s)] \right] \quad (8)$$

$p = k_0 \sin \psi$ ,  $\psi$ : angle entre le vecteur d'onde  $k$  et l'horizontale locale;  $p$  n'est autre que la variable duale de  $h$  pour la transformation de Fourier.

Pour initialiser (8), notre choix s'est porté sur la donnée à  $s=0$  d'une répartition d'amplitude gaussienne dans l'espace direct des  $h$ , dont on peut moduler l'écart-type pour fixer l'angle d'ouverture à 3dB,  $\theta_3$ , de l'antenne de réception embarquée sur le navire.

#### 3.2 Prise en compte numérique des conditions aux limites

L'emploi de la F.F.T. entraîne l'annulation de  $U$  pour les valeurs de  $h$  supérieures à une limite :  $h_{\max}$  et fait apparaître alors des réflexions parasites qui peuvent fausser les valeurs du champ même à la surface de la mer.

Pour amortir ces réflexions parasites, la méthode la plus simple mais néanmoins efficace consiste à dissiper une bonne

partie de l'énergie qui se propage vers les valeurs croissantes de  $h$ , en intercalant une fonction d'apodisation entre  $h=h_{\max}$  et  $h=1,5.h_{\max}$ . Le domaine de calcul des F.F.T. est donc  $[0, 1,5.h_{\max}]$ , mais la solution calculée n'est valable que jusqu'à  $h_{\max}$ .

A la surface de la mer, le cas parfaitement conducteur trouve une solution simplifiée dans l'emploi d'une source image. En pratique, l'équation parabolique est donc résolue sur l'intervalle  $[-1,5.h_{\max}, 1,5.h_{\max}]$  et la solution  $U(h, s)$  y est impaire ou paire selon l'état de polarisation rectiligne fondamental retenu.

Si la mer n'est pas parfaitement conductrice, la solution est une combinaison linéaire des solutions impaires et paires citées précédemment car (5) est elle-même une combinaison linéaire des conditions (7). Cependant, comme la condition (5) n'est pas propagée par l'équation parabolique, les coefficients de la combinaison linéaire doivent être recalculés à chaque étape de la récurrence [4].

Le modèle utilisé dans le cas d'une mer rugueuse est caractérisé par un paramètre unique,  $\sigma_h$ , la hauteur quadratique moyenne des vagues soulevées par le vent. La diffusion sur les rugosités se traduit par un affaiblissement de la réflexion spéculaire. Par conséquent, un coefficient de réflexion modifié est mis en oeuvre dont l'expression est conforme au modèle décrit par MILLER & al. [5].

#### 3.3 Détermination des pas d'échantillonnage

Dans la direction verticale, la détermination de  $\delta h$  repose sur le théorème d'échantillonnage (Shannon). Sa valeur dépend alors de la valeur maximale  $V_{\max}$  de l'angle entre la direction de propagation et l'horizontale locale que l'on souhaite prendre en compte, donc aussi de l'ouverture à 3dB de l'antenne située sur le navire.

De la valeur du pas horizontal,  $\delta s$ , dépend la valeur de l'erreur commise dans la mise en oeuvre de l'algorithme "Split-Step Fourier". Le choix de  $\delta s$  est dicté alors par le niveau d'erreur toléré dans la résolution de l'équation parabolique.

#### 3.4 Validation du logiciel

Le logiciel, élaboré sur les bases théoriques et numériques citées précédemment, a été validé avec succès [6], par comparaison avec MLAYER [7] d'une part, avec PCPEM [8] d'autre part.

#### 4. LE FACTEUR DE COUPLAGE : BASES THEORIQUES

##### 4.1 Définition du facteur de couplage

Le paragraphe 2 a démontré la nécessité de découper la liaison en deux parties qu'il faut donc raccorder.

Puisque le front d'onde issu du satellite est plan, il semble naturel de choisir une interface plane, réduite à une droite pour le problème 2D traité. Comme, en outre, la résolution de l'équation parabolique fournit le champ sur des verticales à la surface de la mer, l'idée la plus simple consiste à choisir une d'entre elles, à l'abscisse  $s=s_0$  (figure 1).

Sur celle-ci, l'onde plane issue du satellite donne une répartition de champ  $E_2(h, s_0)$  équiampitude et à gradient de phase constant. Par ailleurs, le principe de réciprocité permet de remplacer le récepteur du navire par un émetteur fictif. De ce fait, on obtient sur la même verticale une répartition  $E_1(h, s_0)$  provenant de la résolution de l'équation parabolique.

L'étape suivante consiste à définir un lien physique entre les deux parties de la liaison, c'est à dire à évaluer le couplage, en termes de puissance transmise, entre l'espace libre et la propagation guidée. Par référence à la théorie de l'antenne en réception [9], on montre que ce couplage est directement lié au produit de corrélation des deux répartitions défini par:

$$\langle E_1, E_2 \rangle = \int_0^{+\infty} E_1(h, s_0) E_2^*(h, s_0) dh \quad (9)$$

Dans la pratique, le domaine d'intégration est borné,  $h \in [h_{\min}, h_0]$ , et on considère le module au carré de (9) pour assurer l'homogénéité avec une puissance. D'où l'expression du facteur de couplage:

$$\gamma_c = \frac{|\langle E_1, E_2 \rangle|^2}{N} = \frac{\left| \int_{h_{\min}}^{h_0} E_1(h, s_0) E_2^*(h, s_0) dh \right|^2}{N} \quad (10)$$

N est un facteur de normalization explicité plus loin (paragraphe 5).

L'inégalité de Schwartz permet de majorer  $\gamma_c$  par une valeur maximale obtenue si  $E_1$  est associée aussi à une onde plane qui a le même vecteur d'onde que l'onde issue du satellite.  $\gamma_c$  caractérise donc la désadaptation de l'onde issue du navire par rapport à ce cas idéal.

##### 4.2 Interprétation physique de $\gamma_c$

L'onde issue du satellite est plane et sa direction de propagation à un instant donné forme un angle  $\psi$  avec l'horizontale locale à  $s=s_0$ . Au numérateur de (10), on voit apparaître alors l'expression:

$$\int_{h_{\min}}^{h_0} E_1(h, s_0) e^{-jk_{\psi} z(h)} dh \quad (11)$$

cui n'est autre que la composante selon  $k_{\psi}$  dans le spectre angulaire d'ondes planes de  $E_1(h, s_0)$ ,  $h \in [h_{\min}, h_0]$ .

D'autre part, si  $E_1(h, s_0) = 0$  pour  $h \leq h_{\min}$  et pour  $h \geq h_0$ , l'intégrale (11) peut être étendue à  $[-\infty, +\infty]$  et on reconnaît la transformée de Fourier de  $E_1(h, s_0)$ .

En conséquence,  $\gamma_c = f(\psi)$  caractérise le rayonnement en champ lointain de la répartition complexe  $E_1(h, s_0)$ , et, par suite, l'évolution du couplage de l'onde qui s'est propagée dans le conduit d'évaporation avec le satellite supposé à l'infini et qui défile.

##### 4.3 Choix de l'interface de raccordement

-a- Schéma équivalent de la liaison (figure 2)

L'obtention du diagramme de rayonnement à l'infini de  $E_1(h, s_0)$  par transformation de Fourier n'est possible que si la propagation au-delà de l'interface a lieu en milieu homogène, donc en l'occurrence ici, en espace libre. Par conséquent, si pour  $s \leq s_0$  l'onde se propage dans le milieu vrai, celui-ci est remplacé par l'espace libre pour  $s > s_0$ .

#### a- Détermination de $s_0$

Dans la mesure où l'énergie associée à  $E_1(h, s_0)$ , pour  $h \in [h_{\min}, h_0]$ , ne subit plus les effets du conduit d'évaporation au-delà de l'interface de raccordement, le recours au schéma équivalent de la figure 2 est justifié, étant données les hypothèses formulées au 2.1.

Par suite, la méthode de détermination de  $s_0$  est heuristique et consiste à rechercher la valeur minimale de  $s$  au-delà de laquelle le diagramme de rayonnement à l'infini de  $E_1(h, s)$  est invariant. La recherche de la valeur minimale permet une économie du temps de calcul nécessaire à la résolution de l'équation parabolique, partie la plus exigeante du logiciel.

#### -c- Détermination de $h_{\min}$

Le schéma équivalent de la figure 2 montre que l'interposition de l'interface de raccordement à  $s=s_0$  entraîne une "coupure" du conduit d'évaporation, comme si, subitement, sa hauteur passait de la valeur vraie  $h_d$  à  $h_{\min}$ . Par suite, pour  $s > s_0$ , l'énergie comprise entre  $h_{\min}$  et  $h_d$  est propagée en espace libre.

Or, si  $h \leq h_d$ , les gradients verticaux de l'indice de réfraction, inférieurs à -157 unité-N/km, tendent à infléchir les directions qui pointent vers le ciel vers la surface de la mer. En conséquence, on peut prévoir que seule une partie de l'énergie correspondante, fuit effectivement vers les altitudes croissantes. Par contre, si  $h > h_d$ , les directions qui pointent vers le ciel ne retourneront pas vers la Terre car les gradients verticaux de l'indice de réfraction  $\gamma$  sont supérieurs à -157 unité-N/km.

En conclusion, le choix de  $h_{\min} = h_d$  est suffisant pour garantir que l'énergie prise en compte est réellement susceptible de se coupler avec l'onde issue du satellite. C'est une condition suffisante qui n'est cependant pas forcément nécessaire car l'interface supérieure du conduit est floue.

#### 4.4 Domaine de validité de la courbe $\gamma_c = f(\psi)$

Dans l'hypothèse d'une interface de raccordement à  $s=s_0$ , et parce que  $h_{\min}$  est choisi égal à  $h_d$ , le facteur de couplage ne prend en compte que les

directions de propagation situées au-dessus de l'horizontale locale. Par conséquent, la limite inférieure de validité de la courbe  $\gamma_c = f(\psi)$  est  $\psi = 0$  (figure 3).

Cependant, il est intéressant de référencer les angles par rapport à une direction fixe, indépendante de la position de l'interface de raccordement. Le choix le plus naturel pour celle-ci correspond à l'horizon radioélectrique relatif à l'antenne de réception du navire. On définit par rapport à ce dernier l'angle de site  $\alpha$  de la liaison relié à l'angle  $\psi$  (grandeur locale) par:

$$\alpha = \frac{\pi}{2} + \psi - \frac{s_0}{K.a} - \arctg\left(\frac{K.a}{2.h_r}\right) \quad (12)$$

où  $K$  désigne le rapport entre le rayon terrestre fictif et le rayon terrestre vrai;  $K=4/3$  pour l'atmosphère standard.

Pour  $s_0$  assez grand,  $\alpha$  est négatif. Repousser l'interface de raccordement plus loin du navire permet donc d'analyser la liaison lorsque le satellite est sous l'horizon radioélectrique du récepteur au sol.

Pour traiter de manière simplifiée la réfraction à grande échelle due au gradient moyen de l'atmosphère, on remplace donc la Terre vraie par une Terre fictive de rayon égal à  $K$  fois le rayon vrai. Cependant, tant que ce gradient moyen reste supérieur, en valeur algébrique, à -157 unité-N/km, la Terre reste convexe et la figure 3 montre clairement alors que la valeur maximale de l'angle  $\alpha$ ,  $\alpha_{\max}$ , diminue avec  $s_0$ , si par ailleurs  $h_0$  est constante. De plus,  $\alpha_{\max}$  croît avec  $h_0$  à  $s_0$  constante. De ce fait, le choix de  $h_0$  s'oriente naturellement vers la plus grande valeur admissible, soit  $h_0 = h_{\max}$ , limite supérieure du domaine de validité de la solution de l'équation parabolique. De cette manière, l'intervalle angulaire où la courbe  $\gamma_c = f(\psi)$  est valide est le plus large possible.

#### 5. LE FACTEUR DE COUPLAGE : UTILISATION PRATIQUE

##### 5.1 Détermination du dénominateur $N$ de $\gamma_c$

Il s'agit donc d'un terme de normation dont l'expression est la suivante:

$$N = |< E_1, E_1^* >|^2 \cdot |< E_0, E_2^* >|^2 \quad (13)$$

$$\text{avec } |< E_0, E_2^* >|^2 = \left| \int_{-h_{\text{max}}}^{h_{\text{max}}} E_0(h, s_0) \cdot E_2^*(h, s_0) \, dh \right|^2 \quad (14)$$

Le premier terme du produit (13) permet de modifier la valeur de  $s_0$  sans que la valeur du facteur de couplage subisse les effets de l'affaiblissement de  $E_1$  par propagation.

$E_0$  est obtenue par résolution de l'équation parabolique en espace libre, en absence de la Terre, et caractérise donc le rayonnement de l'éclairement initial  $E_1(h, s=0)$  de l'antenne située sur le navire. Par suite, l'adjonction de (14) au dénominateur de  $\gamma_c$  permet de s'affranchir des effets de pondération imputables à la directivité de la source, non isotrope, comme si le récepteur du navire disposait d'un système de poursuite du satellite qui défile.

### 5.2 Les problèmes de troncature

L'intégrale qui figure au numérateur de  $\gamma_c$  est calculée sur un domaine borné et fait donc apparaître une troncature aux deux extrémités de l'intervalle où  $E_1(h, s_0) \neq 0$ ; celle-ci engendre des oscillations parasites, connues sous le nom de phénomène de Gibbs.

Une solution à ce problème consiste à intercaler une fonction d'apodisation entre  $h=h_d$  et  $h=2.h_d$ , fonction dont la forme optimisée est la fenêtre de Hamming. Il en résulte que la répartition de champ  $E_1(h, s_0)$  est un peu modifiée pour  $h \in [h_d, 2.h_d]$  et que, de ce fait, la borne inférieure  $\psi_{\min}$  du domaine de validité de la courbe du facteur de couplage augmente sensiblement. Par exemple, sur la figure 4, on relève  $\psi_{\min}=1,54$  mrd pour  $s_0=50\text{km}$ ; par contre les oscillations de Gibbs sont très nettement atténuées. De plus, pour pallier le resserrement du domaine de validité du facteur de couplage, il suffit d'effectuer le calcul de celui-ci pour une valeur de  $s_0$  plus grande. La figure 4 propose par exemple  $s_0=75\text{km}$  voire même  $s_0=100\text{km}$ .

### 5.3 Validation de la méthode du facteur de couplage

Elle consiste à comparer le champ à l'infini obtenu par la méthode du facteur de couplage à une coupe verticale de la répartition bidimensionnelle de champ calculée directement par l'équation parabolique, ceci le plus loin possible du navire. Compte tenu des limitations en angle de site la coupe est effectuée à  $s_0=160\text{km}$ ; la méthode de validation retenue est illustrée à la fréquence de 5,0 GHz, pour un conduit d'évaporation à 20m.

La figure 5, sur laquelle figurent les deux répartitions de champ auxquelles il est fait allusion ci-dessus, montre la superposition des extréma à 0,2 mrd près. Au vu de ces faibles écarts, on peut donc conclure positivement quant à la validité de la méthode du facteur de couplage.

### 6. INFLUENCE DE LA FREQUENCE SUR LE SIGNAL RECU

La méthode du facteur de couplage est utilisée désormais pour analyser la liaison satellite-navire car, en effet, les courbes  $\gamma_c = f(\psi \text{ ou } \alpha)$  représentent directement l'évolution temporelle du signal reçu à bord du navire lorsque le satellite se lève ou se couche à l'horizon.

#### 6.1 Choix des fréquences d'étude

Celles-ci sont au nombre de trois:

- 1,575 GHz : c'est une des deux fréquences descendantes utilisées par le système de radiolocalisation par satellites GPS-Navstar qui est amené à avoir un secteur spatial important ainsi qu'un grand nombre d'utilisateurs dans un futur assez proche.

- 5,0 GHz : c'est une fréquence de la bande couramment employée par les répondeurs embarqués sur satellite.

- 2,40 GHz : la bande de fréquences concernée est utilisée par les radars de détection. En outre, dans la mesure où les effets du conduit d'évaporation s'amplifient avec la fréquence, il est intéressant d'inclure dans l'étude cette troisième valeur plus forte.

## 6.2 Résultats obtenus

A 1,575 GHz ( figure 6 ) : le décalage des quatre courbes, correspondant à l'atmosphère standard et à trois hauteurs de conduit différentes, est nettement perceptible. Il est dû à l'inflexion des lobes d'interférences vers la surface de la mer. Comme cette inflexion est plus marquée pour les directions les plus inclinées qui subissent les effets du conduit sur des distances plus grandes, il en résulte un décalage des courbes d'autant plus grand que l'angle de site est faible.

En comparant la position du premier maximum, le décalage de la courbe relative au conduit à 26m par rapport à celle de l'atmosphère standard peut être majoré par 2 mrd. Cette valeur passe à 1 mrd si la comparaison des deux courbes porte sur le premier minimum; la faiblesse des effets du conduit d'évaporation à 1,575 GHz se confirme. En outre, il semble difficile de pouvoir donner une estimation de la hauteur du conduit, même à 5 mètres près, simplement en relevant les positions relatives des différents extréma du signal reçu.

Cependant, la figure 6 montre que l'évaluation du niveau de signal reçu aux sites très faibles permet de discriminer les cas de propagation traités ici. En effet, pour  $\psi=0$ , on constate une différence voisine de 20dB entre le conduit à 26m et l'atmosphère standard. Cette différence vaut encore 5dB entre le conduit à 16m et le conduit à 10m. Il semble donc que ce soit un critère à prendre en compte dans la procédure de caractérisation du milieu de propagation.

A 9,40 GHz ( figures 7,8 et 9 ) : il convient de préciser d'abord que les lobes d'interférences sont numérotés à partir du plus incliné, lobe n°1, puis par ordre croissant à mesure que le site augmente.

L'observation de la figure 7, qui correspond à un conduit à 40m, montre que les lobes n°1 et n°2 sont entièrement piégés et que l'énergie qu'ils véhiculent se propage au voisinage de la surface de la mer, dans la partie du conduit que l'on peut qualifier d'efficace. Par contre, si l'inflexion du lobe n°3 est très nette, elle est insuffisante pour que celui-ci soit entièrement piégé et une partie de l'énergie qui lui est associée fuit hors du conduit pour rayonner vers les altitudes croissantes.

Sur la courbe du couplage ( figure 9 ) les lobes n°1 et n°2 ne figurent pas car ils ne sont pas pris en compte. Par contre, la partie non piégée du lobe n°3 se retrouve dans le premier maximum, plus large que les suivants.

Dans le cas où  $hd=10m$  ( figure 8 ), aucun lobe n'est entièrement piégé d'où l'absence de "couche" de forte énergie parallèle à la surface de la mer. Néanmoins, la forme du lobe n°1 suggère qu'une partie de son énergie est guidée et montre clairement alors l'élargissement de celui-ci. Sur la courbe du couplage relative à ce conduit à 10m ( figure 9 ), on observe à nouveau un premier maximum large; la remarque formulée ci-dessus est donc étayée.

Quoi qu'il en soit, la même figure 9 montre que les deux premiers maxima et les deux premiers minima sont presque confondus de sorte qu'il est impossible d'y discerner le conduit à 10m du conduit à 40m. L'analyse effectuée à 9,40 GHz démontre donc que le surplus de supraréfraction engendré par un conduit fort peut conduire à une confusion partielle de celui-ci avec un conduit faible de par la superposition de lobes d'ordres différents. Toutefois, il est possible de lever cette ambiguïté car les seconds minima, par exemple, se distinguent nettement.

La comparaison des courbes de couplage relatives à  $hd=20m$  et à  $hd=40m$  montre également une confusion partielle au niveau du second minimum. Mais, les deux premiers maxima se distinguent nettement.

A 5,0 GHz ( figure 10 ) : La comparaison des quatre courbes de couplage montre globalement une bonne séparation des quatre cas de propagation traités. L'ambiguïté observée à 9,40 GHz ne se retrouve pas ici, car les effets du conduit d'évaporation sont moins marqués. Par exemple, si l'observation de la courbe relative à  $hd=30m$  montre que le lobe n°1 est piégé, elle permet de constater que le lobe n°2 n'est pas suffisamment infléchi vers la surface de la mer pour être confondu avec le lobe n°1 de l'atmosphère standard.

Par ailleurs, le décalage des courbes est plus sensible qu'à 1,575 GHz. Par exemple, le premier minimum relatif à l'atmosphère standard est décalé de 1 mrd par rapport au premier minimum associé au conduit à 10m. Ce même écart s'élève à presque 2 mrd si la comparaison porte sur les conduits à 10m et à 20m. Dans le cas du conduit à 30m, le

lobe n°1, piégé, n'est pas pris en compte de sorte que l'on ne distingue que deux maxima pour  $\psi \leq 14$  mrd, ce nombre s'élevant à trois pour les trois autres cas de propagation.

Par conséquent, la fréquence de 5,0 GHz semble très favorable pour la caractérisation de conduits de hauteurs aussi différentes que 10, 20 et 30m, tant la diversité des informations que l'on peut extraire des courbes du facteur de couplage est importante. De plus, les décalages angulaires constatés sur la figure 10 permettent de prévoir une bonne résolution - au moins 5 mètres - dans l'estimation de la hauteur du conduit.

## 7. INFLUENCE DES PARAMETRES DU MILIEU DE PROPAGATION

L'étude paramétrique réalisée à 5,0 GHz porte sur la rugosité de la mer ainsi que sur l'existence de gradients horizontaux de l'indice de réfraction dans le conduit d'évaporation.

### 7.1 La rugosité de la mer (figure 11)

Le modèle utilisé est le modèle à un seul paramètre,  $\sigma_h$ , décrit au 3.2, et l'étude porte sur trois valeurs de la vitesse du vent,  $u$ , auxquelles correspondent trois valeurs de  $\sigma_h$ , d'après l'échelle de Douglas :

$u = 6 \text{ m.s}^{-1}$	$\rightarrow$	$\sigma_h = 0,23 \text{ m}$
$u = 10 \text{ m.s}^{-1}$	$\rightarrow$	$\sigma_h = 0,61 \text{ m}$
$u = 15 \text{ m.s}^{-1}$	$\rightarrow$	$\sigma_h = 1,53 \text{ m}$

Dans les trois cas,  $h_d=30\text{m}$ , car, dans ce cas, le lobe n°1 est piégé.

Pour  $\sigma_h = 0,23 \text{ m}$  : la comparaison avec le cas de la mer lisse montre peu de différences si ce n'est une légère perte de dynamique entre maxima et minima due à une remontée légère de ces derniers, et un léger glissement des extréma vers les valeurs de  $\psi$  supérieures.

Pour  $\sigma_h = 0,61 \text{ m}$  : les phénomènes décrits ci-dessus sont fortement accentués. Les creux sont beaucoup moins profonds et ils s'élargissent. Ceci est imputable à l'affaiblissement du rayon réfléchi car l'énergie incidente est diffusée par les rugosités de la mer. Le glissement des extréma s'accroît également et le couplage augmente pour les valeurs de  $\psi$  inférieures à 2 mrd. Cette dernière tendance s'explique par l'apparition de fuites hors du conduit d'évaporation; la rugosité de la mer s'oppose au guidage efficace de l'énergie.

Pour  $\sigma_h = 1,53 \text{ m}$  : les phénomènes déjà observés s'accroissent encore. La dynamique entre creux et maxima a presque totalement disparu car le niveau du rayon réfléchi est beaucoup plus faible que celui du rayon direct. Par ailleurs, le glissement des extréma est important, même s'il s'atténue à mesure que l'angle de site croît. Enfin, on peut noter une augmentation sensible du couplage, 10 dB environ, pour les faibles valeurs de  $\psi$ , qui traduit une fuite d'énergie importante en dehors du conduit.

En conclusion, la rugosité de la mer présente des aspects positifs car le couplage avec le satellite est renforcé aux sites faibles par l'apparition de fuites à l'extérieur du conduit d'évaporation. Mais, en contrepartie, les phénomènes d'interférences sont très nettement atténués et la dynamique du signal reçu sur le navire s'en trouve très affaiblie. Si l'on ajoute à cela l'élargissement des minima, la localisation de ceux-ci devient très imprécise et même incertaine si du bruit se superpose au signal utile. Par suite, l'intérêt de la mesure du niveau de signal reçu aux sites très faibles est encore renforcé; la procédure de caractérisation du conduit d'évaporation ne doit pas être focalisée exclusivement sur la localisation absolue ou relative des extréma, mais doit intégrer également cet autre critère.

Précisons tout de même que, si le vent est fort, le brassage de la couche limite est important et le conduit d'évaporation aura une hauteur faible. La coexistence d'une forte rugosité et d'un conduit fort a donc une probabilité peu importante de se présenter.

### 7.2 Les gradients horizontaux de l'indice de réfraction

Si l'hypothèse d'homogénéité horizontale du conduit d'évaporation est communément admise en situation dite "de mer ouverte", c'est à dire au large, elle est remise en cause dès que le bateau est assez proche des côtes pour en ressentir l'influence. Il est très fréquent, alors, d'observer des gradients horizontaux de l'indice de réfraction, conséquences le plus souvent de gradients horizontaux de la température de mer et de la température de l'air.

Les deux cas simulés sont "des cas d'école" et correspondent à un conduit

initialement à 20m qui voit sa hauteur croître jusqu'à 30m sur une distance de 50 km, ou celle-ci décroître de 10m sur la même distance.

Sur la figure 12 sont comparés ces deux cas de propagation avec le cas du conduit homogène à 20m. Les trois courbes ne se superposent pas, surtout pour les directions de propagation les plus inclinées. Lorsque  $h_d$  croît, la supraréfraction s'amplifie et les premiers extréma glissent vers les valeurs de  $\psi$  faibles. Le piégeage du lobe n°1 est également renforcé, d'où une diminution du couplage pour  $\psi < 5$  mrd. Lorsque  $h_d$  décroît, les phénomènes s'inversent; d'où une augmentation des fuites d'énergie hors du conduit perceptibles sur le niveau de couplage aux angles de site faibles.

Si l'on s'en tient à la localisation du minimum des courbes de couplage situé au voisinage de 5 mrd, le décalage angulaire observé n'excède pas 0,5 mrd dans un sens comme dans l'autre. Par conséquent, la sensibilité à l'inhomogénéité horizontale ne semble pas imputable, d'autant plus que celle-ci est grande en proportion puisqu'elle est à 50% et à 100% de la valeur de  $h_d$ .

Néanmoins, la comparaison des niveaux de couplage pour les sites faibles ( $\psi < 5$  mrd) montre des différences marquées entre les différents cas de propagation et permet donc en théorie de les discerner.

L'étape suivante consiste en la comparaison du conduit inhomogène qui voit sa hauteur croître de 20 à 30m avec le conduit homogène à 22m et avec le conduit homogène à 24m (figure 13). Si ce dernier est trop fort pour être confondu avec le conduit inhomogène, par contre la courbe de couplage relative au conduit homogène à 22m se superpose presque parfaitement avec celle du conduit inhomogène, pour les valeurs de  $\psi$  positives. Cependant, pour les valeurs négatives de  $\psi$ , les deux courbes ne coïncident plus, traduction de disparités dans le bilan d'énergie rayonnée à l'extérieur du conduit d'évaporation.

De nouveau, donc, et à deux reprises, est mise en relief l'importance de la mesure du niveau de signal reçu pour les valeurs très faibles de l'angle de site, c'est à dire lorsque le satellite se situe au voisinage de l'horizon radioélectrique du récepteur embarqué sur le navire, voire même en-dessous de cette direction.

## 8. CONCLUSION

Dans cette étude de la caractérisation radioélectrique du conduit d'évaporation, l'intérêt de la méthode du facteur de couplage a été démontré: celle-ci consiste en fait à utiliser le plus possible l'absence d'influence du conduit d'évaporation sur une grande partie de la liaison satellite-navire pour la remplacer par une propagation en espace libre. Alors, le facteur de couplage permet de repérer la distance minimale  $s_0$  à partir de laquelle cette hypothèse est vérifiée.

En ce qui concerne la caractérisation du conduit d'évaporation, l'adéquation de la bande des 5 GHz pour discriminer des conduits de hauteurs très différentes a été démontrée. L'utilisation d'une telle valeur de la fréquence permet donc, de reconnaître l'ensemble des hauteurs de conduit couramment rencontrées, avec, qui plus est, une bonne précision.

Cependant, l'intérêt de la diversité de fréquence ressort clairement puisque l'utilisation simultanée d'une fréquence voisine de 1,5 GHz et d'une fréquence voisine de 5,0 GHz permet de caractériser la hauteur du conduit avec une bonne précision tout en écartant d'éventuelles indéterminations entre conduits faibles et conduits très forts.

L'aspect essentiel de la localisation en angle de site des extréma - et surtout des minima plus pointus - des courbes du signal reçu sur le navire a également été confirmée. Cependant, l'utilisation de ce seul critère peut se révéler insuffisant, notamment si la mer est rugueuse ou s'il existe des gradients horizontaux de l'indice de réfraction. Un deuxième critère s'est avéré très important alors: l'évaluation du niveau du signal reçu lorsque l'angle de site de la liaison est très faible. Les deux critères appliqués conjointement semblent permettre de lever à peu près tous les cas d'indétermination cités au paragraphe précédent.

Dans la pratique, on trouve à la fois une liaison descendante de type télémesure ainsi qu'une liaison assurée par un répondeur émettant de fortes puissances. Par conséquent, les conditions de la diversité de fréquence sont réunies, et, si le satellite défile, il est légitime d'en attendre une

confrontation intéressante du modèle théorique à la réalité expérimentale. Nous espérons pouvoir faire état prochainement des résultats d'une telle confrontation.

# BIBLIOGRAPHIE

- [1] K.D. ANDERSON : "Inference of refractivity profiles by satellite-to-ground RF measurements", Radio Sc., Vol.17, N°3, pp.653-663, 1982.
- [2] V.A. FOCK : "Electromagnetic Diffraction and Propagation Problems", Pergamon Press, 1965, Chaps. 11, 13, 14.
- [3] F.D. TAPPERT, R.H. HARDIN : "Application of the split-step Fourier method to the numerical solution of nonlinear and variable coefficient wave equations", SIAM Rev., 1973, 15, p.423.
- [4] G.D. DOCKERY : "Modeling Electromagnetic Wave Propagation in the Troposphere Using the Parabolic Equation", IEEE, trans. on Antennas and Propagation, vol.36, n°10, October 1988.
- [5] A.R. MILLER, R.M. & M.A. BROWN, E. VEGH : "New derivation for the rough surface reflection coefficient and for the distribution of sea wave elevations", Proc.IEE-H, vol.131, n°2, April 1984.
- [6] N. DOUCHIN, S. BOLIOLI, P. COMBES : "Fluctuations analysis of a near the horizon satellite-ship path", Conference Proc. IEE, ICAP 91, Vol.2, pp.820-823, YORK, 15-18 April 1991.
- [7] H.V. HITNEY, R. VIETH : "Statistical Assessment of Evaporation Duct Propagation", IEEE trans. Antennas and Propagation, 1990, 38, N°6, 794-799.
- [8] K.H. CRAIG, M. LEVY : "A forecasting System Using the Parabolic Equation" 1989, AGARD CP-453.
- [9] J.C. BOLOMEY : "Réponse d'une antenne de réception à une onde incidente non plane", Annales des Telecom., Vol. 34, n°9-10, 1979.

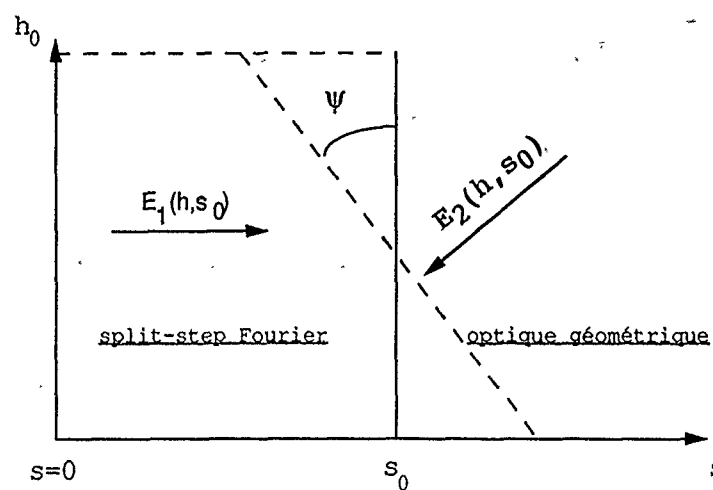


fig.1 - Schéma de principe du calcul du facteur de couplage.

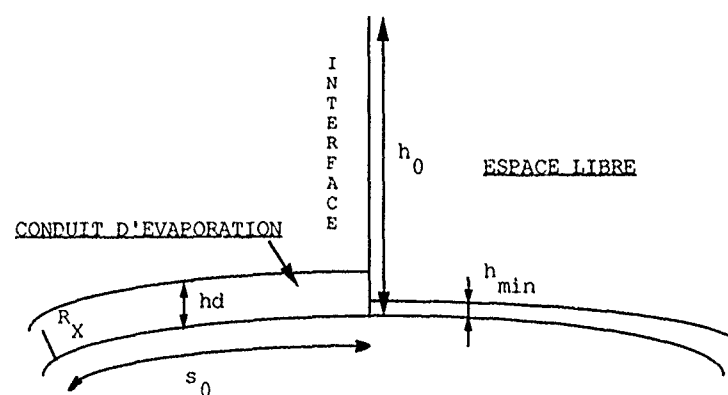


fig.2 - Schéma équivalent de la liaison calculée par la méthode du facteur de couplage.

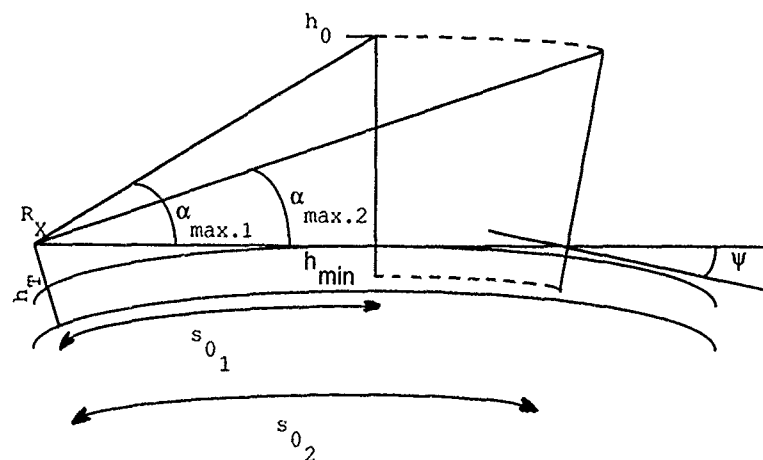


fig.3 - Evolution de  $\alpha_{\max}$  avec  $s_0$ .

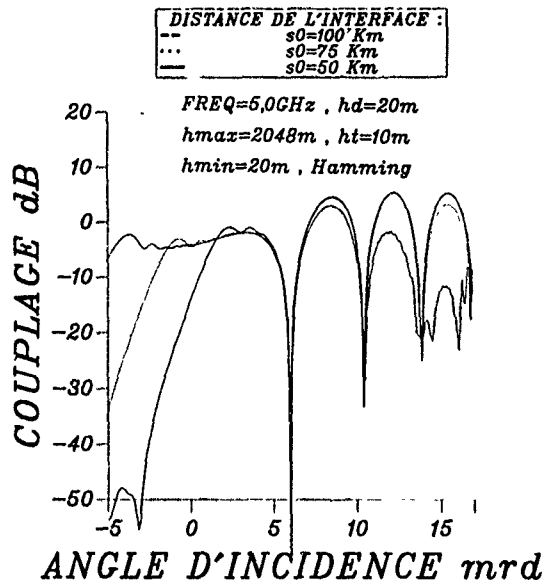
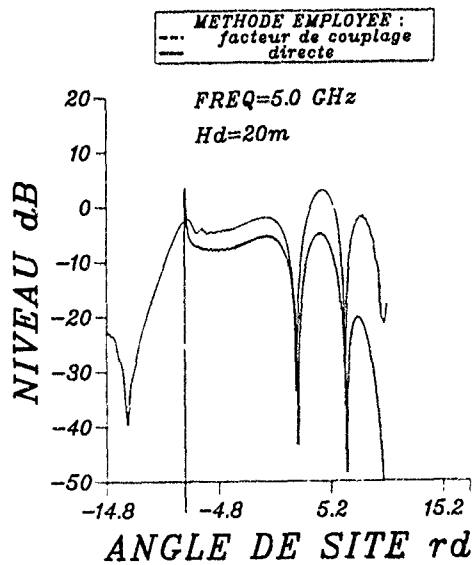
fig.4 - Couplage en fonction de  $y$  pour trois valeurs différentes de  $s_0$ .

fig.5 - Validation numérique de la méthode du facteur de couplage.

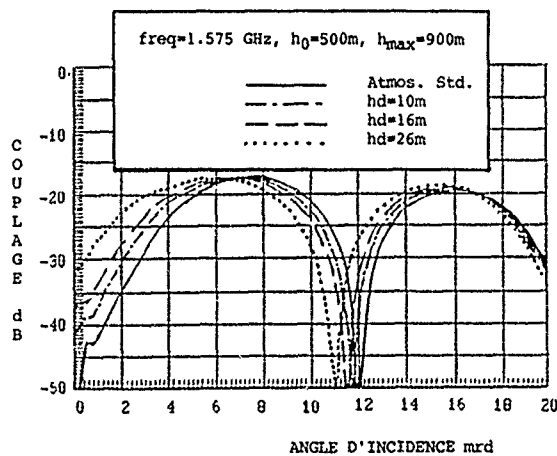
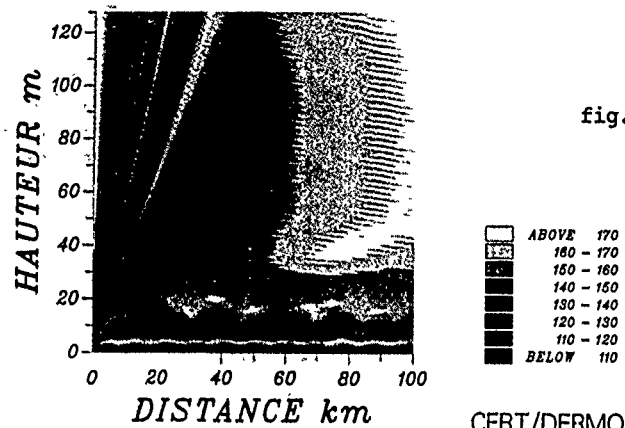
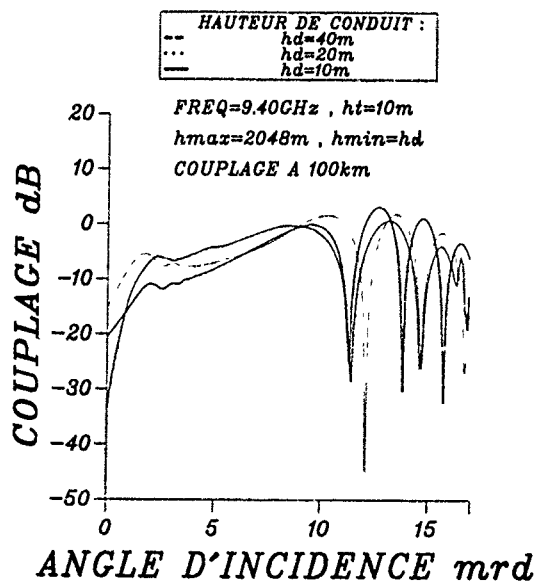
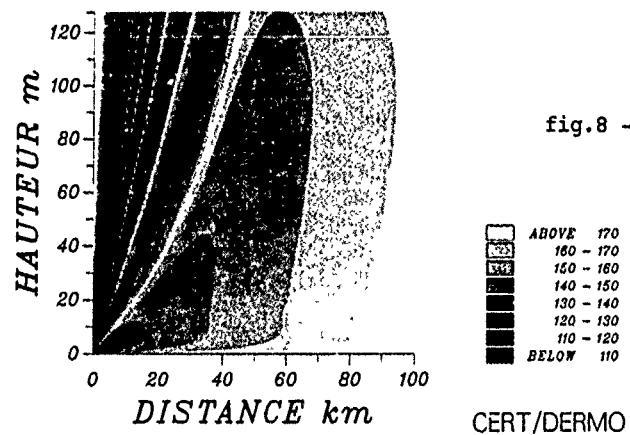


fig.6 - Couplage à 1,575 GHz.

PERTES PAR PROPAGATION A 9,40 GHz  
CONDUIT D'EVAPORATION DE 40m



PERTES PAR PROPAGATION A 9,40 GHz  
CONDUIT D'EVAPORATION DE 10m



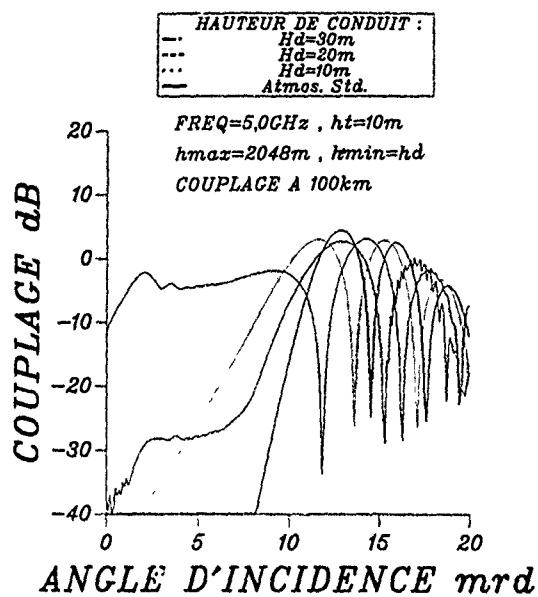


fig.10 - Couplage à 5,0 GHz.

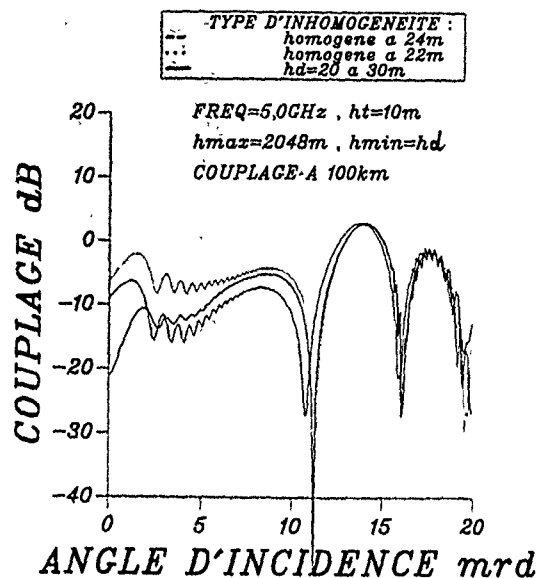


fig.12 - Influence de gradients horizontaux de l'indice de réfraction.

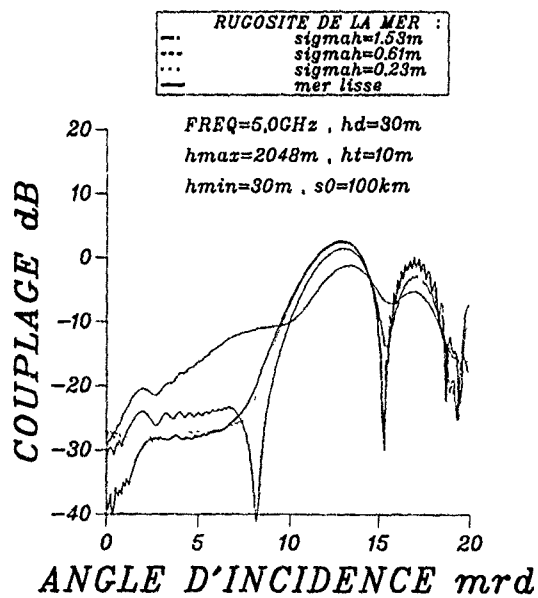


fig.11 - Cas de mer rugueuse.

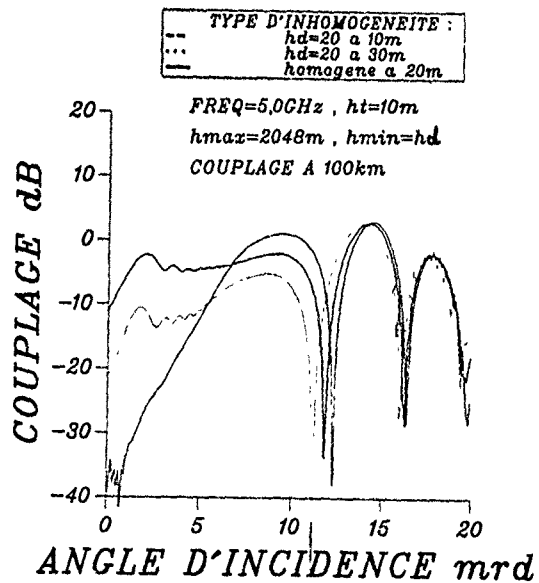


fig.13 - Comparaison entre conduits homogènes et conduit horizontalement inhomogène.

## DISCUSSION

### C. GOUTELAF

Vous avez fait allusion à l'effet ionosphérique, et j'ai cru comprendre que vous le négligiez. Pour le système NAVSTAR à 1.5GHz il ne me paraît pas sûr que l'effet soit négligeable surtout lorsque le satellite est à l'horizon, notamment lorsque des perturbations, notamment les TID sont présents. En fait, négligez-vous ou corrigez-vous les effets ionosphériques?

*You referred to ionospheric effects and I understood from what you said that you had chosen to ignore them. In the case of the NAVSTAR 1.5GHz, it does not seem to me that the effect is negligible, especially when the satellite is on the horizon and when interference, particularly TID, is present. Do you ignore or correct for ionospheric effects?*

### AUTHOR'S REPLY

Une analyse qualitative et quantitative au 1er ordre des effets de l'ionosphère dans cette bande de fréquence (1-18 GHz) a été menée. Elle a conduit à négliger les phénomènes d'absorption et de scintillation afin de simplifier le modèle. Cette dernière pourrait être prise en compte en ajoutant une composante aléatoire, rendant le modèle plus complexe. Outre ces deux phénomènes, seule la réfraction à grande échelle due au gradient d'indice peut être prise en compte simplement en considérant une rotation du front d'onde ( $\approx 1\text{mrad}$ ), et en introduisant un terme correctif sur la position réelle du satellite à un instant donné. L'ensemble de ces hypothèses sera confronté à des résultats expérimentaux qui détermineront si le modèle doit être amélioré; toutefois, la précision et la répétitivité raisonnablement envisageables sur ces expériences laissent entrevoir un bon fonctionnement du modèle simplifié ainsi qu'une bonne adéquation au problème posé.

*A first order qualitative and quantitative analysis of the effects of the ionosphere in this frequency band (1-18 GHz) was in fact carried out. It led us to ignore the phenomena of absorption and scintillation in order to simplify the model. The latter could be allowed for by adding a random component, making the model more complex. Apart from these two phenomena, only large-scale refraction due to the index gradient can be allowed for simply by considering a rotation of the wavefront ( $\approx 1\text{mrad}$ ) and introducing a corrective term to the true position of the satellite at any given time. All these hypotheses will be compared to the experimental results which will determine whether the model should be improved. However, the accuracy and repeatability which can be reasonably expected from these experiments promise satisfactory operation of the simplified model and suitability with respect to the problem posed.*

### J. BELROSE

For satellite-to-ground propagation, you spoke about transmission through the ionosphere and about transmission through the evaporation duct. For Canadian latitudes, propagation through the melting layer (ice above and rain below) and the ionosphere at time of severe high latitude ionospheric disturbance are the important parts of the propagation path. You did not mention propagation through the melting layer. From your studies, is propagation through the evaporation duct the dominant part of the propagation path at latitudes of your interest for satellite-to-ground communications (bearing in mind the elevation angle characteristic of the satellite path)?

### AUTHOR'S REPLY

Dans ce modèle de liaison satellite-navire, la plus grande partie du trajet effectué par l'onde électromagnétique ne s'effectue pas dans le conduit d'évaporation mais dans une zone considérée comme l'espace libre à ces fréquences. Toutefois, le principal objectif de cette étude réside dans la caractérisation du conduit à travers l'analyse d'une telle liaison. Nous n'avons pas encore envisagé l'extension aux latitudes plus froides, qui font intervenir d'autres phénomènes.

*In this satellite-ship model, most of the path travelled by the electromagnetic wave does not occur in the evaporation duct but in an area considered as free space at these frequencies. However, the main aim of the study is to characterise this duct by analysing this type of link. We have not yet envisaged extending the study to colder latitudes, which would bring in other phenomena*

# RADIO REFRACTIVITY PROFILES DEDUCED FROM AEROSOL LIDAR MEASUREMENTS

H. G. Hughes, M. R. Paulson and J. H. Richter

Ocean and Atmospheric Sciences Division  
Naval Ocean Systems Center  
San Diego, California 92152-5000

## 1. SUMMARY

A technique is presented for estimating radio wave ducting conditions from shipboard during cloud-free periods using a lidar (light detection and ranging) system to measure the power from a pulsed laser beam that is backscattered to a receiver from suspended particulates (aerosols) at different ranges. On individual days, the relative humidity measured with altitude using radiosondes launched simultaneously with vertical lidar shots, were highly correlated with the range-compensated power received by the lidar from the same altitude. However, the relationship between the power returns and the relative humidities changed from day to day, indicating an air mass characteristic dependence on the aerosols' optical parameters. Using a combined data set of 13 days, a linear relationship (correlation = 0.73) was determined between the relative humidity at a given altitude and the range-compensated power received by the lidar from the same altitude. While the magnitudes differed in most cases, the gradients in modified radio refractivity calculated using standard vertical lapse rates of temperature and pressure with the experimentally determined relationship were in close agreement with those calculated using the radiosonde measured parameters. Examples of radio signal coverage plots based on the lidar returns are presented and compared with those calculated from the radiosonde data for both elevated and ground-based ducting conditions.

## 2. INTRODUCTION

Balloon borne radiosondes or airborne refractometers are the established methods of determining atmospheric ducting conditions at sea for predicting radar coverages. The radiosonde requires radio signals to transmit the measured meteorological parameters (temperature, pressure and relative humidity) back to the ship. During periods when electromagnetic emissions are not permitted, the radiosonde cannot be utilized. Also, not all ships have radiosonde capability and airborne refractometer information may be available only to aircraft carriers. It has recently been demonstrated by Anderson (Ref 1) that the radiosonde information can be successfully transmitted from altitudes up to 2 km to the ship through a fiber optic tethering cable without violating emission control conditions. Because of the cost involved in obtaining a single refractivity profile, this technique has not yet been deployed in the fleet.

In this paper, the possibility of estimating radio wave ducting conditions is investigated using a lidar system to measure the power from a pulsed laser beam that is backscattered to a receiver from suspended particulate (aerosols) at different ranges. While gradients in temperature are contributing factors, it is the gradients in atmospheric moisture (or relative humidity) which generally determine the gradients in radio refractivity profiles. The relative humidity also has pronounced effect on atmosphere aerosols (suspended particulates). As the relative humidity increases, condensation of water vapor on particles containing water-soluble material cause their sizes, and, consequently, their cross-sections to optical backscatter to increase. Within the well-mixed marine boundary layer, relative humidities are usually high enough that most of the aerosols are hydrated, taking on a spherical shape. Thus, within the layer, the return to a lidar system from a given range can be expected to be directly related to relative humidity at that range. The return, however, will be strongly dependent upon the refractive indices of the aerosols, both at the scattering volume range and along the intervening path. Above the layer, where relative humidities are much lower, unactivated aerosols may be of irregular shape, and little correlation can be expected between their backscattering cross-sections and relative humidity.

## 3. MEASUREMENTS

Measurements of vertical lidar returns were conducted simultaneously with radiosonde launches from the Point Loma peninsula in San Diego in the fall of 1989. The lidar system employed in this study was the AN/GVS-5 rangefinder-based Visioceilometer which was developed by the U. S. Army Atmospheric Sciences Laboratory and has been described elsewhere (Ref 2). The system is a hand-held Nd:YAG laser which nominally emits a 10 mJ, 6 ns pulse at a wavelength of 1.06  $\mu\text{m}$ . The receiver telescope has an aperture of 5.1 cm with a 3 mrad field of view. The range at which the receiver field of view and the transmitter beam overlap is 112.5 m. A signal processing unit clocks the output of a silicon photoavalanche detector at a 20 MHz rate giving a 7.5 m sampling interval. The digitized results are transferred to a microprocessor and then to a Memoryne cassette tape recorder for off-line processing.

The radiosonde system employed was the VAISALA model RS80. When calibrated, the

system measures pressure, temperature and relative humidity with accuracies of  $\pm 0.5$  mb,  $\pm 0.2^\circ\text{C}$  and  $\pm 2\%$ , respectively.

The power  $P(r)$  returned to the lidar detector from a range  $r$  was adjusted to provide a range-compensated signal,  $S(r) = \ln[P(r)r^2]$ , as a function of altitude. While each lidar profile was essentially a snapshot of conditions at the moment, the balloon-borne radiosonde ascended about 200 meters per minute, and frequently drifted southeasterly over the land. Because the lidar frequently showed small-scale fluctuations that the radiosonde did not detect, a 9-point running average of the  $S(r)$  data for each profile was used in the comparison with the radiosonde data. An example of the radiosonde

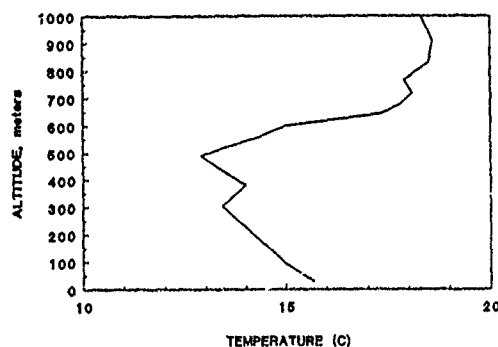


Figure 1. Radiosonde measurement of temperature versus altitude for 13 November 1989.

data taken on 13 November 1989 is shown in Figures 1 and 2b where the measured temperature and relative humidity are plotted versus altitude. Temperature inversions (i.e. an increase in temperature with altitude) occur near 300 m and 500 m which coincide with rapid decreases in relative humidity. In Figures 2a and 2b, the relative humidity (RH) variations with altitude are compared with the range compensated lidar return,  $S(r)$ , for the same day. While minor irregularities occur in both, the two profiles show similar responses to the two temperature inversions. A linear regression analysis was performed between the lidar range-compensated powers and the relative humidity at the corresponding altitudes on each of 13 different days. The regression coefficients ( $a$ =intercept,  $b$ =slope and  $\rho$ =correlation coefficient) for each of the measurement days are listed in Table 1.

While these data demonstrate a definite relationship between the relative humidity and lidar returns on individual days (as shown in Figure 3 for 13 September), there is a significant change in the relationship from day to day. In addition to the temporal and spatial differences between the lidar and radiosonde measurements, the differing relationships most likely are a

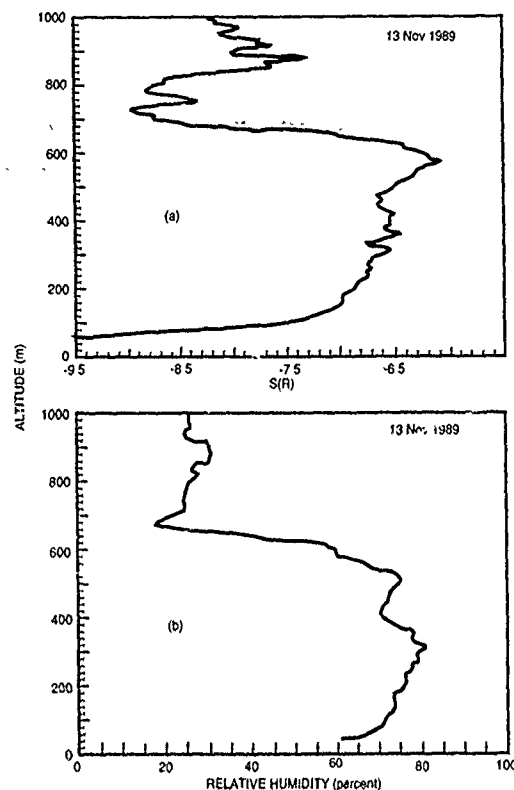


Figure 2. (a) Lidar range-compensated power return,  $S(R)$ , versus altitude for 13 November 1989. (b) Relative humidity, RH, versus altitude for 13 November 1989.

result of the change in the composition of the aerosol from day to day. The extent of this variability is evident from Figure 4 where a linear regression analysis between the relative humidity and range-compensated power was performed using the entire data set to give the relationship,  $RH = 181.9 + 18.5S(r)$ , with  $\rho = 0.73$ . Vertical changes in air mass characteristics may also explain

Date	a	b	$\rho$
12 Sept	241.5	28.4	0.95
13 Sept	178.1	20.8	0.92
18 Sept	218.0	21.6	0.72
20 Sept	226.3	22.8	0.93
26 Sept	270.5	34.3	0.95
27 Sept	305.4	35.4	0.96
28 Sept	304.9	34.1	0.93
29 Sept	186.3	17.8	0.82
2 Oct	234.9	25.1	0.94
3 Oct	328.4	42.1	0.97
24 Oct	161.5	12.1	0.95
13 Nov	219.9	22.4	0.72
21 Nov	378.9	48.4	0.85

Table 1. Linear regression coefficients for relative humidity as a function of range compensated lidar return,  $[RH = a + bS(r)]$

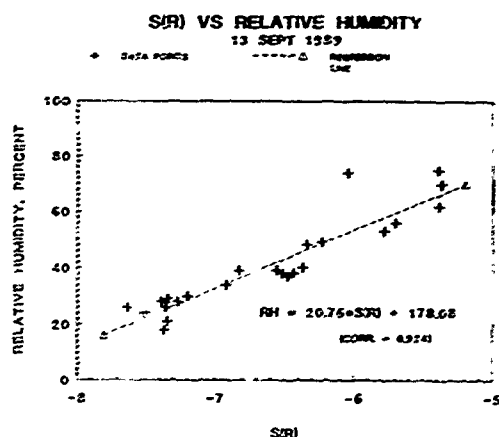


Figure 3. Lidar range-compensated power return,  $S(R)$ , versus relative humidity for 13 September 1989.

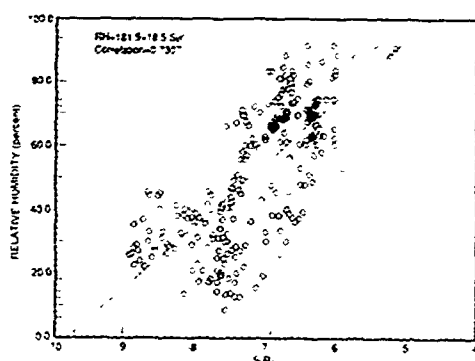


Figure 4. Relative humidity versus lidar range-compensated power return for complete data set listed in Table 1.

vertical variations in the relationship between RH and lidar return for an individual profile.

#### 4. CALCULATION OF REFRACTIVITY PROFILES

Since the real part,  $n_r$ , of the refractive index of air is very close to unity, it is practical to define the "refractivity" of air as  $N = (n_r - 1)10^6$ . For radio waves, the empirical formula for the refractivity is given by (Ref 3)

$$N = \frac{79P}{T} - \frac{11e}{T} + \frac{3.8 \times 10^5 e}{T^2} \quad (1)$$

where  $P$  is the barometric pressure (rb),  $T$  is the temperature (K), and  $e$  is the ambient

water vapor pressure (mb). The ambient water vapor pressure,  $e$ , is related to the saturation water vapor pressure,  $e_s$ , by

$$e = e_s \frac{RH}{100} \quad (2)$$

where RH is the relative humidity in percent and the saturation water vapor pressure can be determined from (Berry et al., 1945)

$$e_s = 6.105 \exp\left[25.22\left(\frac{T - 273.2}{T}\right) - 5.31 \ln\left(\frac{T}{273.2}\right)\right] \quad (3)$$

In raytrace diagrams, it is often convenient to modify the vertical refractivity profile so that the earth may be treated as flat. This leads to the modified refractivity relationship

$$M(h) = N(h) + (h/a) \times 10^6 = N(h) + .153h \quad (4)$$

where  $h$  and  $a$  (earth's radius) are in meters.

In the marine boundary layer, the actual percentage variations of pressure from a standard atmosphere are relatively small, so the pressure of the atmosphere is not a significant factor in creating non-standard refraction. In equation 1, the second term is generally small compared to the third and may be neglected. The actual percentage variations of water vapor from a standard atmosphere are often large in the marine environment, such that water vapor content is the most significant factor. However, the presence of  $T$  and  $T^2$  as denominators of

#### MODIFIED REFRACTIVITY VS. ALTITUDE 13 NOVEMBER 1989

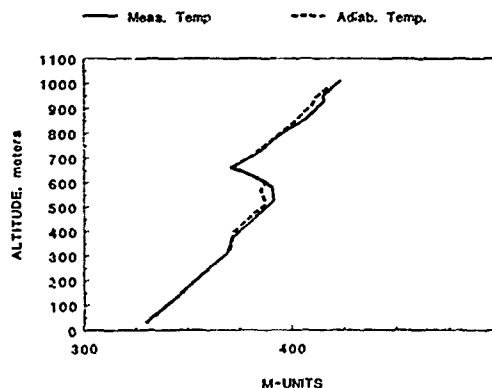


Figure 5. Modified radio refractivity versus altitude calculated using radiosonde measurements of pressure, relative humidity and temperature (solid line) and that calculated with a dry adiabatic lapse rate in temperature.

the pressure and moisture terms and the fairly large percentage variations in  $T$  from a standard atmosphere makes the temperature the other significant factor. If the lidar is to be used as a "stand-alone" instrument for determining refractivity profiles, some assumptions must be made concerning the variations of temperature with altitude. Figure 5 shows the M-unit variations with altitude which were calculated using the measured pressure, temperature and relative humidity profiles and those calculated with a dry adiabatic lapse rate in temperature ( $-0.01^\circ\text{C/m}$ ) referenced to the surface measurement. The close agreement between the two profiles demonstrates the relative insensitivity of the M-unit calculations to the variations in temperature for the southern California data set. Whether the same is true for other locales needs to be determined.

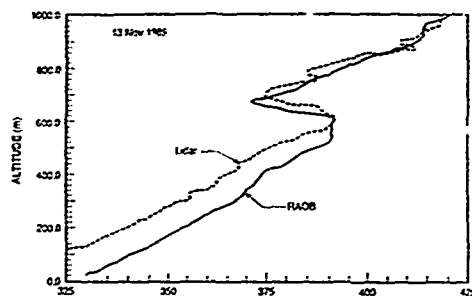


Figure 6. Comparison of M-unit profiles calculated using standard lapse rates of temperature and pressure with the profiles of relative humidity determined from the lidar returns and those calculated from the radiosonde data on 13 November 1989.

In Figure 6, M-unit profiles calculated using standard lapse rates of temperature with the profiles of relative humidity determined from the lidar returns are compared with those calculated from the radiosonde data for the elevated ducting conditions on 13 November (Figure 1). In the calculations using the lidar data, a standard lapse rate of pressure ( $-0.12\text{ mb/m}$ ) from the measured surface value was assumed. This assumption is justified since in the marine boundary layer the actual percentage variations of pressure from a standard atmosphere are relatively small. While there are differences in the magnitudes of the two curves (which may be related to the aforementioned reasons), the gradients in the modified refractivity profiles calculated with the lidar data show quite good agreement with those calculated from the radiosonde data.

An example of the radiosonde data taken on 29 September 1989 is shown in Figure 7 for the case of a ground-based duct. On this day, the M-unit profiles calculated using the lidar data with standard lapse rates of temperature and relative humidity deviate significantly from those calculated using

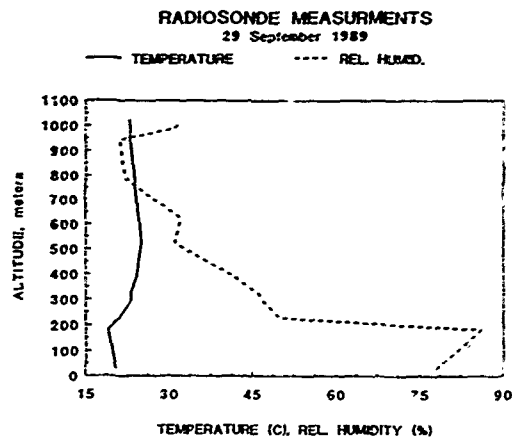


Figure 7. Radiosonde measurements of temperature and relative humidity versus altitude for 29 September 1989.

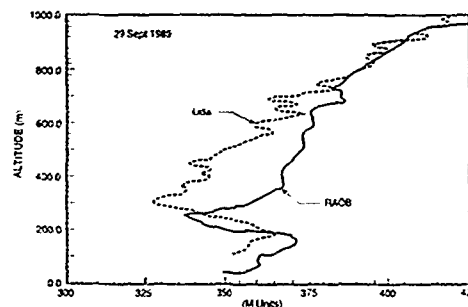


Figure 8. Comparison of M-unit profiles calculated using standard lapse rates of temperature and pressure with the profiles of relative humidity determined from the lidar returns and those calculated from the radiosonde data on 29 September 1989.

the radiosonde data (Figure 8). However, the gradients in both profiles are in good agreement below and through the top of the shallow inversion.

##### 5. COMPARISON OF RADIO SIGNAL COVERAGES

A ray-trace program in the computer code EREPS (Engineer's Refractive Effects Prediction System) (Ref 5) was used to calculate and plot radio signal coverage diagrams for the radiosonde and lidar determined refractivity profiles. Examples calculated using the elevated and ground-based ducting conditions are shown in Figures 9-11. Figure 9a shows the area of coverage on a flat-earth, range-versus-height plot for the elevated ducting condition calculated using refractivity profile determined from the radiosonde data. Figure 9b shows the coverage calculated using the lidar determined refractivity profile. This example is for a

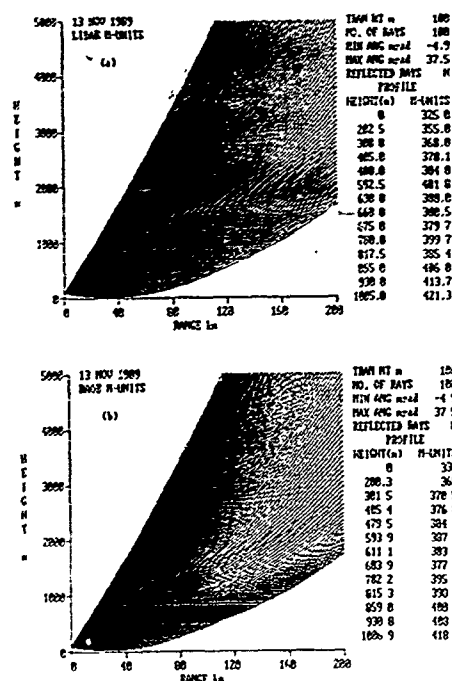


Figure 9. Radio-signal coverage diagrams predicted using M-units determined from (a) lidar data and (b) radiosonde data on 13 November 1989 for a transmitter height of 100 m.

hypothetical transmitter antenna being 100 m above sea level with viewing angles below and above the horizontal of  $-4.9$  mrad and  $37.5$  mrad, respectively. The shaded area in each display corresponds to an area of coverage. The similarity of the coverage diagrams in Figures 9a and 9b is expected since coverage is not dependent on the properties of the elevated duct above. Elevated ducts do, in general, not affect surface-based emitters. If, however, the transmitters were located at a height of 600 m (within the elevated duct) as shown in Figures 10a and 10b, energy is channeled within the duct and a hole in coverage observed just above it. Figures 11a and 11b show coverages for a transmitter located within a ground-based duct using the radiosonde and lidar determined refractivity profiles, respectively. In both of these examples, the coverages predicted with the lidar and radiosonde data are in good agreement. Equally good agreements were obtained for the rest of the data set listed in Table 1.

## 6. CONCLUSIONS

The agreement between the M-unit profiles using the lidar and radiosonde data might be improved upon if a measure of the air mass characteristics could be included in a multiple regression equation relating relative humidity to range-compensated power return of the lidar. While the magnitudes of the M-unit profiles calculated using the lidar and radiosonde data differ, calcula-

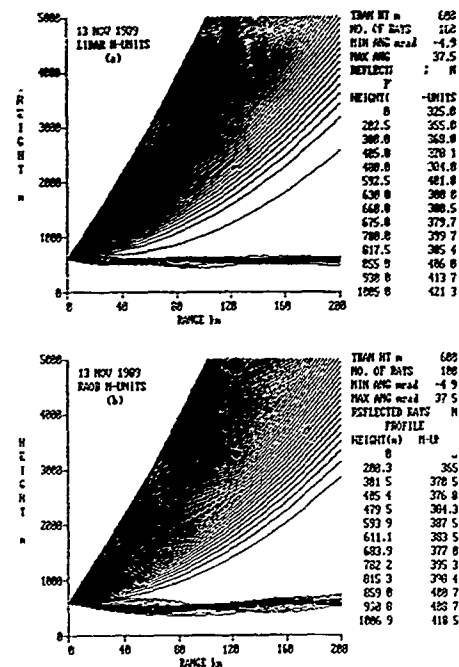


Figure 10. Radio-signal coverage diagrams predicted using M-units determined from (a) lidar data and (b) radiosonde data on 13 November 1989 for a transmitter height of 600 m.

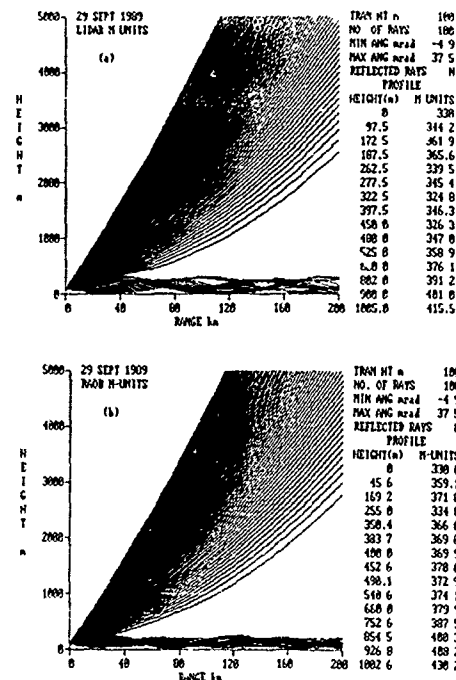


Figure 11. Radio-signal coverage diagrams predicted using M-units determined from (a) lidar data and (b) radiosonde data on 29 September 1989.

tions of radar coverages do not appear to be sensitive to these differences, but rather to the gradients in refractivity. This study has demonstrated that useful radio refractivity information can be obtained from aerosol lidars during cloud-free periods. This approach allows ducting information to be obtained by small ships which are not equipped with radiosonde systems, permits more frequent or continuous assessment of ducting conditions, and involves no radio transmissions (like the radiosonde) which may be intercepted at far away distances.

#### 7. ACKNOWLEDGEMENT

This work was supported by the Office of Naval Technology.

#### 8. REFERENCES

1. Anderson, K. D., "Fiber-Optic Refracti-sonde: Final Report," Naval Ocean Systems Center Technical Report 1403, May 1991.
2. Lindberg, J.D., W. J. Lentz, E. M. Measure and R. Rubio, "Lidar Determinations of Extinction in Stratus Clouds," Appl. Opt., 23, 2172-2177, (1984).
3. Reed, H.R. and C. M. Russel, Ultra High Frequency Propagation, Boston Technical Publishers, Inc., Cambridge, MA., 1966.
4. Berry, F.A., E. Bollay and N. R. Beers, Handbook of Meteorology, McGraw-Hill Book Company, Inc., New York, 1945.
5. Hitney, H. V., A. E. Barrios and G. E. Lindem, "Engineer's Refractive Effects Prediction System (EREPS)," Naval Ocean Systems Center Technical Document 1342, July 1988.

#### DISCUSSION

##### J. GOLDBIRSH

*How do you measure refractivity N using radar?*

##### AUTHOR'S REPLY

*Through a relationship derived by Gossard which connects refractivity with the structure parameters of refractivity and wind velocity which can be sensed by radar. I'll let Dr. Gossard explain this in more detail.*

##### E. GOSSARD

*Surface-based radars can measure elevated gradients of the refractive index through a relationship which connects the gradient of refractivity with parameters that are measured by Doppler radars (see equation (36) of Gossard, E.E. and N. Sengupta, "Measuring gradients of meteorological properties in elevated layers with a surface-based Doppler radar," Radio Science, Vol. 23(4), pp. 625-639, 1988).*

*Whenever reflective layers are present as determined by raob, the clear-air profilers do, indeed, show enhanced backscatter from such layers. Unfortunately, the converse is not true and the profilers often show backscatter from zones that the raob indicates do not have substantial gradients in refractive index. The reason is that many phenomena cause backscatter of radar waves in addition to the turbulent fluctuations of clear-air refractive index associated with the elevated gradients of refractive index that we wish to detect. Such extraneous scatterers include insects and especially clouds. Even at the relatively long wave lengths that have been used for clear-air wind profilers (e.g. 33 cm wavelength), even scattered clouds can compete effectively with the weak signals from the clear air.*

## USE OF MESOSCALE MODELS FOR REFRACTIVITY FORECASTING

M.F. Levy and K.H. Craig  
Radio Communications Research Unit  
Rutherford Appleton Laboratory  
Chilton, Didcot, OX11 0QX  
United Kingdom

### SUMMARY

Three-dimensional forecasts of sensor performance require accurate predictions of refractivity features. Numerical weather models like the U.K. mesoscale model have become sufficiently powerful to provide good refractivity maps. These in turn provide environmental input for parabolic equation models to forecast microwave propagation. This paper briefly describes the U.K. mesoscale model and its application to forecasting sensor performance.

### 1 INTRODUCTION

In recent years, powerful models based on parabolic equation (PE) techniques have been developed to provide predictions for microwave propagation in the troposphere [1]. PE models are extremely flexible, allowing the user to vary frequency, polarization, antenna height and beam pattern, and to specify an arbitrary refractivity structure. Reliable quantitative three-dimensional refractivity forecasts are essential in order to make full use of these methods.

Radiosonde profiles give good vertical resolution, but cannot provide horizontal coverage. Remote sensing by satellites of refractivity profiles is not currently feasible, and it is unlikely that sufficiently refined inversion techniques can ever be developed, in particular for humidity profiles. However parameters like sea surface temperature can now be measured very accurately by satellite. Indirect use of such satellite data through their incorporation into numerical weather models is invaluable for horizontal coverage.

In situations where the 3D variations of the refractivity structure are important, a promising option is to use a numerical weather model incorporating many diverse data sources. With the enormous increase in computer power, numerical weather models have now reached the point where detailed modelling of humidity is available, thus making the forecasting of refractivity structure possible.

### 2 U.K. MESOSCALE MODEL

In 1982, the U.K. Meteorological Office introduced a 15-level numerical weather prediction computer model to provide guidance of forecasters on timescales of 12 hours to 6 days. The regional 15-level model,

which covers the North Atlantic and Europe, has a gridlength of 75 km. The regional model is too coarse to include topographic effects, and does not provide good forecasts of humidity and precipitation.

The mesoscale model developed by the UK Meteorological Office was introduced in order to improve humidity forecasts [2]. It has been in operational use since 1989.

The model has a horizontal resolution of 15 km, and covers the British Isles and most of the North Sea. Figure 1 shows the coverage and horizontal resolution of the U.K. mesoscale model; the map was drawn directly from the orographic height information in the model output. The horizontal gridlength allows a reasonable representation of the orography and coastline, although narrow valleys and steep mountains cannot be represented.

More sophisticated models of boundary layer and surface processes are used than in the regional model, resulting in much better modelling of humidity. Good forecasts can be obtained for parameters like cloud cover, cloud base, visibility and precipitation.

Currently the model produces a 24 hour forecast, with a data assimilation process every 3 hours. The model is closely tied to the regional model, which is used to define boundary conditions. Output from the model includes initial output fields, that is to say the fields obtained right after data assimilation, and forecasts ranging from 3 hour to 24 hour.

The vertical coordinate system is based on the height above the local terrain. Initially the model included 16 vertical levels, with only 6 levels below 2 km. In summer 1990, the vertical resolution was increased to 32 vertical levels, with 15 levels between the ground and 1020 m. Table 1 gives the model levels below 3 km.

A weakness of the current mesoscale model is that it makes no attempt to use radiosonde data directly. The system relies on the regional model data assimilation scheme to analyse radiosonde ascents and incorporate them as part of the background fields [3]. Hence the detailed vertical structure of the ascents is often lost. New data assimilation schemes allowing use of profile data will be introduced next year.

level	height (m)	level	height (m)
1	1.25	11	355.00
2	2.50	12	480.00
3	5.00	13	630.00
4	10.00	14	810.00
5	20.00	15	1020.00
6	40.00	16	1265.00
7	70.00	17	1550.00
8	115.00	18	1880.00
9	175.00	19	2260.00
10	255.00	20	2695.00

Table 1: Mesoscale model levels below 3 km

Refractivity profiles obtained from mesoscale output have been compared to minisonde measurements, with very encouraging results: absolute values of refractivity at the model levels were within 2% of minisonde results. The comparisons were for a coastal site in the south of England in June 1989; at that time only the lower vertical resolution mesoscale model was available. Table 2 shows the percentage errors for each parameter at each of the mesoscale model levels, given in terms of pressure; the temperature error is calculated on the absolute temperature scale. In terms of percentage error in refractivity, the two measurements agree remarkably well. As expected, the water vapour pressure has greater error, although this becomes less significant at greater heights where the dry term in the refractive index formula dominates.

### 3 INTERPOLATION USING POTENTIAL TEMPERATURE

Initially we had hoped to use mesoscale model output to provide a physically meaningful interpolation procedure between radiosonde profiles. The idea was to identify air masses using isentropic coordinates based on equivalent potential temperature, and to use linear interpolation along isentropic lines.

The potential temperature  $\theta$  is defined as the temperature a parcel of air (at temperature  $T$  and pressure  $P$ ) would have if moved isentropically to a reference pressure  $P_0$ , usually 1000 mb. Using the first law of thermodynamics, one can derive the formula

$$\theta = T(P_0/P)^{R_m/c_p}, \quad (1)$$

where  $R_m$  is the specific gas constant of air and  $c_p$  is the specific heat of air at constant pressure [4]. For dry air,  $R_m/c_p = 0.286$ . The variations due to water vapour are usually neglected.

The use of potential temperature eliminates variations due to pressure, but does not take humidity variations into account. For the identification of air masses, it is preferable to use the equivalent potential temperature  $\theta_e$ , which is defined as the temperature a parcel of

air would have if lifted adiabatically until saturation occurs, and then lifted adiabatically until all the moisture has condensed. The equivalent potential temperature is given approximately by

$$\theta_e = \theta \left(1 + \frac{Lw}{c_p T_s}\right), \quad (2)$$

where  $L$  is the latent heat of vaporization,  $w$  is the water vapour mixing ratio and  $T_s$  is the temperature at adiabatic saturation point.  $T_s$  can be calculated using a fixed point method and an approximation to the Clausius-Clapeyron equation.

Equivalent potential temperature can differ substantially from potential temperature: for example for  $P = 1000$  mb and  $T = 300$  K, we have  $\theta = T = 300$  K, while  $\theta_e = 356$  K for saturated air and  $\theta_e = 328$  K for air at 50% relative humidity.

In ducting situations, equivalent potential temperature can be a very useful indicator of layering structures. Figure 2 shows the  $\theta_e$  profile for the De Bilt radiosonde ascent of 2 August 1990 at midday, with the corresponding profile of modified refractivity. This anticyclonic situation is typical of North-West Europe [5]; the discontinuities of the  $\theta_e$  profile are due to a subsiding dry air mass above 1300 m, and advected dry air below 60 m. The modified refractivity profile exhibits a surface duct and a strong elevated duct corresponding to the  $\theta_e$  features.

The situation is not always so clear-cut: the  $\theta_e$  features can be rather complex and difficult to track between vertical profiles. It proved difficult to implement interpolation between radiosondes along isentropic lines. The example we describe below highlights the difficulties of the interpolation approach, and shows the potential of the model for direct use.

The map of Figure 3 shows the location of the radiosonde stations at Hemsby, De Bilt and Essen. Figure 4a shows the  $\theta_e$  profiles obtained from the radiosonde ascents at Hemsby, De Bilt and Essen on 2 August 1990 at 0:00 GMT. The graphs have been offset for easy comparison with Figure 4b. The variations of  $\theta_e$  cannot be described simply, particularly at Hemsby, and it is far from clear how the structures evolve horizontally between the radiosondes.

Figure 4b shows profiles extracted from the mesoscale initial output along the Hemsby-Essen line for the same time. The mesoscale profiles are 45 km apart and have been offset by 20°K for legibility. The mesoscale model has been unable to reproduce the complex features of the Hemsby ascent; it would have performed better with finer vertical resolution, and direct input of radiosonde information. The structure at De Bilt is quite well captured, but the model performs badly at Essen: this is certainly due to boundary problems, as Essen is at the edge of the coverage region of the model.

It is not straightforward to determine isentropic lines. A good automatic procedure would involve complex pattern recognition techniques, and would be lengthy to develop. Then comes the problem of matching the mesoscale derived structure to the radiosonde profiles. This will become easier as the mesoscale model evolves to have sufficient vertical resolution to capture most refractivity features. However at that point, one might as well make direct use of the mesoscale output. We consequently examined the direct use of current mesoscale output for refractivity forecasting.

#### 4 3D VARIABILITY

The mesoscale results showed a surprising amount of horizontal variability. A good example is the horizontal variation of the height of the surface duct which was present over most of the region of interest on 2 August 1990 at 0:00 GMT. Figure 5 shows contours of the advection duct height. There is a clear discontinuity between the North Sea and the English Channel. The contour lines tend to follow the coast, but the variations remain strong even at large distances from the coast.

What is needed ultimately is a forecast of radar performance based on the refractivity maps extracted from mesoscale output. Currently only parabolic equation models are capable of utilizing 2-dimensional refractivity data [1]. Each PE simulation calculates path loss values in a given vertical plane. In order to get a full 3-dimensional picture of the situation, it is necessary to run the PE model for several azimuthal directions.

The following examples show the potential of coupling parabolic equation techniques with mesoscale model output. Simulations were carried out for a site in North Yorkshire, using mesoscale results for 2 August 1990 at 0:00 GMT. The map of Figure 6 shows the location of the antenna and the radials used in the simulations. Figure 7 shows path loss contours for a 3 GHz antenna located 75 m above sea level, in 4/3 Earth conditions. Figure 8 shows modified refractivity profiles extracted from the mesoscale output along the 3 radials of interest. The profiles are taken at 45 km intervals along each radial. The graphs have been offset by 40 M-units for legibility.

Figure 9 shows parabolic equation simulations using the data in Figure 8. Anomalous propagation is taking place along all three radials, but there is strong azimuthal variability, with stronger surface ducting in the southern direction.

#### 5 SSR DATA

The validation of mesoscale/PE techniques is a difficult problem. Direct comparisons of mesoscale output to radiosonde measurements have been carried out with encouraging results, and more of these need to be made. However such comparisons are of neces-

sity limited in time and space, and do not give a global assessment of the model.

In any case the ultimate purpose of the exercise is to produce propagation forecasts, and perhaps the model ought to be judged on its propagation results rather than on its performance as a refractivity forecasting tool. Here again it is difficult to carry out extensive quantitative validation. Expensive airborne trials involving detailed measurements of refractivity and RF signal at 400 MHz have shown the usefulness of the PE method [6]. This type of verification is necessary and should be carried out at higher frequencies, but can only give very localized results.

A more global comparison can be provided by the monitoring of secondary surveillance radar returns from targets of opportunity. This has also been identified as a source of qualitative assessment of anaprop in its own right [7]. SSR responses are routinely monitored by the U.K. Civil Aviation Authority. The map in Figure 10 shows the location of the Debden CAA radar, which operates at a frequency of 1 GHz, and has an operational range of 172 nautical miles. The circular coverage area of the Debden radar is indicated on Figure 10, together with the main airports within range. On days of strong anaprop, returns are obtained from aircraft landing or taking off at Schiphol airport which is normally below the radio horizon.

From the height, range, azimuth and time information included in the SSR responses, it is possible to plot the positions of observed aircraft in a given time interval. Figure 11 shows an example of such a plot when no anaprop is present, for the angular sector between 45° and 135° (see Figure 10). The parabola indicates the 4/3 Earth horizon.

When anaprop is present, aircraft tracks become visible well below the horizon, sometimes right down to the ground. Figure 12 shows SSR responses in the 45°-135° sector between 10:00 GMT and 14:00 GMT on 1 August 1990. The parabolic equation path loss contours obtained from the mesoscale model initial output for 12:00 GMT on 1 August 1990 are shown in Figure 13. Strong anaprop is visible on both Figure 12 and Figure 13. The PE simulation shows a weak surface duct. Although the duct has resulted in extended SSR surface coverage, aircraft landing at Schiphol are lost before reaching the ground. Also note the radar hole in the PE/mesoscale forecast above the low ducting area: this hole is also visible in the SSR data. (A more detailed analysis of the data of Figure 12 shows that most of the aircraft visible at low altitude lie in the 105°-135° sector; the descending tracks near maximum range lie in the 75°-105° sector and disappear at low altitude).

Figure 14 shows the diurnal variation of anaprop on 1 August 1990: the 6 plots each show 4 hours of SSR data in the 45°-135° sector. Anaprop is at its strongest in the morning, with aircraft visible below

the horizon right down to the ground. The low level coverage reduces somewhat in the afternoon, but is seen to return in the late evening, despite less intense air traffic. This diurnal variation could in principle be forecast using the PE with mesoscale model 3-hourly output; this is still under investigation.

## 6 CONCLUSIONS

The extraction of 3D refractivity maps from mesoscale model output is now a realistic alternative to direct measurements of refractivity. The U.K. Meteorological Office mesoscale model already has the capability of providing refractivity forecasts. As the model evolves to allow better vertical resolution and direct assimilation of radiosonde profile data, the quality of refractivity forecasts should improve.

Propagation solvers based on the parabolic equation method provide an ideal tool for exploiting 3D refractivity information. We have shown here the potential of a coupled PE/mesoscale package for 3D anaprop forecasting.

Future work will focus on the difficult and expensive process of validation. While case studies using radiosonde and RF measurements are essential, comparisons with SSR returns provide a useful qualitative assessment of PE/mesoscale predictions. Besides this validation role, the monitoring of SSR returns gives an easily understandable display of propagation conditions at selected sites. This technique would function quite well as a complement to a quantitative forecasting package based on mesoscale output.

## REFERENCES

- [1] Craig, K.H., and Levy, M.F., Parabolic equation modelling of the effects of multipath and ducting on radar systems, *IEE Proc. F* **138**, 153-162, 1991.
- [2] Golding, B.W., The Meteorological Office mesoscale model, *Met. Mag.* **119**, 81-96, 1990.
- [3] Wright, B.J. and Golding, B.W., The interactive mesoscale initialization, *Met. Mag.* **119**, 234-244, 1990.
- [4] Fleagle, R.G. and Businger, J.A., *An Introduction to Atmospheric Physics*, Academic Press, 1980.
- [5] Bye, G., Radio-meteorological aspects of clear-air anomalous propagation in NW Europe, *Br Telecom Technol J* **6**, 1988.
- [6] Levy, M.F., Craig K.H., et al, Airborne measurements of anomalous propagation over the English Channel, *IEE Conf. Proc.* **333**, 1.173-176, 1991.
- [7] Taylor, G.N. and Craig, K.H., Exploitation of anomalous tropospheric propagation in long range air defence radar systems, *AGARD CP* **486**, 1991.

## ACKNOWLEDGEMENTS

Mesoscale data were made available to us by the Short Range Forecasting Division of the Meteorological Office. We particularly wish to thank Mrs. S. Ballard for her continuing help. Thanks are also due to the Meteorological Office for providing radiosonde data.

Thanks are due to the Civil Aviation Authority for the SSR data.

We thank British Telecom Research Laboratory for their assistance in selecting anaprop events.

This work has been carried out with the support of Procurement Executive, Ministry of Defence.

Press (mb)	Temp (C)		Err (%K)	wvp (mb)		Err (%)	Refract (N)		Err (%)
	sond	meso		sond	meso		sond	meso	
1020	23.2	21.3	-0.7	15.6	14.2	-9.3	333.5	329.8	-1.1
1008	22.9	20.0	-1.0	14.8	13.8	-6.7	327.3	326.8	-0.2
985	21.2	18.0	-1.1	13.8	13.3	-3.4	319.3	321.1	0.6
950	18.6	15.1	-1.2	12.1	12.6	3.9	306.0	312.5	2.1
906	15.2	12.8	-0.8	9.6	9.1	-5.8	287.0	287.3	0.1
854	13.3	11.7	-0.6	4.8	6.2	27.5	253.4	260.9	0.4
794	11.5	10.2	-0.5	3.8	3.4	-9.1	233.7	233.4	-0.1

Table 2: Relative errors between minisonde and mesoscale data



Figure 1: The UK Meteorological Office mesoscale model grid.

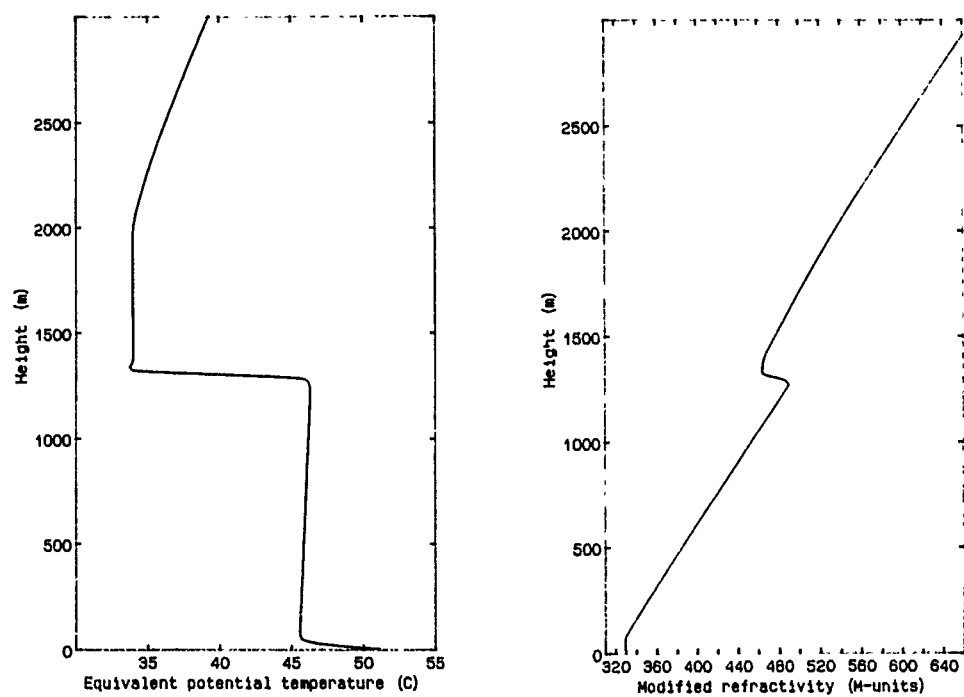


Figure 2: Equivalent potential temperature and modified refractivity profiles from the De Bilt midday radiosonde ascent on 2 August 1990.

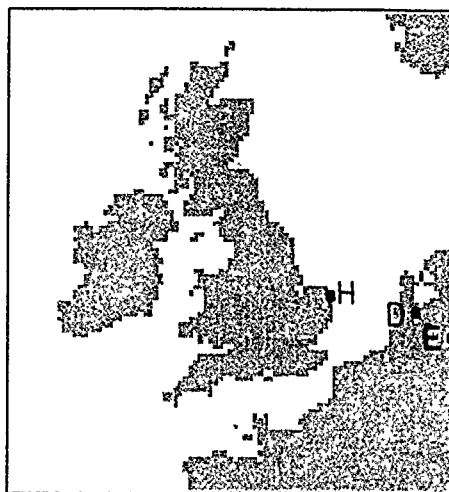


Figure 3: Locations of Hemsby (H), De Bilt (D) and Essen (E) radiosonde stations.

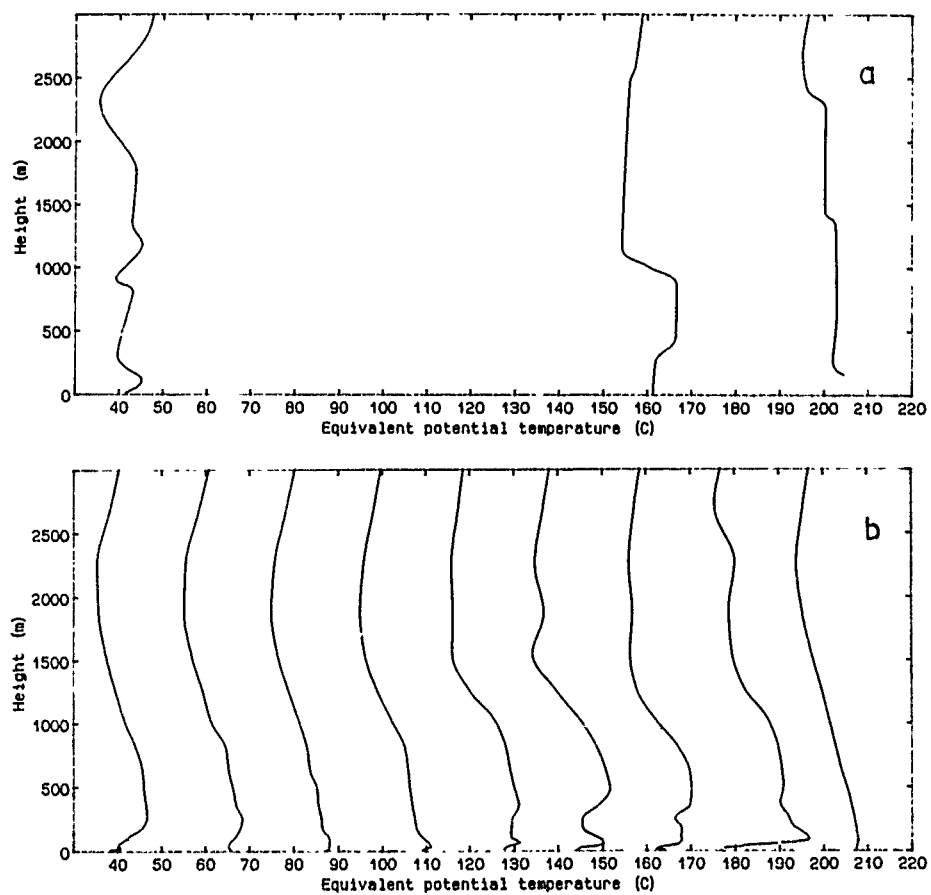


Figure 4: Equivalent potential temperature profiles at 0:00 GMT on 2 August 1990 derived from (a) radiosonde ascents; (b) mesoscale model output.

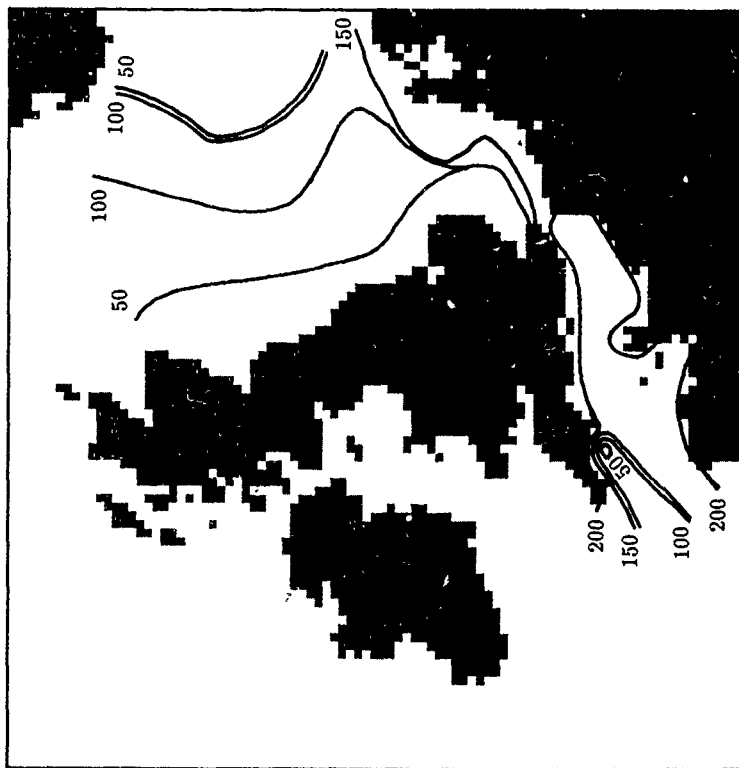


Figure 5: Contours of the advection duct height (m) at 0:00 GMT on 2 August 1990, derived from mesoscale model output.



Figure 6: Location of antenna and the radials used for the results shown in Figures 8 and 9.

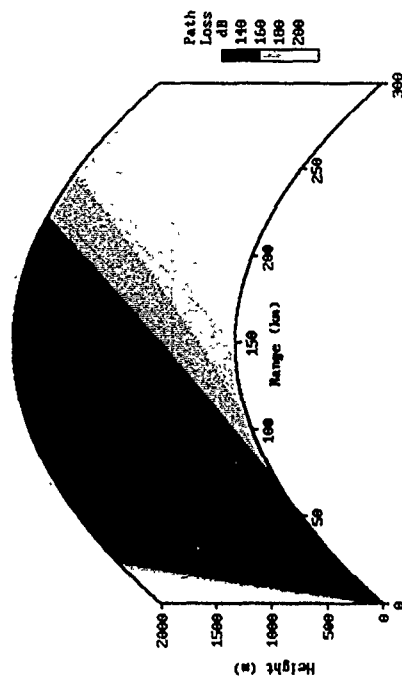


Figure 7: Path loss contours for a 3 GHz antenna in standard conditions.

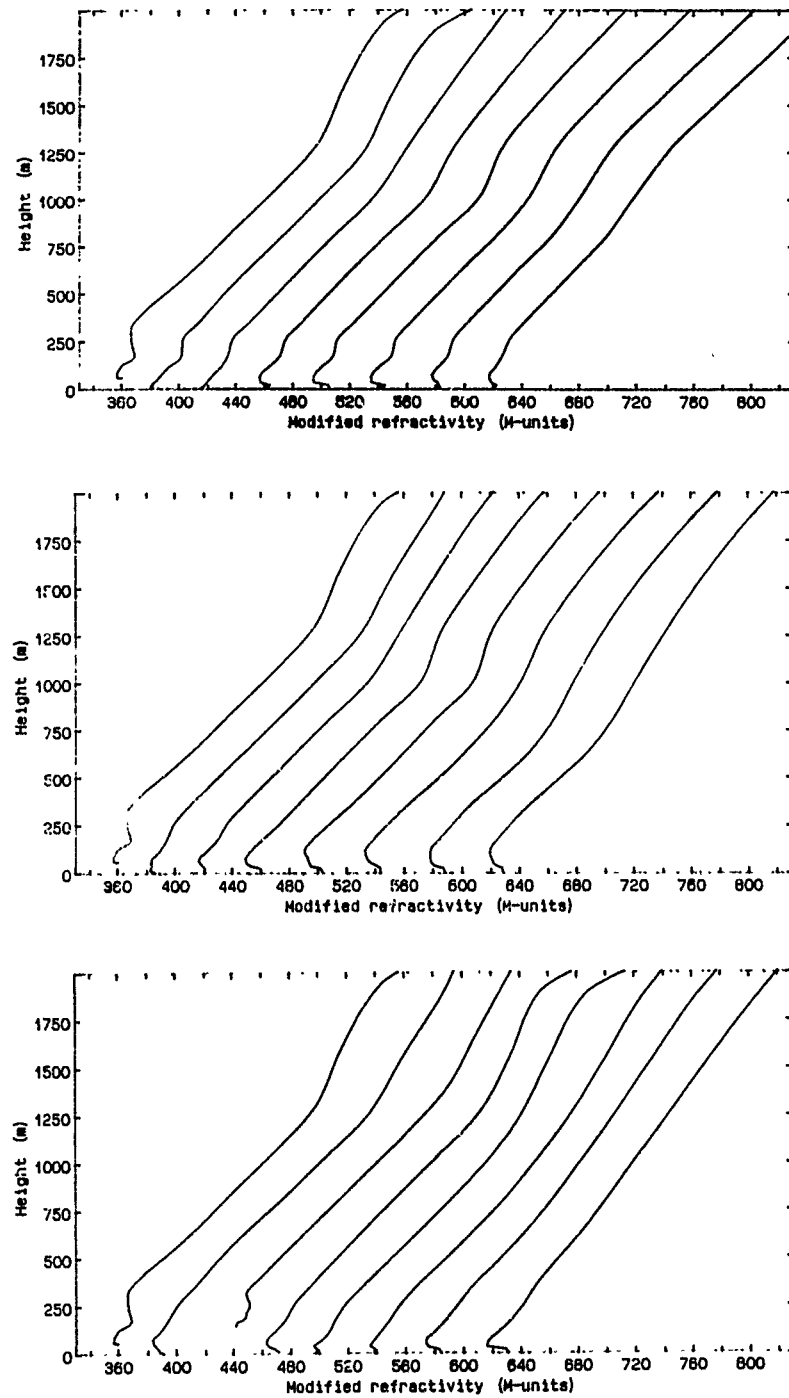


Figure 8: Mesoscale model derived modified refractivity profiles at 45 km intervals along the three radials shown in Figure 6: NE (top), E (middle), SE (bottom).

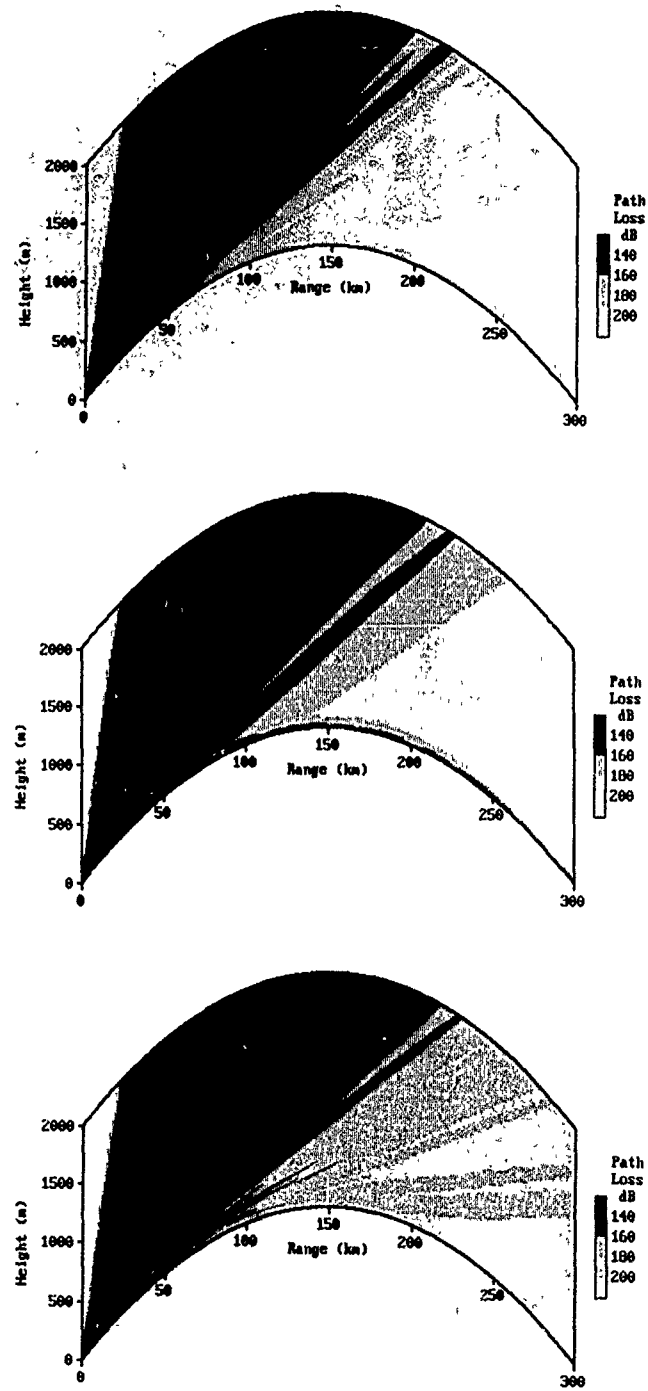


Figure 9: Calculated path loss contours corresponding to the refractivity profiles of Figure 8.

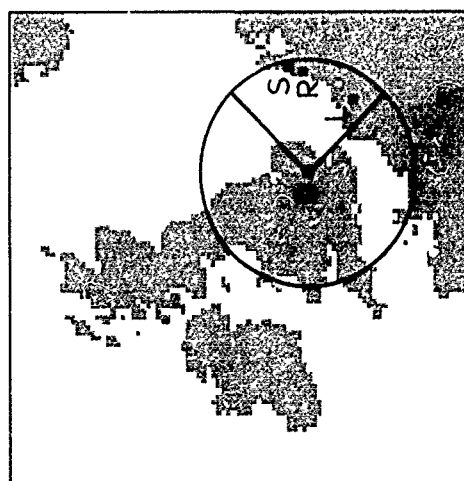


Figure 10: Debden secondary surveillance radar (D); the circle shows the operational limit of the radar. Schiphol (S), Rotterdam (R) and Lille (L) airports are shown.

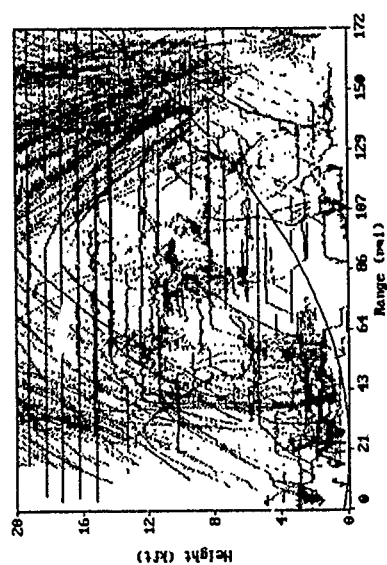


Figure 12: SSR returns in the 45°-135° sector at Debden between 10:00 and 14:00 GMT on 1 August 1990.

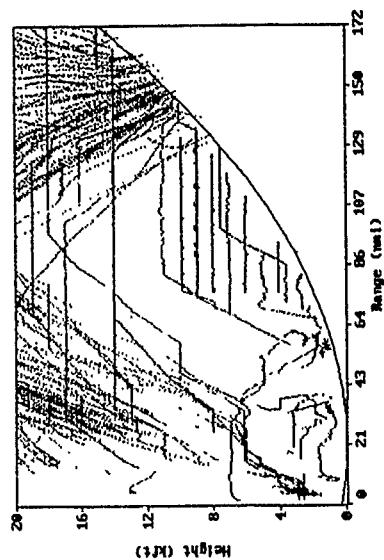


Figure 11: Range-height plot of SSR returns from aircraft under standard conditions. The parabola is the 4/3 Earth horizon for Debden (located at the origin).

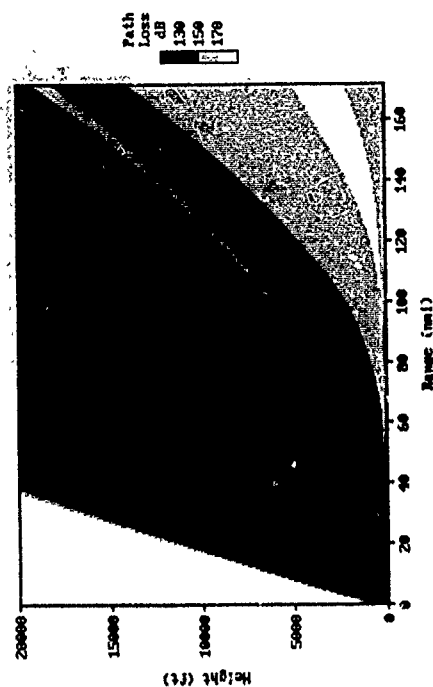


Figure 13: Contours of path loss due east of Debden calculated from mesoscale model output at 12:00 GMT on 1 August 1990.

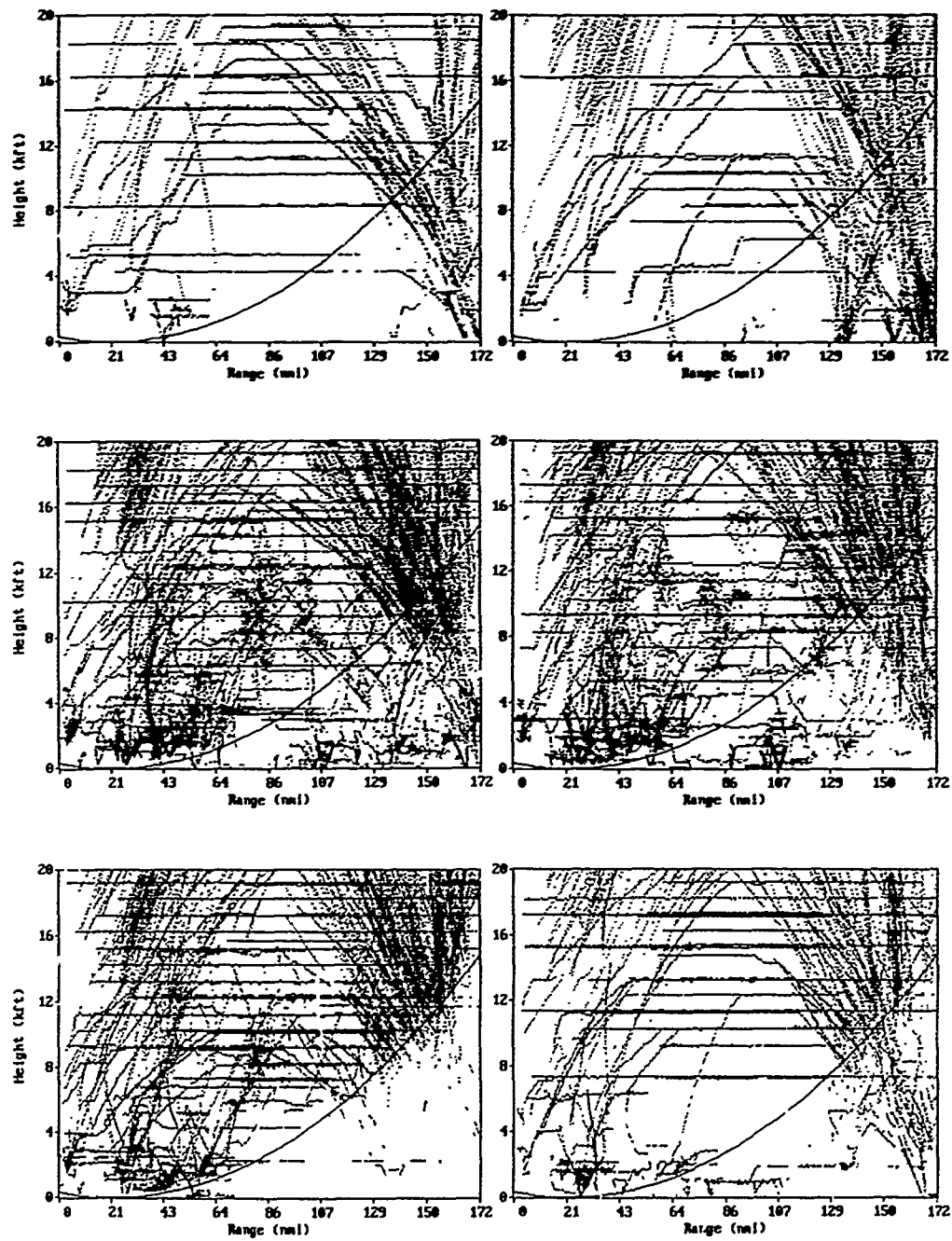


Figure 14: SSR returns observed in the 45°-135° sector at Debden on 1 August 1990. Each plot shows successive four hour periods during the day, beginning at midnight at the top left, and increasing from left to right and top to bottom down the page.

**DISCUSSION**

**K. ANDERSON**

*Are the SSR data used operationally for air-defense systems?*

**AUTHOR'S REPLY**

*As far as I am aware, SSR data have not been used operationally so far.*

**J. GOLDBIRSH**

*Could not low elevation radar measurements of the ocean clutter be a manifestation of the ducting conditions? Why not use this information in the absence of aircraft targets to provide information regarding profile conditions?*

**AUTHOR'S REPLY**

*I agree that sea surface or ground returns from anomalously long ranges could be a useful indicator of anomalous propagation conditions. I think it would be much more difficult to deduce profile information than in the case of SSR data. Of course the SSR data also have the advantage of showing the positions of coverage holes directly.*

## REFRACTIVE ASSESSMENTS FROM SATELLITE OBSERVATIONS

by

Jay Rosenthal and Roger Helvey  
 Pacific Missile Test Center  
 Code 3250  
 Point Mugu  
 CA 93042-5000  
 United States

SUMMARY

Capabilities of estimating ducting conditions for certain ocean regions (and weather regimes) from meteorological satellite data are under development at the Pacific Missile Test Center, in support of the Navy's Electromagnetic Propagation Assessment and Tactical Environmental Support System (TESS) program offices. Visual imagery patterns are used to infer the occurrence, height and intensity of ducts, while processed infrared (IR) and visual imagery are used to infer the spatial distribution of duct heights. Special cloud signature techniques have been developed on a personal computer to help correct for contamination of cloud-top temperatures due to sea and cloud anomaly features which impact the IR-duct technique. Synoptic, mesoscale and geographic influences on the propagation environment are considered as part of the effort to develop a predictive capability.

1 INTRODUCTION

A major need in assessing refractivity conditions over the open ocean is the capability to infer duct occurrence, height

and intensity in areas that are near void of conventional radiosonde data. To address this problem, under the Navy's Electromagnetic Propagation Assessment, and Tactical Environmental Support System (TESS) programs, the PMTC Geophysics Division is developing techniques for relating meteorological satellite data to these duct variables. As discussed by Rosenthal and Helvey, et al [1], both subjective and objective approaches have been used in the development of the techniques. Common to both is the conceptual model of an inversion-dominated weather regime (Figure 1) with low stratus/stratocumulus clouds that are lowest and flattest over the eastern parts of the sub-tropical oceans where the overlying inversion is lowest and strongest. In this model cloud height and convective appearance increase to the west and south along with increasing height and weakness of the inversion. This trend in cloud and inversion characteristics is routinely observed on satellite imagery and is heavily influenced by both the underlying sea surface temperature as well as synoptic and mesoscale weather factors.

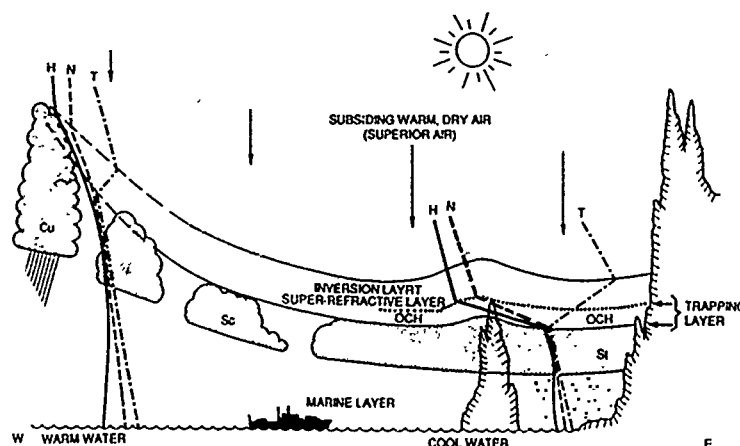


Figure 1. Schematic view of typical inversion conditions over subtropical oceans. (from reference 2) Inversion/super-refractive layer is lower and stronger over eastern side of ocean (with stratus (st) below) and is higher and weaker (with penetrating stratocumulus (sc) and cumulus (cu) in western side of ocean. A typical temperature (T), humidity (H), and refractivity (N) profile is shown at each side. Optimum coupling height (OCH) is near the cloud top.

Also from reference [1] and a previous guidebook prepared by Helvey and Rosenthal [2], is a visual satellite photo (Figure 2) which shows relatively subtle but orderly changes in low cloud appearance and cell size. Also seen are dramatic changes in cloud characteristics associated with frontal systems and open-celled cumulus in the unstable air behind fronts. Superimposed on these satellite features are indications of duct occurrence and height based on derived statistical relationships between cloud appearance and ducting conditions as determined from several thousand radiosonde soundings from the eastern and central Pacific.

Since those earlier models were described in references [1] and [2], and also by Rosenthal, Westerman and Helvey [3], there have been efforts to fine-tune, test and evaluate some of these assumed relationships. This had led to their summarization into rules to be used in an expert system in TESS which factors in synoptic, mesoscale and climatological relationships as well as satellite inferences. While much of these efforts are statistical and quantitative, there is a strong subjective element tied with the interpretation of satellite imagery cloud patterns.

## 2. IR-DUCT TECHNIQUE

In parallel with the subjective-statistical cloud pattern recognition technique has been an on-going effort to

provide more automated, objectively-derived duct height estimates from the processing of infrared (IR) satellite imagery. Termed the IR-duct technique and described in reference [1], the approach was originally developed by Lyons [4], [5], using concepts introduced by Lee [6] for distinguishing stratus from sea surface features, and subsequently refined by Helvey as described by Fisk and Helvey [7]. IR brightness values are used to calculate cloud-top temperatures using and adapting the software first developed by Nagle and Zeleny as described by Schramm, et al [8]. Using this capability, spot cloud-top temperatures are obtained across selected paths or regions of sub-tropical stratus or stratocumulus sheets.

Based on statistics from over 4,000 radiosonde profiles, seasonal mean profiles were derived which then became the basis of converting the cloud-top temperature to a calculated height of duct base, top and optimum coupling height (OCH). These are displayed along with cloud top temperature in an overlay to either visual or IR imagery (Figure 3). The OCH, located at approximately the cloud-top altitude is where the energy in a duct is most effectively coupled. Sea surface temperatures, as discussed by Rosenthal and Helvey [1], [2], have a major impact on the seasonal profiles and duct heights, and was included as a geographical and seasonal factor in the PHIC algorithms used in the IR-duct technique.

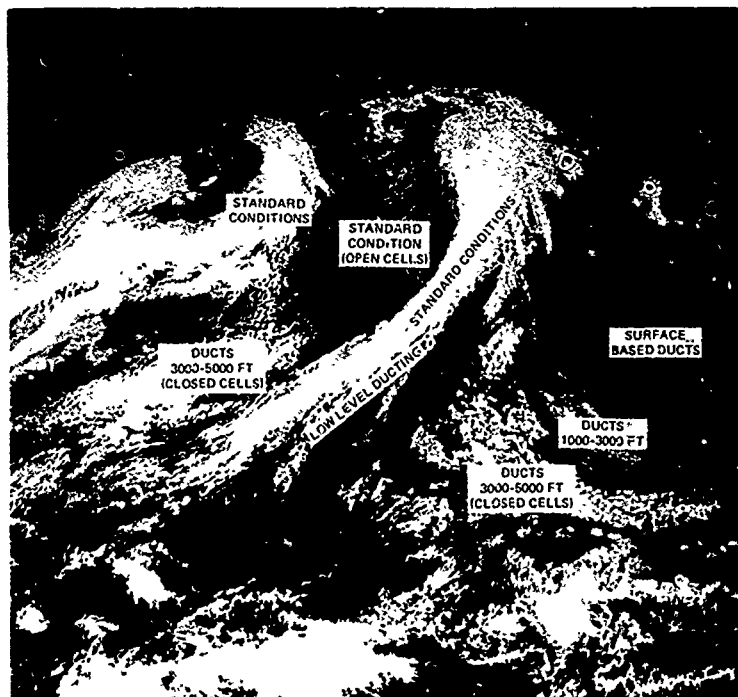


Figure 2. GOES Imagery for 2145 GMT, 15 Nov. 1980, showing typical wintertime synoptic features over north Pacific superimposed by indications of probable refractive structure. (from reference 2)

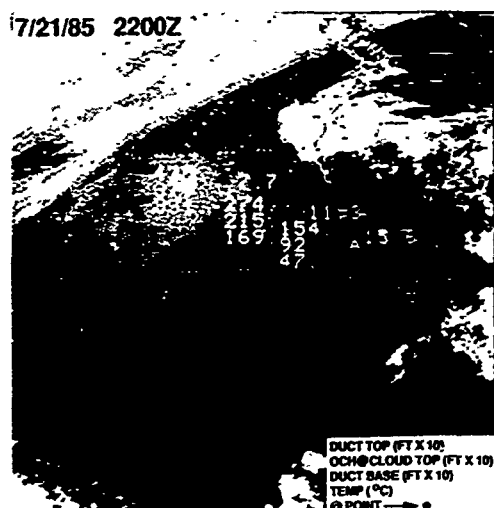


Figure 3. PMTC satellite-IR duct height technique. Shown are 3 sets of values superimposed on IR image with duct top, OCH and duct base (in tens of feet) displayed to left, and cloud top temperature to right of point.

Since the profile shape and intercept point are driving factors in how accurately the duct height can be calculated, work has continued on making the profiles more realistic. Figure 4 is a plot, with best-fit curve of inversion base altitude vs. relative temperature (inversion base temperature minus the sea surface temperature) for a data set obtained by Neiburger, Johnson and Chien [9] during the 1949-1952 UCLA cruise of the Eastern North Pacific.

This figure is an example of results from statistical analysis of one of a number of oceanic upper-air databases being compiled to provide a basis for converting cloud-top temperatures into altitude. The top of the marine layer, tops of imbedded stratocumulus clouds, and the base of the overlying subsidence/trade wind inversion are all more or less coincident. Temperatures are expressed relative to that of the underlying sea surface (SST), since the latter exerts a great influence on conditions in the marine air mass. It is evident from this and other data plots that this temperature offset approaches zero as the marine layer becomes shallower. Thus, the best-fit curve shown was constrained to pass through  $dt=0$  at  $z=0$ . A parabola was used, to accommodate the noticeable tendency for more stable lapse rates overall in the case of deeper marine layers; this may reflect the likely predominance of dry-adiabatic conditions below some typical range of condensation levels, and moist-adiabatic above.

These data were obtained over a rather large region, at various times of year, weather types and cloud conditions. It should be possible to improve the curve fit by consideration of these factors. In particular, the data need to be evaluated for probable low cloud coverage

because of two considerations: The intended application requires presence of marine stratus/stratocumulus to permit detection and remote sensing of cloud top temperatures by satellite; and the cases with substantial marine clouds tend to exhibit a more uniform height-temperature relationship, because of the vertical stirring induced by radiative cooling from the cloud tops. Another factor to be investigated involves atmospheric response to changes in the SST; since this cannot be instantaneous, with greater lag for deeper marine air masses, biases in the local height-temperature relationship can be expected dependent upon wind speed, and direction relative to the SST gradient in the region of interest.

### 3 ANALYZING CLOUD SIGNATURES

One of the inherent limitations of the IR duct technique is the uncertainty in derived cloud-top temperature due to contamination from radiance from the sea surface in areas where cloud cover is thin or incomplete. Also important is the representativeness of the selected cloud-top temperatures in areas where the low clouds exhibit variations in height and/or brightness. In order to provide a means of diagnosing these contaminations, and developing a method for automatic correction of these uncertainties, one of us (Helvey) has developed an interactive cloud signature analysis scheme implemented on an Amiga desktop computer. The technique uses principles previously examined by Maul [10] and Coakley and Bretherton [11]. The underlying assumption here is that typical cloud structures observed regularly on satellite imagery exhibit definable signatures of IR radiance and visual brightness. The approach is to use both the visual and IR data to characterize these cloud signatures, and an insert or window of the derived data can be overlaid on either the visual or infrared image. An example of this approach is shown in Figure 5.

This visual image consists of 260,000 pixels (649 elements by 400 lines), each covering somewhat more than 16 square kilometers. The scene contains ocean, land and various amounts and kinds of clouds. Each type of scene element can be associated with certain characteristic ranges of temperature and radiance (0.5K per raw count value) and brightness (or albedo), as indicated on the scatter plot. The thresholds were selected somewhat arbitrarily, but illustrate how a preliminary classification of pixels can be made to automatically identify the features of interest (ocean and low clouds) for diagnosing marine layer depth and associated duct optimum Coupling Height (OCH).

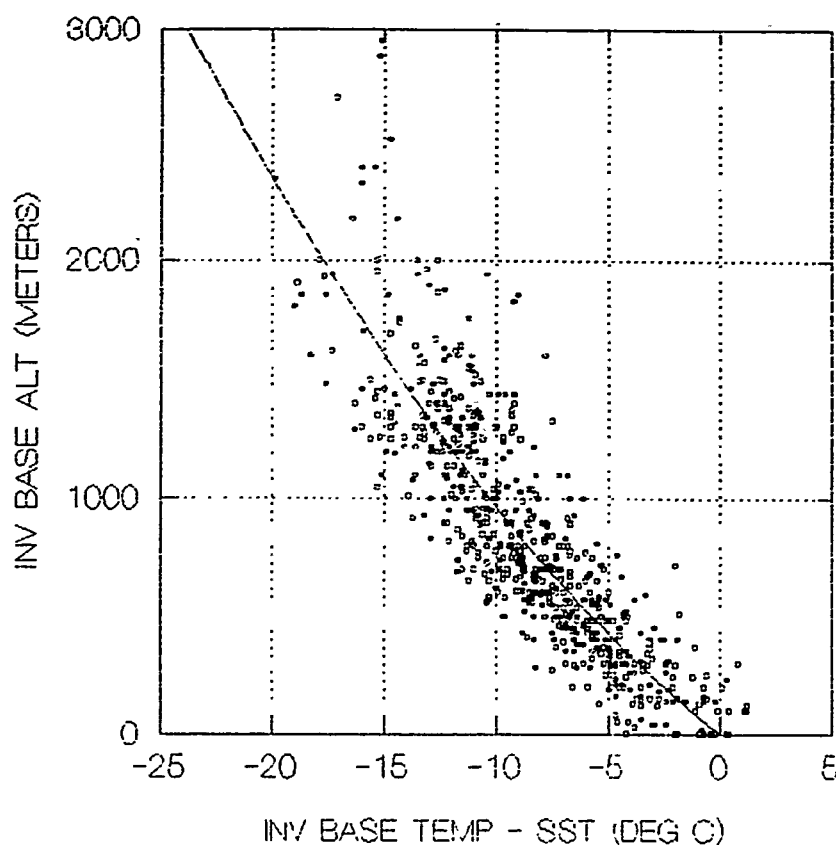


Figure 4. Inversion base height-temperature relationship (for UCLA 1949-1952 Eastern North Pacific Cruise data).

When the technique is applied to situations where there are significant differences in cloud top, height, brightness and type associated with synoptic events, the different signatures are readily distinguishable. For example, in Figure 6 are both extensive stratus/stratocumulus fields off the California and Baja coasts with large cellular and appearance fluctuations, as well as mid and high level clouds associated with an organized frontal band over the Pacific Ocean approaching the West Coast. For those cloud conditions contained in the white boxes over the ocean, coastal and land areas are corresponding IR/visual brightness signatures in the scatter plots shown in the window in the upper right corner of the figure. The pixels in the scatter plot in this and succeeding figures represent averages over about 64 square kilometers. The following differences in appearance and data plots are noted:

- (1) MID/HIGH CLOUDS in frontal area at upper left of image are cold and bright. The degree of scatter indicates considerable inhomogeneity in cloud top altitudes and coverage from pixel to pixel, with multiple layers likely.
- (2) STRATOCUMULUS CLOUDS off the California coast are warmer, with large variations in brightness, but fairly small range in IR temperatures (and cloud top altitudes).
- (3) DESERT TERRAIN in the interior of California and Arizona is very warm (local time is near midday), and of intermediate brightness.

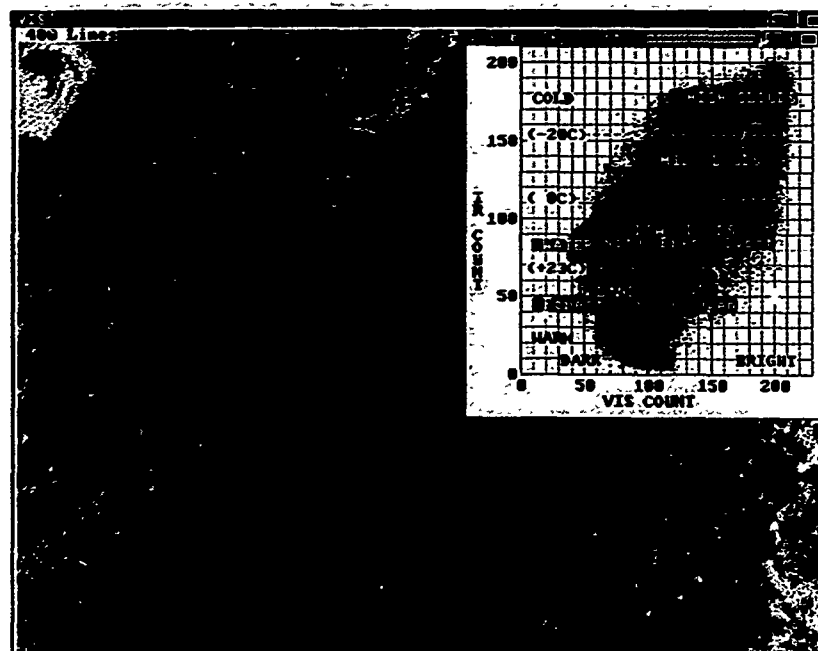


Figure 5. GOES visual image for 2031Z 14 Jul 89 (centered on California) INSET: Scatter plot of IR vs VIS "COUNTS" for all pixels in image.

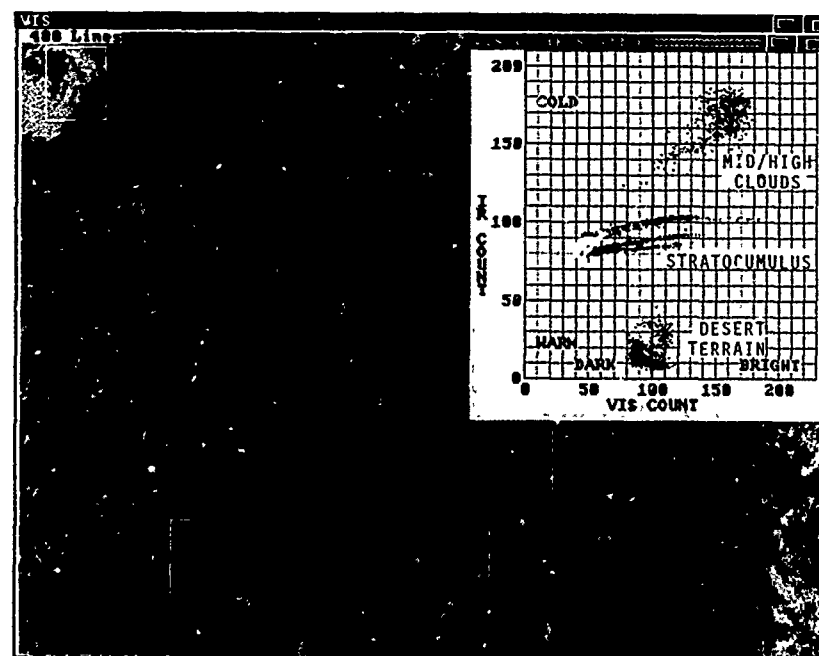


Figure 6. GOES visual image for 2031Z 14 Jul 89 (same as Fig. 5) INSET: IR vs visual pixel scatter plot for areas in boxes on image.

Within each of the areas examined, there are non-uniform fluctuations in brightness. The analysis technique can be applied to much smaller units within these regions so that individual characteristics can be systematically studied. This is shown in Figure 7.

The uppermost distribution is for the indicated portions of an area of stratocumulus off the northern California coast. The temperatures are rather uniformly cold (about 4.8C), so that the tops must be fairly flat and high. Nevertheless, a considerable variation of brightness is apparent.

The next lower distribution is from the cool stratocumulus (about 6.8C) and ocean off central California. Note the uniformly dark and relatively warm cluster (counts VIS=40, IR=88) characteristic of sea surface conditions. Also note the uniformity in IR pixel values for VIS counts greater than about 110; this suggests a threshold in reflectivity beyond which the cloudy pixel is effectively opaque to upwelling radiance from the sea surface. Conversely, below this threshold there is an approximately linear relationship between IR and VIS counts. A similar situation occurs for the next two lower scatter features, representing an area southwest of California (coldest pixels about 11.8C), and another adjacent to Baja California (coldest about 15.3C); the flat IR portion is hardly present, however. This indicates that for these areas there were very few completely cloudy pixels - note the many small stratocumulus elements indicating scattered to broken conditions, or thin and translucent stratus (especially off Baja California).

The accuracy of cloud top temperatures from satellite IR data will have a major impact on reliability of derived elevated duct height estimates. The presence of moisture above the marine layer will tend to make the cloud tops appear too cold, and hence too high. Unless application of more sophisticated multi-band techniques is feasible, this problem may be minimized by limiting the analysis to areas where general synoptic features (and subjective guidance from satellite imagery) indicate dry conditions aloft. On the other hand, as described above, temperatures for pixels which are not completely filled by clouds opaque to IR radiation from the surface, will appear somewhat warmer than representative of cloud tops in the region, and therefore too low. By limiting application of the IR-duct assessment to pixels whose corresponding visual brightness exceeds a certain threshold (dependent on illumination and viewing angles, or date, time and location), it should be possible to avoid this contamination by sea-surface temperature. This is the approach that we have used so far, although it is done subjectively since the appropriate brightness thresholds have not yet been established. Because many regions and individual pixels are not completely cloud-covered, however, a considerable

portion of the region of interest is likely to be excluded thereby from evaluation. A method of correcting for this effect is being developed, to increase the area over which duct height estimates can be made.

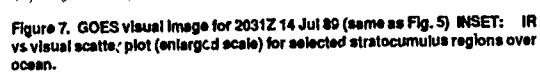
#### 4. PARTIAL COVERAGE CONTAMINATION AND A POSSIBLE SOLUTION

In order to develop an operationally useful and reliable version of the IR-duct technique in TESS, some systematic and consistent basis of correcting for brightness-related ambiguities must be incorporated. The near-linear arrangement of pixels from each region in Figure 7, between the sea surface cluster and the brightness threshold, suggests a basis for correction. The cloud-top temperature can be determined directly from the flat IR portion to the right of the critical brightness threshold, if present. If the region does not contain sufficient numbers of completely cloudy pixels, a cloud-top temperature may be estimated by extrapolating along the sloping part of the scatter distribution, to the IR temperature at the brightness threshold. (A sea surface temperature could be estimated in the same way, by extrapolating down to the IR value at the characteristic ocean brightness.) Simple expressions for the relationship between fractional cloud cover, satellite-measured albedo  $V$  in the visible channel and radiance  $I$  in the thermal IR channel have been given by Chou, et al [12], which can be combined to give:

$$I_{ovc} = I_{clr} + (I_{pix} - I_{clr}) * (V_{ovc} - V_{clr}) / (V_{pix} - V_{clr})$$

where the subscripts are abbreviations for overcast, clear, and actual (observed) pixel values. For the ranges of temperature and albedo values of concern here, raw 'count' units as received from the satellite can be used with little error (as suggested by the more or less linear scatter distribution up to the effective overcast threshold). A special technique for determining the best (least squares) two-segment line fit for the observed scatter distributions has been devised. After more study to establish appropriate brightness threshold values, it should be able to automatically provide equivalent cloud-top IR temperatures, even if not overcast pixels are present, if a statistically sufficient sample of pixels with various lesser cloud amounts is available in the region.

The inset in Figure 8 shows a scatter distribution and fitted lines, for a 32 by 32 kilometer region to the southwest of California. The vertical lines coming up from the base of the graph indicate the total goodness of fit for various positions of the partition between sloping (partly cloudy) and flat (overcast) portions of the distribution. The VIS count at the best-fit partition



position (vertical dotted line) is at the critical brightness threshold value for this particular sample. IR temperatures were determined for this case and a number of other regions where a set of points at uniform IR values gave direct indication of cloud-top or sea surface temperatures; as mentioned above, the slope-extrapolation method is not ready for use yet. The temperatures are plotted on the VIS image in deg C, and appear to be in reasonable agreement with the features in that image, although for interpretation in terms of altitude, the temperature of the ocean surface needs to be taken into account.

##### 5 INTERIM VERSION OF IR-DUCT TECHNIQUE

Until the above analysis scheme is fully automated within the IR-duct technique, certain elements can be combined for use in a semi-manual, interim version for use on a Personal Computer (PC) with data ingest from the MCIDAS-based Meteorological Interactive Data Display System (MIDDS) workstation operational at PMTC. The essential steps of this interim technique are summarized as follows:

- (1) Use MIDDS to pick marine cloud overcast points on VIS image, and obtain coordinates (Lat, Lon).
- (2) Use MIDDS to get temperatures of corresponding points on IR image.
- (3) Use PC program to:
  - a) obtain mean (climatological) or analysis SST for each point by interpolating to given Lat, Lon in SST table for current season, or from analysis if available.
  - b) compute for each point:  $dT = T_c - T_s$   
 where  $T_c$  = IR cloud-top temperature  
 $T_s$  = climatological or analysis SST
  - c) compute altitude for each point, using height vs. temperature relationship for current region and date:  $z_c = b * dT$   
 where  $b$  = parameter for given region & date

NOTE: Analyst must insure that each point selected is overcast, and that there is minimal upper-level moisture (check weather charts, satellite pictures - water vapor imagery).

##### 6 CONCLUSIONS

Both subjective and objective interpretation of meteorological satellite imagery patterns have great potential for inferring duct existence, height and intensity over the open ocean in subtropical inversion-dominated regions typically covered by stratus and stratocumulus clouds. The PMTC IR-duct technique, especially, provides a potentially automated means of mapping out the propagation environment in a way that can quickly address naval operating

problems, and serve as one input to range-dependent propagation models under development by Hitney [13] at NOSC, San Diego.

Contamination of cloud-top temperatures used in this IR-duct technique from sea surface radiance and cloud anomalies is a limitation to its use; however, current cloud signature analysis techniques under development at PMTC offer promise as a means of systematically correcting for these limitations.

##### REFERENCES

- [1] Rosenthal, J.S., Helvey, R.A., Lyons, S.W., Fox, A.D., Szymer, R. and Eddington, L., "Weather Satellite and Computer Modeling Approaches To Assessing Propagation Over Marine Environments", AGARD Conference Proceedings No. 453, AGARD-CP-453.
- [2] Helvey, R.A. and Rosenthal, J.S., "Guide for Inferring Refractive Conditions from Synoptic Parameters", Pacific Missile Test Center Technical Publication TP-5, 1983.
- [3] Rosenthal, J.S., Westerman, S. and Helvey, R.A., "Inferring Refractivity Conditions from Satellite Imagery", Pacific Missile Test Center, Geophysical Sciences Technical Note No. 96, 1985.
- [4] Lyons, S.W., "Satellite-Derived Refractive Duct Height Estimates", Pacific Missile Test Center, Geophysical Sciences Technical Note No. 98, 1985.
- [5] Lyons, S.W., "SPADS Automated Duct Height Statistics", Pacific Missile Test Center, Geophysical Sciences Technical Note No. 100, 1985.
- [6] Lee, T.F., "A Plan For Using SPADS to Distinguish Stratus From Sea Surface Conditions", Pacific Missile Test Center, Geophysical Sciences Technical Note No. 84, 1984.
- [7] Fisk, C. and Helvey, R.A., "Refractive Effects Assessment and Prediction (REAP) Progress Report", Pacific Missile Test Center, Geophysical Sciences Technical Note No. 156, 1990.
- [8] Schramm, W., Zeleny, P., Nagle, R. and Weinstein, "The Navy SPADS, A Second Generation Environmental Display System", 9th Conference Weather Forecasting and Analysis, American Meteorological Society Preprint Volume, 1982.

- [9] Nelburger, M., Johnson, D.S. and Chien, C.W., "Studies of the Structure of the Atmosphere Over The Eastern N. Pacific Ocean in Summer", UCLA, Vol. 1, No. 1, 1981.
- [10] Maul, G., "Application of GOES Visible-Infrared Data to Quantifying Mesoscale Ocean Surface Temperatures", Journal of Geophysical Research, Vol. 86, No. C9, 1981.
- [11] Coakley, J.A. and Bretherton, F.P., "Cloud Cover From High Resolution Scanner Data: Detecting and Allowing For Partially Filled Fields of View", Journal of Geophysical Research, Vol. 87, No. C7, 1982.
- [12] Chou, M.D., Childs, J. and Dorian, P., "Cloud Cover Estimation Using Bispectral Satellite Measurements", Journal of Climate and Applied Meteorology, Vol. 25, 1986.
- [13] Hitney, H., "Remote Sensing of Refractivity Structure by Direct Radio Measurements at UHF", NATO AGARD Symposium on Remote Sensing of the Propagation Environment, Cesme-Izmir, Turkey, 1991.

#### ACKNOWLEDGEMENTS

The authors gratefully acknowledge the considerable efforts of Mrs. Cheryl Von Eschen, Geophysics Division, Ms. Gail Burke, Photographic Laboratory, and Mr. Willie Davis, Visual Information for preparation of the manuscript.

#### DISCUSSION

##### **J. GOLDBIRSH**

*Could you elaborate on validation of the technique to arrive at duct height using cloud measurements?*

##### **AUTHOR'S REPLY**

*Several independent evaluations were conducted previously. These showed that duct heights estimated from the satellite IR duct technique were within about 400 feet of those determined from radiosonde, approximately 80% of the time. Errors are due to both upper level moisture (which can be minimized by using water vapor imagery to select dry areas aloft) and the radiance contamination from the underlying sea surface, which can be minimized by Mr. Helvey's technique that I just described.*

## A "VIRTUAL SENSOR" FOR EVAPORATION DUCTS - THE IMPACT OF DATA UNCERTAINTIES

John Cook

Naval Oceanographic and Atmospheric Research Laboratory  
Atmospheric Directorate  
Monterey, CA 93943-5006

### 1. SUMMARY

For this application, virtually sensed data is defined as the output from a combination of satellite-based remote sensing instruments that have been blended with data from a numerical weather prediction model/data assimilation system and processed by an algorithm. Such a "virtual sensor" is described to assess evaporation ducts over marine regions. In this study, the sensitivity of four evaporation duct height algorithms to data errors are examined and the results are expressed in terms of the duct height error versus parameter error. The data set used was generated parametrically so a large variation of environmental conditions could be considered. The errors imposed on the data represent uncorrelated random errors associated with satellite-based remote sensing inaccuracies. The study shows that although the evaporation duct height algorithms have different genealogies, they have similar sensitivities. The conclusions represent a best case scenario because of the omission of some sources of error and the assumption of horizontal homogeneity in the near-surface refractivity field over a typical satellite sensor footprint.

### 2. INTRODUCTION

The evaporation duct height is defined as the height above the sea surface where the sharp decrease in ambient humidity with height causes the vertical gradient of refractivity to become equal to the critical value required for trapping (Fig. 1). The problem of remotely sensing the evaporation duct is, therefore, closely tied with that of sensing the surface turbulent heat flux, which largely determines the vertical gradients of temperature and moisture, and thus of refractivity as well. Unfortunately, satellite-based remotely sensed measurements of atmospheric refractivity with sufficiently high resolution to describe near-surface profiles, such as those shown in Figure 1, will not be available in the foreseeable future. The evaporation duct height can, however, be inferred from meteorological measurements by using flux-profile relationships that are based on the semi-empirical similarity theory originally developed by Monin and Obukhov (Ref. 1). In general, similarity theory relates bulk measurements of sea surface temperature and reference height values of air temperature, humidity, and wind speed to the near-surface fluxes of momentum, heat and moisture.

In practice, these bulk parameters are difficult to measure accurately using satellite-based remote sensing techniques. Sea surface temperature ( $T_s$ ) and near-surface wind speed ( $U$ ) or stress are the most common and best understood of these satellite measurements. With the improved instruments planned for the Earth Observing System (Eos), such as the Advanced Microwave Scanning Radiometer (AMSR), the Advanced Medium Resolution Imaging Radiometer (AMRIR), and the Moderate-resolution Imaging Spectrometer (MODIS), all weather measurements of  $T_s$  should be consistently available with approximately  $0.5^\circ\text{C}$  accuracy (Refs. 2 and 3). This is comparable with current techniques such as the multichannel sea surface temperature (MCSST) product which utilizes infrared Advanced Very High Resolution Radiometer (AVHRR) data (Ref. 4). The Eos AMSR and scatterometer (SCATT) instruments should also be able to measure  $U$  with approximately  $0.5\text{ m s}^{-1}$  accuracy (Ref. 2), which compares to approximately  $2\text{ m s}^{-1}$  currently reported for both the Scanning Multichannel Microwave Radiometer (SMMR) and the Special Sensor Microwave/Imager (SSM/I) instruments (Ref. 5). The other two parameters, boundary layer air temperature (or air-sea temperature difference) and humidity, are much more difficult to measure using satellite-based remote sensing techniques. Hsu and Blanchard (Ref. 6) apply an algorithm developed by Liu (Ref. 7) to relate measurements of columnar water vapor ( $W$ ) from radiosonde profiles to surface specific humidity ( $q$ ) and report an rms error of approximately  $1\text{ g kg}^{-1}$ , which is about the accuracy reported by Liu and Niiler (Ref. 8) for monthly mean values of  $\bar{q}$  computed using SMMR estimates of  $\bar{W}$ . Developmental satellite-based remote sensing instruments for measuring  $W$ , such as the Eos Advanced Microwave Sounding Unit (AMSU), should be improved by contributions from the Eos Lidar Atmospheric Sounder and Altimeter (LASA). LASA could be used to measure the thickness of the marine atmospheric boundary layer and AMSU should be able to determine  $W$  within the layer to between 5-10% (Ref. 2). The measurement of near-surface air temperatures ( $T$ ) will require the combination of data from AMSU and the infrared radiometers on the High Resolution Imaging Spectrometer (HIRIS) which should result in better measurements than either system alone (Ref. 2). High-resolution temperature retrieval will still be a major challenge; however, by synergistically combining satellite-based remotely sensed temperature and humidity data with output from a numerical weather

prediction model/data assimilation system, a significant amount of the measurement uncertainty may be corrected. Such a system is the best known space-time interpolator of meteorological data (Ref. 9) and if developed specifically for refractivity, would provide a unique means to interpret the measured data. This system can be called a "virtual sensor" because the parameter of interest (the evaporation duct) is not sensed directly, but indirectly through a combination of sensor outputs that are assimilated using the physics of a dynamical model and then processed by a semi-empirical algorithm. This concept is fairly simple, but it is not clear what impact the proposed sensor and data inaccuracies will have when evaporation duct heights are derived in this fashion. The purpose of this study is to assess the magnitude of these errors for a variety of evaporation duct height assessment techniques.

The approach used in this study is to apply a methodology similar to that described in Cook (Ref. 10) for evaluating the sensitivity of operational evaporation duct algorithms to the satellite-based remote sensing data inaccuracies described above. The meteorological data base used here as input to the evaporation duct height algorithms is developed parametrically, thereby easily encompassing a wide range of meteorological situations. Understanding these sensitivities is important because in many cases the calculated duct height is not used independently, it is input to another product, for example, a radar performance depiction or a counterdetection assessment, which may have significant operational consequences.

### 3. EVAPORATION DUCT ALGORITHMS

As implied above, there is no universally accepted scheme for estimating evaporation duct heights. Here, four schemes are chosen for error analysis. All of the algorithms are described in detail in Cook (Ref. 10), but for clarity they are briefly described here. The first algorithm is developed following Cook and Burk (Ref. 11) by noting that meteorological applications of similarity theory are frequently used to compute vertical profiles of potential temperature ( $\theta$ ) and specific humidity ( $q$ ) within the surface layer by using the integrated forms of the similarity expressions (Ref. 12). This methodology was used to compute high resolution  $\theta$  and  $q$  profiles from 0 to 40 m and then the modified index of refraction ( $M$ ) and  $dM/dz$  profiles were constructed from:

$$N = \frac{AP}{T} \left( 1 + \frac{Bq}{eT} \right), \quad (1)$$

$$M = N + \frac{z}{a} \times 10^6 = N + 0.157z,$$

where  $A$  and  $B$  are constants, equal to 77.6 °K mbar<sup>1</sup>

and 4810 °K respectively (Ref. 13),  $\epsilon \approx 0.622$ , and  $a$  is the mean Earth radius,  $6.371 \times 10^6$  m. Pressure,  $P$ , was computed hydrostatically away from the reference height. The duct height ( $\beta$ ) is the level within the profile where  $dM/dz$  reaches its critical value

$$\left( \frac{dM}{dz} \right)_c = \left( \frac{dN}{dz} \right)_c + 0.157 = \frac{-10^6}{a} + 0.157 = 0.$$

Hereafter, values of  $\beta$  calculated with this scheme will be labeled "direct" and written  $\beta_D$ . An example of  $\beta_D$  computed for a specific subset of meteorological conditions is shown in Figure 2a.

Thompson (Ref. 14) describes an evaporation duct height algorithm currently in operational use at the Fleet Numerical Oceanography Center (FNOC). This algorithm is developed by taking the total vertical derivative of refractivity and equating it to the critical refractivity gradient which occurs at the duct height:

$$\left( \frac{dN}{dz} \right)_c = \frac{\partial N}{\partial T} \frac{dT}{dz} + \frac{\partial N}{\partial q} \frac{dq}{dz} + \frac{\partial N}{\partial P} \frac{dP}{dz}. \quad (2)$$

The partial derivatives are computed from (1) and  $dP/dz$  is approximated by the hydrostatic equation. The remaining derivatives,  $dT/dz$  and  $dq/dz$ , are approximated by similarity expressions assuming horizontally homogeneous conditions. Temperature, however, is not a similarity variable; properly, potential temperature should be used instead. This is one of many simplifying assumptions used in this derivation; the resulting expression is plotted in Figure 2b and values of  $\beta$  calculated with this scheme will be labeled "GSCLI" and written  $\beta_G$ . The acronym GSCLI stands for the "Global Surface Contact Layer Interface" model that employs this algorithm at FNOC. The figure shows that for these environmental conditions,  $\beta_D$  and  $\beta_G$  exhibit similar behavior under unstable conditions, but  $\beta_G$  can be significantly less than  $\beta_D$  under stable conditions.

A refractivity quantity that does not vary with pressure is potential refractivity. It has been used by numerous researchers as a similarity variable when investigating near-surface refractivity (e.g., Jeske (Ref. 15); Thompson (Ref. 14); and Paulus (Ref. 16)) and is the basis of the other evaporation duct height algorithms. Potential refractivity ( $\chi$ ) at microwave frequencies is defined as (Ref. 13):

$$\chi = \frac{A}{\theta} \left( P_0 + \frac{B e_p}{\theta} \right), \quad (3)$$

where  $e_p$  is a potential water vapor pressure referenced to the 1000 mb level ( $P_0$ ) (Ref. 17).

Applications of  $\chi$  are used to assess the duct height corresponding to the critical potential refractivity gradient. This is accomplished by assuming  $\chi$  behaves as a similarity variable; this methodology was derived by Jeske and uses a different implementation of similarity theory instead of the Liu et al. (Ref. 12) scheme. As shown in Cook and Burk, however,  $\chi$  does not follow similarity theory under all conditions. The algorithm was subsequently installed in the Integrated Refractive Effects Prediction System (IREPS) (Ref. 18) and is in operational use by the Navy at sea. Evaporation duct height estimates using this technique are shown in Figure 2c and will be written as  $\beta_i$  and labeled "IREPS" hereafter.

A well known undesirable aspect of the IREPS algorithm which can be seen in Figure 2c is the high duct heights computed for near-neutral conditions (air-sea temperature difference (ASTD) close to zero) (Ref. 19). To solve the problems inherent in IREPS, Paulus (Ref. 19) developed an empirical correction. Using high quality buoy data for support, Paulus argued that operationally, error prone environmental data resulted in the use of the stable form of the similarity expressions too frequently. Paulus' correction was to limit  $\beta_i$  to the value computed using an air-sea temperature difference of  $-1^\circ\text{C}$  (with a fixed relative humidity) if the value of  $\beta_i$  associated with the measured data was larger than the value of  $\beta_i$  calculated at the fixed  $-1^\circ\text{C}$  air-sea temperature difference. These results are shown in Figure 2d and show severe truncation under near-neutral and stable conditions. They will be labeled "Paulus" hereafter and denoted  $\beta_p$ .

#### 4. METHODOLOGY

The methodology used here to evaluate the sensitivity of the evaporation duct height algorithms to satellite-based remote sensing data inaccuracies closely follows that described in Cook (Ref. 10) for in situ data errors. Evaporation duct height errors are calculated by first computing the duct height without considering any data errors, then iteratively recomputing the duct height, cycling through each of the data errors one error increment at a time and calculating a new duct height and the difference (error) between the duct heights. The errors for each parameter are evaluated sequentially and classified according to stable or unstable/neutral conditions. The resulting data sets of evaporation duct height error are then averaged for each increment of data error and plotted.

As explained in the previous section, evaporation duct height estimates are functions of sea surface temperature ( $T_s$ ), and reference height values of air temperature ( $T$ ), wind speed ( $U$ ), and specific humidity ( $q$ ). Consistent with operational algorithms (e.g., Paulus (Ref. 16)), the reference height used here is fixed at six meters and the reference height pressure fixed at 1000

mb. Although this is obviously an oversimplification for satellite measurements, Blanc (Ref. 20) found that the influence of typical shipboard barometric pressure and altitude measurement uncertainties combined amounted to less than 1% error in the bulk-derived parameters examined.

Since a large measured data set was not available for this study, a parametric approach was used to generate the necessary data by uniformly cycling through all possible combinations of parameters. This resulted in 6160 sets of  $T$ ,  $q$ ,  $T_s$ , and  $U$  "pseudo-observations" which encompassed a wide range of environmental conditions. Table 1 lists the limits and increments of the parameter values used. Air temperature was computed from the air-sea temperature difference which varied between  $-5^\circ\text{C}$  and  $+5^\circ\text{C}$  in  $1^\circ\text{C}$  increments. Specific humidity was computed using the relative humidity which varied between 98% and 50% according to the values in Table 1. Humidities greater than saturation or less than  $0.2\text{ g kg}^{-1}$  were considered unrealistic and the data sets not included in the analysis.

TABLE 1. Parametric Limits for Variables Used

Variable	Symbol	Maximum	Minimum	Increment
Wind Speed	$U$	$21\text{ m s}^{-1}$	$3\text{ m s}^{-1}$	$2\text{ m s}^{-1}$
Sea Surface Temperature	$T_s$	$20^\circ\text{C}$	$8^\circ\text{C}$	$2^\circ\text{C}$
Air-Sea Temperature Difference	$T - T_s$	$5^\circ\text{C}$	$-5^\circ\text{C}$	$1^\circ\text{C}$
Relative Humidity	RH	98%, 95%, 90%, 85%, 80%, 72%, 62%, 50%		

The error perturbation experiment was executed by imposing a range of errors on the pseudo-observations. The errors are listed in Table 2 and represent a range of accuracies consistent with current satellite-based remote sensing techniques as described above (Refs. 2, 3 and 5). The errors in Table 2 were treated as uncorrelated so the results can be interpreted for each parameter independently, for example, errors in  $q$  when  $T_s$ ,  $T$ , and  $U$  are known precisely. We have, therefore, neglected several important sources of error such as height assignment (vertical resolution and layer averages); the effect of spatial averaging inherent in satellite data; arbitrarily assigning 1000 mb as the reference height pressure; correlation of measurement errors, such as due to measurements using the same instrument or those due to cloud or rain contamination; effects of advection; and differences in the assumptions inherent in the variations of the underlying similarity theories. To estimate effects from more than one

measurement error at a time, the duct height errors can be combined in an rms sense. However, more rigorous experiments that include the neglected errors and the nonlinear influences of errors (e.g., equal over- and under-estimates of parameters may not lead to correspondingly equal differences in evaporation duct heights) should be conducted if a more quantitative understanding is required.

TABLE 2. Measurement Uncertainties

Variable	Uncertainty
U	$\pm 2.0 \text{ m s}^{-1}$
$T_s$	$\pm 1.0^\circ \text{C}$
T	$\pm 5.0^\circ \text{C}$
q	$\pm 2.0 \text{ g kg}^{-1}$

## 5. RESULTS

Figure 3 is a scatter plot of the error-free evaporation duct estimates from the direct method versus stability (represented by the ratio of the reference height,  $z$ , to the Obukhov length,  $L$ ). In the figure, calculated ducts greater than or equal to 40 m and those equal to 0 m are not plotted. The figure demonstrates the discrete nature of the environmental data base and shows that a majority of the environmental conditions considered represent slightly unstable and near-neutral conditions, although the algorithm does predict that evaporation ducts can be present under some stable conditions when the near-surface modified refractivity decreases with height.

Figure 4 represents the duct height errors as a function of error in sea surface temperature (Fig. 4a), near-surface wind speed (Fig. 4b), reference height air temperature (Fig. 4c), and reference height humidity (Fig. 4d) for unstable and neutral conditions ( $z/L \leq 0$ ). As mentioned previously, the range of data errors were chosen to be representative of satellite-based remotely sensed data but the source of the error is unimportant. These errors could also be due to in situ measurements or the resultant errors from a numerical weather prediction model/data assimilation system or virtual sensor. Error here is defined as the erroneous minus the error-free value, so in unstable conditions underestimates (overestimates) of both  $T_s$  and U result in small underestimates (overestimates) of the duct height, respectively. Underestimating  $T_s$  increases the stability towards neutrality as the air-sea temperature difference changes from larger to smaller negative values. This change acts to suppress vertical motions in the surface layer resulting in deeper vertical gradients, with a corresponding tendency for the duct heights to increase. Underestimating  $T_s$ , however,

decreases the refractivity at the surface because the air adjacent to the sea surface is assumed to be saturated; thus decreasing the sea surface temperature also decreases the interfacial specific humidity. This causes the air-sea refractivity difference to become smaller and the duct heights to decrease due to the reduced near-surface gradients. These effects tend to balance each other with the net result a small positive slope in the sensitivity to  $T_s$  errors. For overestimates of wind speed, mechanical turbulence also tends to homogenize the air, driving the stability of the surface layer toward neutrality and again resulting in slightly larger duct heights.

Figures 4c and 4d show duct height error as functions of the errors in near-surface air temperature (or air-sea temperature difference since  $T_s$  is assumed to be known precisely) and errors in specific humidity. Note the change in duct height error scale; all the algorithms are much more sensitive to T and q errors than to  $T_s$  or U errors. This sensitivity seems to be due the change in refractivity at the reference height associated with the errors in T and q. Under unstable conditions, overestimates of T imply greater stability which can result in either thinner ducts for higher humidities or thicker ducts for lower humidities (see Fig. 2 although the curves represent constant relative humidity not q). Overestimating T (with a fixed q) decreases the modified refractivity at the reference height, thus increasing the air-sea refractivity difference, which tends to increase the duct heights due to the enhanced near-surface gradients. These effects reinforce each other at moderate relative humidities (less than about 80%) and result in a large sensitivity to errors in T; above about 80% relative humidity the effects tend to balance each other, however, the mean effect for the data set here is a large positive slope in the sensitivity to T errors. This sensitivity is exacerbated by the large surface air temperature errors associated with satellite-based remote sensing.

The sensitivity to errors in q is also considerable, however, as seen from Figure 4d, the slope is opposite to those for  $T_s$ , U, and T errors. Underestimates of q causes the air-sea refractivity difference to increase and also implies slightly more unstable conditions. As seen from Figure 2, decreasing the humidity at the reference height always leads to increasing duct heights under unstable conditions.

Figure 5 shows the sensitivity of the duct height algorithms to  $T_s$ , U, T, and q errors when the error-free conditions are stable ( $z/L > 0$ ). Under these conditions, overestimates of  $T_s$  (Fig. 5a) result in small overestimates of the duct height. Overestimating  $T_s$  decreases the stability towards neutrality which implies increased mixing as the turbulence acts to keep the mean properties of the surface layer uniform. This

results in weaker vertical gradients and a corresponding tendency for the duct heights to decrease. Overestimating  $T_s$ , however, also increases the refractivity at the surface causing the air-sea refractivity difference to become larger and the duct heights to tend to increase. These effects tend to balance each other and the net result is a small positive slope of the sensitivity to  $T_s$  errors under both stable and unstable conditions.

Figure 5b shows that under stable conditions, overestimates of wind speed tend to decrease duct heights, opposite to the effect under unstable conditions. Here mechanical turbulence tends to drive the stability of the surface layer toward neutrality, eradicating strong gradients, with the result of slightly lower duct heights. The sensitivity of the Paulus technique has a positive slope similar to the unstable results which is due to the truncation of the duct heights at an air-sea temperature difference of  $-1^\circ\text{C}$  under almost all stable conditions.

Figures 5c and 5d show the duct height errors as functions of the errors in near surface air temperature and specific humidity for stable conditions. Again, note the change in duct height error scale necessitated by the increased sensitivity to  $T$  and  $q$  errors. Under stable conditions, underestimates of  $T$  imply decreasing stability which can either result in thinner ducts or thicker ducts depending of the humidity and magnitude of the stability (see Fig. 2). Underestimating  $T$  also increases the modified refractivity at the reference height, thus decreasing, or even changing the sign of the air-sea refractivity difference, which tends to decrease the duct heights. These effects reinforce each other at moderate stabilities and relative humidities (less than about 80%) and result in a large positive slope in the sensitivity to errors in  $T$ .

The sensitivity to errors in  $q$  under stable conditions is also considerable and opposite to those for  $T$  and  $T_s$  errors. As under unstable conditions, underestimates of  $q$  causes the air-sea refractivity difference to increase and also implies slightly more unstable (neutral) conditions. These effects reinforce each other with the net result a large negatively sloped sensitivity under all conditions.

The sensitivities described above can be synthesized into a few simple relationships. If an error drives the surface layer toward neutrality then, under unstable conditions, evaporation duct heights will tend to increase and under stable conditions they will tend to decrease, although there is some humidity dependence to this effect (Fig. 2). If the error implies a larger (smaller) air-sea refractivity difference then the evaporation duct heights will tend to increase (decrease), respectively, except under some stable conditions when the refractivity monotonically increases

with height and there is no evaporation duct present anyway. Such sensitivity to data errors may overwhelm useful information gained by making duct height estimates. For example, Hembree and Kuciauskas (Ref. 21) have demonstrated that evaporation duct height differences of as little as 1 m can more than double the estimated range at which typical shipboard electromagnetic emitters can be covertly detected by threat receivers. It is instructive to briefly investigate what evaporation duct height estimates are used for by such applications. Patterson (Ref. 22, page 31) states "... the evaporation duct height is not a height below which an antenna must be located in order to have extended ranges, but a value which relates to the duct's strength or its ability to trap radiation." Thus, evaporation duct height estimates are used to infer duct strength. Particularly under unstable and near-neutral conditions, most of the deficit in refractivity within an evaporation duct occurs very close to the sea surface (Fig. 1). The nonlinear shape of the refractivity profile provides for a complex coupling between the location of the antenna and energy propagation and results in a frequency dependence for trapping.

## 6. CONCLUDING REMARKS

The sensitivity of four different techniques for computing evaporation duct heights to typical satellite-based measurement errors was investigated. Results presented show that although the techniques have different genealogies, they have similar sensitivities. The error estimates used represent uncorrelated satellite-based remote sensing data inaccuracies but the source of the error for this application is unimportant; they could also represent the uncorrelated error from a numerical weather prediction/data assimilation system or a virtual sensor. So that a wide range of environmental conditions could be evaluated without a large data collection effort, the environmental data base of sea surface temperature and reference height values of air temperature, wind speed, and specific humidity was derived parametrically by uniformly cycling through all possible combinations of parameters.

The use of bulk meteorological techniques driven by remotely-sensed data to estimate evaporation duct heights has been shown to be highly susceptible to measurement error. The patterns of the sensitivities for each technique are similar with the exception of Paulus's algorithm to wind speed errors which is due to the truncation imposed on the duct heights. Additional sources of error that were neglected are height assignment, ambient pressure measurement errors, correlation of errors (e.g., those due to cloud contamination, etc.), spatial averaging by large-footprint satellite sensors, effect of advection on near-surface refractivity, and differences inherent in the different variations of the underlying similarity theories.

The demonstrated sensitivity of the current algorithms to conservative data errors, however, raises questions about the operational applicability of these and more sophisticated models. A troubling assumption is that of horizontal homogeneity of the vertical gradients in the refractivity field over the satellite footprint. If we interpret the errors here in a spatial sense, such as due to weak horizontal temperature or humidity variations, we would expect considerable refractive inhomogeneity or topography associated with the evaporation duct. The impact of this effect will have to be evaluated in the future with range dependent propagation models. A study designed to evaluate the errors for a specific combination of satellite remote sensing instruments or a virtual sensor is feasible using the methodology presented here and could result in measurement accuracy specifications. The results could be verified with data collected during experiments such as those described in Blanc et al. (Ref. 23) which support scatterometer instrument development.

#### ACKNOWLEDGEMENTS

This research has been supported by the Space and Naval Warfare Systems Command, CAPT C. Hoffman, USN, Washington, D.C., Program Element 6704N. NOARL contribution No. 91:122:442. Approved for public release; distribution is unlimited.

#### REFERENCES

1. Monin, A. S. and A. M. Obukhov, Basic laws of turbulent mixing in the ground layer of the atmosphere, Akad. Nauk. SSSR Geofiz. Inst. Tr., 151, 163-187, 1954.
2. NASA, From pattern to process: the strategy of the Earth observing system, Eos Science Steering Committee Report, Vol II, 140 pp., Nat. Aero. Space Admin., Washington, D.C., 1987.
3. Liu, W. T., Remote sensing of surface turbulent heat flux, in Surface Waves and Fluxes, Vol II, edited by G. L. Geernaert and W. J. Plant. pp. 293-309, Kluwer Academic Publishers, The Netherlands, 1990.
4. McClain, E. P., W. G. Pichel, and C. C. Walton, Comparative performance of AVHRR-based multichannel sea surface temperatures, J. Geophys. Res., 90, 11587-11601, 1985.
5. Abbott, M. R. and D. B. Chelton, Advances in passive sensing of the ocean, Reviews of Geophysics Supplement to Vol 29, Part 2, 571-589, 1991.
6. Hsu, S. A. and B. W. Blanchard, The relationship between total precipitable water and surface-level humidity over the sea surface: a further evaluation, J. Geophys. Res., 94, 14539-14545, 1989.
7. Liu, W. T., Statistical relation between monthly mean precipitable water and surface-level humidity over global oceans, Mon. Wea. Rev., 114, 1591-1602, 1986.
8. Liu, W. T. and P. P. Niiler, Determination of monthly mean humidity in the atmospheric surface layer over oceans from satellite data, J. Phys. Oceanogr., 14, 1451-1457, 1984.
9. Bengtsson, L. and J. Shukla, Response to comments on "Integration of space and in situ observations to study global climate change," Bull. Amer. Meteor. Soc., 72, 243-245, 1991.
10. Cook, J., A sensitivity study of weather data inaccuracies on evaporation duct height algorithms, Radio Sci., 26(3), 731-746, 1991.
11. Cook, J., and S. Burk, Potential refractivity as a similarity variable, Accepted for publication in Boundary Layer Meteor., 1991.
12. Liu, W. T., K. B. Katsaros and J. A. Businger, Bulk parameterization of air-sea exchanges of heat and water vapor including the molecular constraints at the interface, J. Atmos. Sci., 36, 1722-1735, 1979.
13. Bean, B.R. and E. J. Dutton, Radio Meteorology, 435 pp., National Bureau of Standards Monograph 92, 1966.
14. Thompson, W. T., The surface evaporative duct height product: an evaluation, NEPRF Technical Report TR 87-05, Naval Oceanographic and Atmospheric Research Laboratory, Monterey, CA, 93943-5006, 55 pp, 1987.
15. Jeske, H., The state of radar-range prediction over sea, Tropospheric Radio Wave Propagation, Part II, AGARD Conference Proceedings No. 70, 50-1 to 50-10, 1971.
16. Paulus, R. A., Specification for evaporation duct height calculations, NOSC Technical Document 1596, Naval Ocean Systems Center, San Diego, CA, 92152, 37 pp, 1989.
17. Jehn, K. H., The use of potential refractive index in synoptic-scale radio meteorology, J.

Meteor., 17, 264-269, 1960.

18. Hitney, H. V., Propagation modeling in the evaporation duct, NELC Technical Report 1947, Naval Ocean Systems Center, San Diego, CA, 92152, 1975.
19. Paulus, R. A., Practical application of an evaporation duct model, Radio Sci., 20(4), 887-896, 1985.
20. Blanc, T. V., The effect of inaccuracies in weather-ship data on bulk-derived estimates of flux, stability and sea-surface roughness, J. Atmos. Ocean. Tech., 3, 12-26, 1986.
21. Hembree, L. A. and A. Kuciauskas, Sensitivity of the Battle Group Vulnerability Tactical Decision Aid to space and time resolution, NOARL Technical Note 31. Naval Oceanographic and Atmospheric Research Laboratory, Monterey, CA, 93943-5006, 44 pp, 1990.
22. Patterson, W. L., Effective use of the electromagnetic products of TESS and IREPS, NOSC Technical Document 1369, Naval Ocean Systems Center, San Diego, CA, 92152, 138 pp, 1988.
23. Blanc, T. V., W. J. Plant, and W. C. Keller, The Naval Research Laboratory's air-sea interaction blimp experiment, Bull. Amer. Meteor. Soc., 70, 354-365, 1989.
24. Kerr, D. E., Propagation of short radio waves, 728 pp., McGraw-Hill Book Company, Inc., 1951.
25. Badgley, F. I., C. A. Paulson and M. Miyake, Profiles of Wind, Temperature, and Humidity over the Arabian Sea, 62 pp., International Indian Ocean Expedition Meteorological Monograph No. 6, Univ. Press of Hawaii, 1972.

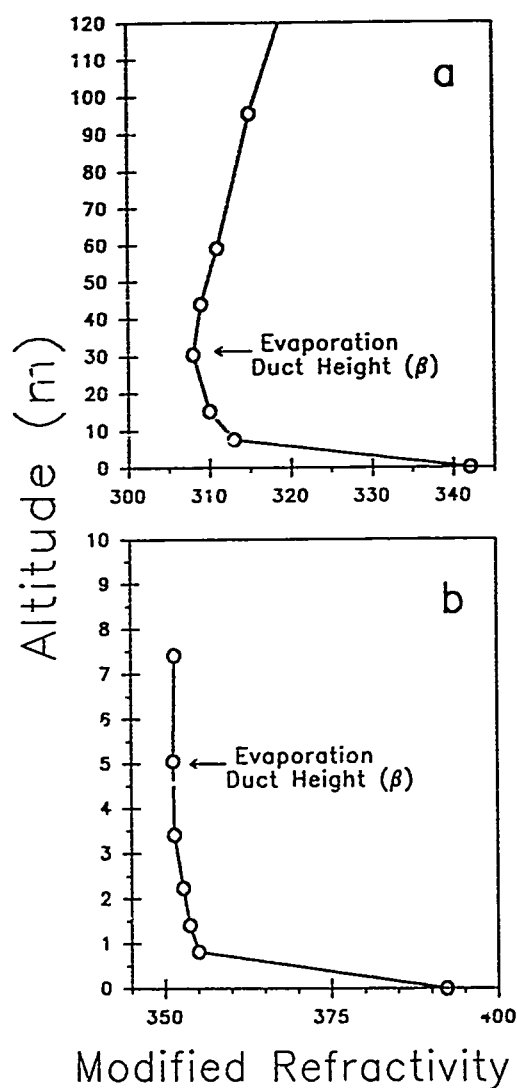


Fig. 1. Examples of observed evaporation ducts. (a) A profile of modified refractivity digitized from a graph by Kerr (Ref. 24, p. 233). The largest refractivity gradient is near the sea surface, and the evaporation duct height ( $\beta$ ) is the inflection point in the profile where the vertical gradient changes sign. (b) A very high resolution profile of modified refractivity close to the sea surface (Ref. 25). The sharp shallow refractivity gradient which characterizes evaporation ducts is underscored.

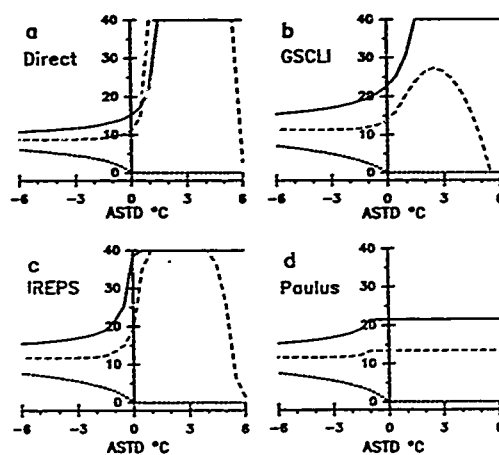


Fig. 2. Evaporation duct height estimates versus air-sea temperature difference ( $T-T_s$ ; denoted ASTD) for air temperature at the reference height of 6 m. (a) Direct method. (b) GSCLI algorithm. (c) IREPS. (d) Paulus' correction to IREPS. The vertical scale is altitude in meters and line type represents relative humidity at the reference height, with solid lines equal to 50%, long-dashed lines equal to 75%, and short-dashed lines equal to 100%. Reference height wind speed is  $5 \text{ m s}^{-1}$ , and sea surface temperature is  $20^\circ\text{C}$  in these examples.

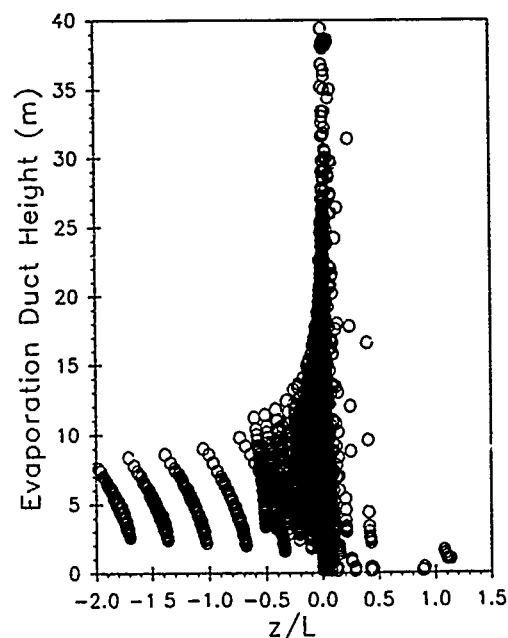


Fig. 3. Scatter plot showing estimated evaporation duct height versus stability ( $z/L$ ) calculated using the direct method for the complete error-free data set. Duct heights equal to 0 or 40 m are not plotted.

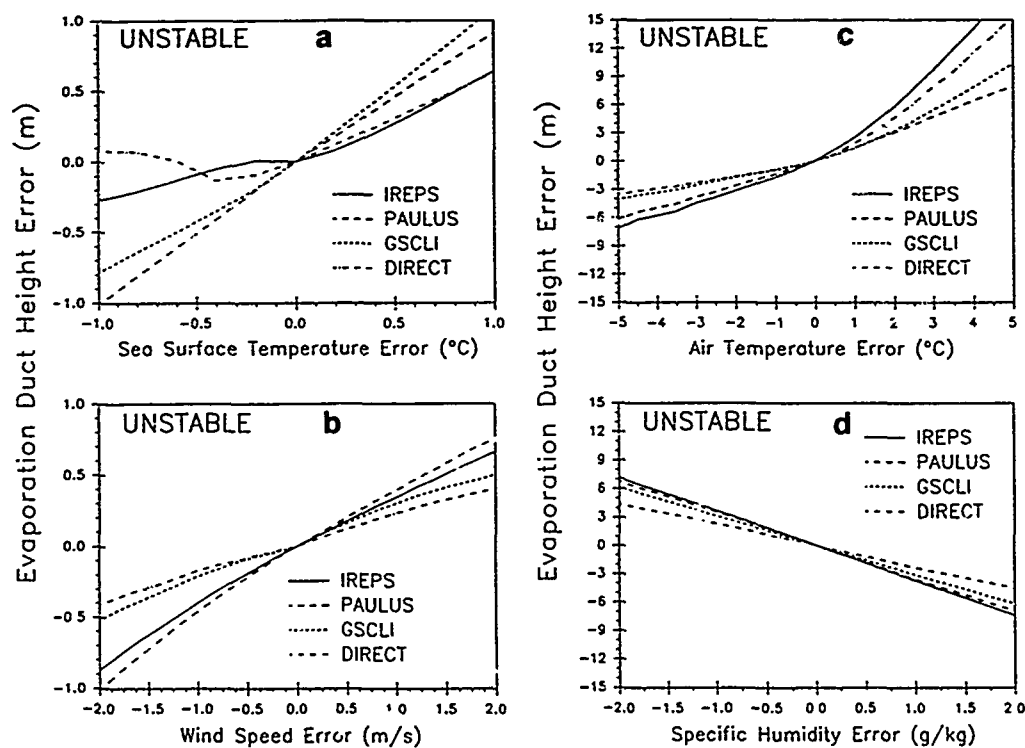


Fig. 4. The errors (erroneous minus error-free values) for four evaporation duct height algorithms versus measurement uncertainty for the input geophysical parameters under unstable and neutral conditions ( $z/L \leq 0$ ). (a) Sea surface temperature error. (b) Reference height wind speed error. (c) Reference height air temperature error. (d) Reference height specific humidity error.

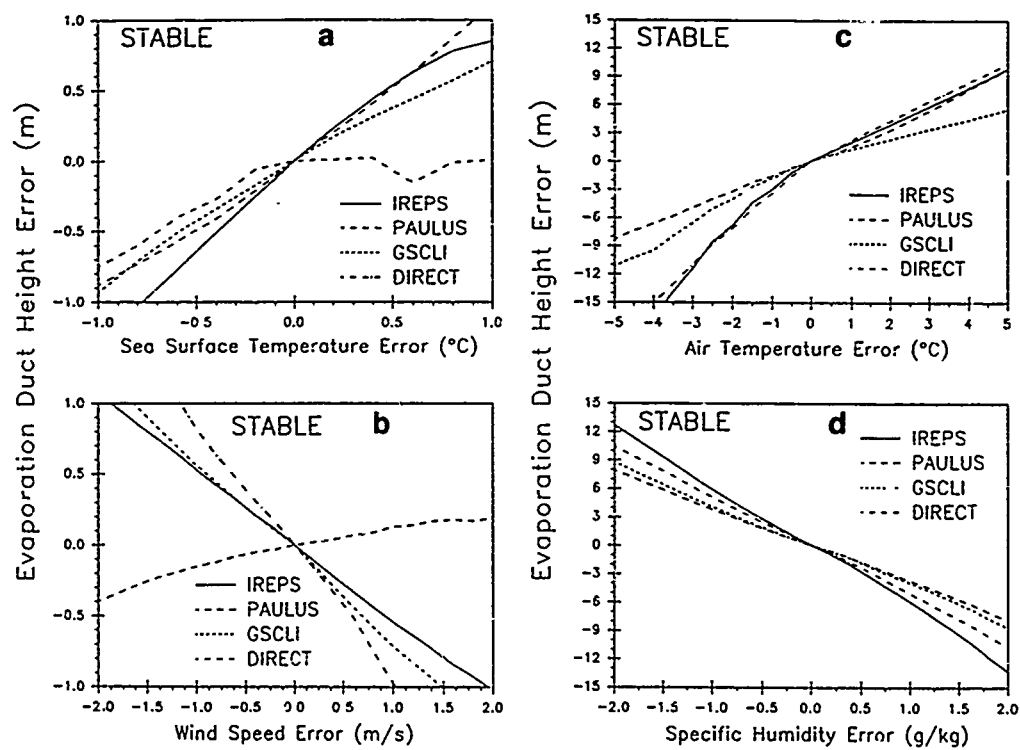


Fig. 5. Same as Fig. 4 except for stable conditions ( $z/L > 0$ ).

## ROSE - A HIGH RESOLUTION, AMPLITUDE CODED, HIGH FREQUENCY OBLIQUE IONOSONDE

by

P.C. Arthur,  
A.H. Dickson  
and  
P.S. Cannon

Applied Ionospheric Physics,  
Defence Research Agency, Aerospace Division,  
Farnborough, Hampshire, GU14 6TD, United Kingdom.

### SUMMARY

A high quality high frequency (HF) oblique ionosonde has been developed for use in propagation research and associated studies of the ionosphere. The ionosonde is known as ROSE (Radio Oblique Sounding Equipment) and requires the connection of a specially designed enhancement to a commercially available chirp sounder receiver (RCS-5) manufactured by the BR Corporation in the USA. Two important features are brought about by the addition of this enhancement. Firstly, an increase in the resolution of an ionogram by a factor of approximately three. This allows the fine structure in the ionospheric returns to be detected. Secondly, colour coding of the ionogram according to the amplitude of the received signal. Detailed mode amplitude information and comparisons of the relative strengths of propagating modes can be achieved. Additional features which are provided include display handling and data storage facilities.

This paper describes the system architecture of the ROSE ionosonde and discusses the type of detailed ionospheric information it can provide from active remote sensing.

### 1 INTRODUCTION

Throughout the world extensive use is made of radio sounding systems to remotely probe the ionosphere. One category of remote sensing system is known as the ionosonde, which is essentially a radar emitting pulses or chirp waveforms to measure the group delay of the return signal bounced back from the ionosphere. The receiver may be co-located with the transmitter, in which case the ionosonde is a vertical sounder, or the transmitter and receiver may be separated by distances of up to several thousand kilometres, in which case the ionosonde is known as an oblique sounder.

### 2 PULSE VERSUS CHIRP SOUNDERS

#### 2.1 Pulse sounders

Pulse sounders transmit a series of short ( $\sim 100 \mu\text{s}$ ) pulses over the band of interest (2 to 30 MHz, for instance). The sounder moves in discrete steps over this band and can transmit up to several hundred pulses on each frequency depending upon the information required. To receive these pulses optimally the receiver must have a large bandwidth, normally  $\sim 20 \text{ kHz}$  or so, and to keep the signal to noise ratio at a reasonable level

transmitter powers up to 10 kW and beyond are required. Due to these large pulsed transmissions the transmitter site has to be carefully chosen to avoid any local interference.

One of the main advantages of pulse sounders is the ease of analysis of the incoming signals. By calculating the time difference between the received pulses the ionospheric propagation modes can be determined. This is a fairly easy task to perform with relatively simple technologies.

#### 2.2 Chirp Sounders

Chirp sounders sweep a phase-continuous signal over the band of interest at rates of up to several hundred kilohertz per second. Due to the method of receiver operation (described later) a comparatively narrow receiver bandwidth is used which is of the order of a few hundred Hertz. This in turn leads to a relatively low transmitter power (10 - 100 W) which is much more practical than the pulse transmitter. There are several trade offs involved in the operational parameters of a chirp sounder. For example, a fast sweep generates an ionogram in a short period of time but requires a larger receiver bandwidth, giving a lower signal to noise ratio which in turn requires the transmitter power to be larger. Conversely, a slow sweep rate leads to lower transmitter powers but the ionogram can take several minutes or longer to collect and ionospheric conditions may have changed during the recording of the ionogram.

One of the main disadvantages of chirp sounders is the complex analysis that must be carried out to determine the ionospheric propagating modes. The advent of specialised digital signal processing (DSP) chips together with other technologies has enabled more extensive development of chirp sounder receivers to be undertaken in recent years.

### 3 CHIRP SOUNDER RECEIVERS

The chirp sounder receiver generates an internal reference signal which is of the same form as that being transmitted at the transmitter site. By carrying out a radio frequency mixing process between this reference signal and the received signal, a baseband signal is obtained which contains a series of frequencies dependant upon the modes of propagation present. The frequencies of the signals are proportional to the time of flight from the transmitter to receiver and, therefore, by carrying out a frequency analysis the relative group delays of the different

propagating modes can be calculated (Fig 1). The absolute time of flight is not known unless the transmitter and receiver have some form of accurate time control. Normally, when the receiver is initiated to gather data on a particular path a searching process is employed to synchronise to the transmitted signal. This process involves adjusting the start time of the internal reference signal until the baseband signals are obtained in the correct frequency range.

### 3.1 RCS-5 sounder receiver

The BR Corporation manufacture a chirp sounder receiver (RCS-5) which is able to receive transmissions from a number of compatible transmitters distributed throughout the world. The RCS-5 is designed to assist the communications operator in selecting the appropriate operating frequency for a particular HF communications link and to this end it displays a simple monochrome ionogram. An indication of either amplitude, automatic gain control (age) or signal quality is also shown, but in each of these cases the displayed value is the integrated value across all the propagating modes at a particular frequency. Therefore, the ionogram cannot show the operator whether, for example, the signal amplitude relates to two modes of similar amplitude or one high amplitude mode and one weak mode.

In the BR system the chirp signal from the transmitter is swept linearly from 2 to 30 MHz in 280 s (ie. at 100 kHz.s<sup>-1</sup>). In the receiver, after mixing, the baseband signal lies between 0 and 500 Hz which corresponds to a group delay of 0 to 5 ms. The RCS-5 spectrally analyses this baseband signal with a 2.5 Hz (0.025 ms group delay) resolution in one second intervals and displays the resulting ionogram on its built-in screen with a resolution of 280 points in the horizontal (frequency) direction and 200 points in the vertical (group delay) direction. The age of the receiver tries to optimise the display to make the propagating modes clear. The main limitation of the monochrome screen is that weak modes are displayed with an equal intensity to strong modes and are therefore indistinguishable.

After an ionogram has been collected the RCS-5 may adjust the sweep start time of its internal reference signal in an attempt to optimise the position of the ionogram on the screen. This adjustment is carried out in 0.5 or 1 ms periods of group delay and is known as 'autoslip'. It is possible to disable this feature to avoid, for instance, the complete loss of the ionogram during a night period when the ionospheric returns may be low and the ionogram may be inadvertently slipped out of range.

### 4 ROSE IONOSONDE PROGRAMME

The RCS-5 receiver is primarily designed for the radio communications operator and its use as a research tool to investigate ionospheric propagation is limited by the constraints described above. To meet the requirements of detailed scientific research ROSE has been developed with the aim of enhancing the output from the RCS-5 whilst both avoiding internal modifications and maintaining compatibility with the current worldwide network of chirp transmissions. Our priority has been to provide a much higher resolution ionogram which also contains detailed signal strength data to enable the amplitudes of various modes to be compared. Furthermore, archiving and data recall facilities have been developed to enable off-line analysis of ionograms.

### 5 ROSE ARCHITECTURE

To achieve the improvements described above, and provide scope for future modifications, an enhancement has been designed for the RCS-5 which duplicates some of its internal functions whilst further analysing the received signal to improve functionality. The enhancement consists of a custom designed digital hardware Processing and Control Unit (PCU) which is connected to the ports at the rear of the RCS-5, and an IBM-compatible Personal Computer (PC) which interfaces to the PCU. The RF front-end of the RCS-5 is still utilised to produce the baseband signal, but then the additional equipment takes over the analysis of the signal and displays the ionogram. Fig 2 shows a corresponding block diagram of the complete ROSE ionosonde.

In ROSE the baseband signal is taken from the RCS-5 and passed to the PCU. In addition, the RS232 remote control interface on the RCS-5 is used to program the receiver and extract information regarding the received signal power levels in the form of receiver age values which can then be used later in the analysis. The baseband output signal from the receiver is digitally sampled and the resultant data stream is arranged into blocks which are weighted using a window function and spectrally analysed by the PCU to give group delay information. The analysis of each block produces 682 values which are displayed on the ionogram as one vertical line with a group delay resolution of 7.3  $\mu$ s (0.73 Hz). The number of vertical lines which constitute a single ionogram (ie. horizontal resolution) is dictated by the rate at which the blocks are analysed during a sweep. A choice is available of either one block per second giving 279 lines, two blocks per second giving 418 lines or three blocks per second giving 836 lines. The latter option produces the highest resolution ionogram of 836 x 682 points - which marks a substantial improvement over the 280 x 200 points of the 'standalone' RCS-5. The former options are of use when computer disc storage space is at a premium or display resolution is limited. The results of the spectral analysis are combined with the age values derived from the RCS-5 to determine the frequency dependant power in each propagating mode. The values are passed to the PC where this detailed signal strength information is displayed by colour coding the ionogram.

Fig 3 summarises the main processes involved in the analysis of the baseband signal. They are discussed in more detail in Section 5.2 below. Table 1 compares the operating parameters of the basic RCS-5 against the full resolution option provided by the ROSE ionosonde.

Table 1.  
Comparison of Operating Parameters

Item	RCS-5	ROSE
Frequency range	2 - 30 MHz	2 - 30 MHz
Horizontal resolution	280 points	836 points*
Vertical resolution	200 points	682 points
Baseband signal bandwidth	500 Hz	500 Hz
Baseband signal resolution	2.5 Hz	0.73 Hz
Group delay resolution	25 $\mu$ s	7.3 $\mu$ s
Vertical lines per second	1	3*

\*maximum resolution option

Normally for ROSE the RCS-5 is operated with the 'autoslip' feature disabled. It has been noticed, however, that there is a long term drift of about 1 ms in a 10 hour period due to inaccuracies between the transmitter and receiver clocks. This problem is yet to be addressed fully and will require careful consideration to avoid loss of data when the ionosonde is used for long periods of time with 'autoslip' enabled.

### 5.1 PCU Hardware

A block diagram of the PCU is shown in Fig 4. A 19 inch 6U KM6 rack construction is used with slide-in modules containing printed circuit cards. The rack has a built-in power supply and the connections for the baseband analogue signal and all the digital data are made via the front panel. The design for the PCU includes enough memory and spare processing capacity to allow for future improvements to be incorporated into the ROSE ionosonde.

#### (a) Processor Boards

The PCU is based around three Texas Instruments TMS32020 digital signal processors which are located on individual circuit boards containing local memory. The processors can communicate with each other, and the outside world, via two buses. The first bus (global memory bus) allows access to a region of global memory so that data can be easily transferred between the three processors. The other bus (interface bus) has the interface devices attached to it such as the RS232 interface, parallel interface, analogue to digital (A/D) converter and the display devices for showing the status of the PCU.

#### (b) Interface Boards

A 14-pole Butterworth low-pass anti-aliasing filter and 12-bit analogue to digital (A/D) converter operating at a sampling rate of 1500 Hz are used to digitise the baseband signal from the RCS-5. The filter corners at 500 Hz to give the required bandwidth (0 - 500 Hz) and provides a stop-band attenuation of at least 80 dB at 1000 Hz. The A/D converter covers a bandwidth of 0 - 750 Hz (as determined by Nyquist) with a dynamic range of 72 dB.

A parallel interface, 16 bits input and 16 bits output, is used to communicate with the PC.

An RS232 interface operating at 9600 baud is used to communicate with the RCS-5 through the built-in remote control port. This allows the PCU to set up the RCS-5, receive start of sweep information, and obtain the receiver agc values which are required for the correct scaling of ionograms.

#### (c) Displays

A liquid crystal display (LCD) is mounted separately in a diecast box and can be located in a convenient place for the operator to view. The display gives information on the status of the PCU, including the sweep set-up parameters and an indication of the progress of the current sweep.

### 5.2 Processor Software

All of the software within the PCU is written in TMS32020 assembly language and its basic function is to perform a spectral analysis on the incoming baseband signal to extract the frequency information required for an ionogram (Fig 3). This process

utilises a computationally efficient Fast Fourier Transform (FFT).

The software consists of three program modules - one for each of the processors. During a sweep the processors share the computational load of real-time analysis of the baseband signal from the RCS-5 by operating in a 'pipeline' fashion. The digitised signal is read by the first processor and formatted into blocks. As each block is generated it is passed on to the second processor for frequency analysis using the FFT algorithm, followed by the third processor for final formatting and transfer to the PC. With this arrangement high data throughput is maintained throughout the sweep. A block size of 2048 samples is used and since the A/D converter operates at 1500 samples per second this covers 1.36 seconds of sweep. This is the period over which the spectral estimate is based, and so gives better processing gain than the RCS-5 which performs its estimate over one second. Frequency resolution is also improved.

A more detailed description of the functions performed by the processor software modules is given below.

After implementation of the software about 30% of the total processing power of the PCU has been used. The remainder is available for future enhancements.

#### (a) Processor one

The data values from the A/D converter are read in by processor one as they are generated (approximately one every 0.67 ms). These values are grouped into blocks of 2048. There is a degree of overlap between the blocks and as a result values generally appear in more than one block. The amount of overlap depends upon the rate at which the blocks are required for analysis, which in turn depends upon the horizontal resolution of the ionogram as selected by the operator. Each of the blocks of values may have a weighted window function applied to it before it is passed on to the next processor. This window attenuates the edges of the data block before the FFT is carried out in order to minimise 'spectral leakage' or 'spreading'. Currently, the operator may select to use either a rectangular window which applies no weighting, or a Kaiser-Bessel window which is very effective at reducing the sidelobes of signal peaks without significantly reducing the signal resolution.

#### (b) Processor two

The FFT algorithm is applied to the windowed data blocks by processor two to convert the signal from the time domain to the frequency domain. The FFT employed has been specifically designed to suit the instruction set used by the TMS32020 processor and comprises eleven stages of calculations. These stages have been optimised for speed by allowing for the limited resolution and bandwidth of the input values and the repeatability of the FFT calculation. In this way only 33% of the calculations normally required for the final stage of the algorithm are actually performed. This is because 50% is repetitious information and the remaining 17% is aliased because it falls in the filter roll-off region of 500 to 750 Hz. The original 2048 time domain samples are converted to 682 frequency domain samples which cover the required bandwidth of 0 to 500 Hz with a resolution of 0.73 Hz. The inherently modular format of the FFT leaves scope to balance the load between the other processors if required in the future.

### (c) Processor three

Every second whilst sweeping the RCS-5 produces an age value ranging from 0 to 40 (each unit corresponds to a 3 dB step) which gives an indication of the level of the incoming signal. These values are read in by processor three and matched to the appropriate data blocks when they arrive from processor two. Since each block covers a sweep period greater than one second consecutive age values need to be weighted and combined to give a figure which more accurately describes the age value applied during the period that the data in the block was received. The age value is used by the PC to tie the values in each block to an absolute magnitude scale. This enables definitive colour coding of signal strength across each ionogram and from one ionogram to the next. Processor three also determines a 'cutoff' level for each block, which is used as a guide as to where the noise floor may lie within the block. The technique used to calculate this level involves arranging all the points within a block into 13 sets according to their magnitudes. The difference between the maximum and minimum group delays represented by the points in each set is calculated and those sets with differences less than a predetermined value (a fraction of the maximum possible difference: 5 ms) are ignored. The 'cutoff' level is then set to the upper magnitude limit of the remaining sets and is transferred to the PC along with the associated data block. The operator may choose either to ignore 'cutoff' levels or to use them to filter out noise on the displayed ionogram by not plotting any points with magnitudes less than the 'cutoff'.

Processor three performs additional tasks apart from handling data during a sweep. At system startup the processor initialises the LCD which is used during system operation to indicate the functions being performed by the PCU and the operating parameters in use.

Furthermore, before data collection begins the processor establishes remote control of the RCS-5 and receives instructions from the PC specifying how it is to be set up. The operator may have chosen to manually program the RCS-5 in the usual way using the receiver's front panel or to let the processor perform the task automatically using data previously recorded by the PC. In the latter case the processor proceeds by sending path details to the receiver and, if required, initiating the signal acquisition function. The processor also acts on further instructions received from the PC which specify the operating rate of the PCU and the type of window to be employed. Before each sweep commences processor three fetches the sweep start time from the RCS-5 and waits for the appropriate moment, as indicated by the real-time clock on the RCS-5, before triggering the data collection routines as a sweep begins.

### 5.3 PC Software

The software for the PC is written in TURBO C++ and performs the following functions:

- (a) reads in the data supplied from the PCU
- (b) displays the values in the form of an ionogram
- (c) stores ionogram data for future use
- (d) provides overall control of the ROSE ionosonde
- (e) supports the operator interface
- (f) provides features for recalling stored ionograms.

The data is read into the PC from the PCU using a high speed parallel interface which utilises direct memory access (DMA). This enables data transfer to occur as a background task whilst

the PC is performing other tasks - such as updating the displayed ionogram. Approximately 700 words of data are passed per vertical line of ionogram (682 values plus control information) and for a high resolution ionogram of 836 lines some  $836 \times 700 = 585$  kwords = 1,170 kbytes of data must be transferred.

As each block of data arrives from the PCU it is displayed as a vertical line on the ionogram. As the sweep progresses the ionogram builds up from left to right in the normal way. A colour scale of absolute magnitude values is also displayed along with data collection details and path information. The highest quality ionogram generated by the ROSE ionosonde has a resolution of  $836 \times 682$  points and contains 32 colours. To display this ionogram in full detail, along with its associated labelling, requires a specially selected screen. A  $1024 \times 768$  pixel screen and appropriate controller is used for the task. However, to maintain compatibility with other PCs the software is designed to also cater for normal VGA displays - although the complete ionogram is then displayed at a lower resolution and using fewer colours. The full screen ionogram represents the normal display mode, however, an alternative mode is available whereby four ionograms are displayed simultaneously at reduced resolutions and updated sequentially. This is useful for showing short term variations in the ionosphere.

The 1,170 kbytes of data which is transferred for a high resolution ionogram represents an impractical amount of data to be stored. Observation of ionograms reveals that only about 20% of the display area contains visible information and the rest is black background. This enables the file size to be reduced to 200 kbytes or less. Data compression techniques may also be selected which further reduce the file size.

As ROSE is primarily a research tool considerable effort has been made to ensure that the software provides control over a large number of system parameters. Before data collection begins the operator is able to select the type of data window to be employed in the PCU, the horizontal resolution of the ionogram and the display mode to be used. Start and stop times for data storage may also be specified. In addition, the operator may choose to remotely program the RCS-5 from the PC instead of using the receiver's manual controls. In this case the PC prompts for the sweep start time of the desired transmitter and instructs the PCU to handle the programming and synchronisation of the RCS-5.

The PC software also provides a number of features for handling ionogram information once it has been stored. In 'replay' mode stored ionograms are displayed sequentially at a high rate to give a 'movie' type of effect. This is useful for visually observing long term changes in the ionosphere. In 'scaling' mode a single ionogram may be recalled and by moving two hair-line cursors certain features of interest may be logged.

### 6 MAIN IMPROVEMENTS

A summary of the main improvements provided by the ROSE ionosonde are listed below.

(a) Ionograms displayed at high resolution (up to  $836 \times 682$  points) so that propagating modes are clearly visible and fine structure is discernable.

(b) Colour coding of signal power (up to 32 colours) against an absolute scale to enable amplitude comparisons across modes on a single ionogram and also comparisons between ionograms.

(c) Storage of information so that ionograms may be recalled when desired. Data compression is also available.

(d) A display format whereby the four most recently collected ionograms are shown simultaneously. *Useful for showing short term ionospheric variations.*

(e) A feature whereby stored ionograms are displayed rapidly in succession giving a 'movie' effect. *Useful for showing long term ionospheric variations.*

(f) Facilities which allow scaling of stored ionograms.

© British Crown Copyright 1991/MOD  
Published with the permission of the Controller of Her Britannic Majesty's Stationery Office

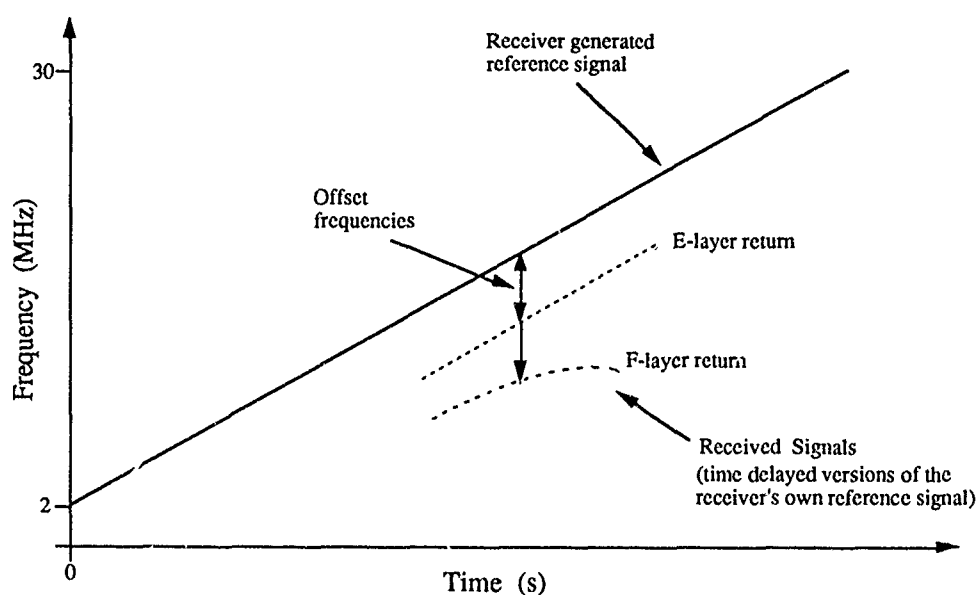


Fig 1. Frequency analysis in a HF oblique chirp sounder

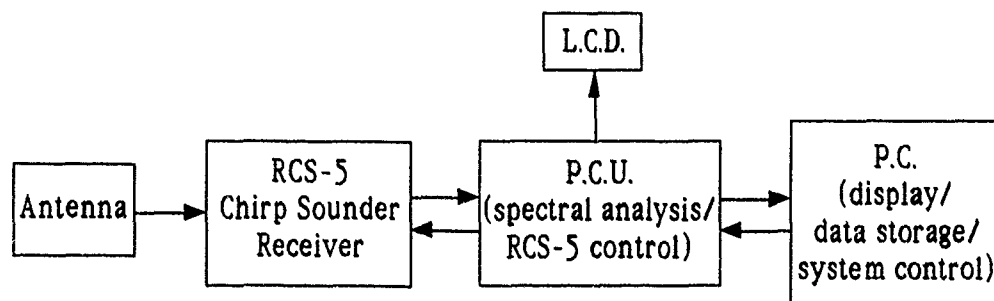


Fig 2. ROSE block diagram

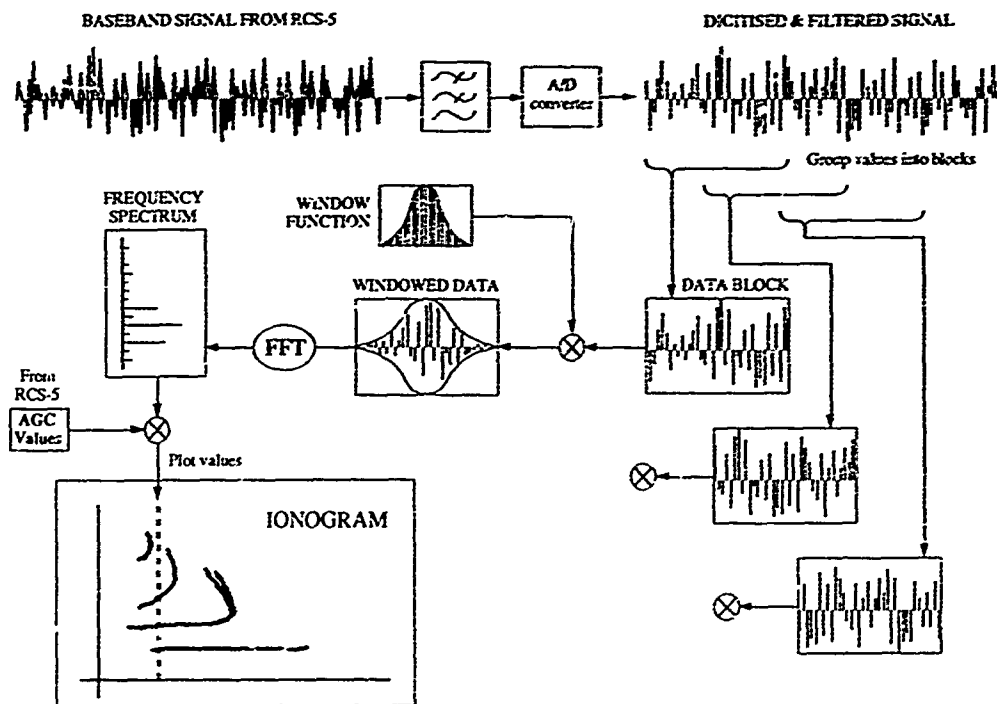


Fig 3. Analysis of the baseband signal in ROSE

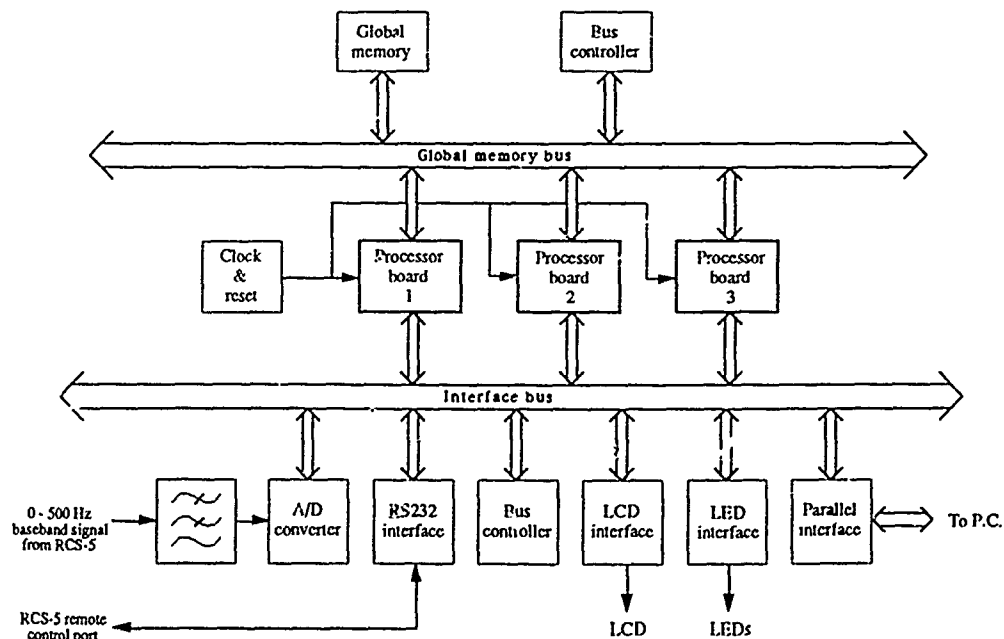


Fig 4. PCU block diagram

### DISCUSSION

#### **B. REINISCH**

*Your oblique ionograms show a good resolution. What is the range resolution of the system's digital processing in  $\mu\text{s}$ ?*

#### **AUTHOR'S REPLY**

*The range resolution of ROSE is  $7.3\mu\text{s}$  (or approximately 2 km). We believe that this range resolution is well matched to the ionosphere. On many occasions we see sporadic-E layers on our ionogram which are only one pixel (2 km resolution) wide.*

THE NEW PORTABLE DIGISONDE  
FOR  
VERTICAL AND OBLIQUE SOUNDING

Bodo W. Reinisch  
D. Mark Haines  
Walter S. Kuklinski  
University of Massachusetts Lowell  
Center for Atmospheric Research  
450 Aiken Street  
Lowell, MA 01854  
USA

### SUMMARY

A small low cost digital ionosonde, the Digisonde Portable Sounder (DPS) has been developed which uses 500 $\mu$ s, 10% duty factor, wide pulses for vertical sounding and 8.5ms pulses for oblique sounding. Intrapulse coding and pulse compression techniques result in a 67 $\mu$ s resolution for both waveforms. A new autoscaling technique for oblique ionograms inverts the oblique echo traces into midpoint electron density profiles that are modeled as a sum of quasiparabolic layers.

### 1. INTRODUCTION

Reliable high frequency (HF) communication, Over-the-Horizon radar tracking, and HF direction finding all depend on good real time knowledge of the ionosphere. In the last decade modern digital ionosondes (Reinisch, 1986) became available that automatically analyze the vertical ionograms and provide, in real time, the vertical electron density profiles for the location of the sounder (Reinisch et al., 1990). For many HF applications the ionosphere must be specified in a large area and a network of ionosondes is required. The new Digisonde Portable Sounder (DPS) has been designed for optimal efficiency in such a network by providing the necessary hardware and software for both vertical and oblique (bistatic between DPS stations) sounding.

For vertical sounding the transmitter pulse width is limited to about 500 $\mu$ s considering the pulse propagation time of 600 $\mu$ s for E region echoes. Intrapulse phase coding and pulse compression techniques provide a range resolution of 67 $\mu$ s (or 10 km). For quasi-vertical or bistatic sounding the DPS transmits 8.5ms pulses at 100% duty cycle with the same range resolution of 67 $\mu$ s. A DPS network can accurately map the ionosphere if both vertical and oblique ionograms are used to specify the electron density profiles at the locations of the sounders as well as at their mid-points. Any successful HF

application requires "now-casting" for the ionospheric propagation medium, i. e. current specification of the ionospheric region used by the HF link. Automatic scaling of the vertical and oblique ionograms in real time provides the inputs for the now-casting.

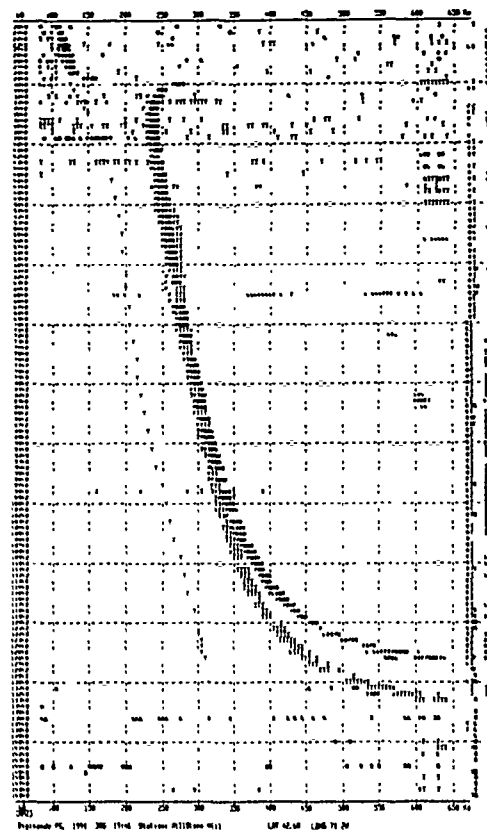
Autoscaling of the vertical ionograms is achieved with the ARTIST software (Reinisch and Huang, 1983, Gamache et al., 1985) which is routinely used in some forty Digisonde 256 sounders worldwide (Reinisch et al., 1990). New autoscaling for oblique ionograms and inversion to midpoint quasiparabolic electron density profiles is described in Section 3 of this paper. Section 2 gives a brief description of the Digisonde Portable Sounder.

### 2. DESCRIPTION OF THE DIGISONDE PORTABLE SOUNDER

Ground based HF observations of the ionosphere rely on the accurate measurement of the following observables:

1. frequency
2. height/range (time delay)
3. amplitude
4. phase
5. Doppler shift or spread (frequency dispersion)
6. wave polarization (left or right hand)
7. angle of arrival

All of these parameters are measured simultaneously by the DPS and as many as five are displayed at once in the various display modes available. For instance, the Doppler Ionogram in Figure 1 (Millstone Hill, 4 November 1991) represents an echo at a given frequency and height by its position in the display. The amplitude (in 2dB) is represented numerically by an optically weighted font, the Doppler shift is represented by shades of color while the polarization is represented by the color group. This paper shows a black/white printout using the letter X to indicate X-echoes. The



automatically scaled leading edges of the E and F-traces are identified by the letters E and F, and the electron density profile is indicated by the letter T.

Accurate measurement of all seven parameters, except the first, depends critically on the signal-to-noise ratio (SNR) of the received signal, therefore vertical incidence ionospheric sounders capable of requiring high quality scientific data have historically utilized powerful pulse transmitters in the 2 to 30kWatt range. For instance, measuring phase to 1 degree accuracy requires a SNR better than 40dB (assuming a

### Physical Layout of the DPS

Figure 3 shows the dimensions and component layout of the DPS. The single 19" rack mountable chassis is installed in a lightweight fiberglass transport case which includes a shock mounted 19" rack. This unit by itself (with the addition of a 24 volt battery and antennas) is ready to make, scale and store automated measurements as soon as power is turned on. A typical installation would also include a keyboard and monitor and two printers for real-time color or black and white outputs of measurement data. The operator can control the system either locally or remotely (via a telephone modem).

## Signal Processing

As mentioned above, the requirement for a good SNR seems incompatible with a small, lightweight, low-cost portable system, however by lengthening the transmitted pulse of a small low voltage solid state transmitter we can transmit an amount of energy per pulse equal to that transmitted by a high power pulse transmitter without having to provide components to handle the large voltages. The range resolution is recovered by phase modulation using an optimized phase code. This intrapulse modulation allows pulse compression in the receiver to restore a 10km resolution to separate the echoes from different ionospheric layers. The compressed pulse must, to an acceptable degree, reproduce a simple rectangular pulse (i.e. the spurious output of the pulse compression process must not obscure other signals of interest) and for monostatic operation (colocated transmitter and receiver) the entire waveform must be transmitted before the first echo of interest is received. Therefore, for vertical incidence sounding we selected an 8



Figure 2a. Digisonde Portable Sounder

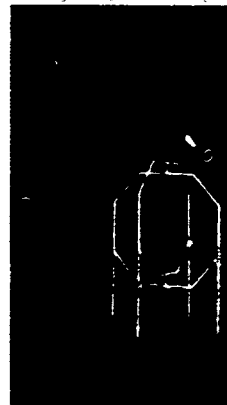


Figure 2b. Turnstyle Antenna

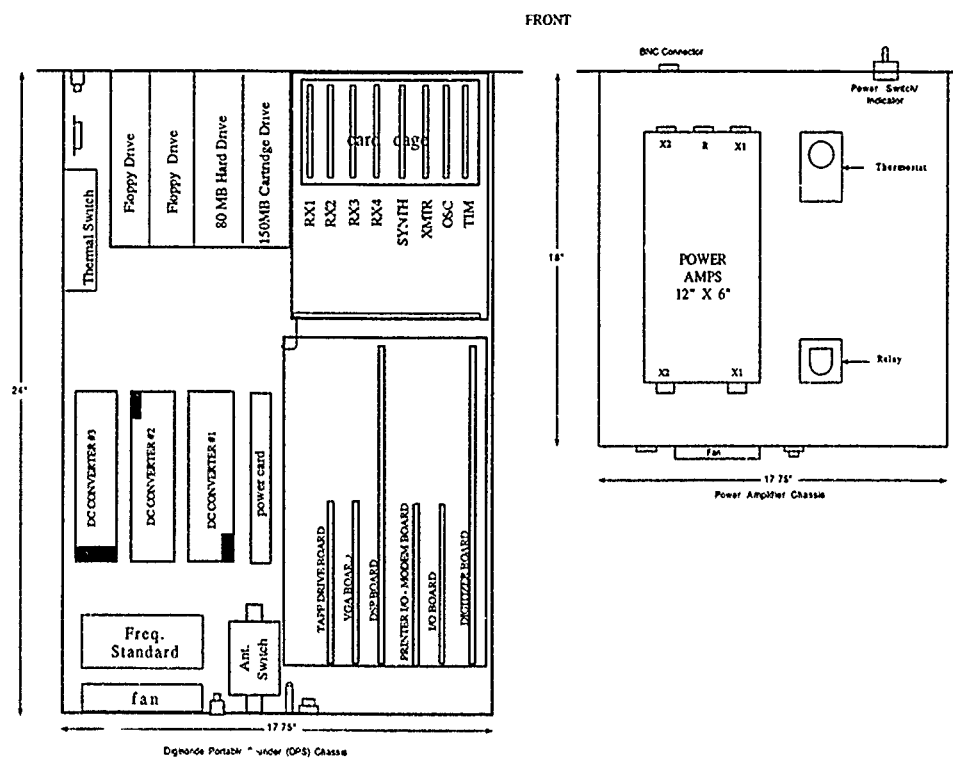


Figure 3. DPS Chassis Configuration

bit complementary (Golay, 1961) phase code pair modulated onto a 533 $\mu$ sec pulse which provides 12dB of SNR improvement upon pulse compression.

For bistatic operation such as oblique sounding or backscatter sounding, a 100% duty cycle CW (continuous wave) waveform can be used since the transmission need not be extinguished prior to sampling data at the receiver. For this mode of operation we have selected the 127 bit maximal length sequence code (Sarwate and Pursley, 1980) which allows pulse compression with a 21dB signal-to-noise ratio improvement while only producing 0.9% spurious amplitude response at ranges (time delays) other than the true range.

Added to the 12 or 21dB of pulse compression gain is the SNR gain offered by the Doppler integration process (also used in the Digisonde 256) which for 128 line Doppler spectra is 21dB. The effect of all this signal processing is tremendous. For instance, compared to the 500Watt DPS oblique waveform with its 42dB SNR improvement, a single pulse, non-integrating measurement system would require 8MWatts of transmitter power to obtain an equivalent SNR. Even a somewhat sophisticated system which coherently integrates 8 pulses (any more than 8 would require "Digisonde-like" Doppler processing due to Doppler induced phase changes over the integration period), would require a 1MWatt transmitter in order to be equivalent.

#### Multiplexing

Using any of the above waveforms, the Digisonde Portable Sounder allows multiplexed Doppler integration of up to 64 separate combinations of frequencies, antennas (the system includes 4 phase matched receiving antennas), and polarizations (i.e. ordinary or extraordinary propagation modes, hereafter referred to as O and X). This multiplexing is implemented by changing the system's operating parameters from pulse-to-pulse. This essentially simultaneous measurement at multiple frequencies, antennas and polarizations is accomplished by synchronizing the computer's data acquisition and signal processing software to the transmitted waveform through a hardware interrupt. The interrupt is timed to occur just 250 $\mu$ sec prior to the occurrence of a transmitted pulse, or coded waveform, such that the frequency, antenna selection, gain, polarization, or waveform can be changed in a pre-computed sequence. The switching of any or all of these parameters is accomplished in 22 $\mu$ sec giving the system ample time (about 200 $\mu$ sec) to settle before transmitting. At the end of the

multiplexed Doppler integration the system contains an entire Doppler spectrum for each resolvable range, each receive antenna, each frequency and each polarization measured, up to 8192 128-line complex spectra. The real-time pulse compression and Doppler processing is performed in a digital signal processor embedded within the system which is fast enough to allow it to keep up in real-time with the data acquisition. The pulse-to-pulse control offers the flexibility to optimize the multiplexing process for any of a number of different types of measurements. A few of these are:

1. Angle of arrival. Since the data on four spaced receiving antennas is acquired quasi-simultaneously, the signal phases measured on each of the antennas can be used to compute an angle of arrival for each range and Doppler component of the received signal.
2. Precise Group Height. By observing the change in phase of a signal as a function of small changes in frequency (e.g. 10kHz), the altitude of a reflecting layer can be determined with high accuracy. The limitation is signal-to-noise ratio dependent, but accuracies of 100's of meters are routinely achievable. The time history of the precise height can be measured by repeated soundings at a fixed frequency.
3. Identification of O or X Propagation Mode. By simultaneously integrating all heights at both polarizations, the detected echo is compared in the two separate data buffers to determine which receive polarization produced a larger response, therefore even elliptically polarized signals can be declared O or X even though some of the echo amplitude "leaks" into the wrong polarization channel.
4. High Doppler Resolution. Although high Doppler resolution could be achieved simply by slowing down the pulse repetition rate or producing extremely large Doppler spectra (e.g. 4096 complex Doppler lines), both approaches increase the time required to make measurements. Since the ionosphere rarely produces more than a few Hertz of Doppler shift the Doppler analysis of pulses transmitted at a 200Hz rate (giving a Doppler range of  $\pm 100$ Hz) is usually inefficient. However, by simultaneously integrating 16 sounding frequencies, the Doppler range is brought down to  $\pm 6$ Hz, which can provide 0.0941Hz Doppler resolution rather than 1.5Hz. At the end of this multiplexed integration 16 frequency steps have been measured and are ready for display. This high Doppler resolution swept frequency ionogram is performed

16 times faster than would be possible with a conventional non-multiplexed mode of operation.

#### Automatic Sequencing

An operator who is only casually familiar with the inner workings of a DPS sounder can easily compose some very complex measurement sequences by selecting programmed measurement parameters from an interactive screen. The parameters presented on the screen specify frequency range, frequency resolution, multiplexing parameters, height resolution, Doppler range and resolution, data storage formats and automatically schedule unmanned operation. Since there are up to 8,192 Doppler spectra in memory at the end of a coherent integration, and typically less than 1% is useful data at the end of a coherent integration, data storage formats allow the user to specify criteria for reducing the amount of data stored:

- a. selection of 1 maximum amplitude in each Doppler spectrum per height measured.
- b. storage of spectra from of a limited number of heights around the leading edge of a layer.
- c. storage of a limited number of Doppler lines around zero for each height measured.
- d. or storage of everything available (i.e., a scattering function which is all Doppler lines at all ranges measured).

The program and schedule settings selected by the user (either remotely or locally) during an interactive editing session are stored in a hard disk file and become the new default settings the next time the system is turned on.

#### Oblique Sounding

Before addressing the use of oblique sounding data for the characterization of the ionosphere at the midpoint, we will describe this operating mode. In addition to the CW waveform, the DPS has optimized oblique channel measurements by providing precision timing, a highly stable frequency source and automatic synchronization with distant transmitters. All timing waveforms are generated from a counter chain which can be driven by a Rubidium frequency standard. The counter chain can be synchronized to an "external" 1 PPS (pulse per second) timing reference (typically GPS, GOES satellite clock, or LORAN) and will maintain synchronization to 1μsec accuracy. The internal timing signals can be offset by a pre-determined amount (i.e. a menu parameter) up to 0.5 seconds to compensate for propagation time delays. Therefore, each transmitted pulse occurs just as the receiving system expects it.

The oblique ionogram data stored for midpoint measurements is a 16 line Doppler spectrum at each of 256 heights (time delays) providing 96 dB of dynamic range in 0.375dB steps. This data is stored on a disk file and on a tape cartridge and the midpoint profile processing can proceed.

### **3. ADAPTIVE OBLIQUE IONOGRAM SCALING AND PROFILE INVERSION**

We have developed an adaptive set of robust algorithms to automatically scale and invert oblique ionograms. These algorithms utilize one or both scaled end point vertical ionograms to estimate the oblique ionogram. This estimate, which is used by subsequent filtering and trace identification algorithms, is updated whenever the vertical ionograms change.

#### Algorithm Development

The automatic oblique ionogram scaling algorithm uses a tracking algorithm (Sun, 1989) to determine the leading edge points of each echo trace. These scaled leading edge points are used directly to calculate a midpoint electron density. The direct inversion process, assumes each ionospheric layer can be modeled with a quasi-parabolic electron density profile. This inversion technique requires the absolute group path information that is provided by the synchronized operation of two Digisonde. The tracking algorithm uses the scaled vertical ionogram, produced in the end point Digisonde, to synthesize the echo traces that would be measured over the oblique link if the midpoint ionosphere and the ionosphere at the transmitter were identical. While the overhead and midpoint ionospheres are typically not equal, they are similar enough to provide an excellent starting point from which any differences between the ionosphere at these two locations can be determined. These synthesized oblique echo traces are also used in a noise suppression filter and subsequent trace identification algorithm. The utilization of these real-time synthesized oblique echo traces produces an adaptive algorithm whose performance is superior to a non-adaptive approach.

#### Frequency Redundancy Filter

The first operation performed on the received oblique ionogram is a frequency redundancy noise suppression. A 100kHz oblique ionogram, which has sufficient resolution for calculating the equivalent midpoint electron density profile, is generated from either 25 or 50kHz sounding data by selecting the highest signal-to-noise ratio channel from each set of four adjacent 25 kHz soundings or two adjacent 50kHz soundings.

### Noise Suppression Wiener Filter

The subsequent noise suppression filter uses an adaptive minimum-mean-square Wiener filtering technique (Andrews and Hunt, 1969, Kuklinski et al., 1990). The 100kHz oblique ionogram is modeled as the sum of a noise/interference signal and the desired noise free oblique autotraces. The Wiener filter is produced by dividing the power spectral density of the synthesized oblique echo traces by the sum of the power spectral densities of the synthesized oblique echo traces and an estimate of the noise power spectral density as shown in equation (1).

$$H(\omega_t, \omega_f) = \frac{P_{et}(\omega_t, \omega_f)}{P_{et}(\omega_t, \omega_f) + P_n(\omega_t, \omega_f)} \quad (1)$$

The noise power spectral density was calculated from ionograms recorded while the transmitter was off, using a two-dimensional periodogram technique. Typical results are shown in Figure 4. The upper panel is a representative 100kHz oblique ionogram with the corresponding filtered ionogram in the lower panel.

The synthesized oblique echo traces, derived from the end point ionograms, are also used to define regions of interest for subsequent processing. These regions of interest, as shown in the upper panel of Figure 5, are defined as all points within a specified number of group path range bins and sounding frequencies of the synthesized oblique echo traces. At present the allowable variations were derived from the variances of an oblique ionogram data base. Any echoes in the region of interest for a particular layer is considered to be part of the echo trace for that layer.

The tracking algorithm determines, at a given sounding frequency, where the echo trace most closely matches an assumed template of echo trace amplitudes. To obtain this optimal location, the template is translated and rotated about an initial estimate. The mean square difference between the actual echo trace amplitudes and the template is used by two sequential gradient searches, one for translation and one for rotation, to determine the optimal location. The results of this local search process are the locations of the center, leading and trailing edges of the echo trace. The algorithm uses this information to estimate the group path of the echo trace at the next sounding frequency to be processed. The template matching procedure is repeated until the entire echo trace is scaled in this manner.

### Midpoint Profile Modeling

Our technique assumes that the ionosphere at the midpoint can be modeled by one or more quasiparabolic (QP) segments (Dyson and Benrett, 1988). In principle, the parameters that define a single QP layer can be calculated from any three pairs of group path vs. sounding frequency data since the ground range between transmitter and receiver is known. In practice however, the numerical sensitivity of the equations that relate the group path and ground range of a ray to the take-off angle and QP layer parameters, causes these three point solutions to be unstable. The tracking algorithm utilized here has the flexibility to produce the required number of scaled leading points for a numerically stable inversion.

The inversion algorithm uses a simulated annealing optimization method to determine the QP electron density profile (Croft and Hoogasian, 1968) for each layer. The QP layer is defined as:

$$N_e = \begin{cases} N_m \left[ 1 - \left( \frac{r - r_m}{y_m} \right)^2 \left( \frac{r_b}{r} \right)^2 \right] & r_b < r < r_m \left( \frac{r_b}{r_b - y_m} \right) \\ 0 & \text{elsewhere} \end{cases}$$

where  $N_e$  = electron density,  $r$  = radial distance from earth center,  $r_b$  = radial distance to the bottom of the layer,  $r_m$  = radial distance of maximum electron density,  $N_m$  = maximum electron density, and  $y_m$  the layer semithickness.

The E layer QP parameters are determined from the scaled oblique E echo points. This QP E layer and the scaled oblique F1 echo points are used to determine the F1 layer QP parameters and, if an F2 trace is present, the E and F1 layer QP parameters and the scaled oblique F2 echo points are used to determine the F2 layer QP parameters.

The multilayer QP model produces the following analytical relationships for the group path,  $P'$ , and the ground range,  $D$ , of a ray in terms of takeoff angle, sounding frequency, and layer parameters.

$$D = \sum g1i(r_{mi}, y_{mi}, N_{mi}, \beta, f) \quad (2)$$

$$P' = \sum g2i(r_{mi}, y_{mi}, N_{mi}, \beta, f) \quad (3)$$

where  $i$  is the layer index,  $\beta$  is the ray takeoff angle, and  $f$  is the sounding frequency.

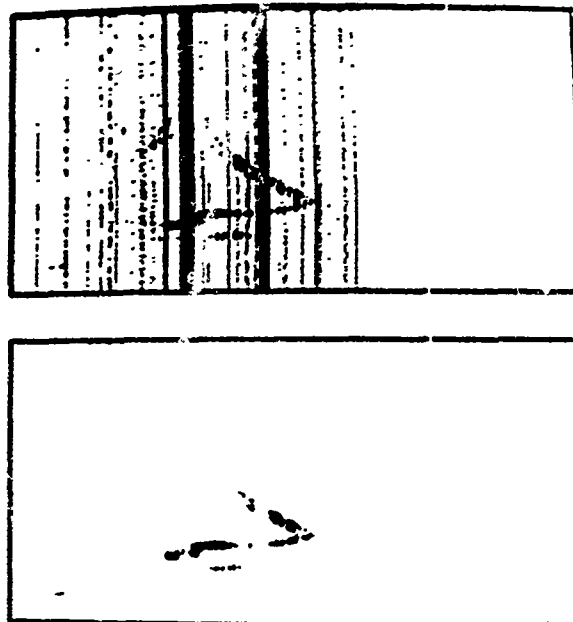


Figure 4. 100kHz Oblique Ionogram Produced via the Frequency Redundancy Technique (Upper). Resulting 100kHz Oblique Ionogram After Processing through the Modified Wiener Trace Enhancement Algorithm and the Noise Suppression Technique (Lower). Goose Bay, Labrador to Millstone Hill, Massachusetts; April 5, 1988, 1908 UT.

Year : 88 Day : 096 Time : 18:59:05

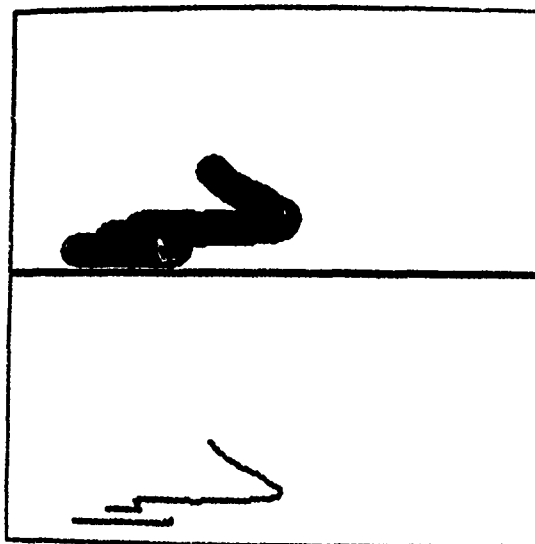


Figure 5. End Point Synthesized Oblique Ionogram via Secant Law (Lower). Region of Interest Calculated from the E and F Layers of the Corresponding Vertical Ionogram (Upper). Goose Bay, Labrador to Millstone Hill, Massachusetts; April 5, 1988, 1859 UT.

The simulated annealing optimization technique we use to determine the QP electron density profile has been applied to solve many large scale combinational optimization problems (van Laarhoven and Aarts, 1988). In these optimization problems an objective function that depends on the configuration of a large set of system parameters is minimized. In the QP electron density profile inversion problem, the system is the collection of quasiparabolic segments used to model the midpoint ionosphere. The objective function used in the electron density inversion is the sum of the squared differences between the group paths calculated from the QP model and those obtained from the scaled oblique ionograms.

Typical results are seen in Figures 6, 7 and 8. The left panels of each figure show the group paths calculated from the QP electron density model (dots) in relation to the oblique ionogram. The right panels are the corresponding ground ranges in relation to the known ground range (straight line). Seven scaled points from the oblique ionogram were used in this example. The upper panels of Figure 6 contain the original scaled oblique ionogram and the known ground range. The middle panel of Figure 5 shows the group paths and ground ranges of the seven rays for the initial estimates of the layer parameters and rays takeoff angles. Any group path differences greater than 500km are plotted as being equal to 500km, hence the four group path points at the top of the left middle panel of this figure. After the first iteration the three low angle ray group paths are within 41km of the actual oblique data, while the three low angle ray ground ranges are within 43km of the actual ground range. Figure 7 contains the data obtained for iterations 3 through 5 in the upper, middle and lower panels respectively, while Figure 8 contains the corresponding data for iterations 6 through 8. As the iterations are performed the algorithm converges to a QP layer that minimizes the total difference between the measured and calculated oblique ionograms. By the eighth iteration (lower panel of Figure 8) the largest group path difference between the actual data and the quasiparabolic model is 4km, while the largest ground range difference is 6km.

#### 4. CONCLUSION

A small low cost ionospheric sounder has been developed and tested that is optimally suited for automated vertical and oblique sounding. Automatic scaling algorithms for the vertical as well as the oblique ionograms provide the vertical electron density profiles at the sounder locations and at the midpoints. While the real time

scaling profile inversion of the vertical ionograms has become a routinely applied technique, the automatic scaling of oblique ionograms in terms of quasiparabolic midpoint profiles is still at an experimental stage.

#### Acknowledgement

This research was in part (autoscaling of oblique ionograms) supported by Air Force Contract No. F19628-90-K-0029 under the "DORIS" subtitle item.

#### 5. REFERENCES

- Andrews H. C. and Hunt B.R., "Digital Image Processing," Prentice-Hall Co., 1969.
- Croft T. A. and Hoogasian H., "Exact Ray Calculations in a Quasiparabolic Ionosphere With no Magnetic Field," Radio Science, 3, p 69., 1968.
- Dyson, P.L. and Bennett, J.A., "A Model of the Vertical Distribution of the Electron Concentration in the Ionosphere and its Application to Oblique Propagation Studies," Journal of Atmos. and Terr. Phys., 50, 3, pp. 251, 1988.
- Gamache, R.R., Kersey, W.T., and Reinisch, B.W., "Electron Density Profiles from Automatically Scaled Digital Ionograms. The ARTIST's Valley Solution," Scientific Report No. 1, AFGL-TR-85-0181, ULRF-434/CAR, Air Force Geophysics Laboratory, 1985.
- Golay, M.J., "Complementary Codes," IRE Transactions on Information Theory, April, 1961.
- Kuklinski W. S., Kitrosser D. F., Reinisch B.W., "Automation of Oblique Propagation Measurements Oblique Trace Identification and Inversion," Scientific Report, No 22, GL-TR-90-0389, ULRF-465/CAR, Air Force Geophysics Laboratory, January 1990.
- Laarhoven van, P.J.M. and Aarts E.H.L., "Simulated Annealing Theory and Applications," D. Reidel Publishing, 1988.
- Reinisch, B.W. and Huang, X., "Automatic Calculation of Electron Density Profiles from Digital Ionograms, 3, Processing of Bottomside Ionograms," Radio Science, 18, 477, 1983.
- Reinisch, B.W., Bibl, K., Kitrosser, D.F., Sales, G.S., Tang, J.S., Zhang, Z.M., Bullett, T.W., and Ralls, J.A., "The Digisonde 256 Ionospheric Sounder," WITS Ionosphere/Thermosphere Study, WITS Handbook, Vol. 2, Ed. by C.H. Liu, December 1989.

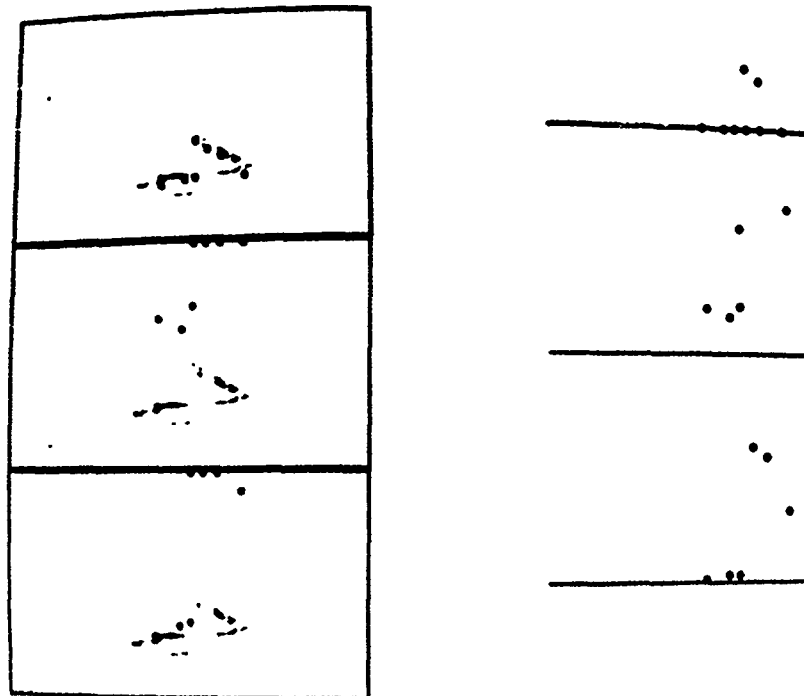


Figure 6. Algorithm Convergence Properties, Iterations 0 through 2.

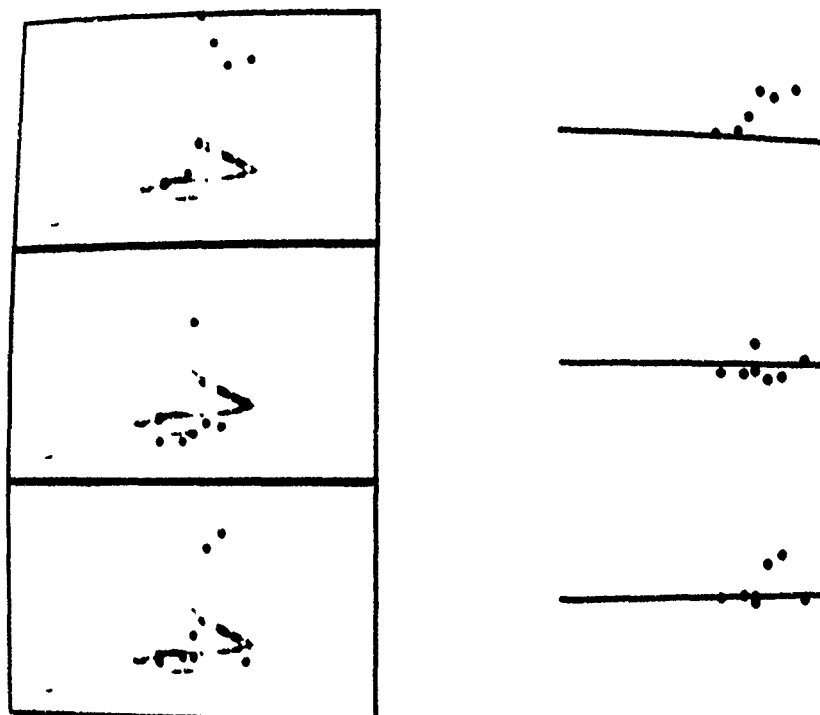


Figure 7. Algorithm Convergence Properties, Iterations 3 through 5.

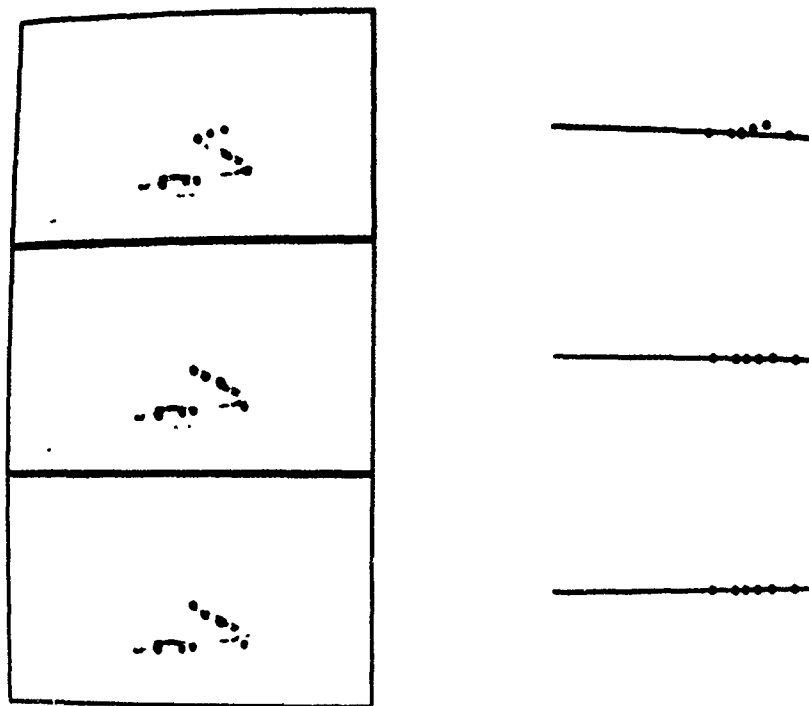


Figure 8. Algorithm Convergence Properties, Iterations 5 through 7.

Reinisch, B.W., Gamache, R.R. and Bossy, L.G., "Ionospheric Characteristics for IRI in Real Time," *Adv. Space Res.*, 10, 8, pp. (8)25-(8)34, 1990.

Reinisch, B.W., "New Techniques in Ground-Based Ionospheric Sounding and Studies," *Radio Science*, 21, 3, pp. 331-341, May-June 1986.

Sarwate, D.V. and Pursley, M.B., "Crosscorrelation Properties of Pseudorandom and Related Sequences," *Proceedings of the IEEE*, 68, 5, May, 1961.

Sun Y., "Development of a Coronary Artery Blood Vessel Tracking Algorithm," *IEEE Transactions on Medical Imaging*, 8, 1, p78, 1989.

## DISCUSSION

### **C. GOUTELARD**

Votre communication est très intéressante et elle m'a passionné au point de vous poser deux questions.

Vous signalez que la puissance équivalente en impulsion de votre système est de 8MW. Il me semble cependant que vous effectuez un traitement post-correlation par transformée de Fourier. Il faudrait tenir compte d'un traitement similaire dans le cas du système impulsionnel. De plus en télédétection où la fonction d'ambiguïté du signal doit être prise en compte les codes continus se trouvent pénalisés. Pouvez-vous faire un commentaire?

Ma deuxième question porte sur le modèle que vous utilisez pour l'ionosphère, un modèle à trois couches quasi paraboliques. Cela permet de mener des calculs analytiques. Nous utilisons un modèle proche de celui de Bradley Dudeney avec 2 couches quasi paraboliques et 1 couche quasi linéaire. Nous menons comme vous des calculs analytiques - par exemple avec des équations de Lagrange - pour modéliser la propagation. Quel est votre avis sur l'opportunité d'utiliser l'un des modèles plutôt que l'autre?

*Your paper is very interesting and it impressed me so much that I should like to ask you two questions:*

*You state that the equivalent pulse power of your system is 8MW. It seems to me however, that you carry out post-correlation processing using a Fourier transform. Similar processing would need to be allowed for in the pulsed system. What is more, the continuous codes are penalised in remote sensing where allowance needs to be made for the ambiguity function of the signal. Would you care to comment?*

*My second question concerns the model which you use for the ionosphere, a model with three quasi parabolic layers. This enables one to make analytical calculations. We use a model similar to the one produced by Bradley Dudeney with 2 quasi parabolic layers and 1 quasi linear layer. Like you, we make analytical calculations - using Lagrange equations for example - to model propagation. What do you think is the advisability of using one model rather than the other?*

### **AUTHOR'S REPLY**

1. For oblique sounding we use the 127 bit maximal length sequence code providing 21 dB S/N improvement. Another 21 dB S/N gain is obtained by the 128 point Doppler integration. 42 dB over 500 W corresponds to 8 MW of a single pulse no-integration system. Without spectral integration (like in the Digisonde) one should not phase-coherently integrate more than 8 pulses (to avoid loss of Doppler shifted echoes). This requires 1 MW for the same S/N ratio.
2. The Bradley-Dudeney profile may have an advantage over the 3 parabola model in that it has less harsh discontinuities between the layers. We prefer the parabolic model since it can be made completely smooth (continuous first derivative) by adding two inverted parabolas between the layer parabolas. Fast analytical ray tracing through parabolic sections of the ionosphere exists. Stability of the inversion solutions is good for our technique, I do not know what it would be for the B-D profile.

### **E. SCHWEICHER**

1. Did you use a Barker code or some other pseudo-stochastic code?
2. Did you perform your pulse compression by software or by hardware?

### **AUTHOR'S REPLY**

1. A complementary 8 bit code is used for vertical sounding in a "moderate" ionosphere. The Barker code is used in a high-Doppler (polar cap) ionosphere.
2. Software pulse compression.

## SENSING THE IONOSPHERIC REFLECTION CHANNEL WITH A SOUNDER

K. C. Yeh

Department of Electrical and Computer Engineering  
University of Illinois at Urbana-Champaign  
Urbana, IL 61801-2991

Haim Soicher

Center for Command, Control and Communications Systems  
U. S. Army Communications-Electronics Command  
Fort Monmouth, NJ 07703-5202

### SUMMARY

The ionospheric reflection channel is known to be dispersive, random and time varying. The dispersion comes about because the ionized medium itself is dispersive as well as the fact that the radio waves at various frequencies within a frequency band follow different ray paths in the reflection process in order for all frequencies within the band of the signal to converge on the fixed receiver. Several decades of sounding and experimentation have cumulated a wealth of evidence to show that the ionosphere usually contains a spectrum of irregularities extending in scale from centimeters to hundreds of kilometers. A convenient way to describe such a plethora of irregularities is to use the stochastic notion, which makes the reflection channel random. The time dependent forcing and the ionospheric winds carrying imbedded irregularities with them render the channel time dependent. All these effects combined make the ionospheric reflection channel dispersive, random and time varying.

A sounder has been designed and constructed to probe the ionosphere for such channel properties. The sounder must be capable of probing the ionosphere for wideband response. The implemented sounder consists of a transmitter located in Platteville, Colorado and a receiver located in Urbana, Illinois separated by a ground distance of 1401 km. The transmitter and receiver are both PC controlled to sound the ionosphere at 6 frequencies selectable by the experimenter in the range 5 to 15 MHz. The sounder can be commanded by a central PC in the laboratory to work in either the ranging mode or the probing mode. In the ranging mode, the time delay is measured while in the probing mode, the quadrature components (or amplitude and phase) are measured. In

this paper we report some experimental results obtained by using this sounder. Specifically some properties of the time dependent transfer function of the channel are described.

### 1. INTRODUCTION

For decades, the Earth's ionosphere has been probed by HF pulse sounders from below the ionosphere by ground based radars (bottomside ionosondes) as well as above the ionosphere on board some satellites (topside ionosondes). The sounding of the ionosphere from a ground based radar can be carried out either in a vertical sounding mode or in an oblique sounding mode. In the vertical sounding mode, the waves are sent vertically upward and the reflected waves are received at a co-located receiving site. On the other hand, in an oblique sounding mode, the receiver and transmitter may be separated by an appreciable distance. A fairly complete description of such techniques can be found in [1]. The obtained data when displayed in the virtual height (distance) vs. frequency format is known as an ionogram. For many applications what is desired are the ionization profiles. Mathematical calculations involved in converting an ionogram into an ionization profile are sometimes referred to as true height calculations. Various methods have been developed to make these true height calculations [2]. In the past the ionogram must be scaled by hand and converted into a digital format understandable by a computer for the true height computation. This step is slow and tedious. It can be circumvented if the ionosonde can produce a machine readable digital ionogram. Therefore, the digital ionosondes are invented [3] followed by the development of the associated algorithms for trace identification and

true height computation [4]. Such software development is likely to be continued.

While digital ionosondes are modern and desirable, for applications to communication such as channel characterization, they are not sufficient at least for three reasons. First, even if the reliable ionization profiles can be computed from ionograms, one needs to trace many rays in order to understand propagation conditions. Thus to obtain the desired communication channel parameters additional computations on a computer are needed. Second, frequently the ionogram is blurred due to presence of spread F irregularities. On such occasions it may be impossible to identify the trace on the ionogram for true height computations. This is the time the channel parameters are of special interest, but the ionograms cannot be used for channel characterization. Third, the current technology brings the wideband transmission and coding into the picture. To understand how signals will behave requires rather sophisticated computer software. Therefore, what seems to be desirable is a channel probe that will measure the channel parameters directly. This area has received increasing interest of late and several probes have been developed for this purpose [5,6].

In this paper we review in section 2 the properties of the ionospheric reflection channel. The experimental system is then described in section 3. We show some preliminary experimental data in section 4 as well as statistical channel properties computed from these data. The paper is finally concluded in section 5.

## 2. PROPERTIES OF IONOSPHERIC REFLECTION CHANNEL

A radio wave propagating through a horizontally stratified ionosphere with embedded random irregularities has its electric field given in the form

$$\vec{E}(\vec{r}) = U(\vec{r}) \vec{E}_0(z) \exp -jk_0 x \sin \theta_0 \quad \text{V/m} \quad (1)$$

where  $E_0(z)$  in V/m is the wave function for the background ionosphere, the dimensionless quantity  $U(\vec{r})$  is the complex amplitude and the exponential factor takes care of the phase shift originating from the Snell's law. The product form of these three factors appearing in (1) is important as it reveals the dependency of the electric field to various ionospheric processes. As mentioned, the exponential factor comes from the Snell's law and is a constant factor for the fixed receiver (i.e. fixed distance  $x$ ). However, as the radio frequency is varied, the incidence angle  $\theta_0$  must also be varied so that the transmitted ray will be "homed" exactly to the receiver. This phenomenon is sometimes known as the frequency splitting phenomenon.

The factor  $E_0(z)$  satisfies the wave equation

$$d^2 E_0 / dz^2 + k_0^2 q^2 E_0 = 0 \quad (2)$$

where  $q^2 = \epsilon(z) - \sin^2 \theta_0$ . At the point of reflection (also known as the turning point),  $q$  vanishes and the ray theory becomes invalid. The usual technique is then to approximate  $q^2$  near the turning point linearly (i.e. the first term in a Taylor's expansion), for which (2) has the solution given in terms of Airy functions. When away from the turning point, the Airy functions are connected smoothly to the WKB solutions. Both theoretical studies [7,8] and experimental studies [9,10] have shown that to the first order the reflection process can be modeled as a quadratic phase channel. The modulus of the complex transfer function for such a channel is constant while the phase variation across the frequency band is approximated by

$$\phi(\omega) = \phi(\omega_c) + \phi'(\omega_c)(\omega - \omega_c) + \frac{1}{2} \phi''(\omega_c)(\omega - \omega_c)^2 \quad (3)$$

where  $\phi(\omega_c)$  is the phase at the carrier (angular) frequency  $\omega_c$ ,  $\phi'(\omega_c)$  is equal to the time delay of a pulse traveling from the transmitter to the receiver via a reflection from the ionosphere, and  $\phi''(\omega_c)$  is known as the dispersion coefficient. In (3), the quadratic term is responsible for pulse dispersion and is therefore a quantity of interest. Past efforts in this direction have been summarized in several books [11]. In a horizontally stratified isotropic ionosphere the dispersion coefficient can be conveniently related to the ionogram by [12,13]

$$\phi''(\omega_c) = \frac{1}{2\pi c} \left| \frac{4h' \cos \theta_0 dh'/df_v}{p' - 2f_c \sin^2 \theta_0 dh'/df_v} \right| \quad (4)$$

where  $c$  is the free space velocity of light,  $h'$  is the virtual height at a frequency  $f_v$  related to the carrier frequency  $f_c$  by the secant law, and  $p'$  is the group path. Thus, if  $h'$  is available from the ionogram, (4) can be used to compute the dispersion coefficient  $\phi''(\omega_c)$  for a given path. A formula such as (4) is very useful because of worldwide availability of ionograms. The use of (4) can yield the dispersion coefficient and the dispersion bandwidth [12] practically on a global basis.

As frequently happens, the ionosphere can be permeated by random irregularities. For waves reflected from such an irregular ionosphere, the otherwise unity complex amplitude  $U$  in (1) becomes a random function. Under the forward scatter approximation,  $U$  is found to satisfy a parabolic equation which can be solved numerically by the phase-screen diffraction layer method [14]. For a given ionospheric model and propagation geometry,  $U$  is solved for many frequencies across the band of interest. The complex amplitude  $U$  as a function of frequency can be viewed as the complex transfer function. The modulus and the phase of the transfer function have been

computer and presented for many cases [15]. The effect of such a transfer function on pulse distortion can be computed and is shown visualized in Fig. 1, where response to a triangular input pulse is plotted at successive distances (or successive times for a moving ionosphere). The distortion from an idealized triangular pulse can be quantified by using the concept of temporal moments [16]. The first temporal moment is related to the time of arrival, the second moment is related to the pulse width, the third moment is related to the skewness, and the fourth moment is related to the kurtosis. These moments have also been studied [15].

As indicated by (1) the combined effects caused by scattering from irregularities and dispersion from background ionosphere enter in a multiplicative fashion. They may cause severe distortion to pulses reflected from the ionosphere.

### 3. DESCRIPTION OF THE EXPERIMENTAL SYSTEM

In order to investigate the wideband response of the ionospheric communication channel, a University of Illinois sounder has been designed, constructed and deployed. The transmitting site is located in Platteville, Colorado (40.18°N, 104.73°W). The supporting electronics are housed in a trailer which was towed to the Platteville site in the spring of 1989. This site is operated by the Wave Propagation Laboratory, National Oceanic and Atmospheric Administration, Department of Commerce. It was previously used for high power ionospheric modification experiments. Such experiments are no longer conducted at the site but the antenna field is still covered by a good ground conducting screen which is now used for our experiment. The transmitting antenna is a log-periodic dipole designed to cover the 5 to 15 MHz band and is fed with an open-wire line coupled to the transmitter with a balun transformer. The complete antenna stands over a wire mesh ground screen. The transmitter is capable of delivering to the antenna up to 500 watts wideband signal in the same frequency range. The transmitter is driven with 6 coherently generated frequency synthesizers, each capable of synthesizing any one of 800 equally spaced discrete frequencies within the 5 to 15 MHz frequency range. This transmitter is both commanded and monitored by a PC in the trailer.

The receiver is located at Urbana, Illinois (40.069°N, 88.225°W) on campus of the University of Illinois. When viewed from Platteville, Urbana is in a direction 85.16° east of true north at a great circle ground distance of 1401.36 km away. Due to space limitations, the receiving antennas consist of two parts: a relatively small (12 × 30 m) and low (18 m) horizontally polarized short dipole array is used for receiving frequencies 10 to 15 MHz and 4 dipoles suspended between two 30 m towers are used for receiving 5 to 10 MHz. The receiver

and the associated recording devices are capable of receiving up to 6 different frequency channels simultaneously. The receiver is commanded by another PC.

The sounder system is capable of operating in two modes: probing mode and ranging mode. In the probing mode, the complex field amplitude at the receiver due to a selected transmitted CW is measured. Up to 6 channels in the 5 to 15 MHz range can be selected. In the ranging mode, total propagation time delay between the transmitter and the receiver via a reflection or more from the ionosphere is measured with 10  $\mu$ s resolution.

All the receiver channels are identical and linear from -50 dBm to 100 dBm. The first LO of each channel is coherently generated for 6 channels and translates the input signal to a standard IF of 60 MHz. When operating in the probing mode, the signal is then further translated to its baseband of 50 Hz and I-Q detected. The I-Q outputs are integrated over 8 ms intervals, digitized by a PC and logged onto magnetic tapes to be processed off-line. This 125 Hz sampling rate is higher than the Nyquist frequency.

The ranging mode uses maximal linear codes [17] to phase modulate the CW that is transmitted. This code has the property that the autocorrelation function is maximum when the code is exactly aligned with itself and has very low side lobes when off aligned. The codes used are 255 bits in length and are clocked at 20 kHz, making it possible to measure a total range delay up to slightly over 10 ms. The onset of the codes are carefully timed in order to synchronize the detection at the receiver. Time synchronization at the transmitter and receiver sites is achieved by locking time codes transmitted by the GOES satellite. Synchronization to within 50  $\mu$ s of the clocks is possible. In the ranging mode, the search for code coincidence starts simultaneously with the code onset at the transmitter. Search rate is 8 ms per step. Each step covers one-fifth of a code chip which is 50  $\mu$ s long. Therefore, a theoretical range resolution of 10  $\mu$ s is possible. It would take 10.2 seconds to search through the length of the code. Mechanism in the receiver search hardware allows leapfrogging a given delay interval such that delays less than a fixed interval can be bypassed to shorten the search time thus enabling us to generate more useful data in less time. The propagation delay determined by the ranging operation can be used to determine the modes of propagation and ease the interpretation of probing data.

### 4. PRELIMINARY EXPERIMENTAL RESULTS

In this section we describe some preliminary experimental results obtained by using this system. We start with some sample data first. We then show a few statistical analyses that have been performed on the data.

Shown in Fig. 2 is an example of ranging data taken on September 11, 1989 at six frequencies with channel 1 (top channel) at 12.7750 MHz and channel 6 (bottom channel) at 12.8250 MHz. As described in section 3, a spike corresponding to a maximum correlation occurs whenever the code that modulates the received signal via a reflection from the ionosphere is aligned with the identical code that is used to modulate the receiver's first local oscillator. The time in seconds (referenced to the start of the experimental run) at which a spike occurs is written next to several spikes. For example, in the top plot, the second spike occurs at 72.888 seconds and the third spike occurs at 83.088 seconds. For our system the ranging code has 255 bits with a bit length of 50  $\mu$ s but an offset of a fifth of the bit length, making the time resolution in the delay measurements to be 10  $\mu$ s and the total number of offsets in a period to be 1275 ( $= 5 \times 255$ ). In the receiver each offset is integrated over a time interval of 8 ms, so that the two codes will be repeatedly realigned every 10.2 s ( $= 1275 \times 8$  ms). To the extreme right of Fig. 2 are periods at which spikes are repeated for that channel frequency. As depicted the values indicated are exactly 10.2 s as expected or very close to it (except for channel 5 where only weak spikes are observed if any).

Since the UT clock at the transmitter did not work properly when the data were taken, the absolute propagation delay is not available. The relative delays between channels (frequencies), however, can be calculated from the data. The relative delays between spikes that occur on different channels using channel 6 as a reference are displayed in a table at the top left corner of the figure. However, each of the six channels had a different starting offset, which can be set to any desired value, and in this case it is 10 bits from one another. This means that there was a 0.50 ms artificial delay in the adjacent channels. True values of the relative delay taking this into account appear in the corrected relative delay column of the table. All the output peaks have 0 relative delay except for channel 3 which occurs 0.01 ms after the other channels. The information of relative delay allows us to estimate the frequency dispersion of the channel. Since the relative time delay at different frequencies is so small (with an upper bound equal to 0.01 ms) for a frequency separation of 0.0625 MHz (between channels 1 and 4), the dispersive coefficient, defined as the second derivative of the phase with respect to the angular frequency  $\phi$  for a communication circuit, can be computed to be  $0.255 \times 10^{-10}$  or smaller. Using the formula given by [12],

$$\Delta f = 0.152 / \sqrt{|\phi''|} \quad (5)$$

the implied dispersive bandwidth  $\Delta f$  can be computed to be 30 kHz or larger. This is quite a reasonable value.

On many occasions the spikes in the ranging data have been found to split into two or even three indicating the presence of multiple discrete modes. During these occasions, the Doppler power spectrum obtained by taking FFT of the complex signal shows multiple lobes. These samples are shown elsewhere [18].

When the sounder operates in the probing mode, the in-phase and quadrature phase components are measured. From these two components, the amplitude and phase can be computed and plotted as a function of time as depicted in Fig. 3(a) and 3(b). The amplitude at all six frequencies is found to fade randomly while the phase varies nearly linearly corresponding to a Doppler shift of about 0.44 Hz. It is suspected that the major contribution to this apparent shift comes from the relative offset between the oscillator at the receiver from that at the transmitter. It is interesting to note that, for channel 4, at a time near 4.7 s the amplitude fades down to zero and correspondingly the phase shows a jump of 180 degrees at the same time. This phenomenon can be alternately illustrated in the complex plane for the complex signal as a locus plot depicted in Fig. 3(c). Here the locus is plotted for the first 10 seconds. At 0 s the amplitude of channel 4 is roughly 1.6 and the phase is slightly larger than  $0.5 \pi$  radians (or slightly larger than  $90^\circ$  degrees). This starting point is marked by a letter s in Fig. 3(c) as well as all points one second apart on the locus. However, some s letters may be masked by the twisting locus curve. As time increases, the phase decreases. On a locus plot the locus for a decreasing phase traces out a clockwise spiral around the origin. At 4.7 s the locus touches the origin at which the amplitude is zero and the phase jumps by 180 degrees. Physically, this phenomenon is caused by multipath resulting in a complete destructive interference. Theoretically such a phenomenon has been predicted by numerical simulations [15]. If this happens near the carrier frequency, the pulse distortion is expected to be very severe at this instant.

When properly adjusted, the amplitude and phase plots such as those in Fig. 3(a) and (b) can be viewed as the transfer function  $H(\omega, t)$  of the ionospheric reflection channel. For communication applications, the transfer function is of most interest. A variety of statistical quantities can be defined based on  $H(\omega, t)$  to characterize the performance of the channel [19,20]. Assuming wide-sense stationarity, a two-frequency two-time correlation function can be defined as

$$B_H(\omega, \Omega, t) = \langle H^*(\omega, t) H(\omega + \Omega, t + \tau) \rangle \quad (6)$$

where  $\omega$  is the carrier angular frequency and  $\Omega$  is the sideband angular frequency. The special case corresponding to  $\Omega = 0$  is the autocorrelation function. One example (after being normalized to unity at zero time lag) obtained at 12:56:00 CST, Febr. 2, 1990 is shown in Fig. 4. From this figure, the coherence time

(time lag at which the autocorrelation function is dropped to a value of 0.5) is approximately 1.86 s, corresponding to a Doppler spread of 0.538 Hz.

The cross correlation function (6) can be similarly computed after being normalized by the autocorrelation function at zero lag. However, experimentally since we probe six frequencies at a time, the computation of (6) can be carried out only for a set of discrete  $\omega$  and  $\Omega$  values. In this regard we wish to examine the generally employed communication model known as "uncorrelated channel." For such an uncorrelated channel, the cross correlation function defined by (6) depends on frequency difference  $\Omega$  only but not on the center frequency  $\omega$ . To test the validity of this hypothesis, the cross correlation function  $B_H$  can be computed from the experimental data for the same  $\Omega$  but for different  $\omega$ . This is done and depicted in Fig. 5. All three curves shown in Fig. 5 are computed for the same frequency separation  $\Omega = 37.5$  kHz but at three different center frequencies: 12.2125 MHz for Fig. 5(a), 12.25 MHz for Fig. 5(b) and 12.325 MHz for Fig. 5(c). Comparison among three curves shows that the cross correlation curves are quite similar between (a) and (b), but dissimilar between (a) and (c). Accordingly the uncorrelated channel model is valid only when the center frequency  $\omega$  does not differ by a range. For Fig. 5 this range is between 37.5 kHz and 75 kHz. Additionally, we notice that the cross correlation functions shown in Fig. 5 do not possess an even symmetry with respect to  $\Omega$  as sometimes assumed by some authors. The frequency separation  $\Omega$  at which the value of the normalized two-frequency two-time function is 0.5 can be defined as the coherence bandwidth. A comparison of Figures 4 and 5 shows that the coherence bandwidth is slightly less than 37.5 kHz. When the separation is doubled (i.e.  $\Omega = 75$  kHz) at the same center frequency, the peak cross correlation drops from 0.4 to slightly less than 0.3. In this case, the cross correlation is found to be very sensitive to the center frequency.

## 5. CONCLUSION

The ionospheric reflection channel is dispersive, random and time varying. Its properties are discussed in section 2 for both the background ionosphere and the perturbed ionosphere. The background ionosphere is responsible for causing dispersive properties of the ionospheric reflection channel. Under idealized conditions, the dispersion coefficient can be related to the ionogram data. This is convenient because of the availability of ionograms on a worldwide basis. On the other hand the presence of ionospheric irregularities is responsible for making the reflection channel random and time varying. The combined effect of a perturbed ionosphere enters in the product form as shown in (1).

An ionospheric probe is next described. It has been designed to investigate the wideband properties of the

ionospheric reflection channel. The probe capable of sounding the ionosphere from 5 to 15 MHz has been deployed over a 1400 km path. Some sample data have been collected. From these data quantities such as dispersive bandwidth, coherence time, Doppler spread, coherence bandwidth can all be found. The curious phenomenon of a phase jump at zero amplitude fade predicted in theoretical simulation is found experimentally. At the instance of this phenomenon occurring at the carrier frequency a severe distortion of the transmitted pulse is expected. An examination of the two-frequency two-time cross correlation shows that the assumption of WSSUS channel as often made by many authors is not realistic for wideband applications. Initial data suggest the ionosphere channel to be very complex. Data are needed in order to characterize the channel more realistically.

## REFERENCES

- [1] Davies, K., "Ionospheric Radio", Chapter 4, Peter Peregrinus Ltd., London, U. K., 1990.
- [2] Radio Science, "Special issue on Analysis of Ionograms for Electron Density Profiles", 2(10), 1967.
- [3] Bibl, K. and B. W. Reinisch, "The universal digital ionosonde", Radio Sci., 13, 519-530, 1978.
- [4] Huang, X. and B. W. Reinisch, "Automatic calculation of electron density profiles from digital ionograms. 2. True height inversion of topside ionograms with profiles fitting method", Radio Sci., 17, 837-844, 1982.
- [5] Basler, R. P., P. B. Bentley and C. L. Rino, "HF channel probe", in "Effect of the Ionosphere on C3I System", edited by J. M. Goodman, National Technical Information Service, Springfield, VA 22161, 147-151, 1984.
- [6] Wagner, L. S. and J. A. Goldstein, "High-resolution probing of the HF ionospheric skywave channel: F2 layer results", Radio Sci., 20(3), 287-302, 1985.
- [7] Terina, G. I., "On distortion of pulses in ionospheric plasma", Radio Eng. and Electron. Phys. (English translation), 12, 109-113, 1967.
- [8] Romanova, T. S. and T. Y. Ryzhkina, "Calculation of the dispersion coefficients of pulsed signals for the oblique propagation of radio waves in the ionosphere", Radio Eng. Electron. Phys. (English Transl.), 21, 1-7, 1976.
- [9] Dhar, S. and B. D. Perry, "Equalized megahertz bandwidth HF channels for spread spectrum communications", Rep. M82-46, MITRE Corp., Bedford, MA, Sept., 1982.
- [10] Salous, S. and E. D. R. "Shearman, Wideband measurements of coherence over an HF skywave link and implication for spread spectrum communication", Radio Sci., 21, 463-472, 1986.

- [11] Budden, K. G., "Radio Waves in the Ionosphere", Cambridge University Press, Chapters 10 and 11, Cambridge, England, 1985.
- [12] Lin, K. H., K. C. Yeh, H. Soicher, B. W. Reinisch and R. R. Gamache, "Vertical ionograms and dispersive bandwidth for an oblique path", Radio Sci., 24, 519-526, July-Aug., 1989.
- [13] Lundborg, B., "Pulse propagation through a plane stratified ionosphere", J. Atmos. Terr. Phys., 52, 759-770, 1990.
- [14] Wagen, J. -F. and K. C. Yeh, "Numerical investigations of two-frequency mutual coherence functions of an ionospheric reflection channel", Radio Sci., 24, 209-223, 1989.
- [15] Rand, T. W. and K. C. Yeh, "Transfer functions and pulse distortion for an ionospheric reflection channel with embedded random irregularities" Radio Sci., 26, 1-14, 1991.
- [16] Papoulis, A., "The Fourier Integral and Its Applications", McGraw-Hill Book Company, New York, 1962.
- [17] Dixon, R. C., "Spread Spectrum Systems", Chapter 3, John Wiley & Sons, New York, 1976.
- [18] Lin, K. H., W. L. Schlegel, K. S. Yang and K. C. Yeh, "Probing the ionosphere with the University of Illinois sounder", Presented at the Ionospheric Effects Symposium 1990, Washington, D. C., May 1990.
- [19] Proakis, J. G., "Digital Communications", 2nd Edition, McGraw-Hill, New York, 1989.
- [20] Belrose, J. S., R. Bultitude, D. Clark, R. W. Jenkins, W. Lauber, G. Noury, N. M. Serinken, and G. Venier, "An overview of Canadian radio propagation/communications technologies research", AGARD-CP-442, "On Propagation Effects and Circuit Performance of Modern Military Radio Systems With Particular Emphasis on Those Employing Bandspreading", paper 2, 1989.
- [21] Lin, K. H. and K. C. Yeh, "Some measured properties of the ionospheric reflection channel at high frequencies", to appear in Proceedings of the 1990 IEEE Military Communication Conference, Sept. 30-Oct. 3, 1990.

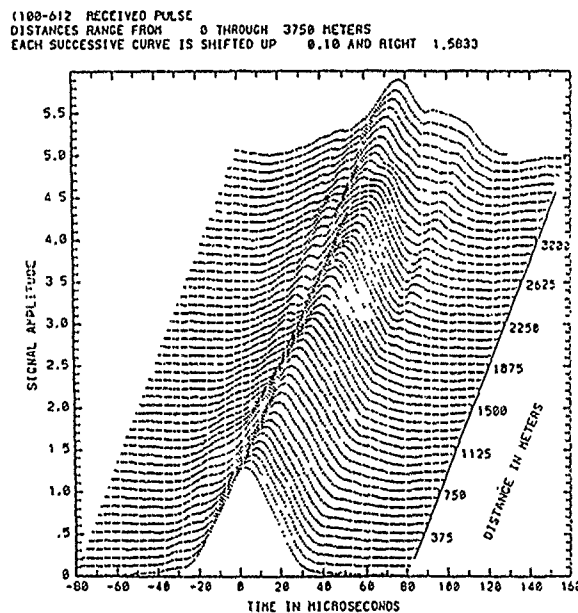


Fig. 1 Simulated response to a triangular input pulse at a carrier frequency of 6 MHz at successive distances [15].

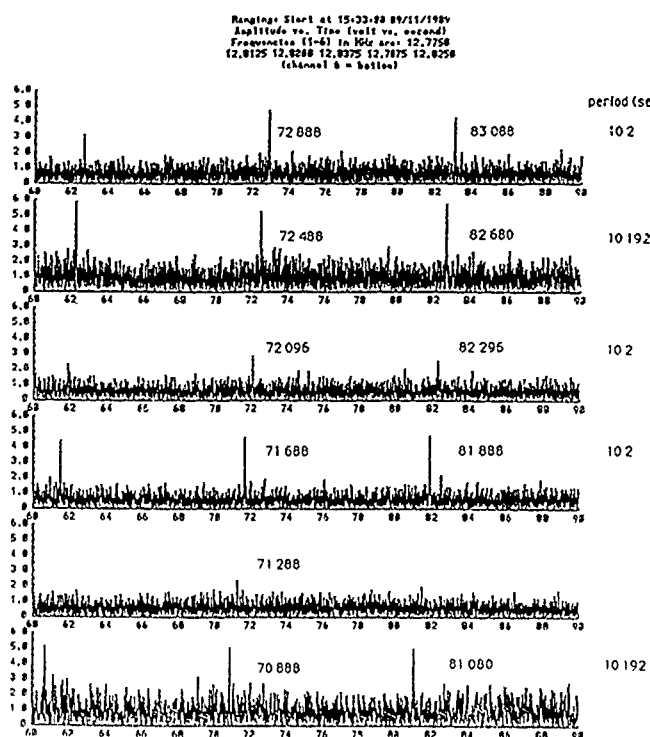


Fig. 2 Sample ranging taken at 15:33 CST, September 11, 1989 showing relative time delays at six frequencies [21].

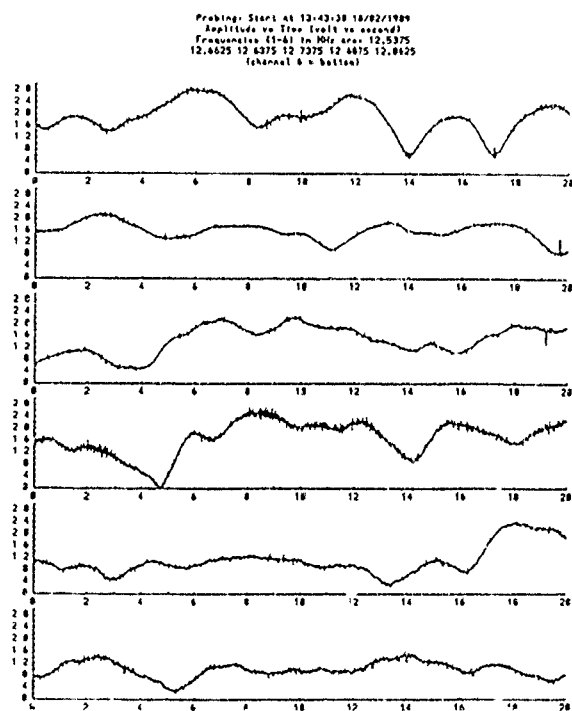


Fig. 3 (a) Amplitude in linear scale as a function of time for six selected frequencies. Data taken at 13:43.30, Oct. 2, 1989.

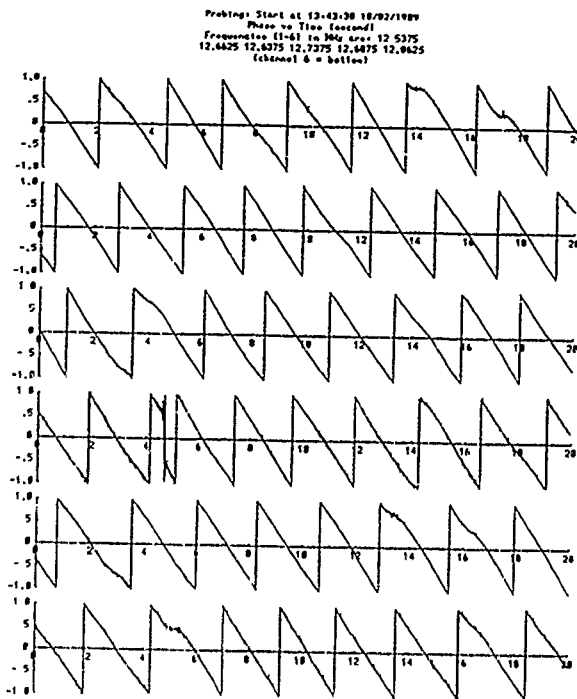


Fig. 3 (b) Phase in  $\pi$  radians as a function of time for six selected frequencies for the same data as (a).

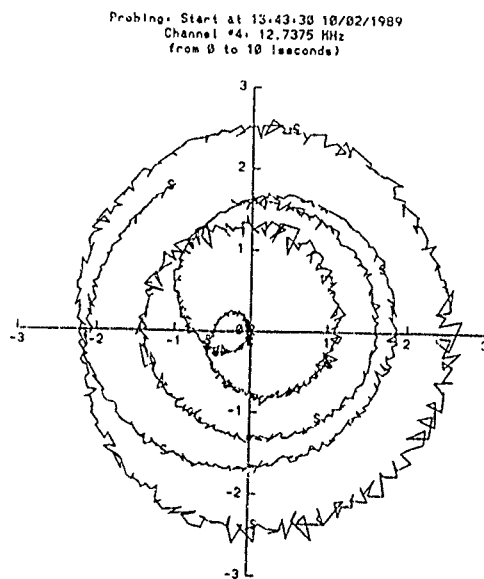


Fig.3 (c) Locus plot of the complex amplitude in the complex plane at a frequency of 12.7375 MHz (channel 4 of (a)) [18].

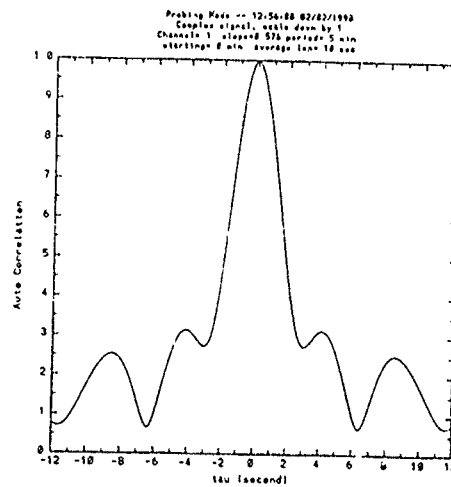


Fig. 4 Normalized autocorrelation function at a frequency of 12.2125 MHz obtained at 12:56:00 CST, Febr. 2, 1990 [21].

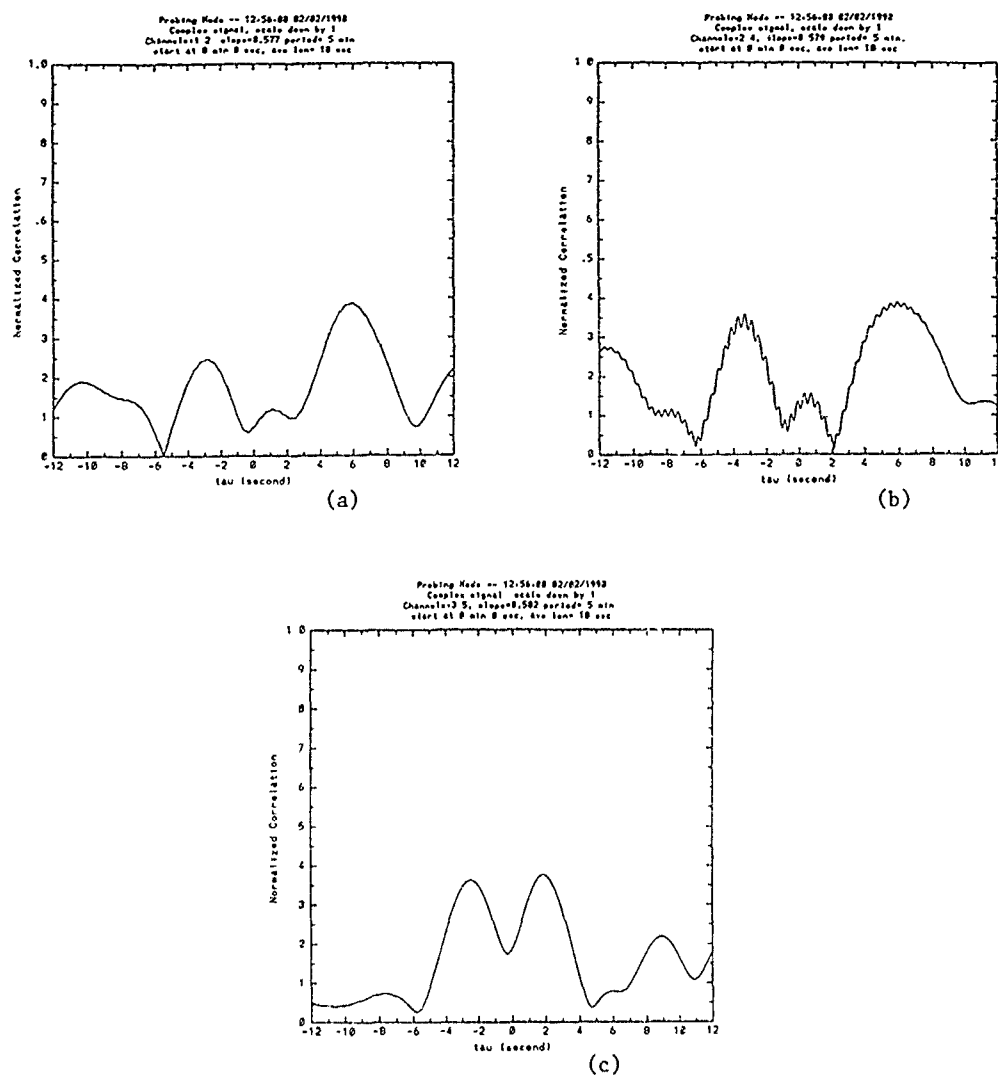


Fig. 5 Normalized two-frequency two-time cross correlation function for a fixed frequency separation of 37.5 kHz but at three different center frequencies [21].

- (a) Center frequency at 12.2125 MHz.
- (b) Center frequency at 12.25 MHz.
- (c) Center frequency at 12.325 MHz.

DISCUSSION

**B. REINISCH**

1. *In your propagation experiments you will encounter superposition of multipath signals (microstructure if single mode). Do you separate signals with different angles of incidence and different polarization?*
2. *Synchronization with GOES satellite signals is unreliable because of msec uncertainties. Have you considered using GPS receivers?*

**AUTHOR'S REPLY**

1. *We rely on time delay to differentiate modes of propagation. The fading is caused by multiple micropaths and is an area of our research interest.*
2. *Currently we hope to upgrade the system by using the GPS system.*

**E. SCHWEICHER**

*Why did you perform I-Q detection?*

**AUTHOR'S REPLY**

*This is done because of our desire to study both amplitude and phase of the received signal.*

**E. TULUNAY**

*Your random model for the ionosphere is nonstationary. However, you use statistical models valid for stationary processes. Could you comment on this?*

**AUTHOR'S REPLY**

*In a simulation study, the ionospheric statistical properties are strictly stationary. There is therefore no problem. However, when one is dealing with real experimental signals, they are usually non-stationary. For short term behavior it is possible to do a statistical testing on a segment of data to assure the statistical properties are varying within some bound. When this happens, the statistical analysis can be performed.*

# Adaptive Remote Sensing of the Ionosphere to Minimise Spectral Intrusion

M. Gallagher & M. Darnell  
Hull-Warwick Communications Research Group  
Department of Electronic Engineering  
University of Hull  
Hull, HU6 7RX  
UK

## Abstract

One of the many information sources needed to control the reliability of a High Frequency (HF) communications link is the current state of the ionosphere. This can be determined in a number of ways which include probing of the ionosphere with an active radiating system (an ionosonde); passive monitoring of broadcast systems (for example, the BBC World Service operates simultaneously on a series of short-wave frequencies); passive monitoring of signals of opportunity such as commercial time, FAX and RTTY signals; finally, the use of the long-term predictions which employ ionospheric forecasting and modelling techniques.

Obviously, there is great advantage in passively monitoring the state of the ionosphere without further congestion of the medium. This paper suggests a rationale for future remote sensing systems using as an example an economic sounding system that employs standard radio system elements. The proposed rationale is based upon a generic architecture which can maximise the information gathered with the minimal active radiation of EM energy.

The system described can passively monitor the outputs from proprietary 'chirp' sounders; it also has the additional capability of radiating its own sounding signals to complement the information gathered from passive monitoring. The active sounding takes the form of a segmented swept FM (SSFM) system. The profile of the sounding signal is produced digitally and can take a number of formats, which include simple linear FM ('chirp') as well as other profiles that are inherently tolerant to other specific propagation problems that exist with the ionosphere; for example, the effects of doppler-shift can be minimised through the use of hyperbolic FM. The sounding system adaptively uses sequences that can sound the channels allocated to the communication system as well as frequency ranges of high importance, such as regions near to the maximum usable frequency (MUF) and lowest usable frequency (LUF). The intelligent and adaptive use of such scanning techniques means that spectrum pollution is minimised, while the information gathered is maximised.

## 1. Introduction

The ionosphere remains one of the most important and flexible propagation media that can be used economically and efficiently (in terms of equipment size, cost and transmission powers) by the long-range radio communicator; therefore, remote sensing of the ionosphere is essential for both the assessment of its current state and comparison with propagation predictions. This is of significant importance for high frequency (HF) communication, ionospheric physics and updating of propagation analysis programs. Remote sensing of the

ionosphere can be achieved by several methods of which terrestrial passive monitoring and active sounding schemes are amongst the most important [1,12,15].

The two above mentioned methods can be used to gather detailed information about the current state of the ionosphere. The main value of passive monitoring methods is in reducing spectral intrusion; however, if active probing of ionosphere must be used then the sounding schemes should be "intelligent" to minimise their spectral intrusion. This is of particular importance for sounders operating in the HF (2-30 MHz) band, since this area of the spectrum has to support a large number of users, has possible world-wide coverage and, hence, is extremely crowded; any further unwarranted transmissions may cause additional problems for HF communications. Even with these limitations, active sounding of the ionosphere remains one of the most important and accurate methods of measuring the current ionospheric state [12].

Passive monitoring of 'transmissions of opportunity' in the HF band, such as broadcast signals, radio beacons, linear frequency modulation (LFM) or "chirp" sounders, time signals and other utilities (such as RTTY FAX and weather stations), make this method much more spectrally efficient (i.e. less-intrusive) than active sounding methods and, hence, can be useful in reducing overall spectral intrusion of the process of gathering data about the ionosphere [2]. This paper will concentrate on the value of LFM signals in the adaptive remote sensing of the ionosphere.

Real-time channel evaluation (RTCE) can be viewed as remote sensing of selected spectral segments of the band, ranging from single channels to large groups of channels (i.e. several MHz), and has traditionally been one of the main methods used by HF communicators to assess the current ionospheric propagation conditions both in, and around, their allocated frequencies [3,16,17]. However, most conventional RTCE philosophies rely on special-purpose equipment used in conjunction with the normal transmission and reception units. This strongly contrasts with the current possibilities where the same equipment can be used both for communication and RTCE purposes, with the only variation being in software reconfiguration. The architecture that can be used in this type of scheme is based on the integration of digital signal processing (DSP) and computer technology into a single multi-functional terminal. The paper will also concentrate on such "embedded" schemes, rather than those based on special-purpose equipment [4].

The chirpsounder network, which is operated by a range of agencies including NATO [5], can provide a detailed description of current ionospheric conditions. This information has great potential value in the channel selection procedure for any frequency management scheme as it can show the multi-path structure across the whole of the HF band. The design of a DSP-based chirp monitoring system that could form an integral part of an adaptive HF system terminal was one of the primary goals

of the HF research within the Hull-Warwick Communications Research Group (HWCGRG). The use of DSP technology in conjunction with standard HF equipment in an integrated architecture means that an embedded solution to many HF problems can be achieved. This type of architecture is intended to exploit the best characteristics of analogue radio systems; however, the full application of digital algorithms means that this type of system can function both as a RTCE device and standard communication terminal.

This paper will initially discuss the parameters and use of the chirpsounder network before briefly detailing the design of the DSP-based chirp monitor. The development of the chirp monitor into a complete LFM sounding system formed an important element in the project; this is discussed before outlining the proposed 'generic' architecture for long-range radio systems and the implications of using such an architecture. Finally, a set of conclusions will be presented.

## 2. The Chirpsounding Network

One of the most important sources of transmissions of opportunity in the HF Band is the world-wide network of chirpsounding transmitters. These sounders are operated as support for both strategic and tactical HF communications, and can provide substantial detail about the current ionospheric propagation conditions.

The linear FM or 'chirp' is a spread-spectrum signal that complies with the following algorithm [6]

$$u(t) = a(t)e^{j\pi kt^2} \quad (1)$$

where

$$k = \frac{B}{T} \quad (2)$$

T = time duration of the signal  
B = bandwidth of the signal

In a nonnormalised form equation (1) becomes

$$u(t) = \frac{1}{\sqrt{T}} \text{rect}\left(\frac{t}{T}\right) e^{j\pi kt^2} \quad (3)$$

This type of signal can be generated with relatively simple equipment and most of the complexity is in the processing of the received signal. In current analogue systems, the receiver is based upon a heterodyne spectrum analyser where the highly stable swept local oscillator is matched to the transmitted sweep and produces a set of base-band (0-500 Hz) frequencies (mixer products) as it traverses the 2-30 MHz band. These mixer products are produced as a consequence of propagation conditions and the offset frequencies are in direct proportion to the current multi-path delays of the path. As the receiver scans across the band, a projection of the multi-path delay versus frequency can be constructed; this type of display is termed an ionogram. The theoretical multi-path resolution of this type of equipment is also directly dependent upon the filter bandwidths

and in the currently deployed networks this is approximately 0.1 ms [7].

The typical parameters of the currently deployed chirpsounding network are:

Sweep rate :	100 kHz/sec or 50 kHz/sec;
Scan time :	280 seconds;
ERP :	5 - 100 W;
Antennas :	various depending on operating agency;
Scan raster :	5/15 minutes;
No. of sounders :	c. 60 (although mainly in US/Western Europe).

In addition, the AGC (automatic gain control) of the receiver is logged as it scans across the band and this information is used to offer a graph of the received signal strength as a function of frequency. The operational principle and a typical ionogram from one of these chirp receivers is shown in figure 1.

Therefore it can be seen that the chirp sounder network offers a dispersed network of "transmissions of opportunity" that can be used to assess the ionospheric state if suitable receiving equipment is available.

It was against this background that a project to design a simple 'chirp monitor' was initiated. This monitor would have a lower resolution than the proprietary chirp receiver, but it could be incorporated into an embedded frequency management architecture of an adaptive HF system at no extra complexity (except in the DSP software). The information would be used to direct the channel selection procedure of the frequency management scheme by initialising and updating an embedded off-line propagation prediction model, for example CCIR 894 [8,13].

## 3. Design and Performance of Chirp Monitor

One of the main aims of the project in the design of a chirp monitor was to use standard commercial HF radio equipment and initially the project was limited to the use of amateur grade equipment and fixed-point DSP devices. This meant a reduced receiver bandwidth and more computation-induced errors. With standard HF receivers, under computer remote control, it is obvious that their maximum scanning rate is directly proportional to their settling time and time taken to change frequency. Therefore, a scanning operation as used in the standard analogue chirp receiver is not realistically possible. Hence, a stepped scanning procedure, as illustrated in figure 2, has been adopted. In this type of operation, the receiver is synchronised to the scan rate of the chirp it is tracking, but steps ahead of the transmission and waits for the chirp signal to pass through a defined set of separated narrowband (3 kHz) channels.

This type of operation has been used successfully by radio amateurs in identifying an approximate MUF, although with human operators the maximum scanning rate is reduced due to the importance of synchronisation. In the DSP-based system, the optimum receiving configuration for the chirp waveform is used, i.e. a matched filter that uses the in-phase and quadrature information (I and Q) contained in the signal to maximise the compression gain that can be achieved. This type of operation is well documented in radar applications [6,9,10], and the

matched filter schematic is outlined in figure 3. The matched filter responds to a 2.7 kHz bandwidth segment of the received chirp signal covering base-band frequencies 300-3000 Hz. A simulated receiving system showing the in-phase and quadrature matched filter outputs, together with the composite output in response to a 'perfect' chirp signal (phase error,  $\phi = 45^\circ$ ) is shown in figure 4. It can also be seen from figure 4 that the matched filter output can be shown to be a good approximation to the impulse response on the channel.

The matched filter envelope,  $\Psi(\tau)$ , is described by

$$\Psi(\tau) = \frac{\sin\{\pi TB(\rho + 1)(1 - \tau)\}}{\pi(\rho \pm \tau)\sqrt{TB}} e^{j\pi\tau T} \quad (4)$$

where

$\phi$  = received phase error  
 $\tau$  = time offset  
 $\rho$  = multipath time offset  
 $T$  = time duration of signal  
 $B$  = bandwidth of signal.

This type of matched filter detection scheme has several limitations: the maximum time resolution is limited by the receiver bandwidth and is in the order of 0.3 ms (for the receiver used here); the matched filter is sensitive both to high levels of certain types interference and input levels which can lead to 'false' triggering; the 10 kHz sampling rate produces a large amount of data, so the synchronisation procedure must minimise the amount of digital data to be interpreted/saved; finally the accuracy of the ionograms produced depends primarily on the peak detection algorithm employed. Although the time resolution of the system is somewhat coarser than that produced by the proprietary chirp receiving system it is comparable with the time resolution for RTCE schemes proposed by the CCIR, i.e. 0.5 ms.

The processing of the received chirp waveform can be carried further than is possible in analogue systems; since all of the impulse responses on the scanned channels are saved, a running or 'past-history' averaging window can be applied to the data to counter the effects of fades and to show long-term trends. In addition, the impulse response and overall trend data can be used to monitor the global ionospheric state for the purpose of updating the prediction models and to control and adapt individual communication system parameters to optimise data throughput in response to multi-path structure and propagation conditions.

The DSP-based system's output is compared with that from a standard chirp receiver in figure 5. These outputs were taken during a trial where both systems were connected to the same antenna so that the input signal would be the identical (with only the processing of the signal being different). In addition, an example channel impulse response from the DSP-based monitoring system is given in figure 6. As can be seen from both these sets of diagrams, although the DSP-based chirp monitor has a resolution limitation of 1/3 ms; overall, in general, the same frequency management decisions would be made if only the DSP-based monitor outputs were available. However, the DSP-based monitor has the added advantage that

the same equipment can then be reconfigured to be a modem that can use the latest propagation information or, alternatively, it can reconfigure as a sounder that will probe the ionosphere to obtain an accurate MUF figure without having to scan the rest of the HF band [10]; this latter capability is described in the following sections.

#### 4. Design and Performance of an Embedded Ionospheric Sounding System

One of the main disadvantages of the passive chirp monitor is that it depends entirely on the availability of chirp transmissions from the chirpsounder network. Therefore, the next phase of the project was to give the adaptive HF communication terminal an economic, embedded and autonomous sounding capability. The sounding capability means that even if there are no 'transmissions of opportunity' on a similar path to that required by the communication system, a capability to probe the ionosphere actively still exists.

Initially the same receiver format, i.e. a chirp matched filter, was used; in addition, it was required to design of a chirp transmitter. The same processing structure was used to generate the chirp signal, and the transmission format was that of a segmented sounding scheme; here the transceiver tunes to frequency, settles, then a chirp segment sounding profile is transmitted, before the transceiver is re-tuned and the process is repeated. This mode of operation is termed segmented swept FM (SSFM).

Since the sounding profile is generated digitally and the transceiver is under remote control and can tune to any frequency in its synthesizer range without any time penalty, it can be seen that the transmitter is not limited to a single sounding profile and can change the overall sounding rate or the frequencies that form the set to be sounded. Therefore, special sounding profiles and scan rates can be used adaptively and in response to ionospheric conditions; for example a hyperbolic FM (HFM) waveform has the property of being, relatively, more tolerant to doppler shifts on the channel than LFM (chirp) [14]. This feature enables a non-uniform sounding raster to be adopted which means that only areas of the spectrum of interest to the communicator need be probed; so, although a complete picture of the ionospheric conditions is not obtained, detailed data on the frequency bands that have direct relevance to the HF communication system are gathered. This type of 'intelligent' active probing means that the overall spectral intrusion in the HF band is reduced with no loss in the quality and amount of relevance of the data gathered. A typical non-uniform raster sounding scheme is shown schematically in figure 7.

For the initial trial of the embedded active sounding scheme it was decided to employ a simple uniform raster to allow the use of the standard chirp monitoring software. Due to RF equipment characteristics, a 200 kHz segmented raster was used and the transmitted LFM signal used the same sweep parameters as a proprietary chirp sounding system. The path to be monitored was the 120 km path from Hull University to Warwick University (in the UK). This short path, although being far from ideal with probable reception being in the range 2 to 9 MHz with near-vertical incidence sky-wave (unless a path with strong sporadic E existed), was suitable for the first trial as the equipment at both ends of the link was under direct experimental control. For initial, approximate synchronisation purposes (the transmitter and receiver only need to be aligned to within 0.5 seconds) the

sounder at Oslo was monitored; but future trials will use a time-standard at both the transmitter and receiver. Figure 8 shows two of the ionograms and impulse responses gathered during the trial. Further trials are scheduled to take place in the near future in order to refine the system parameters and processing.

### 5. Overall HF System Architecture

The adaptive operation of the terminal depends entirely on the implementation of a proposed 'generic' architecture [18,19]. This type of architecture consists of a single, or a number of DSP devices, integrated into a more general purpose computer unit, for example an IBM PC, which operates with a standard radio transceiver. In this type of architecture the general purpose computer unit performs all of the higher level control functions, such as remote control of the transceiver, scheduling of programs and execution of the off-line prediction models; the DSP devices implement all the dedicated signal processing operations which could include interference/propagation assessment, multi-functional adaptive modems or error control codecs. A schematic of this type of architecture is detailed in figure 9.

The terminal that performed all of the operations described in this paper was a standard IBM PC AT clone (286 based PC) that had a AT&T DSP32C floating point DSP device installed on an expansion card. This terminal has the advantage that rapid data integration between the host computer and the DSP device was possible; however, the use of a single DSP device means that scheduling between the various propagation assessment tools must take place, and for efficient operation of the terminal, a trade-off between channel assessment and data transmission must be identified. Therefore, future terminals will use additional DSP devices as a way to run concurrent processes. In this way the chirp monitor could be executed in parallel with an interference assessment program; alternatively, a modem could be configured and tested as the propagation assessment is taking place. In this type of architecture, where software reconfiguration can make the terminal truly multi-functional, the only limit on the adaptivity and functionality of the system is the ingenuity of the software designer and the speed of the hardware.

Another advantage of using this type of architecture is that as hardware improvements in the radio transceiver are made (for example, an all-digital signal path from the IF stage will ultimately exist) then this type of 'generic' architecture has the potential to incorporate and take advantage of the new types of data structures that will be present.

The value of this type of 'generic' architecture is that the terminal has the potential to be a complete embedded system accomplishing the same tasks as many traditional HF system elements. To-date the HWCRG has developed many functional blocks that can be incorporated into this type of architecture and which only depend on software reconfiguration of the DSP device and implementing the correct data presentation and collection operations on the host PC. These operations include an adaptive MFSK modem that has complete in-band spectral agility and a tone raster ranging from a fast-keying FSK to PICCOLO; template correlation; digital synchronisation and speech coding [20,21,22,23,24].

Furthermore, many other embedded RTCE techniques for extracting additional ionospheric and channel data become

possible with this type of architecture. As proposed in [4], these are classified as current channel (CC) and alternative channel (AC) RTCE techniques.

It is obvious that passive or active monitoring of large parts of the spectrum, or parts of the spectrum that can encompass several channels, form part of an AC RTCE system; examples of other HF systems that have successfully used the AC RTCE techniques include the CHEC (channel evaluation and calling) and ALQA (automatic link quality analysis) systems. Additionally, the use of propagation models can be viewed as an AC RTCE technique.

However, the major advantage of this type of digital architecture is that it has enabled a significant increase in the number of CC RTCE techniques. These current channel propagation measures, although only producing data for a small part of the HF spectrum can, if derived correctly, be used in the database of overall ionospheric conditions. These CC measures can be related directly, or indirectly, to the received signal-to-noise ratio (SNR).

Examples of such CC techniques, mostly passive and usually completely embedded within the system architecture, include soft-decision data, error control metrics, synchroniser outputs, data statistics (eg error counting) and zero-crossing statistics [4,21].

### 6. Concluding Remarks

This paper has presented methods for remote sensing the ionosphere in an adaptive manner, using both traditional active sounding techniques and the spectrally less-intrusive passive assessment methods. 'Intelligent' RTCE in overall HF terminal operations have been shown to be a successful way for an HF communicator to gather relevant ionospheric information and, hence, forms an effective method for sensing ionospheric state. The passive monitoring of the extensive chirpsounder network is an economic method of generating detailed ionospheric information or, in the case of the DSP-based chirp monitor, precise frequency management information; however, this depends on the availability of suitable equipment.

For situations, where the chirpsounder network is inappropriate, or other 'transmissions of opportunity' are not available, then active sounding can be considered. The main aim of any active sounder must be the generation of ionospheric information with the minimum of spectral intrusion. One such sounding scheme based upon segmented swept FM (SSFM) has been presented with the capability of adapting both the scan-rate and sounding profiles in response to the amount of data that is required and to counter normal ionospheric effects.

The use of the 'generic' architecture means that sounding the ionosphere is no longer outside the range of functions that an ordinary HF user using a generic communication system terminal can achieve. This type of architecture also offers the prospect of an extremely cost-effective, automatic and adaptive HF system. One use of such a system terminal, when employed in conjunction with a suitable receiver, is as an economic ionospheric remote sensing tool which would be in the cost range of non-specialist users. In addition, since all the useful data can be saved and the terminal can be designed to be economic, compact and operate with many other standard HF elements, monitoring of the ionosphere over large ocean areas

or in third-world countries becomes a reasonable proposal, which would be useful in increasing the flexibility of the current CCIR propagation maps.

The research into the use of the monitoring terminals and the active sounder is continuing and future developments will include:

- (i) multiple simultaneous ionograms;
- (ii) message transmission capability via orthogonal chirp waveforms;
- (iii) alternative complementary sequence (CS) pulse modulated sounding mode [25];
- (iv) jam-resistant non-uniform sounding raster;
- (v) identification of channels subject to frequency selective fading.

Furthermore, it is hoped that the use of the proposed 'generic' digital/DSP architecture offers a suitable alternative to the traditional architecture long-range radio systems.

#### 7. Acknowledgements

The authors gratefully acknowledge the support of the Science and Engineering Research Council (SERC), Roke Manor Research Limited, Siemens-Plessey Defence Systems and DRA-RAE Farnborough.

#### 8. References

1. Davies, K.: "Ionospheric radio", Peter Peregrinus, 1990.
2. Masrani, K. & Riley, N. G.: "Use of passive monitoring techniques in HF radio systems", IEE 5th Int. Conf. on 'HF radio: systems and techniques', CP-339, Edinburgh 1991.
3. CCIR: "Real-time channel evaluation of ionospheric circuits", Report 889, ITU Geneva, 1982.
4. Darnell, M.: "Real-time channel evaluation techniques", 1st Int. Symp. on 'Communication theory and application', Paper No. 64, Crieff, 1991.
5. Report No. ACP 191, US DoD, 1987.
6. Rihaczek, A.W.: "Principles of high resolution radar", McGraw Hill, 1969.
7. Barry, G.H. & Fenwick, R.B.: "Oblique chirp sounding", AGARD Conf. on 'Ionospheric oblique radio wave propagation at frequencies near the lowest usable frequency', Leicester, 1966.
8. Masrani, K. & Riley, N.G.: "Passive monitoring of HF radio signals in determining multi-path", IEE Colloquium on "Methods of combatting multi-path", January 1990.
9. Turin, G.L.: "An introduction to matched filters", Proc IRE on Information Theory, June 1960, pp311-329.
10. Gallagher, M. & Darnell, M.: "An economic ionospheric sounding system using standard HF radio system elements" IEE 5th Int. Conf. on 'HF radio: systems and techniques', CP-339, Edinburgh 1991.
11. Hunsucker, R.D.: "Radio techniques for probing the terrestrial ionosphere", Springer-Verlag, New York, 1990.
12. Hall, M.P.M. & Barclay, L.W.: "Radiowave propagation", Peter Peregrinus, 1990.
13. CCIR, Report No. 894, ITU, Geneva, 1986.
14. Altes, R.A.: "Radar/sonar acceleration with linear-period modulated waveforms", IEEE trans. AES-26, No. 6, November 1990.
15. Villard, O. G.: "The ionospheric sounder and its place in the history of radio science", Radio Sci. 11, 1976, p847.
16. Darnell, M.: "Embedded real-time channel evaluation techniques", AGARD LS-145 on 'Propagation impact on modern HF communication system design', 1986.
17. Darnell, M.: "Channel evaluation techniques for dispersive communication paths" in 'Communications systems and random process theory', Ed. J.K. Skwirynski, Sijthoff & Noordhoff, The Netherlands, 1978.
18. Gallagher, M. & Darnell, M.: "Adaptive architectures for Radio communication systems", 3rd Bangor Symposium on Communications, May 1991.
19. Gallagher, M., Darnell, M. & Clark, P.: "Architectural considerations for adaptive digital signal processing within long-range radio communication system terminals", IEE 6th Int. Conf. on 'Digital processing of signals in communications', Loughborough, September 1991.
20. Speight, T.J. & Darnell, M.: "Suggested improvements to the PICCOLO modulation format", 5th IEE Conference on 'Radio receivers and associated systems', CP-325, Cambridge, July 1990.
21. Grayson, M. & Darnell, M.: "Real-time channel evaluation derived from predicted zero-crossings", 3rd Bangor Symposium on Communications, May 1991.
22. Jowett, A.P. & Darnell, M.: 'Automatic channel selection using template correlation', IEEE Elec. Letts., Vol. 23, No. 22, 1987.
23. Gallagher, M. & Darnell, M.: "The use of template correlation for in-band frequency management", IEE 5th Int. Conf. on 'Radio receivers and associated systems', CP-325, Cambridge, 1990.
24. Darnell, M.: "Distributed long-range radio systems employing multiple propagation mechanisms and an extended frequency range", AGARD CP-433, Crete October 15-20, 1990.
25. Darnell, M.: "Channel estimation techniques for HF communications", AGARD CP-173 on 'Radio systems and the ionosphere', Paper 16, Athens, 1975.

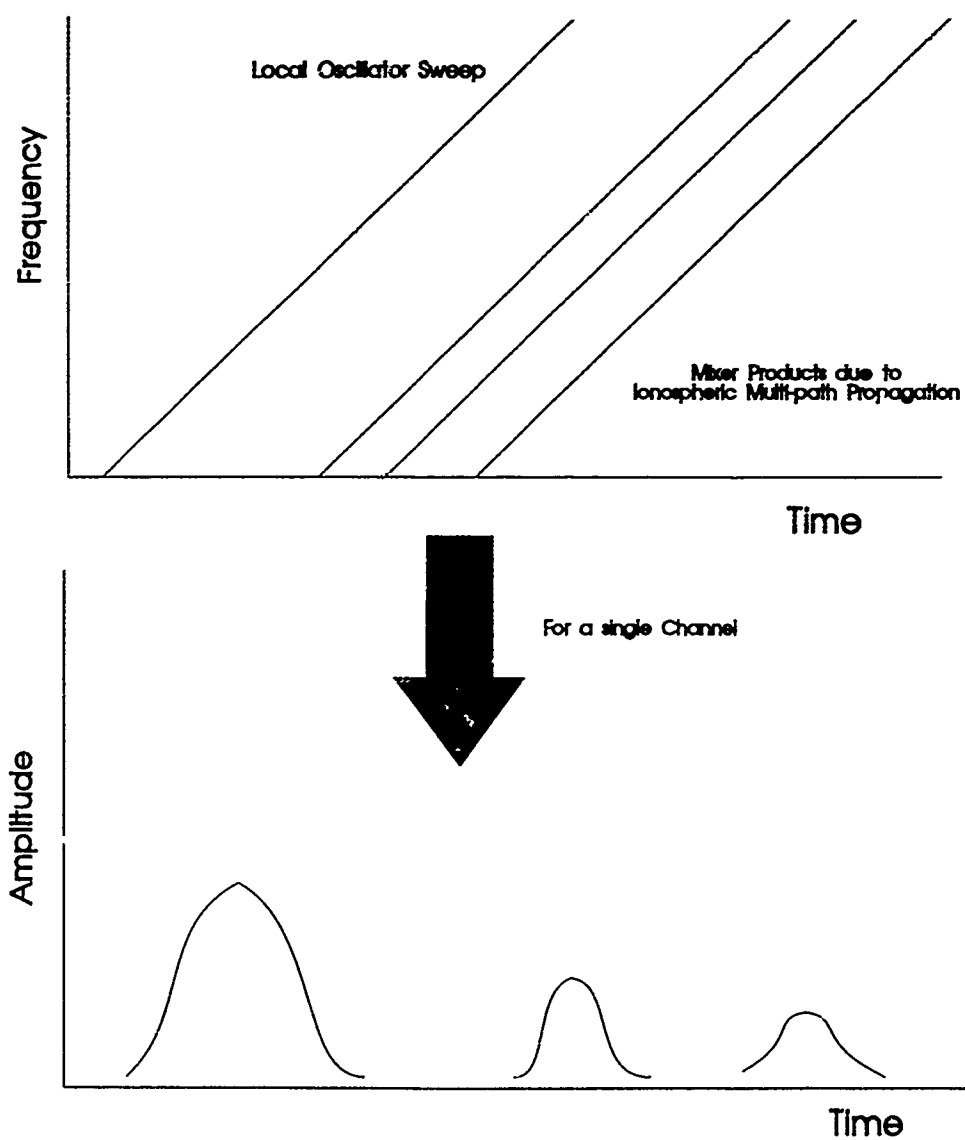


Figure 1a: Schematic of Analogue LFM Detection Scheme

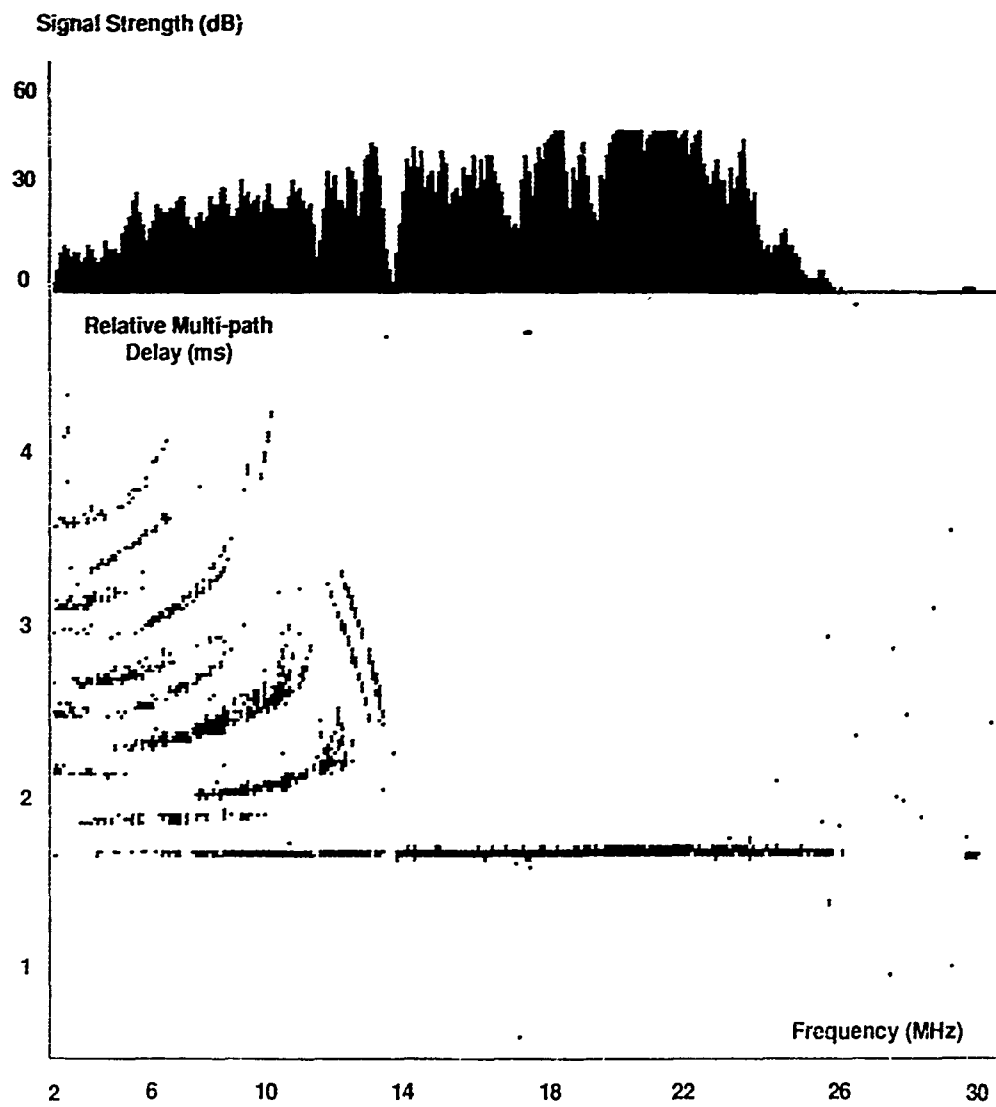


Figure 1b: Example of an Ionogram from Proprietary LFM Receiving System

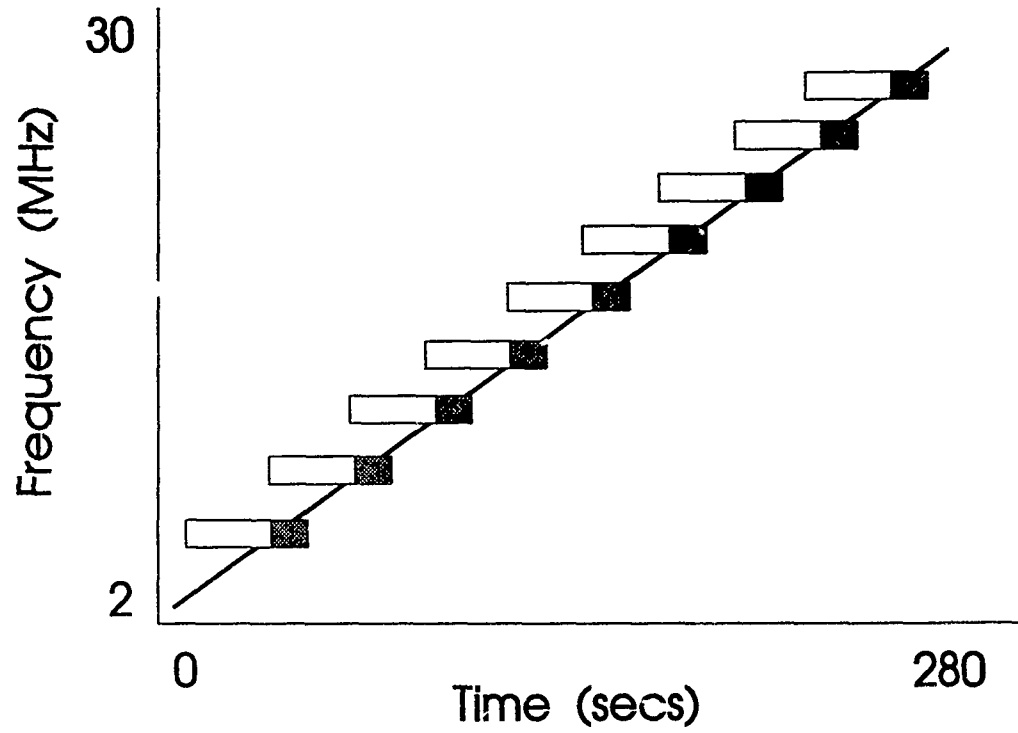


Figure 2: Synchronisation procedure used to track the LFM sweep

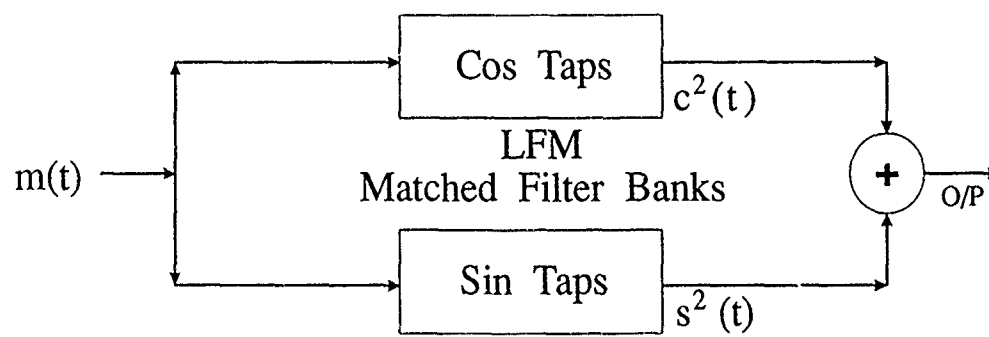


Figure 3a: Schematic of Matched Filter used to detect the LFM signals

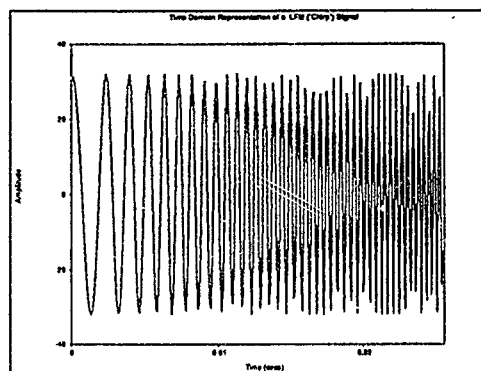


Figure 3b: Un-weighted LFM Signal Profile

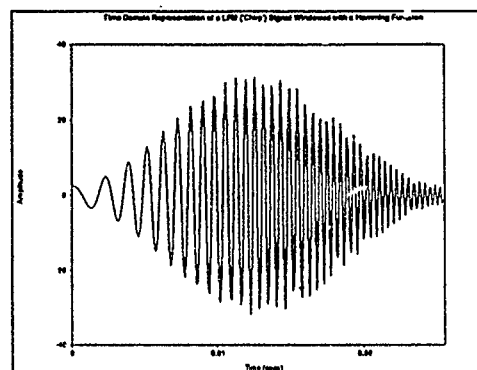


Figure 3c: Hamming Weighted LFM Signal Profile

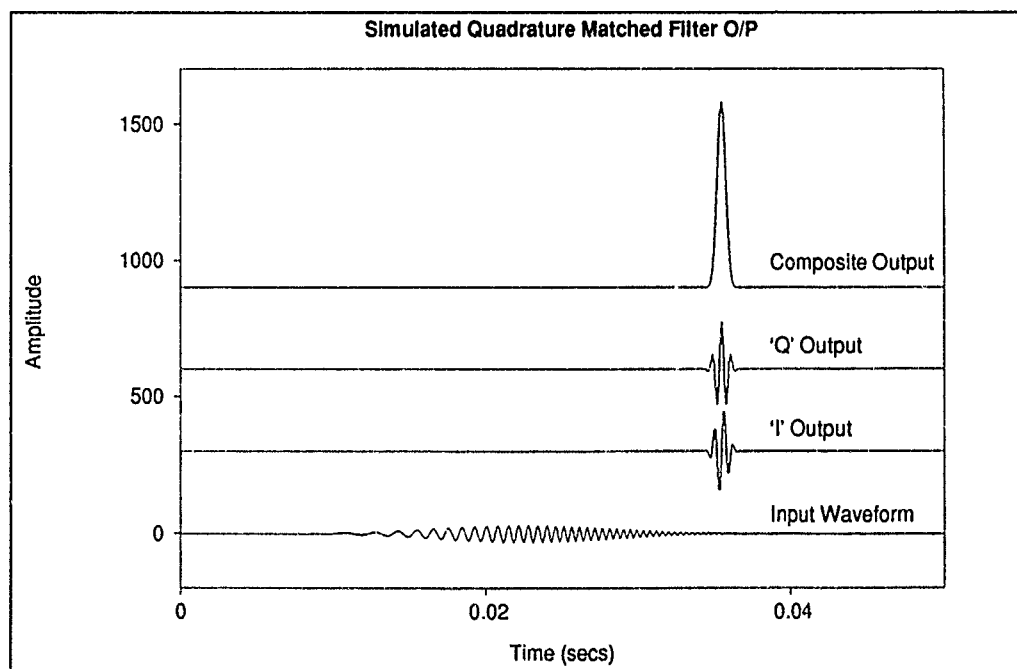


Figure 4: Simulated Matched Filter responses to a Hamming weighted 'chirp' signal

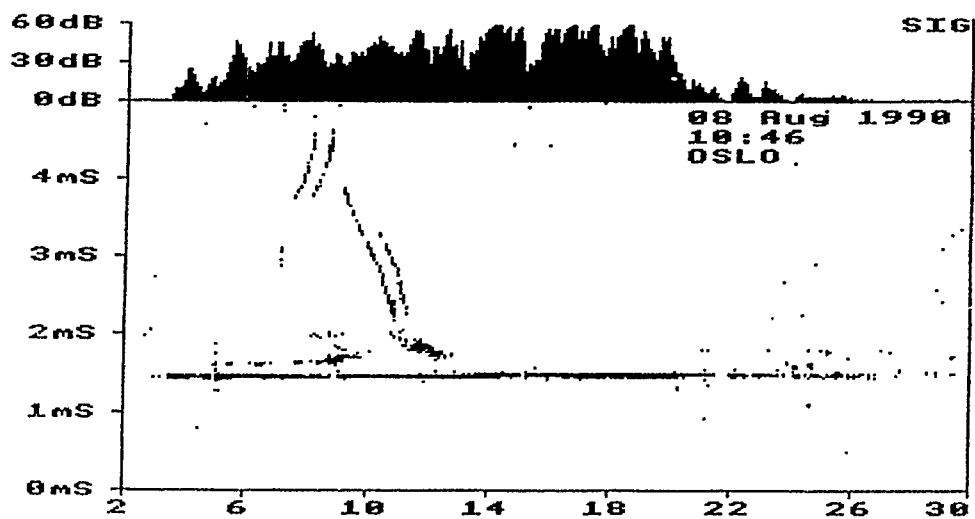


Figure 5a: Ionogram of Path from Oslo to  
Cobbett Hill, (10:41am) 8/8/90

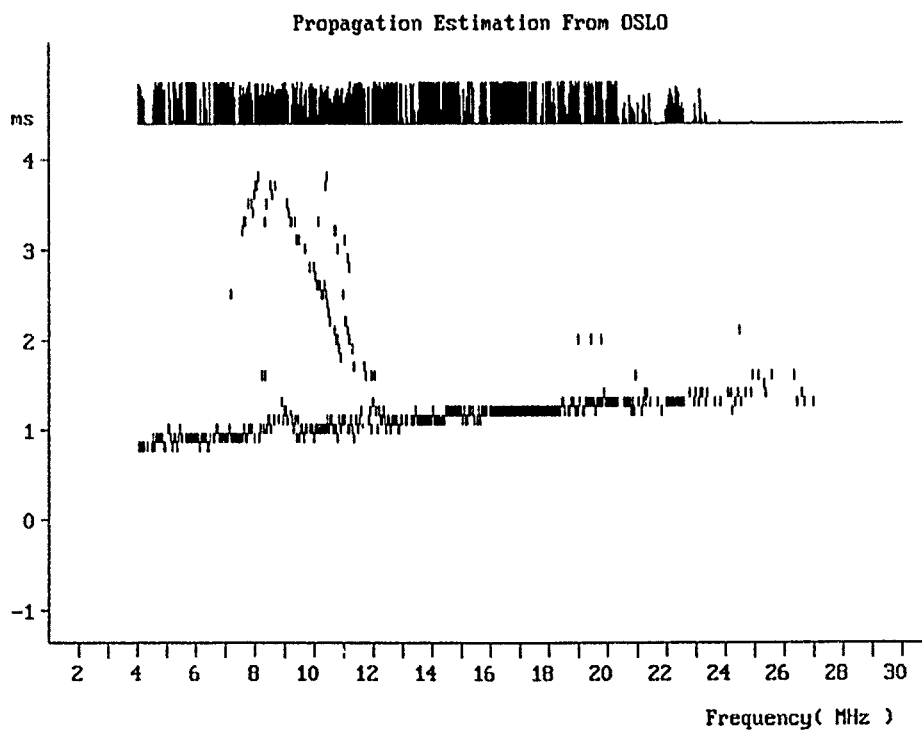


Figure 5b: HWCRG Ionogram of Path from  
Oslo to Cobbett Hill, (10:41am) 8/8/90

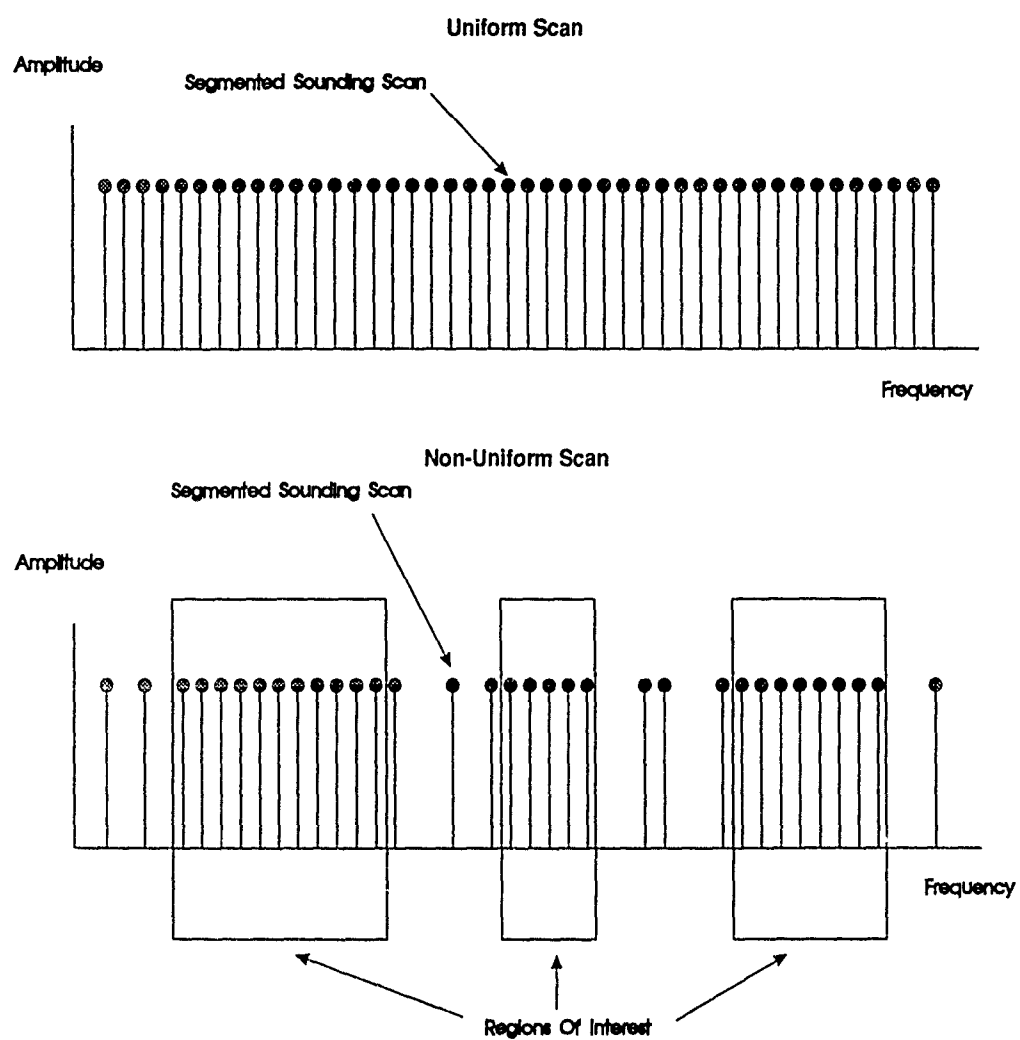


Figure 7a: 'Intelligent' Non-Uniform Scan Option, where sounding confined to regions of interest.



## Time Diversity

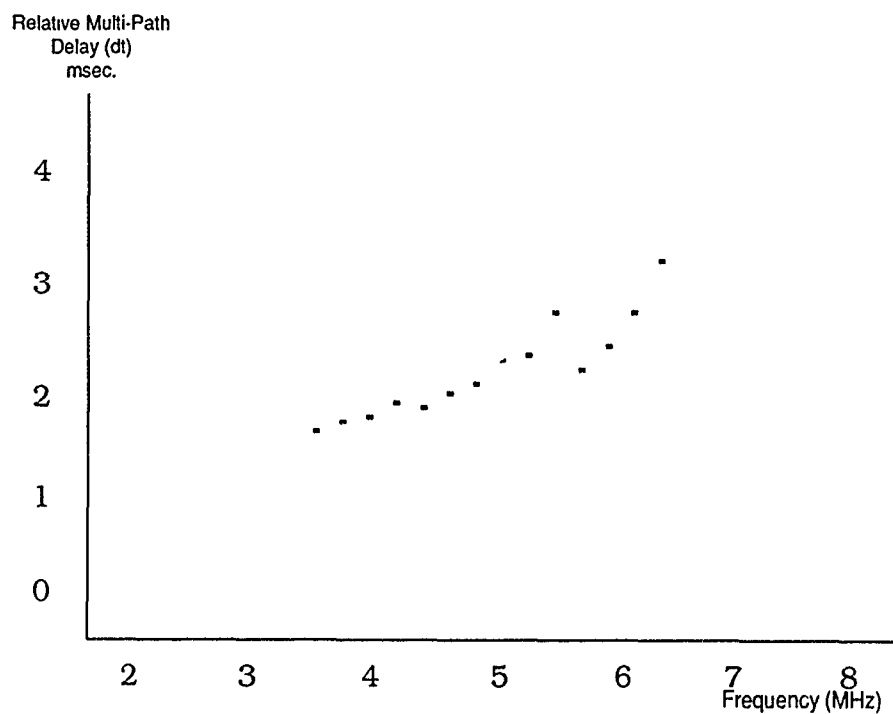


Figure 8a: Ionogram generated by active sounding system on path Hull-Warwick  
c.16.16 16/7/91  
(200 kHz Raster)

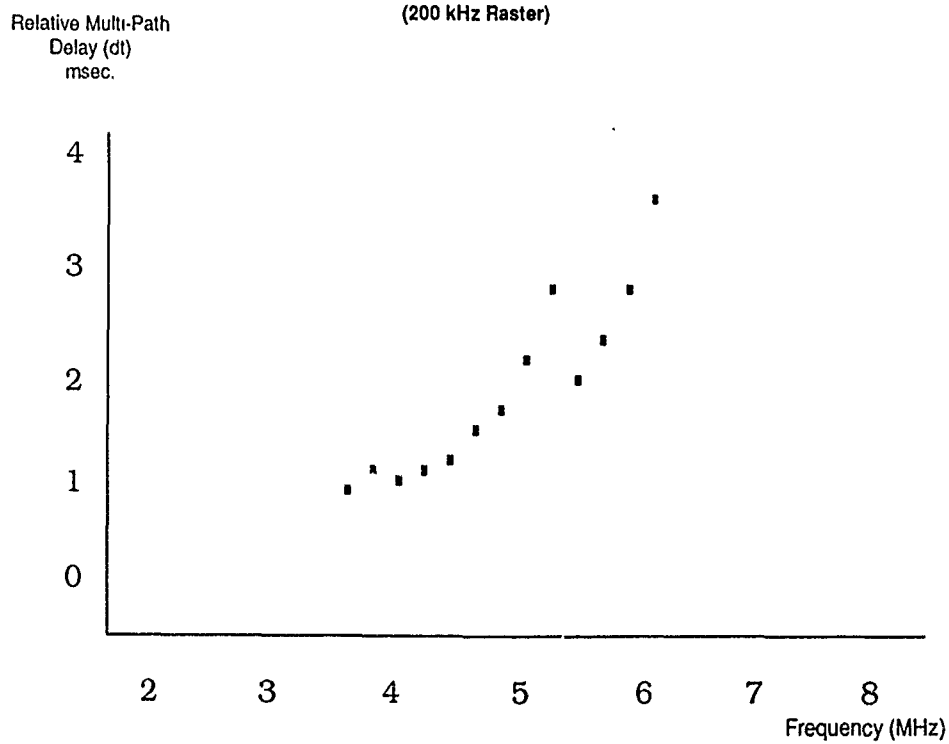


Figure 8b: Ionogram generated by active sounding system on path Hull-Warwick  
c.16.51 16/7/91  
(200 kHz Raster)

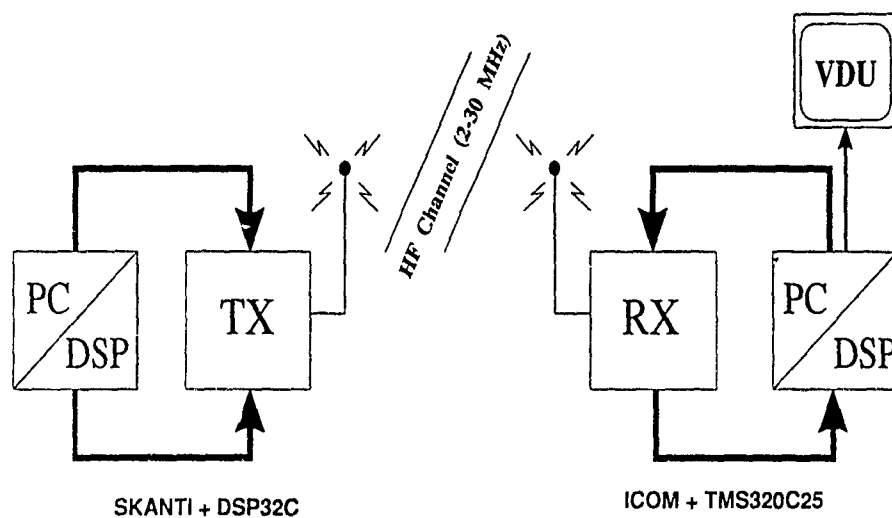


Figure 8d: Equipment Used for Active Sounding Trial

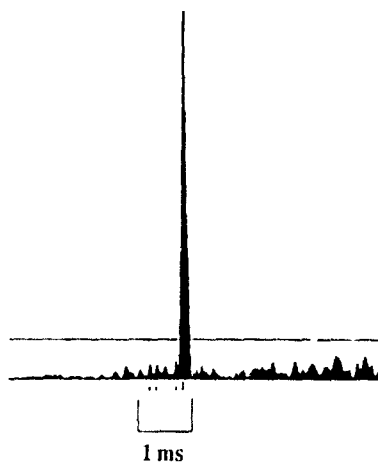


Figure 6: Impulse Response taken from Off-air Chirp c. 8 MHz (Sounder - Oslo)

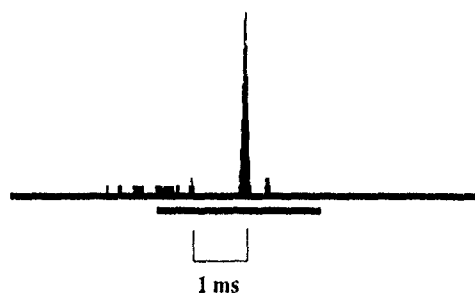


Figure 8c: Impulse Response taken from Sounding Trial (16/7/91)

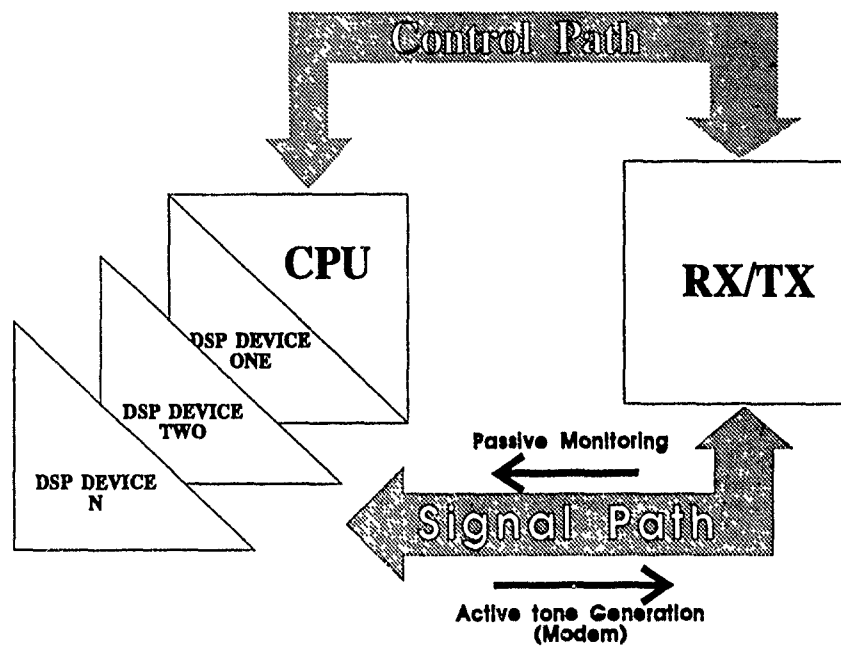


Figure 9: A Schematic of the Proposed 'Generic' Architecture

## DISCUSSION

### **P. CANNON**

1. Does your system have enough processing gain to deal with long distance paths?
2. Your ionograms are very clean. Did you employ a noise 'cleaning' algorithm?

### **AUTHOR'S REPLY**

1. Since a matched filter is the optimum receiver it can approach the theoretical maximum processing gain of '90' (available from using the 3 kHz channel). This is more than adequate to display ionograms on very long distance paths and we have examples of ionograms from the path Cobbett Hill - Hong Kong ( $> 1000$  km).

2. The real-time display algorithm is quite sophisticated and can take account of the average matched-filter "noise". By using this information and the stability of the 'chirp' signal, hence, knowing where the chirp matched-filter return will be placed in the capture frame, a very clean display is possible. All the ionograms displayed are direct 'screen snapshots' from the '286 based PC monitoring system.

In addition, as I mentioned in the test, all the information can be saved in digital form so further "filtering" algorithms can be applied to further reduce 'noise' on the display. This can be done in real-time.

### **C. GOUTELARD**

Have you studied the minimum number of points needed to conserve the pertinent information of the oblique ionogram? I think it's one important point to minimize spectral intrusion.

### **AUTHOR'S REPLY**

We have not made a study to find the optimum number of points that can be used to adequately describe an oblique ionogram, but we feel that areas of the ionosphere that are of little interest to the user should be scanned coarsely, hence minimizing unnecessary spectral intrusion but still giving some ionospheric information; whereas, for areas that have real importance these should be scanned much more finely. As seen from figures 8a and 8b, a 200 kHz raster gives an adequate resolution, so perhaps this should be used as a baseline, with  $< 200$  kHz raster for areas of interest,  $> 200$  kHz for areas of little interest. However, these empirical values obviously need further investigation, and using the work done in backscatter radar (as suggested by you) would be a useful starting point.

In terms of spectral intrusion, the 200 kHz SSFM raster is much more spectrally efficient than continuous LFM systems as if the sounding channels allocated to each system were spaced by 5 kHz, then 40 sounding systems, using SSFM, would only produce the same spectral intrusion as 1 continuous LFM system.

## A REVIEW OF VARIOUS TECHNIQUES FOR COMPUTERIZED TOMOGRAPHIC IMAGING OF THE IONOSPHERE

T. D. Raymond  
1406 W. Green St.  
Wave Propagation Lab  
University of Illinois  
Urbana, IL 61801-2991  
USA

### SUMMARY

Recently, several tomographic techniques for ionospheric electron density imaging have been proposed. Most of these techniques reconstruct a vertical slice image of electron density using total electron content data. The data are measured between a low orbit beacon satellite and fixed receivers located along the projected orbital path of the satellite. By using such techniques it may be possible to inexpensively (relative to incoherent scatter techniques) image ionospheric electron density in a vertical plane several times per day. In this paper, the basic geometry of the problem is reviewed and the various techniques discussed. The satellite/receiver geometry used to measure the total electron content data causes the data to be incomplete; that is, the measured data do not contain enough information to completely specify the ionospheric electron density distribution in the plane between the satellite and the receivers. Most of the proposed techniques include some method designed to overcome this problem. Applications of these techniques made to simulated and real data and the results are compared and discussed.

### 1. INTRODUCTION

The ionospheric electron density distribution can be described approximately by a smooth profile vertically and is locally horizontally homogeneous. A normal ionosphere can contain many deviations from a smooth profile, and these features are of interest. The features can impact many types of HF communication and remote sensing, and can also serve as tracers to other activity in the ionosphere.

Investigations into ionospheric electron density distributions and related ionospheric features use many different techniques; for example, beacon satellites, ionosondes, and incoherent scatter radar have been used [1], [2], [3]. Recently, work on using computerized tomography to image the ionospheric electron density has been done [4], [5], [6], [7], [8]. Ionospheric tomography uses total electron content (TEC) measurements to image the electron density distribution.

This paper reviews the progress of ionospheric tomography. First, Sections 1 through 3 introduce the problem and review earlier series expansion techniques. Next, Section 4 discusses some alternate techniques which have been recently proposed. Section 5 reviews some recent investigations into the limitations of ionospheric tomography. Section 6 reviews recent experimental results, and then Section 7 discusses investigations into three di-

### 2. THE PROBLEM

The goal of ionospheric tomography is to image the electron density in the Earth's ionosphere. To do so, ionospheric tomography uses total electron content measurements as data. Total electron content (TEC) is the line integral between source and receiver of the electron density contained in a column along the integration path. Total electron content measurements can be made by using a radio beacon mounted on a satellite in conjunction with a ground based receiver.

The term *geometry* refers to the satellite positions, ground station locations and the ionospheric image boundary. Tomography requires that the geometry be well known.

The first ionospheric tomographic geometries were two dimensional yielding the electron density distribution in a vertical plane. Figure 1 shows a typical two dimensional ionospheric tomographic geometry after Austen et al. [4]. The satellite orbit is along the arc at the top of the figure. The orbit has an altitude of roughly 1000 km. The receivers are spaced along the ground at the points where the fan beam lines converge. The receivers cover a latitude range of about 20° latitude. The fan beam lines themselves show a representative sampling of the integration paths. In reality, far more TEC measurements can be obtained, but it is not helpful to show all of the integration paths. The grid shows division of the ionosphere into pixels for a finite series expansion reconstruction algorithm.

Recently, some have investigated extending this geometry to three dimensions to image electron density globally. This will be discussed in Section 7. For the most part, it seems that the two dimensional problem and techniques extend to three dimensions.

### 3. SERIES EXPANSION TECHNIQUES

As mentioned above, TEC is the integral of the electron density in a column of unit cross-sectional area along some path.

$$y = \int_P N_e(r, \theta, \phi) ds \quad (1)$$

$N_e(r, \theta, \phi)$  is the electron density along the propagation path  $P$  between source and detector and  $y$  is the TEC. The arguments  $r$ ,  $\theta$ , and  $\phi$  are the altitude, longitude, and latitude respectively. We will assume that geometric optics holds and that the carrier frequencies used to make the TEC measurements are high enough that the path  $P$  is a straight line between source and receiver [4]. We will not assume a specific TEC measurement technique, except that the measurements be absolute TEC (with no unknown phase offsets). For two dimensional ionospheric

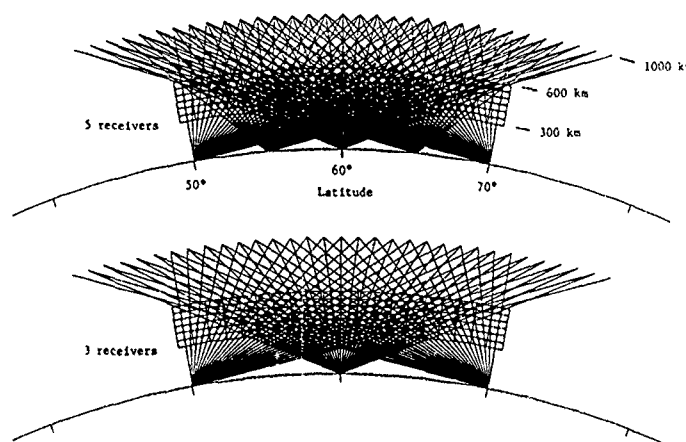


Figure 1. Two ionospheric tomographic geometries. The satellite orbit is along the arc at the top. In the top sketch five receivers are spread along the ground at the points where the fans converge. In the bottom, three receivers are used. The fan beam lines represent integration paths, and the small square boxes represent the pixel grid. After Figure 1 in Austen et al [4]

are aligned along a line of longitude; that is,  $\theta$  is fixed at  $\theta_0$ .

Total electron content (TEC) along some path (say the  $i$ th path or ray,  $P_i$ ) can be approximated as a finite sum of shorter integrals along segments of  $P_i$ . Assume the electron density distribution to be uniform over discrete regions; that is, divide the electron density distribution  $N_e$  into a set of  $N$  pixels,  $x$  where  $x_j$  equals the electron density within the  $j$ th pixel. The reconstruction problem then centers around solving the system

$$y_i = \sum_{j=1}^N A_{ij} x_j + e_i \quad i = 1, \dots, M \quad (2)$$

or (in matrix notation)

$$y_{M \times 1} = A_{M \times N} x_{N \times 1} + e_{M \times 1} \quad (3)$$

where for this problem  $N$  is the number of pixels in the image,  $M$  is the number of TEC values or equivalently, the number of rays or paths,  $y$  is the vector of known TEC data,  $A$  is an array containing the length of the path pixel intersection for each pixel and path,  $x$  is a vector of the electron density in each pixel, and  $e$  is the error vector associated with the series expansion and measurement error. Note that  $y$  and  $x$  are column vectors of TEC and electron density in each pixel respectively.

The solutions based on series expansion techniques categorized into two types: iterative and non-iterative [9]. As discussed by Austen et al. [4], iterative solutions solve (3) by first making an initial guess,  $x^0$ , then calculating the resulting  $y^0$ , and then using the difference between  $y$  and  $y^0$  to modify  $x^0$ , creating  $x^1$ . This cycle is repeated until a satisfactory solution is obtained. Non-iterative techniques compute  $x$  directly from  $A$  and  $y$ . Since the system is usually over determined and inconsistent, the best non-iterative approach seems to be singular value decom-

position of several hundred by several thousand (typically several million entries), an iterative approach requiring less computer memory is usually necessary.

The reconstruction algorithm used by Austen et al. [4] is the algebraic reconstruction technique (ART). This uses an iterative series expansion method for solving (3). Raymond et al. [6] use the multiplicative algebraic reconstruction technique (MART), an iterative approach similar to ART, as the reconstruction algorithm. The multiplicative technique, from the family of entropy optimization algorithms, is similar to ART in constraints and form, but rather than making a correction to  $x^k$  of the form  $x + f(y - y^k)$ , MART uses  $(x)f(y/y^k)$ , making a multiplicative modification to  $x^k$ . This algorithm was first proposed by Gordon et al. [10], more thoroughly discussed by Lent [11], and included in a review of finite series expansion reconstruction algorithms by Censor [9].

Any iterative algorithm requires some initial values,  $x^0$ , before iteration begins. In the ionospheric case, the geometry makes the initial guess very important. This initialization can represent a gross estimate or guess of what the reconstruction might look like; the first iteration of a reconstruction algorithm will begin to correct this guess towards some satisfactory solution. In general, the initial guess should incorporate any *a priori* information about the image; in fact, in the ionospheric case the closer the initial guess is to the correct image, the sooner and more accurately the reconstruction algorithm will converge.

Several of the algorithms mentioned by Censor [9] suggest using an initial guess where a constant value is assigned to every pixel in the image. For ionospheric tomography it has been generally found that some initial guess based on an estimate of the background ionospheric density profile and the measured TEC data yields much better reconstructions.

#### 4. NEWER ALGORITHMS

Recently, several new reconstruction algorithms have been introduced that promise better reconstructions than the series expansion methods. Two are modified series expansion approaches, one uses expansion into empirical orthonormal functions and three others are transform based methods using various convolution back projection algorithms. One other uses diffraction tomography.

##### 4.1 Modified Series Expansion Methods

The Ionospheric Physics Division at the Air Force Phillips Lab has a small in-house effort underway to develop an ionospheric electron density reconstruction algorithm. The algorithm treats the problem as a linear inverse problem, using the same equations as those presented in Section 3. The maximum entropy method has been shown to produce a unique solution which makes optimal use of all available data and makes no assumptions about unmeasured data. The maximum entropy principle is applicable because the set of unknown densities is isomorphic to a set of probabilities, and each observed TEC measurement is a linear combination of these unknown densities [12].

Another series expansion method using simulated annealing was recently applied by Xie [13]. Though there are many images that yield similar TEC values, there are hopefully only a few that yield the exact TEC values measured. Thus the cost surface  $y - y^k$  can be imagined as having many local minima and maybe a few global minima that are deeper than the others. If the initial guess is not good, the series expansion method may converge into one of the local minima, but be far from a global minimum representing a more correct image. Simulated annealing changes the modifications to  $x$  by using "an appropriate cooling schedule". Thus the name. Instead of constantly trying to reduce the error in TEC, the error is sometimes allowed to increase, and is controlled by some random distribution. This way, the algorithm may fall into a local image minimum but if the minimum is not deep enough, it may climb out again and hopefully fall into deeper, more global minimum.

##### 4.2 Empirical Orthonormal Functions

Another reconstruction method, presented by Fremouw and Secan [14] uses empirical orthonormal functions (EOF's). Consider the series expansion method as a sum of orthonormal functions multiplied by coefficients. Each orthonormal function is equal to 1 within a single unique pixel and 0 everywhere else. The coefficient for any particular function is the electron density within the pixel for which the function equals 1. Now suppose a different set of orthonormal functions is used, perhaps one which has more "realistic" properties. Such a set has been suggested and used for a global ionospheric conductivity and electron density (ICED) model [15]. The functions are derived as follows. First a set of example electron density images is obtained. Then, a correlation matrix is formed by correlating the images with each other. The eigen vectors of the correlation matrix form a basis, spanning the set of examples. The basis can be reduced by truncating the number of eigen vectors used based on the magnitude of the corresponding eigen values.

Using the truncated set of basis functions, a system like

tion must be a member of the space of electron density distributions defined by the original example set. While this potentially reduces the reconstruction of unusual features, it does restrict the reconstruction to a "reasonable" solution. That is, the result must be like the original example set.

This method has been used successfully by Fremouw and Secan [14]. Using the same TEC data as that used by Raymund et al. [6], results have been obtained that include a the slant in the ionosphere not detected by the MART algorithm used in the earlier work. The method of reconstruction uses a series of vertical orthogonal functions combined with Fourier reconstruction discussed in the next Section.

A different orthogonal basis function reconstruction algorithm has been proposed by Na [16]. The basic formulation of the problem is still like (3), but the basis functions are proposed to be whole domain functions where each basis function fills the entire image region and may have both horizontal and vertical structure.

##### 4.3 Transform Methods

Recently, several efforts have been made to apply transform techniques. The reconstruction algorithm derived by Yeh and Raymund [17] is a form of convolution back projection. Na and Lee [16] also use this type of technique among others, as have Fremouw and Secan [14].

In general tomographic geometries the region to be imaged is sampled by integration paths passing at all angles through the region. That is, the integral

$$p_\alpha(t) = \int_P f(x, y) ds \quad (4)$$

is measured for some range of  $t$  and for  $\alpha \in [0, \pi]$ . This is sketched in Figure 2 where a line  $P$  at  $t = t_0$  for the projection at angle  $\alpha$  is shown. The sketch of the function  $p_\alpha(t)$  for that  $\alpha$  is also shown. The function  $p_\alpha(t)$  is termed the projection of  $f(x, y)$  at the angle  $\alpha$ . For all  $\alpha$  and  $t$ ,  $p_\alpha(t)$  is called the Radon transform of  $f(x, y)$ .

The Projection Slice theorem or Central Slice theorem relates the Fourier transform of the projection to the two dimensional Fourier transform of  $f(x, y)$ . If we define the respective transforms as

$$S_\alpha(\omega) = \int_{-\infty}^{+\infty} p_\alpha(t) e^{-j2\pi\omega t} dt \quad (5)$$

and

$$F(u, v) = \int_{-\infty}^{+\infty} \int_{-\infty}^{+\infty} f(x, y) e^{-j2\pi(u x + v y)} dx dy \quad (6)$$

where  $f(x, y)$  is the image function, then the projection slice theorem says (see Kak and Slaney [18] for a proof) that

$$S_\alpha(\omega) = F(\omega \cos \alpha, \omega \sin \alpha) \quad (7)$$

The projection slice theorem was first derived by Bracewell [19].

In other words, the one dimensional Fourier transform of  $p_\alpha(t)$  with respect to  $t$  is the same as that along the line

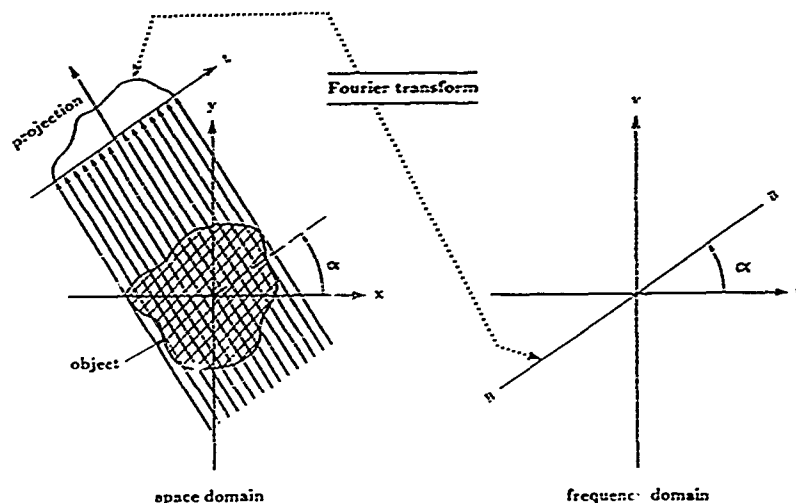


Figure 3: Sketch of the relation between  $S_\alpha(\omega)$  and  $F(u, v)$ . After Kak and Slaney, [18]

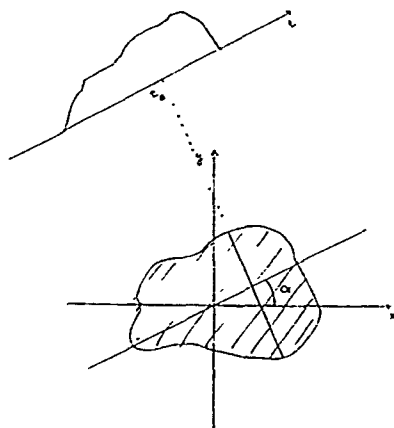


Figure 2: A two dimensional image region and a projection at an angle  $\alpha$ . The integration path for  $t = t_0$  is shown.

spatial frequency domain showing the relation between  $F(u, v)$  and  $S_\alpha(\omega)$  appears in Figure 3.

A good review of transform methods can be found in Lewitt [20]. Kak and Slaney [18] also give a very good introduction to transform techniques.

To apply this to the ionospheric tomographic problem is fairly straight forward. Each TEC measurement can be considered a discrete element of  $p_\alpha(t)$ . After indexing TEC data by projection angle and  $t$ , any of the transform techniques can be applied. For examples, see the refer-

function  $f(x, y)$  reconstructed will really be  $N_e(r, \theta_0, \phi)$ . The change in coordinate systems can be done after the fact or as the last step of the reconstruction.

#### 4.4 Diffraction Tomography

Recently, Kunytsyn and Tereshchenko [21] investigated using diffraction tomography to image ionospheric features. Diffraction tomography includes the effects of scattering and does not assume ray optics. As an inverse scattering problem, the mathematics are not trivial though conceptually the problem is very similar. A good introduction to this type of tomography is given by Kak and Slaney [18] and includes many other references.

#### 5. LIMITATIONS

The ionospheric tomography geometry does not typically include integration paths that traverse the ionosphere horizontally (see Figure 1). In fact, most of the integration paths tend to be vertical or nearly vertical. If there exists an electron density distribution in the imaging region whose path integral is zero in the vertical (or near vertical) direction, it will be undetected, even though it may have a nonzero horizontal path integral. Thus several different ionospheric electron density distributions might produce identical TEC measurements. Clearly with non-unique data, the reconstructions can not be unique either.

An analytic review of the limits of ionospheric tomography has been done by Yeh and Raymond [17]. The ideal geometry is proposed to be a flat earth with a continuous line of receivers extending to  $\pm\infty$  and the satellite orbit extending to  $\pm\infty$  at a constant altitude. From the geometry, two comments about the limits of tomography immediately follow. 1) the TEC data are independent of electron density distributions with line integrals equal to zero in the vertical or the horizontal, and 2) only local electron density distributions can be imaged. The sec-

conditions for the existence of the Fourier transform.

With the above two limits defined, a reconstruction algorithm is derived for the ideal case. The algorithm can reconstruct exactly local distributions without zero line integrals. In reality, it is not possible to configure a continuous line of receivers extending to  $\pm\infty$ ; instead, the number of receivers is discrete and they have some non zero spacing between them. Also, the receivers have some limit on the range of elevation angles at which data can be taken. Usually, the minimum elevation angle is roughly  $15^\circ$ . These two realistic limitations are introduced into the geometry and the resulting degradation from an ideal impulse examined. Figure 4 shows the reconstruction of an Dirac impulse centered in the middle of the image region. The region covers 1000 km of ground distance and 1000 km of altitude and has 10 receivers evenly spaced along the ground. The wings extending from the central peak in the image result from the limit on the minimum elevation angle of the receiver. The wave-like ripples extending horizontally from the peak are due to the finite number of discrete receivers. There are ripples extending vertically from the peak as well, but they die away so quickly that it is hard to see them in the Figure.

The wings are a particularly important effect and have appeared in images obtained using series expansion techniques. Because ionospheric features occur near the peak of the electron density distribution, strong wings can extend from features near the peak into regions where the electron density distribution is low. These wings could be misinterpreted as features.

Another analysis of the limits of ionospheric tomography has been done by Na and Lee [8] and Na [16]. This work is based on a specific reconstruction algorithm, detailed in Na [16]. To analyze the limitations of the algorithm, several problems are identified and their individual contribution to image error analyzed. The finite number of discrete receivers is found to contribute to limitations in the spatial bandwidth. That is, the more closely spaced the receivers are, the less aliasing present in the reconstruction. Through the Central Slice theorem, the effect of limited elevation angles is also qualitatively assessed and the ionospheric tomography problem is identified as a missing cone problem. Figure 5 shows qualitatively the problem, because horizontal line integrals are missing, information is missing in triangular regions of the spectral domain.

The Na algorithm also requires regularly spaced data along each projection and also requires a uniform distribution of projections in angle. The interpolation and binning schemes used to meet this requirement introduce significant amounts of error into the reconstruction. Also, as pointed out by Na [16], some small features may be degraded nearly completely because of the way integration paths sample the image. Figure 6 shows a sketch of several integration paths missing a point feature.

## 6. REVIEW OF RECONSTRUCTION RESULTS

Most work to date has dealt only with simulated TEC data. One simulated data set of some interest is that used by Raymund et al. [6] and Fremouw and Secan [14]. Using a model based on an incoherent scatter radar

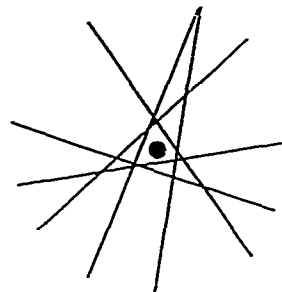


Figure 6: Several integration paths missing a point feature After Na [16].

erated and used for reconstructions. Figure 7 shows a reconstruction of the trough after Raymund et al. [6]. This reconstruction was made using MART, a series expansion based method. Figure 8 shows a reconstruction after Fremouw and Secan [14]. The reconstruction algorithm is based on both orthogonal basis functions and a transform technique. Figure 9 shows the original model. By inspection, it is easy to see that the more recent technique improves on the earlier work by reconstructing the slant in the background.

In December of 1990, a set of stations in the United Kingdom was used to collect TEC data and form a reconstruction of the ionosphere [22]. The reconstruction was made using SIRT, a series expansion technique very similar to ART. The initial guess consists of a Chapman layer with an estimated peak height (325 km) and a scale height based on monthly mean slab thickness data from the 1968-1970 solar maximum. A contour of the reconstruction appears in Figure 10. The reconstruction appears to be a very reasonable one. It is possible the slight depression at 300 km altitude and roughly  $61^\circ$  North is the polar trough. More information about this experiment is to be presented by Walker et al. [23].

## 7. GLOBAL TOMOGRAPHY

Recently, two proposals for global ionospheric mapping have been presented [24], [25]. The techniques and assumptions are very similar to the two dimensional tomography discussed so far, though the geometry is very different.

The TEC data are to be collected using L-band signals from the Global Positioning System (GPS) of satellites. Instead of using ground based receivers, it is proposed that a low orbit satellite receive GPS TEC data could be collected when the integration path skimmed through the Earth's ionosphere. Ground based receivers might

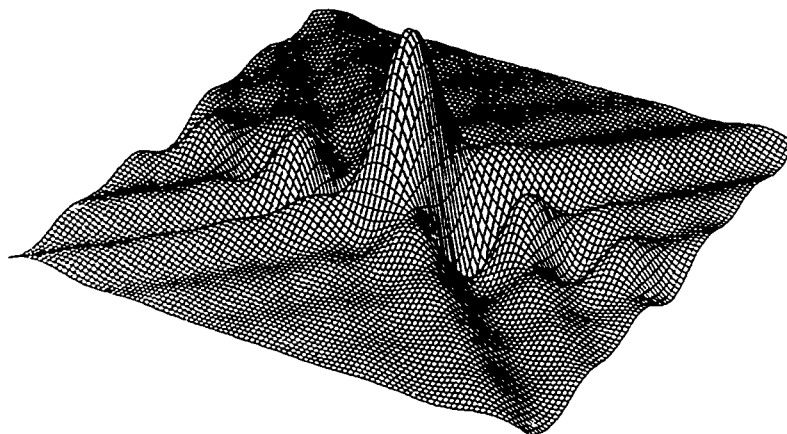


Figure 4: Impulse response for a finite number of discrete receivers with limits on the minimum elevation angle after Yeh and Raymond [17]. The region covers 1000 km horizontally and 1000 km vertically. See the text for discussion of the features

In the plan proposed by Hajj and Yunck [25], singular value decomposition (SVD) is used to solve a linear system like (3.) The pixels have been replaced with voxels (a cube of constant electron density). Now the image region is three dimensional and has been divided into blocks instead of squares.

The method proposed by Chiu et al. [24] is most like the basis function expansion methods, but it does not fit into any one category completely. The TEC data can be binned up into sets where each set corresponds to a particular conjunction of the low orbit satellite and a GPS satellite. The sets are also local to a region of the ionosphere. A local ionosphere is computed based on the TEC data. The gradient of the TEC data is also used and some correction terms generated. The processes is repeated iteratively and the resulting local ionospheres stitched together to form a global map.

## 8. CONCLUSIONS

Though in its infancy, ionospheric tomography is rapidly developing into a usable tool for investigating ionospheric electron density structures. The early history of ionospheric tomography reviewed in Sections 2 through 3, compared with the recent more sophisticated approaches reviewed in 4 shows that methods are rapidly improving. The results mentioned in Section 5, show an increased understanding of the problems of ionospheric tomography, and finally, the results discussed in Section 6, verify some of the promise of ionospheric tomography.

mains a problem. Also, some experiment must be done where another instrument can verify the reconstructed ionosphere. For example, a chain of Transit receivers could be set up along the coast of North America to collect TEC data. The reconstructed ionosphere could be verified using the Mill Stone Hill incoherent scatter radar. Similar experiments could be configured using Eiscat. These experiments would provide valuable insight into the practical problems associated with tomography and would also provide a rigorous test bed for reconstruction schemes.

## REFERENCES

- [1] Huang, Y.-N., Cheng, K. and Chen, S.-W., "Daily observations of the development of the ionospheric equatorial anomaly, by means of differential Doppler shift method", *Radio Sci.*, 22, 1987, pp 433-438.
- [2] Leitinger, R., Hartmann, G.K., Lohmar, F.-J., Lohmar, and Putz, E., "Electron content measurements with geodetic Doppler receivers", *Radio Sci.*, 19, 3, 1984, pp 789-797.
- [3] Weber, E.J., Tsunoda, R.T., Buchau, J., Sheehan, R.E., Strickland, D.J., Whiting, W., and Moore, J.G., "Coordinated measurements of auroral zone plasma enhancements", *J. Geophys. Res.*, 90, 1985, pp 6497-6513.
- [4] Austen, J.R., Franke, S.J., and Liu, C.H., "Ionospheric imaging using computerized tomography",

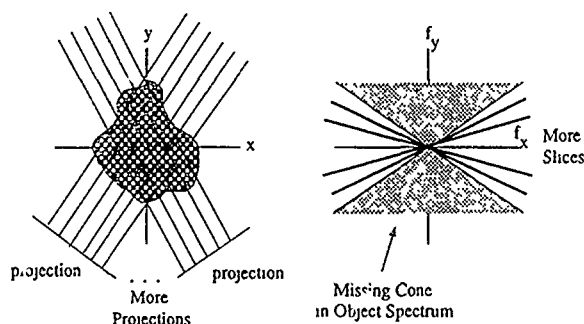


Figure 5: Qualitative description of problems caused by missing horizontal line integrals. The missing line integrals correspond to triangular regions of spectral information. After Na [16]

- [5] Aframovich, E.L., Pirog, O.M., and Terekhov, A.T., "Diagnostics of large-scale structures of the high-latitude ionosphere based on tomographic treatment of navigation-satellite signals and of data from ionospheric stations", USSR Academy of Sciences, Siberian Department, SibIZMIR, Preprint No. 19-89, 1989.
- [6] Raymund, T.D., Austen, J.R., Franke, S.J., Liu, C.H., Klobuchar, J.A., and Stalker, J., "Application of computerized tomography to the investigation of ionospheric structures", *Radio Sci.*, **25**, 1990, pp 771-789.
- [7] Austen, J.R., Raymund, T.D., Liu, C.H., Franke, S.J., Klobuchar, J.A., and Stalker, J., "Computerized ionospheric tomography", in "Proceedings of the Ionospheric Effects Symposium", May, 1990. Available from the Naval Research Laboratory, Washington, D.C.
- [8] Na, H., and Lee, H., "Resolution analysis of tomographic reconstruction of electron density profiles in the ionosphere", *International Journal of Imaging Systems and Technology*, **2**, 1991, pp 209-218.
- [9] Censor, Y., "Finite series-expansion reconstruction methods", *Proc. IEEE*, **71**, 1983, pp 409-419.
- [10] Gordon, R., Bender, R., and Herman, G.T., "Algebraic reconstruction techniques (ART) for three-dimensional electron microscopy and X-ray photography", *J. Theor. Biol.*, **29**, 1970, pp 471-481.
- [11] Lent, A., "A convergent algorithm for maximum entropy image restoration, with a medical X-ray application", in "1976 SPSE Conference Proceedings", edited by R. Shaw, Society of Photographic Scientists and Engineers, Washington, D.C., 1977, pp 249-257.
- [12] Fougere, P., and Klobuchar, J.A., "Maximum entropy ionospheric tomography", presented at the IEEE/AP-S Symposium at the University of Western Ontario, London, Ontario, Canada, June, 1991.
- [13] Xie, J., "Application of computerized tomography technique to ionospheric image reconstruction", Faculty of Graduate Studies, The University of Western Ontario, London, Ontario, Canada, Master's Thesis, March, 1989.
- [14] Fremouw, E.J., and Secan, J.A., "Application of a stochastic inverse technique to ionospheric tomography", presented at the 1991 North American Radio Science Meeting and IEEE/AP-S Symposium at the University of Western Ontario, London, Ontario, Canada, June, 1991.
- [15] Daniell, R.E. Jr., Decker, D.T., Anderson, D.N., Jasperse, J.R., Sojka, J.J., and Schunk, R.W., "A global ionospheric conductivity and electron density (ICED) model", in "Proceedings of the Ionospheric Effects Symposium", May, 1990. Available from the Naval Research Laboratory, Washington, D.C.
- [16] Na, H., "Tomographic Reconstruction Techniques for Imaging Electron Density Profiles in the Ionosphere", Department of Electrical and Computer Engineering, University of Illinois at Urbana-Champaign, Urbana, IL, USA, Ph.D. Dissertation, 1991.
- [17] Yeh, K.C., and Raymund, T.D., "Limitations of ionospheric imaging by tomography", submitted to *Radio Sci.*, 1990.
- [18] Kak, A.C., and Slaney, M., "Principles of Computerized Tomographic Imaging", IEEE Press, 1988 (ISBN 0-87942-198-3).
- [19] Bracewell, R.N., "Strip integration in radio astronomy", *Aust. J. Phys.*, **9**, 1956, pp 198-217.
- [20] Lewitt, R.M., "Reconstruction algorithms. transform

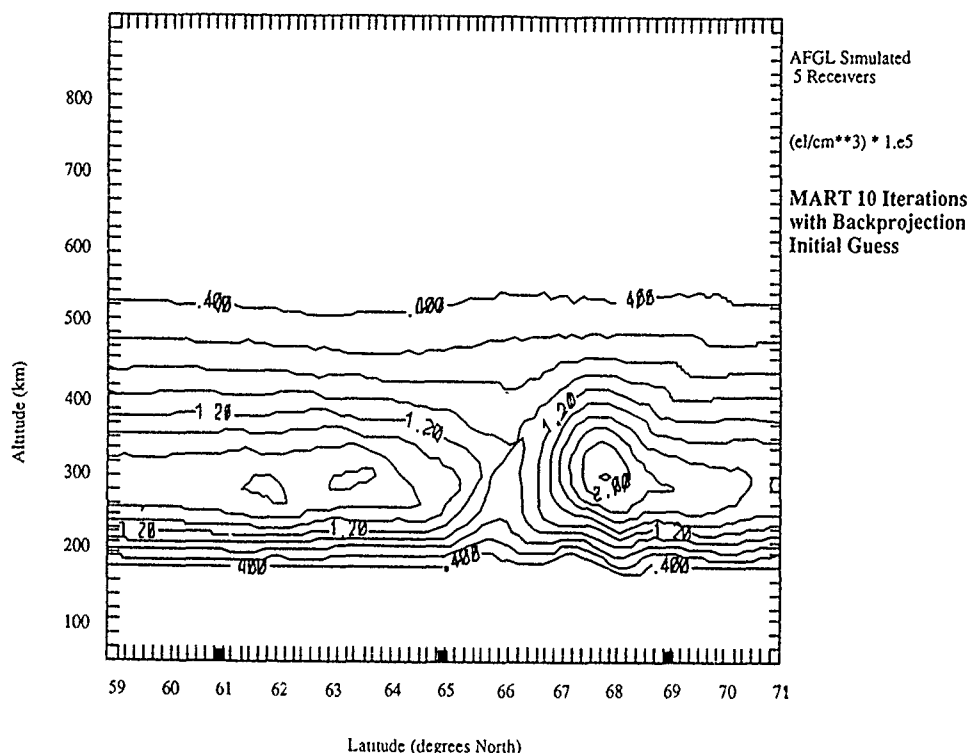


Figure 7: Reconstruction of the polar trough (model) after Raymund et al [6]

- [21] Kunytsyn, V.E., and Tereshchenko, E.D., "The reconstruction of the ionosphere irregularities structure", The USSR Academy of Sciences, Kola Science Center, Polar Geophysical Institute, Preprint PGI 90-01-69, 1990.
- [22] Pryse, S., and Kersley, L., "An Experimental Demonstration of Ionospheric Tomography", presented at the 1991 North American Radio Science Meeting and IEEE/AP-S Symposium at the University of Western Ontario, London, Ontario, Canada, June, 1991.
- [23] Walker, I., Pryse, S., Russel, C, Rice, D., and Kersley, L., "Mapping electron content and electron density in the sub-auroral ionosphere", in "The AGARD 49th Symposium of the Electro magnetic Propagation Panel on the Remote Sensing of the Propagation Environment", AGARD CP, October 1991, Paper 15.
- [24] Chiu, Y.T., Robinson, R.M., Davidson, G.T., and Rinaldi, R.A., "Simulation of Space-Based Ionospheric Tomography", presented at the 1991 North American Radio Science Meeting and IEEE/AP-S Symposium at the University of Western Ontario, London, Ontario, Canada, June, 1991
- [25] Hajj, G A, Yunch, T P "The possibility of 3-D Ionospheric Tomography", presented at the IEEE/AP-S Symposium at the University of Western Ontario, London, Ontario, Canada, June, 1991.

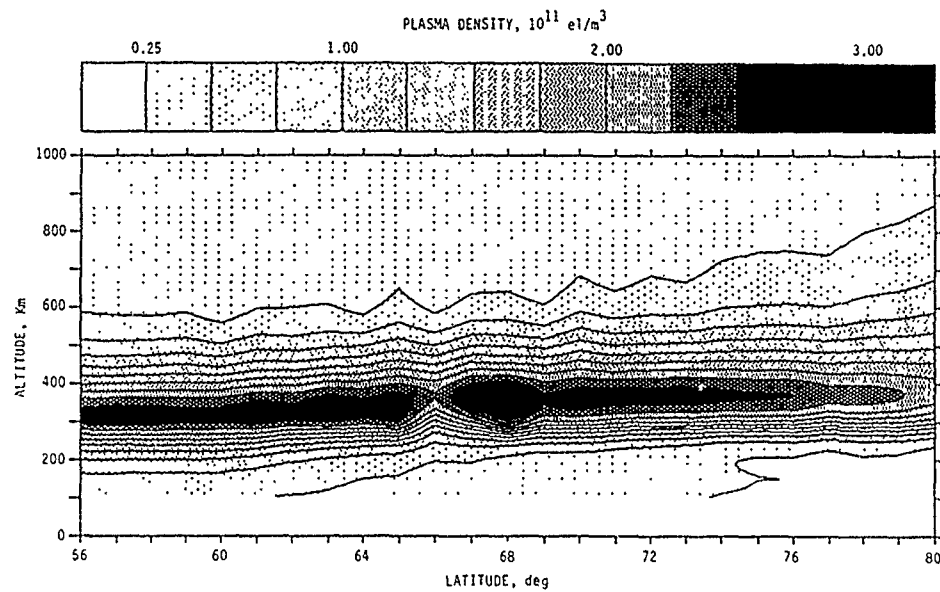


Figure 8: Reconstruction of the polar trough (model) after Fremouw and Secan [14]

As sent to U of Illinois, autumn 1987.

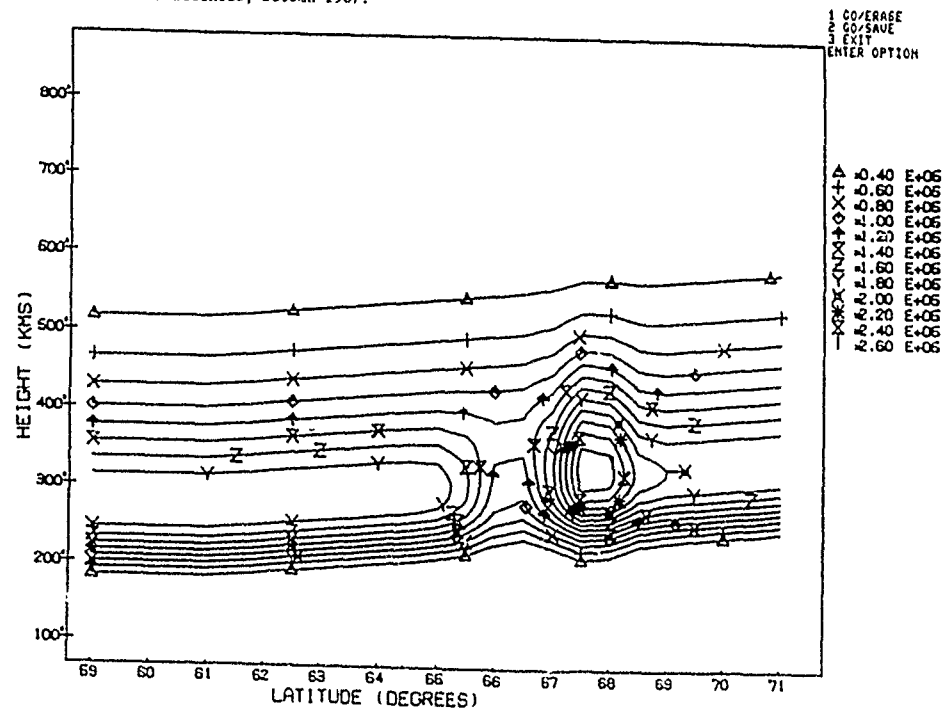


Figure 9 Model of the polar trough TEC data from this model was used to reconstruct images in previous Figures

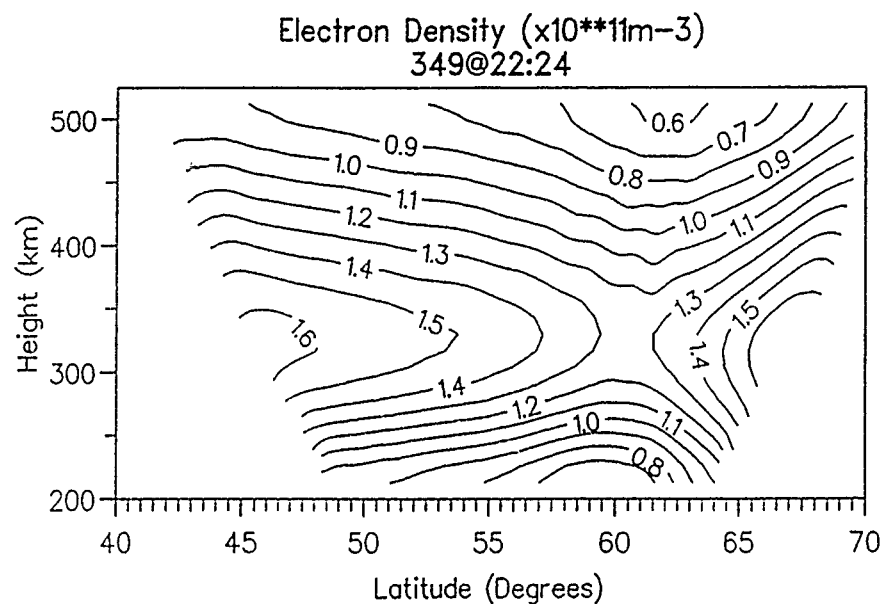


Figure 10 Experimental ionospheric tomography reconstruction after Pryse and Kersley [22] Note the depression at 300 km altitude and 61° North which could be the polar trough.

#### DISCUSSION

##### **B. REINISCH**

*Why don't you have any experimental validation of your technique?*

##### **AUTHOR'S REPLY**

*We have not had sufficient resources to develop the hardware required for a campaign. We hope this will change soon!*

##### **C. GOUTELARD**

*You mention the use of orthonormal empirical functions for the modelling of your calculation. This choice simplifies the treatment by computer and its is very important. Can you describe those functions and your choice?*

##### **AUTHOR'S REPLY**

*The functions are more completely described in the references Daniell [15], Fremouw et al. [14] and Na [16]. Basically, the functions bound the results with the space spanned by some reasonable set of example ionospheres.*

# MAPPING ELECTRON CONTENT AND ELECTRON DENSITY IN THE SUB-AURORAL IONOSPHERE

I.K.Walker, S.E.Pryse, C.D.Russell, D.L.Rice and L.Kersley  
Physics Department, University College of Wales, Aberystwyth, Dyfed. SY23 3BZ. UK

## SUMMARY

Applications involving radio waves propagating through the ionosphere are subject to errors due to effects of the medium. For several of these effects the electron content along the propagation path is a key parameter. At high latitudes, steep gradients in electron content resulting from electron density variations in the vicinity of the ionospheric trough are of particular importance. The present paper describes two methods of mapping electron content and electron density in the sub-auroral ionosphere over northern Europe.

A receiving system for the 150 MHz and 400 MHz transmissions from NNSS satellites has been based at Lerwick in the Shetland Islands for several years. The experiment yields measurements of differential carrier phase from which estimates can be made of the total electron content as a function of latitude for each pass of the satellites monitored. Calibration to obtain absolute values is achieved using spot data from a co-located receiving system for GPS satellites or by means of ionosonde foF2 values and a slab thickness model. The constellation of 7 NNSS satellites in polar orbits gives good temporal coverage of satellite passes so that contour plots can be drawn of electron content behaviour as a function of latitude and time. Results are presented illustrating behaviour of the ionospheric trough.

Simultaneous measurements of electron content made at several stations spaced in the meridian can, in principle, be inverted using the techniques of computerised tomography to reconstruct images of electron density as a function of latitude and height. The paper describes an experimental campaign carried out in the UK in December 1990 during which simultaneous observations were made using the NNSS satellites at 4 stations covering a latitudinal range of some 8 degrees. The resulting measurements of electron content from some 30 satellite passes have been used in a reconstruction algorithm to map the electron density on a two-dimensional grid. The potential usefulness of tomographic techniques in ionospheric sensing is discussed in the light of the results obtained.

## 1. INTRODUCTION

Radio signals propagating in the ionosphere are subject to effects of the medium which can result in system errors. For many applications involving trans-ionospheric propagation the total electron content along the path is a key parameter, while in others the structure of ionospheric electron density is of importance. The present paper describes results obtained from two experimental techniques that have been used to map electron content and electron density in the sub-auroral ionosphere over northern Europe, with a view to obtaining improved knowledge of the propagation medium. The experiments are based on the reception of 150 MHz and 400 MHz phase coherent transmissions from polar orbiting satellites in the Navy Navigational Satellite System (NNSS). Monitoring of the differential carrier phase enables the equivalent vertical total electron content to be obtained as a function of latitude. The constellation of 7 operational NNSS satellites observed at a high latitude site gives good temporal coverage of satellite passes. A mapping technique has been developed to use the observations to display the morphological variations of total electron content for an ionospheric region in the vicinity of the main F-layer trough. The experiment also yields information on the radio-wave scintillation arising from small-scale irregularities in ionospheric electron density. The mapping technique has been applied to the scintillation observations enabling irregularity occurrence to be related to

the larger-scale electron content structures. Results are presented and discussed here illustrating the success of the technique in displaying the temporal development of both large and small-scale features in the ionosphere over a wide latitudinal range in the sub-auroral region.

The second part of the paper is concerned with the development of ionospheric tomography to provide two-dimensional images of electron density. Measurements of electron content made at a latitudinal chain of stations have been used to reconstruct images of electron content in the latitude/height plane. Experimental results are presented showing the development of the main trough which illustrate the potential of ionospheric tomography.

## 2. BACKGROUND

The midlatitude trough and the scintillation boundary are well established features of the sub-auroral ionosphere. The trough has been the subject of considerable study since the mid-1960's. A review by Wrenn and Raitt (1975)<sup>1</sup> details the early work, while more recent studies have been summarised by Moffett and Quegan (1983)<sup>2</sup>. The trough is primarily a nightside phenomenon, extending from dusk through to the dawn sector, though Whalen (1987)<sup>3</sup> has identified a daytime trough at higher latitudes. Rodger et al. (1986)<sup>4</sup> noted that many studies, especially those carried out using satellite observations, concentrate on the location of the trough minimum as this is usually the most readily identifiable feature in the data. Little information is available about gradients in the vicinity of the minimum, though it seems accepted that the poleward wall of the trough is steeper than that on the equatorward side of the depression. It is generally agreed that the latitude of the trough decreases throughout the night and during periods of increased geomagnetic activity the trough is seen at lower latitudes.

The region of small-scale ionospheric irregularities at high latitudes is often characterised by a sharp equatorial boundary. The occurrence morphology of this so-called scintillation boundary has been discussed by many workers (eg. Aarons et al. 1971<sup>5</sup>, Stuart 1972<sup>6</sup>). Early attempts to investigate the relationship between the trough and the scintillation boundary suggested that the two phenomena had statistical behaviours that were broadly similar. However, Kersley et al. (1975)<sup>7</sup> concluded from simultaneous observations that the two features were essentially independent having a relative motion that followed a diurnal pattern. The current work is aimed at exploiting the abundance of suitable passes of NNSS satellites to gain further understanding of the characteristics of the trough as seen in total electron content and the scintillation boundary over northern Europe.

## 3. THE EXPERIMENT

The experiment makes use of the phase coherent signals transmitted on 150 MHz and 400 MHz from the constellation of 7 NNSS polar orbiting satellites. The transmissions are used to estimate ionospheric total electron content using the differential carrier phase technique and to study both amplitude and phase scintillation. The received differential carrier phase is determined at a sampling interval of 0.2 s whilst values of parameters which characterise amplitude and phase scintillation are recorded for every 20 s of satellite pass. The former allow features of the large-scale structure of electron content to be studied as a function of latitude, while

the latter indicate the presence of ionospheric irregularities of sub-kilometre size. The automated receiving and data-logging equipment is located at Lerwick (60.1°N 1.2°W) in the Shetland Islands and has been configured in the manner described above since early 1989. On average some 14 passes per day have been monitored in the long term by the receiving system, with a mean duration per pass of some 15 minutes. Observations from individual passes give information on the latitudinal structure of the ionosphere while slow temporal changes are seen in the measurements from successive passes.

The analysis technique for the reduction of single station differential carrier phase measurements to total electron content is well established. The technique assumes a linear horizontal gradient in electron content in the vicinity of the point of satellite closest approach to estimate the absolute phase difference and hence absolute total electron content. Near the minimum of the ionospheric trough this assumption is open to question and the resulting estimates of total electron content must be treated with extreme caution. Letting et al. (1975)<sup>8</sup> developed a technique using two latitudinally separated stations to provide overlapping measurements and hence overcame the problem that the real ionosphere is not necessarily characterised by a linear gradient in electron content. However, for the bulk of the observations reported here only measurements from the single station at Lerwick are available so alternative methods of calibration have been sought. Two approaches to calibration of the NNSS total electron content measurements have been developed. The first method makes use of another receiving system co-located at Lerwick. This receiver, operated for the Geophysics Laboratory of the US Air Force monitors transmissions from satellites in the Global Positioning System (GPS) and enables absolute total electron content to be determined along a specified line-of-sight. This line-of-sight varies only slowly as a function of time and the resulting GPS observations have been related to the NNSS measurements at the same ionospheric latitude and time, thus allowing calibration of the NNSS observations to obtain absolute total electron content. Where GPS results were not available a different calibration technique was employed. This second approach made use of ionospheric slab thickness, the ratio of total electron content to peak electron density. Ionosonde measurements of the F2-layer critical frequency and hence maximum electron density are often readily available. Knowledge of slab thickness thus allows total electron content to be estimated. An empirical model of slab thickness relevant to European midlatitudes was developed at Aberystwyth during the mid-1970's. The model was based upon harmonic expansions of the known diurnal and seasonal changes, together with solar and magnetic responses, and has been described by Kersley (1980)<sup>9</sup>. Total electron content measurements made at Aberystwyth (52.4°N 4.1°W) using observations of Faraday rotation along the line of sight to geostationary satellites during the period 1967 to 1974 were used in the construction of the model. Despite referring to an ionospheric point well to the south of Lerwick, the model probably represents the best information available on slab thickness variations appropriate to northern Europe. The slab thickness model was used in conjunction with hourly foF2 data from the ionosonde at South Uist (57.4°N 7.3°W), the closest ionosonde to Lerwick, to yield values of total electron content for calibration of the NNSS observations when data from the GPS system were not available.

For the purposes of the present paper GPS total electron content measurements were only available for the periods 21 September to 21 October 1989 and 1 to 31 December 1989. The analysis of NNSS observations and study of the results presented here has been concentrated on these two months, which were near the maximum of the solar cycle.

#### 4. MAPPING TOTAL ELECTRON CONTENT

An NNSS satellite pass provides measurements of differential carrier phase and hence equivalent vertical total electron content as a function of time and hence of latitude. These measurements are then scaled using the appropriate value of

total electron content supplied from either the GPS data base or the slab thickness model at a particular point on the satellite pass to give the variation of absolute equivalent vertical total electron content. Fig.1 shows examples of the resulting variation of equivalent vertical total electron content as a function of latitude for 4 consecutive satellite passes observed between 1750 UT and 2130 UT on the 4 October 1989. It can be seen that a trough-like feature is clearly present in the observations commencing at 1918 UT and again at 2128 UT. In both cases steep gradients in electron content are found on either side of the trough minimum. The position of the trough minimum descends in latitude with time from around 66°N in the observations at 1918 UT to around 63°N at 2128 UT. Whilst the poleward wall of the trough is not apparent in two of the passes, it would appear that the trough minimum was observed in each case and at latitudes that are consistent with a descending pattern.

Through use of extended sequences of satellite passes of this kind it is possible to construct maps illustrating the variation of total electron content not only as a function of latitude but also as a function of time. For this purpose total electron content measurements were binned according to hour and latitude and then averaged to give a single value for each degree of latitude by one hour bin. Plotting of the resulting data made use of Uniras© on-screen interactive graphical processing enabling the appropriate selection of parameter ranges to be made whilst ensuring the integrity of the final output. The resultant maps illustrate the variation of total electron content over some 25° of latitude as a function of time. For the purposes of the present study attention has been concentrated on the 12-hour period from 1600 hours to 0400 hours during which the trough is most likely to be found in the latitudinal range displayed.

#### 5. RESULTS

An example of a contour map showing the variation of total electron content as a function of latitude and time is shown in 3-dimensional form in Fig.2. These data were recorded during the early evening and night of the 11-12 October 1989 and a total of 8 successive satellite passes have been combined to produce the map. The most striking features are the decay in electron content with the progression from early evening into the night and the presence of a trough-like feature. The trough can be seen developing as early as 1700 UT and is clearly in evidence by 1800 UT with a minimum at around 68°N ionospheric geographic latitude. The position of the minimum is seen to descend in latitude with time to around 64°N by 2300 UT. Steep gradients in electron content are evident in both the equatorward and poleward walls of the trough, with the steepest gradients on the northern slope. In this example, the trough becomes gradually merged with the decaying night-time ionosphere in the post-midnight sector, particularly at lower latitudes. Geomagnetic conditions during this period were quiet, with Kp not exceeding 2.

The current experiment also provides information on ionospheric scintillation. In particular, the fluctuations in signal intensity at 150 MHz are characterized by a value of the S4 scintillation index computed every 20 s. A plot of S4 index as a function of latitude for a single satellite pass on 14 October 1989 commencing 1913 UT is shown in Fig.3. A clear increase in signal fluctuation towards the north is seen, with the S4 value rising from 0.2 (weak scintillation) at around 66°N to 0.7 (strong scintillation) near 74°N. This type of plot is typical of the passage of the ray path across the so-called scintillation boundary.

Using techniques similar to those outlined above it is possible to produce maps of S4 as functions of both latitude and time. An example of such a map is shown in Fig.4, illustrating scintillation on the evening and night of the 11-12 October 1989, the same time period of the electron content observations presented in Fig.2. The dominant feature of this plot is the sharp increase in scintillation towards the north associated with the crossing of the scintillation boundary. This feature is sustained throughout the entire period shown

here, moving equatorward in the pre-midnight sector, most sharply at around 2000 UT. It should be noted that some of the isolated structures observed south of the monitoring station at 60.1°N may arise at least partially from effects of the observational geometry. Due to the field-aligned nature of the irregularities an enhancement is seen in S4 when the propagation path lies along a magnetic field line or is confined to an L-shell. A discussion of the observational effects appropriate to observations from Lerwick has been provided by Pryse et al. (1991)<sup>10</sup>.

It is possible to combine the total electron content and S4 observations of the kind shown above to produce 4-dimensional plots like that in Fig. 5. The total electron content is represented by the wire grid and the S4 by the superposed shaded contouring. It can be seen that, for this particular example for the 11-12 October 1989, the steep rise in the S4 scintillation index observed at higher latitudes appears coincident with the poleward wall of the trough and that the latitude variation of the boundary essentially mirrors the movement of the trough. This type of observation is of importance to understanding the nature of the physical mechanisms responsible for the production and growth of the small-scale irregularities causing scintillation. It would appear that in the example shown here the irregularities are associated with gradients in electron content increasing towards the north, suggesting that in this case the plasma convection may have resulted in destabilisation of the gradient. The strongest scintillation around 2200 UT is associated with the steepest northward gradient. A close examination of the region where scintillation was observed south of the station shows that here again there is evidence that the small-scale structure is associated with a weak northwards gradient from about 2000 UT. These results appear to suggest that the gradient drift mechanism may have been responsible for the irregularity development in this case, with northwards gradients being unstable to the prevailing plasma motion.

Another example of a trough-like feature is shown using the 4-dimensional type of map in Fig. 6. This map covers identical time and latitude range to those shown in Fig. 5 and was constructed from observations made in the evening and night of the 4-5 October 1989. Geomagnetic conditions during this period were moderate with Kp not exceeding 2+. Once again total electron content is seen to decrease with the passage from evening into the night. The trough minimum can be identified as early as 1600 UT at a latitude of 65°N and the position of the minimum is observed to descend in latitude with time to around 58°N by 0400 UT. Prior to 2200 UT steep gradients in electron content are seen on both walls of the trough. In the post-midnight sector the poleward wall of the trough exhibits some of the steepest gradients in total electron content but does not extend much beyond 63°N. The region to the north of this latitude is characterised by another broad minimum. In this same sector the equatorward wall of the trough appears to become merged with the gradually decaying night-time ionosphere. This feature of an apparently latitudinally limited poleward wall has been found to be a characteristic of moderate levels of geomagnetic activity. Around midnight the trough minimum is less well defined than at other times. This observation is also characteristic of many of the current observations for intermediate geomagnetic conditions. In this example, no simple relationship is apparent between the variations in the S4 scintillation index and the total electron content. Prior to 2200 UT some scintillation was observed on both walls of the trough, however in the post-midnight sector scintillation was only present at latitudes above the trough minimum. Strong scintillation (S4 > 0.8) was observed continuously at the highest latitudes throughout the period shown.

A limited set of examples is presented here to illustrate the varied response of total electron content and amplitude scintillation to the wide range of geomagnetic activity during the two months under consideration.

#### (i) High Kp

Fig. 6 is a plot showing combined total electron content and S4 scintillation index where Kp had been high (above 4) and was

returning to lower values. A trough-like feature is once again present in the variation of total electron content, however the position of the trough lies much further south than in the examples of troughs discussed above in Figs. 4 and 5. If direct comparisons are made at 2100 UT it can be seen that in this particular example the trough minimum is located at around 59°N, compared to approximately 64°N on the 11-12 October (Fig. 4) and about 63°N on the 4-5 October (Fig. 5). The magnitude of the electron content is generally low throughout the night, another characteristic feature of disturbed magnetic conditions. The scintillation boundary generally follows the north wall of the trough though the maximum S4 is found during a 4 hour period commencing 2000 UT in the latitude range 67°N to 72°N.

Caution must be exercised in trying to generalise about the total electron content behaviour during disturbed geomagnetic conditions. It is well established that low night-time contents are found after storm onsets. Fig. 7 shows an example during a very large geomagnetic storm where Kp reached 8+. The levels of electron content are low throughout the entire latitudinal range and time period. No well defined trough behaviour can be identified, though a poleward gradient in the 58°N to 63°N latitudinal range can be seen in the post-midnight sector. High levels of scintillation activity (S4 > 0.6) are apparent over much of the plot, indicating that the boundary is probably well south of the observing region.

#### (ii) Moderate Kp

Figures 8 and 9 are examples of observations when Kp was generally ~ 2. These data were recorded on the 29-30 September and the 5-6 December respectively. In Fig. 8 a weak trough is apparent in the post-midnight sector with a minimum around 57°N latitude. The poleward wall rises to a maximum at around 65°N and a broad plateau extends beyond this latitude. In the evening sector a trough can be seen at the highest latitudes which descends to about 65°N at 2100 UT. However, this feature does not follow through in a well-defined way to merge into the post-midnight trough. In fact around magnetic midnight the region of the trough minimum shows a general enhancement in the electron content so that the feature becomes less well-defined, a characteristic of many of the observations during conditions of moderate geomagnetic activity. A gradual increase in scintillation was observed towards higher latitudes with a general equatorwards movement of the boundary with the passage of time. In Fig. 9 it is not possible to identify a trough minimum in the post-midnight sector, however the positive gradient in total electron content towards the north at lower latitudes is seen to increase sharply beyond about 57°N to create a poleward wall that maximises at 64°N at 0400 UT. A steady decline in total electron content is observed north of this maximum. In this example, an abrupt scintillation boundary is found apparently coincident with the sudden increase in total electron content which creates the poleward wall after 2100 UT.

#### (iii) Low Kp

Figures 11 and 12 are plots illustrating observations recorded on the nights of 14-15 October and 10-11 December respectively. At no stage during these observations was Kp above 1 for any three-hour period. The trough is not clearly defined in either example though there is some evidence for a weak, broad minimum to develop as the night progresses. On both nights a steady increase in the gradient of the poleward wall is apparent in the post-midnight sector. Lower electron content values and earlier post-sunset decline to a winter night can be seen in the December data. A broad, poorly defined trough after midnight seems to be characteristic of very quiet geomagnetic conditions. In both plots the strongest scintillation is found at the highest latitudes after midnight, with a broad boundary again at higher latitudes than was seen under disturbed magnetic conditions.

## 6. IONOSPHERIC TOMOGRAPHY

Computerised tomography has had a revolutionary effect on medical diagnosis by providing high resolution two-dimensional images of sections of the human body. The

techniques of tomography are now being applied to other fields, including geophysics. The essence of the method is that the line integral of a parameter is measured over a large number of intersecting paths crossing a region of interest with the resulting data set being inverted in a reconstruction algorithm to give a two-dimensional image of the parameter.

The possible application of computerised tomography to the ionosphere was first discussed by a group from the University of Illinois (Austen et al. 1986)<sup>11</sup>. The system envisaged involved the monitoring of radio transmissions from a satellite in low orbit at a network of ground stations to measure ionospheric total electron content along many intersecting paths with the resulting tomographic reconstruction yielding a two-dimensional image of electron density in a vertical section through the ionosphere. The work has been continued by the Illinois group in the form of model studies (Austen et al. 1988<sup>12</sup>, Raymund et al. 1990<sup>13</sup>). Workers in the USSR at the Polar Geophysical Institute and the University of Moscow have published an image of electron density obtained from experimental measurements at a chain of three stations (Andreeva et al. 1990)<sup>14</sup>. Pryse and Kersley (1991)<sup>15</sup> have presented an electron density plot obtained from a tomographic reconstruction in the first independent comparison with an independent measurement of electron density from an incoherent scatter radar.

The present paper describes results from a short campaign of experimental measurements aimed at testing the applicability of ionospheric tomography to the imaging of electron density in the trough region. A chain of four stations was set-up to monitor the differential carrier phase of NNSS satellite signals during a three-day period in December 1990. The stations covered a latitudinal range of some 8 degrees and lay in an approximately straight line with a small longitudinal range of less than 3 degrees (Fig.13). Some thirty satellite passes were monitored simultaneously at the sites, yielding the electron content observations that have provided the basis for the tomographic reconstructions of electron density. The geometry used for the reconstructions is shown in Fig.14. The satellite moves at a height of 1100 km. Total electron content measurements along satellite to receiver paths are taken at intervals of 0.6 degrees latitude of satellite motion. The grid of cells superimposed on the paths extends from a height of 100 to 1000 km. The figure shows the resolution used for the reconstructions, with each cell being approximately 25 km square. The reconstruction algorithm used was the Simultaneous Iterative Reconstruction Technique (SIRT) described by Austen et al. (1988)<sup>12</sup> which required an initial ionisation distribution in the grid. As the algorithm was implemented, the electron densities in the cells intersected by ray paths were modified in accordance with the electron content observations and latitudinal structures in electron density became apparent.

Fig.15 shows the slant total electron content measured at each of the 4 sites as a function of latitude for a pass on the 16 December (day number 350) at 11:25 UT. The curves are similar in shape, with minima displaced in latitude in accordance with receiver site. A best estimate of absolute level has been obtained by using the calibration method of Leitingner et al. (1975)<sup>8</sup> for pairs of stations. The resulting equivalent vertical total electron content profiles for this particular pass are shown in Fig.16. It can be seen that there is close agreement between the observations made at the 4 sites, with total electron content gradually decreasing towards the north in this example of a mid-day pass.

To generate the initial density distribution required by the algorithm, an average electron density was calculated for the grid. This was done by dividing the sum of the total electron content along all satellite to receiver paths by the sum of the path lengths within the grid. This average was then redistributed vertically within the grid according to a Chapman model ionosphere. For this purpose the height of the ionisation peak was set arbitrarily at 325 km for all of the observations and an appropriate scale height assumed. For the case of 11 December at 1125 UT the scale height was taken to be 40 km, a value based on the same observations of slab

thickness made at Aberystwyth during solar maximum in the late-1960's that were used in the construction of the empirical slab thickness model discussed earlier in this paper. This model showed that for December the slab thickness at 1100 UT was only about 170 km, while the scale height for an assumed isothermal ionosphere can be taken to be approximately a quarter of the slab thickness. Having estimated an initial electron density for each cell in the manner described above the SIRT algorithm was implemented. The resulting electron density distribution obtained from the tomographic reconstruction for the pass is shown as a function of height and latitude in Fig.17. It can be seen that there is a peak electron density of some  $20 \times 10^{11} \text{ m}^{-3}$  and a gradual latitudinal gradient with densities decreasing toward the north.

The assumptions involved in the tomographic reconstruction can be verified if independent ionospheric measurements are available. For this particular campaign the only observations available in the region of interest were the published F-layer critical frequencies from the ionosonde at Slough (51.5°N 0.6°W). The ionosonde measurements made around the time of the pass gave a peak electron density of about  $22 \times 10^{11} \text{ m}^{-3}$ . This value is in reasonable agreement with the peak density obtained using the tomographic reconstruction of the electron content measurements.

Observations using 7 NNSS satellites provide good temporal coverage so that it is possible to follow the development of the ionosphere over a prolonged period. Of particular interest is the structure and motion of the trough. Tomographic reconstructions of electron density showing the development of the trough on the night of the 15-16 December 1990 (day numbers 349-350) are presented in Figs.18a to 18h. The latitudinal extent of the reconstructions varies from pass to pass depending on the availability of data. Fig.18a shows the low electron content densities of a winter night, with a decreasing gradient towards the north. Some 30 minutes later (Fig.18b) a trough minimum around 60°N can be seen with a shallow gradient in peak electron density and a much steeper poleward wall. A similar structure can be seen about one hour later in Fig.18c, while from the pass commencing 0133 UT the trough minimum is near 58°N (Fig.18d). This equatorwards motion is confirmed on the next two plots (Figs.18e and f) with the trough minimum being found at 57°N latitude for the pass starting at 0410 UT. A blob-like maximum in density can be seen polewards of the minimum while the overall levels of electron density show that there has been a night-time enhancement. A dawn build-up in density from the south with a northwards recession of the trough minimum to about 60°N can be seen in Fig.18g for 0703 UT. By 0852 UT (Fig.18h) the regular latitudinal gradient of the daytime ionosphere can be seen.

Fig. 19 compares the peak electron density estimated from foF2 measurements at Slough with that obtained from the tomographic reconstructions at 51.5°N throughout the campaign period. In general agreement is good, with for example the enhancement during the first night being confirmed. Some daytime values on day 351 show less good agreement, though it should be noted that these have been qualified and should be treated with some caution. The results indicate that the scale heights assumed for the initial conditions were reasonable. With such agreement at one particular latitude it appears that the simple tomographic technique used here can thus yield additional information on latitudinal structure. The development of the trough illustrated in Figs. 18a to h conforms to well-established understanding of the structure and motion of this feature, providing evidence of the potential usefulness of tomographic techniques to ionospheric sensing.

Much work requires to be done to find conditions of optimal geometry, to develop appropriate reconstruction algorithms and to assess the limits of resolution of the tomographic image. Nevertheless the results of this experimental campaign are sufficiently encouraging to suggest that it is worth pursuing the development of ionospheric tomography as a technique for the remote sensing of the ionosphere propagation environment.

### Acknowledgements

Thanks are due to Mr. Greg Bishop of USAF Phillips Laboratory for making available GPS ionospheric data. This work has been supported in part by the UK National Radio Propagation Programme, the UK Science and Engineering Research Council and the USAF through grant AFOSR 87-0378.

### References

1. Wrenn G.L. and Raitt W.J., "In situ observations of mid-latitude ionospheric phenomena associated with the Plasmopause", *Annls Géophys.* **31**, pp 17-28, 1975.
2. Moffett R.J. and Quegan S., "The mid-latitude trough in the electron concentration of the ionospheric F-layer: a review of observations and modelling", *J. Atmos. Terr. Phys.*, **45**, 5, pp 315-343, 1983.
3. Whalen J.A., "Daytime F layer trough observed on a macroscopic scale", *J. Geophys. Res.*, **92**, pp 2571-2576, 1987.
4. Rodger A.S., Brace L.H., Hoge W.R. and Winningham J.D., "The poleward edge of the mid-latitude trough - its formation, orientation and dynamics", *J. Atmos. Terr. Phys.*, **48**, pp 715-728, 1986.
5. Aarons J. and Allen R.S., "Scintillation boundary during quiet and disturbed magnetic conditions", *J. Geophys. Res.*, **76**, pp 170-177, 1971.
6. Stuart G.F., "Characteristics of the abrupt scintillation boundary", *J. Atmos. Terr. Phys.*, **34**, pp 1455-1468, 1972.
7. Kersley L., van Eyken A.P. and Edwards K.J., "Ionospheric midlatitude trough and the abrupt scintillation boundary", *Nature*, **254**, pp 312-313, 1975.
8. Lehtinger R., Schmidt G. and Tauriainen A., "An evaluation method combining the differential doppler measurements from two stations that enables the calculation of the electron content of the ionosphere", *J. Geophys.*, **41**, pp 201-213, 1975.
9. Kersley L., "An empirical model of slab thickness", AGARD CP 284, May 1980, Paper 23.
10. Pryse S.E., Kersley L. and Russell C.D., "Scintillation near the F-layer trough over northern Europe", *Radio Sci.*, **26**, pp 1105-1114, 1991.
11. Austen J.R., Franke S.J., Liu S.H. and Yeh K.C., "Application of computerised tomography techniques to ionospheric research", *Proc. Beacon Satellite Symposium*, Oulu, Finland, Part 1, pp 25-35, 1986.
12. Austen J.R., Franke S.J. and Liu S.H., "Ionospheric imaging using computerized tomography", *Radio Sci.*, **23**, pp 299-307, 1988.
13. Raymond T.D., Austen J.R., Franke S.J., Liu C.H., Klobuchar J.A. and Stalker J., "Application of computerised tomography to the investigation of ionospheric structures", *Radio Sci.*, **25**, 5, pp 771-789, 1990.
14. Andreeva E.S., Galinov A.V., Kunitsyn V.E., Mel'nichenko Yu.A., Tereschenko E.E., Fihomonov M.A. and Chernyakov S.M., "Radiotomographic reconstruction of ionisation dip in the plasma near the earth", *JETP Lett.*, **52**, pp 145-148, 1990.
15. Pryse S.E. and Kersley L., "A preliminary experimental test of computerised tomography", *J. Atmos. Terr. Phys.*, submitted, 1991.

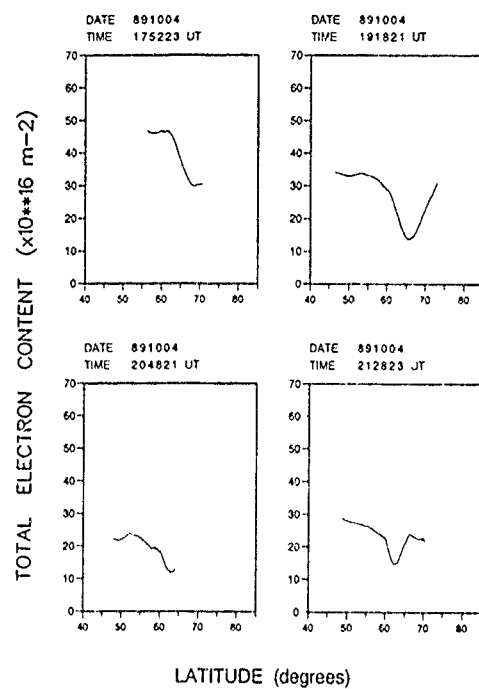


Figure 1.

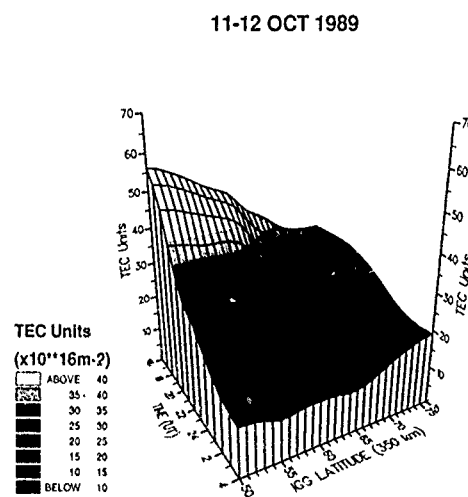


Figure 2.

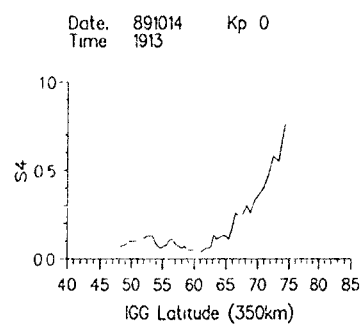


Figure 3.

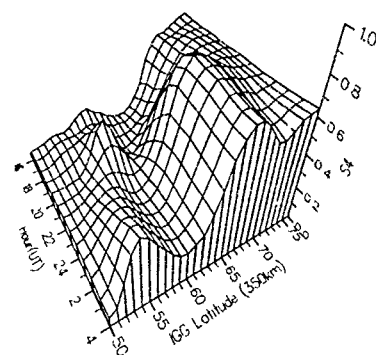


Figure 4.

11-12 OCT 1989

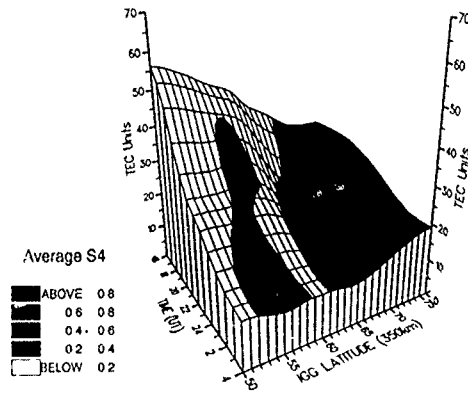


Figure 5.

4-5 OCT 1989

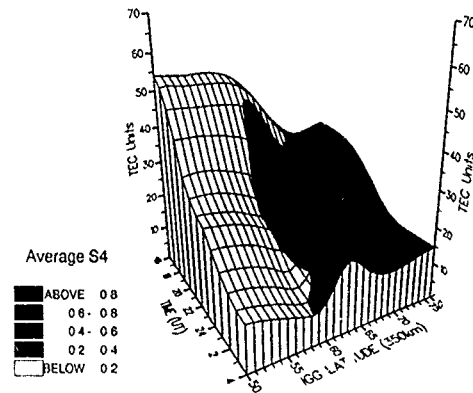


Figure 6.

22-23 SEPT 1989

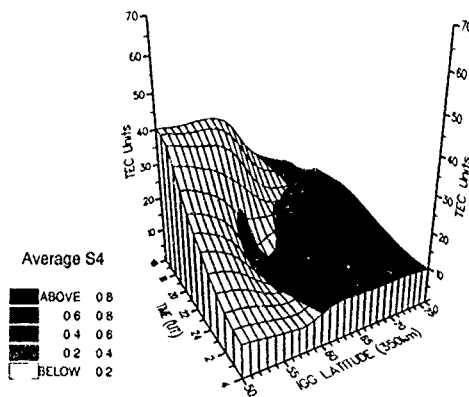


Figure 7.

20-21 OCT 1989

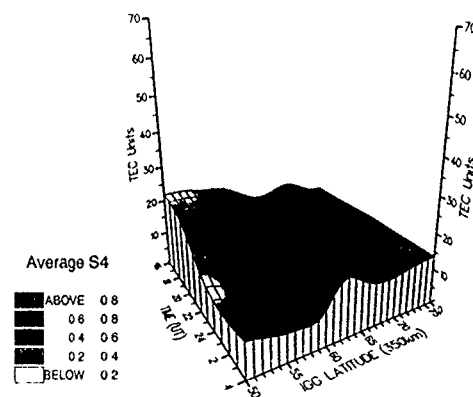


Figure 8.

29-30 SEPT 1989

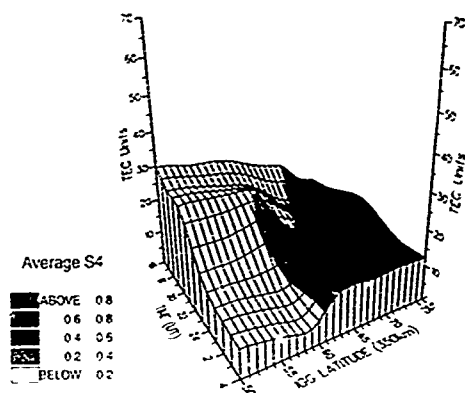


Figure 9.

5-6 DEC 1989

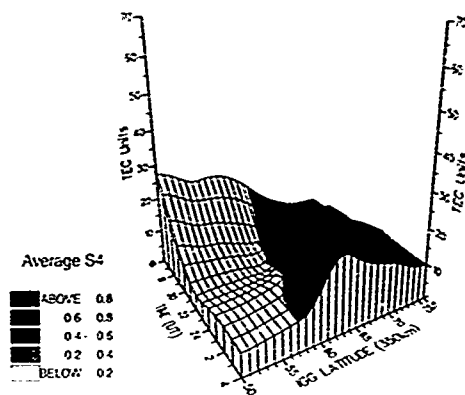


Figure 10

14-15 OCT 1989

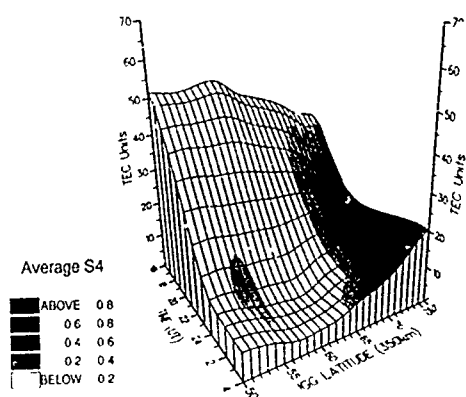


Figure 11.

10-11 DEC 1989

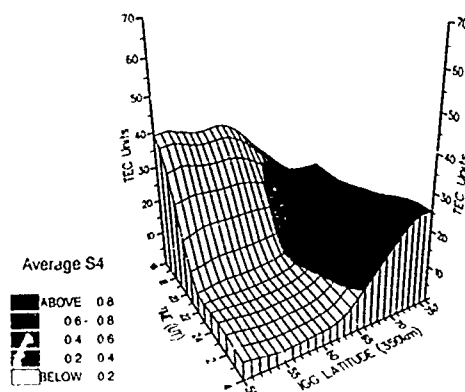


Figure 12.

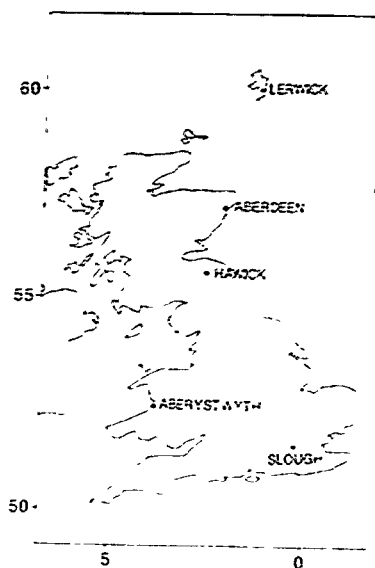


Figure 13.

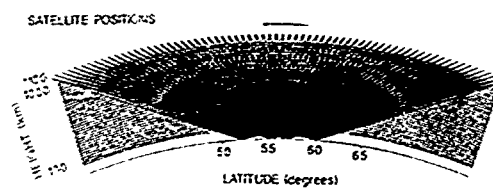


Figure 14.

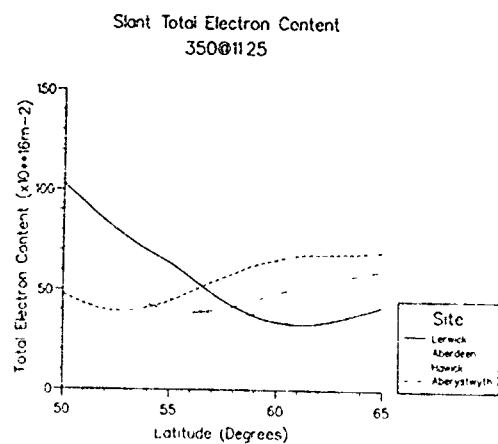


Figure 15.

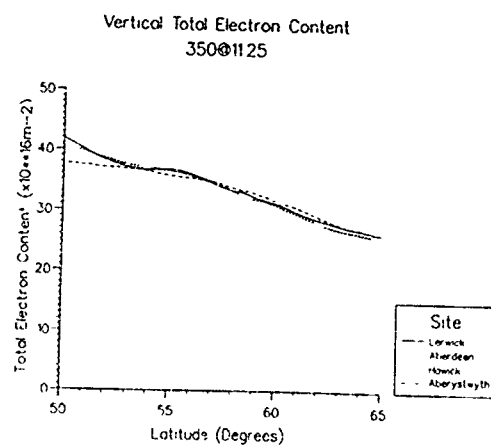
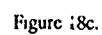
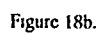
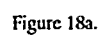


Figure 16.



1100UT foF2=13.4MHz Nmax=22.3x10<sup>11</sup> m<sup>-3</sup>  
1200UT foF2=13.5MHz Nmax=22.6x10<sup>11</sup> m<sup>-3</sup>

Figure 17.



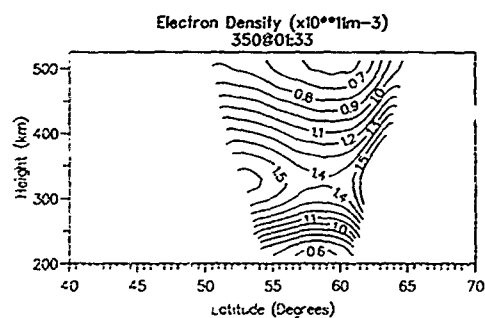


Figure 18d.

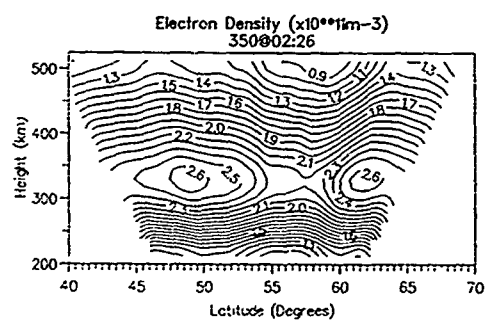


Figure 18e.

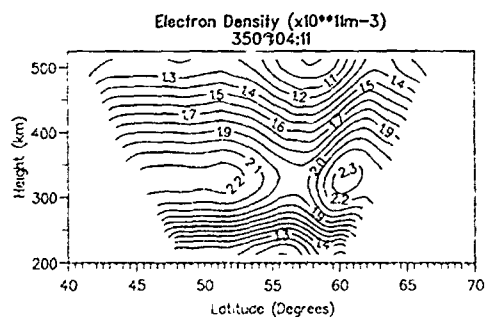


Figure 18f.

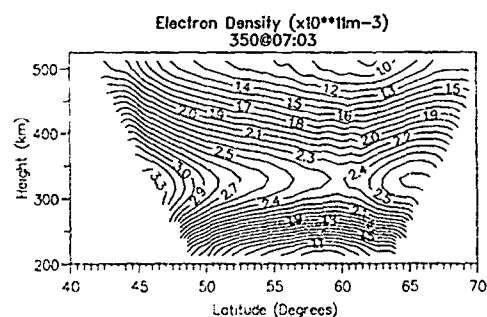


Figure 18g.

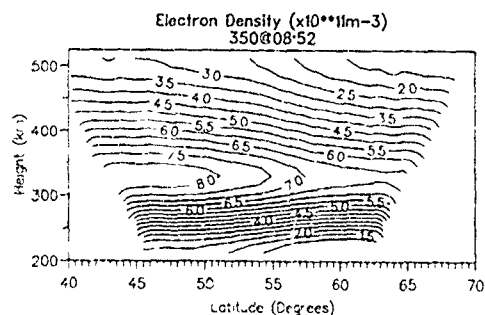


Figure 18h

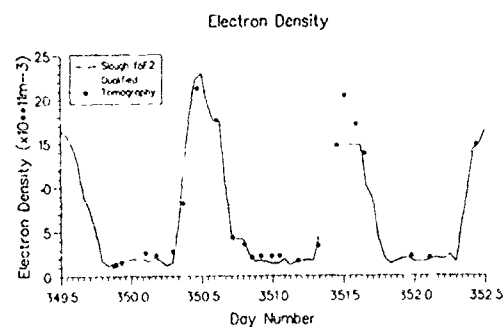


Figure 19

## DISCUSSION

### B. REINISCH

1. *The heights  $h_m F_2$  in the trough are higher by 15% to 40% than outside the trough. How will this effect your results?*
2. *Why do you not use the Slough digisonde profiles or at least  $h_m F_2$ ?*
3. *Which Chapman profile did you use for the F2 layer,  $\alpha$  or  $\beta$ ?*

### AUTHOR'S REPLY

1. *As I stated the height of 325 km was arbitrarily chosen for our first attempt at reconstruction. As yet our reconstruction method is relatively unsophisticated and as I have indicated much work remains to be done. Thank you for your comment which we will bear in mind.*
2. *Again I have to stress that the results are a "1st look" and even with this rough and ready approach we feel that the results are consistent with our knowledge of trough behavior. Future work will hopefully refine our approach/approaches to reconstruction.*
3. *I apologize, I couldn't answer for certain which Chapman model is used - if you wish I can find out for you. I hope you accept that what we have presented here today is very much the start of our investigations.*

### K. YEH (Comment)

*The problem of stability of the reconstructed image and its dependence on the initialization is of course very important. Some studies in this regard have been made by Russians. They show the non-unique nature of the reconstructed image. The difference is caused by the missing cone problem described by Raymund (paper 13) and it shows up in the reconstructed images as "wings".*

### R. BENSON

*Dr. Belrose commented on making use of the vast amount of old data from the Alouette/ISIS program. Dr. Reinisch commented on the need for real time ionospheric information rather than the analysis of old data. I would like to add that great use has been made of these old data to create ionospheric models (such as the International Reference Ionosphere, Nov 1990, Bilitza, National Space Science Data Center, 90-22, Greenbelt, MD, 20771). Have you considered using one of these models rather than a Chapman layer as an input to your method?*

### AUTHOR'S REPLY

*In the future, as I indicated at the end of my talk, we will be looking at refinements to reconstruction - including models other than Chapman layer.*

### C. GOUTELARD

*Les résultats que vous présentez sont tout à fait impressionnants et je pense que c'est une méthode très prometteuse mais je me pose une question sur la stabilité des solutions que vous trouvez. Avez-vous comparé les résultats que vous obtenez en partant d'un modèle initial différent (hauteur max.=325km, facteur d'échelle 40km)? Existe-t-il alors de grandes différences entre les solutions?*

*The results which you present are very impressive and I think this is a very promising method but I wonder about the stability of the solutions which you have found. Have you compared the results which you obtain using a different initial model (max. height =325 km, scale factor 40 km)? Are there major differences between the solutions in this case?*

### AUTHOR'S REPLY

*Thank you for your encouraging comments. I must stress that the results we are presenting are our first attempts at reconstruction. The choice of 325 km was arbitrary and we hope to refine our technique and investigate other options in the future. With regard to stability - we have not directly addressed this problem ourselves (Professor K.C. Yeh made additional comments regarding stability at this point).*

## Ionosphere and Troposphere seen through a Radio Interferometer

T.A.Th.Spoelstra  
Netherlands Foundation for Research in Astronomy  
P.O. Box 2, 7990 AA Dwingeloo, The Netherlands

### 1. SUMMARY

Expectations of the conditions in the propagation environment for the electromagnetic spectrum are based on both knowledge of the long term characteristics and the actual information of this environment. These expectations concern the regular behaviour of the large scale structure as well as any kind of irregularity reflected in relevant physical parameters.

Radio interferometric measurements are highly sensitive to horizontal and vertical gradients in the ionospheric electron distribution and in the tropospheric water vapour distribution. Very Long Baseline Interferometry (VLBI) is also sensitive to integrated effects along the line of sight. Provision of high quality information about the characteristics of the propagation environment is, therefore, inherent to this technique. The way this technique is generally used also enables the determination of these characteristics with a high time resolution, which makes it useful for the study of irregularities in the medium.

The paper describes the possibilities and limitations of this technique for ionospheric sensing and sensing of tropospheric refractivity. It also compares the merits of this technique with some other techniques used to derive the same information. Besides some typical examples, the paper describes the requirements for data handling and processing techniques, while in addition the available "tools" are summarized.

### 2. INTRODUCTION

Radio interferometric observations are affected by tropospheric and ionospheric refraction. At radio frequencies below about 6 GHz tropospheric refraction is basically independent of frequency, while ionospheric refraction varies in inverse proportion to the observing frequency squared. The effects of refraction are visible in two ways:

- (1) as phase errors, which are to first approximation (as long as the ionosphere is "coherent" over the interferometer baseline) linearly proportional to the baseline length in meters;
- (2) as Faraday rotation on polarized signals travelling through a magnetized medium (like e.g. the ionosphere).

The fundamental phenomenon is a delay error. In interferometry it translates into fringe rate or phase errors. Ionospheric refraction is a significant effect for connected element interferometry at frequencies up to about 2 GHz. This has been illustrated by Spoelstra [Ref 20] for the Westerbork Synthesis Radio Telescope (WSRT). Of course there is a smooth transition from refraction into diffraction. Diffraction occurs when the angular scale of ionospheric irregularities is less than the beamwidth of an interferometer element. In that case ionospheric irregularities above the different interferometer elements may be uncorrelated. This effect is then visible in the observations as scintillations in interferometer phase and/or amplitude.

Although often the observing frequencies used in Very Long Baseline Interferometry (VLBI) are higher than 2 GHz, the long baselines involved imply that this technique is also sensitive to ionospheric effects at these high frequencies.

It is evident that interferometric "observables" contain information about ionospheric total electron content and its variations with time and geographical coordinates.

### 3. INTERFEROMETRY

A simple two-element interferometer, the building block of all arrays, is shown in Fig 1. Consider a monochromatic signal of frequency  $\nu$  emanating from a point source whose direction is given by  $\vec{r}$ . Two elements separated by a fixed baseline  $\vec{B}$  intercept the radiation, two samples of which are then transported without loss of characteristics to a common point where they are correlated; i.e., their time averaged sum or product is taken. In

most arrays the radio frequency  $\nu$  is converted to an intermediate frequency (IF)  $\nu_{IF}$  by a superheterodyne process using a common local oscillator of frequency  $\nu_0$ , before transmitting the signals to the correlator point. The time delay  $\tau_D$  is usually inserted analogously or digitally in the IF line to compensate for the geometric time delay difference  $\tau_g$  in the arrival of the radiation to each element.

The time-variable part of the response after correlation is

$$R(\nu, \vec{r}) = S_\nu \exp[j2\pi(\nu \tau_g - \nu_{IF} \tau_D)] \quad (1)$$

where  $S_\nu$  is proportional to the source power. The usual complex notation has been used for the response. The phase of the response is equal to the phase path length difference between the two radiation paths.

The diurnal motion of an extraterrestrial radio source continuously varies the geometric delay causing the response to have a quasi-sinusoidal behavior, so-called fringes. Alternatively the fringes can be described as a "beating" of the two signals which are Doppler shifted to slightly different frequencies at the correlator due to the relative motion of the two elements with respect to the source.

For observations over a larger frequency bandwidth  $\Delta\nu$  the differential time delay  $\Delta\tau$  between the signals at the correlator point must be smaller than  $(\Delta\nu)^{-1}$  to insure that the entire bandwidth adds in phase. Thus the inserted delay  $\tau_D$  is usually varied to compensate for the change  $\tau_g$ . Assuming accurate delay tracking with respect to an angular position  $\vec{r}_0$ , the interferometer response becomes [e.g. Ref 26]

$$R(\nu, \vec{r}) = S_\nu \exp\left[j2\pi \frac{\nu_0}{c} \vec{B} \cdot \vec{r}\right] \exp\left[j2\pi \frac{\nu}{c} \vec{B} \cdot (\vec{r} - \vec{r}_0)\right] \quad (2)$$

The response to an extended source  $I(\vec{r} - \vec{r}_0)$  with a wide bandwidth interferometer having a frequency characteristic of  $\beta(\nu)$  and a primary power pattern  $G(\vec{r} - \vec{r}_0)$  - i.e. the product of the voltage pattern of each element - is given by integrating (2) over  $\vec{r}$  and  $\nu$

$$\begin{aligned} R &= \exp\left[j2\pi \frac{\nu_0}{c} \vec{B} \cdot \vec{r}\right] \iint \beta(\nu) G(\vec{r} - \vec{r}_0) \\ &\quad \exp\left[j2\pi \frac{\nu}{c} \vec{B} \cdot (\vec{r} - \vec{r}_0)\right] d\vec{r} d\nu \\ &= \exp\left[j2\pi \frac{\nu_0}{c} \vec{B} \cdot \vec{r}_0\right] V(\vec{B}). \end{aligned} \quad (3)$$

For simplicity, the angular dependence of the source and the power pattern are assumed to be independent of frequency and normalized at  $\vec{r}_0$ . The response is composed of two parts: the fast time dependence (fringes) is equal to the response of a point source at  $\vec{r}_0$  at an observing frequency  $\nu_0$ . A slower varying quantity  $V(\vec{B})$ , the visibility function, describes the amplitude and phase offsets of the fringes [e.g. Ref 26]. In general, the visibility function is a complicated function of the bandwidth, emission extent, and baseline geometry. The visibility function is closely related to the spatial mutual coherence function used in coherence theory [e.g.: Ref 12].

### 4. PROPAGATION EFFECTS IN MEASURED SIGNALS

In general, the interferometer response for a point source in the direction  $\vec{r}_0$  can be written as

$$R(\nu, \vec{r}) = S_\nu \exp\left[j2\pi \frac{\nu_0}{c} \vec{B} \cdot \vec{r}_0\right] \exp\left[j2\pi \frac{\nu}{c} \vec{B} \cdot (\vec{r} - \vec{r}_0)\right] \quad (2)$$

or

$$R(\nu, \vec{r}) = S_\nu \exp\left[j2\pi \frac{\nu}{c} \vec{B} \cdot \vec{r}_0\right] \exp\left[j2\pi \frac{\nu}{c} \vec{B} \cdot (\vec{r} - \vec{r}_0)\right] \quad (4)$$

where  $B_\lambda$  and  $B_\lambda^0$  is the interferometer baseline expressed in units of wavelengths  $\lambda_0$  and  $\lambda$ , which correspond with  $v_0$  and  $v$ , respectively. As the radio wave passes through a refractive medium, this medium modifies the propagation path and the phase of the wave. The wave emerging from this medium has a correlator response of the form

$$R(v, \vec{r}) = R_0 \exp[j2\pi B_\lambda \vec{r}] \quad (5)$$

where

$$R_0 = S_v \exp[j2\pi (B_\lambda - B_\lambda^0) \vec{r}_0] \quad (6)$$

Then the optical phase path  $r$  can be written as

$$r = \int n(\vec{s}, v) ds \quad (7)$$

where  $n(\vec{s}, v)$  is the refractive index of the medium. The integration is performed along the ray path. The range error  $\Delta r$  is

$$\Delta r = \int_p n(\vec{s}, v) ds - \int_\Sigma ds_0 = \int_\Sigma (n(\vec{s}, v) - 1) ds_0 + \left[ \int_p n(\vec{s}, v) ds - \int_\Sigma n(\vec{s}, v) ds_0 \right] \quad (8)$$

where  $p$  stands for integration along the ray-path,  $\Sigma$  stands for integration along a straight line,  $ds$  is a path element along the ray and  $ds_0$  is a path element along the straight line (the unperturbed ray). The term between brackets on the right hand side of (8) is proportional to  $(n(\vec{s}, v) - 1)^2$  if the refractive index is close to unity everywhere [Ref 28,29]. This condition is fulfilled in the ionosphere and in the troposphere.

As is clear from relations (4) - (8), refraction causes a shift,  $\Delta \vec{r} = (\vec{r} - \vec{r}_0)$ , of the apparent positions of extra-terrestrial objects on the celestial sphere. This shift depends on the geometry of the refractive medium and on the variation of gas or electron density (i.e. manifest in the variation of the refractive index) along the line of sight and perpendicular to it (i.e. gradients in this distribution) [Ref 20,21].

We can write the equation (4) as

$$R(v, \vec{r}) = S_v \exp[j2\pi B_\lambda \vec{r}_0] \cdot \left[ \cos(2\pi B_\lambda \Delta \vec{r}) + j \sin(2\pi B_\lambda \Delta \vec{r}) \right] \quad (9)$$

When a point source is observed and the astrometric and instrumental calibration has been performed correctly, the real part of equation (9) expresses the amplitude of the source. The imaginary part of equation (9) gives the phase error due to refraction effects which is expressed by

$$\Delta \phi = 2\pi B_\lambda \Delta \vec{r} \quad (10)$$

Thus the position error causes an error in the phase difference between signals received at the antennas of two elements of an interferometer (i.e. an error in interferometer phase)  $\Delta \phi$  at a relative distance of  $B_\lambda$ . The relation between position errors and phase errors is given by [Ref 6,7]

$$\Delta \phi = 2\pi B_\lambda (\Delta \alpha \cos \delta_0 \cos t_0 + \Delta \delta \sin \delta_0 \sin t_0) \quad (11)$$

where  $\Delta \alpha$  and  $\Delta \delta$  are the errors in the two coordinates right ascension,  $\alpha$ , and declination,  $\delta$ , respectively,  $t$  is the hour angle (= angular distance from the meridian of the source - west is positive), while the index "0" indicates the 'true' coordinates (i.e. with absence of refraction). These effects are best noticeable for point sources, since the wave front from a celestial point source without any disturbing effects can be taken as perfectly flat and deviations can easily be detected.

Since in the case of connected element radio interferometry one subtracts the phases of two signals that propagate along almost parallel rays separated by a small distance (e.g. a few km), only the gradients in the gas density and the sphericity of the atmosphere will play a role in the case of VLBI, where distances between the interferometer elements are

much greater (> 1000 km), one should also take into account the integrated total effects along the line of sight of each of the interferometer elements [Ref 22].

#### 4.1. Ionosphere

In interferometric observations the refraction produces errors in the interferometer phase. These refraction effects are manifestations of variations of the ionospheric electron density along and perpendicular to the line of sight and with time. The variations can be divided into different time scales and spatial dimensions:

- [1] the ionosphere as a whole, variations between day and night, with seasons and with solar activity
- [2] time scales smaller than one day but larger than minutes, irregularities in the electron density of different spatial scales which may propagate within the ionosphere with different speeds and directions (travelling ionospheric disturbances, TIDs, and acoustic-gravity waves, AGWs).

Large scale TIDs have horizontal speeds of 300-1000 m/s, periods ranging from 0.5 - 3 hours and horizontal wavelengths exceeding 1000 km. They propagate equatorward from the auroral regions, where they are supposed to be generated.

Medium scale TIDs have horizontal phase speeds of 100-300 m/s, periods from about 10 minutes to about 1 hour and horizontal wavelengths of several hundreds of km. They occur more frequently than large scale TIDs. Their origin is unknown.

Small scale TIDs have periods of several minutes and wavelengths of tens of kilometers. They are, therefore, associated with the acoustic branch of the AGW spectrum. As to their origin little is known as for medium scale TIDs.

- [3] small scale irregularities probably frozen in the geomagnetic field which cause scintillation effects.

In particular these irregularities cause trouble in different kinds of applications of radio communication and signal detection.

As long as the ionosphere is coherent over the interferometer baseline these phase errors are to first approximation linearly proportional to baseline length (see equation 10). This is in general the case for connected element interferometry with baselines up to a few km, since even medium scale TIDs have horizontal wavelengths of about 100-200 km. Small scale irregularities with sizes in the east-west direction down to a few hundred meters may give rise to phase and/or amplitude scintillations. Whether these scintillations degrade the observations depends of course on the integration time used and on the primary beam of the elements of the interferometer array. If phase scintillations occur within one integration time the interferometer amplitude is distorted due to decorrelation within the receiver.

Since the presence of the geomagnetic field makes the ionospheric plasma a doubly refractive medium, it will support two orthogonal circularly polarized waves travelling with slightly different phase velocities. The ionosphere affects the state of polarization in the sense that the polarization ellipse is rotated. This is Faraday rotation, which also varies in inverse proportion to the square of the observing frequency. Faraday rotation does not depolarize an arbitrary ray, but can be seen in the interferometric amplitudes.

- (i) the polarization characteristics are expressed in Stokes parameters, which have the dimension of intensity,
- (ii) when in e.g. VLBI due to the inhomogeneities in the ionosphere and its geometry, differential Faraday rotation causes different responses for the different interferometer elements.

Both ionospheric refraction and Faraday rotation depend on the columnar electron density along the line of sight. At mid-latitudes the plasma frequency  $f_p \leq 15$  MHz, the electron gyro frequency  $f_{ce} \approx 1.4$  MHz and the collision frequency  $\nu \leq 10^5$  s<sup>-1</sup>. Hence the refractive index for quasi-parallel propagation can be approximated by

$$n_{\text{ion}}^2 = 1 - \frac{X}{1 \pm Y \cos \kappa} \quad (12)$$

where  $\kappa$  is the angle between the geomagnetic field and the wave vector of the signal,

$$X = \frac{\omega_p^2}{\omega^2} \quad \text{and} \quad Y = \frac{\omega_s^2}{\omega^2} \quad (13)$$

with

$$\omega_p^2 = \frac{e^2 N_e}{m_e \epsilon_0} \quad \text{and} \quad \omega_s^2 = \frac{c H}{\pi r_e} \quad (14)$$

where  $e$  is the electron charge,  $m_e$  is the electron mass,  $H$  is the magnitude of the geomagnetic field,  $N_e$  is the electron density and  $\epsilon_0$  is the vacuum permeability

The interferometric phase error at baseline  $B$  (in m) due to ionospheric irregularities (e.g. TIDs) is a complicated function of the ionospheric electron density [Ref 20,21] and may be approximated for some applications by [Ref 14]

$$\Delta\phi = 84.4 \times 10^{-8} \frac{k p B}{v \cos z} \int_s N(s) ds \quad (15)$$

where  $k$  is the wavenumber of the density wave,  $v$  is the observing frequency (in Hz),  $p$  is the fraction of the total electron content involved in the density waves,  $N$  the electron density (in  $m^{-3}$ ) as a function of position  $s$  along the line of sight, while the zenith angle  $z$  is related to other parameters by

$$\cos z = \sin \delta \sin \beta + \cos \delta \cos \beta \cos t \quad (16)$$

where  $\beta$  is the geographic latitude [Ref 10]. When we use S.I. units the Faraday rotation  $\psi$  can be written as

$$\psi = 2.36 \times 10^4 v^{-2} \int_s N(s) H \cos \theta ds \quad (17)$$

where  $H$  is the strength of the geomagnetic field ( $Wb m^{-2}$ ) and  $\theta$  the angle between the ray and the geomagnetic field (in radians). Then

$$\frac{\Delta\phi}{\psi} = 3.2 \times 10^{-9} v B \quad (18)$$

If a typical density wavelength is 100 km,  $p = 5\%$ ,  $H = 0.5 \times 10^{-4} Wb m^{-2}$ ,  $\theta = 0$ ,  $z = \pi/4$ . This indicates that at all frequencies

$$v \geq 3 \times 10^2 B^{-1} \text{ MHz} \quad (19)$$

the interferometer phase is more sensitive to ionospheric irregularities than Faraday rotation [Ref 23]. This is illustrated in section 4.1.1

#### 4.1.1. Applications

Connected element interferometry is sensitive for ionospheric effects for frequencies below typically about 1 GHz. Due to the long baselines involved VLB observations may be affected by ionospheric effects at higher frequencies as well.

We note that interferometer phase is very sensitive for irregularities in the ionospheric electron density. This implies that an analysis of interferometer phase may provide direct information about irregularities in the refractive medium, i.e. the ionosphere.

Observations with the Westerbork Synthesis Radio Telescope, WSRT, have been used to probe the refractive medium.

The WSRT is located at  $6^\circ 6' E$ ,  $52^\circ 9' N$ . The WSRT is a radio interferometer array described in detail elsewhere [Ref 3,5,8,9,15]. The instrument consists of 14 steerable paraboloids with diameters of 25m each, which are situated along an east-west baseline with a deviation of  $1.2^\circ (\pm 0.1)$  from a perfect east-west baseline (Bregman, 1983: private communication). The maximum baseline between two telescopes is 2.7 km. Ten telescopes occupy fixed positions at 144m intervals. Four additional moveable paraboloids are combined with these fixed to form interferometer pairs. The back end of each of these consists of a correlator system which measures the four complex correlation components necessary to characterize the polarization state of the radiation. The main wavelength bands are 6, 21, 49 and 92 cm

A radio source is observed by tracking it in its diurnal rotation from 6

hours before to 6 hours after meridian transit or over some fraction of this range. The array beam is continuously steered by proper phasing of the elements. This is done with very high precision: the positional accuracy in the sky is better than 0.1, corresponding with a phase accuracy better than 1 mm. This precision is reached by the application of a number of corrections, both for astrometric effects and for known instrumental errors [Ref 21,27 and references therein]

Point sources are observed quite frequently for checking and calibrating the instrument. The standard integration time for these observations is 1 minute. For point sources, we know that the incident wavefront should be perfectly flat; any deviation must be the result of propagation effects giving rise to (also differential) pathlength errors (e.g. Ref 13,20,21). These deviations are visible as phase errors,  $\Delta\phi$ , which are to first order proportional to the baseline between two interferometer elements [equation (10)]. Since the WSRT is mainly sensitive for east-west gradients in the ionospheric total electron content,  $\Delta\phi \sim d/d(\text{TEC})$  [Ref 20,21].

An example of a WSRT registration giving the variation interferometer of amplitude and of  $\Delta\phi$  as a function of time is given in Fig 2. We know that we are dealing with ionospheric refraction effects since the errors correspond with the calculated values and the frequency dependence of  $\Delta\phi$  errors corresponds with what is expected for ionospheric effects [Ref 20,24]. The fluctuations in Fig 2 in  $\Delta\phi$  have different time scales. (a) a large scale slowly varying 'baseline' is caused by the slowly varying component of TEC [Ref 20]; (b) before about 16.30 UT manifestations of medium scale travelling ionospheric disturbances, MSTIDs, are seen, (c) after about 19.00 UT the observation is affected by ionospheric scintillation. Fig 3 illustrates the baseline dependence of ionospheric phase errors, while it also shows that the interferometer amplitude is not affected unless the phase rates are too high (i.e. around  $\pi$  radians per integration period).

Fig 4 illustrates the relative sensitivity of interferometer phase and ionospheric Faraday rotation for ionospheric irregularities an observation of 3C286 at 608.5 MHz and for a baseline of 2.7 km. At this frequency and resolution 3C286 is a point source. This source is 2.4% polarized at this frequency. Fig 4 gives a comparison between interferometer phase  $\phi$  and Faraday rotation  $\psi$  as a function of time. In this case  $\phi$  and  $\psi$  have not been corrected for ionospheric effects. The instrumental noise of the interferometer phase,  $\phi$ , is  $0.14^\circ$ , and of polarization angle,  $\psi$ , is  $4^\circ$ . Fig 4 illustrates that the interferometer phase is indeed more sensitive to ionospheric irregularities than Faraday rotation. According to equation (18)  $\Delta\phi/\psi = 5.3$ .

**- TID parameters and climatology:** The sensitivity of interferometer phase for irregularities in the ionospheric electron density implies that an analysis of interferometer phase may provide direct information about irregularities in the refractive medium, i.e. the ionosphere. This analysis may result in a climatology of different "classes" of ionospheric irregularities, their frequency of occurrence and "strength" (e.g. Ref 18,23,28). This climatology will provide information about the occurrence of these irregularities as a function of time within the day, of day, as a function of season, of solar activity (Spoelstra, in preparation). In particular for predictive estimates for communication quality in the HF range this information may be important.

Kelder and Spoelstra [Ref 18,19] analyzed variations of interferometer phase in WSRT observations in terms of its amplitude ( $A$  - in degrees phase) and apparent period of each irregularity as a function of time for the longest baseline (2.7 km) for observations at 608.5 MHz during the first three months of 1982 and 1983. Fig 5 shows  $A$  as a function of time (0 - 24 hours UT) for the first three months of 1983. The data in Fig 5 show a strikingly systematic pattern for the amplitudes of TID manifestations: a peak being reached around noon, with a secondary peak around midnight. This behaviour is typical for winter observations as has been shown in more comprehensive studies [Ref 15, 1, 28].

The apparent period varies typically from a few minutes (during the night) to 15-20 minutes during daytime. It is also found that the amplitudes of the phase variations are up to about a factor of 2 larger for the very fast irregularities than for the slower ones. Furthermore, within 3 hours around noon more than 90% of the time TIDs are observed during the winter months of 1982 and 1983, on other moments this is about 40%.

It has been observed in WSRT observations that the TID parameters depend on the season [Ref 28]. Furthermore, the amplitudes as presented in Fig 5 show dependence on solar activity as well [Ref 19]. Knowledge of

parameters of ionospheric irregularities and their climatology is, when adequately available, valuable for predictive estimates for communication quality in the HF range. Radio interferometry is one of the tools to provide this information.

This application proved to be also valuable for critical studies of possible excitation mechanisms for ionospheric irregularities [Ref 28]. In addition, by using this method we were able to trace effects of atmospheric tides in the ionosphere [Ref 19].

An additional study of ionospheric irregularities can be performed with a VLBI network. Since the individual interferometer elements are generally a few hundred to a few thousand kilometer apart, the analysis may provide information on the spatial coherence scales of these irregularities.

- *mapping TID motion*: In radio astronomy an arbitrary observation with an interferometer provides a field of view comparable to the angular extent of the beam of an interferometer element in which a number of sources show up (Fig 6). Then for each of the individual point sources the phase errors can be determined as a function of time in principle. Since phase errors are equivalent to position errors, an analysis of those errors for such sources will provide direct information on the propagation direction and speed of ionospheric irregularities. Since in connected element interferometry the extent of the field of view is often of the order of a degree at frequencies below 1 GHz, this type of instrument is particularly useful for this kind of investigation. This information can also be derived from a correlation of interferometer data with differential Doppler measurements of radio signals from satellites of the Navy Navigation Satellite System, NNSS [Ref 19; Spoelstra, in preparation]

Fig 7 gives the calculated azimuth and speed of propagation of medium scale TIDs observed with both the WSRT and by differential Doppler measurements of NNSS signals (for an assumed altitude of 400 km). A histogram of the computed distances between TID ridges is given in Fig 8. These results indicate that for these observations most of the medium scale TIDs which have been analyzed propagate roughly north-south, with a deviation of about 10° to the west [Ref 19; Spoelstra, in preparation].

- *computerized tomography*: Radio interferometers are often constructed as a series of antennas at regular intervals along a straight baseline. In principle this construction enables the application of the computerized tomography method to study the vertical structure of the ionosphere. This method has been applied successfully by e.g. Austin *et al.* [Ref 2], Andreeva *et al.* [Ref 1], Raymund *et al.* [Ref 16]. Observations with the WSRT consisting of 14 telescopes at regular distances of 36 m to 3 km may be used for computerized tomography for a better investigation of the vertical structure of the ionosphere. A preparatory study on this subject has been started.

#### 4.2. Troposphere

In radio interferometry the dominant contribution to the tropospheric refraction error usually stems from the gradient in the water vapour content [Ref 17], which may be caused by e.g. tropospheric turbulence, waves or clouds. Such water vapour content variations are of the order of several tenths of percents, leading to errors of the order of mm. It turns out that the error due to tropospheric refraction becomes negligibly small in comparison with that due to ionospheric refraction at frequencies below 1 GHz.

The refractive index in the troposphere,  $n_{\text{trop}}$ , is given by [Ref 4]

$$n_{\text{trop}} = 1 + 10^{-6} \left[ K_1 \frac{p_d}{Z_d T} + K_2 \frac{p_w}{Z_w T} + K_3 \frac{p_w}{Z_w T^2} \right] \quad (20)$$

where  $p_d$  is the partial pressure of the dry gases in the atmosphere,  $p_w$  the partial pressure of water vapour and  $T$  the temperature.  $Z_d$  and  $Z_w$  are the compressibility factors for dry air and water vapour, respectively. The  $p/T$  dependence in (20) stems from the fact that refraction is proportional to the density of the refracting gas molecules. The additional  $T^{-1}$  in the third term of the right hand side of (20) is due to the dipole character of water molecules. The coefficients  $K_i$  have been determined empirically. Thayer [Ref 25] gave the following best estimates

$$\begin{aligned} K_1 &= 77.60 \pm 0.014 \quad (\text{K/mbar}) \\ K_2 &= 64.8 \pm 0.08 \quad (\text{K/mbar}) \\ K_3 &= (3.776 \pm 0.004) \times 10^5 \quad (\text{K}^2/\text{mbar}) \end{aligned} \quad (21)$$

$K_3$  is approximately equal to  $K_1$ , and the compressibility factors  $Z_d$  and  $Z_w$  are approximately 1. Hence (20) and (21) can be approximated by [Ref 11]

$$n_{\text{trop}} = 1 + 10^{-6} \left[ 77.6 \frac{p}{T} + 3.78 \times 10^5 \frac{p_w}{T^2} \right] \quad (22)$$

where  $p$  and  $p_w$  are expressed in millibars. The first term within brackets in (22) is much larger than the second term. Substitution of the realistic ground values  $p = 1000$  mbar and  $T = 290$  K yields an upper bound of  $2.7 \times 10^{-4}$  for  $(n_{\text{trop}} - 1)$  in the troposphere.

The phase error  $\Delta\phi$  due to tropospheric refraction and allowing for the earth's sphericity, can be written as

$$\Delta\phi = 2\pi \frac{v}{c} B_\lambda (n_{\text{trop}} - 1) \cos \delta \sin t \left[ 1 - \frac{\cos z}{(\cos^2 z + H'^2)^{0.5}} \right] \quad (23)$$

where

$$H' = \frac{R^2 - r^2}{r^2} \quad (24)$$

where  $r$  is the radius of the earth,  $R$  is the radius of the troposphere,  $R = r + H$ , with  $H$  is the equivalent thickness of the troposphere [Ref 6,7]

Hamaker [Ref 13] analyzing WSRT observations noted that in a number of cases the observed interferometer phase phenomena are correlated with meteorological data. This is illustrated in Fig 9, in which we represent rain showers manifesting themselves as variations of  $\Delta\phi$  as a function of baseline with time. It is clear that the tropospheric conditions affect both interferometer amplitude via system temperature (tropospheric emission/absorption) and phase (tropospheric refraction).

#### 4.2.1. Applications

Radio interferometry can be used for tropospheric studies in a similar way as we described for the ionosphere. In particular computerized tomography may be promising. This investigation can be performed for connected element interferometry at frequencies higher than about 2 GHz since at these frequencies the ionospheric effects do not play a role. In addition as is clear from Fig 9, interferometry can be used to investigate tropospheric emission/absorption effects. Or in other words: one is able to investigate tropospheric damping of the radio signals. On the other hand, cloud parameters can be investigated as well. However, in some applications a problem may be that at frequencies  $> 2$  GHz there are fewer sources per observed field.

#### 5. DATABASE, DATA HANDLING AND REDUCTION TOOLS

Radio interferometry is used on a regular basis at a number of radio astronomy observatories.

One of these institutions is the Netherlands Foundation for Research in Astronomy, NFRA, in Dwingeloo, the Netherlands. At its Dwingeloo Radio Observatory in the Netherlands all observations done with the WSRT have been archived and catalogued with great care since it started operations in 1970. The total relevant WSRT-database contains at present in the order of about 100 Gbytes of data. These data are directly accessible for further research. A similar archiving policy is much less developed elsewhere. And since the WSRT is in operation for more than 20 years, this database enables research for a better understanding of the ionospheric electron distribution and irregularities therein for a period of more than 20 years (i.e. more than 2 solar cycles).

A limitation in the use of radio interferometry for sensing the refractive medium is that dedicated software should be available for data handling. However, this software is freely available at the parent institutes responsible for the operations of the radio interferometer. The software contains options as cleaning the measurements of contributions from unwanted sources, facilities to calibrate for astrometric and a variety of instrumental effects, a variety of display facilities (in particular as e.g. used for Fig 2 - 4 and 6 in the present paper), spectral analysis tools for different cross-sections through the data cube of an observation, imaging tools. With these facilities and tools available, radio interferometry turns out to be a powerful tool for ionospheric and tropospheric research [e.g. Ref 28].

#### 6. CONCLUDING REMARKS

Radio interferometry has proven to provide a powerful tool to sense the

refractive medium, in particular to investigate irregularities in this medium. The sensitivity for ionospheric effects in different aspects of radio communication and signal detection depends on the kind of application selected and the analysis of the data. The large scale characteristics cannot be studied very well since interferometry is primarily sensitive for differential effects along the line of sight from the telescope pairs.

The measurements support research of the characteristics of the irregularities in the medium, i.e. in the electron density in the ionosphere and distribution of water vapour and density/temperature variations in the troposphere. The results of the investigations of the ionosphere may provide useful information to add to predictive models, to study excitation mechanisms for irregularities in the electron density. Relevant projects may be the preparation of a climatology of characteristics of ionospheric and tropospheric irregularities, computerized tomographic studies to analyze the vertical structure of the irregularities of interest and for the ionosphere to study position errors within images to determine propagation characteristics of the irregularities.

The WSRT database is probably the only database in the world which contains useful interferometer data over a period of more than two solar cycles.

#### Acknowledgements:

I thank Dr. Ir. L. P. J. Kamp of the Eindhoven University of Technology and Dr. A. R. Foley of the Netherlands Foundation for Research in Astronomy for helpful comments. The Westerbork Synthesis Radio Telescope is operated by the Netherlands Foundation for Research in Astronomy with financial support from the Netherlands organization for scientific research, NWO.

#### 7. REFERENCES

- Andreeva, E. S., Galinov, A. V., Kunitsyn, V. E., Mel'nichenko, Yu. A., Tereschenko, E. E., Filimonov, M. A., Chernyakov, S. M., 1990, "Radiotomographic reconstruction of ionization dip in the plasma near the earth", *JETP Letters* 52, p. 145.
- Austen, J. R., Franke, S. J., Liu, C. H., 1988, "Ionospheric imaging using computerized tomography", *Radio Science* 23, p. 299.
- Baars, J. W. M., Van der Brugge, J. F., Casse, J. L., Hamaker, J. P., Sondaar, L. H., Visser, J. J. and Wellington, K. J., 1973, "The Synthesis Radio Telescope at Westerbork", *Proceedings IEEE* 61, p. 1258.
- Bean, B. R., Dutton, E. J., 1966, "Radio Meteorology", *Nat. Bur. Std. Monograph* 92, Dept. of Commerce.
- Bos, A., Raumont, E. and Van Someren Gréve, H. W., 1981, *Astron. Astrophys.*, 98, p. 251.
- Brouw, W. N., 1969, Netherlands Foundation for Radio Astronomy, Internal Technical Report 78.
- Brouw, W. N., 1971, "Data processing for the Westerbork Synthesis Radio Telescope", Ph.D. thesis, Leiden University.
- Brouw, W. N., 1975, *Methods in Computational Physics* 14, p. 131.
- Casse, J. L., Muller, C. A., 1974, *Astron. Astrophys.*, 31, p. 333.
- Christiansen, W. N., Högbom, J. A., 1969, "Radiotelescopes", Cambridge University Press, Appendix 4.
- Crane, R. P., 1976, "Refraction effects in the neutral atmosphere" in "Methods of experimental physics", Vol. 12B: Radiotelescopes, ed. Meeks, M. L., Academic Press, New York, p. 186.
- Fomalont, E. B., 1973, "Earth-Rotation Aperture Synthesis", *Proceedings IEEE*, 61, p. 1211.
- Hamaker, J. P., 1978, "Atmospheric delay fluctuations with scale sizes greater than one kilometer, observed with a radio interferometer array", *Radio Science* 13, p. 873.
- Hagfors, T., 1976, "The ionosphere", in "Methods of experimental physics", Vol. 12B: Radio Telescopes, ed. M. L. Meeks, Academic Press, New York, p. 186.
- Högbom, J. A., Brouw, W. N., 1974, *Astron. Astrophys.*, 33, p. 289.
- Raymond, T. D., Austen, J. R., Franke, S. J., Liu, C. H., Klobuchar, J. A., Stalker, J., 1990, "Application of computerized tomography to the investigation of ionospheric structures", *Radio Science* 27, 771.
- Resch, G. M., 1984, "Water vapour radiometry in geodetic applications", in "Geodetic refraction, effects of electromagnetic wave propagation through the atmosphere", ed. F. K. Brunner, Springer Verlag, Berlin, p. 53.
- Kelder, H., Spoelstra, T. A. Th., 1984, "Multi-technique study of medium scale TIDs", *Kleinheubacher Berichte* Nr. 27, p. 575.
- Kelder, H., Spoelstra, T. A. Th., 1987, "Medium scale TIDs observed by radio interferometry and differential Doppler techniques", *J. Atmos. terr. phys.*, 49, p. 7.
- Spoelstra, T. A. Th., 1983, "The influence of ionospheric refraction on radio astronomy interferometry", *Astron. Astrophys.*, 120, 313.
- Spoelstra, T. A. Th., 1984, "Correcting Radio Astronomy Interferometry for Ionospheric Refraction" in: "Characteristics of the Lower Atmosphere Influencing Radio Wave Propagation", AGARD conference proceedings No. 346, 15-1.
- Spoelstra, T. A. Th., 1987, "Correcting refraction in radio astronomy", *Publ. Astr. Obs. Beograd* No. 35, 213.
- Spoelstra, T. A. Th., Kelder, H., 1984, "Effects produced by the ionosphere on radio interferometry", *Radio Science* 19, p. 779.
- Spoelstra, T. A. Th., Schulz, R. T., 1981, "Phase Errors in Radio Astronomy Interferometry due to Ionospheric Disturbances", in *Proceedings of the COSPAR/URSI symposium on "Scientific and engineering uses of satellite radio beacons"*, Warsaw, May 19-23, 1980, ed.: A. W. Wernik, p. 315.
- Thayer, G. D., 1974, "An improved equation for the radio refractivity index of air", *Radio Science* 9, 803.
- Thompson, A. R., 1989, "The Interferometer in Practice", in "Synthesis Imaging in Radio Astronomy", ed.: R. A. Perley, F. R. Schwab, A. I. Bridle, *Astronomical Society of the Pacific Conference Series*, vol. 6, p. 11.
- Van Someren Gréve, H. W., 1974, *Astron. Astrophys. Suppl. Series* 15, p. 343.
- Van Velthoven, P. F. J., 1990, "Medium scale irregularities in the ionospheric electron content", Ph.D. Thesis, Eindhoven University of Technology.
- Weenink, M. P. H., 1987, "A new method for the calculation of the phase path in the geometrical-optics approximation", *Manuscripta Geodaeica* 12, p. 99.

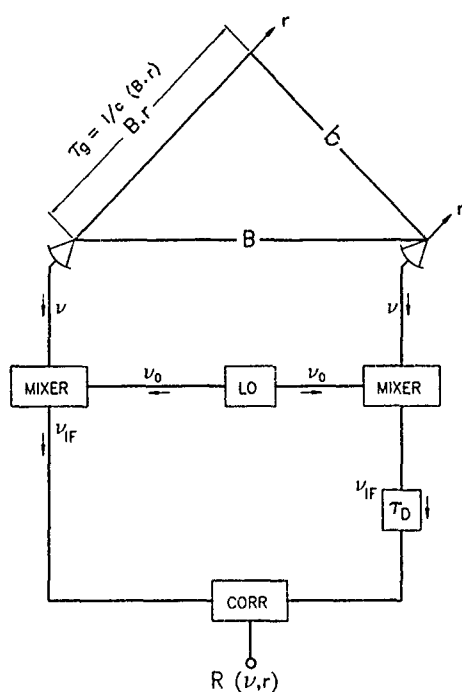


Fig 1. Schematic diagram of a simple two element interferometer

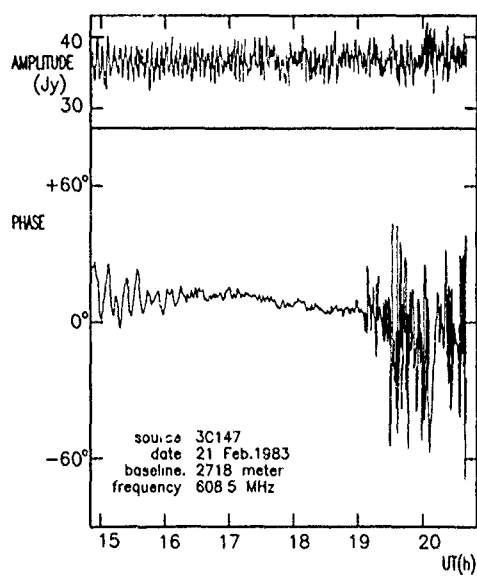


Fig 2 Ionospheric effects observed with the Westerbork Synthesis Radio Telescope, WSRT. The upper frame shows interferometer amplitude and the lower frame the phase errors. The interferometer baseline is 2.7 km. The ionospheric effects are only seen in interferometer phase. This registration shows slowly varying waves during the first 1.5 hours (medium scale TIDs) and rapid variations (phase scintillation) during the last 2.5 hours, both superimposed on a slowly varying background (which is due to the daily variation of the electron content).

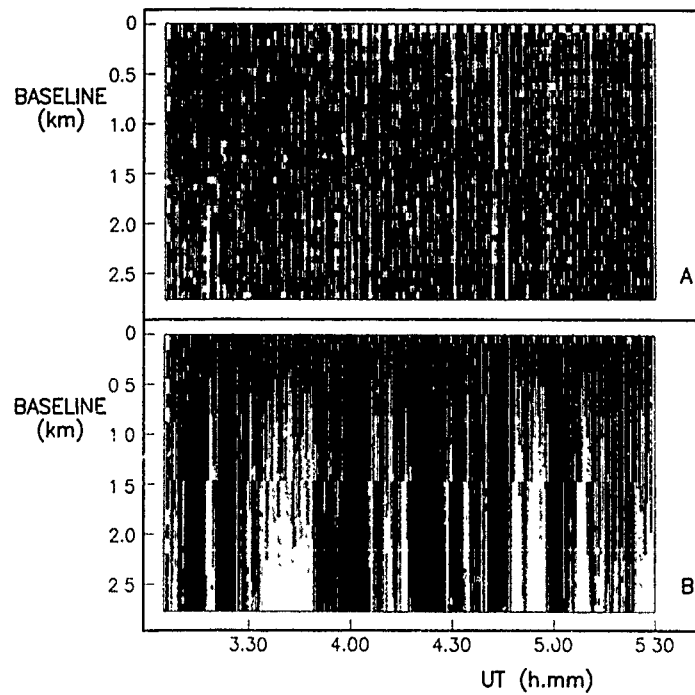


Fig 3 WSRT observation of 3C380 at 14 May 1980 from 3h05m30s to 5h29m20s UT at a frequency of 608.5 MHz. Frame A shows the amplitude and B the interferometer phase differences as a function of baseline. The grey levels indicate deviations from the average value per baseline. The deviations of the amplitude are in % of the mean amplitude: white = -8%, black = +10%. The deviations of the phase are in degrees: white = -30°, black = +40°. The pattern at the shortest baseline is due to solar interference.

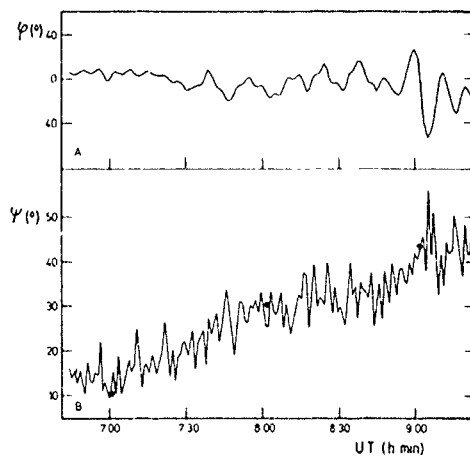


Fig 4 Variations of phase,  $\phi$ , at 2.7 km baseline and polarization angle,  $\psi$ , for radio source 3C286 observed on January 16, 1982, with the Westerbork Synthesis Radio Telescope, WSRT. Note the different scales for the phase and for the polarization angles. The thick dots in the plot of the polarization angles show the Faraday rotation calculated on the basis of observed  $f_0F_2$  values, which represent the critical frequencies for the F2-layer.

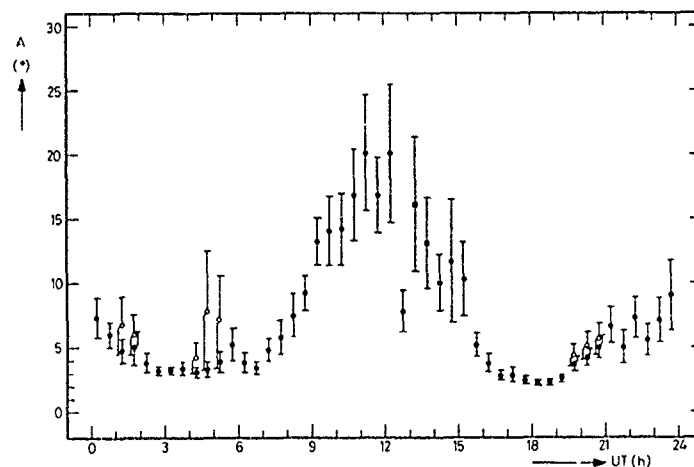


Fig 5 Variation in the amplitude of WSRT-phase variations at a frequency of 608.5 MHz and at 2.7 km baseline due to ionospheric irregularities as a function of time as observed during the winter of 1983. Open symbols indicate that variations with periods less than 10 seconds have been included. Local noon is at 11h33m24s UT.

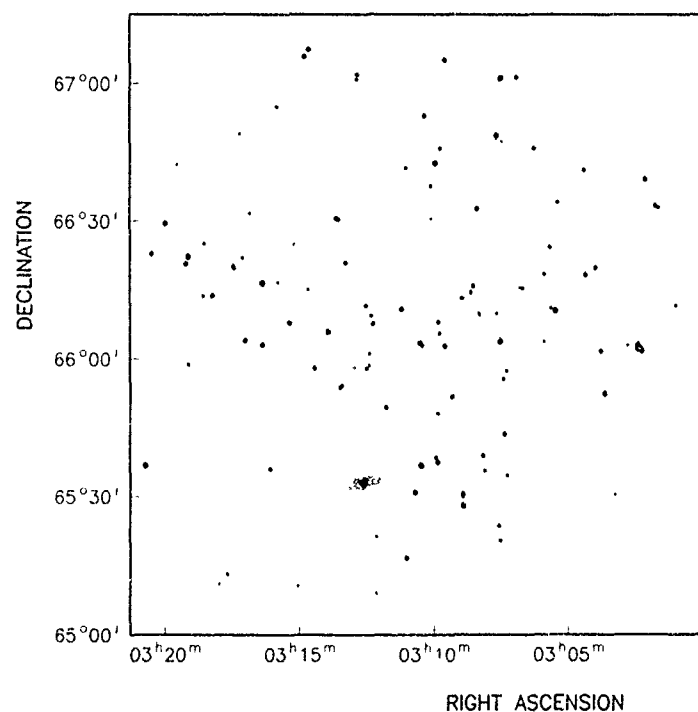


Fig 6 WSRT observation of a field at 608.5 MHz. The synthesized beam is  $28'' \times 28'' \csc \delta$  (where  $\delta$  is the declination of the field centre).

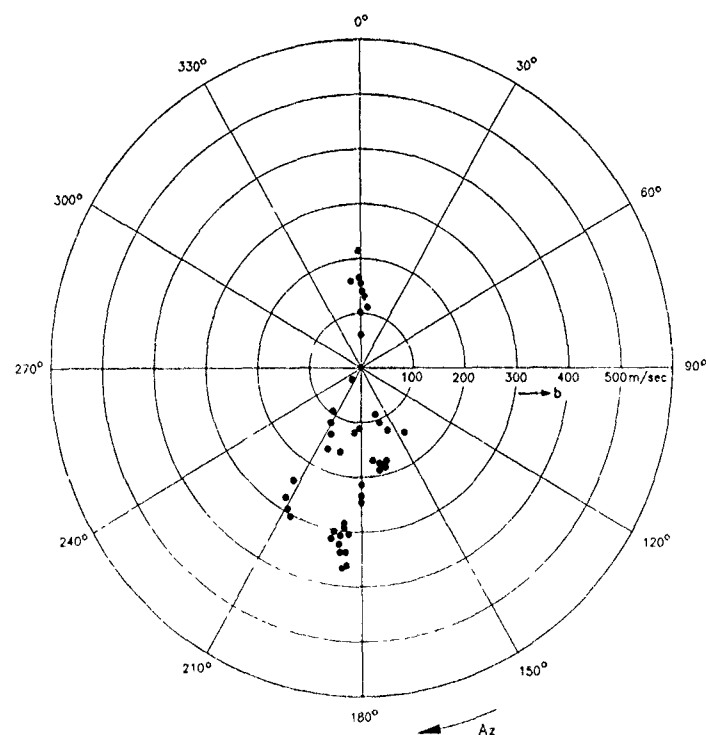


Fig 7 Distribution of azimuths,  $A_z$ , and speeds,  $b$ , of the irregularities from an analysis of combined WSRT and NNSS differential Doppler observations

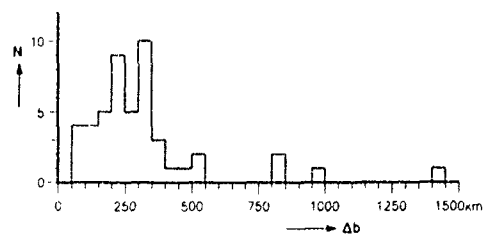


Fig 8 Histogram of the horizontal linear dimensions,  $\Delta b$ , of medium scale TIDs from an analysis of combined WSRT and NNSS differential Doppler observations

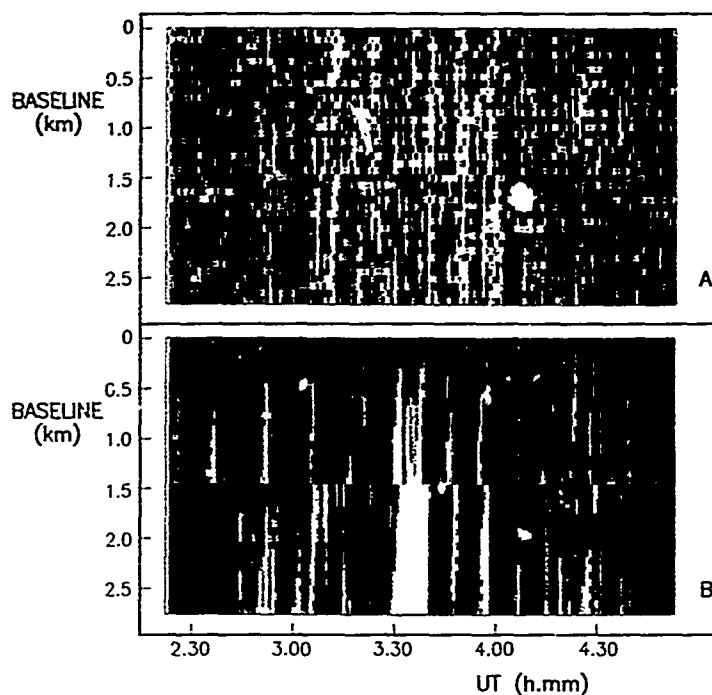


Fig 9. Same as Fig 3, but for an observation of radio source 3C48 at 4995.0 MHz at 28 May 1981 from 2h22m37s to 4h52m27s U.T. The deviations of the amplitude are in % of the mean amplitude: white = -4%, black = +5%. The deviations of the phase are in degrees: white = -40°0, black = +50°0.

## DISCUSSION

E. SCHWEICHER

*Do you change your intermediate frequency (in your interferometer) when you change the wavelength you are looking for?*

AUTHOR'S REPLY

*No. When we change frequency we change the front end receivers.*

W. BOERNER

*Are you working with fixed polarization or adaptively?*

AUTHOR'S REPLY

*We measure all of the four Stokes parameters.*

K. YEH

1. You referred the technique of obtaining ionospheric structures from interferometers as tomographic technique. The real tomography is of course rooted in the back projection theorem. It seems to me you do not make use of this theorem.
2. You compared the relative sensitivity of observing TIDs by Faraday rotation and interferometric phase. In practice these two techniques observe different TIDs as demonstrated in many world campaigns. It seems the interferometer phase is sensitive to gradients and hence more sensitive to small wavelength TIDs while the Faraday rotation is sensitive to large amplitude TIDs. Do you think that it is the right explanation?

AUTHOR'S REPLY

1. Perhaps my explanation was not clear enough. I made a distinction between (a) mapping ionospheric structures within the field of view by analysis of phase errors for discrete sources within this field (e.g. Fig. 6) and (b) the computerized tomographic method which is indeed rooted in the back projection theorem. Mapping ionospheric structures (a) is of course not computerized tomography.
2. Yes. The interferometer phase is indeed highly sensitive to horizontal and vertical gradients in the ionospheric electron content. As I have shown, the relative sensitivity of observing TIDs by Faraday rotation and interferometer phase is directly related to the observing frequency as the interferometer baseline. In the case of the WSRT both techniques are equally sensitive at about 100 MHz. The dependence on observing frequency and interferometer baseline is, as far as I see, the natural explanation of the difference you describe.

# RADAR INTERFEROMETRIC TECHNIQUES FOR INVESTIGATING FIELD-ALIGNED IONOSPHERIC PLASMA IRREGULARITIES

F. Sürücü and E. Kudeki  
Department of Electrical and Computer Engineering  
University of Illinois at Urbana-Champaign  
Urbana, IL 61801-2991  
USA

## SUMMARY

One-dimensional interferometric radar systems with receiver baselines directed in magnetic north-south and east-west directions have been used to study the anisotropy and inhomogeneity characteristics of ionospheric irregularities. In equatorial electrojet aspect sensitivity measurements conducted at Jicamarca, angular spectrum widths as small as  $\sim 0.05^\circ$  have been resolved. The cross-field structures and dynamics of electrojet irregularities have been investigated using an interferometric imaging technique.

## 1. INTRODUCTION

In this paper we review recent developments in radar interferometric probing of ionospheric plasma irregularities at the Jicamarca Radio Observatory near Lima, Peru. The 50 MHz Jicamarca radar system is highly modular and has been used extensively in recent years for interferometric studies of ionospheric plasma irregularities. Radar interferometry was first used at Jicamarca by Woodman [1971] to measure the inclination of the geomagnetic field above the observatory. Farley *et al.* [1981] extended the technique by introducing Doppler sorting in the first interferometric investigations of the equatorial electrojet irregularities. Since then radar interferometry technique has been used successfully at Jicamarca as well as mid- and high-latitudes to study a variety of ionospheric plasma irregularity phenomena [e.g., Kudeki *et al.*, 1981; Providakes *et al.*, 1983; Riggins *et al.*, 1986; Kudeki *et al.*, 1987]. Recently, the technique has also been used for measuring atmospheric wind velocities with MST (Mesosphere Stratosphere Troposphere) and ST (Stratosphere Troposphere) radars [e.g., Kudeki *et al.*, 1990; Larsen *et al.*, 1990; Van Daele *et al.*, 1991].

In this review we shall focus on recent multiple-receiver ionospheric interferometry experiments conducted at Jicamarca. Due to the field aligned nature of ionospheric irregularities [e.g., Fejer and Kelley, 1980] only one-dimensional interferometry measurements with north-south or east-west aligned receiver pair baselines are sufficient to study the anisotropy or inhomogeneity characteristics of the scattering irregularities separately. Minimum-redundancy antenna spacings [e.g., Moffet, 1968] provide the longest sequences of antenna pair baselines in one-dimensional multiple-receiver configurations. In the anisotropy and inhomogeneity experiments to be reviewed here [Kudeki and Farley, 1989; Kudeki and Sürücü, 1991] four-receiver configurations with non-redundant spacing of 1-3-2 were employed. Both the anisotropy and inhomogeneity measurements obtained with north-south and east-west baseline systems can be viewed as one-dimensional brightness spectrum

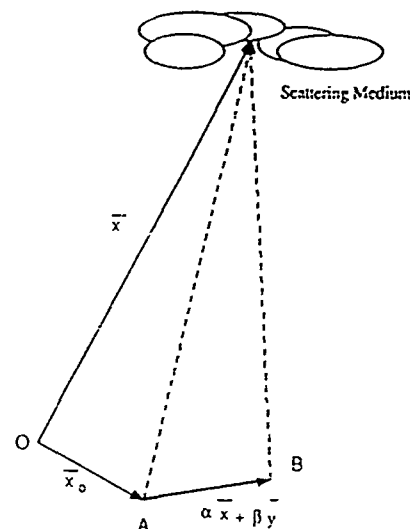


Figure 1: The co-ordinate system used in the derivation of the brightness spectrum.

measurements. In Section 2 we discuss the concept of the brightness spectrum and its relation to receiver pair cross-spectra measured in interferometry experiments. In Section 3 and 4, we discuss the procedures used in estimating the north-south and east-west brightness distributions of ionospheric targets and present sample results obtained in Jicamarca experiments.

## 2. BRIGHTNESS SPECTRUM

Consider the cross-correlation function

$$R(r, \alpha, \beta; t, \vec{x}_0) \equiv \langle s(t, \vec{x}_0) s^*(t + \tau, \vec{x}_0 + \alpha \hat{x} + \beta \hat{y}) \rangle \quad (1)$$

of coherently detected signals  $s(t, \vec{x}_0)$  and  $s(t, \vec{x}_0 + \alpha \hat{x} + \beta \hat{y})$  obtained with two radar receivers (sensors) located at positions  $\vec{x}_0$  and  $\vec{x}_0 + \alpha \hat{x} + \beta \hat{y}$  with respect to the radar transmitter located at O (see Figure 1). In (1),  $\hat{x}$  and  $\hat{y}$  are orthogonal unit vectors, and the position vector magnitudes are measured in units of radar carrier wavelength  $\lambda_0 \equiv c/f_0$ , where  $c$  is the speed of light, and  $f_0$  is the carrier frequency. Assuming a pulsed modulation of the transmitted carrier with some inter-pulse period  $T$  and the quasi-stationarity of the scattering irregularities, the cross-correlation function (1) should be periodic in  $t$  with a period  $T$ , with each value of  $t$  labeling some radar range  $r \equiv ct/2$ . Focusing our attention on radar returns from some fixed range  $r_0$  in the far field, and assuming the quasi-homogeneity of the return signals we drop the labels  $t$  and  $\vec{x}_0$ , and express the cross-correlation function  $R(r, \alpha, \beta)$  as the three dimensional Fourier transform of

the brightness spectrum  $B(f, \theta_x, \theta_y)$  via

$$R(\tau, \alpha, \beta) = \int df e^{i2\pi f \tau} V(f, \alpha, \beta), \quad (2)$$

where

$$V(f, \alpha, \beta) \equiv \iint d\theta_x d\theta_y e^{-i2\pi f \alpha} e^{-i2\pi f \beta} B(f, \theta_x, \theta_y) \quad (3)$$

is to be referred to as the visibility spectrum. In (3),  $\theta_x$  and  $\theta_y$  are the direction cosines with respect to  $\hat{x}$  and  $\hat{y}$  [e.g., Ratcliffe, 1956] which may be regarded as spatial frequencies measured in units of cycles/wavelength, or alternatively, for small values of  $\theta_x$  and  $\theta_y$ , interpreted as the zenith angles measured in  $x$ - and  $y$ -directions in units of radians.

For  $\tau = \alpha = \beta = 0$ , equations (2) and (3) can be combined as

$$R(0, 0, 0) = \iint df d\theta_x d\theta_y B(f, \theta_x, \theta_y), \quad (4)$$

and since  $R(0, 0, 0)$  represents the total echo power, the brightness spectrum  $B(f, \theta_x, \theta_y)$  can be interpreted as the echo power density per unit Doppler frequency  $f$  and viewing angles  $\theta_x$  and  $\theta_y$ . For  $\alpha = \beta = 0$  equation (3) reduces to

$$V(f, 0, 0) = \iint d\theta_x d\theta_y B(f, \theta_x, \theta_y), \quad (5)$$

which indicates that only the frequency distribution of the echo power, i.e., the Doppler spectrum  $S(f) \equiv V(f, 0, 0)$ , can be recovered by using a single receiver. However, the Fourier transform relationship (3) between the visibility spectrum  $V(f, \alpha, \beta)$  and the brightness spectrum  $B(f, \theta_x, \theta_y)$  suggests that a multiple-receiver configuration, which allows an appropriate sampling of the visibility spectrum over the  $\alpha\beta$ -plane, may be useful to measure the brightness spectrum or at least to estimate its lower order moments over  $\theta_x$  and/or  $\theta_y$ . Indeed, radar interferometry consists of measuring one or more non-redundant samples of antenna pair cross-spectra  $V(f, \alpha, \beta)$  and exploiting relationship (3) to deduce the angular distribution of the scattering targets contributing to different frequency bands of the Doppler spectrum  $S(f) = V(f, 0, 0)$ .

For a medium with weak refractive index fluctuations, the backscattering cross-section per unit volume and frequency interval is known to be proportional to the frequency-wavenumber spectrum  $S_n(\omega, \vec{k})$  of the fluctuations evaluated at  $\omega = 2\pi f$  and  $\vec{k} = \vec{k}_B \equiv 2\vec{k}_0$ , where  $f$  represents the Doppler shift from the radar carrier frequency  $f_0$  and  $\vec{k}_B$  is the so called Bragg vector defined as twice the propagation vector  $\vec{k}_0$  of the incident wave [e.g., Booker and Gordon, 1950; Woodman, 1991]. Assuming an incident power density of  $S_i(\theta_x, \theta_y, r)$ , the power return from an infinitesimal volume element of  $r^2 d\theta_x d\theta_y dr$  positioned at some range  $r$  in  $(\theta_x, \theta_y)$  direction and over some frequency band  $df$  centered about  $f_0 + f$  should then be proportional to

$$S_i(\theta_x, \theta_y, r) S_n(2\pi f, \vec{k}_B(\theta_x, \theta_y); \theta_x, \theta_y, r)$$

$$r^2 d\theta_x d\theta_y dr df \frac{A(\theta_x, \theta_y)}{4\pi r^2}, \quad (6)$$

where  $A(\theta_x, \theta_y)$  stands for the effective area of the receiving antenna, and the denominator  $4\pi r^2$  accounts for propagation losses. Note that in the argument list of  $S_n$  we have indicated the direction dependence of Bragg vector  $\vec{k}_B$  as well as possible position dependence of the fluctuation spectrum. The integral of (6) over all  $\theta_x, \theta_y, f$ , and between  $r = r_0$  and  $r_0 + \Delta r$  should be proportional to the total echo power  $R(0, 0, 0)$  coming from the irregularities contained within a scattering volume of depth  $\Delta r$  located at range  $r_0$ . Therefore, a comparison of (4) and (6) suggests the brightness spectrum model

$$B(f, \theta_x, \theta_y) = G(\theta_x, \theta_y) S_n(f, \vec{k}_B(\theta_x, \theta_y); \theta_x, \theta_y), \quad (7)$$

where

$$S_n(f, \vec{k}, \theta_x, \theta_y) \equiv \int_{r_0}^{r_0 + \Delta r} dr S_n(2\pi f, \vec{k}, \theta_x, \theta_y, r) \quad (8)$$

is the radial integral of the fluctuation-spectrum over the depth of the scattering volume, and the function

$$G(\theta_x, \theta_y) \propto \frac{S_i(\theta_x, \theta_y, r_0) A(\theta_x, \theta_y)}{4\pi} \quad (9)$$

includes all implicit proportionality constants and the two way power pattern of the radar system. In obtaining (7), we neglected the  $r$  dependent variation in  $S_i(\theta_x, \theta_y, r)$  with the assumption that the depth of the scattering volume is small compared to its range.

Clearly, (7) suggests that the angular variation of brightness spectrum at each Doppler frequency  $f$  is influenced by three factors: (1)  $\vec{k}$  dependence of  $S_n$ , which has to do with the anisotropy of the scattering irregularities at a fixed  $|\vec{k}| = 2k_0$ , (2) the spatial dependence of  $S_n$  due to irregularity inhomogeneities within the resolution volume, and (3) variations imposed by the two-way power pattern  $G(\theta_x, \theta_y)$ . In most practical cases of interest brightness variation is dominated by the first and/or the second of these effects. For homogeneous scatterers, the brightness spectrum provides a measure of the "aspect sensitivity" of the scattering irregularities with wavenumber  $|\vec{k}_B(\theta_x, \theta_y)| = 2k_0$ . On the other hand, for weakly aspect sensitive or nearly isotropic irregularities the brightness spectrum allows a straightforward visualization of how the scattering irregularities are organized within the field of view. The image structures can then be interpreted in terms of the angular position and extent of the irregularity patches causing the radar echos. The brightness spectrum is dominated by  $G(\theta_x, \theta_y)$  only in the limit of weak anisotropy and inhomogeneity, a situation which rarely arises in ionospheric studies.

Strong magnetic field alignment of ionospheric density irregularities causes the angular variation of  $S_n$  in the direction of the geomagnetic field to be dominated by anisotropy effects, while variations of  $S_n$  in the perpendicular direction to the field may generally be expected to be a manifestation of irregularity structuring. It is therefore possible to study the anisotropy and inhomogeneity characteristics of ionospheric irregularities separately by using one-dimensional interferometry systems with receiver baselines directed in magnetic

north-south and east-west directions, respectively. Although both effects can be studied simultaneously by using two-dimensional receiver distributions, implementation of one-dimensional interferometry is generally easier and experiments to be reviewed in the next two sections were conducted with one-dimensional north-south and east-west baseline systems.

In one-dimensional interferometry, all antenna pair baselines are aligned in one direction, say  $\hat{x}$ , so with  $\beta = 0$ , (3) reduces to

$$V(f, \alpha) = \int d\theta_x e^{-j2\pi\theta_x\alpha} B(f, \theta_x), \quad (10)$$

where

$$V(f, \alpha) \equiv V(f, \alpha, 0), \quad (11)$$

and

$$B(f, \theta_x) \equiv \int d\theta_y B(f, \theta_x, \theta_y) \quad (12)$$

is the one-dimensional brightness spectrum in  $\hat{x}$  direction. Normalizing  $V(f, \alpha)$  and  $B(f, \theta_x)$  by the Doppler spectrum  $V(f, 0, 0) = V(f, 0)$ , and changing the subscript  $x$  for simplicity, we obtain the re

$$v(f, \alpha) = \int d\theta e^{-j2\pi\theta\alpha} b(f, \theta) \quad (13)$$

between the one-dimensional normalized brightness and the visibility spectra satisfying the normalization condition

$$v(f, 0) = \int d\theta b(f, \theta) = 1. \quad (14)$$

Normalized visibility estimates required to recover  $b(f, \theta)$  and therefore  $B(f, \theta) = V(f, 0)b(f, \theta)$  are obtained in practice via

$$\frac{\langle s(f, 0)s^*(f, \alpha) \rangle}{\langle |s(f, 0)|^2 \rangle^{1/2} \langle |s(f, \alpha)|^2 \rangle^{1/2}}, \quad (15)$$

where  $s(f, 0)$  and  $s(f, \alpha)$  stand for  $P$ -point discrete Fourier transform samples of signal time series recorded by using two sensors separated by a distance of  $\alpha$  wavelengths and  $\langle \cdot \rangle$  denotes smoothing over  $K$  contiguous samples.

### 3. NORTH-SOUTH BASELINE ASPECT SENSITIVITY MEASUREMENTS

In ionospheric aspect sensitivity measurements the objective is estimating the characteristic width of the angular spectrum of the return signals in geomagnetic field direction. Using north-south baseline interferometry this amounts to estimating the characteristic width of the one-dimensional brightness spectrum  $b(f, \theta)$ , where  $\theta$  now denotes the zenith angle in northward direction. In view of the normalization condition (14), the characteristic width  $\sigma(f)$  of  $b(f, \theta)$  in  $\theta$  can be defined via

$$\sigma^2(f) = \int d\theta \theta^2 b(f, \theta - \bar{\theta}(f)), \quad (16)$$

where

$$\bar{\theta}(f) = \int d\theta \theta b(f, \theta) \quad (17)$$

denotes the angular position of the brightness peak. Applying the Fourier transform shift theorem on (13) gives

$$v(f, \alpha) = e^{j2\pi\bar{\theta}(f)\alpha} \int d\theta e^{-j2\pi\theta\alpha} b(f, \theta - \bar{\theta}(f)), \quad (18)$$

which implies that for  $b(f, \theta)$  symmetric about  $\theta = \bar{\theta}(f)$ ,

$$\begin{aligned} \frac{d^2 |v(f, \alpha)|}{d\alpha^2} \Big|_{\alpha=0} &= -(2\pi)^2 \int d\theta \theta^2 b(f, \theta - \bar{\theta}(f)) \\ &= -(2\pi)^2 \sigma^2(f). \end{aligned} \quad (19)$$

Taylor series expansion of  $|v(f, \alpha)| = |v(f, -\alpha)|$  about  $\alpha = 0$  is

$$\begin{aligned} |v(f, \alpha)| &= 1 + \frac{1}{2} \alpha^2 \frac{d^2 |v(f, \alpha)|}{d\alpha^2} \Big|_{\alpha=0} + \dots \\ &= 1 - \frac{1}{2} \alpha^2 (2\pi)^2 \sigma^2(f) + \dots, \end{aligned} \quad (20)$$

and therefore, the characteristic width is obtained via

$$\sigma(f) = \sqrt{\frac{-C_2}{2\pi^2}}, \quad (21)$$

where  $C_2$  is the coefficient of the  $\alpha^2$  term of a polynomial fit applied to measured values of  $|v(f, \alpha)|$  at each Doppler frequency  $f$ .

The procedure outlined above has been used in equatorial electrojet aspect sensitivity measurements at Jicamarca [Kudeki and Farley, 1989]. Four receivers were positioned along the north-south diagonal of the Jicamarca incoherent scatter array with 1-3-2 non-redundant spacing. Each receiver was 1/64th module of the array and the unit spacing was  $6\sqrt{2}$  wavelengths. A typical example of the measurements is shown in Figure 2 [Figure 2 in Kudeki and Farley, 1989]. This figure displays daytime electrojet measurements for four range gates obtained with 1-min integration. The top row shows the nearly identical self-normalized Doppler spectra of the four receiver signals. The middle row displays the coherence (the magnitude of  $v(f, \alpha)$ ) for the six different baselines, with symbols changing from triangles to squares to circles to diamonds to crosses to crossed squares as the baseline length increases. The bottom row displays angular (half) width estimates,  $\sigma_x(f)$ , referred to as aspect width. The aspect widths are plotted only when the signal/noise ratio at the corresponding Doppler frequency for all four receivers exceeds some threshold value.

Note that the technique allows the determination of the aspect width as a function of the Doppler frequency  $f$ . This Doppler sorting capability is crucial for differentiating between the aspect widths of high frequency type I and low frequency type II waves responsible for the radar backscatter. Type I and type II electrojet irregularities are known to be generated by distinct physical processes [e.g., Farley, 1985] and one of the findings of these measurements is the enhancement of type II aspect width during strongly driven electrojet conditions, which indicates a nonlinear coupling between directly driven type I waves and linearly damped type II waves with finite wavelengths in the geomagnetic field direction [Kudeki

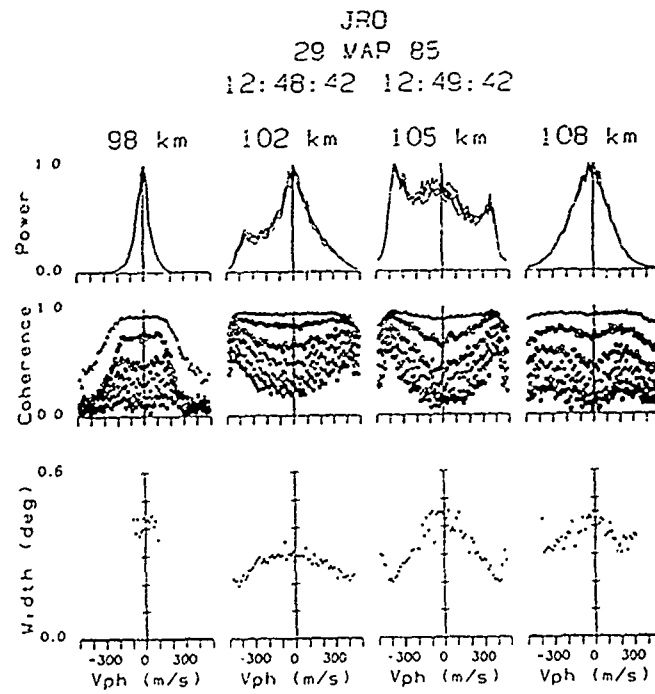


Figure 2: Self-normalized power, coherence, and aspect width spectra for four electrojet during a strongly driven daytime period. The "width" is actually the half width  $\sigma(f)$  (After Kudeki and Farley, [1989])

and Farley, 1969]. Characteristic aspect widths as small as about  $0.05^\circ$  were measured in this experiment.

The procedure used by Kudski and Farley [1989] avoids direct inversion of (13) to estimate the brightness spectrum function  $b(f, \theta)$ , but rather exploits (13) to infer the characteristic width of  $b(f, \theta)$ . Certainly, the characterization of  $b(f, \theta)$  by its width, or more generally, by its low order moments is the most satisfactory when the latter is a single peaked function. This approach is justified in aspect sensitivity measurements when the angular irregularity spectrum  $S_n(f, k)$  is expected to exhibit a single peak as a function of  $k_x$ , the wavenumber in geomagnetic field direction.

#### 4. EAST-WEST BASELINE IMAGING

While the north-south brightness of ionospheric irregularities may be expected to exhibit a single peaked distribution due to the aspect sensitivity effect, in general we have no prior knowledge of the expected shapes of the east-west brightness distributions. Therefore, the "model based" estimation procedure outlined in the previous section is not suitable for the analysis of east-west baseline interferometry data. An alternate procedure referred to as radar interferometric imaging (RII) has been used in the analysis of multiple sensor east-west baseline interferometry measurements conducted at Jicamarca [Kudski and Sürücü, 1991]. RII consists of direct inversion of (13) with the measured normalized visibility samples  $v(f, nD)$ , where,  $n = 0, \pm 1, \dots, \pm N$ , and  $N$  is preferably large compared to unity.

Fourier inversion of (13) yields (where  $\theta$  now denotes the zenith angle in eastward direction)

$$b(f, \theta) = \int d\alpha e^{j2\pi\theta\alpha} v(f, \alpha), \quad (22)$$

which, for  $b(f, \theta)$  band limited to the spatial frequency range  $|\theta| \leq \Theta$ , can also be expressed as

$$b(f, \theta) = \sum_{n=-\infty}^{\infty} D e^{j2\pi\theta nD} v(f, nD) \quad (23)$$

for  $|\theta| \leq \Theta$ , provided that the sampling interval  $D$  of  $v(f, \alpha)$  in  $\alpha$  satisfies the Nyquist criterion  $D \leq 1/2\Theta$ . We shall refer to (23) as the *true image* which is actually inaccessible to RII due to the absence of  $v(f, nD)$  for  $|n| > N$ . However, with the available visibility samples, we can calculate a *dirty image*

$$\hat{b}(f, \theta) = \sum_{n=-N}^N D e^{j2\pi\theta nD} w(n) v(f, nD), \quad (24)$$

where  $w(n)$  is a suitably selected window function such that  $w(n) = 0$  for  $|n| > N$ . In short, RII technique produces a windowed Fourier transform of available visibility samples as an estimate of the brightness spectrum.

The dirty image in (24) is related to the true image via

$$\hat{b}(f, \theta) = W(\theta) * b(f, \theta), \quad (25)$$

where  $*$  denotes convolution over  $\theta$ , and

$$W(\theta) \equiv \sum_{n=-N}^N e^{j2\pi\theta nD} w(n). \quad (26)$$

Therefore, the angular resolution of the dirty image is limited by the characteristic width of  $W(\theta)$ .

Considering a triangular weighting function

$$w(n) = \frac{N+1-|n|}{N+1} \quad (27)$$

for  $|n| \leq N$ , we find that

$$W(\theta) = \frac{\sin^2((N+1)\pi\theta D)}{(N+1)\sin^2(\pi\theta D)}, \quad (28)$$

which implies an angular resolution of

$$\delta\theta = \frac{1}{(N+1)D} \quad (29)$$

radians. If  $D$  is selected to match  $1/2\Theta$ , (29) implies that up to  $2\Theta/\delta\theta = N+1$  features of the true image separated from each other by  $\delta\theta$  or more can be identified in the dirty image. Also, (28) implies that the dirty image is contaminated by -12.8 dB or weaker side-lobes. The matching between  $D$  and  $1/2\Theta$  can be enforced by selecting a transmitting antenna size of  $2D$ , which is well known to be characterized by a BWFN of  $1/D$  radians. Note that (28) is identical to the square of the array factor of a uniformly illuminated  $N+1$  element linear array and that imaging with a triangular weighting function may be viewed as software beam synthesis.

The transmission and reception antenna configurations used in recent Jicamarca electrojet imaging experiments [Kudski and Sürücü, 1991] are shown in Figure 3. Four 1/64th modules of the Jicamarca incoherent scatter array selected with 1-3-2 spacing along its east-west diagonal were sampled independently in reception (labeled R in Figure 3 a). The use of expressions similar to (15) with all module-pair combinations provides normalized visibility samples at  $\alpha = \pm D, \dots, \pm 6D$ . With  $N = 6$ , (29) implies an angular resolution of  $\delta\theta \approx 0.965^\circ$  for a dirty image obtained by using (24) with the measured visibility samples and  $w(n) = (7-|n|)/7$ . Figure 3 b displays the product of the power patterns of the transmission array and one of the reception modules evaluated along the locus of perpendicularity to the geomagnetic field at 100 km altitude. The curve may be regarded as the true image corresponding to a homogeneous distribution of perfectly field aligned plasma irregularities and provides some idea about the expected spatial frequency band of the electrojet images.

Figure 4 displays sequences of seven dirty images  $\hat{b}(f, \theta)$  obtained from 102.3 and 102.6 km daytime electrojet returns. The time and height resolutions were 1.664 s and 300 m, respectively. In each image, the horizontal axis is the Doppler frequency  $f$  in the  $\pm 186.3$  Hz range, corresponding to a maximum Doppler speed of 559 m/s. The vertical axis is the spatial frequency  $\theta$  in the  $\pm 3.38^\circ$  range, which may also be viewed as eastward displacement in the  $\pm 6$  km range measured from the overhead position at 100 km altitude. Positive  $f$  and  $\theta$  correspond to downward motions and eastward directions, respectively. The intensity in each panel varies linearly with self-normalized  $\hat{b}(f, \theta)$  at each Doppler frequency  $f$ , with the darkest and lightest tones corresponding to one and

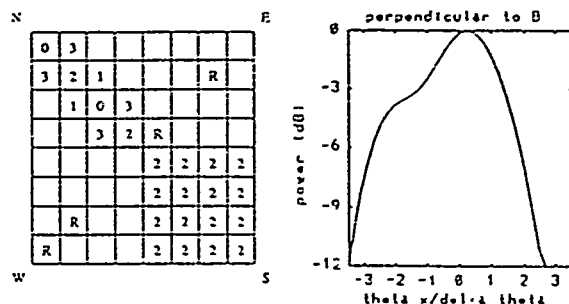


Figure 3: (a) The antenna configuration used on August 6, 1990. The 1/64th modules of the array labeled with *R* were sampled independently in reception. The transmitting array consists of the modules labeled by 0, 1, 2, and 3, which correspond to the applied phasing in units of  $-\pi/2$  radians. Unlabeled modules were not used. (b) The two-way radar beam pattern evaluated at  $(\theta, \tan 2.68^\circ + \theta \tan 4^\circ)$  for  $|\theta/\delta\theta| < 3.5$ , where  $\theta$  is the zenith angle measured along the eastward diagonal of the Jicamarca array and  $\delta\theta = 0.965^\circ$ .

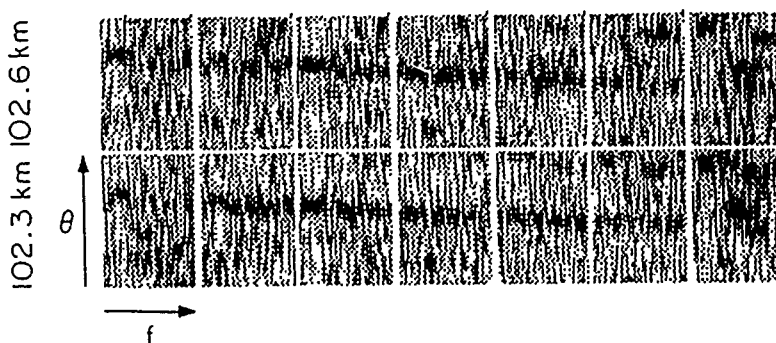


Figure 4: Sequences of seven consecutive images obtained from 102.3 and 102.6 km returns between 12:33:57 and 12:34:07 LT on August 6, 1990.

zero, respectively. Figure 5 displays longer sequences of daytime images obtained from 101.4 and 101.7 km data in a similar format to Figure 4, but only for  $-186.3 < f < 0$  Hz and with a factor of two compression along the  $f$ -axis. Finally, Figure 6 presents samples of nighttime electrojet images from 105.6, and 106.2 km in a similar format to Figure 4.

Both daytime and nighttime image sequences exhibit distinct brightness patches which appear to be displaced in successive images in westward and eastward directions, respectively. Clearly the scattering irregularities are not distributed uniformly in the zonal direction, and the east-west drift speed of enhanced irregularity patches can be directly estimated from the image sequences ( $\approx 300$ - $340$  m/s in Figure 4 and  $\approx 120$ - $150$  m/s in Figure 6). Note that the nighttime images exhibit multiple brightness patches with the upshifted and downshifted brightness patches interleaved in the angular direction. Such signatures can be attributed to kilometer scale primary

waves responsible for the generation of meter scale irregularities detected by the 50 MHz system [e.g., *Kudeki et al.*, 1987]. Also note that the relative positions of upshifted and downshifted brightness patches exhibit some temporal changes which suggest that multiple modes of dispersive kilometer scale waves may be involved in the structuring of meter scale irregularities.

Clearly, the above examples illustrate that radar interferometric imaging constitutes a powerful remote sensing technique for the visualization and investigation of the cross-field dynamics of ionospheric plasma irregularity processes. It is also evident that the amount of useful information which can be obtained with this technique is limited by the resolution of the imaging interferometry system. Certainly, as Figure 6 illustrates, the inherent Doppler sorting capability of the technique helps in differentiating between closely spaced irregularity patches with distinct line of sight motions. But ultimately, the angular system resolution is determined by the longest

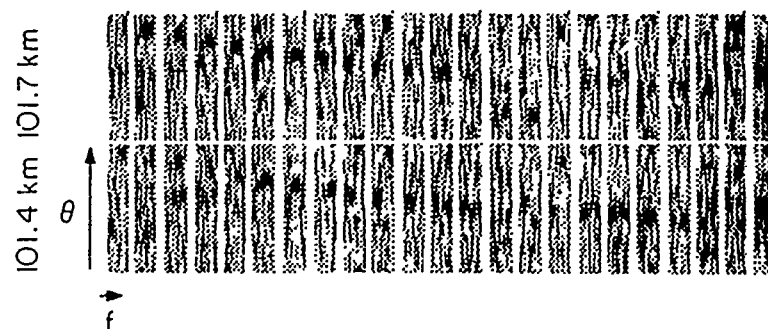


Figure 5: Sequences of twenty-six consecutive images obtained from 101.4 and 101.7 km returns between 12:31:26 and 12:32:07 LT on August 6, 1990.



Figure 6: Same as Figure 3 but for 105.6 and 106.2 km data obtained between 23:05:55 and 23:06:05 LT on August 7, 1990.

available receiver pair baseline (see equation (26)). Finite image resolution is a manifestation of Fourier inversion of (13) with incomplete visibility data, and does not apply in model based estimation of brightness spectrum parameters where the Fourier inversion of (13) can be avoided. One example of model based estimation has been presented in Section 3 in connection with ionospheric aspect sensitivity measurements. Note that the measured aspect widths in the  $\sim 0.45^\circ - 0.05^\circ$  range are significantly smaller than the Fourier resolution of the Jicamarca interferometry system, approximately  $0.965^\circ$ . Clearly, in the case of radar interferometric imaging, information regarding the unpredictable and irregular shapes of the cross-field brightness distributions is exchanged for the high resolution capabilities of model based estimation. Note that when occasionally the imaging method displays single peaked brightness features as in Figure 4, it is possible to return to model based estimation to obtain higher resolution estimates of the zonal dimensions of the irregularity patches. Model based estimation can also be used routinely with east-west baseline systems if the transmission antenna beam is designed to be sufficiently narrow to ascertain the presence of a single irregularity patch within the radar field of view during each estimation interval [e.g., Farley *et al.*, 1981; Kudski *et al.*, 1987]. However, we note that in the latter case it is no longer possible to distinguish between the temporal and spatial variations of irregularity motions and it is difficult to detect rapidly drifting irregularity patches which transit the narrow field of view within a few imag-

ing intervals. Given a sufficiently long baseline, radar interferometric imaging technique appears to be capable of offering a more comprehensive view of the cross-field dynamics of the ionospheric plasma irregularities than the traditional two-receiver interferometry. With the eight-receiver minimum-redundancy configuration being planned for Jicamarca, we hope to achieve angular resolution of  $\sim 0.3^\circ$  in future imaging experiments. This effort will require the construction of four new reception modules to be positioned outside existing antenna array.

A related issue to angular resolution is sidelobe contamination arising from the windowing of the available visibility samples (see equations (24) and (26)). For sufficiently large  $N$  (maximum available spacing), the sidelobe to mainlobe ratio is relatively independent of  $N$ , so the sidelobe problem can not be eliminated by using longer baseline systems. One approach to cope with sidelobe contamination is the CLEAN algorithm developed in the radio astronomy community [e.g., Schwarz, U. J., 1979, Thompson *et al.*, 1986]. CLEAN is basically an iterative deconvolution process, which decomposes the dirty image into point-source responses (i.e., equation (26)), and then reconstructs the brightness spectrum by replacing each point-source response with sidelobe free clean response functions usually taken as Gaussians with a half width equal to the characteristic width of the point source response. Other image enhancement techniques such as the maximum entropy method (MEM) and Capon's high resolution method (HRM) may also prove to be useful in coping with the sidelobe contamination problem. The

results of our preliminary investigation of the CLEAN option will be reported in a separate publication.

## 5. CONCLUSIONS

Recent equatorial electrojet experiments conducted at Jicamarca demonstrate that one-dimensional multiple-receiver radar interferometry is a powerful remote sensing tool for investigating plasma instability process. Its implementation requires the availability of modular radar systems with flexible receiver arrangements. In cross-field imaging applications, system resolution improves linearly with the maximum available antenna pair separation. However, by using minimum-redundancy antenna spacings it should be possible to achieve sufficient resolution with a modest number of receiving antennas in most ionospheric applications. Future measurements at Jicamarca will focus on imaging the structure of spread-F irregularities.

## REFERENCES

- [Booker and Gordon, 1950] Booker, H. G., and W. E. Gordon, A theory of radio scattering in the troposphere, *Proc. IRE*, **38**, 461-412, 1950.
- [Farley et al., 1981] Farley, D. T., H. M. Ierke, and B. G. Fejer, Radar Interferometry: A new technique for studying plasma turbulence in the ionosphere, *J. Geophys. Res.*, **86**, 1476, 1981.
- [Fejer and Kelley, 1980] Fejer, B. G., and M. C. Kelley, Ionospheric irregularities, *Rev. Geophys. Space Phys.*, **18**, 401, 1980.
- [Kudeki and Farley, 1985] Aspect sensitivity of equatorial electrojet irregularities and theoretical implications, *J. Geophys. Res.*, **94**, 426, 1989.
- [Kudeki and Sürücü, 1991] Kudeki, E., and F. Sürücü, Radar interferometric imaging of field-aligned plasma irregularities in the equatorial electrojet, *Geophys. Res. Lett.*, **18**, 41, 1991.
- [Kudeki and Woodman, 1990] Kudeki, E., and R. F. Woodman, A post-statistics steering technique for MST radar applications *Radio Sci.*, **25**, 591, 1990.
- [Kudeki et al., 1987] Kudeki, E., B. G. Fejer, D. T. Farley, and C. Hanuise, The Condor Equatorial Electrojet Campaign: Radar results *J. Geophys. Res.*, **92**, 13561, 1987.
- [Kudeki et al., 1981] Kudeki, E., B. G. Fejer, D. T. Farley, and H. M. Ierke, Interferometer studies of equatorial F region irregularities and drifts, *Geophys. Res. Lett.*, **8**, 377, 1981.
- [Kudeki et al., 1990] Kudeki, E., F. Sürücü, and R. F. Woodman, Mesospheric wind and aspect sensitivity measurements at Jicamarca using radar interferometry and post-statistics steering techniques, *Radio Sci.*, **25**, 595-612, 1990.
- [Larsen et al., 1990] Larsen, M., R. D. Palmer, S. Fukao, R. F. Woodman, M. Yamamoto, T. Tsuda, and S. Kato, An analysis technique for deriving vector winds and in-beam incidence angles from interferometer measurements, *J. Atmos. Ocean Tech.*, (In Press), 1991.
- [Moffet, 1968] Alan T. Moffet, Minimum-Redundancy Linear Arrays, *IEEE Trans. Antennas and Propagation*, Vol. AP-16, pp.172-175, March 1968.
- [Riggin et al., 1986] Riggin, D., W. E. Swartz, J. Proviakes, and D. T. Farley, Radar studies of long-wavelength waves associated with mid-latitude sporadic E layers, *J. Geophys. Res.*, **91**, 8011, 1986.
- [Proviakes et al., 1983] Proviakes, J. F., W. E. Swartz, D. T. Farley and B. G. Fejer, First VHF auroral radar interferometer observations, *Geophys. Res. Lett.*, **10**, 401-404, 1983.
- [Ratcliffe, 1956] Ratcliffe, J., A., Some aspects of diffraction theory and their application to the ionosphere, *Phys. Soc. Reports on Progress in Physics*, **XIX**, 188, 1956.
- [Schwarz, U. J., 1986] Schwarz U. J., The method "CLEAN" - use, misuse and variations, *Image Formation from Coherence Functions in Astronomy*, 197, D. Reide, Dordrecht, Holland, 1979.
- [Thompson et al., 1986] Thompson, A. R., J. M. Moran, and G. W. Swenson, *Interferometry and synthesis in radio astronomy*, Wiley-Interscience, New York, 1986.
- [van Baalen et al., 1991] Van Baalen, J. S., A. D. Richmond, T. Tsuda, S. K. Avery, S. Kato, S. Fukao, and M. Yamamoto, Radar interferometry technique and anisotropy of the echo-power distribution: first results, *Radio Sci.*, **26**, 1315-1326, 1991.
- [van Schooneveld, 1979] van Schooneveld, C., Resolution enhancement; the "Maximum Entropy Method" and the "High Resolution Method", *Image Formation from Coherence Functions in Astronomy*, 197, D. Reidel, Dordrecht, Holland, 1979.
- [Woodman, 1971] Woodman R. F., Inclination of the geomagnetic field measured by an incoherent scatter technique, *J. Geophys. Res.*, **76**, 178, 1971.
- [Woodman, 1991] Woodman, R. F., A general statistical instrument theory of atmospheric and ionospheric radars, *J. Geophys. Res.*, **96**, 7911-7928, 1991.

### DISCUSSION

#### **P. CANNON**

*If you had a radar available in the polar regions, could your technique be employed in that area? For example, are your assumptions of stationarity, etc., applicable in the polar ionosphere?*

#### **AUTHOR'S REPLY**

*I believe the so-called correlation time is much shorter than the one we study at equatorial electrojet. This may require the sampling period (effectively IPP) to be decreased as small as possible so that we can have an observation period (averaging period) being longer than the correlation time and at the same time being shorter than the time scale where irregularities can be assumed stationary.*

# ACTIVE REMOTE SENSING OF THE IONOSPHERE AND THE EARTH SURFACE IRREGULARITIES

Ezekiel Bahar  
Electrical Engineering Department  
University of Nebraska-Lincoln  
Lincoln, NE 68588-0511 U.S.A.

## ABSTRACT

Radio wave propagation in a uniformly stratified propagation environment has been studied extensively, both analytically and numerically. Thus, the propagation environment over the earth's surface has been modelled as multi-layered horizontally stratified, (circular) cylindrically stratified or spherically stratified media. (See Figs. 1, 2) However, naturally occurring propagation paths are more realistically modelled as irregular stratified media (See Figs. 3, 4) Even idealized representations of the earth-ionosphere propagation environment must account for the roughness of the terrain and the sea surface as well as localized (due to lightning) and diurnal variations in the effective height of the ionosphere.

Rigorous analyses of these complex propagation problems necessitate the use of complete electromagnetic field expansions in three dimensions, the imposition of exact boundary conditions and the application of precise analytical procedures. The complete modal expansion of the horizontally and vertically polarized electromagnetic fields (TE and TM) consists of the radiation term, the lateral wave term as well as the trapped waveguide modes. The tangential components of the electric and magnetic fields must be continuous at each of the interfaces of the irregular stratified media. Since the field expansions do not necessarily converge uniformly on the irregular boundaries of the stratified media, Green's theorems should be used to avoid interchanging orders of integration (summation) and differentiation.

The above "full wave" procedures are used to convert Maxwell's equations into sets of generalized telegraphists' equations for the forward and backward propagating wave amplitudes.

Depending upon the location and the performance of the transmitter and the receiver, the propagation environment between them and the frequency of operation, it is necessary to extract only those terms of the complete field expansions that contribute most significantly to the received signals. Thus, if the antennas directly illuminate the ionospheric or terrain irregularities that are remotely sensed, these irregularities can be characterized by a  $2 \times 2$  differential scattering matrix (that accounts for the like- and the cross-polarized scattering radiation fields) for a rough surface differential element. If the remotely sensed irregularities are not directly illuminated by the antennas (beyond the horizon), the scattering phenomenon is characterized by the waveguide mode transmission and reflection scattering coefficients. If the transmitting or receiving antennas are embedded in the earth's crust for instance, it is necessary to consider the scattered lateral waves (associated with the phenomenon of total internal reflection) or the scattered surface waves (associated with the poles of the Fresnel reflection coefficients).

## 1. INTRODUCTION

In Section 2 of this paper, we describe the full wave technique developed to investigate propagation in inhomogeneous anisotropic media such as the ionosphere. The elements of the

permittivity tensor that characterize the medium are functions of position due to the spatial fluctuations in the density of the free electrons and ions of the medium and/or variations in the direction or intensity of the earth's magnetic field.

In regions of critical coupling between the up-going and down-going, ordinary and extraordinary waves, generalized characteristic functions are used to obtain analytical expressions for the electric- and the magnetic-field components. The resulting equations for the coupled wave amplitudes are solved numerically for the reflection and transmission coefficients.

In Section 3, we present the full wave solution to problems of propagation in the earth ionosphere waveguide. These solutions, which account for the earth's curvature, can be applied to problems of propagation over large distances. Thus for these (over the horizon) propagation paths, the transmitter and the receiver are not along a line of sight. Maxwell's equations are reduced to sets of first order coupled equations for the forward and backward travelling mode amplitudes (generalized telegraphists' equations). The mode coupling is due to fluctuations in the effective height of the ionosphere or the earth's ground/sea surface height. The Runge Kutta method is used to numerically solve the discrete set of coupled differential equations. The spurious mode amplitudes together with their propagation coefficients determine the observed fluctuations in the amplitude of the fields due to ionospheric perturbations along the propagation path.

In Section 4, it is assumed that the radar footprint on the remotely sensed random rough surface is visible at the observation point. In this case, the scattered field is expressed completely in terms of the radiation fields, the lateral waves and the surface waves supported by the propagation medium. When the observation point is in the far field, the scattered radiation fields can be used to derive the bistatic like- and cross-polarized radar scatter cross sections, which contain information regarding the remotely sensed parameters of the random rough surface. Since the full wave solutions account for both specular point scatter as well as Bragg scatter in a unified self-consistent manner, it is not necessary to employ two-scale models of the random rough surface. The full wave computer codes for the scattering cross sections contain only measurable ground-truth data (such as, the surface height and slope joint probability density function and the permeability and permittivity of the media). No scaling or normalization factors and no effective media parameters are introduced in these computer codes. Thus, the inverse problem of remotely sensing the propagation environment, using the full wave solutions for the backscatter cross sections or the bistatic cross sections, does not involve any artificial curve fitting parameters. Numerical solutions for the single- and the multiple-scatter cross sections are obtained in terms of multi-dimensional integrals (not integral equations).

## 2. PROPAGATION IN INHOMOGENEOUS ANISOTROPIC MEDIA

Consider an inhomogeneous (horizontally stratified) magnetic-ionic (anisotropic) medium bound on both sides by free

space. (See Fig. 5) The medium is characterized by a  $3 \times 3$  susceptibility matrix of  $M$  whose elements  $M_{\alpha\beta}(\alpha, \beta = x, y, z)$  are functions of position due to fluctuations in the density of the free electrons and ions and/or variations in the direction or intensity of the earth's magnetic field. The direction of the incident wave normal in free space (below the magnetic-ionic medium) is given by the unit vector

$$\hat{n} = s\hat{a}_x + c\hat{a}_y \quad (1)$$

where

$$s = \sin \theta \quad \text{and} \quad c = \cos \theta \quad (2)$$

and  $\theta$  is the angle of incidence. Maxwell's equations for the transverse  $(x, y)$  electromagnetic field components can be expressed in matrix form as follows: (Budden 1962, Bahar 1976)

$$de/dv \equiv e' = Te \quad (3)$$

in which the independent dimensionless variable  $v$  is

$$v = -ikz, \quad d/dv = 1/(-ikdz) \quad (4)$$

and  $k = \omega(\mu_0\epsilon_0)^{1/2}$  is the free space wave number. An  $\exp(i\omega t)$  time dependence of the fields is assumed throughout this work. The dimension of the elements of the  $4 \times 1$  column matrix  $e$  is volts/meter.

$$e = \begin{pmatrix} E_x \\ -E_y \\ H_x \\ H_y \end{pmatrix} \quad (5)$$

In (5)  $E_x$  and  $E_y$  are components of the electric field while  $H_x$  and  $H_y$  are equal to the free space impedance  $\eta_0 = (\mu_0/\epsilon_0)^{1/2}$  times the corresponding components of the magnetic field. The elements  $T_{ij}$  of the  $4 \times 4$  dimensionless matrix  $T$ , which are related to the susceptibility matrix  $M$  are in general also functions of  $v$ .

To facilitate the solution to equation (3), the following linear transformation is introduced

$$e = Sf \quad (6)$$

where the  $4 \times 1$  column matrix  $f$  is the new dependent variable and  $S$  is a  $4 \times 4$  transformation matrix. Thus (3) transforms to

$$f' = S^{-1}(TS - S')f \quad (7)$$

The standard procedure is to determine  $S$  such that

$$S^{-1}TS = D \quad (8)$$

where  $D$  is a  $4 \times 4$  diagonal matrix whose elements are the four characteristic values  $q_i$  of  $T$ . Thus if  $I$  is the  $4 \times 4$  identity matrix

$$|T - q_i I| = \text{determinant of } (T - q_i I) = 0 \quad (9)$$

For the special case when  $T$  is a constant matrix (homogeneous media)  $S' = 0$  and the solutions to (7) are the characteristic functions

$$f_i = f_{i0} \exp\{q_i(v - v_0)\} \quad (10)$$

where  $f_{i0} = f_i(v_0)$  is a constant. For a homogeneous (cold) anisotropic plasma, the four characteristic functions  $f_i$  correspond to the four characteristic waves, the upward and the downward travelling ordinary and extraordinary waves and the four characteristic vectors  $S^i$  that satisfy

$$TS^i = q_i S^i \quad (11)$$

are the four columns of the transformation matrix  $S$

Difficulties in employing the standard procedures to solve (7) using (8) lie in critical coupling regions where there is strong coupling between two or more of the four characteristic waves. In these regions, two or more characteristic values  $q_i$  merge, and the transformation matrix becomes singular ( $S^{-1}$  does not exist). The characteristic vectors do not form a basis for the complete expansion of the fields.

For these interesting cases (which are associated with strong reflections from the ionosphere), Budden used transformation matrices that do not diagonalize the coefficient matrix  $T$ . Thus, approximate solutions to the problem are obtained by solving differential equations of second order.

In this work, non-singular transformation matrices are introduced such that the original set of differential equations are converted into sets of equations for generalized characteristic functions, that can be more readily resolved either analytically or numerically in regions of critical coupling (Bahar 1976, Bahar and Agrawal 1979a). Thus for regions of the media where two characteristic values merge, let

$$v = v_0, \quad T(v_0) = T_0 \quad \text{and} \quad q_3 = q_4 \quad (12)$$

If there are two independent characteristic vectors  $S^3$  and  $S^4$  corresponding to the characteristic values  $q_3 = q_4$ , we proceed in the standard manner (8). If not, in this region we define generalized characteristic values

$$\Delta_i = q_i; \quad i = 1, 2, 3 \quad (13)$$

and

$$\Delta_4 = q_4 + (1/v) \quad (14)$$

The first three characteristic vectors  $S^i$  (columns of the transformation matrix  $S$ ) are defined in the standard manner (11). However, the fourth is defined as the generalized characteristic vector that satisfies the equation

$$(T_0 - I\Delta_4)S^4 = S^{4'} \quad (15)$$

The solution to (15) is

$$S^4 = \left( \frac{A^{14}}{t} + \frac{A^{24}}{t^2} \right) t \quad (16)$$

in which  $A^{14}$  and  $A^{24}$  are solutions to the following equations

$$(T_0 + Iq_4)A^{14} = 0 \quad \text{and} \quad (T_0 - Iq_4)A^{24} = A^{14} \quad (17)$$

Since it is assumed in (12) that  $q_3 = q_4$ ,  $A^{14}$  and  $S^3$  are associated with the same characteristic value, thus, they can be chosen to be equal.

$$A^{14} = S^3 \quad (18)$$

However  $A^{24}$  is a generalized characteristic vector of rank two associated with the characteristic value  $q_4$  of multiplicity two. It can be shown that the three characteristic vectors  $S^i$  ( $i = 1, 2, 3$ ) and the generalized characteristic vector  $A^{24}$  form a set of four linearly independent vectors (Friedman 1956, Bronson 1969, Brogan 1974). Thus a transformation matrix can be found such that

$$S^{-1}(T_0 S - S') = \Delta \quad (19)$$

where

$$S = (S^1 S^2 S^3 S^4) + (1/v)(000A^{24}) \equiv S_0 + S_1/v \quad (20)$$

and  $\Delta$  is the diagonal matrix whose elements are given by (13) and (14). In (20)  $S_0$  is a singular matrix but  $S$  is not singular and  $S^{-1}$  exists. The characteristic wave  $f_4(v)$  corresponding to the generalized characteristic value  $\Delta_4$  (14) is

$$f_4(v) = f_{40} \exp \int_{v_0}^v \Delta_4 dv = f_{40} \left( \frac{v}{v_0} \right) \exp [q_4(v - v_0)] \quad (21)$$

The above solution can be readily generalized to the case in which the matrix  $T_0$  has two characteristic values of multiplicity two. In general, where two or more roots merge we can find solutions to (19) as follows (Bahar 1976, Bahar and Agrawal 1979a). Associated with the characteristic value  $q_i$  of multiplicity  $m$ , there are chains of generalized characteristic values of length  $\ell_i$

$$\Delta_{i+p-1} = q_i + \frac{p-1}{v}, \quad p = 1, 2, \dots, \ell_i \quad (22)$$

where

$$\sum_j \ell_j = m \quad (23)$$

The columns of the transformation matrix  $S$  associated with the chain of length  $\ell_i$  are the generalized characteristic vectors  $A^r$  of rank  $r$ . Thus the generalized characteristic vectors

$$S^{i+p-1} = v \sum_{r=1}^{\ell_i} \frac{A^r}{(p-r)! v^r}, \quad p = 1, 2, \dots, \ell_i \quad (24)$$

are functions of the variable  $v$  (4) (Bahar 1976). In (24)

$$(T_0 - I q_i) A^{1i} = 0 \quad (25)$$

and

$$(T_0 - I q_i) A^r = A^{r-1i}, \quad r = 2, \dots, p \quad (26)$$

Thus

$$(T_0 - I q_i)^p A^p = 0 \quad (27)$$

For the special case  $T = T_0$ , the characteristic waves  $f_1, f_{i+1}, \dots, f_{i+\ell_i-1}$  associated with the chain of length  $\ell_i$  are (for  $p = 1, 2, \dots, \ell_i$ ) given by

$$f_{i+p-1}(v) = f_{i+p-1}(v_0) \left( \frac{v}{v_0} \right)^{p-1} \exp [q_i(v - v_0)] \quad (28)$$

Thus using these non-singular transformation matrices  $S$  the coupled differential equation (7) can be solved analytically (generalized WKB solutions) or numerically (Bahar and Agrawal 1979a) even for critical coupling regions of the inhomogeneous anisotropic (magnetic-ionic) media

It is sometimes convenient to characterize the boundary of an anisotropic medium by a normalized surface impedance dyad  $Z$  as follows

$$\begin{pmatrix} - & E_y^H \\ E_x^V \end{pmatrix} = \begin{pmatrix} Z^{HH} & Z^{HV} \\ Z^{VH} & Z^{VV} \end{pmatrix} \begin{pmatrix} H_x^H \\ H_y^V \end{pmatrix} \quad (29)$$

Thus these solutions can also be used to examine the validity of imposing approximate impedance boundary conditions.

### 3. PROPAGATION IN AN IRREGULAR MODEL OF THE EARTH-IONOSPHERE WAVEGUIDE

When the transmitter and the receiver are at very large distances from each other and the propagation problem can be approximated by a two dimensional geometry, either a ( $z$  independent) cylindrical model (see Fig. 6) or a ( $\phi$  independent) spherical model (see Fig. 7) can be assumed (Bahar 1970, 1980). However in the general case (see Fig. 4), it is necessary to employ complete three-dimensional full wave expansions of the electric and magnetic fields. Thus (Bahar and Fitzwater 1983a,b), the transverse ( $r, \phi$ ) components of the electric and magnetic fields are expressed as follows.

$$\vec{E}^T(r) = \sum_{\nu, m} [E^V(\nu, \theta, m) \vec{e}_r^V]$$

$$+ E^H(\nu, \theta, m) \vec{e}_r^H] \quad (30)$$

in which the electric field transforms are given by

$$E_{\nu m}^P \equiv E^P(\nu, \theta, m) = \int_0^\infty \int_0^{2\pi} E^T(\vec{r}) \cdot (\vec{h}_P^T \times \vec{a}_\theta) r \sin \theta dr d\phi$$

$$P = V, H \quad (31)$$

and

$$\vec{H}^T(\vec{r}) = \sum_{\nu, m} [H^V(\nu, \theta, m) \vec{h}_T^V + H^H(\nu, \theta, m) \vec{h}_T^H] \quad (32)$$

in which

$$H_{\nu m}^P \equiv H^P(\nu, \theta, m) = \int_0^\infty \int_0^{2\pi} H^T(\vec{r}) \cdot (\vec{a}_\theta \times \vec{h}_P^T) r \sin \theta dr d\phi$$

$$P = V, H \quad (33)$$

In (30)-(33) the symbol  $\sum_\nu$  denotes the complete spectrum of spherical waves including a continuous spectrum (integration along the  $Im(\nu)$  axis) and discrete set of waveguide modes ( $\nu_n$  are solutions to the nodal equation). The basis functions  $e_r^P, h_r^P$  and the reciprocal basis functions  $\vec{e}_r^T, \vec{h}_r^T$  satisfy the biorthogonal relationships

$$\int_0^\infty \int_0^{2\pi} \vec{e}_r^P \cdot (\vec{h}_Q^T \times \vec{a}_\theta) r \sin \theta dr d\phi = \delta_{PQ} \Delta(\nu, \nu') \delta_{m, m'} \quad (34)$$

and

$$\int_0^\infty \int_0^{2\pi} \vec{h}_r^P \cdot (\vec{a}_\theta \times \vec{e}_Q^T) r \sin \theta dr d\phi = \delta_{PQ} \Delta(\nu, \nu') \delta_{m, m'} \quad (35)$$

in which  $\delta$  and  $\Delta$  are related to the Kronecker and Dirac delta functions. The vector basis functions are constructed from sets of  $r$  dependent scalar functions  $\psi_\nu^{DP}, \psi_\nu^{UP}$  ( $P = V, H$ ) for the vertically- and horizontally-polarized waves and the functions  $\exp(\pm im\phi)$ . Using these complete field expansions, the biorthogonal relationships and on imposing exact boundary conditions (the electric and magnetic field components tangent to the boundaries are continuous) Maxwell's equations are converted into rigorous sets of coupled first order differential equations for the forward ( $+\theta$ ) and backward ( $-\theta$ ) propagating wave amplitudes  $a_{\nu m}^P$  and  $b_{\nu m}^P$ , respectively. They are given by linear combinations of the field transforms  $E_{\nu m}^P$  and  $H_{\nu m}^P$  (Bahar and Fitzwater 1983b). Since the earth's crust is highly conducting, only the contributions associated with the discrete waveguide modes need to be considered. At large distances from the source and for  $kr_0 \gg 1$  ( $r_0$  is the radius of the earth), the propagation coefficients  $\beta_{\nu m}^\pm$  in the forward and backward directions are approximately the same  $\beta_{\nu m} \approx \nu$ . Similarly, the normalized wave impedance for the forward and backward propagating waves are the same. In these cases, the "generalized telegraphists' equations," (Schelkunoff 1955) for the forward and backward propagating wave amplitudes are

$$\frac{d a_{\nu m}^P}{d\theta} - j\nu a_{\nu m}^P = \sum_{Q, m'} [S_{PQ}^{AA} a_{\nu m'}^Q + S_{PQ}^{BB} b_{\nu m'}^Q] + A_{\nu m}^P \quad (36)$$

$$\frac{d b_{\nu m}^P}{d\theta} + j\nu a_{\nu m}^P = \sum_{Q, m'} [S_{PQ}^{AA} a_{\nu m'}^Q + S_{PQ}^{BB} b_{\nu m'}^Q] + B_{\nu m}^P \quad (37)$$

in which  $S_{PQ}^{\alpha\beta}$  are the transmission ( $\alpha \neq \beta$ ) and reflection ( $\alpha = \beta$ ) scattering coefficients and the subscripts ( $P, Q = V, H$ ) denotes the polarization of the incident ( $Q$ ) and scattered ( $P$ ) waves. The summation  $\sum_{\nu, m}$  is over the spectrum of the incident waves. The source transforms are  $A_{\nu m}^P$  and  $B_{\nu m}^P$ .

The generalized telegraphists' equations may be solved numerically using the Runge Kutta method (Abramowitz and Stegun 1964) subject to the appropriate boundary conditions for the mode amplitudes (Bahar 1970, 1980). From these solutions, one obtains the complete scattering matrix for the waveguide junction that characterizes the irregularities of the ionosphere effective height or the earth's surface.

Accurate solutions to the modal equations for the significant propagating modes in an irregular section of the earth's ionosphere waveguide are critical for obtaining numerical solutions to the propagation problem. The transcendental modal equation involves Bessel functions of complex order  $\nu$  and argument  $kr$ . It is necessary to find the complex roots  $\nu_n$  for the different modes as functions of the effective ionosphere height in the irregular earth-ionosphere waveguide. The algorithm that is used to evaluate these complex roots is described in detail in the literature (Bahar and Fitzwater 1981).

The ionosphere irregularities excite spurious modes that impact on the magnitude and the phase of the total field propagated to large distances from the transmitter. Thus, these analyses can be used either to predict the impact of ionospheric perturbations on navigation and positioning system, or they can be used to remotely sense these perturbations.

#### 4. SCATTERING AND DEPOLARIZATION BY TWO-DIMENSIONALLY ROUGH SURFACES

When the radar footprint on the remotely sensed random rough surface is visible at the observation point, the expansion of the electromagnetic fields in terms of the earth ionosphere waveguide modes is not used since it would be necessary to account for a very large number of coupled modes. In this case, the transverse components of the electromagnetic field  $\vec{E}_T$  and  $\vec{H}_T$  are expressed completely in terms of the vertically- and horizontally-polarized field transforms  $E^P$  and  $H^P$  for the radiation fields, the lateral waves and the surface waves supported by the propagation medium (Brekhovskikh 1960, Bahar 1973a,b)

$$\vec{E}_T(\vec{r}) = \sum_{\nu} \int_{-\infty}^{\infty} [E^V(z, v, w) \vec{e}_T^V + E^H(z, v, w) \vec{e}_T^H] dw \quad (38)$$

$$E^P(z, v, w) = \int_{-\infty}^{\infty} \vec{E}_T(\vec{r}) \cdot (\vec{h}_P^T \times \vec{a}_z) dy dz, \quad P = V, H \quad (39)$$

$$\vec{H}_T(\vec{r}) = \sum_{\nu} \int_{-\infty}^{\infty} [H^V(z, v, w) \vec{h}_T^V + H^H(z, v, w) \vec{h}_T^H] dw \quad (40)$$

$$H^P(z, v, w) = \int_{-\infty}^{\infty} \vec{H}_T(\vec{r}) \cdot (\vec{a}_z \times \vec{e}_P^T) dy dz, \quad P = V, H \quad (41)$$

in which the symbol  $\sum_{\nu}$  denotes summation over the complete wave spectrum while  $\vec{e}_T^P$ ,  $\vec{h}_T^P$ , and  $\vec{e}_P^T$ ,  $\vec{h}_P^T$  are the vector basis and reciprocal basis functions. They satisfy biorthogonal relationships similar to (34) and (35). On following the same procedures outlined in Section (3), Maxwell's equations are converted into sets of generalized telegraphists' equations for the forward and backward travelling wave amplitudes  $a^P$  and  $b^P$  ( $P = V, H$ ) that are linearly related to the electric and magnetic field transforms. These generalized telegraphists' equations are similar to (36) and (37) except that in this case the wave spectrum for the radiation fields and the lateral waves are represented by integrals rather than a discrete sum. The observation point is assumed to be in the far field

scattered by the surface irregularities, thus only the radiation field is considered here.

For plane wave excitations, the full wave solutions for the electromagnetic radiation fields diffusely scattered from two-dimensionally rough surfaces

$$f(x_s, y_s, z_s) = y_s - h(x_s, z_s) = t, \\ -L \leq x_s \leq L, -t \leq z_s \leq t$$

and

$$h(x_s, z_s) = 0, \quad |x_s| \geq L, \quad |z_s| \geq t \quad (42)$$

are expressed as follows in matrix notation

$$G_s^I = \left( \frac{k_0}{2\pi i} \right)^2 \iint \left[ \frac{S_z p'_z h_z + S_z p'_z h_z}{p'_y v'_y} \right] \exp(-i \vec{k}_0 \cdot \vec{r}) \\ \exp[i \vec{v}' \cdot \vec{r}_s] dx_s dz_s \frac{dk'_{0y} dk'_{0z}}{k'_{0z}} G^I \quad (43)$$

in which  $G_s^I$  and  $G^I$  are  $2 \times 1$  matrices whose elements are the vertically and horizontally polarized components of the diffusely scattered and incident fields  $E^{P'}_s$  and  $E^{P'}_i$  ( $P = V, H$ ), respectively. The integration is over the surface variables  $x_s, z_s$  and the wave vector variables  $k'_{0y}, k'_{0z}$  for the radiation fields (Bahar 1973a,b, 1974).

The  $2 \times 2$  scattering matrix  $S$  is given by (Bahar and Rajan 1979, Bahar 1981)

$$S_u(\vec{k}', \vec{k}) = 2 \cos \theta'_0 \cos \theta_0 R_u(\vec{k}', \vec{k}), \quad (u = x, z) \quad (44)$$

The elements of the matrix  $R_u$  are

$$R_u^{VV} = \frac{[\mu_r C'_1 C'_1 C_u - S'_0 S'_0] (1 - 1/\epsilon_r) + (1 - \mu_r) C_u}{(C'_0 + \eta_r C'_1)(C'_0 + \eta_r C'_1)} \quad (45)$$

$$R_u^{HH} = \frac{[\epsilon_r C'_1 C'_1 C_u - S'_0 S'_0] (1 - 1/\mu_r) + (1 - \epsilon_r) C_u}{(C'_0 + C'_1/\eta_r)(C'_0 + C'_1/\eta_r)} \quad (46)$$

$$R_u^{HV} = \frac{-D_u n_r [(1 - 1/\mu_r) C'_1 - (1 - 1/\epsilon_r) C'_1]}{(C'_0 + C'_1/\eta_r)(C'_0 + \eta_r C'_1)} \quad (47)$$

$$R_u^{VH} = \frac{D_u n_r [(1 - 1/\epsilon_r) C'_1 - (1 - 1/\mu_r) C'_1]}{(C'_0 + \eta_r C'_1)(C'_0 + C'_1/\eta_r)} \quad (48)$$

in which the wave vectors in the scatter and incident directions are

$$\vec{k}'_0 \equiv k_0 \vec{n}' = k_0 [\sin \theta'_0 \cos \phi'_0 \vec{a}_x + \cos \theta'_0 \vec{a}_y + \sin \theta'_0 \sin \phi'_0 \vec{a}_z] \quad (49)$$

$$\vec{k}_0 \equiv k_0 \vec{n} = k_0 [\sin \theta_0 \cos \phi_0 \vec{a}_x - \cos \theta_0 \vec{a}_y + \sin \theta_0 \sin \phi_0 \vec{a}_z] \quad (50)$$

and (Bahar and Rajan 1979)

$$C_x = \frac{S'_0 \cos \phi' + S'_0 \cos \phi}{S'_0 \cos \phi' + S'_0 \cos \phi}, \quad C_z = \frac{S'_0 \sin \phi' + S'_0 \sin \phi}{S'_0 \sin \phi' + S'_0 \sin \phi} \quad (51)$$

$$-\frac{p'_z v'_z D_x}{p'_y v'_y} = \sin \phi' \cos \phi' - \frac{S'_0}{S'_0} \sin \phi' \cos \phi', \\ \frac{p'_z v'_z D_z}{p'_y v'_y} = \sin \phi' \cos \phi' - \frac{S'_0}{S'_0} \sin \phi' \cos \phi' \quad (52)$$

Note that in (43), the coefficient of  $h_z$  can be obtained directly from the coefficient of  $h_x$  on making the following transformations:  $k'_x \rightarrow -k'_x$  and  $k'_z \rightarrow -k'_z$  (Bahar 1974).

In (45) through (48)  $\epsilon_r = \epsilon_1/\epsilon_0$ ,  $\mu_r = \mu_1/\mu_0$ ,  $n_r = (\epsilon_r \mu_r)^{1/2}$  and  $\eta_r = (\mu_r/\epsilon_r)^{1/2}$  are the relative permittivity, permeability, refractive index and intrinsic impedance of the medium below the rough interface (42). The sines and cosines of the angles  $\theta_0$  and  $\theta_1$  above and below the rough interface (denoted by  $S_0, S_1$  and  $C_0, C_1$ ) are related through Snell's law.

The vectors  $\vec{r}'$  and  $\vec{r}''$  are given by

$$\vec{r}' = \vec{k}_0 + \vec{k}_0', \quad \vec{r}'' = \vec{k}_0 - \vec{k}_0' \quad (53)$$

and  $\vec{r}_s$  and  $\vec{r}$  are position vectors from the origin to points on the rough surface and to the observation point respectively.

$$\vec{r}_s = x_s \vec{a}_x + h_s \vec{a}_z, \quad \vec{r} = x \vec{a}_x + y \vec{a}_y + z \vec{a}_z = r \vec{n} \quad (54)$$

The partial derivatives of  $h(x_s, z_s)$  with respect to  $x_s$  and  $z_s$  are  $h_x$  and  $h_z$  respectively. To obtain (43) from the "Generalized Telegraphists' Equations" (Bahar 1973a,b, 1974), the slopes are assumed to be small and multiple scatter is ignored. The full wave solutions derived for unbounded, irregular multilayered structures (Bahar 1973a,b) are not based on the approximate surface impedance boundary conditions.

On integrating (43) by parts (Bahar and Rajan 1979, Bahar 1981, Bahar 1988, Bahar and Fitzwater 1988b), it can be expressed as follows

$$G_s^f = \left( \frac{k_0}{2\pi i} \right)^2 \iint S(\vec{k}', \vec{k}) \exp(-i\vec{k}_0' \cdot \vec{r}) \left[ \frac{\vec{r}_s' \cdot \vec{r}_s' + \vec{r}_s' \cdot \vec{r}_s'}{\vec{r}_s' \cdot \vec{r}_s'} \right] \frac{[\exp(i\vec{r}' \cdot \vec{r}_s) - \exp(i\vec{r}'' \cdot \vec{r}_s)]}{\vec{r}_s'} \frac{d\vec{k}_0' d\vec{k}_0}{k_{0x}'} G^i \quad (55)$$

In (55), it is assumed that  $h(x_s, z_s)$  vanishes on the boundaries of the surface (42) and

$$\vec{r}_s = x_s \vec{a}_x + z_s \vec{a}_z = \vec{r}_s - h_s \vec{a}_y. \quad (56)$$

Since  $\vec{r}' \cdot \vec{r}'' = 0$  it follows that

$$-(\vec{r}_s' \cdot \vec{r}_s' + \vec{r}_s' \cdot \vec{r}_s')/\vec{r}_s' \cdot \vec{r}_s' = 1. \quad (57)$$

The expression for the surface element scattering matrix  $S(\vec{k}', \vec{k})$  are given by (44) through (48) with the exception that  $C_u$  and  $D_u$  are replaced by  $\cos(\phi' - \phi)$  and  $\sin(\phi' - \phi)$ , respectively.

Note that the results in (55) are in complete agreement with earlier work (Bahar and Rajan 1979, Bahar 1981) in which it is assumed that the vector  $\vec{n}$  normal to the rough surface is restricted to the  $xy$  plane ( $h_z = 0$ ). This is because the restriction does not constrain the unit vector  $\vec{n}$  to lie in the scatter plan (normal to  $\vec{k}_0 \times \vec{k}_0'$ ).

For the analysis leading to the generalized telegraphists' equations, the vector basis functions used are related to a pair of scalar basis functions for the horizontally and vertically polarized waves  $\psi^H$  and  $\psi^V$  that satisfy the appropriate boundary conditions at an interface between any two media characterized by their permittivity  $\epsilon$  and permeability  $\mu$ . The complete field expansions consist of the radiation fields, the lateral waves as well as the surface waves. For these general two media cases, the reciprocal basis functions are not the complex conjugates of the basis functions  $\psi^H$  and  $\psi^V$  (Bahar 1973a,b).

The second term in (55)  $G_D^f$  can be integrated with respect to  $x_s$  and  $z_s$ . For  $L \rightarrow \infty$  and  $l \rightarrow \infty$  the integrations yield the Dirac delta functions  $\delta(\vec{r}_s')\delta(\vec{r}_s'')$  (Bahar 1988, Bahar and Fitzwater 1988b). Thus this term  $G_D^f$  accounts for the specularly reflected plane wave. The total full wave solution  $G^f$  (55) includes the diffusely scattered field  $G_s^f$  as well as the specularly reflected field  $G_D^f$  for infinitely large surfaces. When the observation point is at a very large distance from the rough surfaces ( $k_{0x} > k_0 L > 1$  and  $k_{0y} > k_0 l > 1$ ), the integration with respect to the scatter wave vector variables ( $k_{0x}', k_{0y}'$ ) can be performed analytically using the stationary phase method. Thus if the observation point is in the direction

$$\vec{n}' = \vec{r}/r = \sin \theta_0' \cos \phi' \vec{a}_x + \cos \theta_0' \vec{a}_y + \sin \theta_0' \sin \phi' \vec{a}_z, \quad (58)$$

the diffuse far fields scattered from the rough surface are

$$G_s^f = G_0 \int_{-L}^L \int_{-l}^l S(\vec{k}', \vec{k}) [\exp(i\vec{r} \cdot \vec{r}_s) - \exp(i\vec{r}'' \cdot \vec{r}_s)] dx_s dz_s \quad (59)$$

The expression for  $S(\vec{k}', \vec{k})$  in (59) is the same as the expression for  $S(\vec{k}', \vec{k})$  in (55) except that the scatter wave vector  $\vec{k}'$  is replaced by  $\vec{k}' = k_0 \vec{n}'$  (58). Furthermore

$$\vec{r} = k_0(\vec{n}' - \vec{n}) \quad (60)$$

and

$$G_0 = k_0^2 \exp[-ik_0 r]/2\pi i r. \quad (61)$$

When the integrations with respect to  $x_s$  and  $z_s$  are performed, the term  $G_D^f$  is shown to be the flat surface diffraction field which is proportional to  $(4Ll/v_x L v_z l) \sin v_x L \sin v_z l$ . The expression for the diffraction term  $G_D^f$  is the same as the expression for the total field  $G^f$  except that  $\vec{r}_s$  in  $G^f$  is replaced by  $\vec{r}_i$  in  $G_D^f$  (56). Thus for  $h(x_s, z_s) = 0$  they are identical and  $G_s^f = 0$ . The physical interpretation of the diffraction field for layered media has also been presented (Bahar and Fitzwater 1988b).

The diffraction term is not included in Rice's (1951) small perturbation scattered field. For surfaces with small Rayleigh rough parameters  $\beta = 4k_0^2 < k^2 < 1$ , it may seem proper to expand the exponent  $\exp(i\vec{r}_s \cdot \vec{r})$  appearing in  $G^f$  in a Taylor series. In this case, the first term in the integrand of (59), which is proportional to  $i\vec{r}_s \cdot \vec{r}$ , is precisely equal to Rice's (1951) first order small perturbation solution. However in view of a convergence problem for surfaces with "very small slopes," this is not done here (Bahar 1991). If the diffracted field  $G_D^f$  is very small in the non-specular direction, it is not necessary to add it to the full wave diffuse scatter solution  $G_s^f$  to obtain the total scattered field in the non-specular direction. Since the contributions to  $G_s^f$  vanish from portions of the surface where  $h(x_s, z_s) = 0$  ( $\vec{r}_s = \vec{r}_i$ ), it is possible to evaluate  $G_s^f$  assuming unbounded plane wave excitations. This is not so for the evaluation of the total scattered field  $G^f$  since it contains the diffraction term.

To remove the small slope restriction used to derive (59), the surface element (differential) scattering matrix  $S(\vec{k}', \vec{k})$  (which accounts for the sources induced on the rough surface by the incident field) is replaced by the following scattering matrix (Bahar 1991).

$$S(\vec{k}', \vec{k}) \Rightarrow T^f S_n(\vec{k}', \vec{k}) T^i = T^f 2C_{0n}^i C_{0n}^f R_n(\vec{k}', \vec{k}) T^i \quad (62)$$

To obtain the quantity  $S_n$  from  $S$ , the unit vector normal to the mean surface  $\bar{a}_y$  is replaced by the unit vector normal to the actual surface (Bahar 1981)

$$\bar{n} = (-h_x \bar{a}_x + \bar{a}_y - h_z \bar{a}_z) / (1 + h_x^2 + h_z^2)^{1/2}. \quad (63)$$

Thus the angles of incidence and scatter with respect to the fixed, reference coordinate system  $(\bar{a}_x, \bar{a}_y, \bar{a}_z)$  are replaced by the angles of incidence and scatter in the local coordinate system  $(\bar{a}_1, \bar{a}_2 = \bar{n} \times \bar{a}_1)$  and the fixed planes of incidence and scatter (normal to  $\bar{n}^i \times \bar{a}_y$  and  $\bar{n}^f \times \bar{a}_y$ ) are replaced by the local planes of incidence and scatter (normal to  $\bar{n}^i \times \bar{n}$  and  $\bar{n}^f \times \bar{n}$ ). The surface element scattering matrix  $S_n$  is invariant to coordinate transformations. The scattering coefficients  $R_{nq}^{PP}$  are assumed to vanish for  $C_{0n}^i = -\bar{n}^i \cdot \bar{n} \leq 0$  and  $C_{0n}^f = \bar{n}^f \cdot \bar{n} \leq 0$  corresponding to self shadow only. The transformation matrix  $T^i$  transforms the vertically and horizontally polarized waves in the fixed (reference) coordinate system to the corresponding vertically and horizontally polarized waves in the local coordinate system while the transformation matrix  $T^f$  transforms the vertically and horizontally polarized waves of the local coordinate system back to vertically and horizontally polarized waves of the reference coordinate system (Bahar 1981). In addition, the rough surface element  $dx, dz$ , in (59) is replaced by

$$dA = dx, dz / (\bar{n} \cdot \bar{a}_y). \quad (64)$$

Note that for the specular direction with respect to the reference coordinate system

$$\bar{n}^f = \bar{n}^i = \bar{n} = 2(\bar{n}^i \cdot \bar{a}_y) \bar{a}_y \quad (65)$$

and the matrix  $R$  reduces to

$$R = \begin{pmatrix} R^V & 0 \\ 0 & R^H \end{pmatrix} \quad (66)$$

in which  $R^V$  and  $R^H$  are the Fresnel reflection coefficient for the vertically and horizontally polarized waves. The corresponding expression for  $R_{nq}^{PP}$  in the local coordinate system reduces to the Fresnel reflection coefficient  $R^P(\theta_0^i)$  at the stationary phase points where

$$\bar{n} \rightarrow \bar{n}_s = \bar{v} / |\bar{v}|. \quad (67)$$

At these specular points, the local angles of incidence  $\theta_0^i$  and scatter  $\theta_0^f$  are given by

$$\cos \theta_0^i = \cos \theta_0^f = -\bar{n}^i \cdot \bar{n}_s = \bar{n}^f \cdot \bar{n}_s. \quad (68)$$

The corresponding expressions for  $R_{nq}^{PQ}$  ( $P \neq Q$ ) vanish (Bahar 1981).

The transformations prescribed in (62) were introduced (Bahar 1981) since it was shown repeatedly by the author that the iterative solutions to the generalized telegraphists' equations are significantly improved whenever basis functions that locally satisfy the boundary conditions were used. Moreover, the resulting full wave solutions are invariant to coordinate transformations. These transformations, however, do not account for multiple scatter. The full wave multiply scattered fields are accounted for either by numerically solving the generalized telegraphists' equations or by replacing the (primary) incident field at the surface  $G^i \exp(-i\bar{k}^i \cdot \bar{r}_s)$  (43) by the total field impressed upon the rough surface (Bahar and El-Shenawee 1991). The expression for the single scattered fields presented here account for, in a self-consistent manner, both (high-frequency) specular point scattering (Beckmann and Spizzichino 1963) as well as (low-frequency) polarization dependent Bragg scattering predicted by Rice (1951), using a small perturbation approach.

In earlier work, the correlation between the height and

the slopes were neglected; and it was assumed that  $p(\bar{n}_1, \bar{n}_2) \rightarrow \delta(\bar{n}_1 - \bar{n}_2)p(\bar{n})$ . Thus for one-dimensionally rough surfaces, the two-point joint probability density function was approximated as follows (Bahar 1987):

$$p(h_1, h_2, h_{x1}, h_{x2}) \rightarrow p(h_1, h_2) \delta(h_{x1} - h_{x2}) p(h_x) \quad (69)$$

Furthermore in the earlier analysis, the diffraction term  $G_D^f$  was added to the full wave diffuse scattering term  $G_D^i$  to yield the total scattered field  $G^f$ . The incoherent scattering cross sections for the one-dimensional surfaces are therefore expressed as follows:

$$\langle \sigma_f^P \rangle = I^P Q \quad (70)$$

in which

$$I^P = \int_{-\infty}^{\infty} f^P(\bar{n}_1, \bar{n}_2) p(h_x) dh_x \quad (71)$$

where  $f^P$  is the product of the scattering coefficients at two points on the surface

$$f^P(\bar{n}_1, \bar{n}_2) = \frac{S_{n1}^{PP}}{\bar{n}_1 \cdot \bar{a}_y} \cdot \frac{S_{n2}^{PP}}{\bar{n}_2 \cdot \bar{a}_y} U(-\bar{n}^i \cdot \bar{n}_1) U(\bar{n}^f \cdot \bar{n}_1) U(-\bar{n}^i \cdot \bar{n}_2) U(\bar{n}^f \cdot \bar{n}_2) \quad (72)$$

in which the unit step functions  $U(\cdot)$  account for self shadow and

$$Q = k_0^2 \int [\chi_2(v_y, -v_y) - |\chi(v_y)|^2] \frac{\exp(i v_x x_d)}{v_y^2} dx_d \quad (73)$$

in which  $\chi$  and  $\chi_2$  are the characteristic and joint characteristic functions of the surface height.

To obtain the first order small perturbation solution of Rice (1951), it is assumed in addition that  $p(h_x) \rightarrow \delta(h_x)$  and that the Rayleigh roughness parameter  $\beta = 4k_0^2 < h^2 < 1$ . Thus in this case

$$I_{SP}^P = f^P(\bar{a}_y, \bar{a}_y) \quad (74)$$

and

$$Q = k_0^2 |\chi|^2 \int_{-\infty}^{\infty} \langle h^2 \rangle C(x_d) \exp(i v_x x_d) dx_d = 2\pi k_0^2 |\chi|^2 W(v_x) \quad (75)$$

where  $W(v_x)$ , the surface height spectral density function is the Fourier transform of the surface height autocorrelation function  $\langle h_1 h_2 \rangle$ . For Gaussian correlation functions (57)

$$W(v_x) = \frac{\langle h^2 \rangle L_c}{2\sqrt{\pi}} \exp(-v_x^2 L_c^2 / 4). \quad (76)$$

For perfectly conducting surfaces

$$I_{SP}^P = \begin{cases} (2 \cos \theta_0^i \cos \theta_0^f \cos(\phi^f - \phi^i))^2 & P = H \\ 4(\cos(\phi^f - \phi^i) - \sin \theta_0^i \sin \theta_0^f)^2 & P = V. \end{cases} \quad (77)$$

To obtain the physical optics solution (Beckmann and Spizzichino, 1963) from the full wave solution, it is necessary to add the diffraction term  $G_D^f$  and to assume that the most significant contributions to the scattered field come from the neighborhood of the stationary phase (specular) points on the surface where  $\bar{n} \rightarrow \bar{n}_s$  (67) (Bahar 1981). Thus in (71)  $p(h_x) \rightarrow \delta(h_x + v_x/v_y)$  and  $I^P \rightarrow f^P(\bar{n}_s, \bar{n}_s)$ .

When slope/height correlations at two points on the rough surfaces are accounted for explicitly in the analysis, it can be shown (on ignoring self shadow) that for one dimensionally (Gaussian) random rough surfaces the (diffuse) scattering width is (Bahar 1991)

$$\begin{aligned}
\langle \sigma_{\epsilon}^P \rangle = & 2k_0 G_0^P \int_0^{2L} \left[ 1 - \frac{z_d}{2L} \right] \\
& \chi(z(\tau_y, -\tau_y)) \\
& [1 + G_1^P \{ \langle h_z^2 \rangle A - \tau_y^2 B^2 \}] \\
& - 2\chi(\tau_y) [1 + G_1^P \{ \langle h_z^2 \rangle A \}] \\
& + 1 + G_1^P \{ \langle h_z^2 \rangle A \} \cos(\tau_y z_d) dz_d \\
& - 2k_0 G_0^P G_1^P \int_0^{2L} \left[ 1 - \frac{z_d}{2L} \right] [\chi(z(\tau_y, -\tau_y)) - \chi(\tau_y)]^2 \\
& 2\tau_y B \sin(\tau_y z_d) dz_d \quad (75)
\end{aligned}$$

and on setting  $R(x_d) \rightarrow 0$  in (75) it follows that the coherent contribution is

$$\langle \sigma_{\epsilon}^P \rangle = 2k_0 L G_0^P \chi(\tau_y) - 1 \left( \frac{\sin \tau_y L}{\tau_y L} \right)^2. \quad (76)$$

In (76)

$$S_{\chi}^{PP}(\bar{u}, \bar{u}_y) = G^P(\bar{u}) = G^P(\bar{u}_y) + h_z G_x^P(\bar{u}_y) = G_0^P [1 + h_z G_1^P] \quad (80)$$

where  $G_x^P = \partial G^P / \partial h_z$ ,  $G_0^P = G^P(\bar{u}_y)$  and  $G_1^P = G_x^P(\bar{u}_y) / G^P(\bar{u}_y)$ . Furthermore

$$R(x_d) = \langle h_1 h_2 \rangle / \langle h^2 \rangle \quad (81)$$

is the surface height normalized autocorrelation function,

$$A(x_d) \equiv \langle h_1 h_2 \rangle / \langle h_z^2 \rangle = - \frac{dR}{dx_d} \langle h^2 \rangle \quad (82)$$

and

$$B(x_d) \equiv \langle h_1 h_{x2} \rangle = - \langle h_2 h_{x1} \rangle = - \frac{dR}{dx_d} \langle h^2 \rangle. \quad (83)$$

In the high frequency limit ( $\tau_y^2 < h^2 \gg 1$ ), the characteristic function  $\chi(\tau_y)$  becomes vanishingly small. In this case (78) and (79) may be approximated, and it can be shown that

$$\begin{aligned}
\langle \sigma_{\epsilon}^P \rangle = & \langle \sigma_{\epsilon}^P \rangle - \langle \sigma_{\epsilon}^{P'} \rangle \\
= & 2k_0 G_0^P \int_0^{2L} \chi_2(\tau_y, -\tau_y) \left[ 1 - 2G_1^P \frac{v_x}{v_y} + G_1^P \frac{v_x^2}{v_y^2} \right] \\
& \cos(v_x z_d) dz_d. \quad (84)
\end{aligned}$$

For the horizontally polarized backscatter cross sections

$$\begin{aligned}
G_0^{P2} \left( 1 - 2G_1^P \frac{v_x}{v_y} + G_1^P \frac{v_x^2}{v_y^2} \right) &= \cos^2 \theta (1 + 2 \tan^2 \theta + \tan^4 \theta) \\
&= \sec^2 \theta. \quad (85)
\end{aligned}$$

Thus in the high frequency limit, (78) is in agreement with the corresponding physical optics (specular point,  $h_x = -v_x/v_z \rightarrow \tan \theta$ ) results for the horizontally polarized backscattered waves (Beckmann and Spizzichino, 1963). Note that (84) cannot be used for near grazing angles at high frequencies since  $\chi(v_y) \rightarrow 1$ , and shadowing cannot be ignored at near grazing angles. Furthermore, for physical surfaces with  $h_{x\max}$  bounded, the probability that the surface contains stationary phase (specular) points is zero for  $\tan \theta > h_{x\max}$ . Thus the stationary phase approximations cannot be used at near grazing angles even in the high frequency limit ( $k_0^2 < h^2 \gg 1$ ).

In the low frequency limit ( $v_y^2 < h^2 \ll 1$ ) on retaining terms of first order in smallness (Rice 1951), (78) reduces to

$$\begin{aligned}
\langle \sigma_{\epsilon}^P \rangle \approx & 2k_0 G_0^{P2} \int_0^{2L} [\chi_2(v_y, -v_y) - \chi(v_y)]^2 \cos(v_x z_d) dz_d \\
\approx & 2k_0 G_0^{P2} \chi(v_y)^2 v_y^2 \int_{-\infty}^{\infty} \langle h_1 h_2 \rangle \cos(v_x z_d) dz_d
\end{aligned}$$

$$= 2k_0 G_0^{P2} \chi(v_y)^2 v_y^2 2\pi W(\tau_y) \quad (86)$$

in which the surface height spectral density function  $W(\tau_y)$  is the Fourier transform of the surface height autocorrelation function  $\langle h_1 h_2 \rangle$ . Thus (78) is in total agreement with the first order small perturbation results.

Note that the analysis also indicates why the approximate full wave results (70) are in good agreement with the full wave results (55) for surfaces with small heights and slopes. The major contribution to the integral (55) comes from the region  $x_d < L$ . In this region  $p(\bar{u}_1, \bar{u}_2) \approx p(\bar{u})\delta(\bar{u}_1 - \bar{u}_2)$  and the term involving the first order height-slope correlation  $B = \langle h_1 h_{x2} \rangle$  drops out of the integrand of (55). Thus the assumption (63) that yields the good approximation results (70) is justified analytically. Note that the above full wave results do not depend on the specific choice of the surface height autocorrelation function  $R(x_d)$ . It is also shown that the full wave results (55) can be used in the very small slope limit  $\langle h_z^2 \rangle \rightarrow 0$  while the corresponding small perturbation results (Rice 1951) diverge (Bahar 1991).

## 5. CONCLUDING REMARKS

The full wave techniques described in this paper have been used to determine the impact of irregular media (anisotropic, inhomogeneous and rough surfaces) effects on electromagnetic propagation. Thus this work can be used to predict the effects of the propagation environment on radio wave communication, navigation and positioning systems. It can also be used to obtain realistic models (based exclusively on ground truth data) of the propagation environment for purposes of remote sensing of the earth and the planets (Bahar and Haugland 1989). The full wave approach has also been applied to problems of propagation in media consisting of random distributions of particles with irregular shape (Bahar and Fitzwater 1988a). Thus the propagation environment can include man made obscurants or planetary dust. It is shown that the full wave approach correctly predicts enhanced backscatter (Flood 1987, Bahar and Fitzwater 1989) therefore it can be used to synthesize surfaces with desired polarimetric surface scattering characteristics (Bahar and Kubik 1991).

Since the full wave approach accounts for Bragg scatter and specular point scatter in a unified self-consistent manner, it is not necessary to adopt two-scale models of the rough surface. Thus artificial scaling and normalization are not introduced and effective medium parameters are not used. Propagation of CW and broad band signals can be analyzed using the full wave approach since the same analytical full wave expressions account for high frequency as well as low frequency phenomena (Bahar and Fitzwater 1978a,b, Bahar 1978, Bahar and Agrawal 1979b,c).

**ACKNOWLEDGEMENTS:** The author wishes to thank the organizing committee of the AGARD-EPP Symposium on Remote Sensing of the Propagation Environment for support to attending the meeting and is grateful to Dr. J. H. Richter for his encouragement. The manuscript was prepared by L. Villalobos, E. Everett, and Dr. M. El-Shenawee.

## 6. REFERENCES

- Abramowitz, M. and I. A. Stegun, 1964, *Handbook of Mathematical Functions with Formulas, Graphs and Mathematical Tables*, Applied Math Series, 55, Nat. Bur. of Stand., Washington, D.C.

- Bahar, E., 1970, Computations of mode scattering coefficients due to ionospheric perturbation and comparison with VLF radio measurements. *Proc. IEE*, 117, 735-738.
- Bahar, E., 1973a, Depolarization of electromagnetic waves excited by distribution of electric and magnetic sources in inhomogeneous multilayered structures of arbitrarily varying thickness-generalized field transforms. *Journal of Mathematical Physics*, 14, 1502-1509.
- Bahar, E., 1973b, Depolarization of electromagnetic waves excited by distribution of electric and magnetic sources of inhomogeneous multilayered structures of arbitrarily varying thickness-full wave solutions. *Journal of Mathematical Physics*, 14, 1510-1515.
- Bahar, E., 1974, Depolarization in nonuniform multilayered structures - full wave solutions. *Journal of Mathematical Physics*, 15, 202-208.
- Bahar, E., 1976, Generalized characteristic functions for simultaneous linear differential equations with variable coefficients applied to propagation in inhomogeneous anisotropic media. *Canadian Journal of Physics*, 54, 301-306.
- Bahar, E., 1978, Transient electromagnetic response from irregular models of the earth's surface. *Radio Science*, 13, 345-355.
- Bahar, E., 1980, Computations of the transmission and reflection scattering coefficients in an irregular spheroidal model of the earth-ionosphere waveguide. *Radio Science*, 15, 987-1000.
- Bahar, E., 1981, Full wave solutions for the depolarization of the scattered radiation fields by rough surfaces of arbitrary slope. *IEEE Trans. on Antennas and Propagation*, AP-29, 443-454.
- Bahar, E., 1987, Review of the full wave solutions for rough surface scattering and depolarization - comparisons with geometric and physical optics, perturbation and two-scale solutions. *Journal of Geophysical Research*, 92, 5209-5224.
- Bahar, E., 1988, Physical interpretation of the full wave solutions for the electromagnetic fields scattered from irregular stratified media. *Radio Science*, 23, 749-759.
- Bahar, E., 1991, Full wave analysis for rough surface diffuse, incoherent radar cross sections with height-slope correlations included. *IEEE Trans. on Antennas and Propagation*, in press.
- Bahar, E. and B. S. Agrawal, 1979a, Generalized characteristic functions applied to propagation in bounded inhomogeneous anisotropic media. *Journal of Atmospheric and Terrestrial Physics*, 41, 565-578.
- Bahar, E. and B. S. Agrawal, 1979b, Ionosphere effects on navigational and positioning signals - full wave solutions. *IEEE Trans. on Antennas and Propagation*, AP-27, 225-232.
- Bahar, E. and B. S. Agrawal, 1979c, Distortion and depolarization by the ionosphere of L band signals coded by phase reversals: full wave solutions. *Radio Science*, 14, 843-853.
- Bahar, E. and M. El-Shenawee, 1991, Use of supercomputers to evaluate singly and multiply scattered electromagnetic fields from rough surfaces. *IEEE Trans. on Magnetics*, in press.
- Bahar, E. and M. A. Fitzwater, 1978a, Transient electromagnetic response from nonparallel stratified models of the earth's crust - part I scattered radiation field. *Radio Science*, 13, 1-10.
- Bahar, E. and M. A. Fitzwater, 1978b, Transient electromagnetic response from nonparallel stratified models of the earth's crust - part II the scattered surface wave. *Radio Science*, 13, 11-20.
- Bahar, E. and M. A. Fitzwater, 1981, Numerical technique to trace the loci of the complex roots of characteristic equations in mathematical physics. *SIAM Journal on Scientific and Statistical Computation*, 2, 389-403.
- Bahar, E. and M. A. Fitzwater, 1983a, Propagation of vertically and horizontally polarized waves excited by distributions of electric and magnetic sources in irregular stratified spheroidal structures of finite conductivity generalized field transforms. *Canadian Journal of Physics*, 61, 113-127.
- Bahar, E. and M. A. Fitzwater, 1983b, Scattering and depolarization of electromagnetic waves in irregular, stratified spheroidal structures of finite conductivity - full wave analysis. *Canadian Journal of Physics*, 61, 128-139.
- Bahar, E. and M. A. Fitzwater, 1988a, Enhancement of the backscattered diffuse specific intensities from random distributions of finitely conducting particles with rough surfaces. *Journal of the Optical Society of America A*, 5, 89-98.
- Bahar, E. and M. A. Fitzwater, 1988b, Full wave - copolarized non specular transmission and reflection scattering matrix elements for rough surfaces. *Journal of the Optical Society of America A*, 5, 1873-1882.
- Bahar, E. and M. A. Fitzwater, 1989, Depolarization and backscatter enhancement in light scattering from random rough surfaces - theory and experiment. *Journal of the Optical Society of America A*, 6, 33-43.
- Bahar, E. and S. M. Haugland, 1989, Interpretation of the Apollo lunar surface data using the unified and the two scale full wave approach. *Proceedings of the IGARSS '89 Conference on Remote Sensing*, Vancouver, Canada, IEEE, #89CH2768-0, 3, 1296-1299.
- Bahar, E. and R. D. Kubik, 1991, Two-dimensional random rough surfaces that exhibit uniform enhanced backscatter for V and H polarizations over a very wide range of incident angles. *Progress in Electromagnetic Research Symposium*, MIT, Cambridge, MA.
- Bahar, E. and G. G. Rajan, 1979, Depolarization and scattering of electromagnetic waves by irregular boundaries for arbitrary incident and scatter angles - full wave solutions. *IEEE Trans. on Antennas and Propagation*, AP-27, 214-225.
- Beckmann, P. and A. Spizzichino, 1963, *The Scattering of Electromagnetic Waves from Rough Surfaces*, (Macmillan: New York).
- Brekhovskikh, L. M., 1960, *Waves in Layered Media* (Academic Press: New York).
- Brogia, W. L., 1974, *Modern Control Theory* (Quantum Publishers, Inc.: New York).

Bronson, R., 1969, *Matrix Methods - An Introduction* (Academic Press: New York).

Budden, K. G., 1962, *Radio Waves in the Ionosphere* (Cambridge University Press).

Flood, W. A., 1957, Wave propagation - although electromagnetic is a mature science new problems are challenging the theoreticians. *Microwaves and R. F.*, 65.

Friedman, B., 1956, *Principles and Techniques in Applied Mathematics* (John Wiley and Sons, Inc.: London).

Rice, S. O., 1951, Reflection of electromagnetic waves from a slightly rough surface. *Communications of Pure and Applied Mathematics*, 4, 251-378.

Schellkunoff, S. A., 1955, Conversion of Maxwell's equations into generalized telegraphists' equations. *Bell System Technical Journal*, 34, 995-1043.

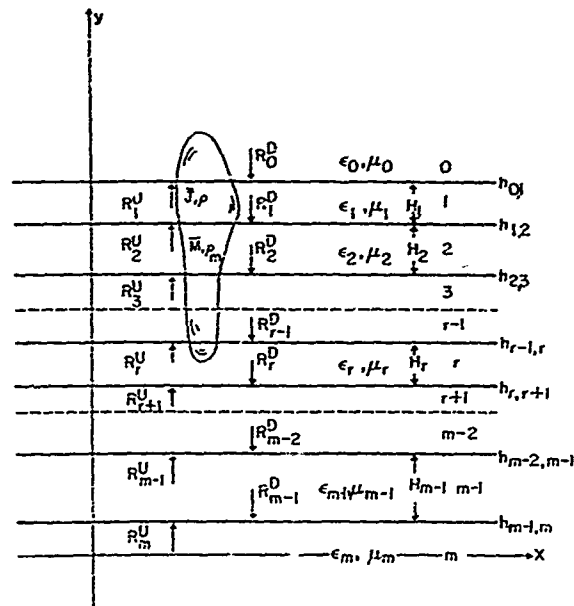


Fig. 1. Electric and magnetic sources distributed in the layers of a uniform multilayered structure.

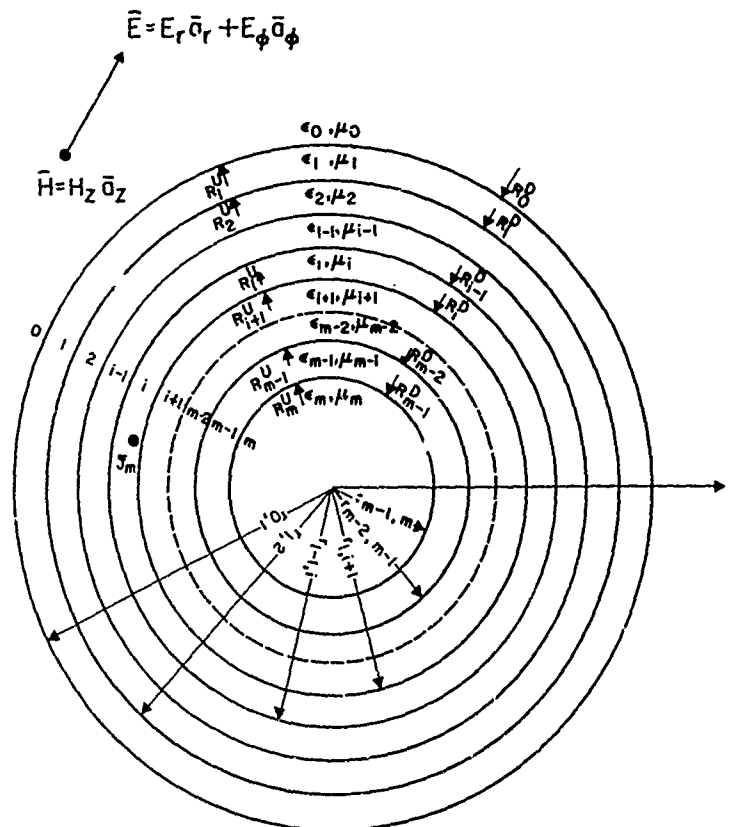


Fig. 2. Magnetic line source parallel to a multilayered circular cylindrical structure.

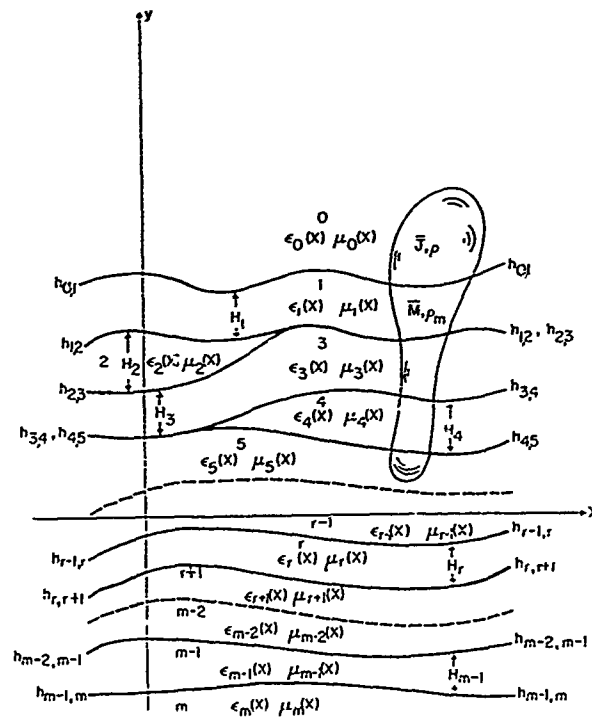


Fig. 3. Electric and magnetic sources distributed in the layers of a nonuniform multilayered structure

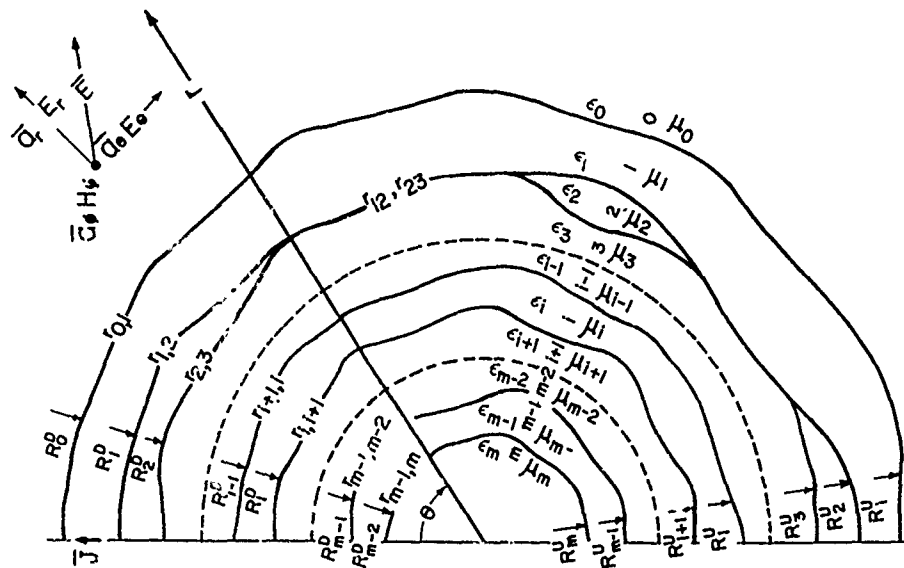
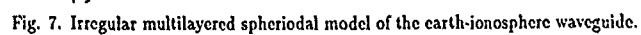
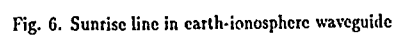
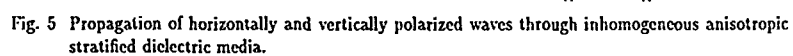


Fig. 4. Radio wave propagation in an irregular stratified spheroidal structure.



# Sensing of ELF Signatures Arising From Space Vehicle Disturbances of the Ionosphere

Jack Y. Dea  
Naval Ocean Systems Center, San Diego, CA 92152-5000, USA

William Van Bise and Elizabeth A. Rauscher  
Magtek Laboratory, 7685 Hughes Drive, Reno, NV 89506, USA

Wolfgang-M. Boerner  
University of Illinois at Chicago  
EECS, Communications and Sensing Laboratory,  
Chicago, IL 60680-4348, USA

## SUMMARY

We report on observations of Extremely Low Frequency (ELF) signatures during exit or reentry of space vehicles through the ionosphere. The two modes regularly observed gave signals that peaked at 5.6 Hz and 11.2 Hz. The evidence points to the lower ionosphere, i.e., the D- and E-layers, as the generator of these signals. The measurements were performed using ground-based multi-turn coil sensors located in Reno and San Diego. The nature of these signals is unclear at present but it is surmised that we are detecting either the evanescent fields of hydromagnetic waves traveling in the ionosphere or the oscillating geomagnetic field associated with these hydromagnetic waves.

## 1. Introduction

Disturbances in the ionosphere can often be monitored on the ground. Examples include High Frequency (HF) fading (or enhancement), phase changes of Very Low Frequency (VLF) waves, and micropulsations. In general, disturbances in the ionosphere and magnetosphere arise from changes in solar activity. We report, perhaps for the first time in the open literature, observations of Extremely Low Frequency (ELF) signatures arising from space vehicle disturbances of the ionosphere. The sharply peaked signatures are observed in the lower ELF band (5 to 15 Hz) but are different from the broader Schumann resonances (1,2) that are also observed in this band. They are different from the Schumann resonances in both frequency and line shape (3).

According to discussions with Robert J. Dinger of Naval Weapons Center (NWC), China Lake, CA, and Mario Grossi of The Harvard-Smithsonian Centre for Astrophysics, Cambridge, MA, the Raytheon Research Laboratory and The Naval Research Laboratory (NRL) conducted a series of experiments in the early 1970s to look for Ultra Low Frequency (ULF) (.01 to 5 Hz) and ELF (5 to 3000 Hz) signals induced by rocket interaction with the ionosphere. It was suggested by Mario Grossi (then of Raytheon Research Laboratory) that the ionized rocket plumes could short-circuit the earth-ionosphere cavity plates and induce a large flow of current from the

ionosphere to ground. This large transient flow of current will ring the ionosphere if any resonant modes exist. Another effect is the introduction of plume ions and water vapor directly into the ionosphere, thus changing its conductivity. The main effect comes from the water vapor which depletes ions and effectively punches a hole in the ionosphere (4). The ionosphere reacts to the change in conductivity in at least two ways: first, currents are induced to normalize the conductivity, and second, any existing natural upper atmospheric currents are diverted in direction. The associated magnetic effects should be observable on ground. Unfortunately, the data obtained were inconclusive and interest was diverted to ground-based stimulation of the ionosphere using high powered HF transmitters (5,6,7).

Acoustic excitation of the ionosphere arising from the eruption of Mount St. Helens, May 18, 1980, in Washington State induced detectable traveling ionospheric disturbances (8,9). Monitoring in Oregon by William Van Bise also revealed ULF signatures in the 3 to 4 Hz range (10). It was hypothesized that the passage of large spacecraft through the ionosphere could also induce such ULF/ELF signatures. The first Space Shuttle mission (Columbia) began with the launch on April 12, 1981 and completed with the landing on April 14, 1981. ELF monitoring in Oregon by William Van Bise during the Columbia's landing period led to the discovery of strong signals peaking at 5.6 Hz and 11.2 Hz that corresponded with the spacecraft penetration of the ionosphere. Further observations of other Shuttle missions indicated possible connections between the ionospheric D-layer with the 5.6 Hz signals and the E-layer with the 11.2 Hz signals. The signals were absent or were very weak during evening launches or landings. The frequencies may vary somewhat, depending upon a variety of parameters. In 1989, an organized effort was launched at the Naval Ocean Systems Center (NAVOCEANSYSCEN), San Diego, CA, to study the validity of this phenomenon. Shuttle missions starting from October 1989 were monitored and valid confirmation data were obtained for several missions. The description of the observations will be given in a later section.

## 2. Instrumentation

This initial study used three sites for the measurements. The sites are located in Reno, NV; in San Diego, CA; and in La Posta, CA. Fig. 1 shows the location of the three sites. The La Posta site is a remote site located 100 km east of San Diego and is linked to NAVOCEANSYSCEN, San Diego, via a commercial telephone link. All the sites use portable directional high turn coil sensors (search coil magnetometers) as the antenna elements. The San Diego and La Posta stations use identical magnetometer systems. Fig. 2 shows a schematic layout of these systems. Each sensor head consists of 90,000 turns of fine wire, wrapped on a mu-metal rod. A low noise instrumentation preamplifier is also located directly at the sensor head in order to avoid amplification of cable noise. The coil and electronics are electrostatically shielded with cylindrically shaped foil covers and are all housed inside a plastic cylinder. Each cylinder measures 10 cm in diameter by 34 cm in length. The three sensor heads are mounted inside a weather proof fiberglass enclosure. The fully loaded enclosure weighs approximately 30 pounds and is highly portable. In the field, the three orthogonally arrayed sensor heads are oriented with the x-sensor pointing east, the y-sensor pointing north, and the z-sensor pointing vertically. A 36 meter cable connects the sensor unit to the external amplifier unit which consists of an amplifier, a 40 Hz low-pass filter and a 60 Hz notch filter for each axis of operation. For general operations at the San Diego station, a spectrum analyzer (HP 3561A) is used for observations of real-time power spectra, and a magnetic tape data recorder (Honeywell 101) is used for data recording. The La Posta remote site uses a PC computer for data collection, processing, and recording. The collected data are stored on hard disk and are also processed with a Fast Fourier Transform (FFT) program. A telecommunications link using the telephone line, modems, and telecommunications software (PC Anywhere) connects the La Posta Station with the NAVOCEANSYSCEN Low Frequency Noise Lab at San Diego. Near real-time power spectrum displays and downloading of data can be performed remotely. Fig. 3 shows a sketch of our monitoring network including the remote link.

The Reno sensor systems (11,12) are basically of the same design as those at San Diego and La Posta, with some differences. The Reno systems consist of single axis sensors; however, three of them together can serve as a three-axis system. The Reno sensors have the preamplifier located at the external amplifier unit rather than at the sensor heads making cable noise a problem if long cables are used. The Reno amplifier units, unlike those at San Diego and La Posta, contain correction elements for adjusting the non-linearity of the coil characteristics to provide a flat output response. This serves to assure uniform system response in the range of 0.1 to 50 Hz. A solid copper casing protects the coils and shields against electrostatic fields and completely excludes electric field components. Fig. 4



Fig 1. Map showing location of ELF monitoring sites at Reno, San Diego, and La Posta.

shows a schematic layout of the Reno sensor system.

The search coil magnetometer systems can measure minute changes in the ambient field. Fig. 5 shows the calibration chart of one axis of the three-axis magnetometer system used in San Diego and La Posta. The output response increases linearly with frequency because the coil sensors measure the derivative of the field and not the field itself. From this calibration chart, we can estimate the minimum field changes that we may expect to observe in the 0.1 to 40 Hz range. The self-noise of the system is approximately  $2.5 \text{ mV(rms)}/\sqrt{\text{Hz}}$ . At 10 Hz, the system outputs 10 volts per gamma (1 gamma = 1 nano-Tesla). An ambient signal to generate an output above the self-noise requires a signal of  $0.00025 \text{ gamma}/\sqrt{\text{Hz}}$  or  $0.25 \text{ milli-gamma}/\sqrt{\text{Hz}}$ . This order of sensitivity is similar to the sensitivity of the US Geological Survey (USGS) search coil magnetometer systems but somewhat less sensitive than the University of California search coil magnetometer systems both described in reference (13). This order of sensitivity is generally sufficient for most low frequency research because the ambient background noise levels are somewhat higher than the minimum levels that can be measured. The Reno search coil sensors are nominally more sensitive having a uniform sensitivity of approximately  $0.05 \text{ milli-gamma}/\sqrt{\text{Hz}}$  in the range of 0.1 to 50 Hz. By contrast, fluxgate magnetometers have a sensitivity of only  $100 \text{ milli-gamma}/\sqrt{\text{Hz}}$ , and low frequency phenomena, such as observed by us, could be missed due to their lack of sensitivity.

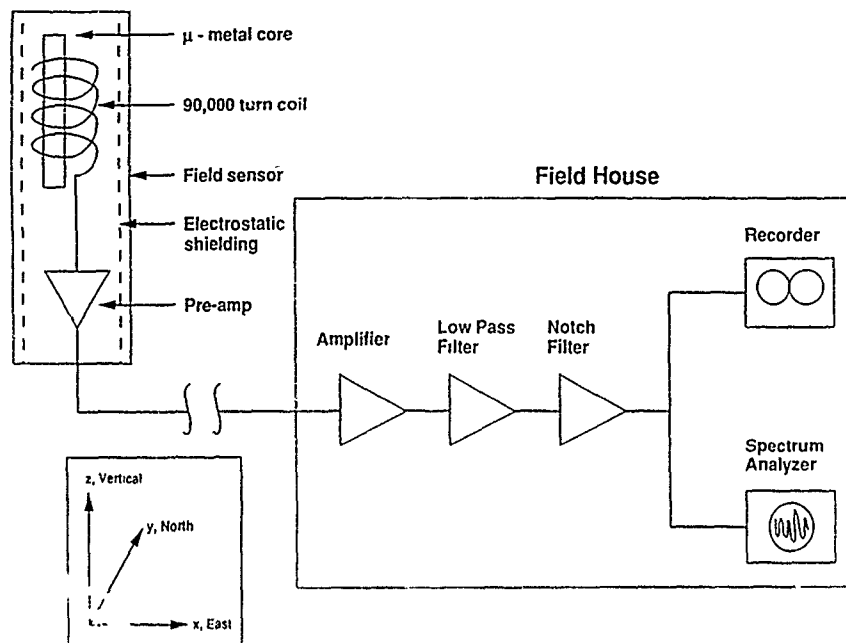


Fig 2. Diagram of one axis of the NAVOCEANSYSCEN three-axis search coil magnetometer system. Insert shows coil orientations.

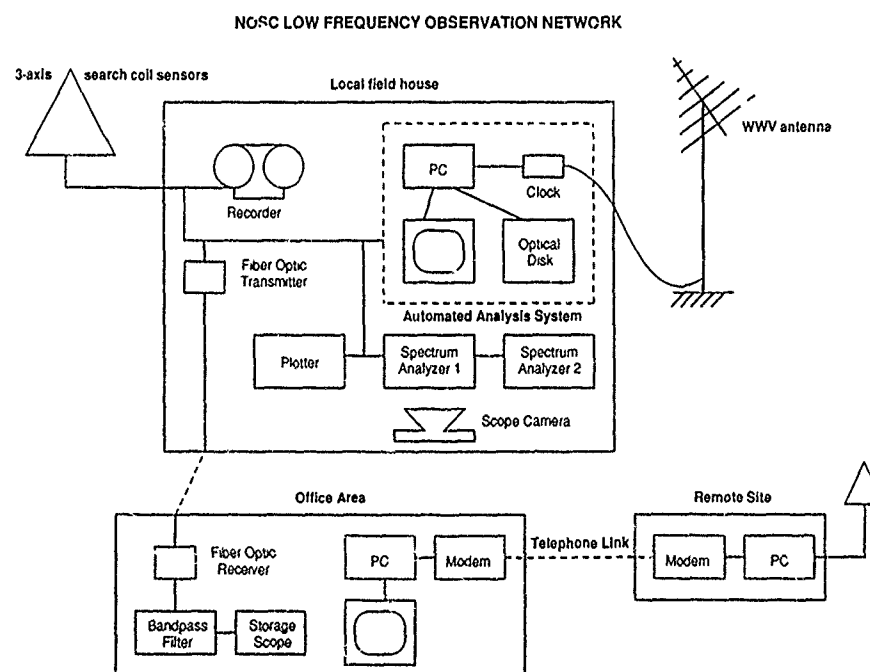


Fig 3. Diagram of the NAVOCEANSYSCEN low frequency observation network.

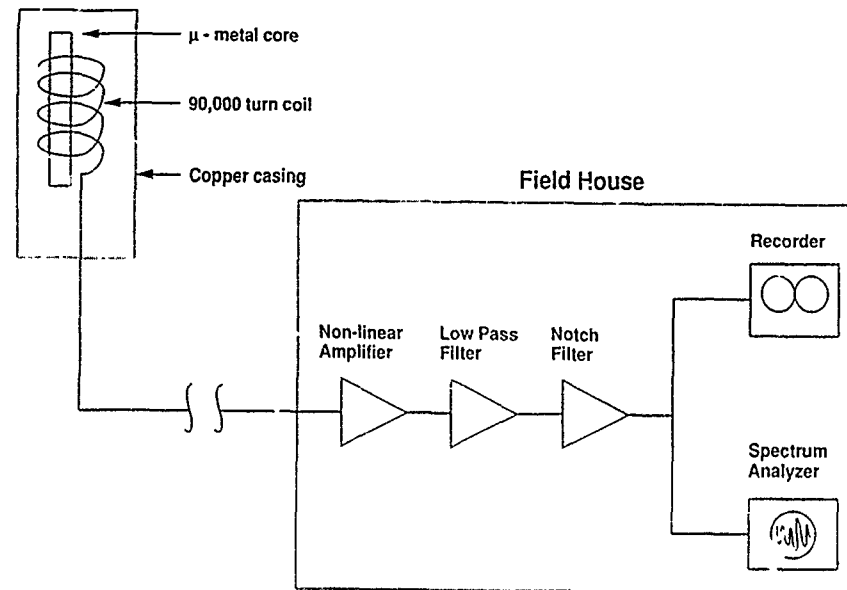


Fig 4. Diagram of the Reno single axis search coil magnetometer system.

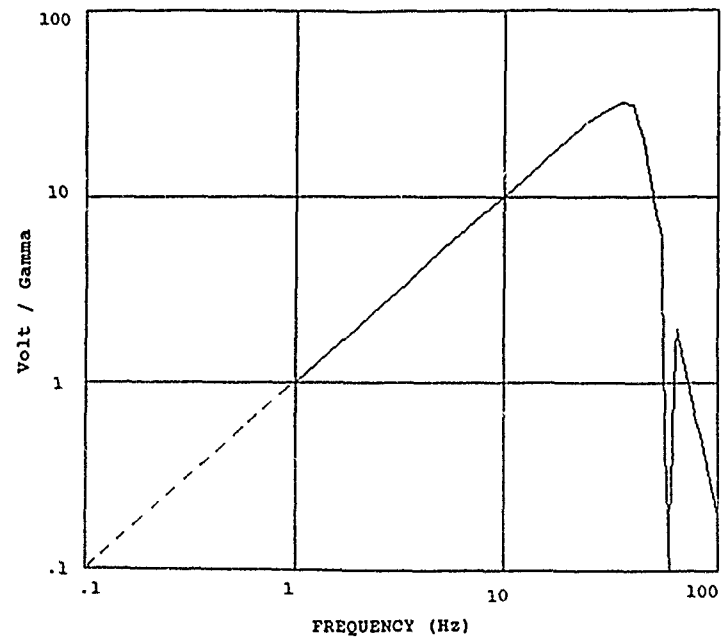


Fig 5. Calibration curve of the NAVOCEANSYSCEN search coil magnetometer system in volts/gamma versus frequency. Dark line indicates measured values; dashed line indicates extrapolated values. Low pass cutoff at 40 Hz and notch filtering at 60 Hz are clearly seen.

### 3. Description of the Observations

Most of the observations of the ELF signatures were taken during Space Shuttle missions. Smaller spacecraft such as Delta rockets, have also been seen to generate similar signatures when traversing the ionosphere. Table 1 lists the recent Shuttle launches since October 1989.

Table 1. Space Shuttle Missions:  
Atlantis=A, Columbia=C, Discovery=D  
(October 1989 to present).

Launch (UT)		Touch Down (UT)
1989, Oct 18, 1753	A	1989, Oct 23, 1732
1989, Nov 23, 0638	D	1989, Nov 28, 0029
1990, Jan 09, 1335	C	1990, Jan 20, 0935
1990, Feb 29, 0750	A	1990, Mar 04, 1608
1990, Apr 24, 1331	D	1990, Apr 29, 1449
1990, Oct 06, 1035	A	1990, Oct 10, 1357
1990, Nov 15, 2247	A	1990, Nov 20, 2043
1990, Dec 01, 0649	C	1990, Dec 10, 0545
1991, Apr 05, 1422	A	1991, Apr 11, 1355
1991, Apr 28, 1133	D	1991, May 05, 1955
1991, June 5, 1326	C	1991, June 14, 1539
1991, Aug 02, 1502	A	1991, Aug 11, 1223

There were many unexpected schedule changes made during these missions, and opportunities for observations have been lost due to these changes.

Typically, recordings are initiated one hour prior to launch time or one hour prior to touchdown. The April 24, 1990 launch of the discovery was recorded on magnetic tape at the Reno station and provided a good example of the signal characteristics. In this particular mission, the Shuttle Discovery was launched at 0531 F (1331 UT) from Cape Kennedy. Four minutes later, signals peaking at 5.7 Hz became prominent. Another two minutes later, signals peaking at 12 Hz also appeared. During the following five minutes the two signals became the two most prominent peaks in the DC (0.1 Hz) to 20 Hz band.

Fig. 6 shows a four-minute average of the DC (0.1 Hz) to 20 Hz background spectrum at 0520, eleven minutes before launch. The averages were performed on an HP3561A Signal Analyzer. No particularly strong signals were observed except for the 15 Hz peak (which most likely was a local artifact). Fig. 7 shows a spectrum observed at 0536, five minutes after launch. The 5.7 Hz peak is clearly visible. Fig. 8 shows a three-minute average spectrum taken from 0538 to 0541. Here the 12 Hz peak dominates the 5.7 Hz peak. The 12 Hz peak is also broader than the 5.7 Hz peak, indicating a lower Q phenomenon. The twin peaks at 1.0 and 4.0 Hz are background noise signals probably not associated with this phenomenon. Fig. 9 shows a time history of the phenomenon showing a one minute average power spectrum every two minutes. The display of the time history clearly shows the appearance and disappearance of the twin peaks. The Shuttle Discovery touched down five days later on 29 April 1990 at 0649 (1449 UT).

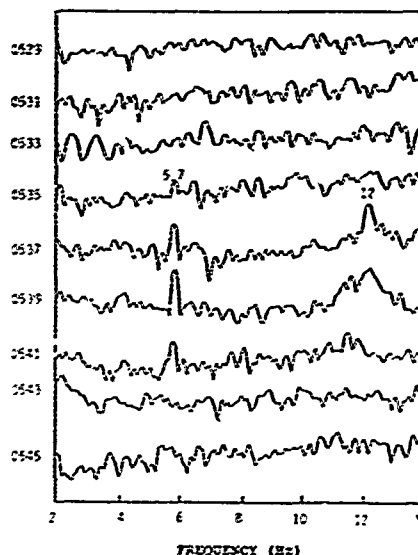


Fig 9. Time history display of the Shuttle launch episode on April 24, 1990. Each curve represents a 1 minute average spectrum. Launch time was 0531 PST. The 5.7 Hz signal begin appearing at 0535 PST, and the 12 Hz signal begin appearing at 0537 PST.

The overall background noise was high that day and the resonant peaks can best be seen through a long time average. Fig. 10 shows a half hour average taken from 0610 to 0640. The peaks have shifted in frequency to 5.3 Hz and 10.55 Hz. The observed peaks at 6.75 Hz and 9.25 Hz do not always appear, and are as yet unexplained.

This series of observations can be correlated with a typical trajectory given by NASA. In launches, the Shuttle reaches 60 km in about five minutes (D-layer) and 100 km in 8.5 minutes (E layer). Then it coasts into orbit at about 240 km traveling at Mach 25. The landing maneuvers can take up to an hour and involve more inclined angles (with respect to the ionosphere) than during launch. Hence during landings the signals generally last longer than during launches. The correlations fit the hypothesis that the 5.6 Hz signals originate from the D-layer and the 11.2 Hz signals originate from the E-layer.

The October 18 to October 23, 1989 mission of the Shuttle Atlantis gave another good example of this phenomenon. Fig. 11 shows a strong 5.16 Hz peak appearing 23 minutes after launch. The low frequency and the long duration of the signal, and the absence of the 10-12 Hz peak, probably indicated changed ionospheric conditions possibly associated with the large October 17 Loma Prieta quake which occurred on the previous day (14). Some mechanisms of the coupling of deep earth geologic processes with the ionosphere are discussed in (15). Fig. 12 shows a strong 11.08 Hz peak at 0910 (1810 UT) on 23 October and Fig. 13 shows a

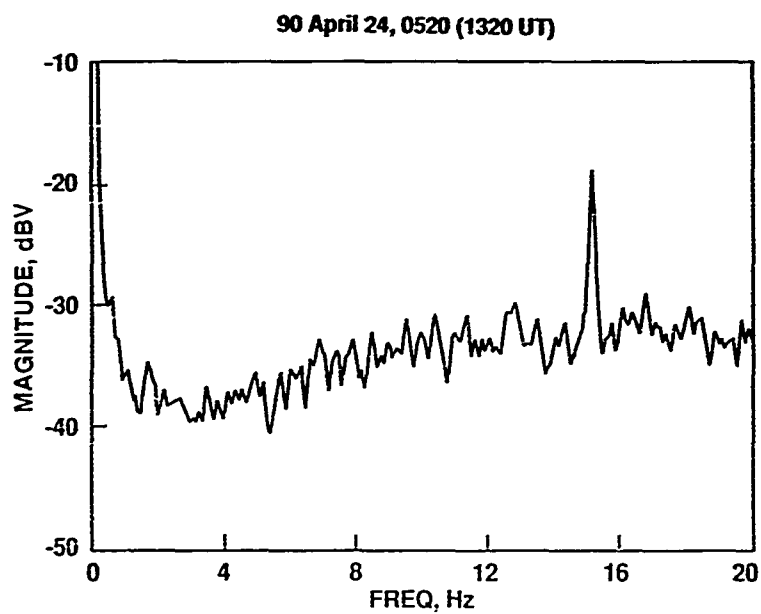


Fig 6. Four minute average power spectrum of background noise. Artifact at 15 Hz. Recorded in Reno eleven minutes before the April 24, 1996 Shuttle launch.

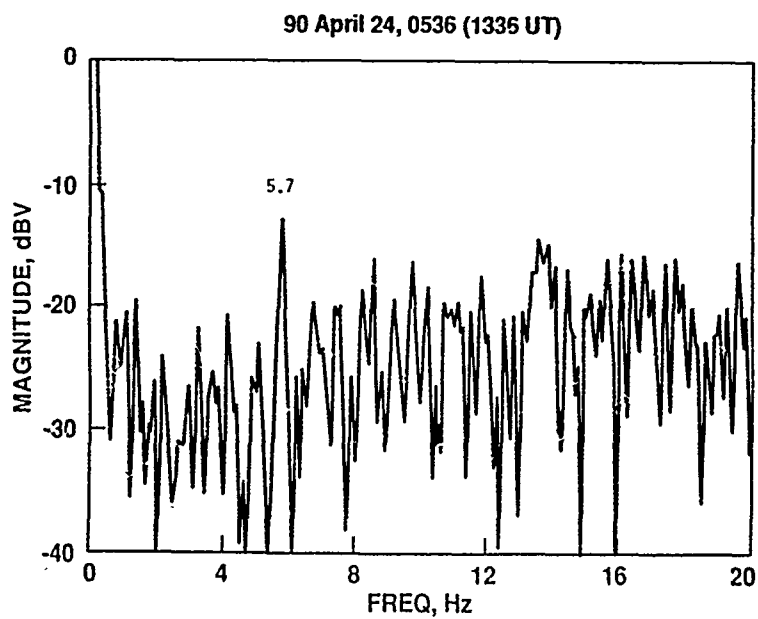


Fig 7. "Snapshot" spectrum taken 5 minutes after the April 24, 1990 Shuttle launch. Peak at 5.7 Hz is clearly visible.

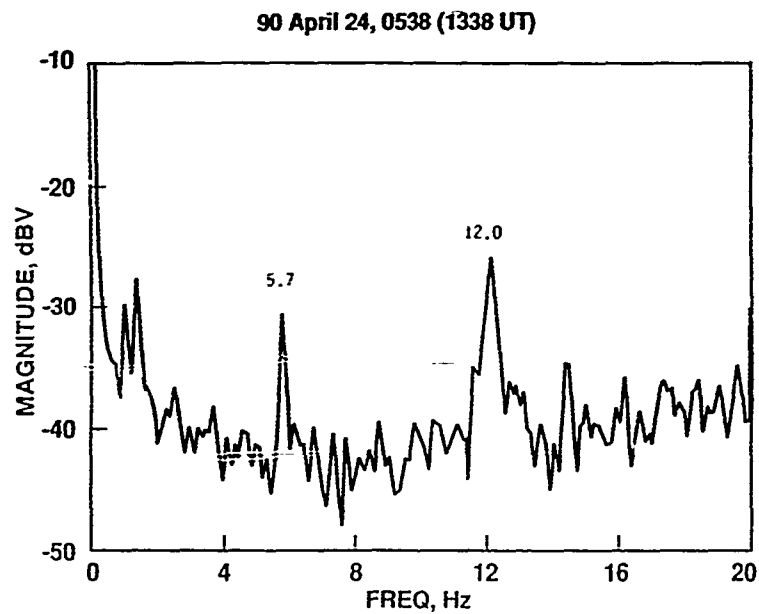


Fig 8. Three minute average spectrum taken 7 minutes after the April 24, 1990 launch. Peaks at 5.7 and 12 Hz predominate.

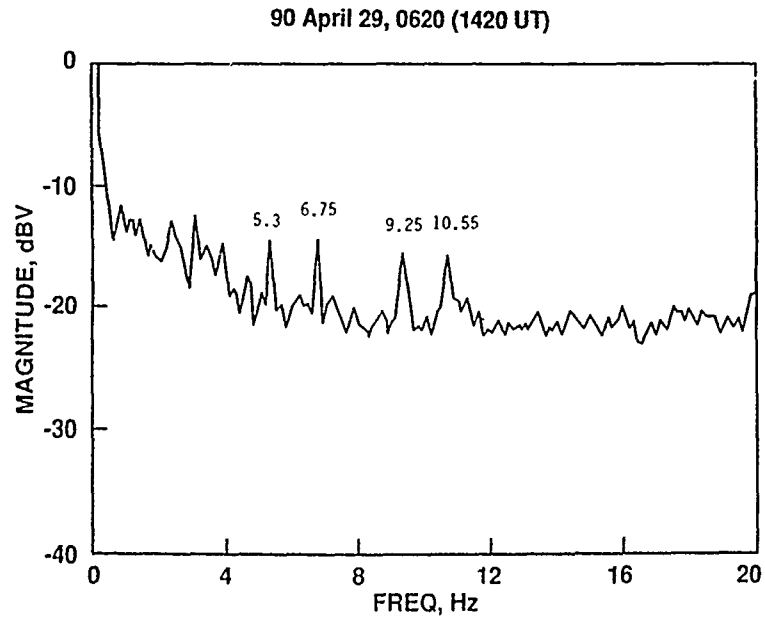


Fig 10. One half hour average spectrum taken during the April 29, 1990, Shuttle landing episode. Strong peaks at 5.3 and 10.55 Hz are present.

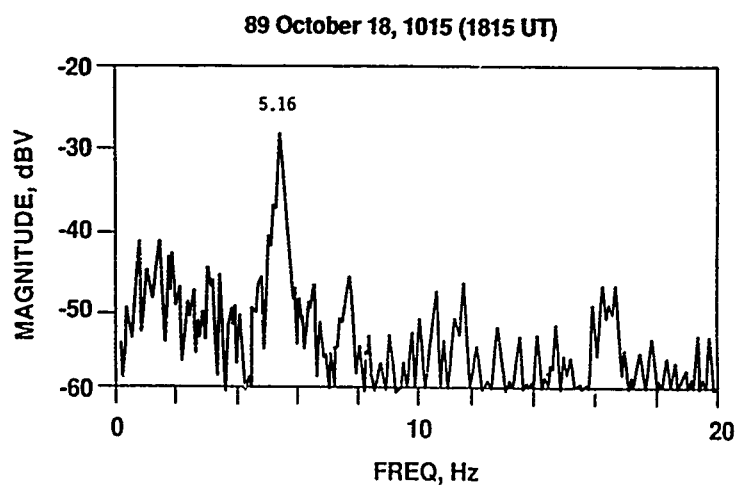


Fig 11. "Snapshot" spectrum taken 23 minutes after the Oct. 18, 1989, Shuttle launch. Recorded in Reno. Strong 5.16 Hz peak is present.

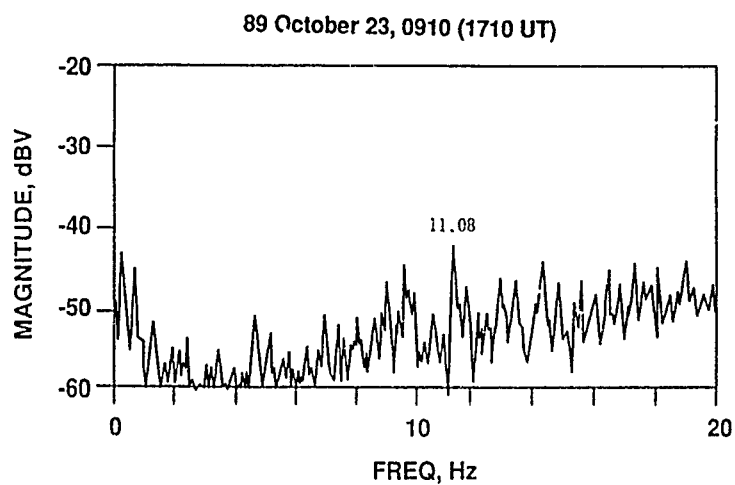


Fig 12. "Snapshot" of spectrum taken 22 minutes before Shuttle touchdown on Oct. 23, 1989. Strong 11.08 Hz peak is present.

89 October 23, 0925 (1725 UT)

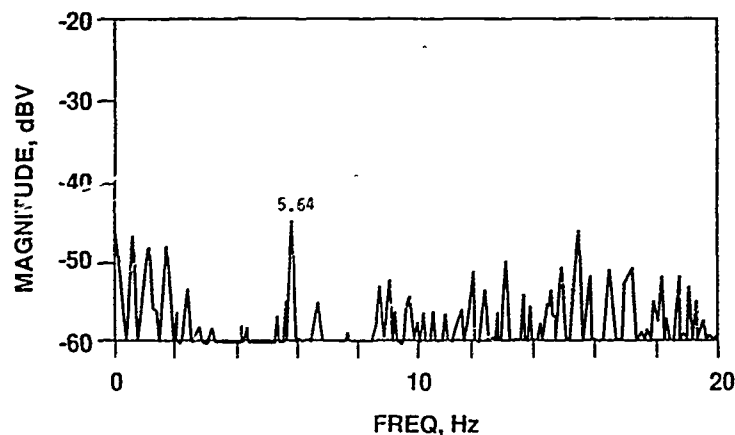


Fig 13. "Snapshot" of spectrum taken 7 minutes before Shuttle touchdown on Oct. 23, 1989. Strong 5.64 Hz peak is present.

strong 5.64 Hz peak at 0925. Touchdown was seven minutes later at 0932. Apparently, the ionospheric conditions had normalized and the peaks had reverted back to the more typical frequencies.

#### 4. Interpretation of Results

As discussed in the previous section, the evidence points to the D-layer as the generator of the 5.6 Hz signals and the E-layer as the generator of the 11.2 Hz signals. The signals, observed in Reno and San Diego simultaneously, indicated a large scale phenomenon. It should be noted that the signatures were observed clearly in Reno but very poorly in San Diego and La Posta. The reason for this difference is yet to be determined. The energy of the phenomenon probably derives from both mechanical contact between the spacecraft and the ionosphere and a shock excitation following the spacecraft. The shock excitation from the reentering Shuttle is strong enough to excite seismic waves (16). In general, the turbulent wake of the spacecraft excites many excitation modes in the plasma fluid. Most modes will be damped out. The undamped modes will be the resonant modes and will propagate for long distances. In the ELF frequency range, two types of plasma waves are seen to be candidates for the signatures observed by us. These candidates are the Alfvén waves and the magnetosonic waves (17, 18). The Alfvén waves are also known as slow hydromagnetic waves and the magnetosonic waves are also known as fast hydromagnetic waves. Hydromagnetic waves are low frequency (less than several hundred Hertz) ion acoustic waves traveling in a region with a magnetic field. Ion acoustic waves are compressional waves formed from the ion background. Slow hydromagnetic waves propagate parallel to the ambient magnetic field while fast hydromagnetic waves

propagate perpendicular to the ambient magnetic field. In hydromagnetic wave propagation, the magnetic field lines and the plasma fluid oscillate together as if the particles were stuck to the lines. The field lines act as if they were mass-loaded strings under tension and a hydromagnetic wave can be regarded as the propagating disturbance occurring when the strings are plucked. A theory that models this phenomenon is called the field line resonance model (19, 20).

A simple formula exists for the velocity of propagation of slow hydromagnetic waves (Alfvén velocity) but unfortunately it is accurate only for fully ionized plasmas. However, a chart of the distribution of the Alfvén velocity with respect to height in the ionosphere has been produced from more detailed calculations (21). The chart shows that the Alfvén wave velocities in the D-layer and E-layer are approximately 600 km/sec and 500 km/sec, respectively. These velocities are much faster than pure ion-acoustic wave velocities which are of the order of several hundred meters/sec. At hydromagnetic speeds East coast to West coast travel time will be less than 10 seconds. This short delay is consistent with observations.

It is surmised that large amplitude hydromagnetic waves are induced by the action of the spacecraft. The waves travel both parallel and perpendicular to the earth's magnetic field. Those waves traveling along the field lines are guided to the bottom of the ionosphere in one direction and guided to the magnetosphere in the other direction. Thus, immediately below the disturbed ionosphere, the disturbance will be seen as evanescent fields. The waves traveling up to the magnetosphere will be seen as evanescent fields at the conjugate location of the planet. The waves traveling East-West will be traveling perpendicular to the earth's field and hence will be fast hydromagnetic

waves. Fast hydromagnetic waves travel somewhat faster than Alfvén waves. What is observed on the West coast during an East coast Shuttle launch is either the evanescent field of the traveling fast hydromagnetic waves or the oscillating magnetic field lines of the earth associated with the passage of the hydromagnetic waves. The exact nature of the observed signals is being explored both experimentally and theoretically.

The question of the resonant nature of the observed peaks is a more difficult question to answer. One approach is to treat the earth, the geomagnetic field, and the lower ionosphere as one giant RLC circuit. The resonant frequency is

$$f = \frac{1}{2\pi\sqrt{LC}}$$

where L and C are the effective inductance and the effective capacitance, respectively. To our knowledge, there are no estimated values of L and C that can be used for this situation. However, there have been rough estimates given for the R, L, and C values for the upper ionospheric/magnetospheric circuit (22,23). The estimates given by Rostoker and Lau (23) gave a resonant frequency for that circuit in the millihertz range which is consistent with only the Pc5 micropulsation frequencies. Fig. 14 depicts a schematic of the equivalent circuit. The existence of the Pc1 micropulsations (up to 5 Hz) give hope that R, L, and C values exist to explain the 5 - 12 Hz oscillations of the type observed by us. At present there is insufficient knowledge to even estimate R, L, and C values for the earth/geomagnetic field/lower ionospheric circuit. More in-depth studies need to be performed to determine the values of geophysical parameters. Because of the large amount of geophysical aeronomical research conducted in Canada and the Northern US including Alaska and the large number of ULF-ELF recording stations located in these regions, we encourage more long term monitoring of the lower ELF band (3 to 40 Hz) which has not been observed as closely as other frequency bands. In particular, it would be important to perform simultaneous sunlit and night sector monitoring during launch and reentry events.

#### 5. Conclusion

We have presented evidence for at least two resonant modes of the lower ionosphere that have not been reported before to the best of the authors' knowledge. These modes occur in the lower ionosphere (D- and E-layers) because they are not usually seen in the evening sectors when sunlight is absent. The nature of the modes are not clearly known at present. It is surmised that the sensors are detecting the evanescent fields of hydromagnetic waves or the oscillating geomagnetic field associated with these waves. The frequencies of these waves are most likely related to the resonant conditions that exist in the earth/geomagnetic field/lower

#### Example of Equivalent Circuit for the Ionosphere/Magnetosphere

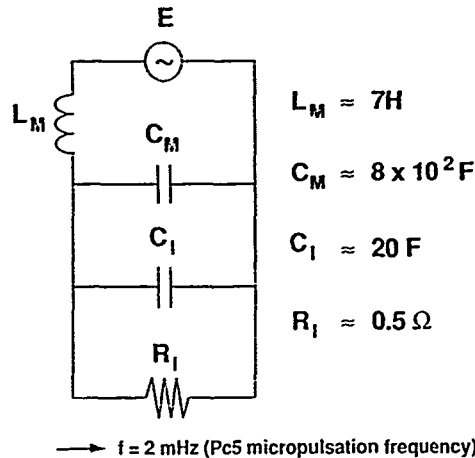


Fig 14. Equivalent circuit explanation of 2 mHz Pc5 micropulsations. E represents energy sources in the magnetosphere. Subscripts M and I refer to magnetosphere and ionosphere, respectively (after ref. 23).

ionospheric cavity. In fact, the observed signatures may indicate the natural oscillations of the lower ionosphere. Intensive investigation is under way to clarify these issues.

#### Acknowledgments

The authors wish to thank Mr. Thomas N. Roy of NAVOCEANSYSCEN for contributing the sensitive search coil magnetometers systems to the project. We thank Dr. James W. Bond, Dr. Peder M. Hansen and Paul A. Singer, all of NAVOCEANSYSCEN, for proofreading the document and providing continual encouragement. We also thank Drs. Anthony C. Frasier-Smith and Robert A. Helliwell of the Stanford University STAR Laboratory; Prof. H. Frank Morrison of the Engineering Geosciences Laboratory within the Dept. of Materials Science and Mineral Engineering of the University of California at Berkeley (UCB); Prof. Tomiya Watanabe of the Geophysical Observatory, UBC, Vancouver, Canada; Prof. Gordon Rostoker of the Geophysics Department of the University of Alberta, Edmonton, Canada; Dr. John Walker of the Geological Survey of Canada and Dr. H. Gordon James of the Canadian Communication Research Center, Ottawa, Ontario, Canada; Prof. Takeo Yoshino of the University of Electro-Communications, Chofu-shi, Tokyo, Japan; Prof. Hiroo Kanamori of the Geophysics Department of the California Institute of Technology; and

Drs. Malcolm J.S. Johnston and Thomas A. Heaton of the US Geological Survey, Menlo Park and Pasadena offices, respectively, for their illuminating discussions. A special thanks is extended to Dr. Robert J. Dinger of the Naval Weapons Center, China Lake, CA, and to Dr. Mario Grossi of the Harvard-Smithsonian Center for Astrophysics, Cambridge, MA, for sharing with the authors the history of the early attempts to seek space vehicle induced signatures from the ionosphere. Support for this work was provided by Independent Research funds of NAVOCEANSYSCEN, Dr. Alan Gordon, coordinator, and a US Navy-ASEE-SFRP Distinguished Professor award.

#### REFERENCES

1. W.O. Schumann. Z. Naturforschung, Teil. 7, 149 (1952)
2. W.O. Schumann. Z. Angew. Phys. 9, 373 (1957)
3. P.V. Bliokh, A.P. Nicholaenko, and Y. F. Philippov. Resonances in the Earth-Ionospheric Cavity. English translation by S. Chomet. Peter Peregrinus Ltd, London. 1982. pp 7-19.
4. M. Mendillo, G.S. Hawkins, and J.A. Klobuchar. Science. 187, 343 (1975)
5. J.R. Davis, J.W. Willis, and E. L. Althouse. MAGIC MODE: Investigation of ULF/ELF Waves in the Ionosphere and Magnetosphere. NRL Report 7552. NRL, Washington, D.C. March 12, 1975.
6. J.W. Willis, and J.R. Davis. Investigation of the Stimulation of ULF Waves. NRL Report 7925. NRL, Washington, D.C. Nov 13, 1975.
7. E.L. Althouse and J.R. Davis. Experimental Investigation of the Characteristics of Pcl Micropulsation Propagation Using a Midlatitude Five-Station Receiving Network. NRL Report 8086. NRL, Washington, D.C. May 18, 1977.
8. R.J. Mueller and M.J.S. Johnston. Physics of the Earth and Planetary Interiors. 57, 23 (1989)
9. M.J.S. Johnston. Physics of the Earth and Planetary Interiors. 57, 23 (1989)
10. E.A. Rauscher and W. Van Bise. Bull. Am. Phys. Soc. 32, 67 (1987)
11. W. Van Bise and E.A. Rauscher. Bull. Am. Phys. Soc. 34, 109 (1989)
12. E.A. Rauscher and W. Van Bise. US Patent 4,724,390 (1988)
13. V.F. Labson, A. Becker, H.F. Morrison, and U. Conti. Geophysics. 50, 565 (1985)
14. A.C. Frasier-Smith, A. Bernardi, P.R. McGill, M.E. Ladd, R.A. Helliwell, and O.G. Villard, Jr. Geophys. Res. Lett. 17, 1465 (1990)
15. J.Y. Dea, C.I. Richman and W.-M. Boerner. Proceedings, NATO-AGARD, 49th EPP Symposium, Remote Sensing of the Propagation Environment, Cesme, Turkey, 30 Sept.-04 Oct. 1991, Session IV, Ionospheric Sensing (B), paper no. 20 (this issue).
16. H. Kanamori, J. Mori, D. Anderson, T. Heaton and L. Jones, Seismic Excitation by the Space Shuttle Columbia (on reentry to Edwards AFB, Aug 13, 1989). CALTECH Geophysics Department Internal Report. Caltech, Pasadena. July 6, 1990.
17. F.F. Chen. Introduction to Plasma Physics and Controlled Fusion. Plenum Press, New York. 1985. pp 99-120.
18. K.C. Yeh and C.H. Liu. Theory of Ionospheric Waves. Academic Press, New York. 1972. pp 167-183.
19. D.J. Southwood. Planet. Space Sci. 22, 483 (1974)
20. W.J. Hughes and D.J. Southwood. J. Geophys. Res. 81, 3241 (1976)
21. J.A. Jacobs. Geomagnetic Micropulsations. Springer-Verlag, Heidelberg. 1970. p 91.
22. T.E. Holzer and G.C. Reid. J. Geophys. Res. 80, 2041 (1975)
23. G. Rostoker and H.-L. Lau. Space Sci. 26, 493 (1978)

#### DISCUSSION

##### P. CANNON

*Could you please comment on the relative amplitudes of the shuttle ELF signatures and the Schumann Resonances?*

##### AUTHOR'S REPLY

*The relative amplitude of shuttle ELF with respect to back ground noise depends on the relative level of solar-terrestrial geo-electromagnetic, electric storm (Schumann resonances), earth-sea-quake and volcano activation of geo-electromagnetic noise. Maximum signal is received with the Z (vert) component of a three axis induction magnetometer, although the horizontal components may also be applicable (independence of magn. latitude/longitude relative to flight path). So far, best results were obtained from magnetometers located at mountain top locations (Reno/La Posta, etc.). More important, the relative amplitude depends on launch/reentry time windows with respect to iono/magneto-spheric parameters and signals for D and E layers were observed only within their day-lit zone of ionosphere. Also, at the transition period from day into night zones of ionospheric illumination, E layer signals were observed but D layer signals rapidly became faint. More measurements at different locations covering the entire North American continent and beyond are required for proper modelling. (For further details see paper.)*

**Sensing of Seismo-Electromagnetic Earthquake Precursor Radiation Signatures Along  
Southern California Fault Zones: Evidence of Long Distance Precursor ULF Signals Observed  
Before a Moderate Southern California Earthquake Episode**

Jack Y. Dea, Charles L. Richman  
Naval Ocean System Center, San Diego, CA/USA 92152-5000

Wolfgang-M. Boerner  
University of Illinois at Chicago,  
EECS, Communications and Sensing Laboratory  
Chicago, IL/USA 60680-4348

### Summary

Although questioned for a long time, there is accumulating evidence for the existence of detectable seismo-electromagnetic phenomena worldwide. California is geologically as well as seismically a unique region for studying these phenomena in depth, because the Southern California geologic province has a multitude of off-shore and inland fault zones with San Diego in its center. At the Naval Ocean Systems Center (NAVOCEANSYSCEN) Low Frequency Noise Laboratory, San Diego CA., we monitor 0.1 - 10 Hz Ultra Low Frequency (ULF) and 10 - 40 Hz Extremely Low Frequency (ELF) signals using mu-metal loaded multi-turn search coil sensors, as well as 10 - 100 KHz Very Low Frequency (VLF) signals using large one-meter-diameter loop antennas. We have observed precursor seismo-electromagnetic emissions of several earthquake events. In this paper, we report on observations of broadband ULF signals before and during the Upland quake of April 17, 1990 ( $M_s = 4.6$ ), centered

200 km north of San Diego. The signals were detected with the vertically oriented search coil sensor and not with the horizontally oriented sensors, which suggests a disturbed ionosphere as the most likely source of these signals. The large pre-quake ULF activity, the rapid decay of ULF activity after the quake, and the absence of any geomagnetic storms indicate that the ULF activity was correlated well with the Upland quake. Although the particular mechanism coupling geologic activity to the ionosphere is not known, we cite a number of hypotheses concerning these mechanisms. An interpretation of our radio observations of seismic activity is presented and extended to earth-quake precursor or predictor studies. We are in the process of expanding this research with the building of more monitoring stations and the improvement of our electric and magnetic field measurement, data collection, formatting, and data processing capabilities.

### 1. Introduction

Although, the existence of seismo-electromagnetic earthquake precursor radiation is yet to be accepted by the majority of the earth science community, it has become an issue of intense international debate. The growing number of reports on the observation of electromagnetic signals before the occurrence of earthquakes has gained greater acceptance for these phenomena and increased curiosity among the earth scientists especially seismologists and geomagnetologists. These reports cover a broad spectrum of frequencies including the Ultra Low Frequency (ULF) (0.01 - 10 Hz), Extremely Low Frequency (ELF) (10 - 3000 Hz), Very Low Frequency (VLF) (3 - 60 kHz), and Low Frequency (LF) (60 - 300 kHz) bands. Examples include many papers published on seismo-electromagnetic effects in a special October 1989 issue (1) in the journal: *Physics of the Earth and Planetary Interiors* (Parrot and Johnston, guest editors). Other examples include ULF observations by Rauscher and Van Bise (2) and Frasier-Smith et al. (3), ELF-VLF observations by Tate and Daily (4), LF observations by Yoshino et al. (5), and

electrotelluric observations by Varotsos and Lazaridou (6). In addition to observations of active emissions, passive ELF-VLF-LF propagation changes have also been observed (4).

Here, at the Low Frequency Noise Laboratory of the NAVOCEANSYSCEN, San Diego, CA, we have been monitoring VLF radio noise for over two decades. The main goal has been the improvement of coverage prediction for Naval communications. More recently (since early 1990) monitoring has been expanded to include coverage of the ULF and lower ELF ranges. Our expanded capabilities include the acquisition of three-axis search coil sensor systems capable of measuring minute magnetic field changes in the frequency range of 0.1 - 40 Hz. Our low frequency broadband surveillance research included a number of observations of seismo-electromagnetic precursor emissions prior to several recent earthquake events in California. In the following sections, we report our intriguing observations of possible precursor magnetic signals in the 0.1 - 5 Hz range, on one of the many recorded events, namely those preceding the occurrence of the April 17, 1990 earthquake ( $M_s = 4.6$ ) centered at Upland, California 200 km north of San Diego. We first describe the equipment used and then discuss the observations made using the monitoring equipment.

### 2. ULF-ELF Instrumentation

A sensitive three-axis search coil magnetometer system, originally designed for underwater ship detection, was used for our ULF/ELF measurements. Fig. 1 shows the schematic configuration of one axis of the three-axis search coil magnetometer systems. Each sensor head consists of 90,000 turns of fine wire, wrapped on a mu-metal rod. A low noise instrumentation preamplifier is also inserted directly at the sensor head in order to avoid subsequent amplification of cable noise. The coil and electronics are electrostatically shielded with cylindrically shaped foil covers and are all housed inside a plastic cylinder. Each cylinder measures 10 cm in diameter by 34 cm in length. The three sensor heads are mounted inside a weatherproof fiberglass enclosure. The fully loaded enclosure weighs approximately 30 pounds, (1 lb = 454g) and is readily portable. In the field, the three orthogonally arranged sensor heads are oriented with the x-sensor pointing east, the y-sensor pointing north, and the z-sensor pointing vertical. A 36 meter cable connects the sensor unit to the external amplifier unit which consists of an amplifier, a 40 Hz low-pass filter, and a 60 Hz notch filter for each axis of operation. For general operations, a spectrum analyzer (HP 3561A) is used to observe real-time power spectra, and a magnetic tape data recorder (Honeywell 101) is used for data recording.

We operate a ULF-ELF station at the NAVOCEANSYSCEN Low Frequency Noise Laboratory in San Diego, and another one at a remote mountain station in La Posta, California, roughly 100 km east of San Diego and 20 km north of the US Mexican border. Fig. 2

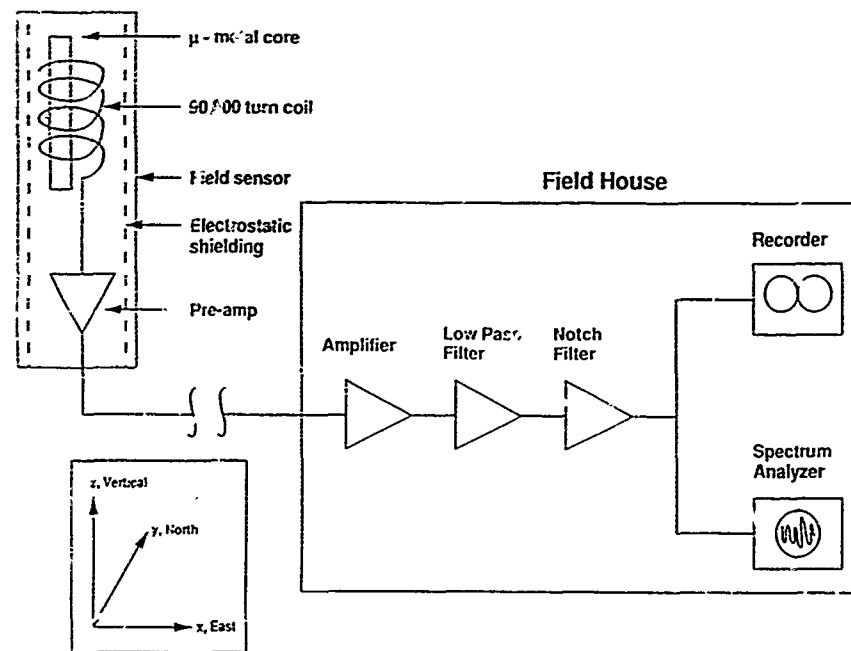


Fig 1. Diagram of one axis of the NAVOCEANSYSCEN three-axis search coil magnetometer system. Insert shows coil orientations.

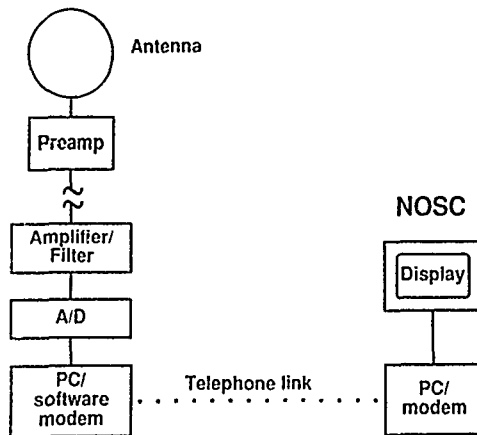


Fig 2. Diagram of the NAVOCEANSYSCEN remote site set-up. The magnetometer system is the same as that shown in Fig 1.

shows a schematic plan of the remote station setup. It uses a personal computer, Fast Fourier Transform (FFT) and telecommunications software, and a high-speed modem in its operation.

The search coil magnetometer systems can measure minute changes in the ambient magnetic field. Fig. 3 shows the calibration chart of one axis of our magnetometer system. The output response increases linearly with frequency because the coil sensors measure the derivative of the field and not the field itself. From this calibration chart, we can estimate the minimum field changes expected in the 0.1 - 40 Hz range. The self-noise of the system is approximately

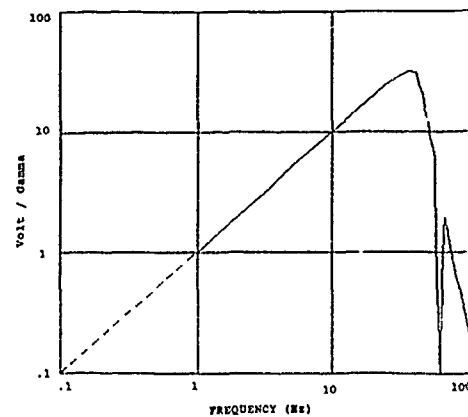


Fig 3. Calibration curve of the NAVOCEANSYSCEN search coil magnetometer system in volts/gamma versus frequency. Solid line indicates measured values, dashed line indicates extrapolated values. Low pass cutoff at 40 Hz and notch filtering at 60 Hz are clearly seen.

$2.5 \text{ mV (rms)}(\text{Hz})^{-1/2}$ . At 5 Hz, the system outputs 5 volts/ $\gamma$  ( $1 \gamma = 1 \text{ nano-Tesla}$ ). An ambient signal to generate an output above the self-noise requires a signal of  $0.0005 \gamma (\text{Hz})^{-1/2}$  or  $0.5 \text{ milli-}\gamma (\text{Hz})^{-1/2}$ . This order of sensitivity of the magnetometer system used is similar to that of the US Geological Survey (USGS) as described in (7), to that of Van Bise and Rauscher (8-10), but

somewhat less sensitive to that used by the University of California at Berkeley (UCB) as is also described in (6). This order of sensitivity is generally sufficient for most geophysical research because the ambient background noise levels are somewhat higher than the minimum levels that can be measured. By contrast, fluxgate magnetometers have a sensitivity of only  $0.1 \gamma (\text{Hz})^{-1/2}$ ; and as a result interesting precursor phenomena could be missed due to this lack of sensitivity.

### 3. Evidence of Pre-Earthquake ULF Signals in Southern California

The Pacific coastal mountain ranges of Canada, the United States and Mexico, represent recent crustal deformations, resulting from the tectonic movement of the Pacific plate along several fault systems. The America-Pacific plate boundary forms part of the so called "ring of fire" which also includes the Aleutian Islands, Japan, and the South Pacific Islands. The Pacific plate is moving northwest with respect to the America plate at an average rate of 6 cm per year. The slippage rate is less than 6 cm per year, and is made up by seismic crustal events. The San Andreas Fault, which forms part of the plate boundary in California, runs from San Francisco in the north to El Centro in the south. Two major adjustments of the Pacific plate-America plate system occurred in the San Francisco area in 1906 ( $M_s = 8.3$ ), and in the San Bernardino-Parkfield region just north of Los Angeles in 1857 ( $M_s = 8.0$ ). The Loma Prieta earthquake of 1989 ( $M_s = 7.1$ ) represented a comparatively minor adjustment. In Southern California, the strain has been accumulating since 1857; a large quake is expected within 30 years along the San Jacinto fault zone near Anza, Ca. Fig. 4 shows the major fault systems in the Southern California region together with the locations of San Diego and La Posta, where the NAVOCEANSYSCEN ULF-ELF observing stations are located. The many active fault systems in this region make it one of the most active seismic regions in the world. Many universities, research laboratories, and the USGS have contributed to two major seismic monitoring sites; one located at Parkfield, CA along the north-central San Andreas fault some 250 km north of Los Angeles (11),

and the other located at Pinon Flat, 150 km south-east of Los Angeles and 30 km east of Anza, Ca. (Fig. 4) to monitor activities along the San Jacinto fault which is one of several active strike-slip faults in Southern California, sub-parallel to the main San Andreas fault. NAVOCEANSYSCEN has contributed an ULF-ELF-VLF monitoring station to the Pinon Flat Observatory, whereas the Stanford University STAR (Space, Telecommunications and Radioscience) Lab has installed a low-frequency monitoring station at the Parkfield observatory.

The NAVOCEANSYSCEN monitoring stations at San Diego and La Posta were originally used to monitor ELF signals emanating from the ionosphere when the ionosphere was perturbed by the passage of a space vehicle (12). For those purposes, the power spectrum ranging from 0.1 Hz - 40 Hz is recorded routinely. The San Diego station has collected background noise signature records starting since January 1990, and the La Posta station since May 1990. The data sets consist of averaged noise background power spectra down-loaded once or twice daily.

The data reported in this paper were taken from these sets of background noise recordings and differs in format from the typical geophysical format, consisting of continuous records of the amplitude of signals within a narrow frequency band. The NAVOCEANSYSCEN data sets consist of time-averaged power spectra. The NAVOCEANSYSCEN data processing and display is being expanded to reflect a more narrow band format, similar to that used by the Stanford STAR Lab and others (3), yet covering the entire frequency spectrum of relevance.

As is well known, signals in the frequency range of 0.1 - 5 Hz can originate from various sources within the magnetosphere and ionosphere (13). However, ascribing some of the signals in this range to geological processes is still debatable. On April 16, 1990 the 0.1 - 5 Hz band seemed particularly active as observed with a spectrum analyzer. Not only was the averaged noise amplitude higher than usual but the noise processes were also fluctuating more rapidly than usual. Fig. 5 shows the noise background power spectrum on a quiet day (April 10, 1990), long before the earthquake precursor arrived. Fig. 6 shows the power spectra taken on April 16, 1990; the 0.1 - 5 Hz power spectra region is elevated (+7 dB) over the quiet levels. On that day, the magnetosphere was quiet, so this broadband noise cannot be attributed to magnetospheric noise. Fig. 7 shows the power spectrum taken on April 17, 1990 at 10:00 PST (18:00 UT); the 0.1 to 5 Hz levels are still elevated. On April 17, 1990, at 15:32 a moderate ( $M_s = 4.6$ ) earthquake struck near

Upland CA, 200 km north of San Diego. Fig. 8 shows the power spectra taken at 17:30, two hours after the quake; the ULF activity has begun to recede. Fig. 9 shows the power spectrum taken on April 18, 1990; the ULF activity has been reduced close to the quiet background level. This series of observations points to possible correlation of high ULF activity with the April 17, 1990 Upland quake. A particularly striking observation is that the ULF activity diminished within a few hours of the quake (as shown in Fig. 8), and then it disappeared after about a day. We are in the process of performing a careful analysis on the statistical variations of the ULF and ELF background levels over long periods as a means of attaching a significance to the observations described which in future should also be correlated to seismic records obtained for this region.

All the data sets shown here have been extracted from the recordings taken from the vertically oriented sensor. The data from the two horizontally oriented sensors showed less elevated activity in the 0.1 - 5 Hz region. This observation can be contrasted with the observation of

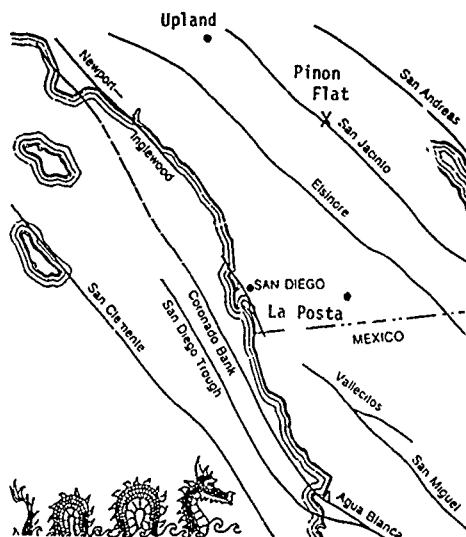


Fig 4. Detail of the active fault systems in the San Diego region. Locations of Upland, La Posta, and San Diego are shown. Location of Pinon Flat Observatory is marked with "x".

pre-quake emissions from the Loma Prieta quake, in which only horizontal sensors were available (3). Another possibility of analyzing the significance of the orientation of the sensors is to measure simultaneously the horizontal and vertical electric and magnetic field components.

We have performed preliminary statistical analysis on natural and cultural background noise levels during times when electric storms, extra-solar-terrestrial, and earth/sea-quake activity were low. In particular, we analyzed the 1 Hz signal levels (within .2 Hz bandwidth) and the 3-4 Hz signal levels of the 1990-1991 data collected by us. It has been found that the signal levels (average of 20 spectra) were stationary during the 1990-1991 period, and the standard deviations are about 1.8 dB and 1.5 dB for the 1 Hz and 3-4 Hz signals, respectively. Thus the observed increase of 5-8 dB above the quiet background level during the Upland earthquake episode is significant. We emphasize that our statistical analysis is still preliminary and we encourage more investigations of a general nature in this area.

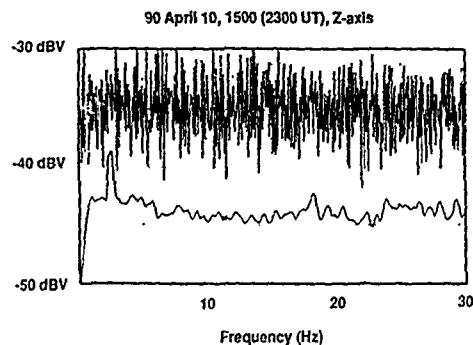


Fig 5. Typical background power spectrum data taken with the vertically oriented search coil sensor. 0.1 to 5 Hz is relatively flat. Actual time series data superimposed on top. (average of 100 frames)

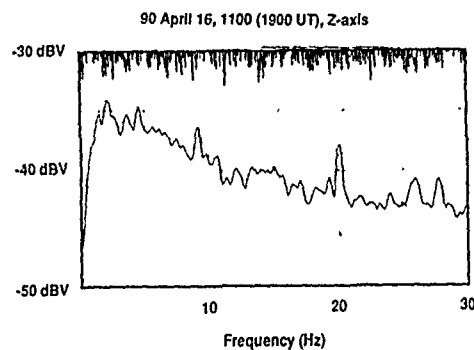


Fig 6. Data taken with the vertical search coil sensor one day before the Upland quake of April 17, 1990, showing high activity in the 0.1 to 5 Hz range. (average of 100 frames)

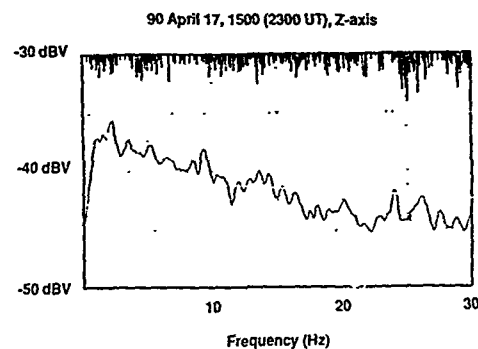


Fig 7. Data taken with the vertical search coil sensor 32 minutes before the Upland quake. Continuing high activity in the 0.1 to 5 Hz range. (average of 100 frames)

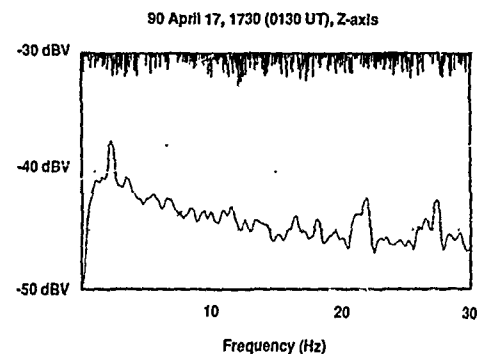


Fig 8. Data taken with the vertical search coil sensor 90 minutes after the Upland quake. 0.1 to 5 Hz activity has diminished within this 90 minutes interval. (average of 100 frames)

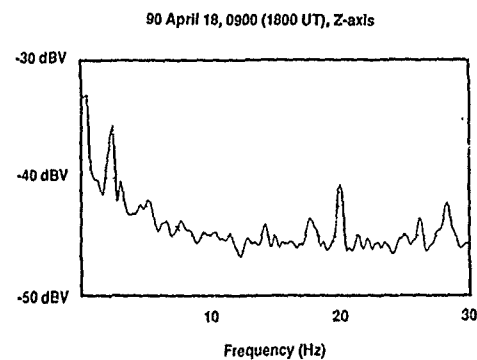


Fig 9. Data taken with the vertical search coil sensor one day after the Upland quake. 0.1 to 5 Hz activity has almost returned to the typical background levels. (average of 100 frames)

#### 4. Possible Mechanisms of Seismo-Electromagnetic Emissions

Our present knowledge of seismo-electromagnetic effects is still very incomplete. This is especially true of the preparatory phase before the occurrence of an earthquake. Laboratory experiments in rock fracturing, piezoelectricity, and triboelectricity have been performed on a sample scale much smaller than the naturally occurring rock sizes to be expected in pertinent fault zones. Hence, we can only infer from these experiments the effects that could occur, which also require high-sensitivity micro-seismic test verification. In the following sections, short summaries of the nature of seismo-electromagnetic effects and other ULF generating mechanisms will be presented.

In general, there are three classes of sources for seismo-electromagnetic emissions: electric, magnetic and acoustic. Of course, combinations of sources can occur. The best known and most studied sources are the electric ones. Piezoelectric effects occur when certain silica rocks, which contain piezoelectric crystals, are subjected to pressure and stress. The crystals become slightly deformed and a displacement of the positive ions (with respect to the negative ones) takes place. The net result is a large electric field in the vicinity of the crystals. Direct laboratory measurement of electromagnetic emissions from stressed rocks show broadband emissions in the 1 - 10 MHz region (14). We did not observe this type of radiation. It is reported, however, in reference (16), that the larger the rock sample is, the lower the observed frequencies of emission, and that a lower limit has yet to be established. The piezoelectric effect, however, can raise the static geoelectric field. According to reference (15), an increase of the geoelectric field, typically several hundred V/m, by an order of magnitude will change the ionospheric electric field by 10 to 100 mV/m. These calculations assume that the surface extent of the disturbance is larger than the ground-to-ionosphere separation. The electric field changes will affect the electron density, the ionospheric conductivity, and the overall height of the lower ionosphere. These changes, if varied over time, will be seen as ULF signals. It should be noted that the upper mantle and the earth's crust contain about 60%  $\text{SiO}_2$  (17). Thus

it is to be expected that piezoelectric effects play a major role in in seismo-electromagnetology. Triboelectrification (charge separation by friction), and piezoelectrification (or rock fracturing) can create non-stationary surface electric charges in seismic preparatory areas (18). Moving charges change the geoelectric field and induce changes in the ionosphere which are seen as ULF and ELF signals.

Recent experimental studies have found that double electric layers (DEL's) are strong sources of electromagnetic radiation (19). DEL's are formed during the fracturing of piezoelectric crystalline rock formations, in which opposite sides of cracks have opposite charges. Many such charge areas form a charge mosaic which can be modeled by a set of capacitors (i.e., dipoles). These dipole elements give off radiation when an acoustic wave passes through, or if strain changes the dipole parameters. Calculations show that the radiation lies in the 1 - 100 MHz range, which is too high to explain our observations. DELs in contact with electrolytes will generate lower frequency radiation, in the 1 kHz - 10 kHz region, which is again too high to explain our observation. However, DEL formation may explain the observation of VLF signals before and during earthquakes, as reported by Yoshino (20).

VLF emissions are likely to be detected only before large earthquakes - when the magnitude on the Richter scale is greater than  $M_s = 7$ . Yoshino et al. (5) used several locations, each with a north-south and east-west loop, for the detection of VLF effects at 81 kHz. A change in ground conductivity associated with dilatancy causes depressions in the strength of the received VLF signals or noise channels (4). These phenomena have occurred before magnitude 6.0 earthquakes (4) and also before volcanic eruptions (20).

Ionic crystal dislocation has produced electromagnetic radiation in the laboratory at ELF frequencies (14). The electromagnetic frequencies produced depend on the repetition rate of fractures. Because ionic fracture does not produce equal positive and negative dipole moments, a net radiation effect is produced. Laboratory experiments produced effects up to 1 kHz. Again the frequencies produced in the laboratory depend on the sample sizes (14). In the fault plane, ELF radiation is greatly attenuated as it passes to surface, leaving only ULF emissions.

Seismic stress relaxation causes seismo-electric activity which is associated with dilatancy. In regions of the fault zone, where there is dilatancy (as opposed to compression) the conductivity of the ground will at first increase and then will undergo a marked decrease (21). Heating eventually evaporates water, which in turn lowers the conductivity (except near the fault face). Friction causes the fault face to collect and concentrate vapor and charges. If this charge accumulation is released, it may produce effects such as corona discharges (Saint Elmo's Fire) or lightning. These effects are called earthquake lights (22). Also, marked changes in the earth's electric field have been noted, which require further analysis.

Magnetic sources of ULF signals include earth currents and changes in the earth's permeability (23, 24) which seem to present one of the most likely candidates for the observed effects. Electrokinetic phenomena occur in the conductive part of the fault face and present a model for the generation of earth currents during the earthquake stress accumulation preparatory period (15, 25). Seismic stress causes the percolation of ground water through porous rocks. This flow of fluid, under certain circumstances, gives rise to an electric current through an electrokinetic effect. A current will only exist if the fluid flows through a region inhomogeneous in resistivity, permeability or coefficient of streaming potential. The streaming potential is created when a liquid is forced through a porous medium. Electro-osmosis exerts an

electromotive force which causes fluid percolation. These underground currents can be detected as disturbances to the local electro-telluric potential. The effects of ionic dislocation and electrokinetic phenomena produce ULF and ELF signals which must pass to the surface. Because attenuation in the earth is proportional to the square root of frequency, commonly only the ULF signals are observed. Fraser-Smith observed signals in the 0.01 - 0.5 Hz range just before the October 17 1989 Loma Prieta earthquake by a horizontal coil antenna (3) placed along the magnetic E-W direction. An electrokinetic model involving deep ground water flow was recently developed at the STAR Laboratory to interpret the Loma Prieta observations (26) which deserves serious consideration.

If a natural electrotelluric potential gradient exists along the fault face, then currents will flow. Geomagnetic pulsations arising from the magnetosphere and reaching into the ground will also induce ground currents along conductive paths in the earth, such as those observed during solar terrestrial storms and especially along electric power transmission systems in auroral and sub-auroral regions (27, 28).

In the last decade, three-dimensional imaging, or seismic tomography has enabled scientists to probe in detail the properties of the crust, upper mantle, lower mantle, outer core, and inner core (29) except for locating deep ground water resources and deep aquifers. However, along with deep sounding magnetotelluric profiling, it is now realized that current systems of charge, heat and fluids much larger and more complex than thought previously, flow in the upper to lower mantle of the earth (17). Those current systems generate the major portion of the static geomagnetic field on the surface of the earth. However, it is still not known how strongly the crustal plates are coupled to the interior electric current systems. If the

coupling is significant, then crustal deformation may have an indirect effect on the earth's static geomagnetic field and should be seen as small variations of the large static field of approximately 1/2 Gauss.

Another seismomagnetic effect occurs when the permeability of the underlying rocks changes. Certain rocks under stress increase their magnetic permeability and will either enhance or oppose the earth's magnetic field. This effect is called tectomagnetism and can be duplicated in the laboratory with piezomagnetic materials (30). The time period for this phenomenon is of the order of days. DC magnetic field perturbations caused by rock magnetic anisotropy were noted in the 1976 Tang-Shan North China earthquake (31). ULF and DC volcano-magnetic effects were noted during and before the 1980 Mount St. Helens eruption (32).

Acoustic waves have already been mentioned in connection with DELs in the generation of high frequency electromagnetic radiation. However, acoustic mechanisms can directly generate ULF, ELF and VLF emissions through interactions with the ionosphere. There are two possible mechanisms. The first is the production of long period acoustic-gravity waves by numerous microshocks before the earthquake and by the main shock (33). One possible response of the ionosphere is the production of medium-scale traveling ionospheric disturbances in the mid-latitude regions (34). ULF magnetic disturbances were caused by this form of acoustic magnetic coupling at the time of Mount St. Helens eruption (35). Low frequency gravity waves propagate azimuthally around the earth while higher frequency acoustic waves are bent upward toward the magnetosphere (36). A second mechanism is the launching of acoustic waves from seismic waves. The acoustic waves, amplified through the atmosphere because of the decreasing atmospheric density with increasing height, induce VLF emission levels which have been detected by satellites (33).

#### 5. Discussion and Interpretation

The intriguing observation at NAVOCEANSYSCEN of high ULF activity during the Upland earthquake episode of April 17, 1990 raises the question of the nature of the observed emissions. The extent of the fault face is too small to directly generate propagating ULF electromagnetic emissions. However, induction fields may be observed near the fault. Induction fields seen 200 km away (the distance from San Diego to Upland), will at best be dipole-type fields. Dipole fields decrease with the cube of the distance. In order for dipole fields to be observed 200 km away, the field strength near the source must be enormous and would cause widespread disruption of electrical equipment. Because this was not reported to have occurred, induction fields from the fault epicenter could not be the cause of the ULF signals. We conclude that these signals originated from the ionosphere and that hydromagnetic waves excited within the ionosphere are the likely sources of these signals.

Acoustic waves launched from the epicenter region and rapid geoelectric or geomagnetic field changes can couple into the ionosphere to generate hydromagnetic waves traveling along the ionospheric fluid layer. Hydromagnetic waves can be detected when they are directly overhead and their evanescent fields reach into the ground. The measurements taken from all of three axes indicated that only the vertical (z) axis showed significant ULF activity prior to the Upland earthquake event. This observation is consistent with the hypothesis that we detected evanescent fields whose sources were overhead.

Another possibility related to the above theories is the concept of field line resonance (37). In field line resonance, hydromagnetic waves cause oscillations of the geomagnetic field lines in ways similar to the plucking of a string. The oscillating field lines should be detected in the vertical sensor and the northerly oriented horizontal sensor. The

vertical component of the geomagnetic field at San Diego on average is nearly twice as large as the N-S horizontal component with the E-W horizontal component being negligible (0.44 G : vertical, 0.24 G : N-S, 0.06 G : E-W), and thus we would expect a larger signal from the vertical sensor. This hypothesis of field-line resonance also appears to be consistent with our observations of strong activity in the vertical sensor and weak activity in the horizontal sensors.

The Stanford observation of high ULF activity, particularly in the 0.01 - 0.5 Hz range, just prior to the Loma Prieta earthquake of October 17, 1989, was recorded only 7 km from the epicenter. In addition, only one horizontally oriented sensor was available. It is believed that the Stanford STAR Lab ULF sensor was detecting only local induction fields which should be detectable in all three axes. Moreover, the Stanford ELF-VLF sensors, horizontally oriented (magnetically E-W), were not able to detect precursor emissions 52 km from the epicenter at another STAR Lab observatory. Thus, if our hypothesis is correct, distant quake precursor events can be detected primarily with the vertically oriented sensor while all three axes can be used to detect precursors to local quakes, which is also consistent with the recent electrokinetic modeling results from the STAR Laboratory showing that deep ground water flow arising from the prequake preparatory phase could result in detectable ULF signatures (36). Several three-axis magnetic and electric field sensor systems should be used to test the feasibility of triangulation. Earthquakes of magnitudes  $M_s = 4$  or larger are good candidates for this method of precursor ULF detection.

#### 6 Summary and Conclusion

We have briefly described, geographically and geologically, the Southern California region. Some of the regional faults form part of the boundary between the Pacific plate and the America plate. Because of the blocking nature of the San Bernardino Mountains near Los Angeles, the Pacific plate cannot slip past and locks onto the thicker crust. Tremendous stresses are built up, and the Southern California region breaks up into a region composed of several major fault lines and numerous smaller fault lines; the fault concentration is greater than most other regions in North America. Similar fault concentrations exist, such as the U.S. Midwest New Madrid fault zone, and the Aleutian-Alaska arc extending down to Vancouver Island.

We have described our equipment, of which the most important was the three-axis search coil magnetometer system. The search coil sensors are sensitive to at least  $0.001 \gamma (\text{Hz})^{-1/2}$ , which is two orders of sensitivity better than the fluxgate sensors geophysicists typically use. This improved sensitivity allows for the observation of weak ULF signals which otherwise would not be detected. We next discussed the observation of broadband ULF signals in the 0.1 - 5 Hz range before the Upland quake of April 17, 1990. The large pre-quake ULF activity, the rapid decay of ULF activity after the quake, and the absence of any geomagnetic storms indicated a possible correlation of the ULF activity with the Upland quake. Next, we briefly described the various hypotheses concerning the generations of ULF, ELF, and VLF signals by seismic activity. These hypotheses include:

- (i) the generation of surface charges by piezoelectrification, triboelectrification, or rock fracturing;
- (ii) acoustic interaction with dipole charge layers;
- (iii) electrokinetic generation of earth currents through groundwater flow;
- (iv) piezomagnetic changes in the underlying rocks;
- (v) acoustic coupling to the ionosphere.

Except for the double-charged layer hypothesis, all these effects can potentially affect the ionosphere which can, in turn, produce traveling waves that can be detected at great distances from the fault zone. Finally, we interpreted our data to be observations of evanescent fields of ionospheric waves traveling overhead. We came to this conclusion because we detected activity from the vertical axis but little from the two horizontal axes. If significant activity were indeed observed from the northerly oriented horizontal axis, then the field line resonance model of an oscillating geomagnetic field would need to be used as well. The major mechanisms that couple the pre-earthquake changes, within the earth's interior, to the ionosphere are unclear at present. However, these observations give rise to the hope that at least some earthquakes may be predicted through the monitoring of precursor ULF signals. We are presently expanding our research by building more monitoring sites and improving our electric and magnetic field measurement systems, data collection, formatting, and data processing capabilities.

Finally, as a result of this study, it is hoped that increased cooperation between U.S., Canadian, Japanese, European and other seismo-electromagnetologists emerges in order to obtain an improved understanding of the underlying mechanisms of these newly discovered phenomena.

#### Acknowledgments

The authors wish to thank Mr. Thomas N. Roy of NAVOCEANSYSCEN for contributing the sensitive search coil magnetometer systems to the project. We thank Dr. James W. Bond, Dr. Peder M. Hansen and Paul A. Singer all of NAVOCEANSYSCEN, for proofreading the document and providing continual encouragement. We also thank Mr. Elizabeth A. Rauscher and Mr. William Van Bise, all of Magtek Laboratory, Reno, Nevada; Dr. Anthony C. Frasier-Smith and Prof. Robert A. Helliwell of Stanford University, STAR (Space, Telecommunication and Radio-Science) Laboratory; Prof. H. Frank Morrison of the Engineering Geosciences Laboratory within the Dept. of Materials Science and Mineral Engineering, of the University of California at Berkeley (UCB); Prof. Tomiya Watanabe of the Geophysical Observatory, UBC, Vancouver, Canada; Professor Takeo Yoshino of the University of Electrocommunications, Chofu-shi, Tokyo Japan; Dr. Walter A. Flood of the US Army Research Office, Geo-Sciences Division at Research Triangle Park, N.C.; and Drs. Malcolm J.S. Johnston and Thomas A. Heaton of the U.S. Geological Survey, Menlo Park and Pasadena offices, respectively, for their helpful discussions. Support for this work was provided by Independent Research Funds of NAVOCEANSYSCEN, Dr. Alan Gordon, coordinator, and a US Navy-ASEE-SFRP Distinguished Professor Award.

#### REFERENCES

1. M. Parrot and M.J.S. Johnston, (guest editors), Special Issue on Seismo-Electromagnetic Effects. *Physics of the Earth and Planetary Interiors* 57, 1-188 (1989).
2. E.A. Rauscher and W. Van Bise. *Bull. Am. Phys. Soc.* 32, 67 (1987).
3. A. C. Frasier-Smith, A. Bernardi, P.R. McGill, M.E. Ladd, R.A. Helliwell, and O.G. Villard Jr. *Geophys. Res. Lett.* 17, 1465 (1990).
4. J. Tate and W. Daily. *Physics of the Earth and Planetary Interiors* 57, 1 (1989).
5. T. Yoshino, I. Tomizawa and T. Shibata. *Annales Geophysicae* 3, 727 (1985).
6. P. VAROTSOS and M. Lazaridou, *Tectonophysics* 188, 321 (1991).
7. V.F. Labson, A. Becker, H.F. Morrison, and U. Conti. *Geophysics* 50, 565 (1985).
8. W. Van Bise and E. A. Rauscher. *Bull. Am. Phys. Soc.* 32, 67 (1987).
9. W. Van Bise and E. A. Rauscher. *Bull. Am. Phys. Soc.* 34, 109 (1989).
10. E. A. Rauscher and W. Van Bise. US Patent 4,724,390 (1988).
11. W.H. Bakun, K.S. Breckenridge, J. Bredehoeft, R.O. Burford, W.L. Ellsworth, M.J.S. Johnston, L. Jones, A.G. Lindh, C. Mortensen, R.J. Mueller, C.M. Poley, E. Roeloffs, S. Schulz, P. Segall, and W. Thatcher. *Parkfield, California, Earthquake Prediction Scenarios and Response Plans*. US Geological Survey, Menlo Park, CA, Open-File Report, No. 87-192 (1987).
12. J. Y. Dea, W. Van Bise, E.A. Rauscher, and W.-M. Boerner, *Proceedings NATO-AGARD, 49th EPP Symposium, Cesme, Turkey, 30 Sept. - 04 Oct. 1991, Session IV, Ionospheric Sensing (B), Paper No. 19. (this issue) (1991).*
13. S.I. Akasofu and S. Chapman. *Solar Terrestrial Physics* Clarendon Press, Oxford 1972.
14. N.I. Gershenzon, M.B. Gokhberg, A.V. Karakin, N.V. Petvaishvili, and A.L. Rykunov. *Physics of the Earth and Planetary Interiors* 57, 129 (1989).
15. H. Mizutani, T. Ishido, T. Yokokura, and S.S. Ohnishi. *Geophys. Lett.* 3, 365 (1976).
16. L.N. Popov, Y.K. Krakovetzky, M.B. Gokhberg, and V.A. Philipenko. *Physics of the Earth and Planetary Interiors* 57, 115 (1989).
17. M.H.P. Bott. *The Interior of the Earth: Its Structure, Constitution and Evolution*. Elsevier, Amsterdam. 1982.
18. V.M. Chmyrev, N.V. Isaev, S.V. Bilichenko, and G. Stanev. *Physics of the Earth and Planetary Interiors* 57, 110 (1989).
19. N.G. Khatiaishvili and M.E. Perelman. *Physics of the Earth and Planetary Interiors* 57, 169 (1989).
20. T. Yoshino and I. Tomizawa. *Physics of the Earth and Planetary Interiors* 57, 32 (1989).
21. K. Meyer and R. Teisseyre. *Physics of the Earth and Planetary Interiors* 57, 45 (1989).
22. D.A. Lockner, M.J.S. Johnston, and J.D. Byerlee. *Nature* 302, 28 (1983).
23. T. Rikitake and Y. Honkura. *Solid Earth Geomagnetism*. D. Reidel Publ. Co., Dordrecht. 1985.
24. T. Rikitake. *Electromagnetism and the Earth's Interior*. Elsevier, Amsterdam, 1966.
25. I.P. Dobrovolsky, N.I. Gershenzon, and M.B. Gokhberg. *Physics of the Earth and Planetary Interiors* 57, 144 (1989).
26. A.B. Draganov, U.S. Inan, and Yu. N. Taranenko. *Geophys. Res. Lett.* Vol 18, #6, 1127-1130 (1991).
27. V.D. Albertson and J.G. Kapperman. *IEEE Spectrum* 27 (March 1990).
28. W.-M. Boerner, J.B. Cole, W.R. Goddard, M.Z. Tarnawsky, L.-F. Shafai, and D.H. Hall. *Space Science Reviews* 35, 195 (1983).

29. T. Lay, J.T. Akrens, P. Olson, J. Smyth, and D. Loper. *Physics Today*. 44 (October 1993)
30. M.J.S. Johnston. *Reviews of Geophysics*. 25, 986 (1987)
31. Z. Zhiĵa. *Physics of the Earth and Planetary Interiors*. 57, 11 (1989)
32. M.J.S. Johnston. *Physics of the Earth and Planetary Interiors*. 57, 47 (1989)
33. M. Parrot and M.M. Mogilevsky. *Physics of the Earth and Planetary Interiors*. 57, 85 (1989)
34. T. Shibata. *Journal of Atmospheric and Terrestrial Physics*. 45, 797 (1983)
35. R.J. Mueller and M.J.S. Johnston. *Physics of the Earth and Planetary Interiors*. 57, 23 (1989)
36. S.H. Francis. *Journal of Atmospheric and Terrestrial Physics*. 37, 1011 (1976)
37. D. J. Southwood. *Planet. Space Sci.* 22, 483 (1974)

# REMOTE SENSING OF AEROSOL EXTINCTION USING SINGLE-ENDED LIDARS

J. H. Richter, H. G. Hughes and M. R. Paulson

Ocean and Atmospheric Sciences Division  
Naval Ocean Systems Center  
San Diego, California 92152-5000

## 1. SUMMARY

Aerosol extinction is one of the primary factors limiting the performance of systems which rely on visible or infrared radiation in the atmosphere. Lidar (light detection and ranging) systems have been used to measure the radiation backscattered to a receiver by aerosols in an attempt to determine extinction. However, the technique of inverting the power returned to a single-ended lidar to obtain range-dependent extinction coefficients requires a knowledge of the relationship between the volumetric backscatter and extinction coefficients along the path. If the atmosphere can be shown to be horizontally homogeneous, the need for knowing the relationship between backscatter and extinction can be eliminated by comparing the powers received from each altitude along two or more different elevation angles, and the extinction coefficient variation in the vertical direction can be readily determined. In this paper, a review is presented of past efforts to determine atmospheric extinction from single-ended lidar measurements of backscatter, and the assumptions made concerning the backscatter/extinction relationships. The degree to which the aerosols within the convectively mixed atmosphere can be expected to be horizontally homogeneous is also discussed. The conclusions are that unless the extinction/backscatter relationship is known, or that the atmosphere is horizontally homogeneous over the propagation path, the accuracies of extinction coefficients determined by a single-ended lidar cannot be assured.

## 2. INTRODUCTION

The utility of a monostatic lidar system as a remote sensor for obtaining temporal and spatial information about the dynamic processes of the atmosphere is well established. By measuring the power backscattered from a laser pulse at a given range to a receiver, the movement and relative concentrations naturally occurring aerosols, of industrial pollutants or battlefield obscuring agents can be monitored, and the bases of clouds determined. Remote mapping of wind velocities and flow patterns over large portions of the atmosphere can also be carried out. In these applications, the lidar is used as a tracer of aerosols which scatter the incident radiation rather than a probe for studying the aerosols' optical properties. There is an extensive amount of literature published on the merits and performance of aerosol tracer lidar techniques (which need not be repeated here). Other lidar systems (Differential Absorption

or DIAL and Raman) which utilize a wavelength dependence or frequency-shifted re-radiation of absorption spectra in the atmosphere have been used to obtain vertical profiles of concentrations of various gases.

The use of visible and infrared electro-optical systems for and weapons and sensor systems require the capability to predict how radiation interacts with atmospheric aerosols in the marine environment. For a given aerosol size distribution, extinction can be determined from Mie theory assuming that they scatter and absorb radiation as if they were spheres of known refractive indices. For example, in the well-mixed marine boundary layer, relative humidities are usually high enough that most of the aerosols are hydrated, taking on a spherical shape. But above the layer, where relative humidities are lower, aerosols may be non-spherical. In such cases, the optical properties predicted for spheres may differ by as much as an order of magnitude from those observed. Estimates of slant-path visibilities are required as inputs to computer codes for scaling selected aerosol size distribution models with altitude to predict the performance of electrooptical systems. Lidars have been used to determine aerosol extinction. However, the technique of inverting the power returned to a single-ended lidar to obtain range-dependent aerosol extinction coefficients have not yet resulted in techniques or instruments with assured accuracy. In this paper, past efforts to use lidar to measure aerosol extinction are briefly reviewed, and the difficulties are pointed out which need to be overcome before lidars can become operationally useful probes for aerosol extinction.

## 3. SOLUTIONS TO THE LIDAR EQUATION

The single-scatter lidar equation is given by the relation

$$S(r) = \ln[P(r)r^2] = \ln K + \ln \beta(r) - 2 \int_0^r \sigma(r') dr' \quad (1)$$

In this equation  $P(r)$  is the power received from a scattering volume at range  $r$ ,  $K$  is the instrumentation constant, and  $\beta(r)$  and  $\sigma(r)$  are the volumetric backscatter and extinction coefficients, respectively. In differential form this equation is

$$\frac{dS(r)}{dr} = \frac{1}{\beta(r)} \frac{d\beta(r)}{dr} - 2\sigma(r) \quad (2)$$

The solution of equation (2) requires knowing or assuming a relationship between  $\beta(r)$  and  $\sigma(r)$ . However, if the atmosphere is homogeneous, the extinction coefficient can be simply expressed in terms of the rate of change of signal with range, i.e.  $\sigma = -1/2 [dS(r)/dr]$ . A plot of  $S(r)$  vs.  $r$  would then yield a straight line whose slope is  $-2\sigma$ .

Various authors (Refs 1 & 2) have presented solutions to equation (2) by assuming a functional relationship between backscatter and extinction to be of the form

$$\beta(r) = C\sigma(r)^k \quad (3)$$

where  $C$  and  $k$  are not dependent upon  $r$ . In this case, only the aerosol number density is allowed to vary with range and not the size distribution. When the integration is performed in the forward direction from a range  $r_0$ , where the transmitted beam and receiver field-of-view overlap, to a final range  $r$ , the extinction coefficient is given by

$$\sigma(r) = \frac{\exp[S(r)]}{\frac{\exp[S(r_0)]}{\sigma(r_0)} - 2 \int_{r_0}^r \exp[S(r')] dr'} \quad (4)$$

where  $\sigma(r_0)$  is the unknown contribution to extinction out to the overlap range.

The instabilities encountered in equation (4) can be overcome by performing the integration in the reverse direction from a final range,  $r$ , in toward the transmitter. In this case the extinction coefficient is given by,

$$\sigma(r) = \frac{\exp[S(r)]}{\frac{\exp[S(r_f)]}{\sigma(r_f)} + 2 \int_r^{r_f} \exp[S(r')] dr'} \quad (5)$$

where  $\sigma(r_f)$  is the unknown value of extinction at the final range. Solutions to the single-scatter lidar equation have been presented for the reverse and forward integration cases (Ref 3) where the relationship between the backscatter and extinction coefficients is assumed to vary with range according to

$$\beta(r) = C(r)\sigma(r)^k \quad (6)$$

where  $k$  is a constant. For the forward integration case the extinction coefficient as a function of range is given by

$$\sigma(r) = \frac{\frac{1}{C(r)} \exp[S(r)]}{\frac{\exp[S(r_0)]}{C(r_0)\sigma(r_0)} - 2 \int_{r_0}^r \frac{1}{C(r')} \exp[S(r')] dr'} \quad (7)$$

and for reverse integration by

$$\sigma(r) = \frac{\frac{1}{C(r)} \exp[S(r)]}{\frac{\exp[S(r_f)]}{C(r_f)\sigma(r_f)} + 2 \int_r^{r_f} \frac{1}{C(r')} \exp[S(r')] dr'} \quad (8)$$

where the constant  $k$  has been chosen to be unity.

#### 4. DISCUSSION

Klett (Ref 1) discussed the instabilities inherent in equation (4) due to the negative sign in the denominator and the uncertainties in the boundary value  $\sigma(r_0)$ . In order to determine the appropriate value of  $\sigma(r_0)$  from the raw lidar return, the values of  $C$  and  $k$  appropriate for the existing air mass must be known. While the value of  $k$  is usually close to unity, a critical problem is determining the proper choice of  $C$ . From the work of Barteneva (Ref 4), a change greater than an order of magnitude can be inferred in the value of  $C$  between clear air and fog conditions. Kunz (Ref 5) proposed that, for situations where the lower levels of the atmosphere appeared horizontally homogeneous,  $\sigma(r_0)$  could be determined from the return of a horizontal lidar shot by means of the slope method, and then used as the boundary value in equation (4) for calculating the extinction in the vertical direction. This approach necessarily assumes that the ratio  $\beta/\sigma$  remains constant with altitude, and that the linear decrease of return signal with range is indeed indicative of a homogeneous atmosphere. Caution must be applied in interpreting linear decreases of  $S(r)$  with range as being related to homogeneous conditions. Kunz (Ref 6) has reported examples of vertical lidar returns beneath clouds which seemingly originated from a homogeneous atmosphere without a reflection from cloud base. In conditions where the aerosol size distribution is increasing with range, an increase in backscattered power can be balanced the decrease in power caused by attenuation.

While equation (2) is "stable", it is difficult to use in a practical sense unless there is another independent determination of  $\sigma(r)$ . For fog conditions, the first term in the denominator of equation (5) becomes negligible, but in these situations the single scatter lidar equation is not applicable. Carnuth and Reiter (Ref 7) used an approach to invert lidar returns beneath stratocumulus clouds by assuming  $\sigma(r)$  to be equal to accepted values of cloud base extinction coefficient ( $10 \text{ km}^{-1} \leq \sigma(r) \leq 30 \text{ km}^{-1}$ ). This approach is still assumes that  $\beta/\sigma$  is invariant with altitude. Lindberg, et al., (Ref 8) have also presented measurements beneath stratus clouds in Europe. Extinction coefficients determined by the reverse integration technique agreed reasonably well with those calculated from balloon borne particle measurements and point measurements of visibility when the atmosphere was horizontally homogeneous and stable. The method by which  $\sigma(r)$  was chosen is not clear since the authors only stated that an iteration procedure was used. Ferguson and Stephens (Ref 9) also used an iterative scheme in an attempt to select the value of

$\sigma(r)$ . The value of  $\sigma(r)$  at a close-in range (where the returned signal is well above the system noise) was varied until the  $\sigma(r)$  determined from equation (5) allowed calculated and measured values of  $S(r)$  to agree. The chosen value of  $\sigma(r)$  was then used as  $\sigma(r)$  in equation (1) to integrate out from the transmitter. This procedure requires the system to be accurately calibrated and the value of  $\beta/\sigma$  to be specified and invariant with range. Hughes et al. (Ref 10) showed the extinction coefficients calculated with this algorithm were not unique and were extremely sensitive to the chosen value of  $\beta/\sigma$ . Bissonnette (Ref 3) pointed out that unless the system calibrations and  $\beta/\sigma$  are accurately known, this algorithm is no more stable than the forward integration solution.

Carnuth (Ref 11) has attempted to verify the reverse integration technique (Klett's method) by making measurements of the visual range using an integrating nephelometer to obtain  $\sigma(r)$  at the end of a slanted lidar path (7 km) up the side of a mountain. Optical depths derived from a transmissionometer operated simultaneously with the lidar were in agreement with those derived from the averages of several lidar returns in cases where the path appeared homogeneous. In other cases, discrepancies were observed which the authors attributed to the variable ratio of  $\beta/\sigma$  along the path (in addition to measurement errors and the neglect of multiple scattering effects). Salemk et al. (Ref 12) determined values of  $\sigma$  and  $\beta$  from horizontal lidar shots using the slope method when the atmosphere appeared to be horizontally homogeneous. They then presented a parameterization between values of  $\beta/\sigma$  and relative humidity ( $33\% \leq RH \leq 87\%$ ). When the parameterization was used to invert visible wavelength lidar returns in the vertical direction, the derived extinction coefficient profiles (using radiosonde measurements of relative humidity) sometimes agreed reasonably well with those measured by aircraft mounted extinction meters. In contrast, de Leeuw et al. (Ref 13) using similar types of lidar measurements did not observe a distinct statistical relationship between backscatter and extinction ratios and relative humidity. Fitzgerald (Ref 14) pointed out that other factors such as the aerosol properties can strongly affect the relationship between  $\beta/\sigma$  and relative humidity and that the power law relationship is not necessarily valid for relative humidities less than about 80%. A unique relationship between  $C(r)$  and relative humidity which is dependent on the air mass characteristics is yet to be developed.

An assumed relationship between the backscatter and extinction coefficients can be eliminated by comparing the powers returned from a volume common to each of the two lidars located at opposite ends of the propagation path. For this double-ended lidar configuration, the range-dependent extinction coefficient can be shown (Refs 15 & 16) to be related to the slope of the difference in the range compensated powers measured by the two lidars (1 and 2) at the common range  $r$  by the equation

$$\sigma(r) = - \frac{1}{4dr} [S(r)_1 - S(r)_2] \quad (9)$$

However, the receiver gain of both lidars must be accurately known since they affect the slope characteristics of the individual  $S(r)$  curves. Although the double-ended technique has a practical limitation for tactical situations, e.g., in slant path measurements at sea, it is feasible to use it in aerosol studies and to evaluate the various single-ended schemes for measuring extinction. Hughes and Paulson (Ref 15) used the double-ended lidar configuration over a 1 km inhomogeneous slant path to demonstrate that if the value of  $C(r)$  varies with range, but is assumed to be a constant, neither the single-ended forward or reverse integration algorithms will allow range-dependent extinction coefficients to be determined with any assured degree of accuracy even if the initial boundary values are specified. If, however, the manner in which  $C(r)$  varies is specified, both the forward and reverse single-ended inversions reproduce the double-ended measurements remarkably well.

In situations where the different layers of the atmosphere are horizontally homogeneous, the need for knowing the relationship between the backscatter and extinction coefficients can be eliminated by comparing the range compensated powers received from each altitude along two or more different elevation angles (Refs 17 & 18). Assuming extinction and backscatter coefficients to vary only in the vertical direction, the optical depth,  $\tau$ , between any two altitudes can be shown to be

$$\tau = \frac{[S(R_1) - S(R_2)] - [S(R_1) - S(R_2)]}{2(1/\sin\phi_1 - 1/\sin\phi_2)} \quad (10)$$

where  $S(R_1)$  and  $S(R_2)$  are the range compensated powers returned along slant ranges  $R_1$  and  $R_2$  from an altitude  $h_1$  with the lidar elevated at angles  $\phi_1$  and  $\phi_2$ , respectively, with  $\phi_1 < \phi_2$ . Similarly,  $S(R_3)$  and  $S(R_4)$  refer to the range compensated powers returned from an altitude  $h_2$  with the lidar elevated at an angle  $\phi_2$  where  $\phi_1 < \phi_2$ . In principle, if the atmosphere were horizontally homogeneous, the lidar beam could be swept in elevation and the method used between closely separated angles to obtain an incremented profile of extinction and backscatter (Ref 19). The smaller angular separations, however, place stringent requirements on the accuracies to which the range compensated powers must be measured (Ref 18). Also, the works of Russell and Livingston (Ref 17), and Spinhirne et al. (Ref 20) concluded that the atmosphere within the convectively mixed marine boundary layer rarely, if ever, has the degree of homogeneity required. Atlas et al. (Ref 21) presented examples of lidar returns observed from an aircraft above the marine boundary layer. The returns from within the mixed layer were shown to be associated with updrafts carrying aerosol-rich air upward and conversely. These effects were enhanced by increasing humidity updrafts and decreases-

ing humidity downwards that operate to increase and decrease aerosol sizes within small scale sizes between 200 and 500 meters superimposed upon the large scale (1-2 km) undulations of the inversion.

It has been demonstrated by Paulson (Ref 18) that the double angle technique can be used to determine the extent to which the atmosphere is horizontally homogeneous. In these studies, data were taken beneath a thin stratus cloud layer at about 500 meters. Two calibrated Visioceilometer lidars (Ref 8) were operated side-by-side on the west side of the Point Loma Peninsula at San Diego, Calif. and pointed west over the Pacific Ocean. A series of nearly simultaneous shots were made with the one lidar elevated at an angle of 25° and the other at 50°.  $S(r)$  values for each of the lidars (determined using 5-point running averages of the raw data) showed increasing returns with increasing range and fluctuated about one another at different ranges which indicated an inhomogeneous condition. The optical depths between different altitudes determined from Equation 10 are shown in the following table:

TABLE 1. Optical depths calculated from different altitudes up to a maximum altitude of 475 meters on 17 May 1989.

Lower Altitude (meters)	Optical depth
100	0.811
125	0.437
150	0.584
175	0.597
200	0.647
225	0.584
250	0.688
275	0.150
300	0.260
325	0.260
350	0.342
375	0.492

The optical depth between 275 and 475 meters is only 0.15, while that from 375 to 475 meters is more than three times greater (0.49). If the data were representative of a horizontally homogeneous condition, the optical depth up to 475 meters should consistently decrease as  $h_i$  increases. These data demonstrate that, even though the magnitude of  $S(r)$  from a horizontal lidar return decreases linearly with range, horizontal homogeneity can only be assured if optical depths within the boundary layer measured by the two-angle method decrease as contributions from the close-in returns are eliminated.

#### 5. CONCLUSIONS

Range-dependent extinction coefficients cannot be determined from single-ended lidar measurements with any assured degree of accuracy unless the backscatter/extinction coefficient ratio is known along the propagation path or the atmosphere is horizontally homogeneous. If the conditions exist for which the forward inversion algorithm is stable, the double-ended lidar work has shown that a single-ended lidar inversion technique would be possible when augmented with a close-in measurement of extinction and measurements to relate  $C(r)$  to air mass characteristics and relative humidity.

While the works of Mulders (Ref 22) and de Leeuw et al. (Ref 13) have concluded no relationship exists between  $C(r)$  and relative humidity, their measurements did not account for changes in the air mass characteristics. Simultaneous lidar measurements and air mass characteristics (e.g., radon and condensation nuclei) need to be conducted to identify their relationship to relative humidity profiles. Whether or not such a relationship can ever be identified in a practical sense is yet to be determined.

For a single-ended lidar to become a useful operational tool, innovative concepts need to be pursued. A novel single-ended lidar technique has been recently proposed by Hooper and Gerber (Refs 23 & 24) to measure optical depths when used down-looking from an aircraft or satellite at the ocean surface and when the reflection properties of the surface are known. In this technique, two detectors are used: one with a narrow field-of-view, which measures the power directly reflected off the rough ocean surface and another with a wide field-of-view where the directly reflected photons are blocked (aureole detector). The accuracy of the system is presently being evaluated by comparing the optical depths inferred from the direct and aureole scattered returns to those calculated from size distributions measured simultaneously from an aircraft. Should the aureole system be proven reliable it would be most useful if the optical depths determined using visible or near infrared wavelengths could be scaled directly to the mid or far infrared wavelength bands at which many important EO systems operate.

#### 6. ACKNOWLEDGEMENT

This work was supported by the Office of Naval Technology.

#### 7. REFERENCES

1. Klett, J.D., "Stable Analytical Inversion Solution for Processing Lidar Returns," Appl. Opt., 20, 211 (1981).
2. Kohl, R.H., "Discussion of the Interpretation Problem Encountered in Single-Wavelength Lidar Transmissometers," J. Appl. Meteorol., 17, 1034 (1978).
3. Bissonnette, L.R., "Sensitivity Analysis of Lidar Inversion Algorithms," Appl. Opt., 25, 2122 (1986).
4. Barteneva, O.D., "Scattering Functions of Light in the Atmospheric Boundary Layer," Bull. Acad. Sci. USSR Geophys., Ser. 12, 32 (1960).
5. Kunz, G.J., "Vertical Atmospheric Profiles Measured with Lidar," Appl. Opt., 22, 1955 (1983).
6. Kunz, G.J., "Lidar and Missing Clouds," Appl. Opt., 26, 1161 (1987).
7. Carnuth, W., and R. Reiter, "Cloud Extinction Profile Measurements by Lidar Using Klett's Inversion Method," Appl. Opt., 25, 2899 (1986).

8. Lindberg, J.D., W. J. Lentz, E. M. Measure, and R. Rubio, "Lidar Determinations of Extinction in Stratus Clouds," *Appl. Opt.*, 23, 2172 (1984).
9. Ferguson, J. A., and D. H. Stephens, "Algorithm for Inverting Lidar Returns," *Appl. Opt.*, 22, 3673 (1983).
10. Hughes, H. G., J. A. Ferguson, and D. H. Stephens, "Sensitivity of a Lidar Inversion Algorithm to Parameters Relating Atmospheric Backscatter and Extinction," *Appl. Opt.*, 24, 1609 (1985).
11. Carnuth, W., "Verification of Klett's Method by Comparison of Lidar and Transmissometer Measurements," AGARD Conference Proceedings No. 454, Paper No. 30, 1989.
12. Salemink, H.W.M., P. Schotanus, and J.B. Bergwerff, "Quantitative Lidar at 532 nm for Vertical Extinction Profiles and the Effect of Relative Humidity," *Appl. Phys.*, B34, 187 (1984).
13. de Leeuw, G., G. J. Kunz, and C. W. Lamberts, "Humidity Effects on the Backscatter/Extinction Ratio," *Appl. Opt.*, 25, 3971 (1986).
14. Fitzgerald, J. W., "Effect of Relative Humidity on the Aerosol Backscattering Coefficient at .694 and 10.6  $\mu\text{m}$  Wavelengths," *Appl. Opt.*, 23, 411 (1984).
15. Hughes, H. G., and M. R. Paulson, "Double-Ended Lidar Technique for Aerosol Studies," *Appl. Opt.*, 27, 2273 (1988).
16. Kunz, G. J., "Bipath Method as a Way to Measure the Spatial Backscatter and Extinction Coefficients with Lidar," *Appl. Opt.*, 26, 794 (1987).
17. Russell, P. B., and J. M. Livingston, "Slant-Path Extinction Measurements and Their Relation to Measured and Calculated Albedo Changes," *J. Clim. and Appl. Meteor.* 23, 1204 (1984).
18. Paulson, M. R., Atmospheric Horizontal Inhomogeneity Effects on the Optical Depths Determined by the Double Elevation Angle Lidar Technique, Naval Ocean Systems Center Technical Document 1600 (1989).
19. Kunz, G. J., "A Method for Measuring the Vertical Extinction and Backscatter Profile with a Scanning Lidar," TNO Physics and Electronics Laboratory, Report No. FEL 1988-65 (1988).
20. Spinhirne, J. D., J. A. Ragan and B. M. Herman, "Vertical Distribution of Aerosol Extinction Cross Section and Inference of Aerosol Imaginary Index in the Troposphere by Lidar Technique," *J. Appl. Meteor.*, 19, 426 (1980).
21. Atlas, D., B. Walter, S. Chou and P. J. Sheu, "The Structure of the Unstable Marine Boundary Layer Viewed by Lidar and Aircraft Observations," *J. Atmos. Sci.*, 43, 1301 (1986).
22. Mulders, J. M., "Algorithm for Inverting Lidar Returns: Comment," *Appl. Opt.*, 23, 2855 (1984).
23. Hooper, W. P., and H. Gerber, "Down Looking Lidar Inversion Constrained by Ocean Reflection and Forward Scatter of Laser Light," *Appl. Opt.*, 21, 689 (1986).
24. Hooper, W. P., and H. Gerber, "Monte Carlo Simulations of Laser-Generated Sea Surface Aureole," *Appl. Opt.*, 27, 5111 (1988).

## DISCUSSION

### J. GOLDBIRSH

*Have dual frequency lidars been considered where we take simple ratios of the power to remove the calibration constants and improve estimations of extinction and backscatter?*

### AUTHOR'S REPLY

*They have, but, to my knowledge, have not resulted in readily available extinction measurement devices.*

### D. HOEHN

*Have you analyzed the applicability of a single-ended, single-frequency lidar for  $\sigma$ -determination also under the condition, that the type of the actual aerosol size distribution may be classified by meteorological information, so that you would not have to consider the whole range of possible aerosol size distribution for determining the C-value, rather than only this class?*

### AUTHOR'S REPLY

*If you make assumptions concerning aerosol properties, air mass characteristics, homogeneity, etc., you may infer  $\sigma$  from single-ended lidars. The point of our paper was, that without such assumptions, single-ended lidars don't give you  $\sigma$  with any assured degree of accuracy.*

### C. WERNER (Comment)

*I'd like to add that the German Aerospace Research Establishment together with Impulsphysik GmbH have developed a lidar-slant visual range (SVR) measuring device for installation at airports. This SVR lidar is now installed at the Hamburg-Fuhlsbüttel airport for operational use in visibility conditions less than 500 m. This system can handle multiple scattering also and uses multiple scattering contributions for determining visibilities below 200 m. Reference: DLR-Institute of Electronics, SVR-measuring device, Report No. 88-42 (1988).*

# PROBING OF THE ATMOSPHERE WITH LIDAR

G.J. Kunz  
TNO-Physics and Electronics Laboratory  
P.O. Box 96864  
2509 JG The Hague, THE NETHERLANDS

## SUMMARY

Lidar (optical radar) is a generally accepted technique which can be used for remote sensing of atmospheric properties over ranges of kilometers within a few microseconds. Different inversion techniques to derive the required information from the lidar signal are discussed. The lidar properties determine which kind of information can be obtained. In this paper we present an overview of results obtained with two different lidar systems. The results include the assessment of the systems, long term studies of the vertical infrared structure of the atmosphere, and fast dynamic processes.

## 1. INTRODUCTION

Optical radar or lidar (light detection and ranging), is widely used for remote sensing of atmospheric quantities over ranges of kilometers. The simplest types of lidar systems are mono-static, operate at one wavelength and use direct detection. These so-called Mie lidars are applied, e.g., to measure visibility, vertical extinction and backscatter profiles, cloud base height and wind. They can also be used as cloud mapper, range finder or imaging system.

The principle of lidar is similar to that of radar, with the difference that lidars operate in the micrometer region of the electro-magnetic spectrum instead of the mm or cm region. The maximum detection ranges in homogeneous atmospheres vary with the actual weather condition and are less than 1 km for the smaller systems (Bonner, 1979 and Lentz, 1982) to more than 50 km for the largest ones (Shimizu, 1985). (See also Appendix A for a mathematical derivation of the maximum range.) The measured waveforms are a function of the spatial backscatter coefficient and the transmission losses.

The latter are a function of the path-integrated extinction coefficient. All other atmospheric parameters that can be measured with (direct detection Mie) lidar are derived from the backscatter and the extinction.

In this paper we give an overview of existing techniques for inverting data from Mie lidar systems. Some of the results obtained with two lidar systems are presented. A low-repetition rate lidar (0.1 pps) is used to investigate long term atmospheric effects. A high repetition rate lidar (10 pps) is used to study dynamic atmospheric processes. An extensive literature reference is given.

## 2. INVERTING LIDAR RETURNS

The generally accepted model describing the single-scatter return of lidar systems with direct detection is given by equation (1). This model can be applied to ranges which are large with respect to the length of the laser pulse and is the basis for inverting the backscatter and the extinction coefficients.

$$(1) \quad P(R) = \frac{K \cdot B(R)}{R^2} \cdot \exp\left(-2 \cdot \int_0^R \alpha(x) \cdot dx\right)$$

where:

$P(R)$  = received power from range  $R$  in  $W$   
 $R$  = range in  $km$   
 $K$  = system constant in  $W \cdot km^3$   
 $B(R)$  = backscatter coefficient in  $km^{-1}$   
 $\alpha(R)$  = extinction coefficient in  $km^{-1}$

From the physical point of view information on both the backscatter and the extinction coefficient are available from the signal. However, mathematically it is not possible to derive two unknowns from a single equation. Therefore additional information is required. Two different approaches are generally applied.

The first one assumes that the atmosphere is homogeneous. This implies that the backscatter and the extinction are constants. To derive these, linear regression analysis is applied on the logarithm of the range compensated signal.

$$(2) \quad \ln(P(R) \cdot R^2) = \ln(K \cdot B) - 2 \cdot \alpha \cdot R$$

The intercept and the slope of (2) are a measure for the backscatter and the extinction coefficient respectively. The method was first proposed by Collis (1966) and is generally referred to as the 'slope method'. Other references to this subject are, e.g., Carswell (1972), Werner (1981), Klett (1981), Ferguson and Stephens (1983) and Measures (1984). The maximum range over which the lidar can measure in a homogeneous atmosphere depends on the system parameters and the atmospheric conditions. An expression for this maximum range is derived in Appendix A.

The second method to invert lidar returns is based on the assumption that there is a relation between the extinction and the backscatter. (Results from Mie calculations show that the kind of relation depends on the aerosol. See e.g. De Leeuw and

Lamberts, 1987.) This leads to a Bernoulli differential equation in either of the two quantities. This differential equation can be solved provided that either the total transmission losses over the path are known (Fernald, 1972) or that a solution somewhere on the trace (boundary condition) is known (or assumed). The method of using the Bernoulli differential equation was proposed by Hitschfeld and Bordan (1954) to invert the rain rate from radar returns and has been used for lidar by e.g. Barret and Ben-Dov (1967), Viezee et al. (1969), Davis (1969), Kohl (1978) and Klett (1981). Nowadays this method is generally referred to as the Klett method. Other authors who discuss the problem of the boundary condition are Kunz (1983), Ferguson (1983), Fernald (1984), Sasano (1985), Hughes et al. (1985), Klett (1986) and Bissonnette (1986). Effects of the relation between backscatter and extinction on the solution of the lidar equation have been described by, e.g., Sasano (1984), Klett (1985) and Keastner (1986). Gonzalez (1988) published a recursive equation to solve the lidar equation with an *a priori* knowledge on the spatial relation between the extinction and the backscatter. However, this approach is essentially not different from the analytical solution.

In summary, all the efforts made to solve the inhomogeneous lidar equation are hampered by two problems: - the relation between extinction and backscatter and - the boundary condition.

Two alternative techniques are available to measure the backscatter and the extinction profile with a lidar in an inhomogeneous atmosphere. The first one is based on simultaneous measurements along the same path with two lidars operating in opposite directions. The combination of the two lidar signals provides sufficient information to solve both the backscatter and the extinction along the path. This method has been described by Paulson and Powers (1986), Kunz (1987) and by Hughes and Paulson (1988). A disadvantage of this so-called 'bipath' or 'double-ended' method is that two synchronized systems are required. In general, it is not possible to mount lidar systems at both ends of the path. In particular, for the most useful application of lidar, i.e. remote sensing of atmospheric profiles only single-ended systems can be applied. However, the double-ended method has merits for the verification of existing inversion techniques (e.g. Kunz, 1989) and in particular situations where *in situ* measurements are impossible.

The second alternative technique is based on the assumption of horizontal stratification of the atmosphere. The vertical extinction and backscatter profiles can be inverted from a (large) number of measurements under different elevation angles (in one vertical plane). The basic idea for this method was proposed by Hamilton (1969) and has been further elaborated by Russel and Livingstone (1984), Paulson (1985) and Kunz (1988). Russel and Livingstone (1984) pointed out that this technique is less suitable for vertical structure measurements because the atmosphere is not horizontally stratified, while also the atmosphere may change during a measurement. Paulson (1985) performed a sensitivity analysis for a two-angle slant

path measurement. Kunz (1988) derived an analytical expression for deriving the backscatter and the extinction profiles from a large set of measurements.

In summary, several methods exist to invert lidar returns. In homogeneous situations, the slope method is best suited to invert both the backscatter and the extinction coefficient over the range of the system. For inhomogeneous situations the lidar return is best solved via Bernoulli's differential equation which leads to a backscatter and/or an extinction profile. It should be kept in mind, however, that *a priori* information is necessary in this case. The values of the boundary condition and of the backscatter/extinction ratio used in this procedure can severely influence the final results. The double-ended method provides both the backscatter and the extinction profile without any additional information but can only be used in some specific situations.

### 3. SOME RESULTS

In this section some of the results obtained with two different lidar systems are presented. The first lidar is capable of measuring with a maximum repetition rate of 6 shots per minute and is used to study long term atmospheric effects. The second lidar operates with a maximum repetition rate of 10 measurements per second and is used to measure dynamic atmospheric processes.

#### 3.1 Results with a low repetition rate lidar system

A calibrated small lidar system, wavelength 1.06  $\mu\text{m}$  and laser energy about 100 mJ, has been used by the TNO Physics and Electronics Laboratory since 1983 in several field experiments and other projects conducted from our establishment. A review of the results is presented, starting with comparisons with other measurements on the atmospheric vertical structure.

##### 3.1.1 Assessment of the reliability of lidar for vertical structure measurements

In a common NATO experiment, see e.g. Lindberg et al. (1987), vertical lidar data were compared with balloon-borne AEG point visibility meter data. The lidar data were inverted to extinction profiles using Bernoulli's differential equation. The boundary value was obtained from a single horizontal lidar measurement using the slope method. The relation between extinction and backscatter was assumed to be linear, and constant over the vertical range. Figure 3.1 shows a comparison between the lidar data and the extinction profiles derived from the point visibility meter, for four different situations.

The differences between the profiles from the AEG and the lidar below the clouds (Figure 3.1C and D) are due to the measurement principle, the integration time of the nephelometer and the different wavelengths. In the cloud, the nephelometer

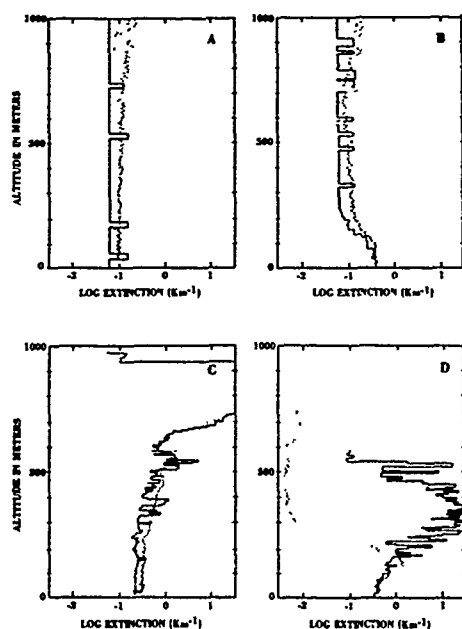


Figure 3.1: Examples of  $1.06 \mu\text{m}$  extinction profiles determined by the lidar (dotted line) and from the airborne AEG visibility meter data (solid curve). A a vertically homogeneous atmosphere, B a ground haze C a situation with a mid altitude stratus cloud and D a low altitude stratus cloud.

could measure the actual extinction. The lidar, on the other hand, could not penetrate deep enough into these optically thick clouds. It has been concluded from the analysis of this trial that lidar is a reliable tool to measure quantitatively the vertical extinction and/or backscatter profiles to altitudes of several kilometers. In cases of clouds, however, the capabilities of the lidar are limited by the maximum penetration depth of the laser pulse (Lindberg et al., 1987).

It has been shown recently by Rosen and Kjöme (1991) that comparison of balloon-borne scatterometer data with the results of lidar, are still of current interest to obtain complementary data on the aerosol from within clouds.

### 3.1.2. Lidar measurements over the sea

During a NATO aerosol measurement campaign in the North Atlantic in 1983, the lidar system has been operated continuously during a period of 5 weeks aboard a weather ship (De Leeuw et al. 1984, 1986-a). Measurements under negative and positive elevation angles as well as in horizontal direction were performed to determine the extinction from close to the sea surface to an altitude of about 1.5 km. A gyro-controlled platform was used to provide a stable horizontal reference plane. Examples of inverted extinction profiles have been published in De Leeuw et al. (1986-a,c). The profiles were described by a mixed-

layer model including relative humidity effects on the aerosol size distribution (De Leeuw, 1989). The relation between the backscatter and the extinction over a period of one day was shown by Mulders (1984). The relations between the extinction and the backscatter versus the wind speed were published by De Leeuw (1986-c).

### 3.1.3 Marine boundary layer studies in a tropical environment

The TNO lidar has also been operated from Florida Keys as part of the KEY90 experiment to evaluate the Naval Oceanic Vertical Aerosol Model (NOVAM) (De Leeuw et al., 1989; Gathman et al., 1989) in a tropical marine environment. An example of the behaviour of the vertical structure, during a period of about 4.5 hours, is presented in Figure 3.2. In the original presentation, the data was coded in false colour but for reproduction reasons the figure was coded in gray tones which reduced the contrast somewhat.

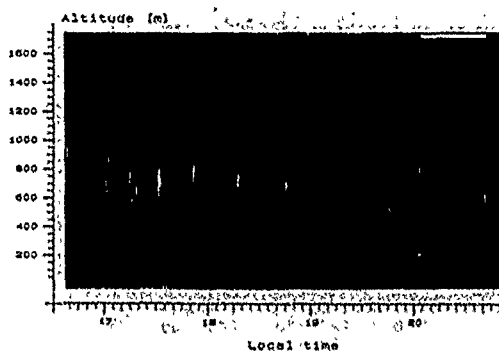


Figure 3.2: Backscatter profiles, coded in gray tones, as measured in a tropical marine environment in a height versus time figure. Horizontal axis: 16:37-20:54 hours. Vertical axis: 25-1350 m altitude.

The lidar data has been converted to absolute backscatter profiles because of the very low extinction. The measured profiles show a strong variability in the backscatter at altitudes of about 600 m, which is ascribed to the occurrence of convective plumes. Profiles with relatively low backscatter interspersed with profiles with relatively high backscatter also points in this direction. Sometimes, the convective plumes end in small patches of clouds (light-gray spots). Similar observations were made with airborne lidar (Hooper, 1989) during KEY90 and during other experiments (Melfi et al., 1985).

### 3.1.4 VISA (Vertical Infrared Structure of the Atmosphere)

The VISA experiment was conducted during a period of about two years. The lidar was operated continuously (24 hours/day), from a room at the roof of TNO-Physics and Electronics Laboratory in The Hague, in a coastal area at about 3 km from the sea.

Vertical extinction and backscatter profiles were measured together with meteorological parameters. The lidar generated about ten profiles per hour and performed several horizontal measurements to derive the horizontal backscatter and extinction. Some of the results of this experiment are presented in the subsequent figures.

#### Relation between $\alpha$ and $\beta$

One of the most interesting subjects is the relation between backscatter ( $\beta$ ) and extinction ( $\alpha$ ). Figure 3.3 shows examples

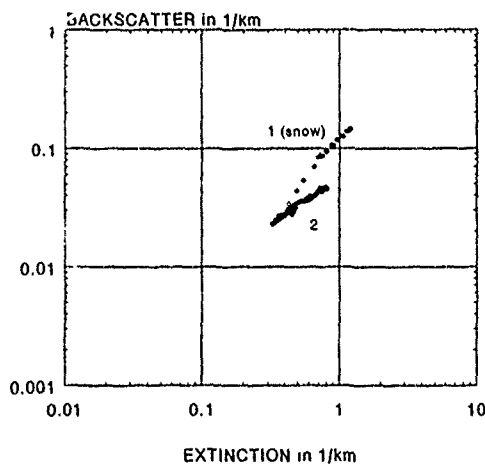
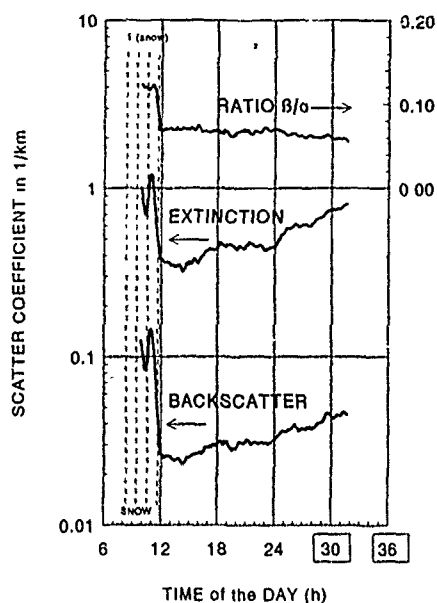


Figure 3.3: Time series of backscatter, extinction, ratio  $\beta/\alpha$  and scatter plot of the backscatter versus the extinction. The period with light snow-fall has been indicated by (1). During period (2) there was no precipitation. Data 15 and 16 January 1985.

of time serial plots of horizontal backscatter, extinction and their ratio  $\beta/\alpha$ . The relation between backscatter and extinction is also shown in a scatter diagram. From 10:00 to 12:00 a.m., light snow resulted in high backscatter and extinction coefficients. After 12:00 it stopped snowing and both the backscatter and the extinction dropped. However, because the snow effected the backscatter more than the extinction, their ratio also dropped. During the following 20 hours  $\beta/\alpha$  remained fairly constant (variation less than 10 %) although both the backscatter and the extinction gradually increased by more than a factor 2.

In contrast to period (2) in Figure 3.3, the time serial diagram of  $\beta/\alpha$  in Figure 3.4A shows strong fluctuations. These data were from lidar measurements during a period of ground haze with clear sky in which the backscatter and the extinction were strongly variable. These fluctuations are not obvious from a scatter plot, as shown in Figure 3.4B. The data in this figure approximate a straight line which, in this double logarithmic plot, suggesting a power law relation. This may be a coincidence.

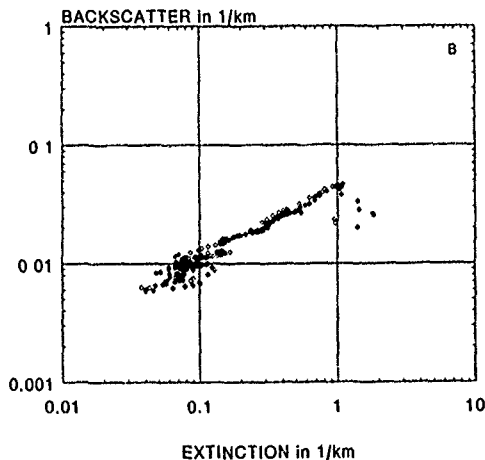
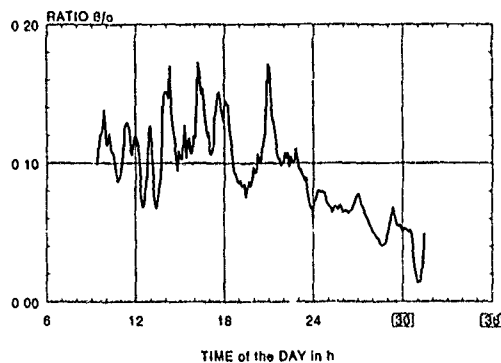


Figure 3.4: Variation of the ratio  $\beta/\alpha$  on 5 and 6 February 1985 (A). Scatter plot of the backscatter versus the extinction (B).

In Figure 3.5 we present the relation between the backscatter and the extinction averaged over all data recorded during this two year period. The figure was created by partitioning  $\log(\alpha)$  in 50 intervals and calculating the mean and the standard deviation of the backscatter for each interval.

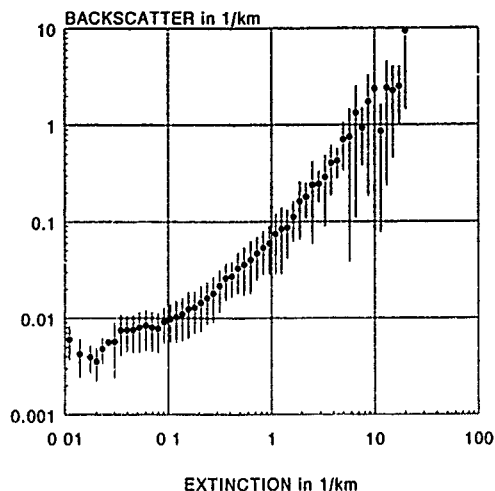


Figure 3.5: Relation between backscatter and extinction as derived from about 22,000 measurements during a two year period. All data were used unconditionally.

The results in Figure 3.5 indicates a non linear relation between  $\beta$  and  $\alpha$  which can be used to predict the  $\beta/\alpha$  ratio. The relation becomes less evident for extinctions larger than about  $3 \text{ km}^{-1}$ . This is probably due to local fluctuations in  $\alpha$  and  $\beta$ . For extinctions smaller than  $0.03 \text{ km}^{-1}$  accurate determination of the extinction is the limiting factor as shown by Kunz (1992). In that case the backscatter can be determined more reliably. The results from Figure 3.5 indicate that the relation between backscatter and extinction is reliable within a factor 2 for extinctions from about  $0.03$  to about  $3 \text{ km}^{-1}$ .

#### Relative humidity effects

The relation between the relative humidity and the backscatter, the extinction and the ratio  $\beta/\alpha$  is an other subject of interest (e.g. De Leeuw, 1986-b and Tonna, 1991) because the relative humidity tends to increase with height in the atmospheric boundary layer. If a definite relation between  $\beta/\alpha$  and the RH could be found, than this relation could be used to solve the lidar equation. In many data files, the backscatter and the extinction vary only slightly (about 15 %) for relative humidities between about 50 % and about 90 %. Above this value, the backscatter and the extinction depend stronger on the relative humidity. Examples of this effect are shown in Figure 3.6.

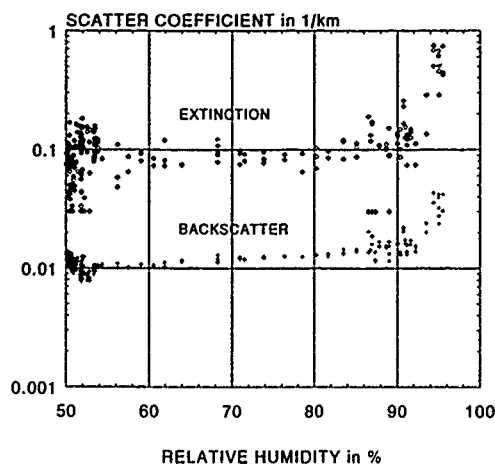


Figure 3.6: Extinction and backscatter versus relative humidity. Data were recorded over a period of 24 hours on 20 and 21 February 1985.

In many cases, the relation between backscatter and relative humidity shows a kind of hysteresis loop which is a common phenomenon for hygroscopic aerosol as shown e.g. by Winkler (1971). An example of this behaviour is given in Figure 3.7.

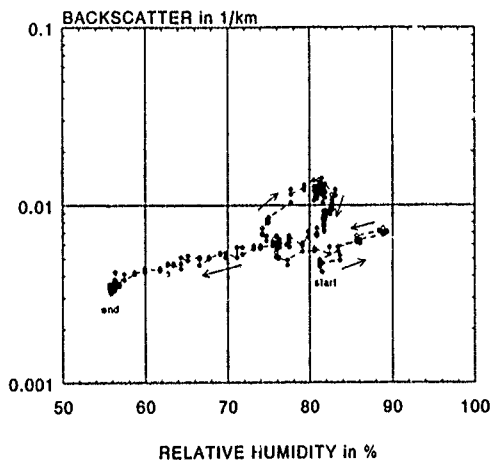


Figure 3.7: Relation between the horizontal backscatter and the relative humidity over a period of 24 hours. Date 7 February 1985. Note the loop between RH of 74 and 82 %.

#### Visibility

Extinction determines the visibility. However, because of the difference in wavelength, the relation between the lidar derived extinction ( $1.06 \mu\text{m}$ ) and the visibility (photopic spectrum) depends on the aerosol characteristics (particle size distribution and complex refractive index).

Relations between the visibility (measured with an AEG point visibility meter) and the horizontal backscatter or extinction measured with the lidar have been published by e.g. Lamberts and De Leeuw (1986). Results from the VISA data base show that there is, in many cases, a relation between the visibility and the backscatter or the extinction. Examples of a good correlation are shown in Figure 3.8. However, such good correlations are not always obtained, as evidenced by the data in Figure 3.9. A more detailed analysis of the data base is required to investigate the conditions for which the backscatter and the extinction are well-correlated with visibility. Interesting questions are why in other cases the correlation is reduced, and what the frequency of occurrence of such situations is. A limited data base of simultaneously measured aerosol particle size distributions is available, which could be useful to find answers to these questions.

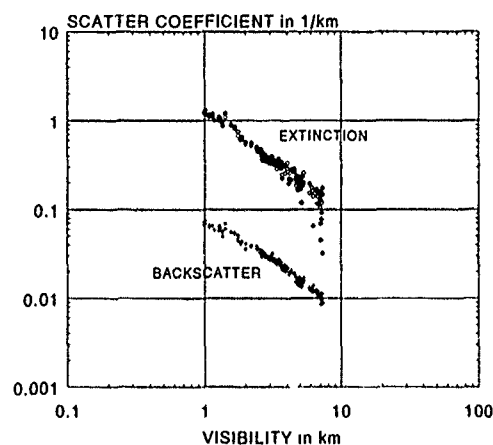


Figure 3.8: Scatter plot of the horizontal extinction and the horizontal backscatter as a function of the visibility. The data were recorded on 10 March 1986 during a period of 24 hours, starting at 09:00 a.m.

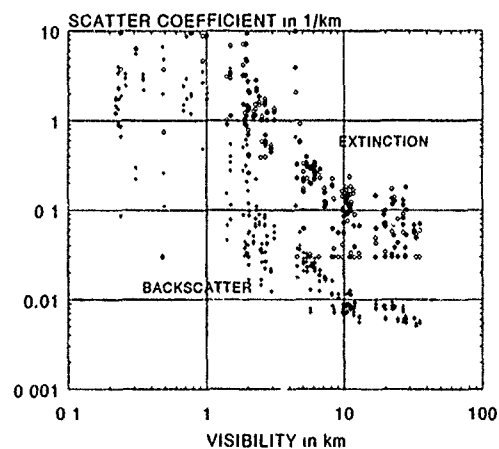


Figure 3.9: Scatter plot of the horizontal extinction and the horizontal backscatter as a function of the visibility. The data were recorded on 21 February 1985 during a period of 24 hours, starting at 09:00 a.m.

#### Cloud base monitoring

Cloud base has been monitored during part of the VISA project. Cloud base is important in avionics but also in meteorology and other fields. Although there is no unique definition for cloud base, see e.g. Pruppacher (1980), Heaps (1982) and Eberhard (1986), the results of commercial cloud base instruments are in good agreement despite the different techniques applied (WMO report 1986). With lidar, the cloud base has been defined in two different ways. The first criterion is based on a local maximum in the recorded waveforms caused by cloud reflection. The second criterion uses the height where the extinction exceeds a certain value (Duncan, 1980).

Results from application of both criteria on the lidar signals, recorded during a overcast period of 33 hours, are shown in Figure 3.10.

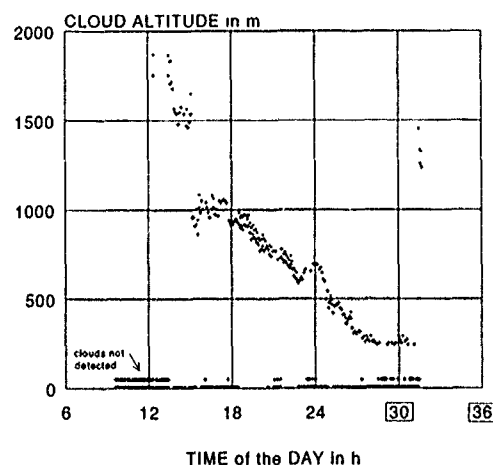


Figure 3.10: Cloud base altitude as a function of time on 20 and 21 February 1985. Dots indicate the results from a simple relative maximum criterion and plus signs indicate the results from the extinction criterion.

The extinction criterion provides a better detection probability. The pulse-height criterion often fails. This occurs in situations where the increase in backscattering from cloud droplets is compensated by the extinction. As a result the lidar signal cannot be distinguished from signals from a homogeneous atmosphere. This effect has been discussed by Kunz (1987) and has been elaborated mathematically in Appendix B.

#### Extinction profiles

Extinction profiles to an altitude of 1 or 2 km were recorded semi-continuously during VISA. Figure 3.11 shows an example of the results during a one-week period. The altitude has been plotted along the vertical axis and the time has been plotted along the horizontal axis. Hourly intervals are indicated by small white tics. The separation between the days is indicated by

the white vertical lines. The extinction has been coded in false color. For this B/W presentation, however, the false colors have been converted to gray tones which reduces the resolution.

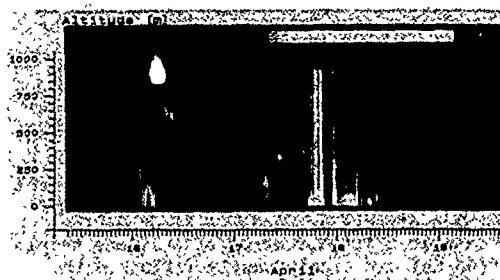


Figure 3.11: Vertical extinction profiles coded in gray tones, in the period 15-19 April 1985. Maximum altitude 1000 m. No precipitation has been observed in this period.

Discussion. On April 15 at 08:50 a.m. the measurements started under a cloudy sky with cloud base at about 500 m. After 09:00, the extinction in the mixed layer decreased until about 23:00 hours. Then a cloud was detected at about 1000 m and the extinction at ground level increased rapidly. At 05:00 a.m. on April 16 a new cloud layer was detected at about 700 m altitude which remained there until about 20:00 hours. Note that the extinction below the cloud started to increase already at an altitude of about 300 m. Between 17:00 and 19:00 hours a haze layer was observed to move in from the sea. This resulted in an increase in the extinction between 200 and 600 m altitude. During the night from April 16 to 17 a ground haze developed. The depth of this layer slowly decreased. Minimum altitude was reached between 03:00 and 04:00 a.m. From that time on, the top of the ground fog layer ascended from about 100 m to about 250 m. A second layer was detected which rose from about 250 m to about 50 m altitude. At 09:00 a.m. the top of the mixed layer rose to about 700 m. From 13:00 to 15:00 hours the atmosphere was clear above 100 m. At about 16:00 hours cumulus clouds were observed and at 17:00 hours a new ground fog layer developed which stayed until 13:00 the next day. At that time the extinction decreased due to deepening of the mixed layer. From about 16:00 hours to about 02:00 a.m. on April 19 the thickness of the mixed layer decreased. Then a new layer was detected at an altitude of about 700 m which descended slowly until 10:00 a.m. to an altitude of about 100 m. From that time on this layer ascended and dissolved.

### 3.2 Results with a high repetition rate lidar system

For mapping dynamic atmospheric processes, like smoke plumes and wind driven aerosol patches having life-times on the order of seconds, lidar systems are required with a repetition rate of at least 10 Hz. Such a system has been realized and applied by TNO-Physics and Electronics Laboratory. It operates at a wavelength of  $1.06 \mu\text{m}$ , has a pulse energy of about 20 mJ and a telescope diameter of 50 cm. It is fully computer controlled and has been mounted on a

platform for scanning in any desired direction. Examples of results obtained with this system during the NATO smoke experiment 'BEST ONE' were published in the workshop proceedings on this trial (Kunz, 1987).

Some of the results from atmospheric measurements with this system are presented in the next set of figures. The dynamic behaviour of the atmosphere during a period of 125 seconds and up to an altitude of 1140 m is presented in Figure 3.12. The measurements were made in a fixed direction during a period of high relative humidity (99 %), wind speed of 1.5 m/s and visibility of 3.5 km. Figure 3.12 shows that the atmosphere below an altitude of 300 m is very turbulent while above this level the variations are much slower.

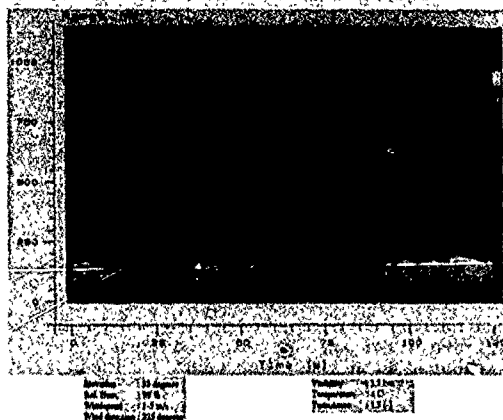


Figure 3.12: Atmospheric scattering, coded in gray tones, as measured with a vertically pointing lidar in a height versus time representation.

A vertical cross-section of the atmospheric scattering can be mapped by scanning the lidar in a vertical plane. An example of such a measurement, also called RHI (Range to Height Indicator), is shown in Figure 3.13. Relatively high atmospheric scattering is observed below a broken cloud layer. Above this cloud layer, cloud patches are observed at an altitude of about 650 m, despite the attenuation of the lower clouds.

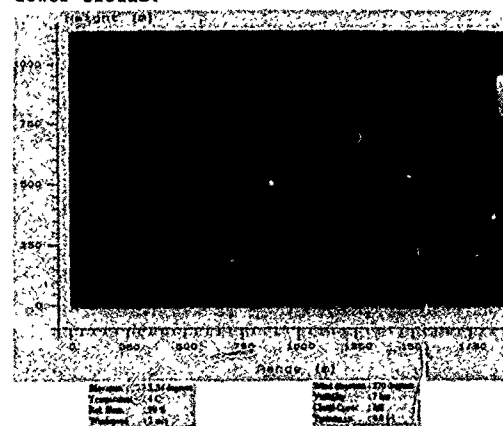


Figure 3.13: A vertical cross-section of atmospheric scattering measured with a scanning lidar. Visibility 7 km, relative humidity 99 %, wind speed 2 m/s.

The results presented in Figure 3.14 were obtained during a session where the lidar was pointing in the direction of the wind at a fixed elevation angle of 15 degrees. A large number of aerosol eddies were mapped which were not visible by eye. Because these eddies move with the wind they can serve as a tracer for wind speed measurements. Application of this phenomenon has been described by e.g. Eloranta (1975), Sasano et al. (1982), Zuev (1986) and Hooper and Eloranta (1986).

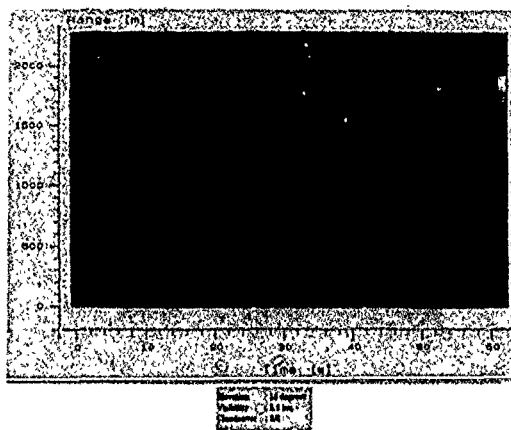


Figure 3.14: Atmospheric scattering as measured with the lidar under a fixed elevation of 15 degrees. The aerosol eddies are drifted by the wind, away from the system.

#### 4. DISCUSSION

For investigating atmospheric parameters and processes over ranges of kilometers, lidar can be used as a convenient remote sensing tool. Even relatively simple systems can provide invaluable information, in an efficient way. The spatial and temporal backscatter and extinction can be monitored as a function of height during extended periods of time. No other technique provides this feature.

Lidar can be applied to determine both the backscatter and the extinction in homogeneous situations from atmospheres with relative low aerosol content (Rayleigh) to situations with dense fog. In situations with low extinction, the range of the lidar should be large enough to invert this parameter reliably. The backscatter on the other hand can be determined more reliably in those situations (Kunz, 1992).

Single-ended lidar data from inhomogeneous atmospheres can only be handled if additional information is available (or is assumed). A number of useful methods to invert the lidar equation has been proposed thus far. It is noted that each of these has certain limitations. The performance of these lidar techniques has been evaluated from several field experiments by comparing the results with data obtained with other equipment.

Accurate measurements, as well as

understanding of the possibilities and limitations of the electronic system, are required to reliably invert the basic quantities from the lidar return. The influence of the hardware on the accuracy of the measurement is rarely discussed in literature. Experience has shown that in many situations the receiver is the most critical part of a lidar system. This component converts the relatively fast transient optical signals with a large dynamic range to corresponding electrical signals. Furthermore the accuracy of the base line, the resolution of the waveform recorder and the accuracy of the trigger moment are of significant influence on the final results. In many practical systems these effects are under-estimated. For example a trigger error of only one sample (50 ns) can significantly influence the calculated extinction. The laser on the other hand should be single pulsed with a pulse duration which is short compared to the minimum detectable range and the desired range resolution.

#### REFERENCES

- Barret, E.W. and O. Ben-Dov, "Application of the lidar to air pollution measurements", *J. Appl. Meteor.*, Vol. 6, 1967, pp 500-515.
- Bissonnette, L.R., "Sensitivity analysis of lidar inversion algorithms", *Appl. Opt.*, Vol. 25, No. 13, 1 July 1986, pp 2122-2125.
- Bonner, R.S. and W.J. Lentz, "The visiocellometer: a portable cloud height and visibility indicator", *Atmospheric Sciences Laboratory, White Sands, NM, USA; ASL-TR-0042*, Oct. 1979.
- Carswell, A.I., "Remote probing by laser radar", *Can. Aeronautics & Space Journ.*, Dec. 1972, pp 335-336.
- Collis, R.T.H., "Lidar: a new atmospheric probe", *Quart. J. of the Royal Meteor. Soc.*, Vol 92, 1966, pp 220-230.
- Davis, P.A., "The analysis of lidar signatures of cirrus clouds", *Appl. Opt.*, Vol 8, No. 10, Oct. 1969, pp 2099-2102.
- De Leeuw, G., L.H. Cohen and M.M. Moerman, "Survey of aerosol and lidar measurements at the North Atlantic (25 May-28 June 1983)", *Physics and Electronics Laboratory TNO, The Hague, PHL 1984-01*, March 1984.
- De Leeuw (a), G., S. Parashar, P.M. Park, S.J. Perry, P.L. Roney and M.H. Smith, "Aerosol study in the North Atlantic 1983", *NATO AC/243 (PANEL IV/RSG.8)*, Report 1986-01.
- De Leeuw (b), G., G.J. Kunz and C.W. Lamberts, "Humidity effects on the backscatter/extinction ratio", *Appl. Opt.*, Vol. 25, No. 22, 15 Nov. 1986, pp 3971-3974.
- De Leeuw (c), G. "Lidar measurements in the marine atmosphere", *Int. Conf. on Optical and mm-wave Propagation and scattering in the atmosphere*, May 27-30, 1986, Florence, Italy, pp 101-104.
- De Leeuw, G. and C.W. Lamberts, "Influence of refractive index and particle size interval on Mie calculated backscatter and

extinction", *J. Aerosol Sci.*, Vol. 18, No. 2, 1987, pp 131-138.

De Leeuw, G., K.L. Davidson, S.G. Gathman and R.V. Moonkester, "Physical models for aerosol in the marine mixed-layer". AGARD Electromagnetic Wave Propagation Panel Specialists, meeting on "Operational decision aids for exploiting or mitigating electromagnetic propagation effects", San Diego, CA, USA, 15-19 May 1989. Proceedings pp 40-1 to 40-8.

Duncan, L.D., J.D. Lindberg and R.B. Loveland, "An empirical model of the vertical structure of German fogs", Atmospheric Sciences Laboratory, White Sands NM, USA; ASL-TR-0071, Nov. 1980.

Eberhard, W.L., "Cloud signals from lidar and rotating beam ceilometers compared with pilot ceiling", *J. Atm. and Ocean Technology*, Vol. 3, Sept. 1986, pp 499-512.

Eloranta, E., "The determination of wind speeds in the planetary boundary layer", *J. of Appl. Meteor.*, Vol. 14, Dec. 1975, pp 1485-1489.

Ferguson, J.A. and D.H. Stephans, "Algorithm for inverting lidar returns", *Appl. Opt.*, Vol. 22, No. 23, 1 Dec. 1983, pp 3673-3675.

Fernald, F.G., B.M. Herman and J.A. Reagan, "Determination of aerosol height distribution by lidar", *J. of Appl. Meteor.*, Vol. 11, April 1972, pp 482-489.

Fernald, F.G., "Analysis of atmospheric lidar observations: some comments", *Appl. Opt.*, Vol. 23, No. 5, 1 March 1984, pp 652-654.

Gathman, S.G., G. De Leeuw and K. Davidson, "The NAVAL Oceanic Vertical Aerosol Model: Progress Report", AGARD 45th symposium of the Electromagnetic Wave Propagation Panel on "Atmospheric Propagation in the UV, Visible and mm-Wave region and Related System Aspects", Copenhagen, Denmark, 9-13 October 1989, Proceedings pp 17-1 to 17-11.

Gonzalez, R., "Recursive technique for inverting the lidar equation", *Appl. Opt.*, Vol. 27, No. 13, 1 July 1988, pp 2741-2745.

Hamilton, P.M., "Lidar measurement of backscatter and attenuation of atmospheric aerosol", *Atm. Environ.*, Vol. 3, 1969, pp 221-223.

Heap, M.G., "A vertical structure algorithm for low visibility/low stratus condition", Atmospheric Sciences Laboratory, White Sands NM, USA; ASL TR 0111, June 1982.

Hitschfeld, W. and J. Bordan, "Errors inherent in the radar measurement of rainfall at attenuating wavelengths", *J. of Meteor.*, Febr. 1954, pp 58-67.

Hooper, W.P. and E. Eloranta, "Lidar measurements of wind in the planetary boundary layer; the method, accuracy and results from a joint measurements with radiosonde and kyttoon", *J. of Climate and Appl. Meteor.*, Vol. 25, No. 7, July 1986, pp 990-1001.

Hooper, W.P., Private Communications 1991.

Hughes, H.G., J.A. Ferguson and D.H. Stephans, "Sensitivity of a lidar inversion algorithm to parameters relating atmospheric backscatter and extinction", *Appl. Opt.*, Vol. 24, No. 11, 1 June 1985, pp 1609-1613.

Hughes, H.G. and M.R. Paulson, "Double-ended lidar technique for aerosol studies", *Appl. Opt.*, Vol. 27, No. 11, 1 June 1988, pp 2273-2278.

Keastner, M., "Lidar inversion with variable backscatter/extinction: comment", *Appl. Opt.*, Vol. 25, No. 6, 15 March 1986, pp 833-835.

Klett, J.D., "Stable analytical inversion solution for processing lidar returns", *Appl. Opt.*, Vol. 20, No. 2, 15 Jan. 1981, pp 211-220.

Klett, J.D., "Lidar inversion with variable backscatter/extinction ratios", *Appl. Opt.*, Vol. 24, No. 11, 1 June 1985, pp 1638-1643.

Klett, J.D., "Extinction boundary value algorithm for lidar inversion", *Appl. Opt.*, Vol. 25, No. 15, 1 Aug. 1986, pp 2462-2464.

Kohi, R.H., "Discussion of the interpretation problem encountered in single-wavelength lidar transmissometers", *J. Appl. Meteor.*, Vol. 17, 1978, pp 1034-1038.

Kunz, G.J., "Vertical atmospheric profiles measured with lidar", *Appl. Opt.*, Vol. 22, No. 13, 1 July 1983, pp 1955-1957.

Kunz, G.J., "Bipath method as a way to measure the spatial backscatter and extinction coefficients with lidar", *Appl. Opt.*, Vol. 26, No. 5, 1 March 1987, pp 794-795.

Kunz, G.J., "Lidar and missing clouds", *Appl. Opt.*, Vol. 26, No. 7, 1 April 1987, p 1161.

Kunz, G.J., "Lidar measurements during the BEST ONE experiment", in: Rogge, J. Proc. of the Workshop on measuring and modeling the battlefield environment, 15-18 June 1987, Royal Military Academy, The Netherlands. NATO Report DS/A/DR(87)307

Kunz, G.J., "A method for measuring the vertical extinction and backscatter profile with a scanning lidar", TNO-Physics and Electronics Laboratory, FEL 1988-65.

Kunz, G.J. and H.G. Hughes, "Similarities between lidar inversion algorithms", *Appl. Opt.*, Vol. 28, No. 12, 15 June 1989, p 2195.

Kunz, G.J., "On inversion of lidar signals with the slope method", in preparation for publication in *Applied Optics* 1992.

Lamberts, C.W. and G. de Leeuw, "Aerosol-induced visibility reduction in the Netherlands". In: S.D. Lee, T. Schneider, L.D. Grant and P.J. Verkerk (Eds). *Aerosols. Research, risk assessment and control strategies*. Lewis, ISBN 0-87371-051-7, pp 793-807.

Lentz, W.J., "The visioceilometer: a portable visibility and cloud height lidar", Atmospheric Sciences Laboratory, White Sands, NM, USA; ASL-TR-0105, Jan. 1982.

Lindberg, J.D., M.G. Heaps, G.J. Kunz and P.E. Rasmussen, "Comparison of selected data from the European vertical structure experiment", NATO AC/243 (PANEL IV/RSG.8), Report 1986-2, April 1987.

Measures, R.M., "Laser remote sensing: fundamentals and applications", John Wiley and Sons, New York 1984, ISBN 0-471-08193-0.

Melfi, S.H., J.D. Spinhirne and S-H. Chou, "Lidar observations of vertically organized convection in the planetary boundary layer over the ocean", J. of Climate and Appl. Meteor., Vol. 24, No. 8, Aug. 1985, pp 806-821.

Mulders, J.M., "Algorithms for inverting lidar returns: comment", Appl. Opt., Vol. 23, No. 17, 1 Sept. 1984, pp 2855-2856.

Paulson, M.R., "Sensitivity of two elevation angle method for obtaining integrated extinction to errors in S(R) measurements", Naval Ocean Systems Center San Diego, TN 1402, June 1985.

Paulson, M.R. and W.J. Powers, "Description of a two-lidar technique for determining aerosol extinction coefficient profiles", Naval Ocean Systems Center San Diego, TN 1449, April 1986.

Pruppacher, H.R., "Microphysics of clouds and precipitation", Reidel Publishing Company, 1980.

Rosen, J.M. and N.T. Kjome, "Backscattersonde: a new instrument for atmospheric aerosol research", Appl. Opt., Vol. 30, No. 12, 20 April 1991, pp 1552-1561.

Russel P.B. and J.M. Livingstone, "Slant-Lidar aerosol extinction measurements and the relation to measured and calculated albedo changes", J. Climate and Appl. Meteor., Vol. 23, August 1984, pp 1204-1221.

Sasano, Y., et al., "Horizontal wind vector determination from the displacement of aerosol distribution patterns observed by a scanning lidar", J. of Applied Meteor., Vol. 21, No. 10, Oct. 1982, pp 1516-1523.

Sasano, Y., "Significance of the extinction/backscatter ratio and the boundary value term in the solution for the two component lidar equation", Appl. Opt., Vol. 23, No. 1, 1 Jan. 1984, pp 11-13.

Sasano, Y., "Observational study on the atmospheric mixed layer and transition layer structures using Mie lidar", J. Meteor. Soc. of Japan, Vol. 63, No. 3, June 1985, pp 419-435.

Shimizu, H., et al., "Large scale laser radar for measuring aerosol distribution over wide area", Appl. Opt., Vol. 24, No. 5, 1 March 1985, pp 617-626.

Tonna, G., "Backscattering, extinction, and liquid water content in fog: a detailed study of their relations for use in lidar systems", Appl. Opt., Vol. 30, No. 9, 20 March 1991, pp 1132-1140.

Viezee, W., E.E. Uthe and R.T.H. Collis, "Lidar observations of airfield approach conditions: an exploratory study", J. of

Appl. Meteor., Vol. 8, April 1969, pp 274-283.

Werner, Ch., "Slant range visibility determination from lidar signatures by the two-point method", Optics and Laser Techn., Febr. 1981, pp 27-36.

Winkler, P., and C.E. Junge, "Comments on: Anomalous deliquescence of sea spray aerosols", J. Appl. Meteor., Vol. 10, 1971, pp 159-163.

World Meteorological Organization, "Final Report International Ceilometer Intercomparison", Beaufort Park, U.K., Spring 1986

Zuev, V.F., "Laser sounding of instantaneous and mean wind speed using correlation method", Proc. International Laser Radar Conference, Toronto 1986.

#### APPENDIX A.

The maximum range of lidar in a homogeneous atmosphere

The range of a lidar system is a function of both the properties of the system and the actual weather condition. The maximum detection range for single shot operation is defined as that range where the received power is equivalent to the noise equivalent power of the receiver. The receiver noise is determined by electronic noise and the amount of background radiation. In the general case of an inhomogeneous atmosphere, it is not possible to predict the maximum detection range. However, in the special case of a homogeneous atmosphere, this maximum range can be calculated by assuming a linear relation between backscatter and extinction. The starting point for the derivation of the maximum range is the common model for lidar signals from a homogeneous atmosphere.

$$(A.1) \quad P_n = \frac{K \cdot B}{R_{\max}^2} \cdot e^{-2 \cdot \alpha \cdot R_{\max}}$$

where:

$P_n$  = noise equivalent power in W  
 $K$  = system constant in  $W \cdot m^3$   
 $R_{\max}$  = maximum range in km  
 $B$  = backscatter coefficient in  $km^{-1}$   
 $\alpha$  = extinction coefficient in  $km^{-1}$

The lidar system constant K includes the receiver's area and sensitivity as well as the energy of the laser. After taking the logarithm of (A.1) and substitution  $K' = K/P_n$  we obtain:

$$(A.2) \quad 2 \cdot \alpha \cdot R_{\max} + 2 \cdot \ln(R_{\max}) = \ln(K' \cdot B)$$

The maximum range  $R_{\max}$  can now be calculated if either  $\alpha$  and  $B$  are known or if a relation between  $\alpha$  and  $B$  is assumed like  $B = \alpha^k \cdot C_A$  (generally  $k=1$ ). The first situation occurs only in Rayleigh atmospheres while the second situation, which is more general, occurs if we are dealing with a (homogeneous) Mie atmosphere. In this case  $R_{\max}$  is solved as a function of the system parameter  $K'$  and the ratio of  $B$  and  $\alpha$ ,  $C_A$ . The solution is

is found by taking the total derivative of (A.2):

$$(A.3) \quad 2 \cdot \alpha \cdot dR_{\max} + 2 \cdot R_{\max} \cdot d\alpha + \frac{2}{R_{\max}} \cdot dR_{\max} = \frac{d\alpha}{\alpha}$$

The extinction at which the maximum range occurs is found by explicitly writing  $dR_{\max}/d\alpha$  and equating this term to zero. This results in:

$$(A.4) \quad \alpha_{R_{\max}} = \frac{1}{2 \cdot R_{\max}}$$

Finally, the maximum range  $R_{\max}$  is found by substituting (A.4) in (A.2). This provides:

$$(A.5) \quad R_{\max} = \left[ \frac{K' \cdot C_A}{2 \cdot e} \right]^{1/3}$$

where  $e$  is the base of the natural logarithm.

This mathematical derivation shows that the maximum range of a lidar in homogeneous Mie atmosphere is directly proportional to the third root of the product of the system constant and the ratio  $\beta/\alpha$ . The maximum range is obtained when the atmospheric extinction coefficient is equal to the inverse of twice this maximum range.

#### APPENDIX B.

Situations where a cloud reflection cannot be distinguished from the return of a homogeneous atmosphere

Assume that the inhomogeneous layer starts at range  $R_0$ . The range compensated lidar signal from this layer can be described as follows:

$$(B.1) \quad S_1(R) = \beta(R) \cdot \exp(-2 \cdot \int_{R_0}^R \alpha(x) \cdot dx)$$

A homogeneous layer at the same range which provides the same signal is described by:

$$(B.2) \quad S_2(R) = \beta_0 \cdot \exp(-2 \cdot \alpha_0 \cdot (R - R_0))$$

If these layers provide the same lidar signal than both the strength and the slopes are equal:

$$(B.3a) \quad S_1(R) = S_2(R) \quad \text{and}$$

$$(B.3b) \quad S_1'(R) = S_2'(R)$$

in which  $S'$  equals  $dS/dR$ .

The first derivative of (B.1) and (B.2) leads to a differential equation in  $\beta(R)$ :

$$(B.4) \quad \frac{d\beta(R)}{dR} - 2 \cdot \beta(R) \cdot (\alpha(R) - \alpha_0) = 0$$

A linear but different relation between extinction and backscatter is assumed for both layers:

$$(B.5) \quad \beta(R) = k_i \cdot \alpha(R) \quad \text{inhomogeneous layer}$$

$$(B.6) \quad \beta_0 = k_h \cdot \alpha_0 \quad \text{homogeneous layer}$$

With (B.5), the differential equation for  $\beta(R)$  becomes:

$$(B.7) \quad \frac{d\beta(R)}{dR} - \frac{2}{k_i} \cdot \beta^2(R) + \alpha_0 \cdot \beta(R) = 0$$

This differential equation can be solved by substituting:

$$(B.8) \quad Q(R) = 1/\beta(R)$$

which results in a differential equation for  $Q(R)$  according to (B.9):

$$(B.9) \quad Q'(R) + \frac{2}{k_i} - 2 \cdot \alpha_0 \cdot Q(R) = 0$$

A general solution for  $Q(R)$  is:

$$(B.10) \quad Q(R) = A + B \cdot e^{-CR}$$

The constants  $A$  and  $C$  can easily be found by substituting (B.10) and the first derivative of (B.10) in (B.9). The results are:

$$(B.11) \quad A = \frac{1}{k_i \cdot \alpha_0}$$

$$(B.12) \quad C = -2 \cdot \alpha_0$$

The backscatter profile for the inhomogeneous layer can now be found by substituting (B.8), (B.11) and (B.12) in (B.9), resulting in:

$$(B.13) \quad \beta(R) = \frac{\alpha_0 \cdot k_i}{1 + \alpha_0 \cdot k_i \cdot B \cdot e^{2 \cdot \alpha_0 \cdot R}}$$

The constant  $B$  is found by the condition that for  $R=R_0$  the value of the backscatter profile equals the backscatter of the homogeneous layer.

$$(B.14) \quad \beta(R_0) = \beta_0$$

Substituting (B.14) in (B.13) gives the value of  $B$ :

$$(B.15) \quad B = \frac{\alpha_0 \cdot k_i - \beta_0}{\alpha_0 \cdot \beta_0 \cdot k_i} e^{-2 \cdot \alpha_0 \cdot R_0}$$

Finally the equation for the backscatter profile, which provides the same lidar signal as from a homogeneous layer, is found by substituting (B.6) and (B.15) in (B.13), which results in:

$$(B.16) \quad \beta(R) = \frac{\beta_0 \cdot b_0}{\frac{k_h}{k_i} - \left( \frac{k_h}{k_i} - 1 \right) \cdot e^{2 \cdot \beta_0 (R - R_0) / k_h}}$$

# LIDAR REMOTE SENSING TECHNIQUES FOR DEVELOPING AND EVALUATING ATMOSPHERIC AEROSOL MODELS

by

D. R. Jensen  
H. G. Hughes  
M. R. Paulson

Ocean and Atmospheric Sciences Division  
Naval Ocean Systems Center  
San Diego, CA 92152-5000 USA

## 1. SUMMARY

A technique has been developed by which lidar returns can be used to adjust simultaneously observed/ modeled aerosol size distributions to represent existing atmospheric conditions. This technique has been used to evaluate the U. S. Navy Maritime Aerosol model (NAM) and the U. S. Navy Oceanic Vertical Aerosol Model (NOVAM). The evaluation of NOVAM indicated that, when scaled to visibility, good agreement exists between the lidar scaled extinction and backscatter coefficients and the predicted profiles. While adjustments of the NAM aerosol number densities can be made to match the modeled S(R) profiles to that measured by lidar in the first few meters above the surface of the ocean, the large adjustments for low wind speed indicates that the modeled aerosol size distribution shape near the ocean surface may not be correct.

## 2. INTRODUCTION

Lidar systems have been extensively used in an attempt to model atmospheric structure by measuring the radiation backscattered into a receiver by aerosols at different ranges within the beam of a pulse lidar. Accuracies of aerosol extinction coefficients determined by inverting the single-ended lidar returns have been questioned and cannot presently be assured (Ref 1). However, a technique has been developed by which lidar backscattered returns, without question of the inversion accuracies, can be used to adjust simultaneously measured or modeled aerosol size distributions (total number densities) to represent existing atmospheric conditions. Using this technique, models of aerosol size distributions can be evaluated as to their representativeness of actual atmospheric conditions. Presently, the U. S. Navy's development and evaluation of electro-optical systems utilize the LOWTRAN propagation codes (Refs 2 & 3) which incorporates several different atmospheric aerosol models. One such model for calculating aerosol scattering and absorption properties is the Navy Maritime Aerosol Model (NAM), (Ref 4). Another model being developed that is destined for LOWTRAN is the Navy Oceanic Vertical Aerosol Model (NOVAM), (Ref 5). The Navy Maritime Aerosol Model is a surface based model and is the sum of three log normal size distributions. In addition to the surface wind speeds (current and 24-hour averaged) and relative humidity, the model requires the input of an air-mass factor which identifies the origin of the aerosols as either marine or continental (an integer value of one for pure oceanic air masses and ten for coastal region continental air). Also, when an observed surface visibility is available as an input, the model is adjusted to make the visibility calculated at a wavelength of 0.55  $\mu\text{m}$  the same as the observed value. The accuracy by which the model can predict infrared transmission has been given by Gathman and Ulfers (Ref 6) and radiance by Hughes and Jensen (Ref 7). NOVAM is being developed to include the vertical structure of the aerosol extinction coefficients within the marine boundary layer (MBL) using NAM as the kernel. It is based on a combination of empirical and physical models (Refs 4, 8, 9, & 10) which describe the dynamic behavior of aerosols. A summary of the initial evaluation of NOVAM has been given by Gathman, et al., (Ref 5). This paper presents the technique by which lidar returns can be used to validate or adjust simultaneously measured or

modeled aerosol size distributions to represent existing atmospheric conditions. In this paper case studies are presented for the evaluation of the NAM for number densities near the ocean surface for low wind speeds, and NOVAM for vertical profiles of aerosol extinction. While this technique is not a stand-alone concept, a single-ended lidar system, when operated in conjunction with other aerosol and meteorological measurements, is shown to be useful in adjusting aerosol models to existing atmospheric conditions.

## 3. PROCEDURE

The lidar S(R) quantity is given by

$$S(R) = \ln[P(R) R^2] \quad (1)$$

where P(R) is the power received from the scattering volume at a range R. In terms of extinction and backscatter, the lidar single-scatter equation is given by

$$S(R) = \ln(C_1) + \ln[\beta(R)] - 2 \int_0^R \sigma(x) dx \quad (2)$$

where  $\sigma(R)$  and  $\beta(R)$  are the range-dependent volumetric extinction and backscatter coefficients, respectively, and  $C_1$  is the lidar instrumentation constant. Equ 2 relates the calculated aerosol extinction and backscatter coefficients from either unscaled measured or modeled aerosol size distributions to the lidar backscattered signal S(R). By using these extinction and backscatter coefficients from measured or modeled distributions, an expected S(R) profile can be calculated for the aerosol data as a function of range (S(R)). Following the technique developed by Hughes and Paulson for adjusting aerosol model densities to match lidar S(R) returns (Ref 11), the aerosol-size distribution data, i.e., the aerosol number density and resulting extinction and backscatter coefficients, can be adjusted to allow the calculated S(R), values from Equ 2 to match the measured lidar S(R)<sub>m</sub> returns, or

$$S(R)_c = S(R)_m \quad (3)$$

To do this, Equ 2 is expressed in terms of a scaling quantity, k, as

$$S(R)_c = \ln(C_1) + \ln[k\beta(R)] - 2 \int_0^R k\sigma(x) dx \quad (4)$$

where k is the multiplier of the measured size distribution which allows Equ 3 to be satisfied. The k value is determined from the measured and calculated data by expressing Equ 4 in terms of altitude, h (atmosphere assumed to be composed of

finite layers at altitude  $h_1, h_2, \dots, h_n$ , and solving it by iteration for  $k$  at each altitude until Equ 3 is satisfied (Ref 11). The aerosol extinction and backscatter coefficients at each altitude are then sequentially adjusted by  $k$  such that the calculated and the measured lidar  $S(R)$  return from each altitude agree.

#### 4. NOVAM MODEL VALIDATION

On 30 March 1989, nearly simultaneous measurements of atmospheric structure were made by using the Naval Ocean Systems Center (NOSC) airborne platform (Piper Navajo aircraft), (Ref 12), and the Army's Visioceometer (lidar), (Ref 13). The lidar was mounted on the aircraft so as to be pointing vertically downward. Aerosol-size distribution measurements were made with the PMS ASSP-100 aerosol-size spectrometer. The aircraft made a slow ascending spiral over the ocean just south of Pt. Loma, San Diego, CA, from 30 to 1525 m in approximately 8 minutes. Air temperature, pressure, and relative humidity were measured and recorded every 5 seconds (height resolution of 4.5 m). A complete aerosol spectrum was obtained every 4 seconds (3.6 m resolution). At 300 m intervals the aircraft leveled momentarily while the lidar was fired vertically downward. The measured aerosol-size distribu-

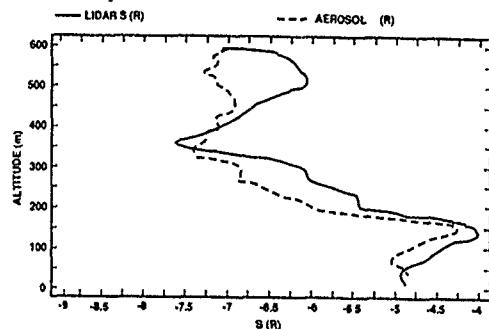


Fig 1. Comparison of the  $S(R)_{\text{lidar}}$  and calculated  $S(R)_{\text{aerosol}}$  profiles.

tions were used to calculate (via MIE theory) the extinction and backscatter profiles. The lidar shots were combined to generate a received backscattered lidar signal profile  $S(R)$  as a function of altitude (Equ 1).

Using the aerosol extinction and backscatter profile coefficients, an expected  $S(R)$  profile can be calculated for the aerosol data  $S(R)_a$  from Equ 2. The  $S(R)$  profile taken by the lidar at 600 m ( $S(R)_L$ ) and the corresponding  $S(R)_a$  aerosol profile are compared in Fig 1. Good agreement exists between the two profiles up through the inversion (region of higher aerosol density), but the profiles differ significantly above the inversion (region of lower aerosol density). Above 250 m the aerosol  $S(R)_a$  data are consistently less than those measured by the lidar (with the exception near 350 and 600 m). These lower extinction and backscatter-derived  $S(R)$  values undoubtedly resulted from: 1) the statistical sampling period required for low aerosol concentration sampling was not sufficient to obtain an adequate data sample (Ref 14), 2) the ASSP-100 was designed and calibrated to size pure spherical water droplets, an unlikely condition above the inversion on a clear day, 3) particles above the inversion were more likely solid, non-spherical, and inactivated (not growing with relative humidity), (Ref 15), and 4) the dynamic range of the PMS spectrometer was limited to sample smaller particles (minimum diameter of 0.45  $\mu\text{m}$ ). Fig 2 shows the scaling factor,  $k$ , required to match the aerosol and lidar  $S(R)$  data to within 0.1 percent;  $k$  varied from 0.7 to 2.25 below the inversion and up to 3.4 above. This result is in agreement with that found by Jensen, et al., (Ref 16). They reported that extinction coefficients derived from PMS spectrometer data could vary from ground truth measurements by as much as a factor of three for clear, dry days.

NOVAM used the measured surface meteorological data for 30 March 1989 and the corresponding profile of air temperature,

relative humidity, and pressure to calculate the predicted vertical profile of aerosol extinction. The inversion base was at 150-200 m (shallow surface haze layer). Surface winds were northwesterly at 4.9 m/s and the visibility was between 12 and 13 km. Calculations were made for both marine and continental air-mass factors (AMFs) of 1 and 10, respectively. The measured AMF was not available for 30 March 1989. Fig 3 compares the NOVAM extinction predictions for a wavelength of 1.06  $\mu\text{m}$  with those calculated for both the scaled ( $k$  multiplier) and unscaled aerosol data. These data show the strong dependency of NOVAM on AMF. When the AMF was varied from 1 to 10, the predicted NOVAM extinction coefficients changed by more than an order of magnitude. The aerosol extinction profiles (both scaled and unscaled) exceeded the predicted NOVAM values for both AMFs. Similar comparisons were made for wavelengths of 0.53, 3.5, and 10.6  $\mu\text{m}$ . For all wavelengths, except the visible, NOVAM underestimated the extinction values.

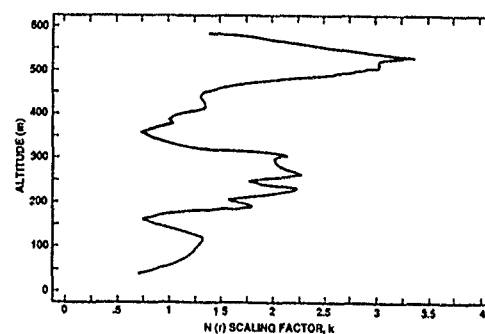


Fig 2. Scaling factor  $k$  to make the  $S(R)_{\text{aerosol}}$  and  $S(R)_{\text{lidar}}$  match.

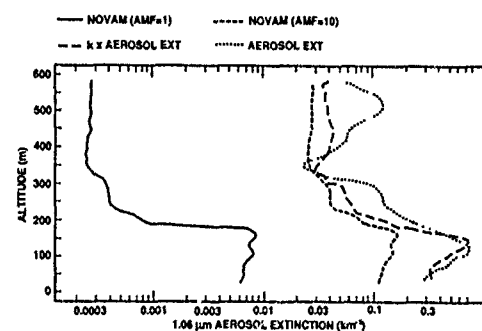


Fig 3. Comparison of NOVAM-predicted 1.06  $\mu\text{m}$  extinction profiles with those calculated using aerosol data (both scaled and unscaled).

The underestimated extinction values partially resulted from NOVAM not being scaled to surface visibility. Figs 4 and 5 show the 0.53  $\mu\text{m}$  NOVAM calculations for AMFs of 1 and 10, respectively, scaled to the observed surface visibility of 12 km. This scaling forces the lowest level extinction values to be equal. A better agreement now exists between the NOVAM-predicted and the scaled-aerosol extinction profiles. Below the inversion base (150-200 m) the NOVAM-predicted values did not increase as rapidly as did those obtained from the aerosol data. At the inversion height, an excellent agreement existed, especially for the AMF of 10. Above the inversion (250 m), the occurrence of a larger variation can be attributed to the aerosol sampling problems previously discussed. Figs 6 and 7 show the NOVAM calculations for the far infrared (10.6  $\mu\text{m}$ ) and AMFs of 1 and 10, respectively, scaled to the 0.53  $\mu\text{m}$  surface visibility of 12 km. Even though the structural details below the inversion (150-200 m) are evident in both profiles, NOVAM still underestimated the extinction magnitude for 10.6  $\mu\text{m}$ .

### 5. NAM MODEL VALIDATION

During the summer of 1990, lidar measurements of atmospheric structure within the first 10 m of the ocean surface were made using the Visioceilometer. The lidar was mounted at the end of Scripps Pier, La Jolla, CA, at an elevation of 10 m above mean sea level and a distance of 0.4 km from the shore line. It was mounted so as to be pointing seaward and tilted downward at an angle such that the range between the lidar and the point where the beam would strike the ocean surface was approximately 330 m (height resolution of 0.23 m). Simultaneous measurements of air temperature, barometric pressure, relative humidity, wind speed, and sea-surface temperature were made at the 10 m level.

Following the procedure developed by Paulus (Ref 17), the profile of relative humidity from 10 m to the surface was generated as an input to NAM. This procedure assumes a logarithmic decrease of relative humidity with altitude from 100 percent at the surface to the value measured at 10 m. The shape of the profile is dependent on the stability of the intervening media.

During each measurement period, several lidar shots were averaged to minimize the effects of the horizontal inhomogeneities. NAM was then used to generate the aerosol-size distributions as a function of altitude above the sea surface and were used to calculate (via MIE theory) the extinction and backscatter profiles near the ocean surface. The lidar provided a received backscatter lidar signal profile ( $S(R)_a$ ) as a function of altitude. Fig 8 shows the vertical profile of the modeled relative humidity for 30 July 1990. Surface visibility was greater than 20 km. Winds were moderate at 4.9 m/s with a 24-hour average of 4.1 m/s. The NAM generated extinction and backscatter coefficients were used in the lidar  $S(R)$  equation (Equ 2) and adjusted by the scaling factor  $k$ , for each level, so that the modeled

aerosol  $S(R)_a$  profile would match the  $S(R)_a$  profile measure by the lidar. Fig 9 shows the lidar  $S(R)_a$  profile for 30 July 1990. Fig 10 shows the corresponding profile of  $k$ -factor needed to match the  $S(R)_a$  profile with the  $S(R)_a$  profile for AMFs of 1, 3, 5, 7, and 10. These profiles show that, for a  $k$ -factor close to 1, an AMF of about 7 or 8 is required for NAM to represent present atmospheric conditions near the ocean surface (AMF was not measured). For an AMF of 7 and a wavelength of 10.6  $\mu\text{m}$ , Fig 11 shows the predicted NAM extinction profile and the lidar adjusted profile for 30 July 1990. The very high NAM predicted extinction at zero elevation is caused by the 100 percent relative humidity at the surface as determined by the

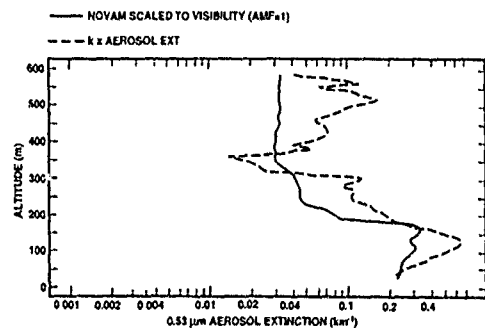


Fig 4. Comparison of NOVAM-predicted 0.53  $\mu\text{m}$  extinction profiles scaled to surface visibility with that calculated using aerosol data. AMF = 1.

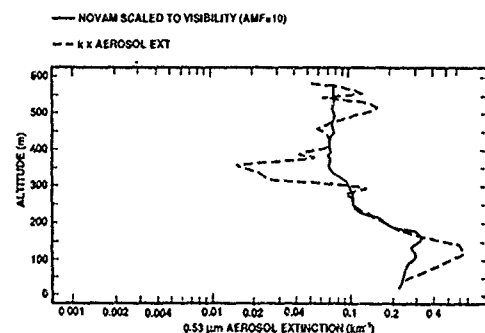


Fig 5. Comparison of NOVAM-predicted 0.53  $\mu\text{m}$  extinction profiles scaled to surface visibility with that calculated using aerosol data. AMF = 10.

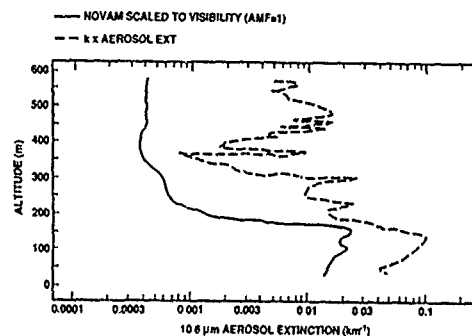


Fig 6. Comparison of NOVAM-predicted 10.6  $\mu\text{m}$  extinction profiles scaled to surface visibility with that calculated using aerosol data. AMF = 1.

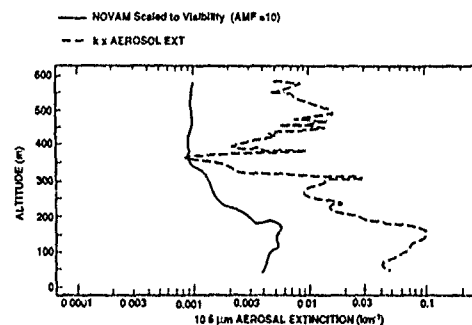


Fig 7. Comparison of NOVAM-predicted 10.6  $\mu\text{m}$  extinction profiles scaled to surface visibility with that calculated using aerosol data. AMF = 10.

07/30/90 U=4.9 m/s U(24)=4.1 m/s

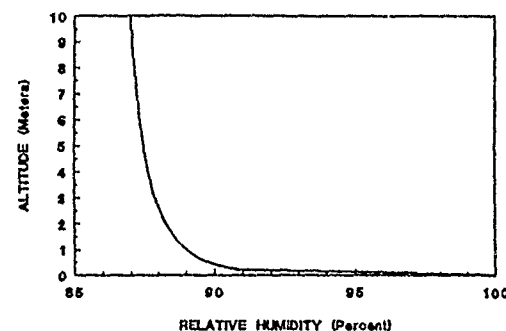


Fig 8. Calculated relative humidity profile for 30 July 1990. U = 4.9 m/s, U(24) = 4.1 m/s.

relative humidity program of Paulus (Ref 17). The lidar adjusted profiles do not show the large increase of extinction at the surface that the NAM model predicts based on relative humidity. Correction factors at the surface ranged from 0.53 to 1.5 in order to match the NAM predicted and the lidar observed extinction profile.

A similar comparison was made for data taken on 26 July 1990. Winds were light with a current wind speed of 1.8 m/s and a 24-hour average of 2.7 m/s. Fig 12 shows the required k-factor for AMFs of 1 and 10 required to match the lidar S(R) data to the NAM modeled. k-factors varied from 35 to 40 for an AMF of 1 to 3 for an AMF of 10. To get a k-factor near 1 would require an AMF greater than 10. This is outside the allowable range for AMF in NAM.

Similar comparison were made for a total of 21 observational periods. k values ranged from 0.8 to 433 for an AMF of 1 and from 0.4 to 26 for a AMF of 10. The large variation of k values indicate that the NAM model, in its present form, cannot be used with any realistic degree of accuracy at  $1.06 \mu\text{m}$  in the coastal regions near the surface of the ocean.

## 6. CONCLUSIONS

The Navy Oceanic Vertical Aerosol Model was evaluated by using nearly simultaneous measurements of atmospheric aerosol structure made with an airborne lidar and a PMS aerosol-size

spectrometer. Profiles of measured aerosol-size distributions were scaled to the lidar returns and compared with the NOVAM predictions. The NOVAM predictions underestimated the extinction values for all AMFs. However, when the predicted extinction values for a given AMF were scaled to surface visibility (scaling not incorporated in NOVAM), better agreement existed between the predicted and the measured vertical profiles of extinction. Atmospheric vertical structural characteristics agreed well with those observed by PMS aerosol spectrometers and lidar returns, especially below the inversion.

The magnitude of the NOVAM extinction predictions is critically dependent upon identifying the air mass as either marine or continental. For AMFs between 1 and 10, the predicted extinction coefficients vary by more than an order of magnitude. Because of this NOVAM dependency on AMF and the difficulty in obtaining a good AMF determination from either radon concentration measurements or an air-mass trajectory analysis, Gathman (Ref 18) is incorporating into NOVAM a technique whereby AMF is deduced from visibility measurements.

The Navy Oceanic Vertical Aerosol Model shows potential for predicting the vertical aerosol structure within the marine boundary layer. Scaling to visibility and incorporating a technique to better estimate the AMF are expected to improve NOVAM for calculating scattering and the absorption properties of the MBL.

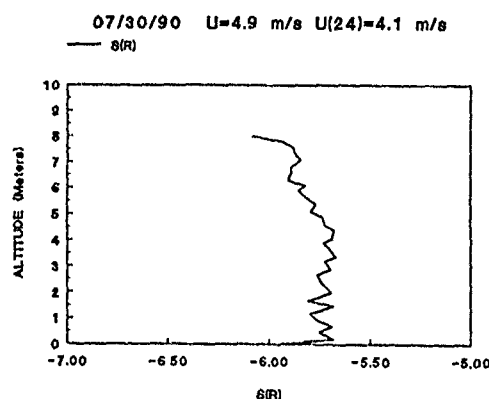


Fig 9.  $S(R)_{\text{lidar}}$  profile for 30 July 1990.  $U = 4.9 \text{ m/s}$ ,  $U(24) = 4.1 \text{ m/s}$ .

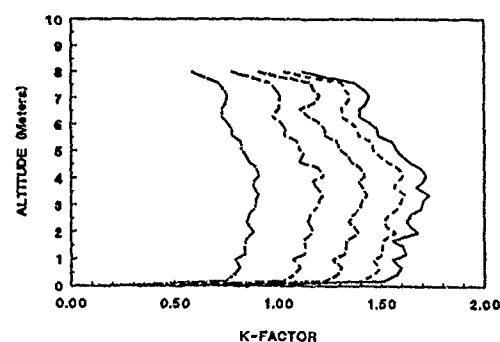


Fig 10. k factor profiles needed to match the  $1.06 \mu\text{m}$   $S(R)_{\text{lidar}}$  profile for 30 July 1990 for air-mass factors of 1, 3, 5, 7, and 10 (right to left, respectively).  $U = 4.9 \text{ m/s}$ ,  $U(24) = 4.1 \text{ m/s}$ .

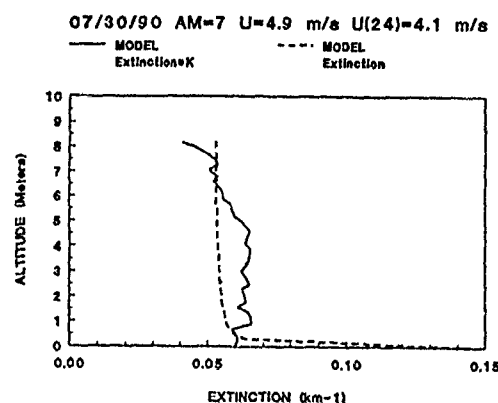


Fig 11. Comparison of the lidar-adjusted extinction coefficient profile at  $1.06 \mu\text{m}$  with that calculated by NAM for 30 July 1990. AMF = 1.  $U = 4.9 \text{ m/s}$ ,  $U(24) = 4.1 \text{ m/s}$ .

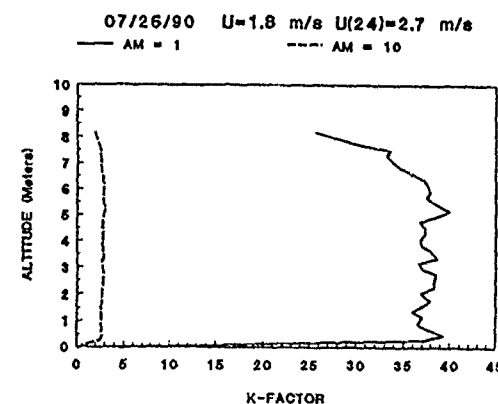


Fig 12. k factor profiles needed to match the  $1.06 \mu\text{m}$   $S(R)_{\text{lidar}}$  data for 26 July 1990. AMFs = 1 and 10.  $U = 1.8 \text{ m/s}$ ,  $U(24) = 2.7 \text{ m/s}$ .

NAM in its present form, cannot be used with any realistic degree of accuracy at 1.06  $\mu\text{m}$  in the coastal region near the surface of the ocean. The program greatly underestimates the extinction and backscatter coefficients for low wind speed conditions. Average adjustment factors up to greater than 400 were required for an air-mass factor of 1 and wind speeds around 1 to 2 meters per second. Since it is very difficult, if not impossible, to determine what the air-mass factor should be, an air-mass factor of 10 was used as well. Even when the air-mass factor is set to its maximum value, to try to compensate, the adjustment factor was usually considerable greater than unity.

## 7. RECOMMENDATIONS

While adjustment of the NAM aerosol number densities can match the model S(R) profile to that measured by the lidar, the large adjustment factors required for low wind speeds would suggest the shape of the aerosol size distribution is probably not correct. The model would then give incorrect results if it were used for the longer wavelengths. A better approach would be to use the lidar, along with the wind, AMF, and aerosol size distribution measurements, to try to adjust the appropriate parameters in the NAM model so the model and the lidar give the same S(R) with adjustment factors close to unity.

## 8. ACKNOWLEDGEMENTS

This work was supported by the Office of Naval Technology.

## 9. REFERENCES

1. Hughes, H. G., and M. R. Paulson, "Double-ended lidar technique for aerosol studies," *Appl. Opt.*, Vol. 27, 1988, pp 2273-2278.
2. Kneizys, F. X., E. P. Shettle, W. O. Gallery, J. H. Chetwynd, Jr., L. W. Abreu, J. E. A. Selby, S. A. Clough, and R. W. Fenn, "Atmospheric transmittance/radiance: computer code LOWTRAN 6," Air Force Geophys. Lab. Technical Report No. 83-0187, Aug 1, 1983.
3. Kneizys, F. X., E. P. Shettle, L. W. Abreu, J. H. Chetwynd, Jr., G. P. Anderson, W. O. Gallery, J. E. A. Selby, and S. A. Clough, "Users Guide to LOWTRAN 7," Air Force Geophys. Lab. Tech. Report No. 88-0177, Aug 1988.
4. Gathman, S. G., "Optical properties of the marine aerosol as predicted by the Navy aerosol model," *Opt. Eng.*, Vol. 22, No. 1, 1983, pp 57-62.
5. Gathman, S. G., G. de Leeuw, K. L. Davidson, and D. R. Jensen, "The Naval Oceanic Vertical Aerosol Model; Progress Report," AGARD Conference Proceedings No. 454, Copenhagen, Denmark, 9-13 Oct 1989, pp 17-1 to 17-11.
6. Gathman, S. G., and Ulfers, B., "On the accuracy of IR predictions made by the Navy Aerosol Model," American Meteorology, Society Ninth Conf. on Aerospace and Aeronautical Meteorology, 1983, pp 194-198.
7. Hughes, H. G., and Jensen, D. R., "Aerosol model selection using surface measurements of IR horizon radiances and satellite detected visible radiances," *Appl. Opt.*, Vol. 27, 1988, p 4367.
8. Davidson, K. L., and C. W. Fairall, "Optical properties of the marine atmospheric boundary layer; aerosol profiles," *Ocean Optics VIII*, Proc. SPIE, Vol. 637, 1986, pp 18-24.
9. Fairall, C. W. and K. L. Davidson, "Dynamics of modeling of aerosols in the marine atmospheric boundary layer," E. C. Monahan and G. Mac Niocaill, eds., in *Oceanic Whitecaps*, Dordrecht, D. Reidel, 1986, pp 195-208.
10. Noonkester, V. R., "Profiles of optical extinction coefficients calculated from droplet spectra observed in marine stratus cloud layers," *J. Atmos. Sci.*, Vol. 42, 1985, pp 1161-1171.
11. Hughes, H. G., and M. R. Paulson, "Lidar techniques for adjusting aerosol model number densities to existing conditions," Naval Ocean Systems Center Technical Document 1637, Sept 1989.
12. Jensen, D. R., "Aerosol measurements in the marine boundary layer at San Diego," Naval Ocean Systems Center, Technical Report 168, 1978.
13. Lentz, W. J., "The visioceilometer: A portable visibility and cloud ceiling height lidar," Atmospheric Sciences Laboratory TR-0105, Jan 1989.
14. Noonkester, V. R., "Droplet spectra observed in marine stratus cloud layers," *J. Atmos. Sci.*, Vol. 41, No. 5, Mar 1984, pp 829-845.
15. Fitzgerald, J. W., "Approximation formulas for the equilibrium size of an aerosol particle as a function of its dry size and composition and the ambient relative humidity," *J. Appl. Meteorol.*, Vol. 14, 1975, pp 1044-1049.
16. Jensen, D. R., R. Jeck, G. Trusty, and G. Schacher, "Intercomparison of PMS particle size spectrometers," *Opt. Eng.*, Vol. 22, No. 6, 1983, pp 746-752.
17. Paulus, R. A., "Specification for environmental measurements to assess radar sensors," Naval Ocean Systems Center Technical Document 1685, Nov 1989.
18. Gathman, S. G., Private Communication

24-6

DISCUSSION

**C. WERNER**

*Do you have a computer simulation program for lidar returns for different atmospheric conditions?*

**AUTHOR'S REPLY**

*We do not have such a simulation program.*

## FAR-INFRARED CHARACTERIZATION OF HORIZONTAL PATH IMAGE DEGRADATION

Wendell R. Watkins  
 Atmospheric Sciences Laboratory  
 U. S. Army Laboratory Command  
 White Sands Missile Range, New Mexico 88002-5501, USA

## SUMMARY

Modelers beware! There are important issues that must be considered in modeling of infrared systems that are not being appropriately extrapolated for applications of today's more complex and sophisticated sensors to ever increasing ranges. What is measured vertically may not be directly applicable to horizontal paths. The degradation of the atmosphere for far-infrared imaging systems is not merely an absorption coefficient derived from LOWTRAN calculations, nor can the spatial degradation due to propagation be considered as an atmospheric modulation transfer function (AMTF) of unity, especially for hot desert regions of current interest. The same is true for the non-uniformity of aerosol obscuration whose spatial degradation is not fully characterized by a single extinction coefficient but rather requires a complex point spread function or AMTF.

Recent measurements by the Mobile Imaging Spectroscopy Laboratory (MISL) have shed new light on the real degradation produced by atmospheric propagation on far-infrared imaging systems. By the hot and cold bars and the unique measurement technique of closeup and distant simultaneously collected matched imagery of a large area blackbody target board, the AMTF has been shown to be definitely nonzero for both atmospheric horizontal path turbulence and aerosol clouds. In addition observations of the target board without the bar pattern and uniform backgrounds have been used to compare the MISL measured contrast transmission with LOWTRAN calculations.

## LIST OF SYMBOLS

AMTF - atmospheric modulation transfer function  
 LOS - line of sight  
 FLIR - forward-looking infrared  
 ASL - Atmospheric Sciences Laboratory  
 MISL - Mobile Imaging Spectroscopy Laboratory  
 FTS - Fourier transform spectrometer  
 TCC - Target Contrast Characterizer  
 NF - near field  
 FF - far field  
 $h_i(x,y)$  - imager impulse function  
 $h_d(x,y)$  - deterministic degradation point spread function  
 $f(x,y)$  - ground truth image function  
 $f_{NF}(x,y)$  - closeup image function  
 $f_{FF}(x,y)$  - distant image function  
 \* - two-dimensional spatial convolution  
 LOWTRAN - Low-Resolution Atmospheric Transmission Code  
 R - range

$\tau_c(R)$  - contrast transmission for range, R  
 $C(0)$  - inherent target contrast  
 $C(R)$  - target contrast from range, R  
 $\nu$  - spectral frequency  
 $F(\nu)$  - system spectral response function  
 $\nu_1$  to  $\nu_2$  - limits of system spectral response function  
 $L_p(R,\nu)$  - path spectral radiance over range, R  
 $L_b(0,\nu)$  - inherent background spectral radiance  
 $\bar{T}(R)$  - system weighted atmospheric transmission over range, R  
 $\Delta T$  - change in temperature between target and background  
 $BBT_c$  - target board hot bar to cold bar contrast transmission  
 $BBT_b$  - target board hot bar to vegetative background contrast transmission  
 IFOV - instantaneous field of view  
 SRF - slit response function  
 DFT - discrete Fourier transform  
 MTF - modulation transfer function

## 1. INTRODUCTION

With the ever increasing sophistication of today's weapon systems, characterization of the propagation environment has increased in its importance. This is especially true for the horizontal lines of sight (LOS) near the ground (Ref 1). While airborne active and passive remote sensors can accurately profile temperature, humidity, winds, and extinction, the extrapolation of these parameters to horizontal infrared imaging system performance requires great care. As recent events have shown, ground warfare can occur at lightning speed; and the unit that "sees" best in the battlefield environment has a tremendous advantage. With increasing spatial resolution of second and third generation forward-looking-infrared (FLIR) systems, target acquisition is being degraded by more than just an extinction coefficient as longer range detection is sought. Optical turbulence, which is recognized in the visible as shimmer above hot asphalt pavement in the daytime and twinkling of distant city lights at night, has been shown to degrade infrared imagery as well (Ref 2). This distortion has been characterized as a complex point spread function or atmospheric modulation transfer function (AMTF) (Refs 3 and 4). In addition to the thermally induced degradation, there is also nonuniformity in extinction coefficients along the LOS to the individual scene areas comprising the pixels of the target and background, which alters the AMTF and contrast transmission as well as

solar loading changes that also influence the contrast transmission (Ref 5). This paper discusses these topics.

## 2. BACKGROUND

For several years the Atmospheric Sciences Laboratory (ASL) has been developing a unique research tool--the Mobile Imaging Spectroscopy Laboratory (MISL) (Refs 6 and 7). The MISL is comprised of a Fourier transform spectrometer (FTS) and an imaging component termed the Target Contrast Characterizer (TCC). It is the use of the TCC that is stressed here. The TCC has two far-infrared 8- to 14- $\mu$ m imagers that are used to characterize the atmospheric AMTF. The complex means to accomplish this are described in detail elsewhere (Refs 3 and 4); but, in essence, the target and background of interest are viewed with two optically matched imagers along a common LOS. One imager is placed at close range or in the near field (NF); the other imager is placed at a distant location or in the far field (FF) and is equipped with a compensating telescope. The resulting images are registered pixel for pixel with an image processing system and remote control and data transfer via fiber optics. Paramount to the success of this alignment process is the use of single detector scanning imagers, even though their spatial resolution and sensitivity are less than most FLIRs. Also the development of a large area (1.78 by 1.78 m) blackbody with uniform surface temperature was essential. The unique design of tilting the oven surface of this blackbody back to allow the heating air to rise along the backside of the front surface, coupled with an offset see-through front bar pattern for near perfect hot to cold bar transition, has made the measurement of the AMTF and contrast transmission with the TCC possible.

In theory, characterization of the AMTF is straightforward with the TCC (Refs 3 and 4). If the imagers are noiseless with identical impulse functions,  $h_1(x,y)$ , and the degradation is a deterministic point spread function,  $h_d(x,y)$ , then the zero-range or "truth" image,  $f(x,y)$ , as observed by the closeup imager is  $f_{NF}(x,y) = f(x,y) * h_1(x,y)$ , where  $*$  denotes a two-dimensional spatial convolution. The image,  $f(x,y)$ , as observed by the distant imager is  $f_{FF}(x,y) = f(x,y) * h_1(x,y) * h_d(x,y)$ . The AMTF (the Fourier or Laplace transform of the degradation point spread function) is simply the ratio of the Fourier (or Laplace) transforms of the long- and short-range images.

$$\begin{aligned} \text{AMTF} = H_d(x,y) &= \frac{F_{FF}(x,y)}{F_{NF}(x,y)} \\ &= \frac{F(x,y) \cdot H_1(x,y) \cdot H_d(x,y)}{F(x,y) \cdot H_1(x,y)} \end{aligned} \quad (1)$$

In practice, however, several difficulties arise. The imagers are not identical and each has an associated noise process that must be characterized. Each imager exhibits a different line-to-line scan anomaly, and the imagers are neither line-to-line nor frame synchronized. Finally, the AMTF is not a deterministic point spread function but, rather, a complicated nonstationary random process.

Spatial degradation along horizontal paths is only one issue that must be considered in assessing imaging system performance. Another is the contrast loss due to propagation and weather related conditions. Many assessments of FLIR system performance are based on an absorption coefficient derived from LOWTRAN or, better yet, an extinction coefficient that includes scattering losses. But the quantity that is really needed for assessment is contrast transmittance,  $\tau_c(R)$ , which is the ratio of the distant range,  $R$ , to inherent range (zero) contrasts or  $C(R)/C(0)$ . Watkins et al. give detailed derivations that allow a simplified expression for  $\tau_c(R)$  (Ref 8).

$$\tau_c(R) = \frac{C(R)}{C(0)} = \frac{1}{1 + \frac{\int_{v_1}^{v_2} L_p(R,v) F(v) dv}{\int_{v_1}^{v_2} L_p(0,v) F(v) \tau(R,v) dv}} \quad (2)$$

where  $v$  is the spectral frequency;  $F(v)$  is the system response function that spans frequencies  $v_1$  to  $v_2$ ;  $L_p(R,v)$  is the path spectral radiance over the distance,  $R$ ;  $L_p(0,v)$  is the background spectral radiance at zero range; and  $\tau(R,v)$  is the spectral atmospheric transmission over the distance,  $R$ . Note that optimization of  $\tau_c(R)$  for humid conditions requires proper selection of the system response function,  $F$ , which has been accomplished for the TCC imagers through use of cold finger filters based on FTS measurements (Ref 9).

Now, for the condition where the path spectral radiance does not have an appreciable component from external sources such as cold sky or solar reflections or pyrotechnic smokes (not in general a good battlefield environment assumption), the expression for contrast transmission reduces to

$$\tau_c(R) \approx \frac{1}{1 - \frac{1 - \bar{\tau}(R)}{\bar{\tau}(R)}} = \tau(\bar{R}) \quad (3)$$

where  $\bar{\tau}(R)$  is the system weighted atmospheric transmission given by

$$\bar{\tau}(R) = \frac{\int_{\nu_1}^{\nu_2} \tau(R, \nu) F(\nu) d\nu}{\int_{\nu_1}^{\nu_2} F(\nu) d\nu} \quad (4)$$

The TCC is ideally suited to measure directly contrast transmission because the NF imagery can be used to obtain an excellent approximation of the zero-range contrast,  $C(0)$ ; and the FF imagery to obtain the distant contrast,  $C(R)$ . The computational procedures for arriving at the value of  $r_c$  from measured target and background apparent temperatures described by Watkins et al. (Ref 8) can be approximated within a couple of percent for target and background temperatures near 300 K by simply taking the ratio of the FF and NF difference temperatures,  $\Delta T_s$ , or

$$r_c(R) = \frac{T_s(FF) - T_b(FF)}{T_s(NF) - T_b(NF)} \quad (5)$$

Measurements of  $r_c(R)$  using the TCC can be compared with LOWTRAN 7 (Ref 10) calculations by using Eqs. (4) and (5), but there are some spatial resolution issues that must be addressed if the problems experienced previously (Ref 8) are to be avoided. To overcome these problems the large area blackbody was used without a front bar pattern to produce a resolvable uniform hot surface for NF to FF comparisons.

The issue of image resolution brings up an interesting question of how best to describe image degradation. If the NF and FF images are compared pixel by pixel to obtain values of contrast transmission, the values obtained will vary greatly because of the spatial resolution differences. The optical turbulence degradation, AMTF, will increase these differences. The issue of how best to use TCC comparison of NF to FF images for overall image degradation quantification is still under investigation. One metric, the "complexity measure," is currently being used (Ref 11). The complexity measure is a quantity from 0 (disjoint distributions) to 1 (indistinguishable distributions) based on the overlap of the distributions of gray scale values in equal pixel areas of target and background.

### 3. MEASUREMENT AND ANALYSES

The TCC measurements of atmospheric degradation will begin with the conceptually simpler contrast transmission instead of the AMTF. The TCC 8- to 14- $\mu$ m

imagers were positioned at NF = 96 m and FF = 1,637 m from the large area (1.78 by 1.78 m) target board with a large evergreen tree for the background. The FF was matched to the NF with a 17X lens whose transmission properties were determined by initially positioning it at the NF location and comparing target and background temperatures measured by the NF and FF imagers. To obtain the apparent target and background temperatures for the contrast transmission value, the average target temperature was calculated for a square region in the center of the target board with 1/4 the length and height of the target board as in Fig. 1a.

A comparable square region in the background was used to obtain the average background temperature. This was done for both the NF (Fig. 1a) and FF (Fig. 1b), and the resulting  $r_c = 0.80$  was obtained by using Eq. (5). The meteorological parameters used in LOWTRAN 7 calculations at this time were temperature of 21 °C, pressure of 1,006 mbar, relative humidity of 53 percent, typical minor constituent concentrations, and rural aerosols with 20 km visibility. The resulting LOWTRAN 7 calculations for the path difference between the NF and FF resulted in a  $\bar{\tau} = 0.82$ , which considering the uncertainty in the LOS aerosol extinction is quite good compared to previous measurements with a small area target board (Ref 8).

Now, the question is what happens when the bar pattern target board required to measure the AMTF is used as in Figs. 2a and 2b. The same square averaging region cannot be used. If a vertical strip is taken as the new averaging region to obtain the average temperatures for the hot and cold bar centers as well as the background, a couple of options are possible. The target to background contrast temperatures can be between hot and cold bars or hot bar and cold vegetative background. The resulting values for  $r_c$  are for bar to bar,  $r_{bb} = 0.13$ , and for hot bar to vegetation,  $r_{bv} = 0.65$ . The discrepancies between the  $r_c$  values obtained with these contrast sources and the exposed whole target board to uniform background are related to spatial resolution and the AMTF.

The manufacturer-specified instantaneous field of view (IFOV) for the single detector scanning imager is 2 mrad for the 1X lens, which is positioned 96 m from the target board with 25 cm separation between the vertical bars. Figure 2a shows the resulting infrared image with a 4X electronic blowup and an implied 19 by 19 cm IFOV; the imager slit response function (SRF) should be around 0.7. This was verified by measuring the uniform blackbody surface with the bar pattern removed to show that only 40 percent of the inherent bar pattern  $\Delta T$  was detected in good agreement with an SRF of 0.7. When the recorder MTF was considered, the resulting area in the image, which was averaged to obtain a single scene pixel value, was 21 pixels high and

26 pixels wide--the bars being 15.5 pixels wide. The results in the FF using a 17X lens at 1,637 m were essentially the same under quiescent atmospheric conditions. Figure 2b shows that during most of the day optical turbulence was present, resulting in marked distortion of the target board bar pattern. It is this spatial distortion that produces significant errors in the contrast transmission values derived from the narrow hot bars of the target board that are not present when the central portion of the whole 1.78 by 1.78 m blackbody source is used. The large errors in the bar pattern measured  $r_c$  values would be less if an FLIR with better resolution were used, but they would not disappear. For a better understanding the magnitude of the optical turbulence distortions must be quantified as an AMTF.

Again all the details of deriving the AMTF from images such as Figs. 3a and 3b using Eq. (1) are given elsewhere (Refs 3 and 4). The derivations will only be summarized here. To begin, an approach utilizing one-dimensional discrete Fourier transforms (DFTs) of horizontal scans through the target board pattern instead of two-dimensional fast Fourier transforms was used because the noise reduction and field-to-field phase correction algorithms needed for the latter process are still under development for the recently acquired database presented here. Line scans horizontally through the center of the target board bars in Figs. 3a and 3b are shown in Fig. 4 for 256 by 256 pixel portions of the scenes. With a 15.5-pixel spacing between bars or a 31-pixel cycle, the DFT of these line scans will have a peak at index 8 associated with the 3.5-cycle bar target. This is shown in Fig. 5 where the whole target board has a significant peak at index 1 and harmonics at indices 3 and 5. The energy content of indices 12 and above are basically noise because these frequencies cannot be resolved with the imager. Note that there is about a 70 percent loss of energy content for the index 8 between the NF and FF because of optical turbulence. This translates into a significant loss in the resolving capability of 0.1 mrad features, which the bars represent at 1.6 km over a horizontal path when the temperature is only 25 °C. This measure of AMTF was consistent over frames spaced 10 s apart (Fig. 6), and the average of these three images yields an AMTF whose shape based on the high-energy indices 1, 3, 5, and 8 shows a consistent falloff and represents an average or slow AMTF in (Fig. 7). Before these measurements the AMTF was always considered to be unity for the far infrared over horizontal paths. The only other AMTF measurement in the infrared was for the near infrared (Ref 12) and was not measured in the field. The bottom line is that the increased spatial resolution of today's FLIRs are going to be degraded by optical turbulence over horizontal paths near the ground in warm climates such as those of current interest.

The issue of dust cloud obscuration will now be addressed. Often the attenuation produced by large clouds of vehicular dust is uniform. By observing a vehicular dust cloud that passed between the NF and FF during a time of minimal optical turbulence distortion, the effect of the obscuring attenuation was observed as a resulting change in AMTF. First the contrast reduction of the FF image of the target board is illustrated in Fig. 8. The DFTs of lines through the FF target board image with no dust are shown in Fig. 9. The corresponding DFT plots with dust and contrast reduction are shown in Fig. 10. When gain is applied to reestablish the index 1 peak in Fig. 11, the DFT plots for dust (Fig. 11) and no dust (Fig. 9) are almost identical, and the dust modulation transfer function (MTF) is essentially unity. Unfortunately, battlefield obscurants are not uniform and can have significant emissive or reflective components that can influence the overall AMTF by adding clutter to the target scenes. This can be illustrated by observing the dust cloud produced by a tank going down a sandy road in the desert on a clear day. Viewing the dust cloud produced at near normal incidence indicates the cloud is essentially the same apparent temperature as the road in Fig. 12. As the viewing angle to the top of the cloud becomes a grazing one, the cloud begins to reflect the cold far-infrared sky temperature as in Fig. 13.

Now, another measure of changes in target contrast is the "complexity measure" (Ref 11), which essentially is the overlap of equal area target and background intensity distributions. Like the AMTF the complexity measure is essentially independent of attenuation or gain change. Figure 14 shows the low NF and FF complexity measure values when the complexity measure was applied to TCC imagery of an exposed tank against a vegetative background at midday. Three separate simulated artillery dust events occurred during this 7.5 min time interval. During the heavy dust event, the attenuation was so severe that the target scene became blank; and, hence, the target and background areas were identical (complexity of 1.0). During the other two events, the dust cloud attenuation was not uniform and was mixed with hot explosion by-products. The result was that the complexity measure, which like the AMTF is insensitive to uniform attenuation, increased significantly because of the nonuniform attenuation and path radiance characteristics of simulated battlefield conditions. Finally, even though the baselines of the NF and FF complexity measures track each other quite well, they are not constant. In fact, the NF complexity changes from 0.2 to 0.1 in less than 7 min due to solar loading changes.

The dramatic influence that solar loading changes have on target contrast is not fully appreciated when remote sensing is applied to characterizing the vertical

structure for extrapolation to the ground level propagation environment. What goes on under the clouds is remarkable. As it turns out, the windspeed is the driving parameter for contrast changes of camouflage netting and vegetative backgrounds (Ref 5). For 2 days with nearly the same relative humidity, temperature, and variability of solar loading, a change of from 2 to 3 m/s windspeed to 5 to 6 m/s windspeed can have tremendous impact on target contrast. During the higher wind conditions, the camouflage net has a high complexity value or blends well with the background over an 8-min time interval (Fig. 15). The exposed tank complexity starts out near 0.2 for sunny conditions and then drops sharply to 0.05 when the target area is shaded. During the low windspeed conditions, a remarkable change occurs. The camouflage net cannot follow the cooling cycle of the vegetative background, as illustrated in Fig. 16. Only during shady conditions does the camouflage net blend into the background (high complexity). When the sun comes out, the low thermal mass camouflage net actually becomes easier to see than the exposed vehicle (lower complexity). In fact, the camouflage net almost flickers as the solar loading changes. What a difference windspeed can make!

In summary this material may prove useful to individuals tasked with modeling of far-infrared imaging system performance for horizontal path applications based on remotely sensed atmospheric parameters. Because of the increased spatial resolution for longer range applications, FLIRs are now susceptible to degradation from optical turbulence. The magnitude of this AMTF degradation is not easily estimated from remotely sensed vertical profiles, nor is the nonuniformity of aerosol obscuration that can include cold sky reflection as well as emissive path radiant clutter. Besides the spatial distortions that must be included in system performance modeling, target contrast reduction due to natural attenuation cannot be fully characterized with a single absorption coefficient. The more accurate measure of the degradation due to atmospheric propagation (the contrast transmission that includes path radiance contributions and inherent contrast changes) can be correlated to LOWTRAN calculations; but for this measurement-to-prediction comparison, extreme care must be used. Of interest are target metrics that are least sensitive to the propagation environment. The complexity measure metric was used to illustrate uniform attenuation insensitivity, but solar loading changes coupled with low levels of wind-speed caused dramatic fluctuations in this metric. The research continues for better methods of longer range target detection, and proper characterization of cloud cover induced contrast changes may be useful in these pursuits.

#### 4. ACKNOWLEDGEMENTS

The author thanks Richard Dutro for his assistance in obtaining the LOWTRAN calculations; Jay Jordan for data reduction and figures; and Fernando Palacios, Daniel Billingsley, and Young Yee for their assistance in collecting the AMTF and contrast transmission related imagery data.

#### 5. REFERENCES

1. Watkins, W. R., F. T. Kantrowitz, and S. B. Crow (NATO Restricted), "Dynamic Changes in Images and Scenes to Environmental Factors (U)," in "Atmospheric Propagation in the UV, Visible, IR and MM-Wave Region and Related System Aspects," AGARD-CP-454 (Supl), October 1989, pp 44-1, 44-12.
2. Miller, W. B., J. C. Ricklin, and D. H. Marlin, "Effect of Atmospheric Turbulence on Electro-Optical Systems," in "Atmospheric Propagation in the UV, Visible, IR and MM-Wave Region and Related System Aspects," AGARD-CP-454, October 1989, pp 45-1, 45-10.
3. Watkins, W. R., D. R. Billingsley, F. R. Palacios, S. B. Crow, and J. B. Jordan, "Characterization of the Atmospheric Modulation Transfer Function Using the Target Contrast Characterizer," SPIE Conference Proceedings, Vol. 1486, Orlando, FL, April 1991.
4. Watkins, W. R., and J. B. Jordan, "Characterization of Turbulence Effects on Infrared Imagery," ICO Topical Meeting Proceedings on Atmospheric, Volume, and Surface Scattering and Propagation, Florence, Italy, 27-30 August 1991.
5. Crow, S. B., W. R. Watkins, F. R. Palacios, and D. R. Billingsley, "Technique for Measuring Effects on Image Metrics," SPIE Conference Proceedings, Vol. 1486, Orlando, FL, April 1991.
6. Watkins, W. R., F. T. Kantrowitz, and S. B. Crow, "Characterization of Atmospheric Effects on Target Contrast," SPIE Conference Proceedings, Vol. 926, Orlando, FL, April 1988.
7. Watkins, W. R., S. B. Crow, and F. T. Kantrowitz, "Characterizing Atmospheric Effects on Target Contrast," Optical Engineering, October 1991.
8. Watkins, W. R., F. T. Kantrowitz, and S. B. Crow, "Transmission Measurements With the Target Contrast Characterizer," SPIE Conference Proceedings, Vol. 1115, Orlando, FL, March 1989.

9. Kantrowitz, F. T., W. R. Watkins, D. R. Billingsley, and F. R. Palacios, "Characterization and Optimization of Infrared Imager Detector Response for Long Path Research," SPIE Conference Proceedings, Vol. 1311, Orlando, FL, April 1990.
10. Kneizys, F. X., E. P. Shettle, L. W. Abreu, G. P. Anderson, J. H. Chetwynd, W. O. Gallery, J. E. A. Selby, and S. A. Clough, Users Guide to LOWTRAN 7, AFGL-TR-88-0177 (NTIS: AD A206773), 1988.
11. Carlson, J. J., J. B. Jordan, and G. M. Flacks, "Tasks Specific Complexity Metrics for Electronic Vision," SPIE Conference Proceedings, Vol. 901, Los Angeles, CA, January 1988.
12. Kuga, Y., and A. Ishimaru, "Modulation Transfer Function and Image Transmission Through Randomly Distributed Spherical Particles," J.O.S.A.A., Vol. 2, p 2330, 1985.

#### 6. ILLUSTRATIONS



Fig. 1a. Closeup or NF (96 m range) 8- to 14- $\mu$ m image with 65 by 87 mrad field of view showing the exposed 1.78 by 1.78 m blackbody (right) and evergreen tree background (left) on a 50 °C full-scale setting.



Fig. 1b. Distant or FF (1,637 m range) 8- to 14- $\mu$ m image with 4 by 5 mrad field of view showing the exposed 1.78 by 1.78 m blackbody (right) and evergreen tree background (left) using a 20 °C full-scale setting.

120 110 100 90 80 70 60 50 40 30 20 10 0

A high-contrast, black and white image of a textured, rectangular object, possibly a piece of fabric or paper, with a dark, irregular border. The object has a mottled, grainy appearance with varying shades of gray and black, suggesting a rough or aged surface. The lighting is uneven, with brighter areas in the center and darker, more shadowed regions towards the edges. The overall effect is abstract and somewhat mysterious.

The image is a dark, grainy, high-contrast scan of a document page. It features a central, bright, textured area that appears to be a large, irregularly shaped object or a heavily illuminated section of the page. The background is predominantly black, with scattered white specks and noise, suggesting a low-quality scan or a very dark original document. The central area has a mottled, almost crystalline appearance with varying shades of gray and white, indicating different textures or materials. There are no discernible text, figures, or tables visible in this image.

Fig. 3b. FF blowup image of the target board with bar pattern in the afternoon with 25 °C ambient temperature showing optical turbulent distortion of the bars.

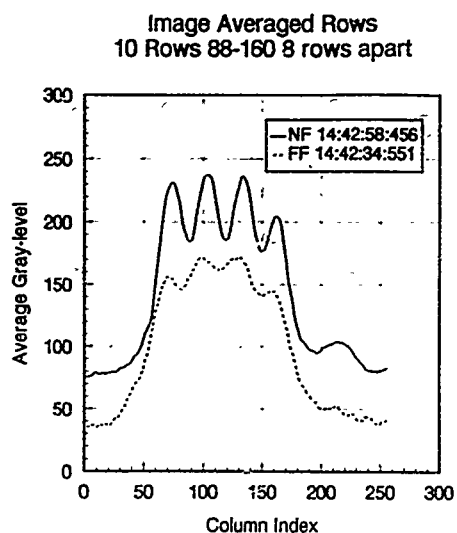


Fig. 4. Average gray scale plots of 10 horizontal line scans through NF and FF scenes illustrated in Figs. 3a and 3b.

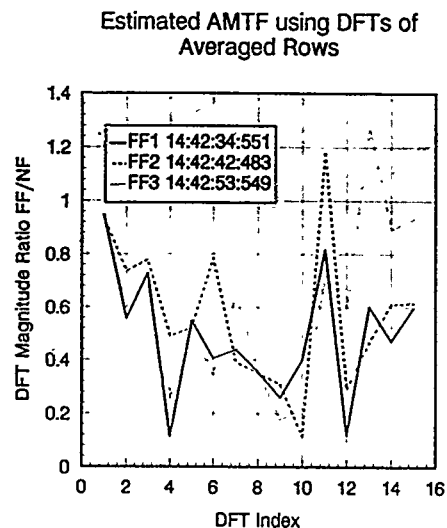


Fig. 6. Set of three ratios of FF/NF DFTs like Fig. 5 yielding estimates of the AMTF for image pairs spaced approximately 10 s apart.

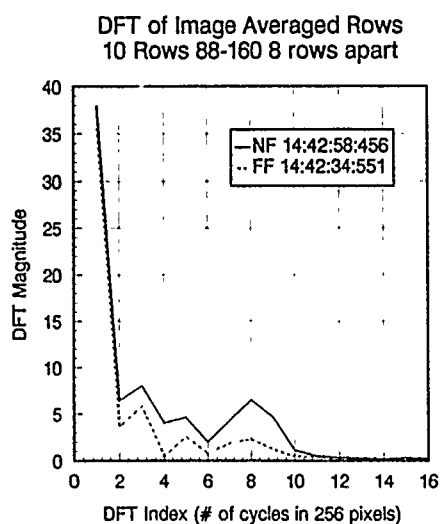


Fig. 5. DFTs of plots shown in Fig. 4 with the peak at index 8 corresponding to the bar pattern spatial frequency.

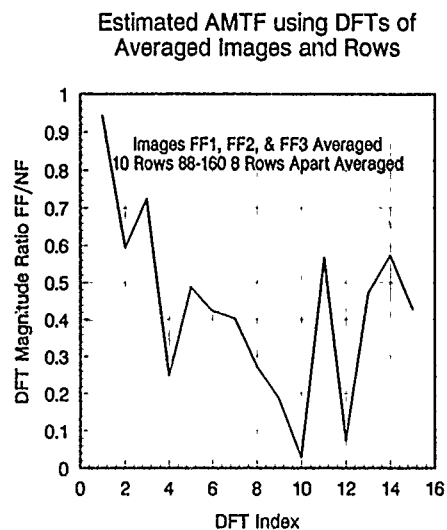


Fig. 7. Smoothed estimate of the AMTF using the averaged images from Fig. 6 showing a 70 percent drop in energy content for the bar pattern frequency at index 8.

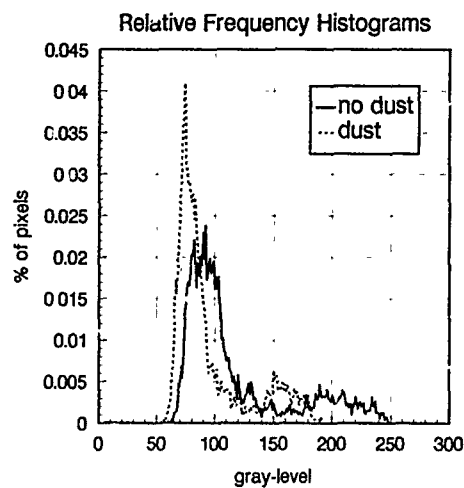


Fig. 8. Histograms of FF images of the target board as in Fig. 3b for no dust and a couple second later dust attenuated (shift to lower gray level) image.

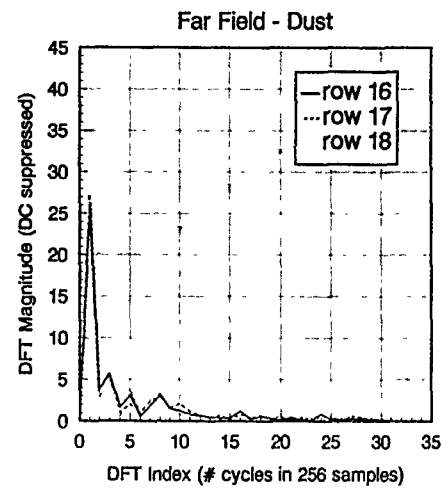


Fig. 10. Set of the same three horizontal line DFT plots as in Fig. 9 with dust attenuation present.

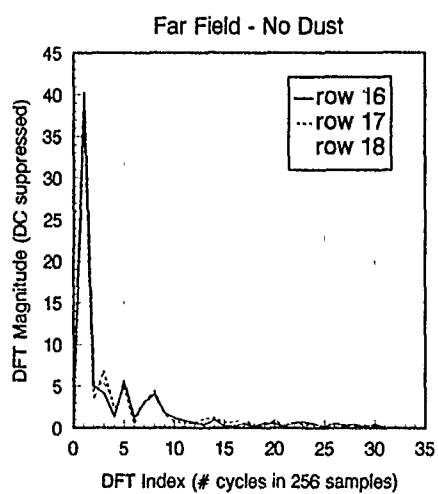


Fig. 9. Set of 3 horizontal line DFT plots through the center of the target board with no dust attenuation.

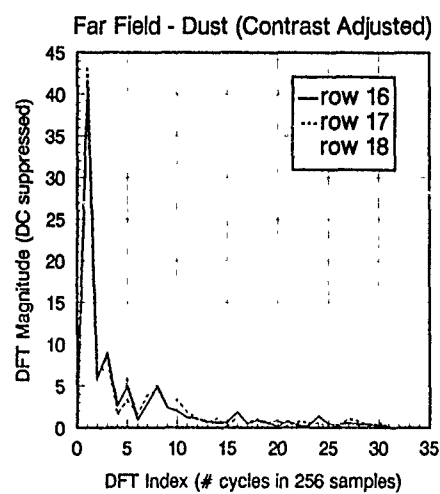


Fig. 11. Set of contrast adjusted (based on Fig. 8) DFT plots in Fig. 9 showing no MTF distortion of the target board bars from the Fig. 9 DFT plots.



Fig. 12. Far-infrared image of tank driving down a hot, sandy road with trailing dust cloud blending into the road apparent temperature.



Fig. 13. Far-infrared image of the same tank as in Fig. 12 just 17 s later with trailing dust cloud top surface grazing view angle now reflecting the clear, cold sky and highly contrasted against the warm road.

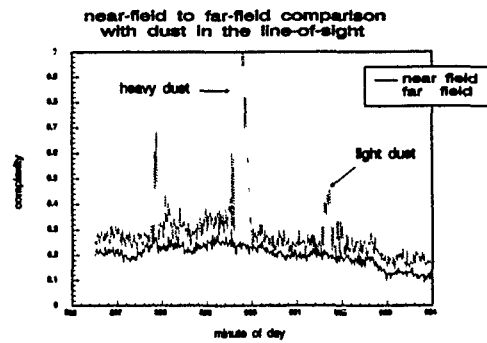


Fig. 14. NF versus FF tank-to-background complexity for dust clouds in the line of sight.

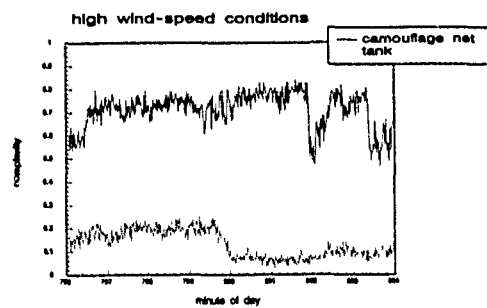


Fig. 15. Complexity during high wind-speed conditions for a target of high thermal mass (tank) compared to a target of low thermal mass (camouflage net).

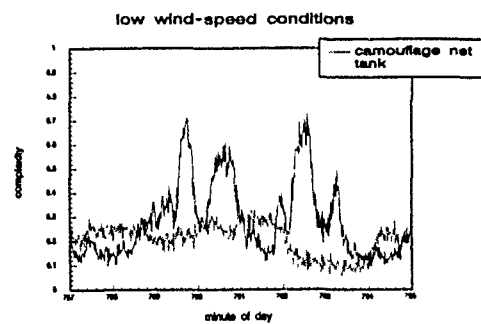


Fig. 16. Complexity during low windspeed conditions for a target of high thermal mass (tank) compared to a target of low thermal mass (camouflage net).

## DISCUSSION

### E. SCHWEICHER

1. Your definition of contrast does not comply with the definition of the MTF. Can you explain?
2. Why did you use a 1.8m x 1.8m target instead of the standard NATO 2.3m x 2.3m target?
3. How do dust clouds perform on 8-12 $\mu$  images compared to 3-5 $\mu$  images?

#### AUTHOR'S REPLY

1. I have used to U.S. Army Night Vision definition of contrast for measurement and prediction of the contrast transmission. A denominator of the sum of the background and target radiances could have been used as well. The MTF measurements were derived strictly from the comparison of image spatial content and not contrast.
2. The choice of 1.8m was for expedience because aluminum sheets are much easier to obtain in the U.S. in 6 ft. widths.
3. The dust clouds vary differently depending upon the precise environmental condition. For clear sky conditions the 8-12 $\mu$  image would typically show colder sky reflections than the 3-5 $\mu$  because the 8-12 $\mu$  sky is colder than the 3-5 $\mu$  and generally the reflection at longer wavelengths is greater. However, there may be emissive components in the 3-5 $\mu$  dust cloud to consider.

### D. HOEHN

You found cases of thermal contrast loss created by atmospheric turbulence. Have you also observed cases of contrast created by real thermal path variance in the atmosphere?

#### AUTHOR'S REPLY

In order to enhance our sensitivity to measure long range atmospheric distortions due to turbulence and aerosol attenuation, the 3-5 $\mu$  and 8-12 $\mu$  images have cold finger spectral filters to greatly reduce the effect of inherent atmospheric path radiance. The effects of emissive clutter caused by, for example, explosive dust clouds will affect the 3-5 $\mu$  more than the 8-12 $\mu$ . Also the size of the emissive clutter will have the most impact when its spatial dimensions are of the same size as the target features of interest.

### E. TULUNAY

Isn't the function  $h_i(x,y)$  time dependent?

#### AUTHOR'S REPLY

There is a time dependence of  $h_i(x,y)$ , but its magnitude is small compared to the physical effects being characterized. One reason for this is because the imagers that use the Target Contrast Characterizer are single detector scanning radiometers. The normal mode of operation is in a highly oversampled fashion meaning that the instantaneous field of view is much larger than the individual pixel sizes resulting in temporal averaging already being present in the imagery.

# Compact Laser Doppler Anemometer

Ch. Werner, M. Klier, H. Herrmann, E. Biselli, and R. Häring  
DLR-Institute of Optoelectronics  
8031 Oberpfaffenhofen  
Federal Republic of Germany

## 1. Summary

Wind profiles in the atmospheric boundary layer are a very important parameter also to study atmospheric exchange processes. A small laser Doppler anemometer was designed, constructed and tested. The system consists of the laser Doppler anemometer mounted on a pedestal and controlled by a personal computer. A sine wave fitting computer program is used to get the wind velocities and wind direction for the levels selected. This sophisticated program can distinguish between cloud and aerosol signals and uses also the azimuthal angle-velocity for extracting the direction of the wind.

## 2. Introduction

The wind field in the atmospheric boundary layer is highly variable in spatial and temporal scales. For a few possible applications a more frequent wind sensing is necessary, i.e.

- for airports located in low level jet areas,
- for chemical plants to get information of the transport of toxic gases from leakages,
- for military application (artillery).

Only a few techniques can be applied to get the wind field in the boundary layer. The laser Doppler systems are a candidate.

There are a few laser anemometry projects performed during the past years (Woodfield and Vaughan, 1983; Köpp et al., 1984). RSRE designed and manufactured with GEC a LAser True Airspeed Sensor (LATAS), a very compact system in the early 80's. Also RSRE and GEC designed and manufactured a cw-laser Doppler system for DLR in 1981. This system was installed in a container and has been operated at airports, artillery ranges and on a Northsea research platform (Werner et al., 1986). Pulsed systems with larger range capacity are in use at NOAA-Boulder (M.J. Post, 1990).

This paper summarizes the principle technique, gives the special design of the new compact system and presents test and simulation results.

The requirements for the system are a compact design and an automatic or half-automatic operation. The required windspeed measurement capability is listed in table 1.

Table 1: Required Windspeed Measurement Capability

Windspeed	Maximum 30 m/s
	Minimum 1 m/s
	Accuracy 1 m/s
Wind direction	Accuracy 5 degree at max. windspeed
Measurement points:	Typically 5 height levels between 10 m and 300 m above ground.
Measurement time:	Typically 60 seconds per level
Mode of operation:	nearly fully automatic

## 3. Principle of Doppler Lidar Technique

Figure 1 shows the principle. For the continuous wave (cw) CO<sub>2</sub>-laser, the energy is focused by the telescope into the region of investigation. Some of the radiation is backscattered by small aerosol particles drifting with the wind speed through the sensing volume. Aerosol particles moving with the wind are the targets for the Doppler lidar, therefore a reasonable number of particles is necessary to produce a signal. The backscattered radiation is collected by the telescope and detected by coherent technique. In that way, the Doppler frequency shift can be extracted which directly determines the line-of-sight component of the wind vector. At CO<sub>2</sub>-laser wavelengths of 10.6 micrometers a velocity component of 1m/s corresponds to 189 kHz frequency shift.

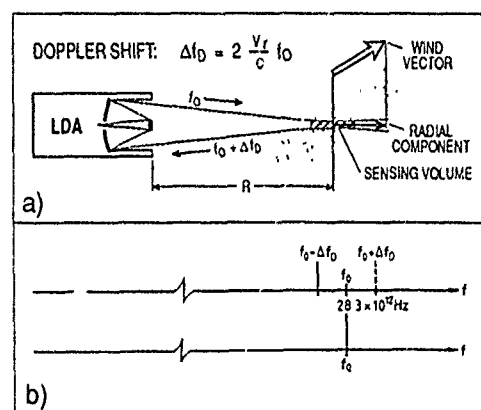


Figure 1: Laser Doppler Anemometer

a) principle

b) frequency scale

The frequency scale is shown in figure 1b. The center frequency is the laser output frequency which is for the wavelength of 10.6 micrometer  $28.3 \times 10^{12}$  Hz. The Doppler shifted radial velocity for the atmospheric wind is between 0 and 25 MHz.

The coherent detection technique uses part of the output energy of the master oscillator laser (1) for an offset locking loop (2) that maintains the local oscillator laser (3) at a constant frequency difference from the master (Figure 2).

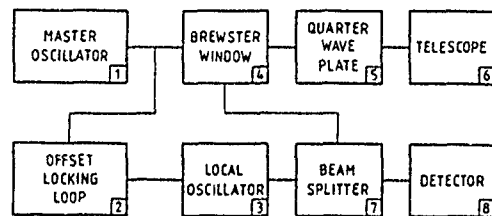


Figure 2: Block Diagram of the Coherent Detection Technique

The radiation passes through a Brewster window (4), aligned for horizontal polarization, through a quarter-wave plate (5) to rotate the polarization to circular, and into a telescope (6). The telescope collimates the beam and transmits it into the atmosphere. The return beam, Doppler shifted and rotated in polarization, comes back along the same path into the telescope (6) and to the quarter-wave plate (5). Because of the reverse polarization of the return beam, the radiation passing through the quarter-wave plate now becomes vertically polarized. The beam is reflected by the Brewster window (4) to a beam splitter (7), where it is combined with the local oscillator beam and transmitted to the detector (8). The coherent mixing of the two beams is called heterodyning and results in an interference pattern imaged on the surface of the detector. If one uses the master laser also as a local oscillator, one can reduce the amount of components necessary for such a system. One gets a homodyne system.

The interference pattern fluctuates according to the difference in frequency of the two beams, thereby resulting in an electrical signal coming out of the detector in the form of a frequency modulated wave with the modulation frequency being equal to the Doppler shift of the return beam. The signal processor necessary for the frequency analysis gives an output resolution depending on the processor. For cw-laser Doppler systems normally the Surface Acoustic Wave analyzers are used with a resolution in the order of 20 kHz. These cw-laser Doppler systems are used as ground based systems to get wind profiles in the atmospheric boundary layer. The range resolution depends on the focus size of the telescope used.

With the described laser Doppler method one gets the radial wind component. To determine the magnitude and direction of the horizontal wind, some form of scanning in azimuth and elevation is required (Schwiesow et al., 1985). Lhermitte and Atlas (1961) showed that it is possible to retrieve mean horizontal wind magnitude and direction from radial velocity data around horizontal

circles centered on the vertical axis of the scanner (Figure 3).

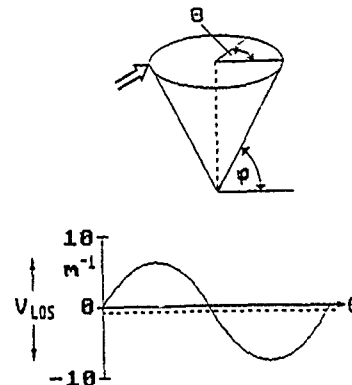


Figure 3: Velocity-Azimuth-Display (VAD) Scan Technique

This type of pattern is called a conical scan because the lidar beam sweeps out a cone with the apex at the scanner. The representativeness of wind values derived from scans over parts of a full circle were determined by Schwiesow et al. (1985). The task is to fit the measured radial velocity  $v_{LOS}$  vs. azimuth data to a function of the form

$$v_{LOS} = [u \sin\theta \cos\phi + v \cos\theta \cos\phi + w \sin\phi]$$

where

$u$  is the east-west wind component,

$v$  is the north-south wind component,

$w$  is the vertical wind component,

$\theta$  is the scan angle clockwise from north, and

$\phi$  is the elevation angle,

using a standard least-square procedure. The calculation can be made also for an azimuth angle region (sector) in the order of 45 degree. As known from other fitting procedures, one needs a number of data points to get the accurate wind vector. As known from the equation shown above at least there are data sets necessary at two different azimuth angles to get the horizontal wind components  $u$  and  $v$ . Figure 3 shows below the different radial wind components versus the azimuth angle. For a homogeneous wind field these components form a sine wave. The deviation from the zero line is direct proportional to the vertical wind component (dashed line).

#### 4. Design of the Compact Laser Doppler Anemometer (LDA)

The following sections describe the design of the laser system, its principle operation and its signal processing.

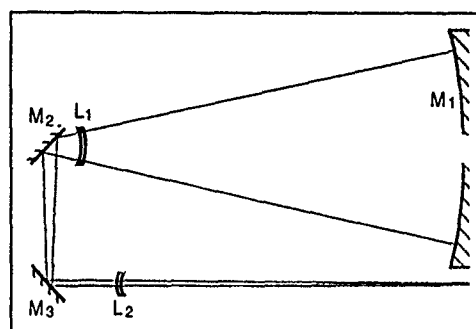
##### 4.1 Introduction

The block diagram in figure 4 shows the different units of the compact LDA

The scanner and the LDA are operated and controlled by the electronics. Two racks are used. One contains a power supply (220 v ac vs. 24 v dc) and the scanner control. The second rack (separated in figure 4 by the thick solid line) contains the computer (Compaq 386), the LDA control and the signal processing (SAW) and integration unit.

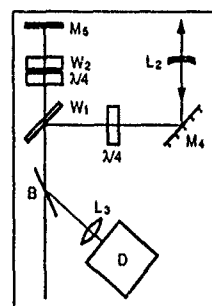
To keep the system compact, the transceiver optics is a compromise. On one side one has the requirements for a good range resolution and therefore for a large primary mirror, on the other side is the problem of compactness. The maximum distance at which wind measurements can be made is determined by the amount of laser radiation which is backscattered from atmospheric aerosols within the focal volume of the transmitted beam and by the proportion of backscatter which is then collected by the receiver telescope. The length of the focal volume,  $L$ , can be determined as follows

where  $\lambda$  is the laser wavelength,  $R$  is the distance at which the measurement is made and  $D$  is the diameter of the telescope. This relation used for the CO<sub>2</sub>-laser and a telescope with 250 mm aperture, at a distance of 300 m the extend  $L$  of the focal volume is 72 m. Figure 5 shows the transceiver optics.



Laser: CM 1000  
beam diameter 2.8 mm  
Mirror M1: diameter 250 mm  
focal length -500 mm  
Lense L1: ZnSe  
focal length -97 mm  
Lense L2: ZnSe  
focal length - 34 mm  
(for range positioning)  
flat mirrors M2 M3

The interferometer performs several functions including the separation of the transmitted and received beams, the combination of the received beam with the local oscillator and the monitoring of the spectral output of the CO<sub>2</sub>-laser for the purpose of stabilizing it on one mode. Figure 6 shows the layout of the interferometer.



The laser radiation is passing a Brewster window B and is split by the window W1 (95% reflection) into the two beams. The reflected beam is passing a Germanium quarter-wave plate before entering the lens L2 (see also figure 5). This is the transmitted beam into the telescope. The lens L2 is motor driven in position for range

control. The local oscillator radiation originates from the mirror M5. Another quarter-wave plate and a neutral filter W2 is used to get the correct polarization and power. The two beams, received backscatter radiation and local oscillator are combined at the Brewster plate B directed into the SAT MCT Joule-Thomson cooled detector. A lense L3 and a field stop is placed between the Brewster plate and the detector.

The optics and the laser including the power supply built the LDA measurement head. The cooling for the laser and the ballast resistors of the high-voltage is located adjacent to the head (figure 4).

#### 4.3 Scanner

The scanner is an ORBIT AL4371 scanner, elevation over azimuth. This unit is a standard for microwave antennas and is used in a modified version to allow an azimuthal scan velocity of 20 degree per second. The LDA head is mounted on one side of the scanner, on the other side is the Nitrogen bottle for the Joule-Thomson cooler. On top of the scanner the laser cooling device is placed. The system is controlled manually or via IEEE bus. The range scanning is performed by moving the lense L2 (figure 5) manually or also by IEEE bus routine.

#### 4.4 Signal Electronics

The detector output is preamplified and the signal is fed into mixers where the beat frequency (figure 1) is extracted. This frequency is then measured by a spectrum analyzer and the output is transferred to a digital integrator where the signal to noise is improved prior to analysis by the wind vector processor. Figure 7 shows the block diagram of the signal processing.

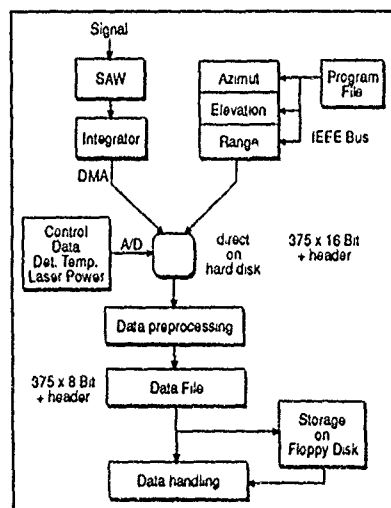


**Figure 7: Block diagram of the signal processing**  
The preamplified signal reaches the SAW device (MESL) and the integrator (GEC). It is a modified unit with a digital output the computer can handle via Direct Memory Access (DMA).

#### 4.5 Signal Processing

As shown in figure 7 the signal is at the integrator. A computer Compaq 386 (modified for  $\pm 4$  v dc operation) is used to get the stored data. Additionally the scanning procedure is performed via a preselected programmable file. Together with control data on the performance of laser and detector via an A/D board the data of each record is stored on the hard disc of the computer. After finishing the scan program, the raw data are preprocessed to produce the data file which can further be stored on a floppy disc. Direct - on-line - data handling is possible.

#### 4.6 Data Handling

Figure 8 shows a typical spectrum from the spectrum analyzer and integrator. The scales are signal voltage vs. line-of-sight (LOS) velocity (on the bottom) and the digital bins (on the top). The integrator produces frequency spectra which carry the wind information, averaged over selectable time periods from 1.6 to 52 milliseconds. Specifically, the peak position in the spectrum corresponds to the magnitude of the most probable radial wind components in and outside the sensing volume. Fog and cloud scatterers can produce signals that can have their origin from outside the sensing volume (Werner et al., 1987).

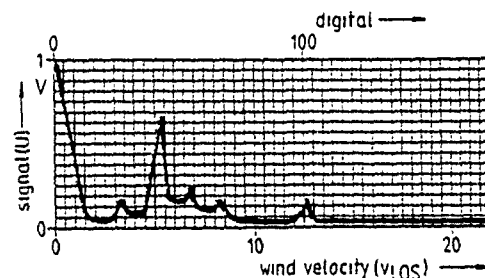


**Figure 8: Doppler Spectra in a Digital Frame**

The block header contains the focused position and the complete spectrum. Using the LDA as a homodyne system as described, one cannot determine the sign (plus or minus) of the radial velocity. Therefore a special procedure (see below) is introduced. The data system is able to handle 50 millisecond averaged data. The flow diagram to compute the wind field is shown in figure 9.

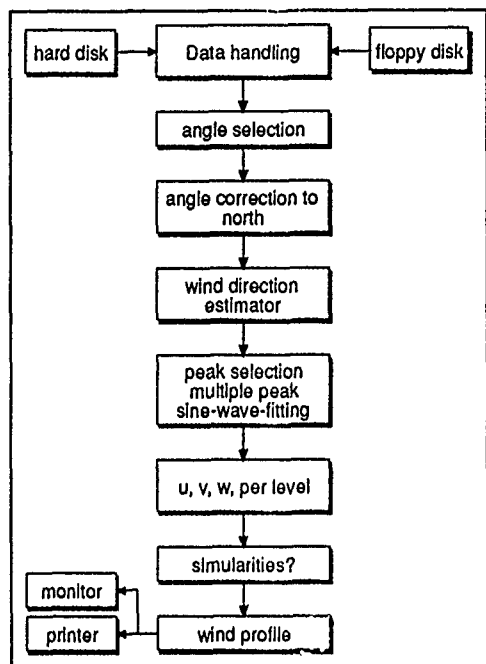


Figure 9: Flow Diagram of Data Handling

On-line data handling from the hard disc or later computation from a floppy disc starts with the angle selection. Each line-of-sight wind signal for an azimuth angle is selected. If two signals for the same azimuth angle exist, an averaging is done. The position of the van in direction to North is corrected in the subprogram "angle correction". The scanner has a fixed angle encoder to its own zero.

The procedure "wind direction estimator" uses the following approach (Biselli and Werner 1989, Hausmann and Davis 1990): Most of the operational cw-LDA systems use an eccentric scan pattern. Eccentric means that there is an additional movement introduced by the scan mirror. The rotational velocity is small compared to the wind component. Normally this component is neglected. Using a fast digital data system one can use this additional component to determine the sign of the wind direction for a homodyne lidar. If one scans with the wind direction, the rotational component is added. If one scans against the wind, the component is subtracted. The different frequency shifted values between both scans can be measured.

The sine wave fitting computer program is starting with the peak selection. Each peak in order to amplitude and frequency is determined. The fitting routine uses the amplitude as a parameter. It determines the  $u, v$ , and  $w$  components of the wind vector for each altitude level. If similarities of the determined wind exist between the levels, a procedure to fit the wind profile is used. This procedure is based on the fact that a low level cloud base can contribute by measuring from lower level to higher one with an increasing amplitude to the determined signal. The amplitude is an indicator for this behaviour.

#### 4.7 Special Setups

The nearly automatic operation of the compact LDA needs some control mechanism. The control starts after switch-on with a supervizing of the detector temperature and of laser power and mode control. The protective housing of the LDA can be opened by the computer to start the measurements. After finishing the measurements, a close-up procedure starts. The operator have to select the program file and has to answer a few questions during the operation, for example the direction of the small van with respect to North.

#### 5. Tests

A test procedure was developed to show the influence of noise in the signal on the wind vector determination. The described case with a low level cloud explains the procedure. Figure 10 shows an example of the signals during a scan from 0 degree to 120 degree in azimuth (range is 424 m, elevation 45 degree). Two intensities show a sine wave shape with some noise in the frequency scale.

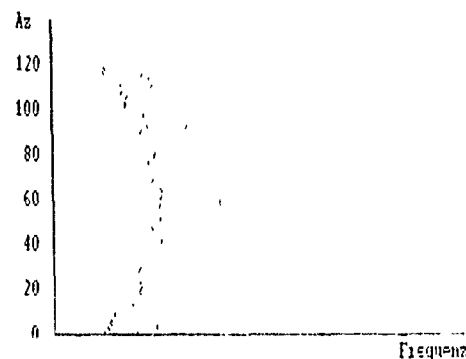


Figure 10: Simulation Example of a Scan

The intensity is noisy also but split into two regimes. Figure 11 shows the data for the same simulation. Three regimes of intensities are selected. The first two regimes contain the information.

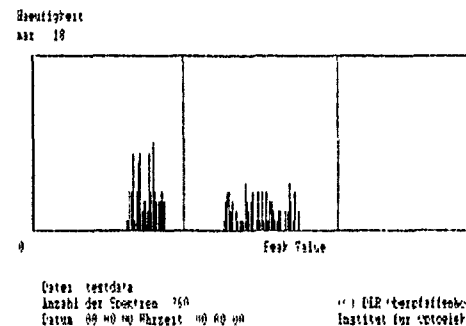


Figure 11: Example of Intensity Selection

These two intensities can be fitted. For the test a wind profile was assumed. Table 3 shows the result.

**Table 3: Results of a Simulated Wind Profile using the LDA Data Handling Procedure**

Level	Height (m)	I	$v_x$	$v_y$	Cloud Influence
1	50	$I_1$			
2	100	$I_1$	6,1		
3	200	$I_1$	4,9	9,0	
		$I_2$	10,1	15,1	*
4	300	$I_1$	10,0	15,1	*
		$I_2$	6,1	10,1	
5	400	$I_1$	10,0	15,0	*

Five levels were chosen in heights from 50 m to 400 m. The intensities  $I$  of the signal (see figure 11) contain noise and a cloud influence with a cloud base height in 400 m. The determined horizontal wind components  $v_x$  and  $v_y$  show similarities (see flow diagram in figure 9) in three levels. The intensity changes caused by the cloud influence between levels 4 and 5.

Tests of the sign of the wind can be performed also. The method depends on the noise in frequency (and intensity) also as on the number of points used for the fitting. The eccentric rotation is assumed to contribute as an additional z-component of the wind vector. If one can separate the computed z-component for the two rotational directions, one can determine the sign or - with other words, one can apply the method. Table 4 shows the results of a few cases.

**Table 4: Influence of Noise and of the Sector Size on the Determination of the Sign**

Input	$v_x = 10 \text{ m/s}$	$v_y = 10 \text{ m/s}$	$v_z = \pm 0,2 \text{ m/s}$
Output	$v_x$	$v_y$	$v_z$
$I = 1, F = 1, S = 360$	10,0	10,0	0,2
	10,0	10,0	-0,2
$I = 8, F = 8, S = 360$	10,0	10,1	0,3
	9,9	10,1	0,1
$I = 1, F = 1, S = 90$	10,1	10,1	0,1
	9,9	10,0	-0,2
$I = 8, F = 8, S = 90$	10,0	10,4	0,2
	10,1	10,5	0,7

$I$  = Intensity / bit     $F$  = frequency / channel     $S$  = sector

It was assumed to have a homogeneous horizontal wind field ( $v_x = v_y = 10 \text{ m/s}$ ). The z-component is caused only by the rotation (no natural z-component). The sector size ( $S$ ) was varied and the noise. The noise in intensity ( $I$ ) is given in bits, the noise in frequency ( $F$ ) is given in channels (out of 375). The result in the horizontal wind estimates is within the requirement (table 1). The sign ( $v_z$ ) is separable also out of noisy data from a sector.

## 6. Measurements

The first field test was performed end of August 1991 on the Meppen Proving Ground. Figure 12 shows one result.

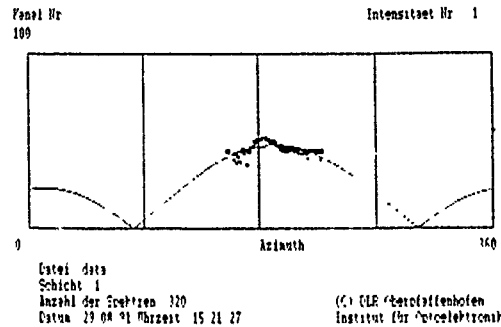


**Figure 12: Result of a Wind Measurement**

Within the 360 degree azimuth angle there are the data points and there is the fitted sinus. The data were measured between 150 degree and 230 degree under 25 degree elevation and at a range of 100 m. The result of the wind sensing was a horizontal wind with 3.3m/s out of 192 degree.

## 7. Conclusion

We have developed a compact laser Doppler anemometer to measure wind profiles in the atmospheric boundary layer. The problem to handle the system nearly automatically was described. The system development gave experiences on the way to the development of a spaceborne global wind sensor.

## 8. References

- Woodfield, A.A., and J.M. Vaughan: Airspeed and Windshear Measurements with an Airborne CO<sub>2</sub>-Continuous wave laser. RAE Technical Report 83061 (1983).
- Köpp, F., R.L. Schwiesow, and Ch. Werner: Remote Measurements of Boundary Layer Wind Profiles using a cw Doppler Lidar. Journ. Climate and Appl. Meteor. 23, 148-154, (1984).
- Werner, Ch., F. Köpp, Eu. Biselli, and Ef. Biselli: Laser Doppler Wind Profile Measurements over Sea Surfaces. ESA-TT 971, (1986).
- Post, M.J., and R.E. Cupp: Optimizing a Pulsed Doppler Lidar. Appl. Opt. 29, 4145-4158, (1990).
- Schwiesow, R.L., F. Köpp, and Ch. Werner: Comparison of cw-Lidar Measured Wind Values Obtained by Full Conical Scan, Conical Sector Scan and Two-Point-Technique. Journ. Atmospheric and Oceanic Technology 2, 3-14, (1985).
- Lhermitte, R.M., and D. Atlas: Precipitation Motion by Pulse Doppler, Reprints Ninth Weather Radar Conference, Kansas City, Amer. Met. Soc. 218-223, (1961).
- Werner, Ch., F. Köpp, and R.L. Schwiesow: Influence of Clouds and Fog on LDA Wind Measurements. Appl. Opt. 23, 2483, (1984).
- Biselli, Eu., and Ch. Werner: Determination of the Direction of Motion on the Basis of CW Homodyne Laser Doppler Radar. Appl. Opt. 28, 915-920, (1989).
- Hausmann, D., and B.W. Davis: Sign of the Wind Vector, Appl. Opt. 29, 2919-2928, (1990).

### DISCUSSION

#### **F. DAVARIAN**

*In one of your viewgraphs you showed measured wind speed distribution. The chart showed a signal component at the origin (dc). Would you comment on why the dc component exists?*

#### **AUTHOR'S REPLY**

*The zero frequency originates from the mixing of the outgoing laser frequency  $f_0$  with radiation reflected from different optical parts back to the detector. For a very frequency stable  $\text{CO}_2$ -laser this zero component is in the order of 100 kHz, for the  $\text{CO}_2$ -waveguide laser we use it is in the order of 200 kHz corresponding to 1 m/s wind velocity.*

## Remote Sensing of the Atmosphere by Multi-Channel Radiometers

Faramaz Davarian  
Jet Propulsion Laboratory  
California Institute of Technology  
4800 Oak Grove Drive  
Pasadena, CA 91109, U.S.A.

### 1. ABSTRACT

To characterize Earth/space communication links, The Jet Propulsion Laboratory's (JPL's) Radiowave Propagation Program supports a number of propagation studies. Low-availability satellite links and their propagation vagaries at Ka and millimeter-wave bands constitute a major effort within this program. Since 1987, this program has funded the Wave Propagation Laboratory (WPL) of the National Oceanic and Atmospheric Administration (NOAA) to conduct multiple-frequency radiometric observations of the atmosphere. The Wave Propagation Laboratory has extensive experience in using two- or three-frequency radiometers at 20, 31, and 90 GHz. These instruments provide unique observations of precipitable water vapor and liquid. Equally useful are the microwave attenuation characteristics that these devices can easily provide. Attenuation statistics are needed for the design of satellite communication systems.

Measurements of atmospheric emission and attenuation at 20, 31, and 90 GHz at different locations are presented. Single-station and joint-station statistics are derived. A linear regression scheme for the prediction of fade statistics in one channel using fade data of the other two channels is presented.

### 2. INTRODUCTION

Physically compact satellite ground terminals operating at Ka and higher frequency bands are attracting the attention of both commercial and military service providers. Such terminals could vary in antenna size from about a meter to about 10 cm. Unfortunately, due to the limited antenna gain of a compact ground terminal, the satellite link is likely to suffer from the lack of adequate margin to support a high link availability. Therefore, a low-margin link can benefit from fade (mostly rain fade) compensation. In theory, the received signal strength can be monitored at the ground terminal and an approaching fade can be detected. The detection of a fade would start a process that would boost the link margin for the period of the fade event.

Many fade compensation schemes, including uplink power control, data rate reduction, and signal encoding, have been discussed in the literature. The success of

any fade compensation scheme hinges upon the timely detection of an approaching fade. Fade detection may be performed by the monitoring of a satellite-transmitted beacon and the use of already available signal attenuation statistics.

To accumulate signal attenuation statistics, the Propagation Program at JPL has three ongoing efforts. Two of these efforts use Ka-band beacons transmitted from spacecraft, namely, the Olympus [1] and ACTS [2] satellites. The third uses ground-based radiometers at Ka and millimeter-wave bands. Ground-based radiometers have proven to be practical and very cost effective means of atmospheric attenuation measurement. Although the main objective is to collect statistics on atmospheric microwave attenuation and emission, atmospheric water vapor and liquid content measurements are also possible as byproducts of the studies supported by the program.

WPL has designed, constructed, and operated ground-based multi-frequency microwave radiometers in the past. Data from these instruments can be used to provide information useful for radio propagation research. Since late 1987, investigators from WPL have participated in the Propagation Program and, employing the NOAA ground-based radiometers, have provided the propagation community with valuable data. Some of the results from WPL experiments will be presented in this paper.

### 3. ATTENUATION AND BRIGHTNESS TEMPERATURE

The atmospheric microwave radiation is described by the brightness temperature,  $T_b$ , which depends on frequency. For a nonscattering atmosphere,  $T_b$  is related to the absorption coefficient of the medium via the radiative transfer equation. Assuming a mean physical temperature for the medium, denoted by  $T_m$ , the radiative transfer equation can be simplified to:

$$T_b = \frac{T_e}{L} + T_m \left(1 - \frac{1}{L}\right) \quad (1)$$

where  $T_e$  represents the radiation entering the atmosphere (cosmic radiation), and  $L$  is the loss factor

due to the absorbing medium. Equation 1 can be solved for  $L$  to yield the following result:

$$L = \frac{T_m - T_e}{T_m - T_b} \quad (2)$$

Note that  $L$  ranges from a large value (opacity) to 1 (perfect transparency). In practice,  $T_m$  is estimated from surface temperature measurements and/or radiosonde data,  $T_b$  is obtained from radiometric observation of the atmosphere, and 2.75 K is the value assumed for  $T_e$ .

#### 4. TWO-FREQUENCY MEASUREMENTS

Dual-frequency measurements were made at two locations in 1988 [3], and both single-station and joint-station statistics will be presented in this section. The stations are 50 km apart, located in Denver and Platteville, Colorado, and are at about the same altitude with similar climates. The Denver radiometer has a  $2.5^\circ$  beamwidth for both frequencies, whereas the Platteville radiometer has a  $5^\circ$  beamwidth for both frequencies. The experiments were conducted in two seasons, the winter and summer of 1988.

Figure 1 shows the time series of zenith brightness temperatures at 20.6 and 31.6 GHz on September 13, 1988. The sharp maxima in brightness temperature are due to liquid-bearing clouds. The vapor response is more significant at 20.6 GHz, and liquid response is more significant at 31.6 GHz.

Single-station cumulative distributions of zenith attenuation are given in Figure 2. Attenuation data were obtained by the use of Equation 2 where  $T_m$  is obtained from climatological radiosonde data: the values of 255 K and 275 K were used for winter and summer, respectively.

To derive joint-station statistics, the Platteville and Denver data were placed into one-to-one correspondence within a time uncertainty of  $\pm 1$  min. Next, for each 2-min time interval, the maximum and minimum of the two attenuation values were determined. Then, two additional time series of the minimum and maximum values were constructed. From these derived time series, cumulative distributions for the winter and summer seasons were developed. The results are shown in Figure 3. Note that at the 0.01% level, only 1 to 2 dB are gained by diversity during winter conditions. However, in summer, when significant attenuation from clouds can occur, a margin of 8 dB is gained at 31.6 GHz.

#### 5. ACCURACY OF ATTENUATION DATA

The accuracy of attenuation data depends on how well  $T_b$  and  $T_m$  can be measured. The absolute accuracy of the radiometers is about 1 K. The standard deviation of error in estimating  $T_m$  by climatology is about 6 or 7 K. To investigate the effect of a change in  $T_m$  on the calculated amount of  $L$ , Figure 4 shows plots of  $L$  as a function of  $T_b$  for two values of  $T_m$ , 275 K and 265 K. The difference between the two curves is also shown on the same chart and is labeled "Error." As is evident from Figure 4, an uncertainty of 10 K in the measured value of  $T_m$  will not significantly affect the calculated value of  $L$  for small attenuations, but for attenuations larger than 10 dB, the error is significant. For example, for  $T_b = 250$  (where attenuation is about 12 dB), the uncertainty in calculating  $L$  is 2 dB for an error of 10 K in  $T_m$ .

#### 6. THREE-FREQUENCY MEASUREMENTS

The three-frequency measurements presented herein were conducted by WPL investigators using the NOAA three-frequency steerable radiometer at Denver, Colorado, and San Nicolas Island, California [4]. The three frequencies are 20.6, 31.6, and 90 GHz. All three channels on this radiometer have equal beamwidths of  $2.5^\circ$  and point in the same direction from the same location; hence they are capable of simultaneously measuring emission and deriving attenuation for the same volume of air.

Representative brightness temperatures measured simultaneously at each operation frequency are shown in Figure 5 for San Nicolas and Denver. Note the large increase in brightness temperature at 90.0 GHz relative to 20.6 and 31.6 GHz as clouds pass through the radiometer antenna beam. Due to higher amounts of water vapor, brightness temperatures at all frequencies at Denver during August are higher than in December.

Attenuation statistics were developed by processing the measured brightness temperatures. The cumulative distributions at three frequencies are shown in Figures 6-8. Note that the sea-level altitude of San Nicolas Island always results in dry attenuation greater than that at Denver. Oddly, the two curves corresponding to attenuation statistics at 20 and 30 GHz for winter Denver data cross each other. At high percentage values (low attenuation), dry weather prevails and hence 30-GHz attenuation is higher than that of 20 GHz. At low percentage values (high attenuation), cloud liquid attenuation is the dominant factor and hence 30-GHz attenuation is higher than that of 20 GHz. In the intermediate region, water vapor attenuation is the important factor and therefore 20-GHz attenuation is higher than that of 30 GHz.

#### 7. FREQUENCY SCALING

Data from three-frequency measurements at Denver and San Nicolas Island were used to develop prediction models of attenuation between various frequencies [4]. Regression relationships between the various channels

for clear, cloudy, and ail conditions were determined. The general form of the linear regression is:

$$L(\text{dependent}) = c_0 + c_1 L_1(\text{independent}) + c_2 L_2(\text{independent}) \quad (3)$$

where attenuation,  $L$ , is given in dB. The result of the regression analysis has shown that there is a high degree of correlation and predictability between the channels, and if care is taken to distinguish between clear and cloudy conditions, the correlation coefficients between measured and predicted attenuations are greater than 0.9. To provide the reader with an example, the following prediction model was obtained using data from the San Nicolas Island observations in July 1987 (all conditions):

$$L(90.0) = -0.499 - 0.463L(20.6) + 5.64L(31.6) \quad (4)$$

The correlation coefficient of the above prediction is 0.998.

#### 8. SUMMARY

Propagation data are needed for the design and development of low-margin ground terminals of advanced communications satellite systems. Data can be obtained through recording signals transmitted by a satellite or by the use of radiometers. Ground-based radiometers are used by WPL for collecting atmospheric emission and attenuation statistics at Ka and millimeter-wave bands as part of an effort supported by the Propagation Program at JPL.

Data from experiments using two-frequency and three-frequency radiometers were presented. It was shown that sky brightness temperature measurements can easily be converted to atmospheric attenuation data. The accuracy of this conversion depends on how well the mean temperature of the atmosphere is measured or estimated. For data presented in this paper, with an uncertainty of 6 or 7 K in the atmospheric mean temperature, the attenuation data are reliable below the values of 10 or 12 dB.

Single-station and joint-station statistics of attenuation were presented. Seasonal effects were also shown. A regression method for predicting 90-GHz attenuation from 20- and 30-GHz attenuations was provided.

#### 9. ACKNOWLEDGMENTS

The author would like to express his appreciation for the valuable data provided to JPL's Propagation Program by Dr. E. Westwater and J. Snider of WPL. The author would also like to thank them for their assistance in preparing this paper.

The research conducted in this paper was funded by the Jet Propulsion Laboratory, California Institute of Technology, under a contract with the National Aeronautics and Space Administration.

#### 10. REFERENCES

1. Arbesser-Rastburg, B., "OPEX Propagation Measurements and Studies," Proc. NAPEX XIV, JPL Publ. 90-27, July 1991, pp. 29-35.
2. Davarian, F., "ACTS Propagation Program," Proc. NAPEX XIV, JPL Publ. 90-27, July 1991, pp. 23-28.
3. Fionda, E., Falls, M., and Westwater, E., "Attenuation Statistics at 20.6, 31.65 and 52.85 GHz Derived from Emission Measurements by Ground-based Microwave Radiometers," IEE Proc.-H, Vol. 138, No. 1, February 1991, pp. 46-50.
4. Westwater, E., Snider, J., and Falls, M., "Ground-Based Observation of Atmospheric Emission and Attenuation at 20.6, 31.65, and 90 GHz: A Comparison of Measurements and Theory," IEEE Trans. Antennas Propagation, Vol. 38, No. 10, October 1990, pp. 1569-1580.

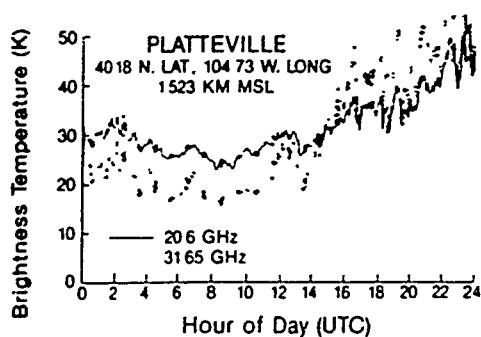
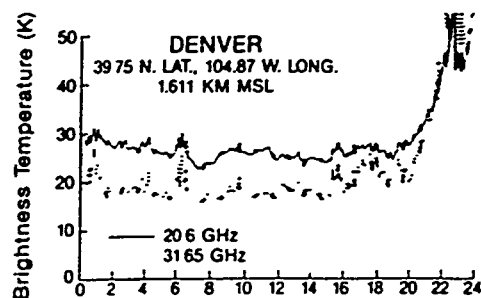


Fig. 1 Time series of zenith brightness temperatures, 13th September 1988

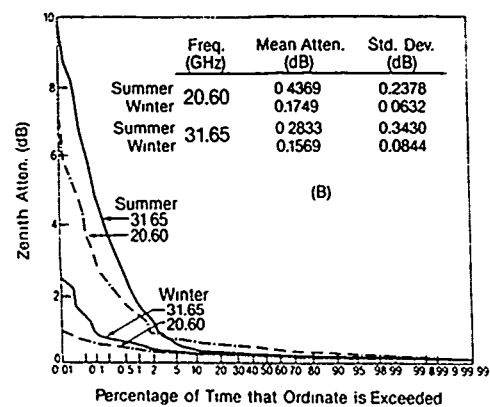
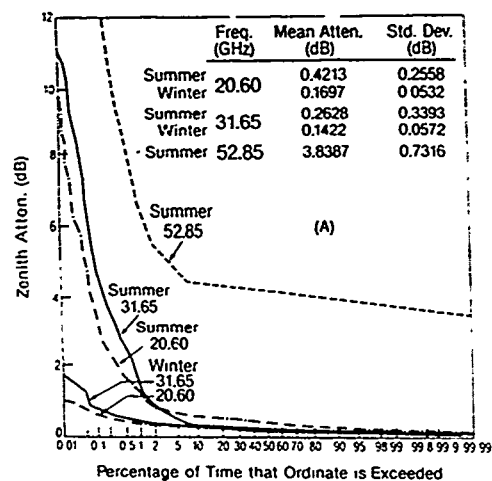


Fig. 2 Single-station cumulative distributions of zenith attenuation

(A) Denver, Colorado

	Frequency (GHz)	Mean attenuation (dB)	Standard Deviation (dB)
Summer	20.60	0.4090	0.2548
Winter	20.60	0.1697	0.0532
Summer	31.65	0.2669	0.4625
Winter	31.65	0.1422	0.0572
Summer	52.85	3.8387	0.7316

(B) Platteville, Colorado

	Frequency (GHz)	Mean attenuation (dB)	Standard Deviation (dB)
Summer	20.60	0.4436	0.2196
Winter	20.60	0.1749	0.0632
Summer	31.65	0.2809	0.3330
Winter	31.65	0.1569	0.0844

Sample size: summer 46538, winter 41238

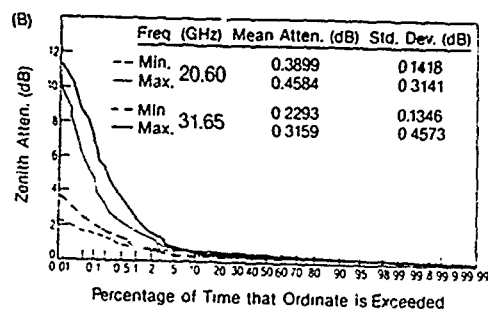
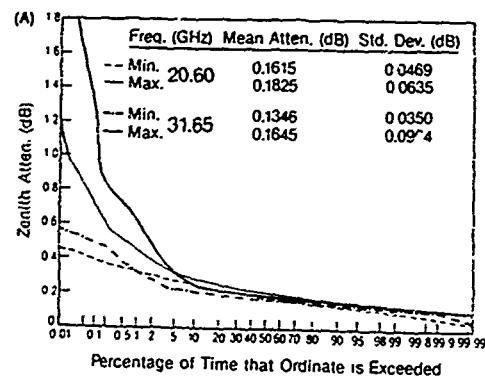


Fig. 3 Joint-station cumulative distribution of maximum and minimum zenith attenuation measured at Denver and Platteville, Colorado

(A) Winter 1987/1988

Frequency (GHz)	Mean attenuation (dB)	Standard Deviation (dB)
Minimum 20.60	0.1815	0.0469
Maximum 20.60	0.1825	0.0635
Minimum 31.65	0.1346	0.0350
Maximum 31.65	0.1645	0.0904

(B) Summer 1988

Frequency (GHz)	Mean attenuation (dB)	Standard Deviation (dB)
Minimum 20.60	0.3899	0.1418
Maximum 20.60	0.4584	0.3142
Minimum 31.65	0.2309	0.1427
Maximum 31.65	0.3221	0.5797

Sample sizes given in the caption of Fig. 2

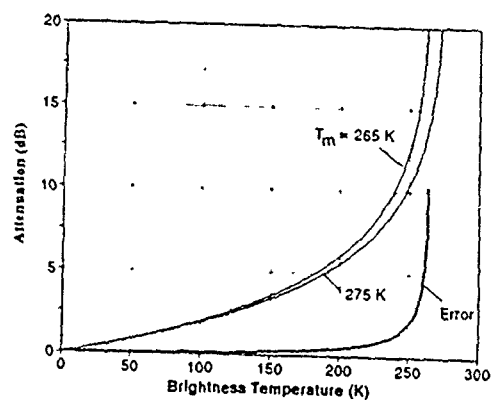


Fig. 4 Attenuation as a function of brightness temperature

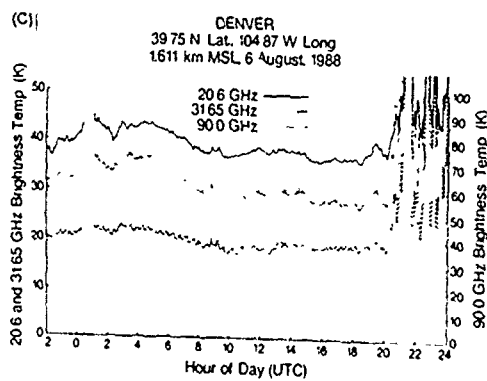
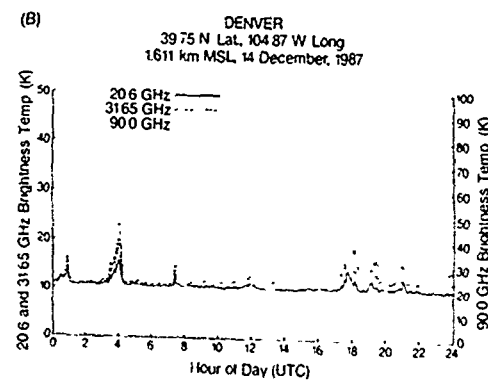
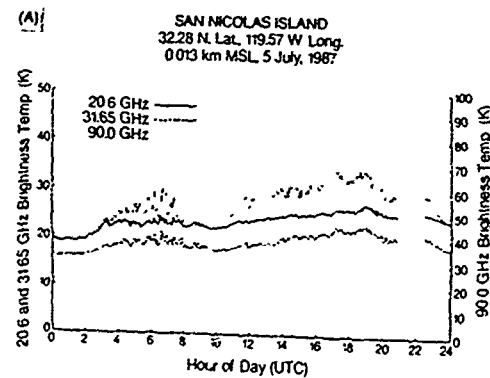


Fig. 5 Time series of brightness temperatures measured by a three-channel zenith-viewing radiometer.  
(A) San Nicolas Island, CA, July 5, 1987.  
(B) Denver, CO, December 14, 1987.  
(C) Denver, CO, August 6, 1988.

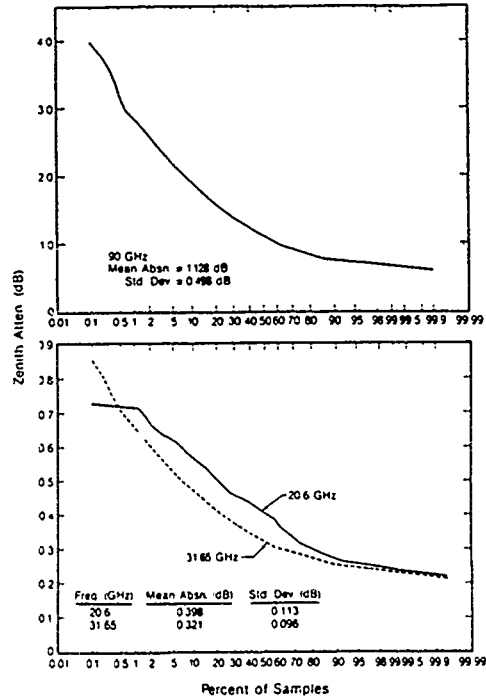


Fig. 6 Cumulative distribution of zenith attenuation measured by a three-channel radiometer at San Nicolas Island, CA, July 1987. Data consist of 4805 5-min averages.

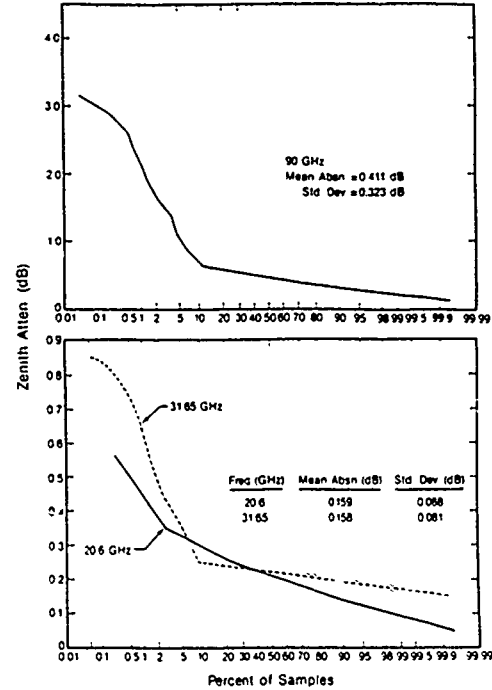


Fig. 7 Cumulative distribution of zenith attenuation measured by a three-channel radiometer at Denver, CO, December 1987. Data consist of 14 181 2-min averages.

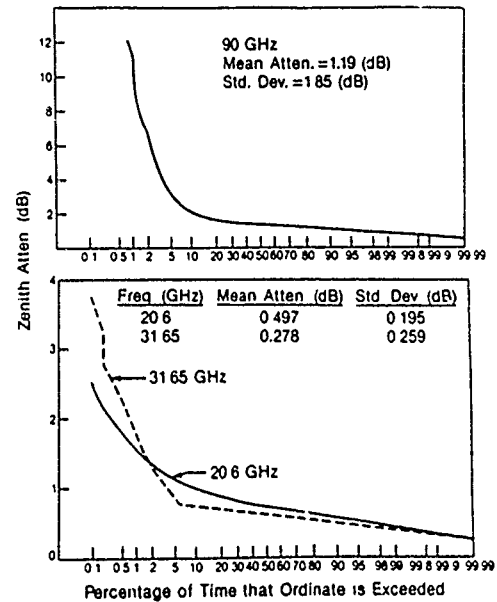


Fig. 8 Cumulative distribution of zenith attenuation measured by a three-channel radiometer at Denver, CO, August 1988. Data consist of 17 792 2-min averages.

### DISCUSSION

#### **D. HOEHN**

*Why do you use a purely empirical modelling approach for your "frequency scaling," even if there exists a physical relationship for the atmospheric attenuation at the frequencies considered?*

#### **AUTHOR'S REPLY**

*Developing an experimental model is cost free for us because we have already collected the data. Furthermore, an empirical model has statistics associated with it, i.e., percentages which a theoretical model does not.*

#### **J. GOLDBIRSH**

*The previous question involved arriving at the scaling of fades for different frequencies using theoretical means. The equations Dr. Davarian showed, however, have the added dimension of probability. Those relations were equi-probability ones. Theory does not give this.*

#### **AUTHOR'S REPLY**

*Yes, I agree.*

## OPTICAL REFRACTION IN THE ATMOSPHERIC SURFACE LAYER

James B. Gillespie and David H. Tofsted  
 Atmospheric Sciences Laboratory  
 U.S. Army Laboratory Command  
 White Sands Missile Range, New Mexico 88002-5501, USA

## SUMMARY

Recent developments in the Middle East have highlighted the need to sense refraction within the atmospheric surface layer since apparent vertical variations of location of distant objects can result in significant errors in tank lay position under certain conditions. The U.S. Army Atmospheric Sciences Laboratory has investigated the nature of atmospheric refraction and developed criteria when refraction may cause errors in tank gunnery in deserts.

Refraction can be remotely sensed as a function of time through point-to-point measurements of the elevation of a distant object relative to the atmospheric neutral events that occur approximately one-half hour before sunset and one-half hour after sunrise. The vertical position change of a distant object can be measured using either another object close enough to the observer that effects will be minimal (thus providing a fixed reference point) or a theodolite that has its own internal reference through the leveling bubble. We have made extensive measurements of diurnal variations in elevation of distant objects at White Sands Missile Range (WSMR), New Mexico. Lessons learned from these experiments include accounting for numerous potential error sources when taking readings using theodolites and the photographic techniques necessary to cope with changing light levels and atmospheric turbulence effects. We have also made measurements at Aberdeen Proving Ground, Maryland; Fort Stanton, New Mexico; and other locations that exhibit similar vertical shifting characteristics. A surface-energy-budget model was developed to predict refraction situations based on meteorological measurements. An optical ray tracing model was developed utilizing terrain characterization and temperature gradient information to predict horizontal refraction. We provided "rules of thumb" for horizontal surface refraction based on our experimental results and modeling efforts.

## 1. INTRODUCTION

When one is viewing a target with an electro-optical (EO) sensor, the atmosphere can be thought of as an optical system component. The atmosphere is not as homogeneous an optical system as it appears to the human eye. Phenomena such as scattering and extinction by aerosols and scintillation by optical turbulence both affect how clearly a target can be seen. These subjects have been dealt with extensively in the literature. A third phenomenon, optical path bending (or atmospheric refraction), has largely

been ignored for EO sensors that look horizontally along paths near the earth's surface. The impact that refraction has upon aiming accuracy is the subject of this paper.

Historically, atmospheric refraction has primarily been studied by astronomers for very long slant paths through the earth's atmosphere, while the more spectacular phenomena of mirages and looming have been studied by scientists for horizontal paths. More recently, surveyors have examined the effects of refraction on paths horizontal to the earth's surface. Because most EO sensor targeting has been for path lengths of less than 2 km, vertical aiming errors caused by refraction have been ignored for military considerations. Figure 1 illustrates the effect of refraction for a tank on the left viewing a target on the right. The image of the target does not propagate in a straight line from the target to the receiver. Instead, the image propagates along an optical path that takes a minimum time for the light to propagate. The incoming ray thus arrives at an angle different from zero degrees. The viewing angle will be increased for nighttime refraction and decreased for daytime refraction. Since the sensor looks tangent along the incoming ray, the vertical aiming angle will be in error--sometimes by as much as a milliradian or more for long paths in desert type situations.

## 2. BACKGROUND

The vertical bending of the optical path of a beam of light propagating horizontally is caused by a vertical refractive index gradient. This gradient is produced by the temperature gradient resulting from diurnal solar heating of the earth's surface. Refraction in a non-homogeneous medium such as the earth's atmosphere can be quite adequately described by classical geometrical optics (which uses the assumption that the wavelength of the light is negligibly small). Refraction can be described by either Huygen's wave front construction method, Fermat's principle

$$\int n ds = 0 ; \quad (1)$$

Snell's law

$$n_1 \sin \theta_1 = n_2 \sin \theta_2 ; \text{ or} \quad (2)$$

the eikonal equation

$$(\text{grad } L)^2 \approx n^2 ; \quad (3)$$

where  $L$  is the optical path length,  $ds$  is the incremental change in path of the ray,  $n$  is the refractive index, and  $\theta_i$  is the angle of propagation in the  $i$ th layer.

Using Eq. (3), we can derive the following expression for atmospheric ray tracing for horizontal, near-surface propagation:

$$d\phi = \frac{ds}{n} \frac{\partial n}{\partial z} \quad (4)$$

where  $d\phi$  is the incremental angular change of the optical path with respect to some fixed axis,  $z$  is the vertical dimension, and propagation is nearly horizontal.

For propagation paths near the surface, the atmosphere does not follow a spherical symmetry; instead the optical path is more strongly dependent on distance from the local surface. The surface fluxes of latent and sensible heat dominate the structure of temperature and humidity. The temperature gradient has a much stronger influence on density gradient than does the pressure gradient. This temperature gradient is largely a function of the degree of heating or cooling occurring at the surface. During the day sensible heat flows upward as the surface transfers this heat to the near surface air by convection. During the night, as the surface cools, the atmosphere closest to the surface also cools, setting up an inversion condition (Ref 1). The effect of daytime atmospheric heating is to couple the structure of the temperature lapse rate to the immediately surrounding terrain. An adequate model of this would be to calculate the structure of the air temperature with height for an average case and then apply that profile to the terrain along the line of sight over which we wish to propagate. By determining the height of the line of sight above this terrain at any particular point along the line of propagation, we could calculate the temperature gradient at that point. The approach for a nighttime situation is handled similarly.

The refraction of the atmosphere is conveniently described in terms of a parameter,  $N$ , called the refractivity. It is defined as

$$N = (n - 1) \times 10^6 \quad (5)$$

For most atmospheric conditions,  $N$  has a value near 250. It varies with wavelength, temperature, pressure, and absolute humidity (Ref 2). The refractivity can be written as the sum of two contributions--a dry air part and a water vapor part:

$$N = N_{\text{dry}} + N_w \quad (6)$$

$$N_{\text{dry}} = \{1 + (5.337 - .0157T) \times P \times 10^{-6}\} (.3789) P N_0 T \quad (7)$$

$$N_w = [1 - .0109\lambda^{-2}] \times [-.0059] A \quad (8)$$

where  $P$  is the pressure,  $T$  is the temperature,  $A$  is the absolute humidity,  $\lambda$  is the wavelength, and  $N_0$  is a wavelength dependent refractivity term.

Using the hydrostatic equation,

$$dP = \frac{mg}{kT} P dz \quad (9)$$

along with Eqs. (6) through (9), we can derive an expression for the gradient of  $n$ :

$$\frac{dn}{dz} = -78.2 \times 10^{-6} P T^{-2} \left( \frac{dT}{dz} + .0344 \right) \quad (10)$$

We model the terrain profile by using a local terrain profile,  $H(x)$ , and the distance between the ray and the local surface,  $z'$ . The local height can be described by

$$z' = z - H(x) \quad (11)$$

Disregarding any  $y$  dependence for  $H$ , we can write the gradient of the refractive index as

$$\text{grad}[n] = \frac{\partial n}{\partial z'} \left\{ \frac{\partial z'}{\partial x} \hat{i} + \frac{\partial z'}{\partial z} \hat{k} \right\} \quad (12)$$

Using Eq. (11), Eq. (12) can be rewritten as

$$\text{grad}[n] = -78.2 \times 10^{-6} P T^{-2} \times \left\{ \frac{\partial T}{\partial z'} + .0344 \right\} \left\{ -\frac{\partial H}{\partial x} \hat{i} + \hat{k} \right\} \quad (13)$$

We utilize two methods to obtain a terrain profile--assume a flat earth or survey the terrain and interpolate between the surveyed points. Our refraction ray tracing model, REFRAC (Ref 3), uses a Fourier series to fit to the terrain.

Temperature gradients for our model are obtained through application of Similitude Theory (Ref 4). In general, the temperature gradient goes as  $z^{-1}$  for neutral conditions, as  $z^{-4/3}$  for day conditions, and as  $z^{-2/3}$  for night conditions. However, the night conditions can be highly terrain dependent--pockets of cool air can accumulate in depressions and flow downhill. Targets may appear to move vertically dramatically (greater than 0.5 mrad) within a few minutes.

In addition to an atmospheric ray tracing model, we have developed surface energy budget (SEB) models to infer strengths of turbulence ( $C_n^2$ ) and temperature gradients from standard meteorological data (Ref 5). A basic model called SURFA is a near

copy of a model described by Deardorff (Ref 6); TGRAD is an upgrade of SURFA that incorporates new methods for determining heat flux, solar radiation, and foliage temperature; and TGEN is a modification of TGRAD that includes algorithms that account for water phase change during freeze or thaw. These models take as input variables such as temperature, pressure, relative humidity, cloud cover, percentage of foliage cover, surface roughness height, soil moisture content, soil type, windspeed, time of year, longitude, latitude, and time of day. The model will then determine the diurnal values of  $C_n$ , the temperature gradient, the vapor pressure gradient, the Obukhov length, the friction velocity, vertical wind structure, and similarity parameters. Paulson's (Ref 7) 1970 paper on this subject is a key reference.

The SEB is the balance of radiative, convective, and conductive fluxes of heat, both to and from the earth's surface. Mathematically it is described by

$$S\downarrow - S\uparrow + R\downarrow - R\uparrow - H - LE = G \quad (14)$$

The arrows describe the direction of the flux of the radiation, downward to the surface or upward from the surface.  $S$  represents the visible solar light incident from the sun or reflected from the earth's surface.  $R$  represents the thermal radiation flowing from the heat sink of the atmosphere and from the ground.  $H$  is the sensible heat, and  $LE$  is the latent heat flux due to evaporation, where  $L$  is the latent heat of vaporization and  $E$  is the flux of water into the atmosphere.

That the SEB model can be used to predict refractive effects was verified from optical refraction and meteorological data taken at WSMR, New Mexico, in June 1983 over a relatively flat, desert terrain. The verification is shown in Fig. 2.

### 3. MEASUREMENTS

The vertical structure of the near-surface refractive index can be remotely sensed as a function of time through optical measurements. This technique measures the variation in elevation of distant objects relative to the fixed elevation of some reference. The two references typically used are the fixed elevation of some nearby object or the reference leveling bubble of a theodolite. The nearby object will be unaffected by refracting effects since refractive error increases linearly with range.

From relative elevation positions, the absolute error angles can be determined. Zero refraction can be observed during the day when clouds cover the optical path. There are also two neutral events that occur near sunrise and sunset when the apparent elevations of objects transition from appearing high (night) to low (day). However, these transition periods

can be rapid, resulting in ambiguity. During testing, a technique was developed whereby a line of sight was surveyed and posts were placed along the optical path. From the survey data, marks could be placed on the posts such that under neutral conditions the marks would appear to line up. Under daytime (unstable) atmospheric conditions the marks would appear to tail off downward with distance, while at night the marks would appear higher on the more distant posts. The closer posts would also provide a reference that would not change with time.

The vertical structure of refractivity can then be inferred by observing the temporal change in apparent elevation of the distant posts. From the assumed vertical structure of temperature with height, the known terrain profile, the equation for the gradient of refraction (13), and Eq. (4), we have a model for determining the refractive profile.

The authors have made extensive diurnal measurements of variations in elevation of distant objects at WSMR, New Mexico, using both photographic techniques and theodolite measurements of elevations. Numerous lessons were learned while developing these techniques.

Use of a theodolite yielded highly accurate readings at night, but during the day the wooden legs of the theodolite's tripod would expand and contract, depending on their exposure to direct sunlight. This effect caused the level to vary continuously and required constant attention. The observer had to take special care that he stood in the same location relative to the legs for each measurement. An umbrella was used to shade the legs, but keeping all the legs simultaneously shaded was tedious.

Photographing the targets was relatively trouble free compared to theodolite measurements, but two references had to be included in each image. The first was needed to convert from measured distances on the photograph to angular values in the field of view. The second provided the nearby fixed elevation point. Often these two measures were placed on the same nearby post. Use of photographic means eliminated the difficulties of maintaining the leveling bubble. The permanent records of photographs also eliminated the unfortunate drawback of theodolites that the readings depend on the skills of the individual making the measurement and cannot be verified later.

Figure 3 is a typical daytime scene taken through the telescope. We used a Cassegrainian telescope with a 2000-mm focal length and an 8-inch receiving aperture. A 35-mm camera recorded the data. Figure 4 shows the telescope setup. During the day the 8-inch aperture was stopped down to around 1.5 inches to reduce turbulent image blur. At night the aperture stop was removed to allow for faster exposure time. Depending on the power available to the line of sight, the exposure time could be as long as 7 s. When power was available electric lights were

run to each target post. In many cases, however, power was unavailable and flashlights were connected to car batteries so the target posts could be viewed throughout the night.

Figures 3 and 4 are from a field test conducted on 1 April 1986 over a grassy field near Fort Stanton, New Mexico. This site is located approximately 40 km east of Carrizozo, New Mexico, in the foothills of the Sacramento mountains. Seven target posts were surveyed in along the 1980-m optical path. The nearest post served as both the reference post and the angular reference (each bar represents 0.2 mrad).

Figure 5 shows the line of sight under a typical neutral condition. With clouds shielding the line of sight from direct sunlight, the marks on the posts appear in almost a straight line. Comparing Figs. 3 and 5, one can see that under unstable conditions (Fig. 3) the marks on the more distant posts appear lower.

In addition to the optical instrumentation, sites were typically instrumented with a micrometeorological tower to measure several variables related to computing the surface energy budget at the site (Fig. 6). If the surface energy budget can be estimated (including the sensible heat flux) using flux profile techniques, the temperature gradient can be estimated. We thus have direct measurement of the vertical structure of temperature through tower measurements; we can infer the vertical structure through the observed movement of the distant targets; and we can model this structure through a surface energy budget model.

The results of the Fort Stanton test are seen in Fig. 7. Overall, a day-to-night shift of 0.7 mrad was observed, with an extensive cloud cover and some rain from 0200 through 0630. Similar tests were conducted at WSMR during the summer of 1987. The results of these tests are seen in Figs. 8 and 9. The weather conditions for these two tests were good for refraction. We were testing to determine the effects of the height of the line of sight on prediction and tactical choices of terrain. The results in Fig. 8 were for a 2-km path approximately 8 m above the terrain. The results in Fig. 9 are for a 3-km path 10 through 15 m above the terrain. These figures illustrate the  $-4/3$  power law decrease in refractive gradients compared to the  $-2/3$  nocturnal power law. Daytime effects are largely eliminated while nocturnal effects remain.

We also discovered during these investigations that the point measurement of the vertical temperature structure through the tower measurements could only reasonably model the refractive structure of the air during the day. At night the tower data was usually an inappropriate estimate of the atmospheric state over the entire path because the temperature gradient would vary from point to point

along the path due to irregular flow of pockets of air mentioned previously. The Fort Stanton site was somewhat of an anomaly in this regard, simply because our observation site was located at the upper end of a shallow draw. At night the katabatic flow off Sierra Blanca mountain carried the same air mass we were observing our effects through directly past our met tower. In the WSMR measurements we were observing lines of sight where the wind was moving air masses transverse to the line of sight. Thus a met tower set up at any point along one of these paths would only detect a fraction of the overall atmospheric characteristics at night. A sample data plot showing this problem is given in Fig. 10.

#### 4. RESULTS AND CONCLUSIONS

To quantify the effects of refraction observations for direct fire weapons systems in a Middle East environment, we developed a simplified refraction algorithm to correct for refraction bias based on model calculations from our TGRAD SEB model. Ten years of weather data from Beersheba, Israel, collected at 3 h intervals was used for the calculations. A height of 2.3 m was used for the observation height, and a range of 2 km was selected for the target distance. A diurnal temperature gradient resulted and was converted into a refraction correction angle in milliradians. The shape of the diurnal effect was nearly a cosine with maxima of about 0.4 mrad occurring in the afternoon and in the middle of the night. Neutral (no refraction correction) points occurred near sunrise and sunset. With little or no loss in prediction accuracy, the cosine shape (a 9-term Fourier series fit) was replaced with a simpler series of four straight lines as shown in Fig. 11. This algorithm was applied to experimental observations and produced good results when applied to situations that met the circumstances for which the model was derived. It will produce errors if applied to cases where there is cloud cover, wet soil, high winds, or highly uneven terrain.

As an alternative to an actual computational algorithm that would be built into a firing control system, we developed a set of "rules of thumb" for direct-fire aiming. These rules are depicted in Fig. 12. Basically, they say to aim a little higher in the daytime; aim a little lower at night; and aim in the middle of the target for rough terrain, dawn or dusk, or high winds.

#### 5. REFERENCES

1. Oke, T. R., "Turbulent Transport Near Ground in Stable Conditions," *J. Appl. Meteorol.*, 9, 1970, pp 771-786.

2. Hill, R. J., S. F. Clifford, and R. S. Lawrence, "Refractive Index and Absorption Fluctuations in the Infrared Caused by Temperature, Humidity, and Pressure Fluctuations," J. Opt. Soc. Am., 70, 1980, pp 1182-1205.

3. Tofsted, D. H., "EOSAEL 87, Volume 25, Optical Path Bending Code Module REFRAC," ASL-TR-0221-25, U.S. Army Atmospheric Sciences Laboratory, 1987.

4. Obukhov, M., "Turbulence in an Atmosphere with a Non-uniform Temperature," English Translation in Boundary Layer Meteorology, 1971, pp 7-29.

5. Tofsted, D. H., and J. B. Gillespie, "Comparing Results from Three Surface Energy Budget Models," In Proceedings of the Sixth Annual EOSAEL/TWI Conference, Vol. 2, R. C. Shirkey Ed., February 1986, pp 401-412.

6. Deardorff, J. W., "Efficient Prediction of Ground Surface Temperature and Moisture, with Inclusion of a Layer of Vegetation," J. Geophys. Res., 83, No. C4, 1978, pp 1889-1903.

7. Paulson, C. A., "The Mathematical Representation of Wind and Temperature Profiles in the Unstable Atmospheric Surface Layer," J. Appl. Meteorol., 9, 1970, pp 857-861.

#### 6. ILLUSTRATIONS

##### FIRING FROM BORESIGHT

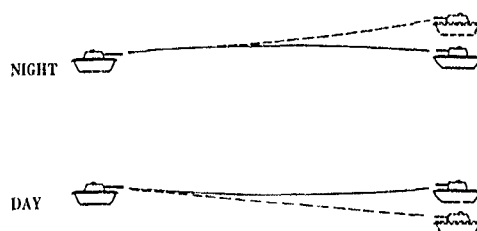


Fig 1. Sighting scenario illustrating diurnal variations in apparent target location.

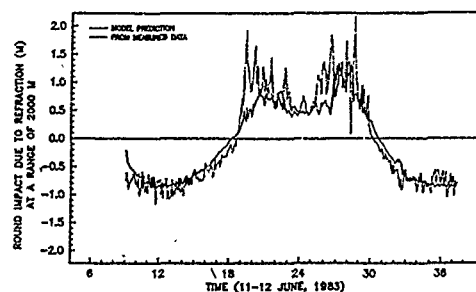


Fig. 2. Comparison of surface energy budget model estimates of refractive elevation change of a distant target and observed vertical motions of the target.



Fig. 3. Under strong daytime refraction the marks on the posts appear lower with distance. Note level of grassy region relative to the closest post.



Fig. 4. Telescope and camera used for photographic measurements. The telescope aperture was stopped down for daytime operation.

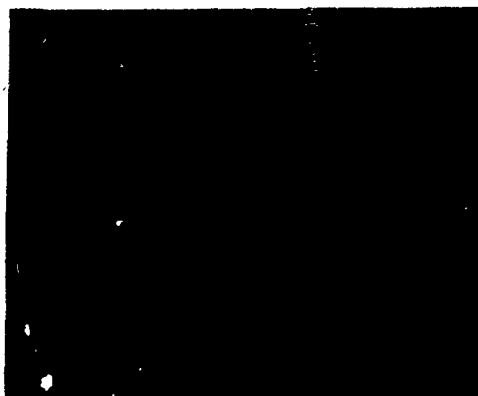


Fig. 5. Neutral condition refraction close to sunset. Targets and cattle are clearly visible in low turbulence.



Fig. 6. View of towers and low hill to the south of the line of sight.

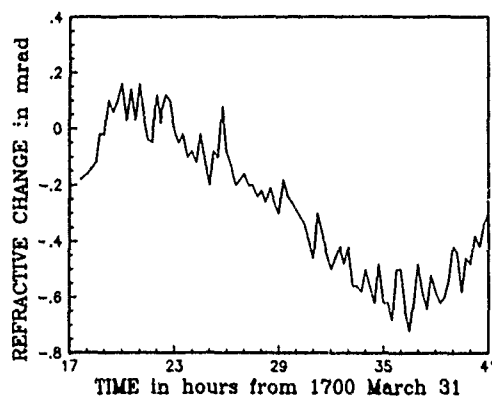


Fig. 7. Fort Stanton optical test results: observed elevation changes of the 1980-m target.

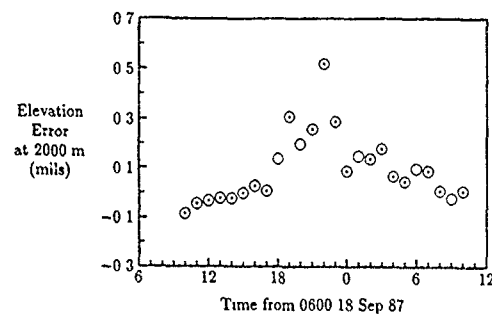


Fig. 8. "C" Station optical test results at WSMR, NM: observed elevation changes of a 2000-m target, hourly results.

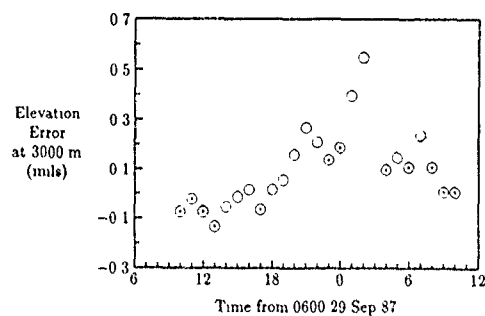


Fig. 9. Southwest WSMR optical test results: observe elevation changes of a 3000-m target, hourly results.

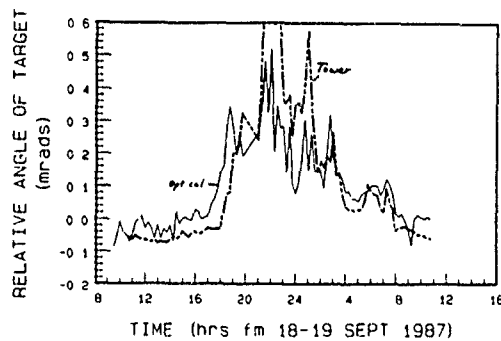


Fig. 10. Time plot of optical elevation changes for the "C" Station optical test compared to elevation changes inferred by tower temperature measurements. Lack of prediction is caused by nocturnal horizontal inhomogeneities in temperature structure.

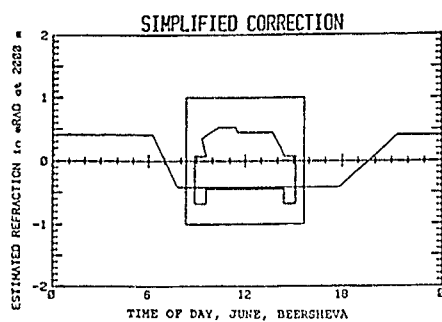
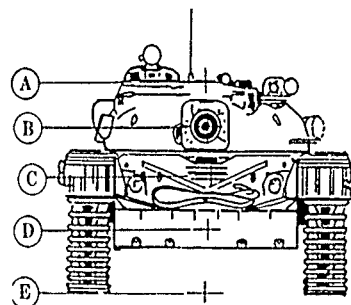


Fig. 11. Typical June day refraction plot, Beersheva, Israel.



Condition:

- a. Clear sky, flat desert, daytime, winds <10 mi/h, 2500 to 3500 m range
- b. Clear sky, flat desert, daytime, winds <10 mi/h, 1500 to 2500 m range
- c. Cloudy sky, rugged terrain, dawn or dusk, high winds or range <1500 m
- d. Clear sky, flat desert, night, winds <4 mi/h, 1500 to 2500 m range
- e. Clear sky, flat desert, night, winds <4 mi/h, 2500 to 3500 m range

Fig. 12. Rule of thumb refraction corrections.

# INVERTING RADIOMETRIC MEASUREMENTS WITH A NEURAL NETWORK

Edward M. Measure  
Young P. Yee  
Jeff M. Balding  
Wendell R. Watkins  
Atmospheric Sciences Laboratory  
U.S. Army Laboratory Command  
White Sands Missile Range, New Mexico 88002-5501, USA

## SUMMARY

A neural network scheme for retrieving remotely sensed vertical temperature profiles has been applied to observed ground-based radiometer measurements. The neural network used microwave radiance measurements and surface measurements of temperature and pressure as inputs. Because the microwave radiometer is capable of measuring 4 oxygen channels at 5 different elevation angles (9°, 15°, 25°, 40°, and 90°), 20 microwave measurements are potentially available. Because these measurements have considerable redundancy, we experimented with a neural network, accepting as inputs microwave measurements taken at 53.88 GHz, 40°; 57.45 GHz, 40°; and 57.45 GHz, 90°. The primary test site was located at White Sands Missile Range, New Mexico, USA. Results are compared with measurements made simultaneously with balloon borne radiosonde instruments and with radiometric temperature retrievals made using more conventional retrieval algorithms.

The neural network was trained by using a Widrow-Hoff delta rule procedure. Functions of date to include season dependence in the retrieval process and functions of time to include diurnal effects were used as inputs to the neural network.

## LIST OF SYMBOLS

- $T_{bv}$  - downwelling cosmic microwave background brightness temperature above the atmosphere
- $T_{bv}$  - downwelling microwave brightness temperature at frequency  $\nu$
- $T(s)$  - temperature at height  $s$
- $\alpha_\nu(s)$  - absorption coefficient
- $\mathbf{o}$  - vector of output temperatures
- $\mathbf{W}$  - matrix of weights
- $\mathbf{i}$  - vector of inputs
- $\Delta w_{ij}$  - change in weight  $w_{ij}$
- $\eta$  - learning rate factor
- $t_i$  - target output from the  $i$ th unit
- $o_i$  - actual output from the  $i$ th unit
- $i_j$  -  $j$ th input

## 1. INTRODUCTION

This paper describes the results of simulations of a neural network for retrieving vertical profiles of atmospheric temperature from various radiometric measurements. The term neural network has been applied to a large

variety of computational architectures, but all have the notion of simulated neurons and synapses in common. The implementations of the simulated neurons and synapses vary widely, being more or less faithful to what is known about their biological antecedents (which are themselves rather various, depending on their functional specialization). A simulated neuron (Fig. 1) is generally considered to be an entity with multiple inputs and a single (usually subsequently branching) output. The neuron's output is a function of its current state, its current inputs, and possibly its past state history. The output of a neuron is connected to the inputs of other neurons by synapses, each of which has a weight (or multiplying factor) associated with it. The values of the weights, in conjunction with the initial state of the system, determine the computation performed by the network.

## 2. THEORETICAL BACKGROUND

Ground-based measurements of atmospheric brightness temperature at several microwave frequencies permit some inference about the vertical temperature structure of the atmosphere (Ref 1). In the 20- to 60-GHz region, the measured brightness temperatures satisfy (to a good approximation) the following equation:

$$T_{bv} = \int_0^\infty T(s) \alpha_\nu(s) \exp[-\int_0^s \alpha_\nu(s') ds'] ds + T_{bv}^* \exp\left[-\int_0^\infty \alpha_\nu(s) ds\right], \quad (1)$$

where

- $T_{bv}$  = the downwelling microwave brightness temperature at frequency  $\nu$
- $T(s)$  = temperature at height  $s$
- $\alpha_\nu(s)$  = the absorption coefficient
- $T_{bv}^*$  = the downwelling cosmic microwave background brightness temperature above the atmosphere

Inferring atmospheric temperature structure from microwave brightness temperature measurements thus becomes the problem of solving Eq. (1) to

find  $T(s)$ . Problems of this type are often referred to as inverse problems, since it is relatively simple to compute  $T_i$  from a knowledge of  $T(s)$  but more difficult to obtain  $T(s)$  from  $T_i$ . Although many techniques are used for attacking such problems (Ref 2), each technique has its limitations. Our intent in this paper is to investigate the applicability of a technique based on the idea of the neural network.

### 3. CONSTRUCTION OF A NEURAL NETWORK FOR THE INVERSION PROBLEM

Much of the work with neural networks has focused on simulation of brain function, associative memory, and pattern recognition. For reasons to be discussed in the following sections, we believe that neural network techniques may also have advantages for certain types of computational tasks that are usually addressed by more conventional computational techniques.

In discrete approximation, the right-hand side of Eq. (1) takes a set of temperatures defined at discrete heights and produces from them the corresponding microwave brightness temperatures at discrete frequencies. Although this direct computation is fairly straightforward, various obstacles exist for the inverse computation (Ref 3). Our objective is to perform the inverse calculation with a neural network simulation. Inputs to the neural network will be measured microwave brightness temperatures and other relevant measurements such as surface measurements of temperature and pressure. Outputs will be estimated temperature at various atmospheric heights. The simulated neurons produce outputs that are functions of the weighted sums of the inputs. The weights, analogous to the strength of the synapses of biological neurons, contain the network's knowledge about how to solve the inversion problem. For a simple linear network, the outputs are given as functions of the inputs by

$$o = \sum i \quad (2)$$

In Eq. (2),  $o$  is the vector of output temperatures;  $\sum$  is the matrix of weights; and  $i$  is the vector of inputs comprised of a bias input, deviations from the mean of the surface measurements, and the microwave brightness temperatures.

Equation (1) has much in common with the transformation of Eq. (2); although the transformation involved is not, in general, linear. The neural network transforms the inputs into the outputs; and for this linear transformation, the weights are the elements of the transformation matrix. More general neural networks are possible since the state may be (and for biological systems is) a nonlinear function of the weighted inputs. Other generalizations include replacing the weighted sum of the inputs with a more general function of the

weighted inputs. In our current work, we have restricted ourselves to the linear case, except that we have not required the weight matrix to be square, that is, the number of inputs and outputs may be different.

Since values of the weights determine the transformation of the input vector, specification of the weights is equivalent to programming the neural network.

We find the neural networks interesting because they can be arranged to learn by experience, that is, to adjust their weights based on inputs and outputs. The learning mechanism applied in this paper is Widrow-Hoff or delta-rule learning (Refs 4 and 5). The delta-rule learning is a type of learning where weights are modified to reduce the difference between the desired output and the actual output of a processing element, that is, a neuron-like unit.

Delta-rule learning requires a training set, that is, a set of inputs together with the corresponding outputs. Initially, the weights are set to small random values. Inputs are supplied, the corresponding outputs are obtained and compared with the desired outputs, and an error signal is generated. This error signal is used to generate corrections to weights as follows:

$$\Delta w_{ij} = \eta (t_i(t) - o_i(t)) i_j(t), \quad (3)$$

where  $\Delta w_{ij}$  is the change in weight  $w_{ij}$ ;  $\eta$  is a learning rate factor;  $t_i$  is the target output from the  $i$ th unit;  $o_i$  is the actual output from the  $i$ th unit; and  $i_j$  is the  $j$ th input.

In our work, the neural network was trained with the delta-rule training scheme. This requires a teaching set of inputs and their corresponding outputs. Because it is straightforward to do the direct radiometric computation, there is a natural way to get such a teaching set. In our case, we have assembled a large set of radiosonde (meteorological balloon) observations of atmospheric temperature profiles. From each profile, Eq. (1) was used to compute a vector of corresponding microwave brightness temperatures. This vector of brightness temperatures (augmented by surface observations or other data) then served as the input vector  $i$  and the radiosonde temperature observations served as the training outputs  $o$ . This neural network is indicated schematically in Fig. 2 for a network with three radiometric inputs.

### 4. RESULTS

Our training set consisted of 525 radiosonde observations taken at White Sands Missile Range, New Mexico, from 1984 to 1987. The trained networks were tested on a set of radiosonde observations taken during the same period. In each case, the radiosonde observations were used in a somewhat more sophisticated

version of Eq. (1) that included elevation angle and refraction effects to compute microwave brightness temperatures that would be observed by a four-channel, elevation scanning oxygen radiometer.

Because microwave radiometer measures 4 oxygen channels at 5 different elevation angles (9°, 15°, 25°, 40°, and 90°), 20 microwave measurements are potentially available. Because these measurements have considerable redundancy, we experimented with a neural network, accepting as inputs functions of date and time, surface temperature, surface pressure, and simulated microwave radiances at 53.88 GHz, 40° elevation; 57.45 GHz, 40° elevation; and 57.45 GHz, 90° elevation.

The weight matrix of each neural net was initialized with small random values and trained by using Eq. (3). Training consisted of supplying the network with the selected surface measurements and computed radiances from radiosonde profiles scaled by 0.001, comparing the networks output temperature to the radiosonde temperatures to compute the error at each height, and applying the correction of Eq. (3) to the weights. The complete training cycle, which was concluded when the residual weight changes were sufficiently small, involved cycling each member of the training set through the procedure numerous times.

After the network was trained, it was tested on the test set of radiosonde observations by supplying the selected radiances and surface observations to the network, by comparing the output temperatures to the radiosonde observations, and by computing the errors for each height.

Figure 3 illustrates good agreement between a representative sample radiosonde temperature profile and the corresponding neural network inferred profile. Figure 4 illustrates the case of an upper level temperature inversion layer at approximately 3 km in which the neural network was unable to adequately infer from ground radiometric measurements. The inferred profile was produced by the neural network illustrated in Fig. 2 and Table 1.

Table 2 shows the error between the desired output temperature values and the neural network inferred output temperature values. Improvement in the error at most of the atmospheric heights is significant between the 10,000 training iterations and the 30,000 training iterations. Some improvement is shown from 30,000 to 1,000,000 iterations, especially at atmospheric heights of 10.7 and 27.4 km.

One objective of the study was to determine methods to include date and time functions. Inputs to the processing element representing the date were normalized to radians for the year

and the sine was taken such that the maximum peak is June 30 and the minimum is December 30. Times were normalized to  $2\pi$  for a 24-h period and the sine was taken such that the maximum peak is at 1500 and the minimum is at 0300.

## 5. CONCLUSION AND RECOMMENDATION

One of the unique features of neural computing is that it provides an inherently clean and simple mechanism for dividing the computational task into subunits. This inherent parallelism makes it an ideal candidate for highly parallel architectures.

The neural network did an excellent job of retrieving temperature profiles for the White Sands Missile Range, New Mexico, training set. The type of neural network tested was a simple kind--the linear network. There might be situations in which a more general, nonlinear type of neural network would have advantages. This possibility is still being explored.

## 6. REFERENCES

1. Barber, T. L., Young P. Yee, Edward M. Measure, and D. R. Larson, "Tactical Weather Intelligence for Artillery," In Proceedings of the Seventh EOSAEL/TNI Conference, U.S. Army Atmospheric Sciences Laboratory, White Sands Missile Range, New Mexico, April 1987.
2. Westwater, E. R., and W. B. Sweezy, "Profile Retrieval Algorithms Used in Thermal Sounding of the Atmosphere," In Proceedings of SPIE Conference on Inverse Optics, Arlington, VA, 1983.
3. Twomey, S., 1977, Introduction to the Mathematics of Inversion in Remote Sensing and Indirect Measurements, Elsevier, NY, pp 237.
4. Rumelhart, D. E., G. E. Hinton, and J. L. McClelland, "A General Framework for Parallel Distributed Processing," Parallel Distributed Processing, David E. Rumelhart and James L. McClelland, eds, Massachusetts Institute of Technology Press, Cambridge, MA, 1986, pp 45-76.
5. Rumelhart, D. E., G. E. Hinton, and R. J. Williams, "Learning Interval Representations by Error Propagation," Parallel Distributed Processing, David E. Rumelhart and James L. McClelland, eds, Massachusetts Institute of Technology Press, Cambridge, MA, pp 318-362.

## 7. ILLUSTRATIONS

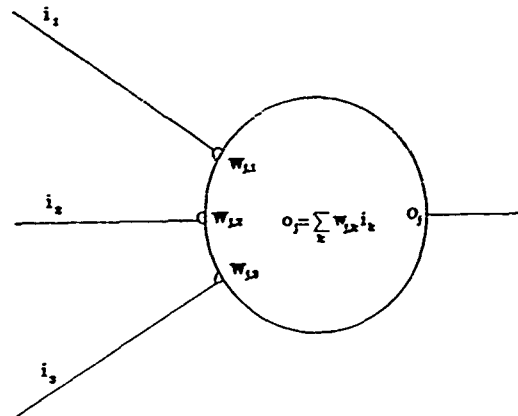


Fig. 1. A model neuron.

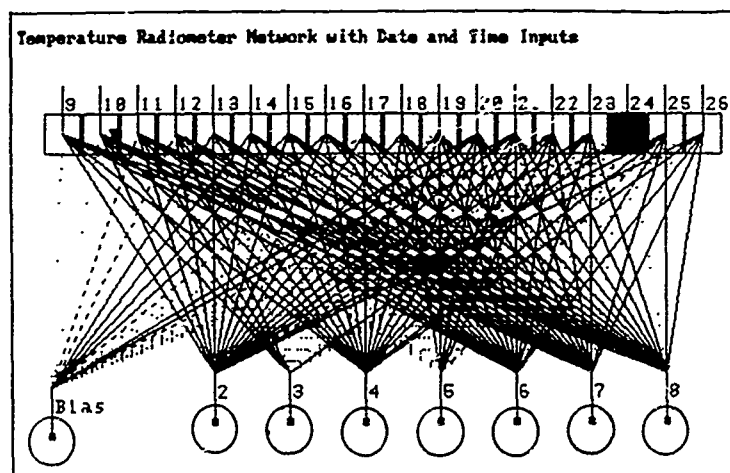


Fig. 2. Neural network diagram with an input layer located at the bottom (circled processing elements) and an output layer located at the top (squared processing elements).

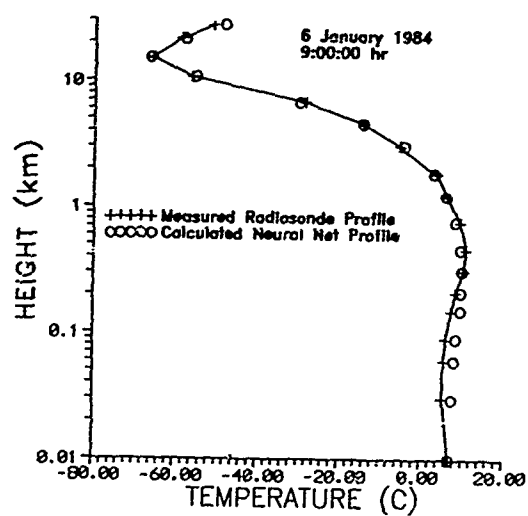


Fig. 3. Semilog graph of temperature versus height comparing a measured radiosonde temperature profile with the corresponding calculated neural network profile. Date: 6 Jan 1984. Location: White Sands Missile Range, New Mexico, USA.

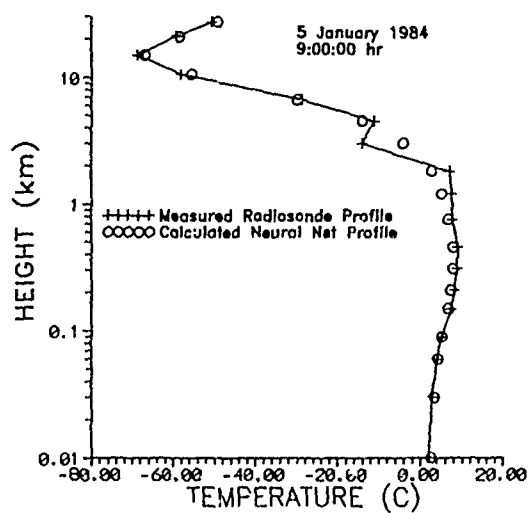


Fig. 4. Semilog graph of temperature versus height comparing a measured radiosonde temperature profile with the corresponding calculated neural network profile. Date: 5 Jan 1984. Location: White Sands Missile Range, New Mexico, USA. Depiction of an upper level temperature inversion at approximately 3 km.

Table 1. Matrix of weights of the neural network after 1,000,000 training iterations. Input values are scaled by 0.001 before applying the weights of the networks.

	Height (km)	BIAS PE1	DATE PE2	TIME PE3	T, PE4	P, PE5	R <sub>1</sub> PE6	R <sub>2</sub> PE7	R <sub>3</sub> PE8
PE9	0	0	27	62	972	10	-37	81	-20
PE10	.03	0	24	39	759	-1	-41	187	93
PE11	.06	0	19	22	565	-11	-42	286	193
PE12	.09	0	14	8	374	-20	-40	382	288
PE13	.15	0	-8	-8	23	-27	-32	552	468
PE14	.21	0	-11	-8	-99	-35	16	576	528
PE15	.31	-1	-16	-4	-257	-41	92	595	602
PE16	.46	-1	-14	3	-312	-50	215	512	621
PE17	.76	-2	-16	3	-345	-57	400	389	584
PE18	1.22	-2	12	-24	-315	-16	611	219	480
PE19	1.83	-2	16	-35	-243	70	807	59	297
PE20	3.05	-3	-4	-22	-127	110	854	-64	110
PE21	4.57	-3	-1	-15	-41	111	1105	-144	-114
PE22	6.70	-1	77	-84	98	-16	1396	-312	-318
PE23	10.7	0	168	-44	310	-191	809	-324	-583
PE24	15.2	1	260	-38	126	-125	-880	125	129
PE25	21.3	0	252	-110	186	-23	234	-90	-192
PE26	27.4	-4	421	-161	192	15	-69	7	51

Table 2. The error for each of the output processing elements representing temperatures at various atmospheric heights is compiled for (a) 10,000 training iterations, (b) 30,000 training iterations, and (c) 1,000,000 training iterations.

PROCESSING ELEMENT	HEIGHT (km)	ERROR AFTER 10,000 ITERATIONS	ERROR AFTER 30,000 ITERATIONS	ERROR AFTER 1,000,000 ITERATIONS	AVERAGE TEMPERATURE (C degrees)
PE9	0	-2.22	805	169	14.99
PE10	03	-1.55	530	031	15.19
PE11	06	-1.42	258	-.025	15.37
PE12	09	-1.21	.096	-189	15.54
PE13	15	-92	-523	-551	15.84
PE14	21	-31	-367	-807	15.77
PE15	.31	57	-182	-1.16	15.60
PE16	.46	110	-132	-233	14.88
PE17	.76	137	150	-412	13.12
PE18	1.22	2.06	547	-392	10.28
PE19	1.83	1.64	415	-383	6.42
PE20	3.05	85	-629	-652	-1.65
PE21	4.57	71	-125	-256	-11.63
PE22	6.70	334	183	-386	-26.49
PE23	10.7	5.93	297	-466	-53.45
PE24	15.2	-4.55	203	221	-67.14
PE25	21.3	78	100	138	-56.98
PE26	27.4	283	-323	644	-46.69

# CLEAR-AIR WIND PROFILERS AS CLOUD MONITORS AND HYDROMETEOR IDENTIFIERS

by

E. E. Gossard

Cooperative Institute for Research in Environmental Sciences  
University of Colorado  
Boulder, Colorado

S. Y. Matrosov, R. G. Strauch, and D. C. Welsh  
NOAA/ERL, Wave Propagation Laboratory  
Boulder, Colorado

## SUMMARY

Clear-air-sensing radars, which are used for wind sounding from surface platforms, are now widely deployed. They are usually designed to measure the Doppler-sensed movement of clear-air refractive index inhomogeneities, but they also provide an excellent tool for sensing ice and water particles in clouds. These radars usually have a very low detection threshold and long averaging time so that size distributions of particles as small as 100  $\mu\text{m}$  diameter with mean vertical fall velocities ( $V_f$ ) as small as 0.2  $\text{ms}^{-1}$  can be accurately measured. We present data from two events in which clouds form, intensify, and finally produce precipitation. Height profiles are displayed and analyzed as  $ZRV_f$  plots vs. height, where  $Z$  is the radar reflectivity factor,  $R$  is liquid flux (rain), and  $V_f$  is the mean fall velocity in quiet air derived from the radar-measured vertical velocity. It is shown how these radars can provide 1) cloud layer structure above lower overcast, 2) height profiles of liquid mean dropsizes, 3) the ice-water transition level compared with the  $0^\circ$  isotherm, 4) height profiles of rain rate, and 5) inferences about the identity of hydrometeors vs. height.

## LIST OF SYMBOLS

$A$	Cross sectional area of drop
$C_d$	Drag coefficient
$D$	Drop diameter (mm)
$D_t$	Diameter of mode of lognormal distribution
$D_m, D_L$	Liquid mass median diameter, liquid mass weighted average diameter
$F_L, F_i, F_s$	Vertical mass flux ( $\text{g m}^{-2} \text{s}^{-1}$ ): liquid, graupel, snow
$g$	Acceleration of gravity
$K$	$(1 - \epsilon)/(2 + \epsilon)$
$K_w, K_i$	$K_w$ (water), $K_i$ (graupel, snow)
$N, N_i$	Drop number spectral density ( $\text{m}^{-3} \text{mm}^{-1}$ ) water, ice (graupel)
$N_0$	Number density at $D = 0$ .
$R, R_w, R_i$	Equivalent rain rate ( $\text{mm hr}^{-1}$ ): liquid, graupel, snow
$S_r, S_w, S_i$	Reflectivity factor spectral density: liquid, graupel, snow
$S_{LW}, S_{iW}$	Mass spectral density ( $\text{g m}^{-3} \text{mm}^{-1}$ ): liquid, graupel
$V_f$	Fall velocity in quiet air
$V_z$	Reflectivity factor weighted mean fall velocity
$Z, Z_w, Z_i$	Reflectivity factor ( $\text{mm}^6 \text{m}^{-3}$ ): liquid, graupel, snow
$Z_e$	Equivalent reflectivity factor if population had been liquid drops
$\epsilon$	Dielectric constant
$\lambda$	Radar wavelength (m)
$\eta$	Radar reflectivity ( $\text{m}^{-1}$ )

$\mu$  Viscosity of air ( $\text{g m}^{-1} \text{s}^{-1}$ )  
 $\rho_L, \rho_i, \rho_s$  Density: liquid, graupel, snow  
 $\rho_0, \rho(825), \rho(700)$  Air density: sea level, 825 mb, 700 mb

## 1. INTRODUCTION

The sensitive Doppler radars now available for monitoring the height "profiles" of the horizontal wind can also provide a wealth of information on hydrometeor populations. Most previous work has focused on the use of research radars that provided the complete Doppler fall velocity spectrum from which dropsizes spectra can be deduced. Experiments were carried out by many investigators; e.g., Lhermitte<sup>[1]</sup>, Rogers and Pilie<sup>[2]</sup>, Wilson<sup>[3]</sup>, Caton<sup>[4]</sup>, Foote and DuToit<sup>[5]</sup>, Gorelik et al.<sup>[6]</sup>, and Beard<sup>[7,8]</sup>. A comprehensive discussion of the state of the methodology of that time was given by Atlas et al.<sup>[9]</sup>. The dropsizes vs. fall velocity in quiet air is fairly well known (e.g., Gunn and Kinzer<sup>[10]</sup>); so in quiet air the conversion of a measurement of the fall velocity spectrum to a dropsizes spectrum is straightforward. However, complications arise when the particles are not in quiet air, but are, in fact, embedded in a turbulent medium that may have a net updraft or downdraft. Until the advent of clear-air radars this complication was insurmountable although, as noted above, many experiments were done under conditions when the investigators believed atmospheric conditions to be relatively quiet. They neglected turbulence, and they used various methods to estimate the mean vertical wind. The accuracy of the estimated vertical wind was only about 1  $\text{m s}^{-1}$ , which was not accurate enough for determining the size distributions of the smaller particles (Atlas et al.<sup>[9]</sup>).

It was pointed out by Wakasugi et al.<sup>[11,12]</sup> and Gossard and Strauch<sup>[13]</sup> that clear-air radar wind profilers provide the necessary information on clear-air structure to allow the crucial corrections for a non-quiescent medium to be made, and Doppler radars can now collect accurate spectra of drop number density and liquid water density remotely for a wide range of liquid water clouds using the water droplet backscatter.

However, it is not presently planned that the operational "wind profilers" will routinely provide continuous Doppler spectra to the user. Only the spectral moments [i.e., power, mean Doppler frequency shift (wind) and spectral width] will be routinely provided, but occasional spectra from selected range gates will also be available for removing up/downdrafts. We here show how such measurements can provide new cloud information. The potential use of mean vertical fall velocity as a direct measurable related to size and liquid flux in a precipitating population has also been pointed out by Martner and Battin<sup>[14]</sup>, and by Srivastava<sup>[15]</sup>. In this paper we present radar-measured fall velocity, reflectivity, and liquid flux measurements from a wind profiling system described by Strauch et al.<sup>[16]</sup>, and point out their relevance to the identification of hydrometeor type, size and location within precipitating systems.

## 2. OBSERVATIONAL DATA

The necessary data are obtained from the zero and first moments of the Doppler spectra, although occasional spectra are required to remove up/downdrafts from the data. The interpretation of radar-measured fall velocity and the calculation of mean or median drop size is unambiguous only if the form of the drops size number density distribution is known or can be reliably inferred. Figures 1 and 2 show radar measurements of the development of cloud systems that eventually produced rain at the ground. Both events occurred on 28 September 1990 when the synoptic situation was as shown in Figure 3. The radiosonde observations (RAOBs) at 0900 and 1200 UTC are shown at the appropriate hour. The top frames show the time-height record of radar reflectivity where the radar reflectivity factor,  $Z$ , ( $\text{mm}^6 \text{m}^{-3}$ ) is related to drop size,  $D$  (mm), and number density,  $N$  ( $\text{m}^{-3} \text{mm}^{-1}$ ), as follows (e.g., Doviak and Zrnic<sup>[17]</sup>):

$$Z = \int_0^\infty N D^6 dD.$$

In Figures 1 and 2 the radar reflectivity is calculated from the received power and is expressed as  $Z$  in decibels (dBZ). The lower frames show the time-height records of radar-sensed fall velocity ( $\text{m s}^{-1}$ ). The hourly surface observations at Denver's Stapleton Airport, which is also the site of the radar, are given at hourly intervals above the top frames. The reflectivity and fall velocity data are averaged over a half hour from 30 s data acquired every 2 minutes. The radar-indicated cloud layers are labeled as "upper" and "lower." Note that no precipitation reached the ground until 0500 UTC in the first event or until 1400 UTC in the second event. Although the precipitation was then recorded as "light rain" or "light rain showers," the enhancement in reflectivity and in mean fall velocity was often very substantial even in the (half-hourly) averages. We will show how height profiles of flux (rain) and of mean drop size can be monitored from data such as these. The synoptic situation at 1200 UTC is shown in Figure 3. The cloud system was generally stratiform, wide-spread, and time-stationary.

The data in Figures 1 and 2 are found by calculating the zero and first moments of the Doppler spectra. Figure 4 shows an example of the Doppler spectra recorded by the radar in a 30-minute period from 1400-1430 UTC, stacked in height. The lowest spectrum shown is 500 m above the radar (AGL), and the highest is at 3.3 km. The 1200 UTC RAOB shows the zero degree isotherm to be at 2200 m AGL, and the melting process taking place below that height is obvious in the change in spectral form. The velocity associated with the reflectivity spectral peak in gate 9 prior to melting is about  $1 \text{ m s}^{-1}$ . The peak moves quickly out to about  $5.5 \text{ m s}^{-1}$  in gate 7 as melting proceeds. At lower heights the mean fall velocity remains about the same for gates 6 and 5, and gates 1 and 2 show the drops size spectra below cloud base. The spectra from the third and fourth range gates have been deleted because the data at these ranges are contaminated by scatter from traffic on Interstate 70, located about 1 km from the radar, entering through the antenna sidelobes. (We note here that a high signal-to-noise ratio in the fall velocity measurement is needed, because the fall velocity is raised to the second or higher power in the denominator of the equation for flux (rain rate).)

The zone between the melting level and the height at which traffic noise overwhelms the cloud backscatter (about 800 m) is too thin to show evidence of the drop growth by liquid accretion discussed by Gossard et al.<sup>[18]</sup>

Each spectrum shown in Figure 4 is normalized to a common maximum spread for the stacked display. The Doppler velocity spectrum can be converted to the number density vs. size spectrum using known fall velocity vs. size relationships, so the moments of

the Doppler spectra provide height-profile information about drop number vs. size.

Below the cloud base, the spectral peak near  $V_f = 0$  is caused solely by backscatter from the clear-air at those ranges where ground "clutter" can be ignored. Higher up the clear-air backscatter is overwhelmed by the cloud return at our radar wavelength (0.328 m), and there is no clear separation. For cloud studies it would obviously be desirable to use a longer wavelength radar that is less sensitive to droplet scatter. Cloud backscatter is proportional to  $\lambda^{-4}$  compared with refractive index backscatter which is proportional to  $\lambda^{-2}$  where  $\lambda$  is the wavelength.

If there were no fall velocity and no up/downdrafts, the backscatter would all appear at  $V_f = 0$ . If the scatterers are moving randomly due to turbulence, some of the scattering ensemble will be moving upward and some downward within the pulse volume at any given moment, so the spectral line at  $V_f = 0$  will then be spread over a Gaussian distribution about zero. This spread is, in fact, a measure of the vertical component of turbulent intensity.

## 3. PARTICLE SPECIES IDENTIFICATION

### 3.1 The $Z$ - $R$ - $V_f$ Relationship

Cloud data acquired with a vertically pointing Doppler radar provide direct fall velocity information so the flux ( $R$ ) can be calculated, thus adding another dimension to the classical  $Z$ - $R$  relationship. After removal of up/downdrafts in the medium, the velocity sensed by the radar is the reflectivity-weighted mean fall velocity over all sizes of drops, i.e.,

$$\bar{V}_Z = \frac{\int_0^\infty V_f S_Z(V_f) dV_f}{\int_0^\infty S_Z(V_f) dV_f}, \quad (1)$$

where  $S_Z(V_f)$  is the spectral density of  $Z$  vs.  $V_f$ . The flux (i.e., rain rate) is given by

$$F = \int_0^\infty V_f S_{LM}(V_f) dV_f, \quad (2)$$

where  $S_{LM}(V_f)$  is the mass spectral density of cloud liquid water.  $F$  is flux in  $\text{gr m}^{-2} \text{s}^{-1}$ , which is easily converted to rain rate,  $R$  ( $\text{mm hr}^{-1}$ ).

The spectrum of  $Z$  vs. drops size is defined by:

$$S_Z(D) = N(D) D^6 \quad (3)$$

where  $D$  is the diameter of small (Rayleigh) liquid drops. The corresponding spectrum of liquid water is

$$S_{LM}(D) = \rho_L \frac{\pi}{6} N(D) D^3 = \rho_L \frac{\pi}{6} S_Z(D) D^{-3} \quad (4)$$

where  $\rho_L$  is the density of liquid water.

Therefore, if the radar measures the spectrum of radar reflectivity,  $S_Z(V_f)$ ; and if the relationship between size and fall velocity is known so that  $S_Z(D) = (\partial V_f / \partial D) S_Z(V_f)$ , the reflectivity spectrum measured by the radar can provide height profiles of  $Z$ ,  $R$  and  $\bar{V}_Z$  in contrast to the empirical  $Z$ - $R$  relationships which have been the subject of many past investigations (e.g., see Battan<sup>[19]</sup>).

Operational wind profiling radars do not output raw spectra, but rather the moment data  $Z$  and  $\bar{V}_Z$  (see the top and bottom frames

of Figures 1 and 2). If the spectral form  $N(D)$  is known, or can be reliably inferred, the necessary integrations in (1) and (2) can be carried out. If  $N(D)$  is exponential, as is very commonly assumed (e.g., Marshall and Palmer<sup>(10)</sup>), the integrations are simple and an analytic relationship between  $Z$ ,  $R$  and  $\bar{V}_z$  is easily obtained if the  $V_f(D)$  function is also chosen to be exponential. For other functions, the integrations were carried out numerically. We note that, instead of a  $Z$ - $R$  relationship, we are now dealing with an unambiguous  $Z$ - $R$ - $V_f$  diagram. We specifically analyze water drops, graupel, and snow.

### 3.2 Water Drops

Doppler radars have long been used to measure fall velocity (e.g., Battar<sup>(17)</sup>; Rogers and Yau<sup>(21)</sup>).

The early literature and experimental data relating terminal fall velocity of water droplets in quiet air to their size is extensive (e.g., Gunn and Kinzer<sup>(18)</sup>; Foote and DuToit<sup>(19)</sup>; Beard<sup>(9)</sup>). It has been reviewed and discussed by Gossard and Strauch<sup>(13), (22)</sup>, and we concluded that this relationship represents one of the lesser errors in the technique if the embedding medium can be considered truly quiescent. In the present paper, three relationships for three dropsizes ranges of the spectrum are used. For very small drops with fall velocity  $< 0.40 \text{ m s}^{-1}$ , the Stokes relationship for the terminal fall velocity is used (Beard and Pruppacher<sup>(23)</sup>).

$$D = (18\mu V_f/g)^{1/2} \quad (5a)$$

where  $g$  is acceleration of gravity ( $\text{m s}^{-2}$ ),  $D$  is drop diameter (mm), and  $\mu$  is the viscosity of air. [For pressure and temperature conditions corresponding to about 3 km MSL in a standard atmosphere,  $\mu = 0.0167 \text{ (g m}^{-1} \text{ s}^{-1})$ .] For other ranges of  $V_f$ ,

$$D = 0.225 \left( \frac{\rho}{\rho_0} \right)^{0.4} V_f^{1.09} \text{ for } 0.40 \text{ m s}^{-1} \leq V_f < 2.50 \text{ m s}^{-1}, \quad (5b)$$

and, (Atlas et al.<sup>(9)</sup>),

$$D = -1.667 \ln \{ [9.65 - V_f \rho / \rho_0^{0.4}] / 10.3 \} \text{ for } V_f > 2.5 \text{ m s}^{-1}, \quad (5c)$$

where  $\rho$  is air density and  $\rho_0$  is air density at 1000 mb. [Equations (5a)-(5c) represent a slightly improved match of derivatives where the ranges join, compared with similar relationships in our earlier papers (e.g., Gossard et al.<sup>(14)</sup>).] These conditions are applied to clouds in Colorado at typical heights corresponding to a pressure near 700 mb (about 1500 m AGL at Denver). Figure 5 compares the above relationships (solid curve) with measured fall velocities from many sources summarized by Mason<sup>(24)</sup> in his Table B.1 (solid points). The open circles and the crosses show the function

$$V_f = 10.5 (1 - e^{-0.2C}) \quad (6)$$

for the values of  $C$  indicated. The expressions (5) were used in the numerical integrations for the  $Z$ - $R$ - $V_f$  plots in our figures and the integrations were carried out to  $V_f = 10 \text{ m s}^{-1}$ . However, it is useful to illustrate the results with the approximation (6), integrating over  $V_f$  to  $\infty$ , so that simple analytical approximations are obtained for discussion.

Using (6) and choosing the exponential dropsizes distribution:

$$N(D) = N_0 e^{-3.67 D/D_0} \quad (7)$$

where  $D_0$  is the mass median diameter of the population, (1) and (7) yield

$$D_0 = 3.67 C [\gamma^{-1/3} - 1] \quad (8)$$

where

$$\gamma = 1 - \frac{\bar{V}_z}{10.5}.$$

Combining (2) and (7) then yields the liquid flux (rain rate)

$$R (\text{mm hr}^{-1}) = \rho_L \left( \frac{\pi}{6} \right) 0.315 Z \left( \frac{\gamma^{3/2}}{C^3} \right) \left( \frac{1 - \gamma^{4/3}}{(1 - \gamma^{1/3})^3} \right) \quad (9)$$

where we note that  $Z$  and  $\bar{V}_z$  are directly measured by the radar. In (9),  $D$  is in mm,  $Z$  is  $\text{mm}^6 \text{ m}^{-3}$ , and  $\rho_L$  is the density of water in  $\text{g cm}^{-3}$ . Together with the calculated flux (converted to rain rate,  $R$ ) they constitute the  $Z$ - $R$ - $V_f$  diagrams on which we have plotted our data. For other assumed dropsizes distributions the integrations were carried out numerically. These include the log-normal and modified Cauchy distributions to be discussed later. Figure 5 shows that  $C = 5/3$  provides a good overall fit to the solid curve, but  $C = 2$  provides a better fit at small diameters where the large number densities dominate the integrals. Therefore in (9),  $C = 2$  provides a better fit than  $C = 5/3$  to the numerically integrated values of  $F$  found from the solid curve in Figure 5A

### 3.3 Graupel and Hail

Radar observations provide no direct determination of the state (ice or water) of the scattering particles, so an apparent or equivalent  $Z$  (often written  $Z_e$ ) is the quantity calculated (e.g., Sassen<sup>(25)</sup>). For particles small in the Rayleigh sense, the reflectivity, found from the received power, is related to  $Z$  by

$$\eta = \frac{\pi^5}{\lambda^4} |K|^2 \int_0^\infty N(D) D^6 dD \quad (10)$$

where  $K = (e - 1)/(e + 2)$  and  $e$  is the complex permittivity of the scatterers, which is not a priori known. The appropriate value for water ( $|K_w|^2 = 0.93$ ) is therefore used so that

$$Z_e = \eta \frac{\pi^5}{\lambda^4} \frac{1}{|K_w|^2}.$$

If we had a priori knowledge that the particles were ice, we could have calculated a true reflectivity factor,

$$Z_i = \int_0^\infty N_i(D) D^6 dD,$$

given by

$$Z_i = \eta \frac{\pi^5}{\lambda^4} \frac{1}{|K_i|^2}$$

so the measured quantity,  $Z_e$ , is related to the size distribution of the particulate population (about which we seek information) by

$$Z_e = \frac{|K_i|^2}{|K_w|^2} \int_0^\infty N_i(D) D^6 dD \quad (11)$$

For ice particles, we pursue a derivation similar to that for water drops. Figure 5B shows fall velocity vs. size data for graupel and hail collected by Auer et al.<sup>(26)</sup> at a pressure-height of about 825 mb and found to be in good agreement with data collected in the  $N(\text{ational})$   $H(\text{ail})$   $R(\text{esearch})$   $E(\text{xperiment})$  reported by Heymsfield<sup>(29)</sup>

We have used their least squares fit of  $V_f$  to  $D$  to approximate a linear relationship and calculate the equivalent liquid flux for the ice particulates they studied. In our calculations, we assume:

$$V_f = 0.95 D^{0.911} = 0.86 D \quad \text{at } 825 \text{ mb.} \quad (12)$$

$$N_i(D) = N_{oi} e^{-3.67 D/D_{oi}}, \quad (13a)$$

$$S_{oi}(D) = \frac{|K_i|^2}{|K_w|^2} N_i(D) D^6 \quad (13b)$$

$$S_{oi}(D) = \rho_i \left( \frac{\pi}{6} \right) N_i(D) D^3 \quad (13c)$$

where ice particles are indicated by the subscript "i" and water by the subscript "w." The quantity  $|K_i|^2/|K_w|^2$  depends strongly on the ice particle density,  $\rho_i$ , (Cumming<sup>[27]</sup>; Rosenberg<sup>[28]</sup>), which is highly variable in graupel and hail (Heymsfield<sup>[29]</sup>).

To relate  $D$  to  $V_f$  for different air densities, we note (Beard<sup>[6]</sup>) the general relationship balancing buoyancy against frictional stress, for particles larger than the Stokes range, is

$$V_f = \left[ \frac{2}{A} \frac{\pi}{6} \frac{g}{C_D} \left( \frac{\rho_i - \rho}{\rho} \right) D^3 \right]^{1/2} \quad (14a)$$

Thus, assuming  $\rho_i \gg \rho$

$$V_f^2(z) = V_f^2(0) \left[ \rho_o / \rho(z) \right] (\rho_i / 0.4) \quad \text{for } \rho_i \gg \rho \quad (14b)$$

where  $\rho_o$  is the air density at the pressure-height level at which the empirical measurements were made,  $C_D$  is the drag coefficient (assumed independent of density),  $\rho_i$  is particle density (average assumed to be  $0.4 \text{ gr cm}^{-3}$  in the data sample which led to (12),  $\rho$  is air density,  $g$  is the acceleration of gravity, and  $A$  is the cross-sectional area of the particle. [ $A = (\pi/4) D^2$  for a sphere.] Therefore, for heights  $z$ , other than the 825 mb level, to which (12) applies:

$$V_f^2(z) = V_f^2(825) \left[ \frac{\rho(825)}{\rho(z)} \frac{\rho_i}{0.4} \right] = V_f^2(825) f(\rho). \quad (15)$$

For the Standard Atmosphere,  $\rho(825) = 0.997 \text{ kg m}^{-3}$ . We will assume the 700 mb level to be the typical cloud height above Denver and use it for our ZRV plots. Therefore,  $\rho(700) = 0.912 \text{ kg m}^{-3}$  so (12) gives  $V_f(700) = 1.0 D^{0.911} = 0.9 D$ .

From (1), (12), and (15) we find

$$\bar{V}_z = (0.86)(7) f(\rho)^{1/2} \left( \frac{D_{oi}}{3.67} \right), \quad (16)$$

and from (2), (13c), and (16),

$$R_{oi} = 0.623 \pi \left( \rho_i \frac{|K_w|^2}{|K_i|^2} \right) [f(\rho)]^{1/2} \frac{Z_o}{\bar{V}_z^2} \times 10^{-3} \quad (17)$$

where  $R_{oi}$  is the equivalent rain rate ( $\text{mm hr}^{-1}$ ) in the ice particulates.

For water,  $|K_w|^2 = 0.93$  at temperatures  $< 20^\circ\text{C}$  for radar wavelengths greater than 10 cm (e.g., Battan<sup>[30]</sup>). For ice, the ratio  $K_i/\rho_i = 0.49 \pm 0.015$  over the range of  $\rho_i$  of interest (Cumming<sup>[27]</sup>). Therefore, to a very good approximation,

$$\rho_i \frac{|K_w|^2}{|K_i|^2} = \frac{4.00}{\rho_i} \left( \frac{\text{g}}{\text{cm}^3} \right) \quad (18)$$

The graupel curves in Figures 6, 7, and 8 have been plotted from (18) using  $\rho_i = 0.4 \rho_L$  (an intermediate value in the range found by Heymsfield<sup>[29]</sup>) and assuming a pressure level of 700 mb (about 1.4 km above Denver).  $F_i$  has been converted to equivalent "rain rate" in  $\text{mm hr}^{-1}$ , and plotted parametrically on dBZ and  $\bar{V}_z$  axes.

### 3.4 Snow

To relate fall velocity to size of a snow particle, we adopt the empirical relationship of Magono and Nakamura<sup>[30]</sup> (see discussion by Ihara et al.<sup>[31]</sup>); i.e.,

$$V_f = 8.8[(\rho_s - \rho)(0.1) D]^{1/2} = 2.78(\rho_s - \rho)^{1/2} D^{1/2} \quad (19)$$

where  $D$  is the diameter of a snow "sphere" in mm,  $\rho_s$  is the density of snow ( $\text{gr cm}^{-3}$ ), and  $\rho$  is air density ( $\text{gr cm}^{-3}$ ).

The measurements of Magono and Nakamura<sup>[30]</sup> were made at air densities corresponding to a pressure-height near sea level, so with reference to other heights, we assume that

$$V_f = 2.78 \left[ \frac{\rho_o}{\rho(z)} \right]^{1/2} \left( \frac{\rho_s - \rho(z)}{\rho_L} \right)^{1/2} D^{1/2} = 2.78 f(\rho)^{1/2} D^{1/2} \quad (20)$$

where  $f(\rho)$  is defined by (20). Assuming the forms of (13a,b,c) to be applicable to snow, and integrating (1), we find

$$\bar{V}_z = 3.77 f(\rho)^{1/2} D_{oi}^{1/2} \quad (21)$$

and integrating (2) and using (21), we find, assuming an exponential size distribution (Braham<sup>[32]</sup>),

$$R_{oi} = 0.533 \pi \left( \rho_s \frac{|K_w|^2}{|K_s|^2} \right) f(\rho)^3 \frac{Z_o}{\bar{V}_z^3} \quad (22)$$

The snow curves in Figures 6, 7, and 8 have been plotted from (22) using (18). In Figure 7b, curves for dry snow ( $\rho_s = 0.05 \rho_L$ ) and wet snow ( $\rho_s = 0.2 \rho_L$ ) are both shown for  $R = 1 \text{ mm hr}^{-1}$ .

## 4. INTERPRETATION OF THE ZRV DIAGRAMS

It is instructive to analyze the cloud-layer information in Figures 1 and 2 on ZRV diagrams. There are two dominant cloud layers in both events, but the double layer structure is especially evident in Figure 1 where there is clearly one cloud layer that forms at a height of 2 km at about 1230 UTC and another layer, initially at a height of about 7.6 km, that descends during the period and finally merges with the lower layer at about 1530 UTC. The hourly surface observations report rain showers at the ground at 1400 UTC, becoming light rain by 1600 UTC. The top frames, showing the magnitude of the reflectivity in dBZ, illustrate the value of these radars for monitoring the morphology of the cloud layers as they develop. They are especially valuable for observing cloud layer structure above a broken or overcast layer of lower clouds. We note, for example, that the upper layer, originally estimated to be at 7.6 km AGL by the surface observer, descended steadily through the period. However it became obscured from surface observation by the cloud layer developing at 2 km and continued to be reported at 7.6 km as originally estimated. The lower frames show the reflectivity-weighted vertical fall velocity as sensed by the radar. They show ice precipitation in the upper cloud layer

throughout the period. Significant water precipitation develops in the lower layer after about 1230 UTC, although it was not reported at the ground until about 1400 UTC. We note that the rate of descent of the upper layer was about  $0.2 \text{ m s}^{-1}$ , while the average reflectivity-weighted fall velocity was about  $1 \text{ m s}^{-1}$ . The radio-sonde observations taken at 0000 and 1200 UTC are plotted at the time of the corresponding radar sounding. We note that the  $0^\circ$  isotherm was at about 2.1 km AGL at 1200 UTC. Thus, the lower cloud layer was constantly below the melting level and the upper layer was above it.

The pattern of cloud development shown in Figure 2 was similar to that in Figure 1, but it was less intense. Although there was a lower cloud layer at 1-2 km, the fall velocities associated with it were generally too small to be reliably extracted from the ambient noise in "backscatter" at this height because the traffic "noise" from I-70, mentioned earlier, degraded the quality of the reflectivity and fall velocity information during busy times of the day. Therefore, lower cloud data were rejected unless the fall velocity was relatively large ( $> 0.5 \text{ m s}^{-1}$ ) compared with the noisy background. The lower cloud layer in Figure 1 generally satisfied this criterion, but the lower cloud layer in Figure 2 (5 PM to 10 PM local time) only produced large enough fall velocities when precipitation began to reach the ground at 0500 UTC. These data are plotted in Figures 6 and 7 where the zones of the various particles species are shown on ZRV diagrams.

The various time and height intervals analyzed are shown in Figure 6 and all of the data from the centers of the upper (U) and lower (L) layers have been combined in Figure 7a. We see that the zones in which the data lie correspond essentially to snow for the upper layer, and to drizzle or light rain for the lower layer. For reference, the Marshall and Palmer<sup>(20)</sup> Z-R relationship is shown dotted on Figure 7a. The Z-R relation not only cuts sharply across the theoretical flux curves and it implies average fall velocities of  $4\text{--}5 \text{ m s}^{-1}$  for drizzle and light rain. It is noteworthy that measurements of R, in most of the Z-R relations, were made at the ground below the clouds after considerable size-sorting has occurred. Evidently the fall velocities provided by vertically pointing wind profilers can add significantly to the understanding of possible relationships between radar data and rain rates.

The upper and lower cloud radar data provide sets that lie in different zones of the ZRV diagrams and therefore such plots offer aid in identifying the nature of the particles scattering the radar waves (see 7b). We note very good agreement between the theoretical flux curves for snow and the Z,  $\bar{V}_z$  values observed by the radar near the center of the upper layer. The data suggest little change in the nature of the particles or in the mass flux (about  $0.25 \text{ mm hr}^{-1}$ ) as the layer lowers, but the reflectivity and fall velocity both increase with time as the layer descends and the ambient temperature rises. In Figure 6c there is a clear pattern in fall velocity and reflectivity (dBZ), with time, as the upper cloud layer develops and lowers. Between 1100 and 1500 UTC the reflectivity at the center of the layer increases from 3 dBZ to 25 dBZ and the layer lowers from about 5.5 km AGL to 2.5, corresponding to an increase in temperature from about  $-20^\circ\text{C}$  to  $-4^\circ\text{C}$ . The mean fall velocity increases with increasing backscatter, and the  $\bar{V}_z$  vs. dBZ relationship agrees well with the theoretical relationship for a flux of about  $0.25 \text{ mm hr}^{-1}$  and a snow density of about  $0.5 \text{ g cm}^{-3}$ . In the 0000-0400 UTC event, no similar pattern is evident.

The ZRV plots are also useful in the analysis of individual reflectivity profiles. Figure 8 shows half-hourly averaged profiles of backscattered power with their corresponding ZRV diagrams at 1400-1430 UTC - top, (the time the spectra were recorded), and at 1530-1600 UTC - bottom. The latter case is interesting because it shows what may be an ice particle transition to snow, beginning at range gate 17. We note that the fluxes throughout the height domains of the different particles remain roughly the same at about

$0.25 \text{ mm hr}^{-1}$ . The transition from ice to water is shown dotted on the ZRV plots.

In no case is there a very well defined "bright band", although there is some enhanced reflectivity seen in the dashed zone of the ZRV's at 1500 and 1600 UTC. Although this enhancement is not trivial (amounting to perhaps 5 dBZ), the sharp increase in fall velocity associated with the melting is a more impressive feature of the records. In general, proceeding downward through the upper layer, the diagram shows that initially the reflectivity increases without much change in fall velocity. Below the maximum reflectivity (nose) there is some increase in fall velocity as the reflectivity decreases toward the melting level. This may suggest that the intercloud zone is made up of fewer but larger particles. At the melting level the enhancement in reflectivity precedes the increase in fall velocity. Unfortunately, spurious scatter from vehicles on I-70 makes interpretation of data from the third and fourth range gates (900-1300 m) uncertain in this critical height range, and they have been deleted.

## 5. PROFILES OF DROPSIZE

For exponential dropsize and fall velocity distributions such as (6) and (7), measurements of  $\bar{V}_z$  are easily converted to  $D_o$  (the mass median diameter for the exponential distribution). For other functions, the necessary integrations of (1) are carried out numerically. Instead of  $D_o$ , we have chosen to plot the more generally definable "liquid-weighted average" diameter,  $D_L$ , of the size distribution, i.e.:

$$D_L = \frac{\int_0^\infty D S_{LM}(D) dD}{\int_0^\infty S_{LM}(D) dD} \quad (23)$$

where  $S_{LM}(D)$  is given by (4)

We consider (1) exponential, (2) log-normal, and (3) modified Cauchy distributions, where we choose to define them as follows.

(1) Exponential distribution [see (7)] (Note that  $3.67/D_o = 4/D_L$ )

(2) Log normal distribution:

$$N(D) = N_o e^{-\frac{(\ln D - \ln D_o)^2}{2 \ln^2 \sigma_z}} \quad (24)$$

where  $D_o$  is a scale representing the mode of the distribution,  $N_o$  is the modal number density, and  $\sigma_z$  is a width scale equal to about 1.43 (Feingold and Levin<sup>(13)</sup>)

(3) Modified Cauchy distribution:

$$N(D) = \frac{N_o}{1 + \left(\frac{D}{D_w}\right)^y} \quad (25)$$

where  $D_w$  is a diameter at which  $N(D)/N_o = 1/2$  and  $y$  is its slope on a log log plot when  $D \gg D_w$ . Our data suggest  $y$  is between 7 and 8. The ZRV plots for water drops for the three distributions are shown in Figure 9 for comparison.

The exponential is a two parameter distribution, while the log normal and Cauchy are three parameter distributions. The results are shown in Table 1 where  $D_L$  is given for the various parameters of the distributions. Figure 10 shows the relationship between the radar-measured vertical velocity,  $\bar{V}_z$ , and the liquid-weighted mean diameter  $D_L$  for several distributions, and we note that  $\bar{V}_z$  can be translated into the dropsizes,  $D_L$ , within fairly narrow error

limits if the real droplet distribution resembles any of the commonly chosen functional forms. Figure 11 shows height profiles of liquid-averaged droplet size [calculated from (20) assuming an exponential distribution] from 1330 to 1500 UTC. We have interpolated across gates 3 and 4 (dashed zones). Melting, beginning at 2100 m AGL, is complete by about 1800 m. The liquid-weighted mean droplet size of the distribution is then about 0.2 mm.

Table 1

	$D_L/D_0$	
Exponential	1.09	
Log normal	$\sigma_z$	$D_L/D_0$
	1.3	2.30
	1.43	1.77
	1.5	1.45
Cauchy	$\gamma$	$D_L/D_w$
	7	1.25
	7.5	1.148
	8.0	1.08

## 6. CONCLUSIONS

The new generation radar wind sounders will provide a useful new class of cloud/precipitation data that will be continuous in time and available over dense spatial networks. 1) They will permit cloud layer structure to be monitored above lower overcasts that preclude optical observation. 2) They will allow height profiles of cloud population droplet size to be monitored continuously as precipitating systems evolve. 3) They will allow the transition zone of ice to water to be monitored continuously and, with RASS, compared with the 0° isotherm. 4) They will allow height profiles of liquid flux (rain) to be monitored continuously as cloud systems develop precipitation. 5) They offer promise of hydrometeor identification and observation of hydrometeor evolution in time and height.

## 7. REFERENCES

1. Lhermitte, R., "The Use of Special 'Pulsed Doppler Radar' in Measurements of Particle Fall Velocities", in *Proceedings, Eighth Weather Radar Conference*, San Francisco, CA, American Meteorological Society, 1960, pp. 269-275.
2. Rogers, R. R. and Pile, R. J., "Radar Measurements of Droplet Size Distribution", *J. Atmos. Sci.*, 19, 1962, pp. 503-506.
3. Wilson, D. A., "Droplet Size Distribution as Recorded by Pulsed Doppler Radar", M. A. Thesis, 64 pp., University of Arizona, Tucson, 1963.
4. Caton, P. G. F., "The Measurement of Wind and Convergence by Doppler Radar", in *Proceedings, Tenth Weather Radar Conference*, Washington, DC, American Meteorological Society, 1963, pp. 290-296.
5. Foote, G. B., and duToit, P. S., "Terminal Velocity of Raindrops Aloft", *J. Appl. Meteor.*, 8, 1969, pp. 249-253.
6. Gorelik, A. G., Gritskiv, I. V., Penzay, L. A., and Tsykunov, V. V., "Results of Simultaneous Radar and Ground Measurements of the Microstructure of Precipitation", *Izv. Akad. Nauk SSSR, Ser. Fiz. Atmos. Okeana*, 3, 1967, pp. 961-966.
7. Beard, K. V., "Terminal Velocity Adjustment for Cloud and Precipitation Drops Aloft", *J. Atmos. Sci.*, 34, Aug., 1977, pp. 1293-1298.
8. Beard, K. V., "Simple Altitude Adjustments to Raindrop Velocities for Doppler Radar Analysis", *J. Atmos. Oceanic Technol.*, 2, Dec., 1985, pp. 468-471.
9. Atlas, D., Srivastava, R. C., and Sekon, R. S., "Doppler Radar Characteristics of Precipitation at Vertical Incidence", *Rev. Geophys. Space Phys.*, 11, 1973, pp. 1-35.
10. Gunn, R., and Kinzer, G. D., "The Terminal Velocity of Fall for Water Droplets in Stagnant Air", *J. Meteorol.*, 6, 1949, pp. 243-248.
11. Wakasugi, K., Mizutani, A., Matsuo, M., Fukao, S., and Kato, S., "A Direct Method for Deriving Droplet Size Distribution and Vertical Air Velocities from VHF Doppler Radar Spectra", *J. Atmos. Oceanic Technol.*, 3, 1986, pp. 623-629.
12. Wakasugi, K., Mizutani, A., Matsuo, M., Fukao, S., and Kato, S., "Further Discussion on Deriving Droplet Size Distribution and Vertical Air Velocities Directly from VHF Doppler Radar Spectra", *J. Atmos. Oceanic Technol.*, 4, 1987, pp. 170-179.
13. Gossard, E. E., and Strauch, R. G., "Procedural Guide for the Retrieval of Droplet Size Distributions in Water Clouds from Ground-Based Clear-Air-Sensing Doppler Radar Observations", NOAA/ERL Technical Document, 44 pp., July, 1988.
14. Martner, B. F., and Battan, L. J., "Calculations of Doppler Radar Velocity Spectrum Parameters for a Mixture of Rain and Hail", *J. Appl. Meteorol.*, 15, May, 1976, pp. 491-498.
15. Srivastava, R. C., "A Method for Improving Rain Estimates from Vertical-Incidence Doppler Radar Observations", *J. Atmos. Ocean. Tech.*, 7, Oct., 1990, pp. 769-773.
16. Strauch, R. G., Merritt, D. A., Moran, K. P., Earnshaw, K. B., and van de Kamp, D., "The Colorado Wind Profiling Network", *J. Atmos. Oceanic Technol.*, 1, 1984, pp. 37-49.
17. Doviak, R. J., and Zrnic, D. S., (Eds.), *Doppler Radar and Weather Observations*, Orlando, FL, Academic Press, 1984, 458 pp.
18. Gossard, E. E., Strauch, R. G., and Rogers, R. R., "Evolution of Droplet Size Distributions in Liquid Precipitation Observed by Ground-Based Doppler Radar", *J. Tech.*, 7, Dec., 1990, pp. 815-828.
19. Battan, L. J., "Radar Observation of the Atmosphere", 323 pp., Chicago, IL, The University of Chicago Press, 1973.

20. Marshall, J. S., and Palmer, W. M. K., "The Distribution of Raindrops with Size", *J. Meteorol.*, 5, 1948, pp. 165-166.
21. Rogers, R. R., and Yau, M. K., "A Short Course in Cloud Physics", Oxford, England, Pergamon Press, 1987, 293 pp.
22. Gossard, E. E., and Strauch, R. G., "The Retrieval of Drops Size Distributions in Water Clouds from Ground-Based, Clear-Air-Sensing Doppler Radar Observations", *Meteorol. Rundschau*, 42, June, 1990, pp. 165-173.
23. Beard, K. V., and Pruppacher, H. R., "A Determination of the Terminal Velocity and Drag by Means of a Wind Tunnel", *J. Atmos. Sci.*, 26, 1969, pp. 1066-1072.
24. Mason, B. J. (Ed.), "The Physics of Clouds", Oxford, England, Clarendon Press, 1971, 659 pp.
25. Auer, A. H., Marwitz, J. D., Vali, G., and Veal, D. L., "Final Report to the National Science Foundation", 94 pp., Department of Atmospheric Resources, University of Wyoming, Laramie, WY, 1971.
26. Cumming, W. A., "The Dielectric Properties of Ice and Snow at 3.2 Centimeters", *J. Appl. Phys.*, 23, 1952, pp. 768-773.
27. Rosenberg, V. I., "Scattering and Extinction of Electromagnetic Waves by Atmospheric Particles", *Gidrometeoizdat, Leningrad, USSR*, 1972, 348 pp.
28. Sassen, K., "Ice Cloud Content from Radar Reflectivity", *J. Clim. Appl. Meteorol.*, 26, Aug., 1987, pp. 1050-1053.
29. Heymsfield, A. J., "The Characteristics of Graupel Particles in Northeastern Colorado Cumulus Congestus Clouds", *J. Atmos. Sci.*, 35, 1978, pp. 284-295, 1978.
30. Magono, C., and Nakamura, T., "Aerodynamic Study of Falling Snowflakes", *J. Meteorol. Soc. Japan*, 43, 3, 1965, pp. 139-147.
31. Ihara, T., Furuhashi, Y., and Tohma, K., "Measurement of Depolarization Due to Snowfall at 34.5 GHz", *Trans. IECE of Japan*, E65, Jan., 1982, pp. 16-22.
32. Brahm, R. R., "Snow Particle Size Spectrum in Lake Effect Snow", *J. Clim. Appl. Meteorol.*, 29, Mar., 1990, pp. 200-207.
33. Feingold, G., and Levin, Z., "The Lognormal Fit to Raindrop Spectra from Frontal Convective Clouds in Israel", *J. Clim. and Appl. Meteorol.*, 25, 1986, pp. 1346-1363.
34. Sekon, R. S. and Srivastava, R. C., "Snow Size Spectra and Radar Reflectivity", *J. Atmos. Sci.*, 27, 1970, pp. 299-307.

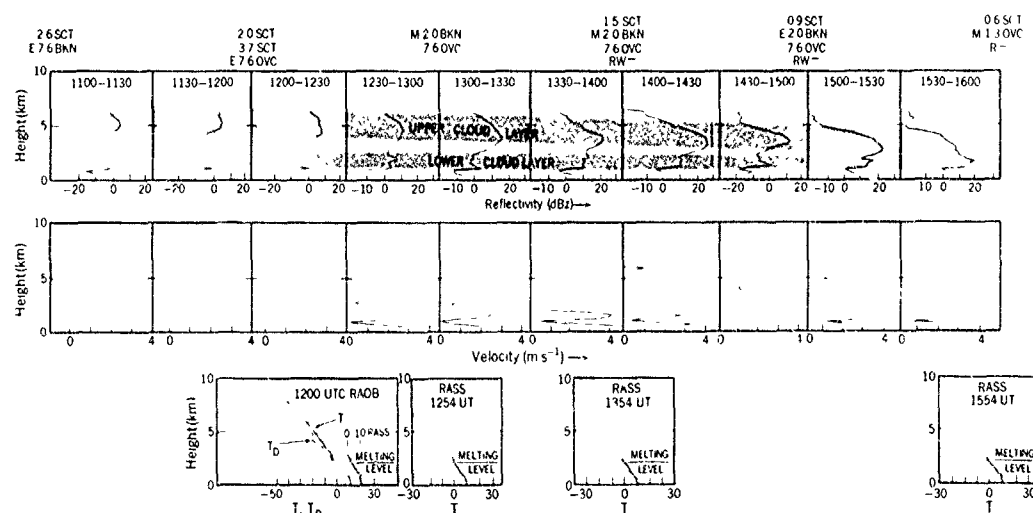


Figure 1. Soundings on 28 September 1990 from a vertically-pointing radar located at Stapleton Field, Denver. Top frames: Height profiles of dBZ averaged over half-hourly intervals. Lower Frames: Profiles of vertical velocity measured with antenna pointing vertically averaged over half-hourly intervals. Bottom: Stapleton radiosonde shown at the time it was obtained and temperature soundings by RASS. Hourly surface airway observations at Stapleton are shown above the top frames, where OVC = overcast (>0.9 sky cover), SCT = scattered clouds (0.1-0.5 sky cover), BKN = broken clouds (0.6-0.9 sky cover), RW - rain showers, R - light rain.

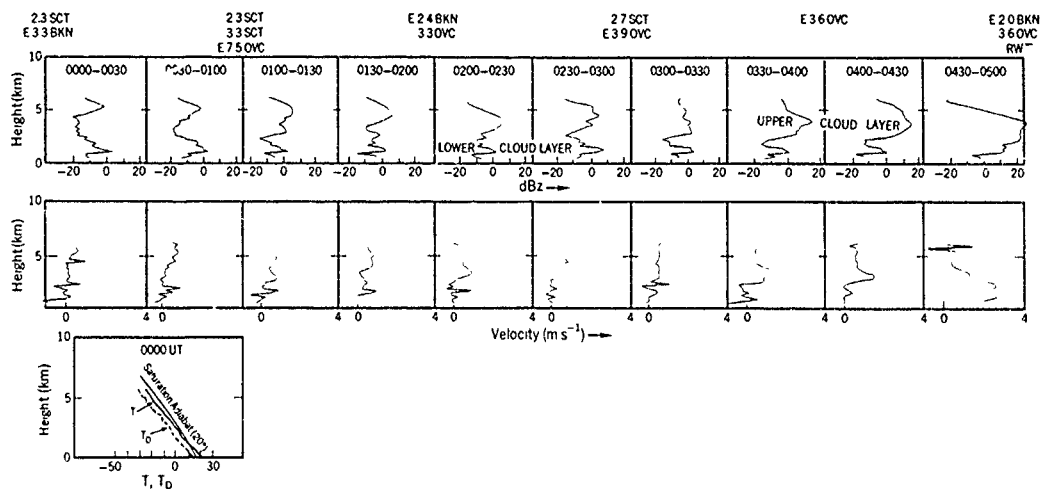


Figure 2. Same as Figure 1, except different time and no soundings by RASS are shown.

FRIDAY, SEPTEMBER 28, 1990

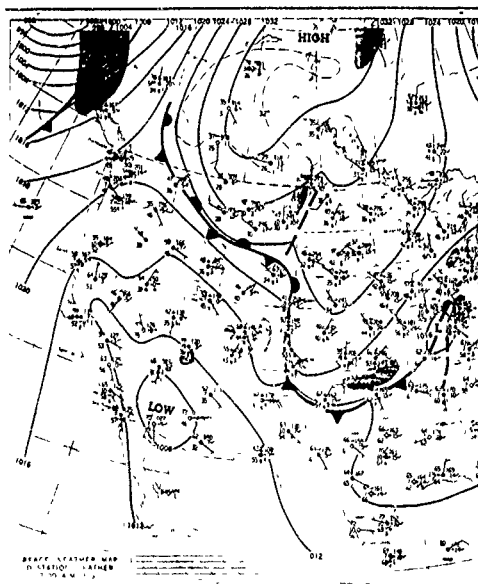


Figure 3. Synoptic surface weather map of 1200 UTC on 28 September 1990.

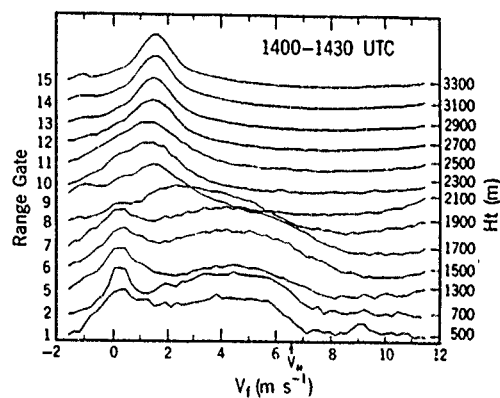


Figure 4. Doppler spectra stacked in height, from the 1406-1430 UTC time interval of the record shown in Figure 2. In these plots the spectra of log-power (vertical axis) are all normalized to the same spread. Range gates 3 and 4 (heights 900-1300 m AGL) are omitted because of "clutter" from traffic on I-70 in this range interval. The two lowest spectra are below cloud base. The melting level is at 2100-2300 m AGL.  $V_N$  is the Nyquist, or folding, frequency.

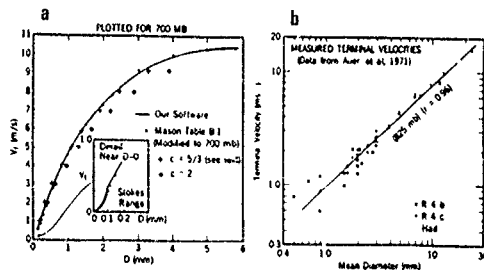


Figure 5. (a) Data and functions relating terminal fall velocity of water drops in quiet air to their diameter. Solid curve is a three-segment fit of the functions (5) to experimental data published by Mason<sup>[24]</sup>, (Table B.1), adjusted to a pressure-height of 700 mb. (b) Fall velocity of ice particulates measured by Au et al.<sup>[25]</sup> R4b is lump graupel, R4c is conical graupel.

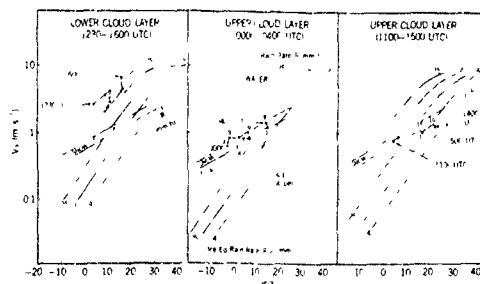


Figure 6. Location of lower (L) and upper (U) cloud layer points on a ZRV diagram whose background curves are plots from (9), (17), and (22). Fall velocities and dBZ are the maximum values for each of the two layers. Times at beginning and end of records are shown, and numbers beside points are degrees (C) below 0°C

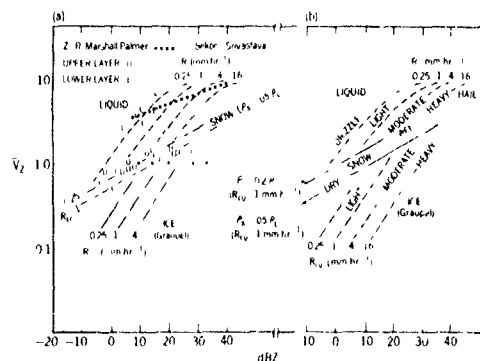


Figure 7 (a) Composite of all upper layer and lower layer points from Figure 6, and (b), diagram of the zones on ZRV plots where various hydrometeor types may be expected to lie. The Marshall-Palmer<sup>[30]</sup> (liquid) and Sekon-Srivastava<sup>[14]</sup> (snow) Z-R relations are shown for comparison.

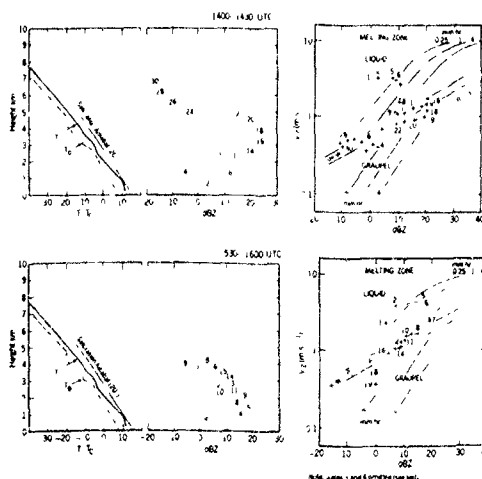


Figure 8. Top frames: Average profile of dBZ from 1400-1430 UTC shown with corresponding ZRV diagram and closest RAOB. Lower frames: Average profile of dBZ from 1530-1600 UTC shown with corresponding ZRV diagram

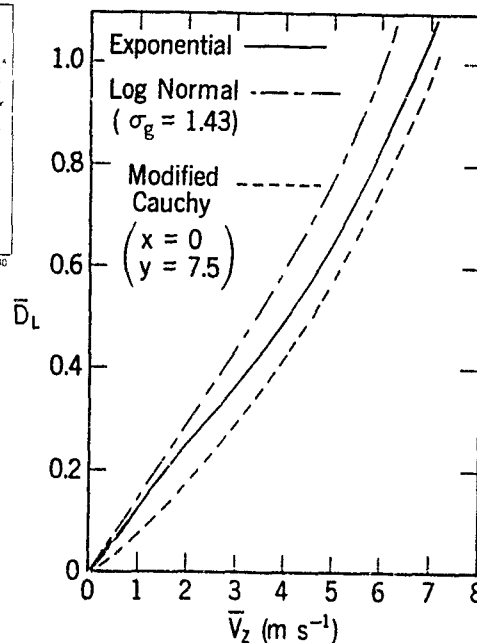


Figure 9. Theoretical ZRV plots for lognormal liquid droplet distribution [see (24)], modified Cauchy distribution [see (25)], and exponential distribution [see (7)], from numerical integration of (1) and (2)

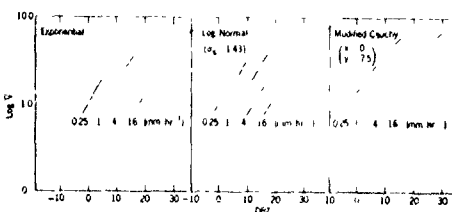


Figure 10. Plot of relationships between radar-measured fall velocity  $V_z$  and liquid-weighted mean droplet size [found from (1) and (23)], for three functions sometimes used to describe droplet size distributions [see (7), (24), and (25)].

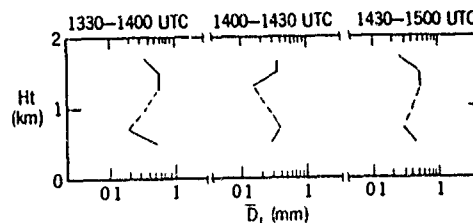


Figure 11. Profiles of liquid-weighted mean diameter vs. height calculated from radar-measured  $V_z$  using (23) and adopting (6) and (7) with  $C = 2$ . Dashed portions are interpolated over gates 3 and 4.

The frequency scale is shown in figure 1b. The center frequency is the laser output frequency which is for the wavelength of 10.6 micrometer  $28.3 \times 10^{12}$  Hz. The Doppler shifted radial velocity for the atmospheric wind is between 0 and 25 MHz.

The coherent detection technique uses part of the output energy of the master oscillator laser (1) for an offset locking loop (2) that maintains the local oscillator laser (3) at a constant frequency difference from the master (Figure 2).

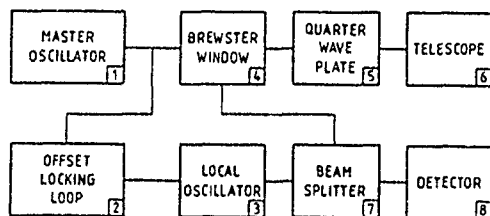


Figure 2: Block Diagram of the Coherent Detection Technique

The radiation passes through a Brewster window (4), aligned for horizontal polarization, through a quarter-wave plate (5) to rotate the polarization to circular, and into a telescope (6). The telescope collimates the beam and transmits it into the atmosphere. The return beam, Doppler shifted and rotated in polarization, comes back along the same path into the telescope (6) and to the quarter-wave plate (5). Because of the reverse polarization of the return beam, the radiation passing through the quarter-wave plate now becomes vertically polarized. The beam is reflected by the Brewster window (4) to a beam splitter (7), where it is combined with the local oscillator beam and transmitted to the detector (8). The coherent mixing of the two beams is called heterodyning and results in an interference pattern imaged on the surface of the detector. If one uses the master laser also as a local oscillator, one can reduce the amount of components necessary for such a system. One gets a homodyne system.

The interference pattern fluctuates according to the difference in frequency of the two beams, thereby resulting in an electrical signal coming out of the detector in the form of a frequency modulated wave with the modulation frequency being equal to the Doppler shift of the return beam. The signal processor necessary for the frequency analysis gives an output resolution depending on the processor. For cw-laser Doppler systems normally the Surface Acoustic Wave analyzers are used with a resolution in the order of 20 kHz. These cw-laser Doppler systems are used as ground based systems to get wind profiles in the atmospheric boundary layer. The range resolution depends on the focus size of the telescope used.

With the described laser Doppler method one gets the radial wind component. To determine the magnitude and direction of the horizontal wind, some form of scanning in azimuth and elevation is required (Schwiesow et al., 1985). Lhermitte and Atlas (1961) showed that it is possible to retrieve mean horizontal wind magnitude and direction from radial velocity data around horizontal

circles centered on the vertical axis of the scanner (Figure 3).

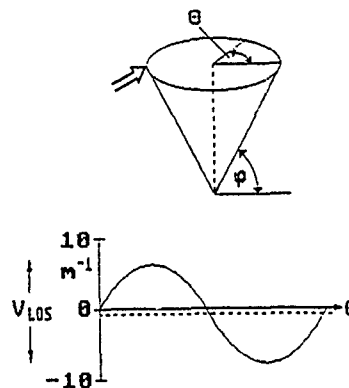


Figure 3: Velocity-Azimuth-Display (VAD) Scan Technique

This type of pattern is called a conical scan because the lidar beam sweeps out a cone with the apex at the scanner. The representativeness of wind values derived from scans over parts of a full circle were determined by Schwiesow et al. (1985). The task is to fit the measured radial velocity  $V_{LOS}$  vs. azimuth data to a function of the form

$$V_{LOS} = |u \sin\theta \cos\phi + v \cos\theta \cos\phi + w \sin\phi|$$

where

$u$  is the east-west wind component,

$v$  is the north-south wind component,

$w$  is the vertical wind component,

$\theta$  is the scan angle clockwise from north, and

$\phi$  is the elevation angle,

using a standard least-square procedure. The calculation can be made also for an azimuth angle region (sector) in the order of 45 degree. As known from other fitting procedures, one needs a number of data points to get the accurate wind vector. As known from the equation shown above at least there are data sets necessary at two different azimuth angles to get the horizontal wind components  $u$  and  $v$ . Figure 3 shows below the different radial wind components versus the azimuth angle. For a homogeneous wind field these components form a sine wave. The deviation from the zero line is direct proportional to the vertical wind component (dashed line).

#### 4. Design of the Compact Laser Doppler Anemometer (LDA)

The following sections describe the design of the laser system, its principle operation and its signal processing.

##### 4.1 Introduction

The block diagram in Figure 4 shows the different units of the compact LDA

## DISCUSSION

### **K. CRAIG**

*Could you comment on the relative merits of Doppler wind profiler radars and dual-polarization radars for sensing of hydrometeor types.*

### **AUTHOR'S REPLY**

*Both techniques can identify many of the possible hydrometeor populations. Since the techniques are fundamentally independent physically, they are complementary rather than competitive with each other. However, the method described in the paper provides cloud flux and mass density information directly, while the polarization techniques do not.*

### **W. BOERNER**

1. Polarization diversity - which polarization state for antenna systems is used?
2. Ambiguity of hydrometeor species could be removed with "complete polarimetric (scattering matrix) radar."
3. Note that polarimetric Doppler signatures are not identical for inhomogeneously swirling hydrometeor masses, e.g., down bursts, tornado, etc.

### **AUTHOR'S REPLY**

1. Our radar does not have dual polarization. The antenna points vertically so horizontal/vertical polarization loses much of its meaning.
2. We agree that polarization capability would remove ambiguity in the particle identification.
3. Interesting point.

### **J. GOLDBIRSH**

1. In further answering Ken Craig's question about the difference between multiple polarization radars and Dr. Gossard's techniques, they both do the same thing. They both measure Drop Size Distribution (DSD); but using different techniques. Dr. Gossard's System is furthermore operational.
2. Have you done anything by way of validation? At rain rates of 4 mm/h and greater, a ground based rain gauge disdrometer could be very helpful for validation.

### **AUTHOR'S REPLY**

*We intend to employ the technique at higher rain rates; however at the wavelength we are using (33 cm), the "clear air" backscatter quickly becomes obscured by the cloud backscatter at the higher rain rates. At our wavelength the most useful conditions are drizzle and light rain. We hope to get similar data with a 74 cm wavelength radar soon.*

## Digital channel sounder for remote sensing of scatterers in mobile radio environment

Rudolf Werner Lorenz and Gerhard Kadel  
Forschungsinstitut der Deutschen Bundespost Telekom  
D-6100 Darmstadt, Federal Republic of Germany

### 1. INTRODUCTION

Computer programs for the estimation of area coverage in mobile radio are based, at the present time, on the two-dimensional analysis of diffraction along the direct path between base and mobile stations. Mobile radio propagation, however, is characterized by multipath transmission. Partial waves scattered from mountains or large buildings may reduce the path loss considerably if significant obstructions attenuate the direct wave. Large estimation errors occur in areas where due to heavy obstruction of the direct path a large portion of the received signal is composed of scattered waves. Three-dimensional propagation models are to be developed to improve prediction in these crucial areas. This requires the availability of wide-band measurement results to determine the scattering from obstacles in the terrain for estimation of multipath power distribution.

Several channel sounders having bandwidths of 5 MHz or more have been described in the literature, e.g. [1]. A pseudo-random sequence (PNS) is transmitted and the impulse response (IR) is gained by correlation of the received signal with the replica of the PNS. Surface-acoustic-wave devices (SAW) are used for correlation. These set-ups suffer, however, from the following drawbacks:

- The sensitivity is poor. Due to the large bandwidth it is difficult to get reliable results in areas where the path loss is large.
- Internal reflections of the SAW devices result in poor dynamic range of the IRs.
- The wider the bandwidth the larger is the amount of data to be recorded and analyzed. This makes it difficult to store the data quickly which is required for the investigation of the time variation of the received signal. Moreover, the amount of data impedes the analysis of large measurement campaigns.
- Because of the limited radio spectrum, it is very difficult to perform wideband radio transmission without interference of or by other radio services.

A new channel sounder, called "RUSK 400", has been developed. Its bandwidth is as low as 400 kHz. The correlation is performed by digital signal processing. The dynamic range and the sensitivity are larger than achieved by SAW devices. On the other hand, the resolution of the IR is as poor as 5  $\mu$ s compared to 0,2  $\mu$ s or more by the set-up described in [1].

RUSK 400 is capable of measuring complex IRs. The main purpose for its development was to gain data for system simulation of the new Pan-European digital mobile radio transmission system, the GSM-system [2]. Nevertheless, RUSK 400 is suitable to achieve useful estimation of the three-dimensional multipath power distribution and its allocation to obstacles in the terrain. This is demonstrated in the following.

### 2. THE CHANNEL SOUNDER

#### 2.1 Multipath propagation in mobile radio

It is well-known that radio coverage in a deep valley having steep slopes is often better than in a flat valley having moderate slopes. The scattering at the opposite slope depends on its steepness, its

roughness, its size and the angles of incidence. Its contribution to the received signal depends on the obstructions in the surroundings of the mobile. It is most likely that a large portion of power is transmitted via scattering at the slope, if

- there is free line of sight (LOS) from the mobile to the slope,
- the direct LOS between mobile and base station is heavily obstructed, and,
- there is free LOS from the base station to the same area of the slope which is seen from the mobile.

Two-dimensional propagation models considering only diffraction theory at wedges of the direct path fail in these cases. Planning of mobile radio cells requires not only the estimation of the path loss but also of frequency selectivity in case of wide-band radio transmission. The duration of the IRs should not exceed a specified value which is determined by the performance of equalizers in the receiver. Otherwise, the mobile radio communication is deteriorated by intersymbol interference even if the received power well exceeds the noise level.

#### 2.2 Correlation measurement

In case of RUSK 400 the maximum resolvable excess delay  $\tau$  is limited to  $T = 127 \mu$ s, the period of the PNS. The IR is gained not by direct crosscorrelation of the received signal with the replica of the PNS but by multiplication of the Fourier Transform ( $\mathcal{F}$ ) of the received signal with the conjugate complex of the  $\mathcal{F}$  of the replica of the PNS. This yields shorter signal processing time. A further advantage of this procedure is that equalization of the transfer function of the entire set-up and pulse shaping of the IR can be performed without spending extra processing time. For this purpose the transfer function of the entire set-up is to be measured by back-to-back connection before the radio propagation measurement is started. The  $\mathcal{F}$  of the PNS is then multiplied with the reciprocal of the  $\mathcal{F}$  of the set-up transfer function and the  $\mathcal{F}$  of the desired pulse shape.

It turned out that the equalization of the transfer function of the entire set-up improved the dynamic range of RUSK 400 considerably. It avoids distortions arising especially from the double balanced mixer and from the power amplifier at the transmitter, e.g. AM-PM conversion. Therefore, back-to-back measurements are to be repeated whenever components within the set-up have been replaced, even after variation of the signal input-level at the power amplifier. This is the reason why the power amplifier has to operate during back-to-back measurements at the output power to be adjusted in radio operation. Good shielding between transmitter and receiver is necessary to avoid spurious interference paths in back-to-back operation which falsifies not only the calibration of power levels but also the transfer function of the set-up. The latter reduces the dynamic range considerably. For pulse shaping a cosine filter with roll-off factor of  $\gamma = 1$  has been chosen. This ensures low sidelobes of the IRs and also approximates the GSM spectrum well (Fig.1).

Discrete samples of the complex IR are computed in real time by the signal processor of RUSK 400 and recorded in increments of 1  $\mu$ s at a total duration of  $T = 127 \mu$ s. Together with information on vehicle location the data are stored on the hard disk of a vibration proof PC. A maximum repetition rate of 22.86 ms was achieved. A detailed description of the set-up is given in [3,4].

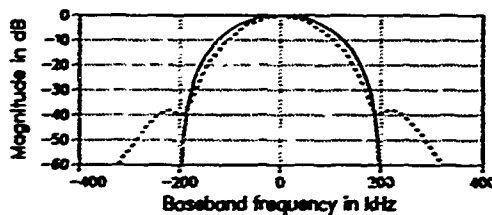


Fig.1 Cosine shaped transfer function of the channel sounder (solid line) and power spectrum envelope of the GSM-system signal (dashed line).

### 2.3 Dynamic range

Fig.2 shows two examples of IRs measured by connecting transmitter and receiver back to back. No multipath propagation should occur in this case and the shape of the IR should be determined by the Fourier transform of the cosine filter. The receiver input power levels were -70 dBm and -90 dBm, respectively. Nevertheless, spurious signals occur due to quantization distortions of the digital processing and due to noise in the analogue components. The level difference between the minimum of the IR and the highest peak of the noise is defined as the dynamic range of the receiver. The dynamic range is a function of the input power level. In Fig.3 mean and minimum dynamic ranges are plotted versus input power. These results were gained from 1,000 IRs measured at each input level. The dotted line gives the average dynamic range. The continuous curve in the middle depicts the minimum dynamic range gained from the measured 1,000 IRs. The lower dash-dotted line indicates the threshold which has been chosen for further evaluations of the measured IRs. This threshold is indicated by the dotted line in Fig.2. Signal components below are set to zero.

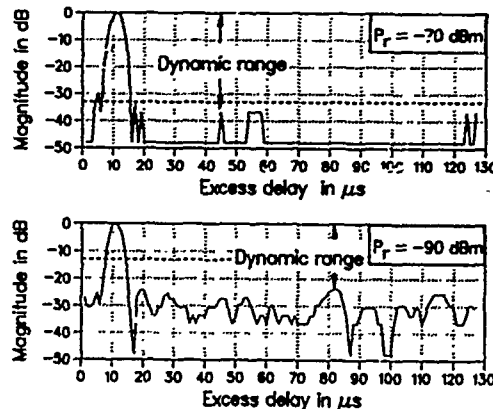


Fig.2 Examples of two impulse responses at high and low power levels of the received signal.

### 3. CALIBRATION OF THE PATH LOSS

In the following we describe the complex IR by the function  $h(\tau, x)$  in terms of excess delay  $\tau$  at location  $x$ . In case of a moving vehicle care must be taken that the displacement of the mobile during the measurement of  $h(\tau, x)$  is sufficiently small. The measurement of one IR lasts about  $2T = 254 \mu s$ , the double of the period of the PNS. The local variation of the standing wave pattern of the superimposed partial waves can be neglected if the displacement of the mobile within the time interval  $2T$  is less than  $\lambda/40$ . Therefore, the following condition must be met:

$$\frac{v_{max}}{km/h} \leq \frac{106}{f/GHz} \quad (1)$$

where  $v_{max}$  is the maximum speed of the mobile and  $f$  is the radio frequency.

The power received at the location  $x$  is given by

$$P_r(x) = c \int_{-\infty}^{\infty} |h(\tau, x)|^2 d\tau \quad (2)$$

where  $c$  is a calibration constant and  $T = 127 \mu s$  is the period of the PNS. As described in section 2.2, the IR  $h(\tau, x)$  is computed by correlation of the received signal with the replica of the PNS. The mean received power  $P_r(x)$  can be measured by a thermal power meter averaging the received modulated RF signal. The calibration constant  $c$  can be determined from  $P_r(x)$  and  $h(\tau, x)$  by back-to-back measurement and application of Eq.(2). This procedure enables us to determine by RUSK 400 the absolute value of the received power.

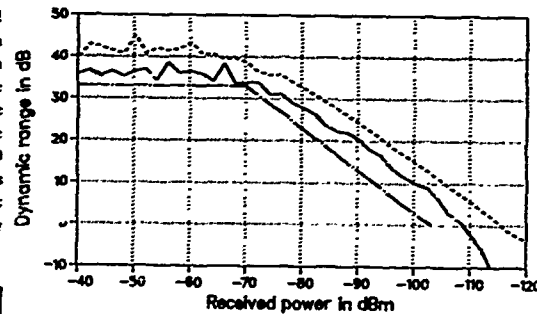


Fig.3 Dynamic range of the channel sounder

A key objective of propagation measurements is the determination of the basic transmission loss

$$L(x) = 10 \lg P_t - 10 \lg P_r(x) + 10 \lg G_t + 10 \lg G_r \quad (3)$$

where  $P_t$  is the transmitter power and  $G_t$  and  $G_r$  are the isotropic gains of the transmitter and receiver antennas, respectively. For computing  $L(x)$  it is necessary to have knowledge of  $G_t$  and  $G_r$  as accurate as possible. The antennas for the measurement should be the same as those which are provided by the mobile radio service. Therefore, a monopole mounted in the middle of the car roof was used for the measurements. The gain of the monopole is in general lower than the gain valid for the same monopole being mounted on a very large flat conducting plane. This is due to the finite extension of the roof and its vaulting. The determination of the gain was done by measurement of  $L(x)$  on a flat test range at short path lengths.

A measured example is plotted in Fig.4 (oscillating curve). The result was compared with a two-ray model considering reflection on plane earth characterized by its dielectric constant  $\epsilon_r$  and its conductivity  $\kappa$ . Agreement between measurement and theory was improved when the reduction of the power density of the reflected ray due to the roughness  $\Delta h$  of the earth's surface was taken into account by the experimental specular reflection coefficient of the earth [5]. The effective antenna gain was determined by fitting the two curves by proper selection of the parameters. This process was performed for several different base station antenna heights. The experimental analysis was repeated using CW-measurement equipment. The same

measurements were carried out on the 1.8-GHz band using similar antennas. The best fit was achieved in both cases for  $\epsilon_r=4$ ,  $\kappa=10$  mS/m and  $\Delta h=0.1$  m. The gain of the mobile antenna obtained by this method was about 2.6 dB smaller than the value given in the manufacturer's specification which is based on a monopole mounted on a large perfectly conducting plane.

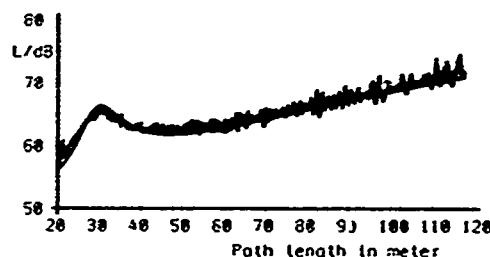


Fig.4 Measured and fitted two-path model transmission loss for determination of the antenna gain of the mobile station. Parameters:  $\epsilon_r = 4$ ,  $\kappa = 10$  mS/m and  $\Delta h = 0.1$  m.

#### 4. REMOTE SENSING BY DOPPLER ANALYSIS

##### 4.1 Fundamentals of Doppler analysis

Due to multipath propagation the angles of arrival at the mobile differ. The motion of the mobile causes the frequency shift

$$f_d = (v/\lambda) \cos \alpha \quad (4)$$

where  $v$  is the velocity of the mobile,  $\lambda$  is the wavelength and  $\alpha$  is the angle of arrival of the wave with respect to the direction of motion. The maximum of the Doppler shift is  $f_d = \pm f_{d \max} = \pm v/\lambda$ . However, larger frequency shifts may happen to occur due to moving scatterers, e.g. other vehicles or tree branches. For evaluation of Doppler power spectra IRs are to be recorded within sample intervals

$$\Delta t < 1/(2 f_{d \max}) = \lambda/(2 v) \quad (5)$$

to fulfil the sampling theorem. The displacement of the mobile during the measurement of subsequent complex IRs converts the location

$$x(t) = v(t) t \quad (6)$$

into the recording time  $t$ . We use the notation  $h(\tau, t)$  where  $\tau$  is the excess delay and  $t$  is the time when the IR has been measured. Thus,  $h(\tau, x)$  converts into  $h(\tau, t)$ . The assumption that an IR should be measured while the displacement of the mobile is less than  $\lambda/40$  means that  $t$  can be regarded to be constant within  $T = 127 \mu s$ , the maximum duration of the IR.

To fulfil the sampling theorem according to Eqs.(5,6) the maximum local distance between two subsequently measured IRs should be less than  $\lambda/2$ . The maximum repetition rate of RUSK 400 is 22.86 ms. This results in a maximum speed

$$\frac{v_{\max}}{\text{km/h}} \leq \frac{23.6}{f/\text{GHz}} \quad (7)$$

This condition is more stringent than Eq.(1).

The sampling of the spacial frequency of the standing wave pattern becomes periodic for constant velocity  $v$  of the mobile and constant sampling clock. Then, the Doppler shifts can be calculated by Fourier

transform for every excess delay  $\tau_m$  from a sequence of  $n = 1 \dots N$  complex IRs  $h(\tau_m, t_n)$ . Fourier transform requires a large number  $N \rightarrow \infty$  of subsequently measured IRs. Due to the local variation of the scattering and shadowing objects in the environment of the mobile station, however,  $h(\tau_m, t_n)$  does not represent a stationary statistical process. This is because the angle of incidence  $\alpha$  of the partial waves is a function of location  $x$ . Hence,  $\alpha$  varies with  $t_n$ . Therefore, the Doppler shift  $f_d$  is, according to Eq.(4), no more constant along the measured run. Fourier transform, however, assumes constant  $f_d$ . This is a stringent argument why the analysis is to be restricted to a rather small number  $N$  of measured IRs. In other words, short-term Doppler power spectra are to be determined. This reduces the resolution of  $f_d$ . Depending on the size of scatterers and their distance to the mobile the requirement of stationarity may be violated within run lengths in the order of 10 meters. At 900 MHz this results in a run length of only about 30  $\lambda$ .

The instantaneous Doppler shift can be estimated by the discrete delay-Doppler transfer function [6]

$$H(\tau_m, f_d) = \sum_{n=1}^N g(t_n) h(\tau_m, t_n) \exp(-2\pi j f_d n \Delta t) \quad (8)$$

$g(t_n)$  is an appropriately chosen windowing function to reduce the sidelobes in the Doppler frequency domain. For practical purposes a cosine window has been taken, similar to the cosine filter according to Fig.1 in the transfer function of RUSK 400. This window reduces the first sidelobes of the IRs to about -30 dB below peak level, as depicted in the upper curve of Fig.2.

The average delay power density  $\langle S(\tau, f_d) \rangle$  can be computed by Fourier transform of the autocorrelation function of the IR. It can be estimated also in good approximation by averaging over the magnitudes square of instantaneous delay-Doppler transfer functions:

$$\langle S(\tau_m, f_d) \rangle = \mathcal{F} \{ \text{ACF}(h(\tau_m, t)) \} = \langle |H(\tau_m, f_d)|^2 \rangle \quad (9)$$

where  $\mathcal{F}$  denotes the Fourier transform and ACF the autocorrelation function.

The following restrictions hold for determination of the angles of incidence of the partial waves at the mobile receiver:

- The  $N$  sampling functions  $h(\tau_m, t_n)$  cover a relatively short total time interval  $T_T = N \Delta t$ . The FFT results in  $N$  sample functions  $H(\tau_m, f_{d,n})$ . The Doppler frequency interval between two adjacent spectral samples is  $\Delta f_d = 1/(N \Delta t)$ .
- The cosine function (Eq.(4)) results in a left-right ambiguity of the angle of arrival. The estimation is restricted to  $|\alpha|$ :

$$S(|\alpha|) = \sin(|\alpha|) \cdot S(f_d) \quad (10)$$

$$\text{for } f_d = f_{d \max} \cdot \cos \alpha$$

- Because of the nonlinear relation between  $f_d$  and  $\alpha$  the samples of  $\alpha$  are not equidistant. For  $|\alpha| = 0$  and  $|\alpha| = \pi$  the resolution becomes very poor.

##### 4.2 General restriction of the resolution of the delay-Doppler power spectra

Restricted bandwidth  $B$  of the channel sounder and limited number  $N$  of measured sampling functions of the IRs  $h(\tau_m, t_n)$  confine the resolution of the delay-Doppler power spectra:

- The bandwidth of RUSK 400 is limited to  $B = 400$  kHz. The cosine filter (Fig.1) reduces the zero-value interval of the IR in time domain to  $4/B = 10 \mu s$ .

- The total interval of the measured ensemble is confined to  $T_{T1}$ . The FFT yields  $N$  spectral lines being  $\Delta f_d = 1/T_{T1}$  apart from each other. The larger  $T_{T1}$  becomes the higher is the resolution of the Doppler power spectrum. The cosine window  $g(\nu_d)$  in Eq.(8) results in a zero-value of the Doppler frequencies of  $4/T_{T1}$ . Therefore, three adjacent spectral lines are generated by one received partial wave.

Fig.5 shows the "cell of resolution" achieved by Doppler analysis of the measured IRs.

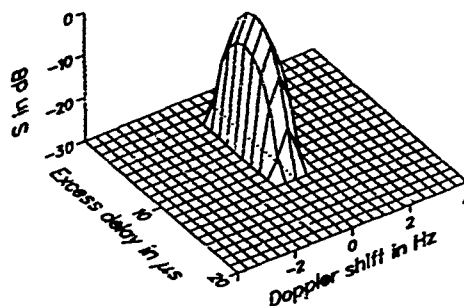


Fig.5 Resolution of the Doppler analysis for one partial wave depicting the "cell of resolution" obtained by RUSK 400.

#### 4.3 Reliability of Doppler power spectrum estimation

A special model of the Doppler power spectrum was first described by Jakes [7,8]. It assumes uniformly distributed angles of arrival  $\alpha$   $[0...2\pi]$  with a large number of partial waves each of them transmitting equal power. These assumptions result in the Doppler power spectrum

$$S_D(f_d) = \frac{1}{\pi f_{d \max} \sqrt{1 - (f_d/f_{d \max})^2}} \quad \text{for } |f_d| \leq f_{d \max} \quad (11)$$

Fading simulators have been developed to test the performance of mobile radio equipment. One of the important specifications of the simulator is the determination of the Doppler power spectra. The Jakes model was one of several Doppler power spectra which were specified by the working group COST 207 [9]. The digital frequency-selective fading simulator DFS 6/15, which is described in [10], approximates the Jakes model very well. The stochastic modulation in the fading simulator is stationary in contrast to the "real world". DFS 6/15 has been used to investigate the reliability of the power spectrum estimation by measurements with RUSK 400 and evaluation of Eqs. (8-10). The total time interval  $T_{T1}$  was chosen such that at the simulated velocity of the mobile a runlength of about 2.4 m was recorded, that is about  $7\lambda$  in the 900-MHz band. Care was taken that the sampling theorem Eq.(7) was fulfilled. The results are presented in Fig.6 where  $S(|\alpha|)$  is plotted in polar diagram. Because of the low resolution at  $|\alpha| \approx 0$  and  $|\alpha| \approx \pi$  the curves are not plotted in these parts. The mirror symmetry of the continuous and dotted curves indicate the left-right ambiguity. Ensembles of sufficient large number  $N$  of IRs should result in  $S(|\alpha|) \approx \text{const.}$  One ( $K=1$ ) short-term power spectrum (Fig.6a) or averaging over two ( $K=2$ ) power spectra (Fig.6b) yields no good estimation. Averaging over  $K=5$  or  $K=10$  Doppler power spectra (Fig.6c and d) indicate good estimation of  $S(|\alpha|) \approx \text{const.}$  Similar results were gained by

application of the ACF on only one but longer total time interval  $K \cdot T_{T1}$ . In other words, the reliability of estimation of the Doppler power spectrum is equivalent if either it is gained by averaging over  $K$  Doppler power spectra computed from  $K$  different ensembles of  $N$  IRs ( $\gamma_{m-f_d}$ ), each of them having the total interval length  $T_{T1}$ , or Eq.(9) is applied on one larger ensemble having the total interval length  $K \cdot T_{T1}$ .

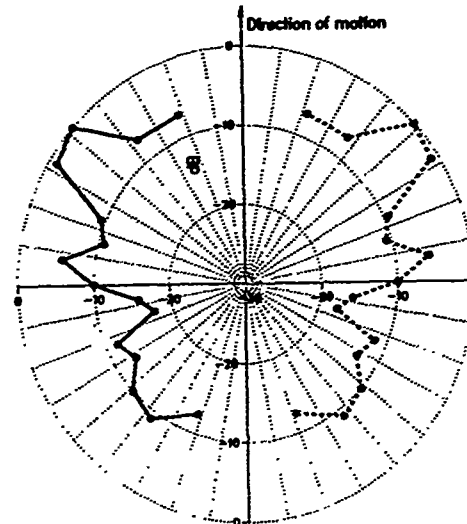


Fig.6 a Estimation of  $S(|\alpha|)$  based on one ( $K=1$ ) short-term Doppler power spectrum  $S(f_d)$ .

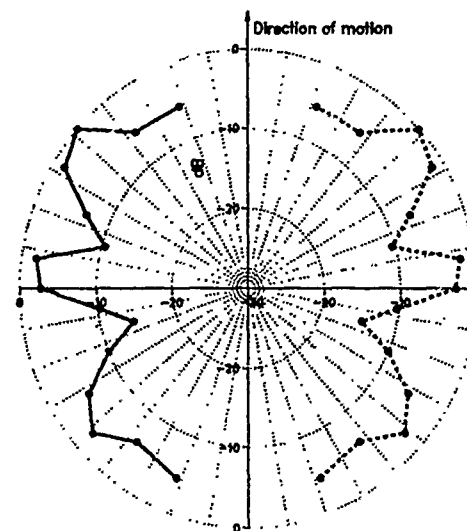


Fig.6 b Estimation of  $S(|\alpha|)$  based on the average  $\langle S(|\alpha|) \rangle$  of  $K=2$  uncorrelated Doppler power spectra  $S(f_d)$ .

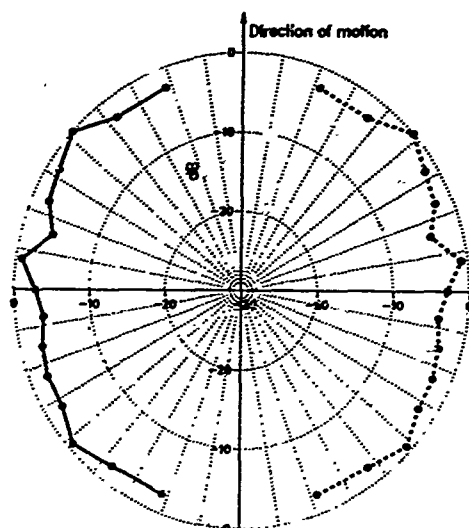


Fig.6 c Estimation of  $S(|\alpha|)$  based on the average  $\langle S(|\alpha|) \rangle$  of  $K=5$  uncorrelated Doppler power spectra  $S(f_d)$ .

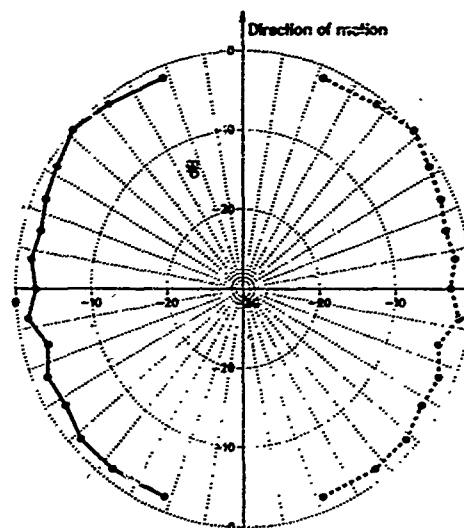


Fig.6 d Estimation of  $S(|\alpha|)$  based on the average  $\langle S(|\alpha|) \rangle$  of  $K=10$  uncorrelated Doppler power spectra  $S(f_d)$ .

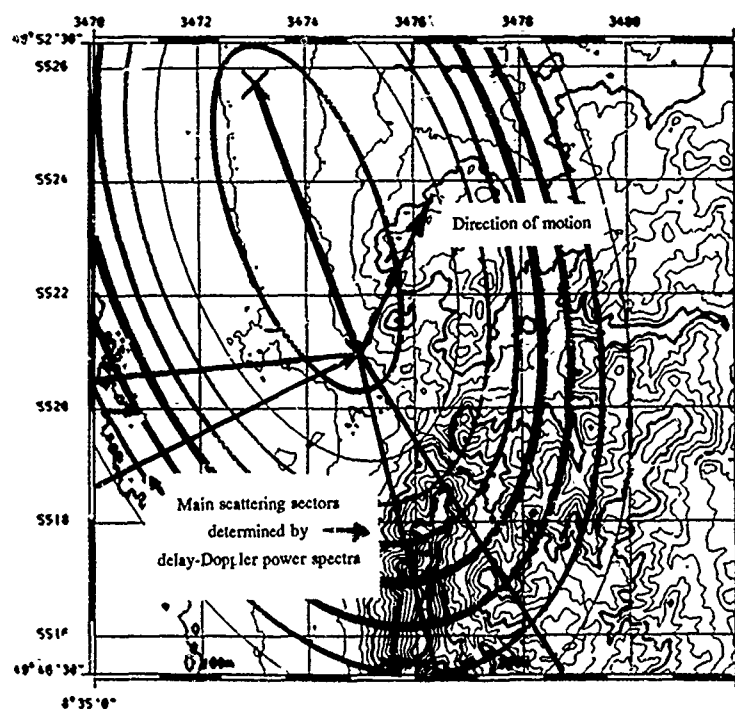


Fig.8 Map of the area in Darmstadt where the delay-Doppler power spectrum depicted in Fig. 7 was measured. The scattering mountains are situated in the sector towards south-south east.

In mobile radio environment, the stationarity of the fading does not allow for long measured runs as explained above. The estimation of angles of arrival could be improved, however, if identical runs were measured several times and the measured ensembles of  $IRs h(r_m, t_m)$  were uncorrelated. This was investigated and it was found that the correlation between different measurements taken at the identical run was 0.25 and less. Therefore, a reasonable estimation can be achieved by averaging  $S(r, \alpha)$  over 5 to 10 measurements at an identical location.

#### 4.4 Results determined by Doppler analysis.

An example measured at 943 MHz in the city of Darmstadt, Germany, is shown in Fig.7. The base station height was 50 m above ground. The path length was 5 km and the direct path was not

obstructed by terrain undulations. Nevertheless, at the location of the mobile station direct LOS towards the base station was obstructed by houses of a residential area. In the opposite direction, however, there was quite a good view towards the north-eastern slopes of the Odenwald mountains. The distance mobile-slopes was about 3 to 4 km. This results in an excess path length of 6 to 8 km and excess delay of 20 to 27  $\mu s$ , respectively. These values are varified in the mean IR shown in Fig.7. Fig.8 depicts a map of the area, the locations of the base and the mobile stations and direction of the motion of the vehicle. The area where the scattering occurs can be estimated from  $S(r, \alpha)$ . In spite of the left-right ambiguity the sectors in Fig.8 doubtless allow for allocation of the scattering slope, because the left sector is situated in a completely flat area.

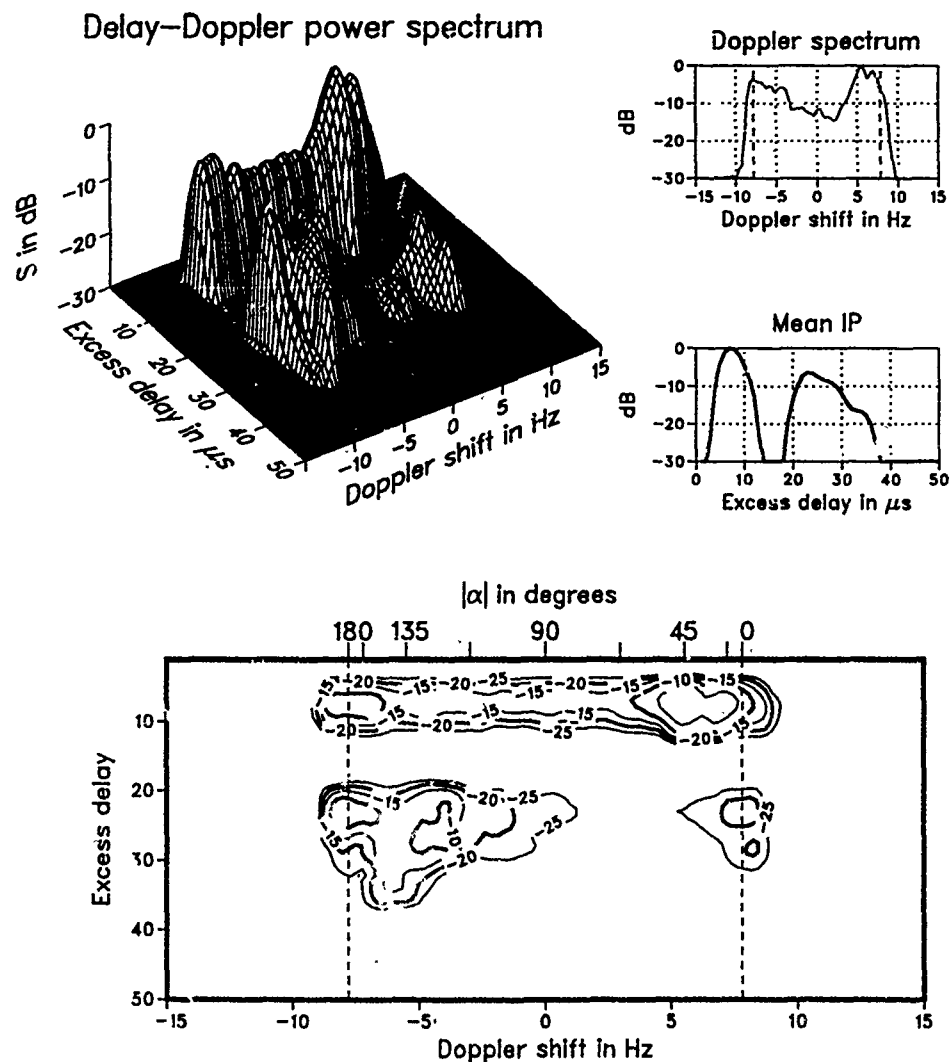


Fig.7 Delay-Doppler power spectrum measured at the edge of a residential area in the city of Darmstadt, Germany. The direct path was obstructed by houses and trees. The echoes are caused by mountain slopes to which free line of sight existed from the mobile and from the base station.

A good means for checking the excess-path length ellipses was a measurement in Mannheim where the direct path was heavily obstructed. A very large facade of a power station resulted in a two-path model with excess delay of about 17 $\mu$ s and large stable magnitude of the scattered path. A directional antenna was used at

the base station to exclude prominent scatterers in other directions as much as possible. Fig.9 shows the map and the ellipses superimposed. The location of the power station between the northern bank of the river Rhine and the southern part of the ellipses is verified rather well.

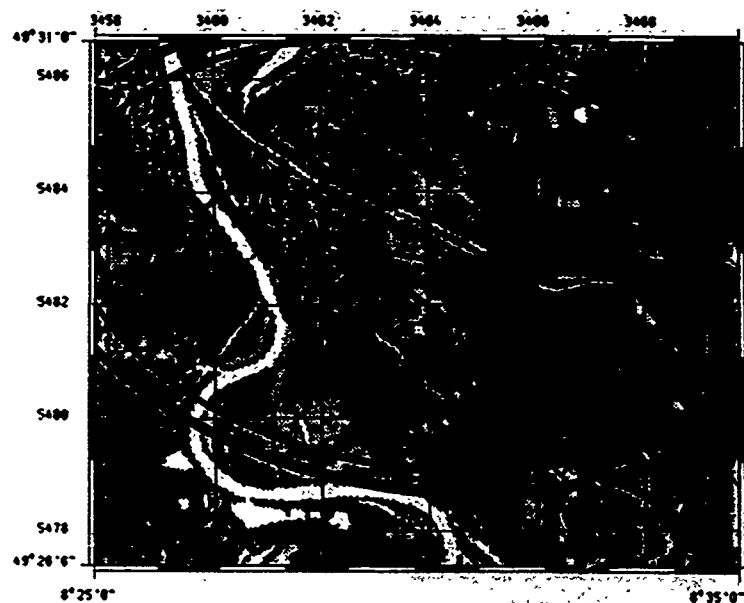


Fig.9 Map of the area of Mannheim where the direct path was heavily obstructed and scattering at the facade of a large power station was predominant. The building is situated at the north bank of the Rhine where the ellipse runs tangential to the river.

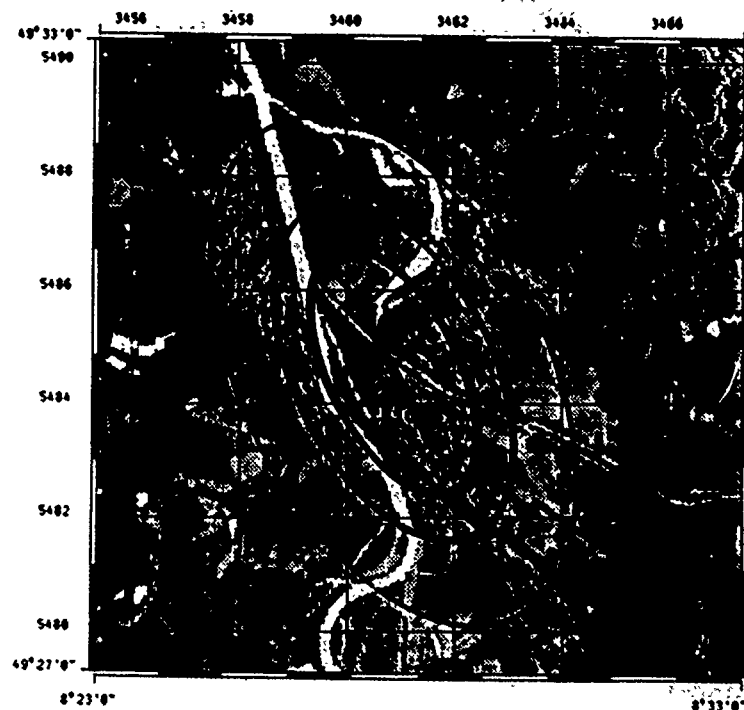


Fig.11 Map of the area where the measurement depicted in Fig.10 was taken. The scatterers are located somewhere close to the ellipses. The direction of the scatterers cannot be determined because of secondary scattering in the vicinity of the mobile.

Another example is depicted in Fig.10 showing the evaluation of a measurement which was taken in the industrial harbor area of Mannheim, Germany. The terrain is flat. The radio frequency was 943 MHz. The base station antenna height was 30m above ground. The path length was 3 km. There was free LOS from the base station antenna to the area where the measurement was taken, however, the path was obstructed by 2 to 4 % or high industrial buildings in the vicinity of the mobile. The location where the measurement was performed is close to the rivers Rhine and Neckar. The rivers and big harbor basins allow for long, unobstructed paths to large store-

houses and chemical complexes of the BASF company, oil refineries and power stations. Their large facades cause reasonable reflections and excess delays up to 25  $\mu$ s were observed, i.e. excess path lengths up to 7.5 km. However, the three-dimensional plot and the contour plot in Fig.10 do not allow for estimation of the angles towards these obstacles. This is because multiple scattering at the relatively small facades in the vicinity of the mobile modify the angles of arrival and broaden the sectors within which the long-excess delay partial waves would be received if there were no obstructions close to the mobile.

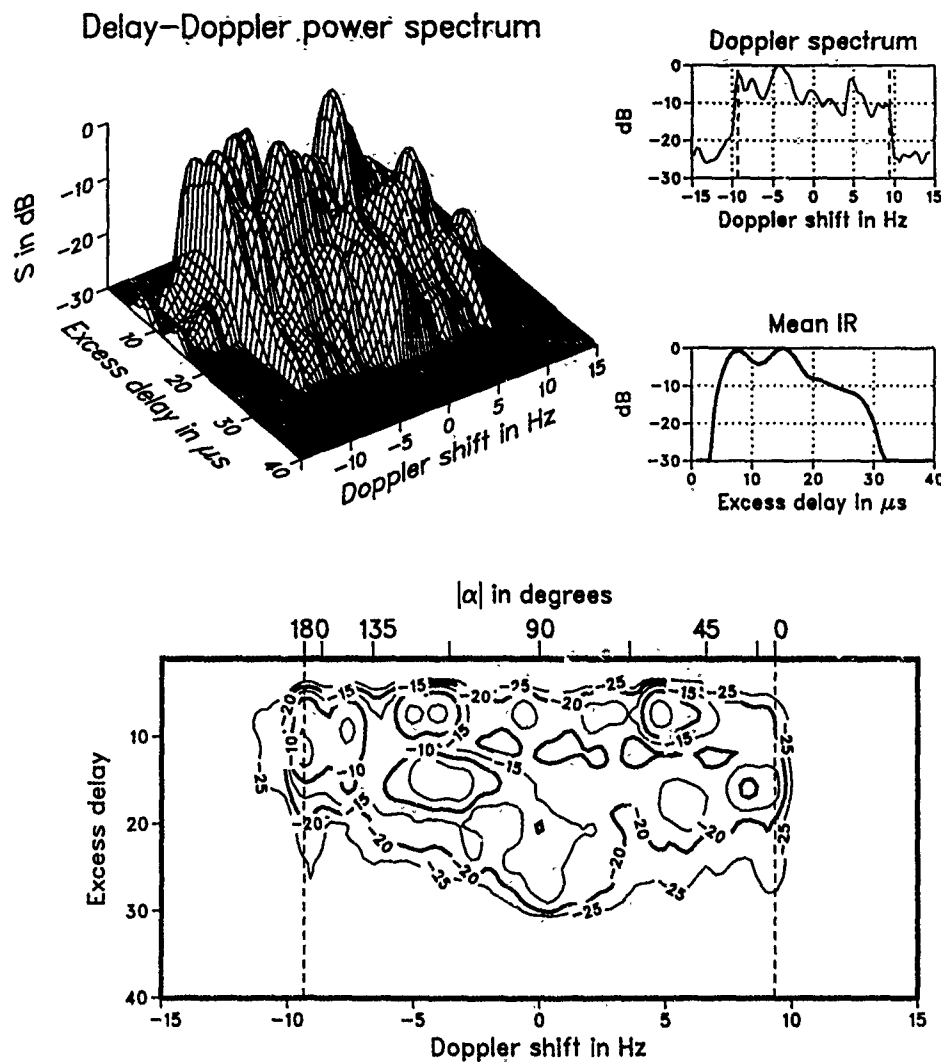


Fig.10

Delay-Doppler power spectrum measured in an industrial area in the city of Mannheim, Germany. The echoes are caused by the facades of large industrial complexes. Secondary scattering at small facades in the vicinity of the mobile modify the angles of arrival at the mobile.

#### 4.5 Conclusions for application of RUSK 400 for remote sensing by Doppler analysis in mobile environment

The examples have demonstrated that scattering in the vicinity of the mobile may strongly modify the angles of arrival. The Doppler analysis is applicable only if there is reasonable free LOS from the location of the mobile to the scattering obstruction. Then, RUSK 400 can be applied for the quantitative analysis of the contributions of scatterers to multipath propagation in mobile radio.

The angle of arrival cannot be determined in areas where the direct LOS to the scattering objects is obstructed. It is still possible, however, to locate these obstructions on confocal ellipses because additional excess delays due to multiple scattering in the vicinity of the mobile can be neglected compared to long excess delays which are resolved by RUSK 400. Fig.11 shows the map of the harbor of Mannheim where the measurement depicted in Fig.10 was performed. The widths of the ellipse lines indicate the magnitude of the echoes. The position of the scattering objects can be found somewhere on the ellipses.

#### 5. Summary

A channel sounder called RUSK 400 was described. It is capable to record complex impulse responses (IRs) in mobile environment. Thanks to digital signal processing RUSK 400 measures IRs with large dynamic range. RUSK 400 has been calibrated carefully to allow for quantitative analysis. Doppler analysis of the measured results can be performed because the data are stored rapidly, and, therefore, the sampling theorem can be fulfilled. For determination of delays the resolution is restricted to about 5  $\mu$ s because of the small bandwidth of only 400 kHz. Nevertheless, the resolution is good enough to perform propagation measurements with the goal of improving of propagation models which use topographical terrain data bases.

The determination of angles of arrival is restricted due to the following facts:

- Stationarity of multipath fading allows for the estimation of Doppler power spectra only for short run lengths. The quality of estimation of these short-term spectra is poor. However, it can be improved considerably by averaging over 5 to 10 power spectra measured subsequently along identical runs. It turned out that the individual data of these runs are almost uncorrelated. This is the reason why averaging improved the results considerably.
- The nonlinear relation between Doppler shift and angle of arrival results in poor quality of estimation of the angle of arrival in direction of motion of the mobile.
- Doppler shift does not allow for distinction whether the estimated angle of arrival with respect to the direction of motion is positive or negative.

The shortcomings of poor resolution and left-right ambiguity can be overcome if it is possible to measure complex IRs at the same location by driving in different directions.

RUSK 400 will be used for quantitative determination of magnitudes of waves scattered by terrain slopes. The results will be used to improve automatic field-strength prediction methods and estimation of the delay spread caused by mountains.

The resolution of RUSK 400 is too small for determination of delay parameters in urban microcell environment because of its small bandwidth. For this purpose RUSK 5000 has been developed. This new device is based on the same concept as RUSK 400, i.e. digital signal processing for correlation and recording of complex IRs. The bandwidth of RUSK 5000, however, is 5 MHz. This yields 12.5 times better resolution of delays than RUSK 400. On the other hand, the amount of data to be handled for analysis is increased by the same factor.

#### REFERENCES

- [1] de Weck, J.-P., Ruprecht, J.: Real-time ML estimation of very frequency-selective multipath channels. IEEE Global Communications Conference GLOBECOM'90 (1990), San Diego, USA.
- [2] Lorenz, R.W. and Kadel, G.: Propagation measurements using a digital channel sounder matched to the GSM-System bandwidth. International Conference on Communications ICC'91 (1991) pp. 548-552.
- [3] Hermann, S., Martin, U., Reng, R., Schüssler, H.W. and Schwarz, K.: Ein System für Ausbreitungsmessungen in Mobilfunkkanälen - Grundlagen und Realisierung. Kleinheubacher Berichte (1990) Vol. 34 pp. 615-624.
- [4] Hermann, S., Martin, U., Reng, R., Schüssler, H.W. and Schwarz, K.: High resolution channel measurement for mobile radio. Conference Proceedings EUSIPCO 90, Barcelona (1990) pp. 1903-1906.
- [5] Beckmann, P., Spizzichino, A.: The scattering of electromagnetic waves from rough surfaces. Pergamon Press 1963, pp. 316-321.
- [6] Parsons, J.D. and Bajwa, A.S.: Wide-band characterization of fading mobile radio channels. IEE Proc. Pt. F Vol. 129 (1982) pp. 95-101.
- [7] Jakes, W.C. (Editor): Microwave mobile communications. John Wiley (1974) pp. 20-24.
- [8] Jakes, W.C.: A comparison of specific space diversity techniques for reduction of fast fading in UHF mobile radio systems. IEEE Trans. VT-20 (1971) pp. 81-92.
- [9] COST 207: Digital land mobile radio communications, Final Report. Published by the Commission of the European Communities in the Series on Information Technologies and Sciences (Brussels 1989). ISBN 92-825-9946-9. pp.135-197.
- [10] Schüssler, H.W., Thielecke, H., Preuss, K., and Gerken, M.: A digital frequency-selective fading simulator. Second Nordic Seminar on Digital Land Mobile Radio Communication. Stockholm (1986) pp. 331-336.

# BASIC EQUATIONS OF RADAR POLARIMETRY AND SOLUTIONS THE SENSING OF PROPAGATION PATH POLARIZATION STATE CHANGES

Wolfgang-Martin Boerner, Wei-Ling Yan, An-Qing Xi  
University of Illinois at Chicago, USA  
Department of Electrical Engineering & Computer Science  
Communications & Sensing Laboratory  
UIC-EECS/CSL, M/C 154  
840 W. Taylor St., SEL-4210  
CHICAGO, IL 60680-4348

Yoshio Yamaguchi  
Niigata University, Faculty of Engineering  
Department of Information & Sensing Engineering  
Radar Sensing and Probing Laboratory  
Ikarashi 2-8050, Niigata-Shi 950-21, JAPAN

**Summary:** Basic principles of radar polarimetry are introduced. The target characteristic polarization state theory is developed first for the coherent case using the three step, the basis transformation, and the power (Mueller) matrix optimization procedures. Kennaugh's and Huynen's theories of radar target polarimetry are verified for the monostatic reciprocal case. It is shown that there exist in total five unique pairs of characteristic polarization states for the symmetric scattering matrix of which the two pairs, the cross-polarization null and co-polarization max pairs are identical; whereas, the cross-pol max and the cross-pol saddle-point pairs are distinct. These three pairs of orthogonal characteristic states are also mutually orthogonal on the polarization sphere. The fifth pair, the co-pol null pair lies in the plane spanned by the co-pol max/-cross-pol null and the cross-pol max pairs which determines the target characteristic circle on the polarization sphere reestablishing Huynen's "polarization fork" concept. The theory is verified by an example for which next to the polarization fork also the copolarized and cross-polarized power density plots are presented. In a next step, the partially polarized case for completely polarized wave incidence is presented and compared with the results for the coherent and the partially coherent cases, the latter still being unresolved.

## 1. Introduction

The basic principle of radar polarimetry is based on the concept of characteristic polarization states first introduced by Kennaugh [1], who demonstrated that there exist radar polarization states for which the radar receives minimum/maximum power. This min/max polarization state theory was extended primarily by Huynen [2], who introduced the "polarization fork" concept, and more recently by us [3-9]. With the advent of dual polarization coherent radar [10] and Pol-SAR [11] systems, radar polarimetry has become a subject of recurring and globally intensifying interest in recent years [12-14]. In spite of extensive studies of this theory, a final rigorous and complete formulation still is warranted. Different approaches were introduced for determining these characteristic polarization states by using the voltage

equation [1], the eigenvalue problem of the power scattering matrix [2,4], the unitary transformation techniques [3,6,7], the three-step procedure [3,5], and the Mueller matrix approach for the "degenerate coherent Stokes vector case" [8,9]. All of these methods are compared and it is shown how each of them contributes partially for a complete understanding, although more approaches may still be required for completely resolving all unanswered questions for the coherent case, for example, such as recently presented in [15]. Whereas, a unique optimization method for the general partially coherent case still does not exist, considerable progress was made in determining an optimization approach for the partially polarized case [8,16] for which it is assumed that the wave incident on a vibrating scatterer is completely polarized. However, it is noted that there exist physical realizability conditions to which the elements of the  $4 \times 4$  Mueller matrices are subjected in order to identify erroneous measurement results such as of scattered waves with degree of polarization greater than unity [17] which apply, in general, also in the partially polarized case.

This paper is concluded by identifying the useful application of these basic principles of radar polarimetry to practical problems in ultra-wideband polarimetric impulsive radar target imaging [18]; to high resolution air/-space-borne POL-SAR imaging [19,20] or in polarimetric matched filtering [20,21].

## 2. Optimal or Characteristic Polarization States for the Coherent Case

The "Optimal Polarization State" problem is to find such polarization states of the transmitted and received waves for a target of known scattering matrix  $[S]$ , that the voltage developed across the receiving antenna terminals is maximized (or minimized).

### 2.1 The three-step optimization approach

This method enables one to treat symmetric, asymmetric, monostatic and bistatic cases in an identical manner [18] as was first considered in [5].

## Step 1

The total energy density  $P_W$  in the scattered wave [22,23,24,25] is given by

$$P_W = \vec{E}_S^* \vec{E}_S = ([S] \vec{E}_T)^* [S] \vec{E}_T = \vec{E}_T^* [S]^* [S] \vec{E}_T = \vec{E}_T^* [G] \vec{E}_T \quad (1)$$

where  $\vec{E}_S$  and  $\vec{E}_T$  are the scattered and transmitted waves, and the superscript  $(\cdot)^*$  denotes the conjugate and transpose, i.e.,  $(\cdot)^* = (\cdot^T)^*$ .

We need to find such an  $\vec{E}_T$  for which  $P_W$  is an extremum for a given  $[S]$ . It translates into the following eigenvalue problem:

$$[G] \vec{E}_{T,OPT} = \lambda \vec{E}_{T,OPT} \quad (2)$$

with the solution

$$\lambda_{1,2} = \frac{1}{2} [\text{Tr}([G]) \pm \sqrt{\text{Tr}^2([G]) - 4\det([G])}]$$

The eigenvalues  $\lambda_1$  and  $\lambda_2$  are real because the power scattering matrix  $[G]$  is hermitian which agrees with their physical interpretation as power. The eigenvector  $\vec{E}_{T,OPT}$  is the polarization state of a transmitter so that the power in the scattered wave is maximized.

## Step 2

Compute this scattered wave by using the known scattering matrix  $[S]$  and  $\vec{E}_{T,OPT}$

$$\vec{E}_{S,OPT} = [S] \vec{E}_{T,OPT} \quad (3)$$

so that the scattered polarization state  $\vec{E}_{S,OPT}$ , associated with the optimal transmitting polarization state  $\vec{E}_{T,OPT}$ , is completely specified.

## Step 3

In order to ensure polarization match i.e., to receive all of the power contained in the scattered wave, one must adjust the receiver polarization state, which results in

$$\vec{E}_{R,OPT} = \frac{\vec{E}_{S,OPT}^*}{||\vec{E}_{S,OPT}||} = \frac{([S] \vec{E}_{T,OPT})^*}{||[S] \vec{E}_{T,OPT}||} \quad (4)$$

This polarization match (4) completes the three-step optimization process. Note, by using the "three step procedure", we can obtain the maximum polarization state for optimal reception, i.e., for satisfying the condition of the matched two-antenna case, but we cannot determine the other pairs of additionally existing characteristic polarization states, which will be derived next.

## 2.2 The critical point method [7]

This method using the polarization basis transformation formulation can determine all existing characteristic states for which the radar receiver obtains maximum/minimum power backscattered from the targets and for which optimal polarization phase ( $\delta$ ) instabilities may occur. In our

case, the power expression can be written as

$$P = |V|^2 = |\vec{E}_R^T [S] \vec{E}_T|^2 = |\vec{E}_R^T [S'] \vec{E}_T'|^2 \quad (5)$$

where  $'$  represents reference to any new basis (AB) which is obtained after unitary transformation from the original basis (HV). For the co-pol channel, the co-polarized power  $P_C$  can be calculated as

$$\vec{E}_R = \vec{E}_T = \vec{E} \text{ and } \vec{E}_T' = \vec{E}' \text{ as}$$

$$P_C = |V_C|^2 = |\vec{E}^T [S] \vec{E}|^2 = |\vec{E}'^T [S'] \vec{E}'|^2 \quad (6)$$

Similarly, the cross-polarized power  $P_X$  can be calculated for  $\vec{E}_R = \vec{E}_T^\perp = \vec{E}_\perp$  and  $\vec{E}_T' = \vec{E}_\perp^\perp = \vec{E}_\perp'$  with  $(\perp)$  denoting the orthogonal vector as

$$P_X = |V_X|^2 = |\vec{E}_\perp^T [S] \vec{E}|^2 = |\vec{E}_\perp'^T [S'] \vec{E}'|^2 \quad (7)$$

In mathematics, the maximum and minimum of a function can be found at the critical points of the function. Here we apply the critical point method to the power functions (6) and (7). A more direct way of doing so is by diagonalizing the scattering matrix  $[S]$  in functions (6) and (7) by implementing the unitary transformation, i.e., let

$$[S'(AB)] = \begin{bmatrix} S'_{AA} & S'_{AB} \\ S'_{BA} & S'_{BB} \end{bmatrix} = [U]^T \begin{bmatrix} S_{HH} & S_{HV} \\ S_{VH} & S_{VV} \end{bmatrix} [U] \quad (8)$$

where  $S_{HV} = S_{VH}$  and  $S'_{AB} = S'_{BA}$  for the monostatic scattering case.

To diagonalize the scattering matrix  $[S'(AB)]$ , we let  $S'_{AB} = 0$  and find the diagonalizing factor  $\rho_{1,2}$  as:

$$\rho_{1,2} = \frac{-B \pm \sqrt{B^2 - 4AC}}{2A} = |\rho_{1,2}| e^{j\delta_{1,2}} \quad (9)$$

$$\text{where } A = S_{HH}^* S_{HV} + S_{HV}^* S_{VV},$$

$$B = |S_{HH}|^2 - |S_{VV}|^2,$$

$$C = -A^*$$

Therefore, the scattering matrix is in diagonal form

$$[S'(AB)] = \begin{bmatrix} S'_{AA} & 0 \\ 0 & S'_{BB} \end{bmatrix} = \begin{bmatrix} \lambda_1 & 0 \\ 0 & \lambda_2 \end{bmatrix} = [S_d] \quad (10)$$

with

$$\lambda_1 = S'_{AA}(\rho_1) = (1 + \rho_1 \rho_1^*)^{-1} (S_{HH} + 2\rho_1 S_{HV} + \rho_1^2 S_{VV}) e^{2j\psi_1} = |\lambda_1| e^{j\phi_1} \quad (11a)$$

$$\lambda_2 = S'_{BB}(\rho_1) = (1 + \rho_1 \rho_1^*)^{-1} (\rho_1^2 S_{HH} - 2\rho_1^* S_{HV} + S_{VV}) e^{2j\psi_1} = |\lambda_2| e^{j\phi_2} \quad (11b)$$

The function of the power return to the co-pol and cross-pol channels of the

receiver are determined from the bilinear form (5) to become:

- (i) For the function of the power returned to the cross-pol channel ( $\vec{E}_R = \vec{E}_T$ )

$$P_x = |V_x|^2 = |\vec{h}_T^T [S_d] \vec{h}|^2 = (1 + \rho' \rho'^*)^{-2} (|\lambda_1|^2 \rho' \rho'^* - \lambda_1 \lambda_2^* \rho'^2 - \lambda_1^* \lambda_2 \rho'^2 + |\lambda_2|^2 \rho' \rho'^*), \quad (12)$$

where  $\rho'$  is the polarization ratio of the transceiver in the new basis. The critical points are some  $\rho'$ 's with which the first derivative of  $P_x$  with respect to  $\rho'$  and  $\rho'^*$  vanishes. These critical points found in function  $P_x$  are:

$$\rho'_{xn1} = 0 \quad (13a)$$

$$\rho'_{xn2} = \infty \quad (13b)$$

$$\rho'_{xm1,2} = \pm i \left( \frac{\lambda_1 \lambda_2^*}{\lambda_1^* \lambda_2} \right)^{1/2} = \pm e^{j(2v+\pi/2)} \quad (13c)$$

$$\rho'_{xs1,2} = \pm \left( \frac{\lambda_1 \lambda_2^*}{\lambda_1^* \lambda_2} \right)^{1/2} = \pm e^{j2v} \quad (13d)$$

- (ii) For the function of the power returned to the co-pol channel ( $\vec{E}_R = \vec{E}_T$ )

$$P_c = |V_c|^2 = |\vec{h}_T^T [S_d] \vec{h}|^2 = (1 + \rho' \rho'^*)^{-2} (|\lambda_1|^2 + \lambda_1 \lambda_2^* \rho'^2 + \lambda_1^* \lambda_2 \rho'^2 + |\lambda_2|^2 \rho'^2 \rho'^*), \quad (14)$$

the critical points are determined from (14) are

$$\rho'_{cm1} = \rho'_{xn1} = 0, \quad \rho'_{cm2} = \rho'_{xn2} = \infty, \quad (15a, b)$$

$$\rho'_{cn1,2} = \pm \left( -\frac{\lambda_1}{\lambda_2} \right) = \pm \left( \frac{|\lambda_1|}{|\lambda_2|} \right)^{1/2} e^{j(2v+\pi/2)} \quad (15c)$$

Note that the following conditions are satisfied

$$\rho'_{xn1} \rho'_{xn2} = -1 \quad (16a)$$

$$\rho'_{xm1} \rho'_{xm2} = -1 \quad (16b)$$

$$\rho'_{xs1} \rho'_{xs2} = -1 \quad (16c)$$

that means  $\rho'_{xm1}$ ,  $\rho'_{xm2}$  are orthogonal and so are  $\rho'_{xs1}$  and  $\rho'_{xs2}$ ,  $\rho'_{xn1}$  and  $\rho'_{xn2}$ .

#### X-POL Null and CO-POL Maximum States

It can be shown for the monostatic reciprocal case that the X-POL Nulls and the CO-POL Maxima are identical as shown in (15a, b). The power return to the cross/co-pol channels are

$$P_x(\rho'_{xn1}) = P_x(\rho'_{xn2}) = 0 \quad (17a)$$

$$P_c(\rho'_{cm1}) = |\lambda_1|^2 \quad (17b)$$

$$P_c(\rho'_{cm2}) = |\lambda_2|^2 \quad (17c)$$

#### CO-POL Nulls, X-POL Maxima and X-POL Saddles

The  $\rho'_{xm1,2}$  of (13c) are the cross-pol maxima and  $\rho'_{xs1,2}$  of (13d) the cross-pol saddles. The corresponding power returns to the receiver of the cross/co-pol channels are:

$$P_x(\rho'_{xm1,2}) = 1/4(|\lambda_1| + |\lambda_2|)^2 \quad (18a)$$

$$P_c(\rho'_{xm1,2}) = 1/4(|\lambda_1| - |\lambda_2|)^2 \quad (18b)$$

$$P_x(\rho'_{xs1,2}) = 1/4(|\lambda_1| - |\lambda_2|)^2 \quad (18c)$$

$$P_c(\rho'_{xs1,2}) = 1/4(|\lambda_1| + |\lambda_2|)^2 \quad (18d)$$

The  $\rho'_{cn1,2}$  of (15c) are the co-pol nulls, because the power returned to the co-pol channel becomes zero, i.e.,

$$P_c(\rho'_{cn1,2}) = 0 \quad (19)$$

In Table 1 and Figs. 1a/b, the theory is verified by an example for which a symmetric scattering matrix of the form  $[S(HV)] = \begin{bmatrix} 2j & .5 \\ .5 & -j \end{bmatrix}$  was used, also used in [5,6], is presented.

TABLE 1: Results of critical point method for the example of  $[S] = \begin{bmatrix} 2j & 0.5 \\ 0.5 & -j \end{bmatrix}$

	new basis(AB)		old basis(HV)						power	
	$\rho'$		$\rho$		$\vec{g}$					
	$ \rho $	$\delta^\circ$	$ \rho $	$\delta^\circ$	$g_0$	$g_1$	$g_2$	$g_3$	$P_x$	$P_c$
$\rho_{yn1}$	0	arb.	0.4142	90.0	1.0000	0.7071	0.0000	0.7071	0	4.871
$\rho_{xn2}$	$\infty$	arb.	2.4142	-90.0	1.0000	-0.7071	0.0000	-0.7071	0	0.629
$\rho_{xm1}$	1.0000	90.0	1.0000	0.0	1.0000	0.0000	1.0000	0.0000	2.25	0.50
$\rho_{xm2}$	1.0000	-90.0	1.0000	180.0	1.0000	0.0000	-1.0000	0.0000	2.25	0.50
$\rho_{xs1}$	1.0000	0.0	0.4142	-90.0	1.0000	0.7071	0.0000	-0.7071	0.50	2.25
$\rho_{xs2}$	1.0000	-180.0	2.4142	90.0	1.0000	-0.7071	0.0000	0.7071	0.50	2.25
$\rho_{cn1}$	1.6684	-90.0	1.4142	-159.2	1.0000	-0.3333	-0.8819	-0.3333	1.75	0
$\rho_{cn2}$	1.6684	90.0	1.4142	-20.7	1.0000	-0.3333	0.8819	-0.3333	1.75	0

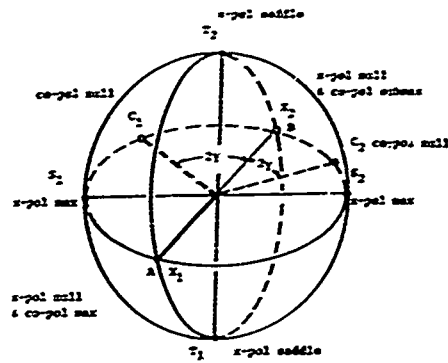


Fig. 1a The characteristic polarization states on the Poincaré sphere of Example (1) referenced to the new basis (AB) for the scattering matrix  $[S] = \begin{bmatrix} 2j & 0.5 \\ 0.5 & -j \end{bmatrix}$  with the characteristic polarization ratios:

$$\begin{aligned} \rho'_{xn1} = \rho'_{cn1} = 0, (X_1), \rho'_{xn2} = \rho'_{cn2} = \infty \\ (X_2), \rho'_{xm1,2} = \pm j (S_1, S_2), \rho'_{xs1,2} = \pm 1 \\ (T_1, T_2), \rho'_{cn1,2} = \pm 1.668j (C_1, C_2). \end{aligned}$$

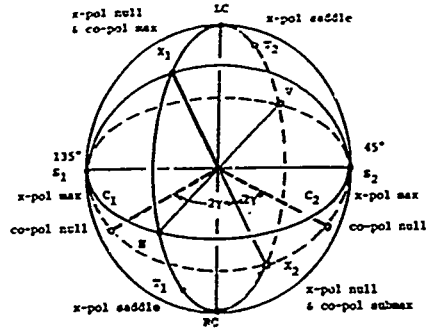


Fig. 1b The characteristic polarization states on the Poincaré sphere referenced to the old basis (HV) for the scattering matrix  $[S_1]$  of the same Example with the characteristic polarization ratios:

$$\begin{aligned} \rho_{xn1} = \rho_{cn1} = 0.414 e^{j90^\circ} (X_1), \\ \rho_{xn1} = \rho_{cn2} = 2.414 e^{-j90^\circ} (X_2), \\ \rho_{xm1,2} = \pm 1 (S_1, S_2), \rho_{xs1} = 0.414 e^{-j90^\circ} (T_1), \\ \rho_{xs2} = 2.414 e^{j90^\circ} (T_2), \\ \rho_{cn1} = 1.414 e^{-j159^\circ} (C_1), \\ \rho_{cn2} = 1.414 e^{-j20.7^\circ} (C_2), \end{aligned}$$

and the geometric parameters:

$$\nu = 0.0, \gamma = 30.9, \delta_m = 90.0, \alpha_m = 22.5, \phi = 0.0, \tau_m = 22.5$$

### 2.3 Optimization approach using Stokes vector and Stokes reflection matrices formulae with example [8,9]

Using the Lagrange multiplier method applied to the received power expressed in terms of the Stokes reflection matrices  $[\bar{H}_c]$ ,  $[\bar{H}_x]$  and  $[\bar{H}_2]$ , respectively; this method enables one to obtain characteristic polarization states for the symmetric (reciprocal), asymmetric (unreciprocal), monostatic and bistatic cases.

#### Coherent one-antenna case

For the coherent one-transceiver-antenna case (monostatic), we can derive the received power separately for the co-pol channel and the x-pol channel, respectively, as follows [8,9]

$$P_c = |\bar{H}_c^T [S] \bar{E}_T|^2 = \bar{g}_T^T [\bar{H}_c] \bar{g}_T / |\bar{g}_T|^2 \quad (20a)$$

where  $||\cdot||$  indicates the norm, with the Stokes reflection matrix  $[\bar{H}_c]$  of the co-pol channel given by:

$$[\bar{H}_c] = ([A]^{-1})^T \{ [S] \otimes [S]^* \} [A]^{-1} = [C] [M] \quad (20b)$$

where  $[M]$  is the Mueller matrix;

$$P_x = |\bar{H}_x^T [S] \bar{E}_T|^2 = \bar{g}_T^T [\bar{H}_x] \bar{g}_T / |\bar{g}_T|^2 \quad (21a)$$

where the symbols  $\otimes$  and  $\perp$  denote the Kronecker product [26] and the orthogonal channel, and the Stokes reflection matrix  $[\bar{H}_x]$  of the cross-pol channels is given by

$$[\bar{H}_x] = ([A]^{-1})^T \begin{bmatrix} 0 & 0 & 0 & 1 \\ 0 & -1 & 0 & 0 \\ 0 & 0 & -1 & 0 \\ 1 & 0 & 0 & 0 \end{bmatrix} \{ [S] \otimes [S]^* \} \quad (21b)$$

where

$$[C] = \frac{1}{2} \begin{bmatrix} 1 & 0 & 0 & 0 \\ 0 & 1 & 0 & 0 \\ 0 & 0 & 1 & 0 \\ 0 & 0 & 0 & -1 \end{bmatrix}, [X] = \frac{1}{2} \begin{bmatrix} 1 & 0 & 0 & 0 \\ 0 & -1 & 0 & 0 \\ 0 & 0 & -1 & 0 \\ 0 & 0 & 0 & 1 \end{bmatrix}$$

#### Coherent two-antenna case

For the case that one antenna system serves as a transmitter and the other as the receiver (coherent bi-static) including slightly bi-static (monostatic separated antennas), the optimum received power  $P_2$  using the matching condition

$$\bar{H}_R = \bar{E}_S^* / |\bar{E}_S| \quad (22)$$

is given by:

$$P_2 = \bar{g}_T^T [\bar{H}_2] \bar{g}_T \quad (23a)$$

where

$$[\bar{H}_2] = [\bar{H}_c] + [\bar{H}_x] = \begin{bmatrix} 1 & 0 & 0 & 0 \\ 0 & 0 & 0 & 0 \\ 0 & 0 & 0 & 0 \\ 0 & 0 & 0 & 0 \end{bmatrix} [M] \quad (23b)$$

For simplicity, we always choose the transmitting wave  $\bar{g}_T$  as a normalized, completely polarized wave; i.e., the components of  $\bar{g}_T$  satisfy the following constraint

$$g_{T0} = \sqrt{g_{T1}^2 + g_{T2}^2 + g_{T3}^2} = 1 \quad (24)$$

The received power expressions  $P_c$ ,  $P_x$  and  $P_2$  are functions of  $g_{T1}$ ,  $g_{T2}$ , and  $g_{T3}$  which are subject to the above constraint. This requirement dictates the use of the method of Lagrangian multipliers to find the extremum of the received power  $P$  [8].

Let our equation of constraint be given by:

$$\Phi(g_{T1}, g_{T2}, g_{T3}) = \sqrt{g_{T1}^2 + g_{T2}^2 + g_{T3}^2} - 1 = 0 \quad (25)$$

then the Lagrangian multipliers method for finding the extreme value of the power  $P$  ( $g_{T1}$ ,  $g_{T2}$ ,  $g_{T3}$ ) results in

$$\frac{\partial P}{\partial g_{Ti}} - \mu \frac{\partial \Phi}{\partial g_{Ti}} = 0 \quad (i = 1, 2, 3), \quad (26)$$

#### Example

The scattering matrix  $[S]$ , also used for Section 2.2 (Table 1 and Fig. 1), and the Stokes reflection matrices  $[\bar{R}_c]$ ,  $[\bar{R}_x]$ ,  $[\bar{R}_2]$  and  $P_c, P_x, P_2$  are obtained by solving (20b), (21b), (23b), (20a), (21a), and (23a), respectively.

Applying the Lagrangian Multiplier method on  $P_c$  yields four solutions (two maxima and two nulls), and on  $P_x$  yields six solutions (two maxima, two saddle points, and two nulls, where the latter are identical to the co-pol max pair). Optimizing  $P_2$  yields two solutions, which are the same as the co-pol max pair, which are identical to those determined by the critical point method listed in Table 1 and illustrated in Figs. 1a,b and Fig. 2

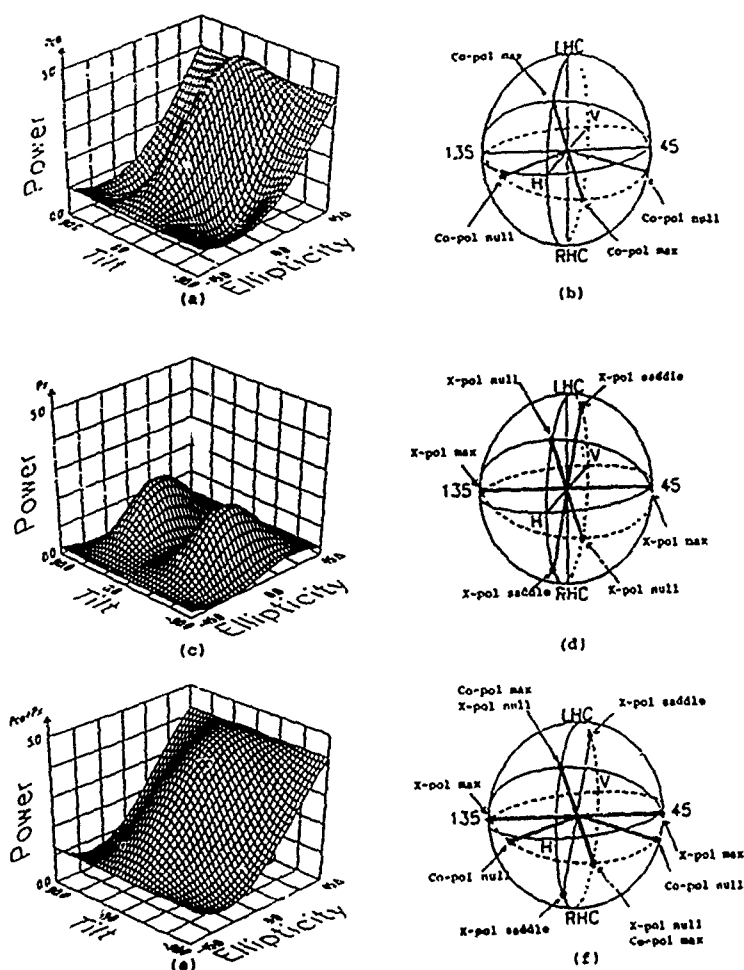


Fig. 2 Polarization characteristics for the scattering matrices  $[S]$  and  $[M]$   
 (a) Co-polarized power spectrum, (d) X-polarization states  
 (b) Co-polarization states, (e) Power spectrum for matched  
 (c) X-polarized power spectrum two-antenna case  
 (f) Generalized polarization Fork

### 3. Optimal Polarization States for the Partially Polarized Case

Consider a time-dependent scatterer which is illuminated by a monochromatic (completely polarized) wave  $\vec{E}_T$ , for which the reflected wave  $\vec{E}_S$  is, in general, non-monochromatic; and therefore, partially polarized. Consequently, the Stokes vector and Mueller matrix formalism will be employed. The following optimization criteria result for the scattered energy density arriving at the receiver, which may be separated into four categories [1]:

- $g_{S0}$  Total energy density in the scattered wave before it reaches the receiver; (27a)
- $pg_{S0}$  Completely polarized part of the intensity; (27b)
- $(1-p)g_{S0}$  The unpolarized part; (27c)
- $(1+p)g_{S0}/2$  Maximum of the total receivable intensity. (27d)

There are three types of energy density terms, next to the total energy density  $g_{S0}$ , that can be optimized according to (27b, 27c, 27d).

#### 3.1 Optimization of the adjustable intensity $pg_{S0}$

The energy density  $pg_{S0}$ , contained in the completely polarized part, is called the adjustable intensity because one may adjust the polarization state of the receiver to ensure the polarization match. We can rewrite the scattering process index notation as [16,18]:

$$g_{Si} = \sum_{j=0}^3 M_{ij} g_{Tj} \quad (28a)$$

where  $j = 0, 1, 2, 3$ . The adjustable intensity  $pg_{S0}$  has the following property:

$$pg_{S0} = \left( \sum_{i=1}^3 g_{Si}^2 \right)^{1/2} = \left[ \sum_{i=1}^3 \left( \sum_{j=0}^3 M_{ij} g_{Tj} \right)^2 \right]^{1/2} \quad (29)$$

where  $g_{Ti}$ 's are the elements of the Stokes vector of the transmitting wave. The partial derivative of  $(pg_{S0})^2$  with respect to  $g_{Tk}$  can be derived as:

$$\begin{aligned} \frac{\partial (pg_{S0})^2}{\partial g_{Tk}} &= \sum_{i=1}^3 \frac{\partial g_{Si}^2}{\partial g_{Tk}} = 2 \sum_{i=1}^3 g_{Si} M_{ik} \\ &= 2 \sum_{i=1}^3 \sum_{j=0}^3 M_{ij} M_{ik} g_{Tj} \end{aligned} \quad (30)$$

For optimizing the adjustable intensity, we apply the method of Lagrangian multipliers, which yields

$$\begin{aligned} \frac{\partial (pg_{S0})^2}{\partial g_{Tk}} - \mu \frac{\partial \Phi}{\partial g_{Tk}} &= 2 \sum_{i=1}^3 \sum_{j=0}^3 M_{ij} M_{ik} g_{Tj} \\ - \mu g_{Tk} &= 0 \end{aligned} \quad (31)$$

where  $\Phi$  is the constraint equation of (25). Equation (31) is a set of inhomogeneous linear equations in  $g_{T1}(\mu)$ ,  $g_{T2}(\mu)$  and

$g_{T3}(\mu)$ . Then, the straightforward solutions for the  $g_{Ti}(\mu)$  are three functions of  $\mu$ .

Substituting  $g_{Ti}(\mu)$ , ( $i = 1, 2, 3$ ) into the constraint condition of (25) leads to a sixth-order polynomial equation of  $\mu$ . For each  $\mu$  value, we calculate  $g_{T1}$ ,  $g_{T2}$ ,  $g_{T3}$ , and  $pg_{S0}$  according to the formula in (31). The largest (or smallest) intensity is the optimal intensity, the corresponding  $\vec{g}_T$  is the optimal polarization state of the transmitted wave.

#### 3.2 Minimizing the noise-like energy density term: $(1-p)g_{S0}$

An unpolarized wave can always be represented by an incoherent sum of any two orthogonal completely polarized waves of equal intensity [9], which leads to a 50% efficiency for the reception of the unpolarized wave. We would like to minimize the noise-like energy so that as much energy as possible may be received. The total energy density of the unpolarized part of the scattered wave is given by:

$$(1-p)g_{S0} = g_{S0} - pg_{S0}$$

$$= \sum_{j=0}^3 M_{0j} g_{Tj} - \sqrt{\sum_{i=1}^3 \left( \sum_{j=0}^3 M_{ij} g_{Tj} \right)^2} \quad (32)$$

Hitherto, no simple way was found giving the analytic closed form solution for the minimum solution, instead, computer numerical analysis must be used.

#### 3.3 Maximizing the receivable intensity in the scattered wave: $1/2(1+p)g_{S0}$

The total receivable energy density consists of two parts: 100% reception efficiency for the completely polarized part of the scattered wave and 50% reception efficiency for the unpolarized part. We may write the following expression for the total receivable intensity:

$$\begin{aligned} 1/2(1+p)g_{S0} &= pg_{S0} + 1/2(1-p)g_{S0} \\ &= \frac{1}{2} \sum_{j=0}^3 M_{0j} g_{Tj} + \frac{1}{2} \sqrt{\sum_{i=1}^3 \left( \sum_{j=0}^3 M_{ij} g_{Tj} \right)^2} \end{aligned} \quad (33)$$

Also, this equation can only be solved using numerical analysis.

#### 3.4 Numerical example

Consider the following Mueller matrix, which corresponds to experimental data taken for a combined collimator-radiometer system [7].

$$M = \begin{bmatrix} 0.7599 & -0.0623 & 0.0295 & 0.1185 \\ -0.0573 & 0.4687 & -0.1811 & -0.1863 \\ 0.0384 & -0.1714 & 0.5394 & 0.0282 \\ 0.1240 & -0.2168 & -0.0120 & 0.6608 \end{bmatrix} \quad (34)$$

The polarization states  $\vec{g}(\mu)$  and its intensities, are displayed in Table 2 and illustrated in Fig. 3.

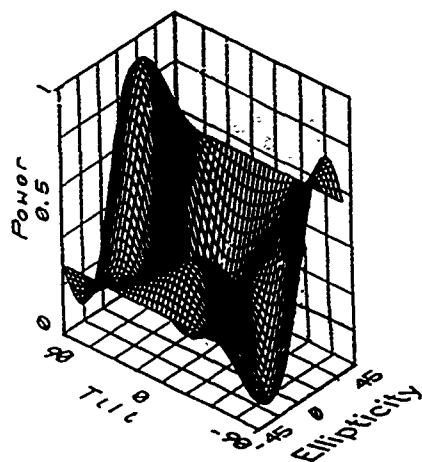


Fig.3 Polarization dependence of the adjustable intensity in terms of the tilt and ellipticity angles.

The noise-like energy  $(1 - p)g_{S0}$  was minimized and the receivable intensity  $=(1 + p)g_{S0}$  was maximized by numerical analysis as shown in Table 3.

#### Interpretation and Comparison of Results

We have demonstrated that there exist several different approaches for determining the optimal polarization states in radar polarimetry. For the coherent case, the basis transformation method [6,7] of Section 2.2 is the most complete one for determining the characteristic polarization states of the given  $2 \times 2$  Sinclair matrix  $[S(A,B)]$ , whereas, the Lagrangian multiplier method using the  $4 \times 4$  Stoke reflection matrices  $[\vec{M}_c]$ ,  $[\vec{M}_x]$  and  $[\vec{M}_2]$  is most suitable for determining the

optimal polarization states of the given target as is shown in Section 2.3 and verified for one example. It is, thus, shown and proven that Kennenough's target characteristic operator theory of the coherent case is correct and Huynen's polarization fork concept is valid in the coherent case. For the partially coherent case, no complete optimization procedures for determining the optimum polarization states yet exists; however, in Section 3, it was shown that for the partially polarized case, for which the wave incident on the scatterer is completely polarized, a solution can be found. In all of the cases investigated, it was demonstrated that, also for the partially polarized case, there exist five pairs of characteristic polarization states [18]; however, whereas, for the coherent case ( $p = 1$ ) the absolute (normalized) power maximum at the co-pol  $\max(\rho_{cm1})$  and co-pol null  $(\rho_{cn1,2})$  locations, respectively becomes

$$P_{\max}^C(\rho_{cm1})/m^2 = 1 \quad (35a)$$

$$P_{\text{cn1,2}}^C(\rho_{cn1,2})/m^2 = 0 \quad (35b)$$

we find that for the partially polarized case ( $0 > p > 1$ ) the maximum normalized value will always be reduced by  $(1 - p)/2$  and the achievable minimal normalized power can never be less than  $(1 - p)/2$ , and that according to (27d) for the completely unpolarized case ( $p = 0$ ), the minimal and maximal achievable normalized powers become equal and in the limit approach by  $g_{S0} = .5$ ; i.e., the power density plot is flat in the extreme unpolarized case as illustrated in Fig. 4.

Thus, from the comparison of our results, we conclude that the optimal polarization state theory will also be highly useful for treating the partially dual polarization radar reception problem. In extension of previous results it was found that there exist eight distinct characteristic polarization states for the symmetric matrix case, the three pairs of orthogonal pairs whose diameters are mutually orthogonal on

Table 2. Roots, intensities and Stokes vectors for the characteristic polarization states of the adjustable intensity optimization

Root Number	Root $\mu$	Intensity $pg_{S0}$	$g_{T0}$	$g_{T1}$	$g_{T2}$	$g_{T3}$
1	0.8019	0.9677	1	-0.5807	0.3378	0.7408
2	0.5739	0.6942	1	0.6134	-0.4203	-0.6686
3	0.3548	0.5923	0.997	0.3894	-0.8702	0.2918
4	0.3170	0.5342	1	0.0221	0.6619	-0.7492
5	0.0734	0.2776	1.006	0.8710	0.4486	0.2301
6	0.0633	0.2404	1.009	-0.6812	-0.4777	-0.5707

TABLE 3. The intensities and the Stokes vectors of the optimal polarization states of the different types of energy density

Method	Intensity	$g_{T0}$	$g_{T1}$	$g_{T2}$	$g_{T3}$
Maximum of $pg_{S0}$	0.9677	1	-0.5807	0.3375	0.7408
Minimum of $(1 - p)g_{S0}$	-0.07	1	-0.6108	0.3893	0.6894
Maximum of $\frac{1}{2}(1 + p)g_{S0}$	0.9311	1	-0.5602	0.3090	0.7686

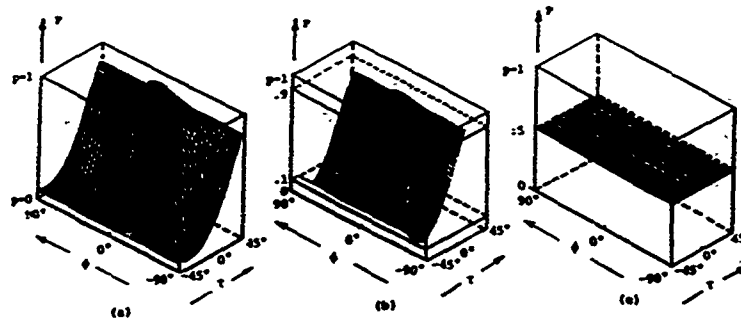


Fig. 4 Dependence of received power density plots on degree of polarization  $p$ : (a)  $p = 1$ , (b)  $p = .8$ , and (c)  $p = 0$ .

the polarization sphere: the X-pol null pair (identical to co-pol max pair), the x-pol max pair and the x-pol saddle (turning point) pair. In addition, there exists a pair of co-pol nulls lying in the plane spanned by the x-pol-null and the x-pol max pairs, the target characteristic plane with the line (diameter) joining the two x-pol nulls bisecting the angle between the two co-pol nulls on this target characteristic circle. As a result of these unique polarization fork properties, one can show that once the two co-pol nulls have been found, the entire polarization fork can be recovered; i.e., for the description of a radar target we require the specification of two distinct points on the polarization sphere, whereas, only one for the description of a completely polarized wave. In particular, our polarization transformation ratio  $p$  formulation is in complete agreement with Huynen's formulation and shows, given a measured matrix  $[S]$ , that the Huynen target characteristic parameters  $m$ ,  $\phi_m$ ,  $\nu$ ,  $\gamma$ ,  $\delta_m$  and  $\alpha_m$ , can be uniquely determined; or inversely, given these parameters the scattering matrix  $[S]$  can be uniquely reconstructed [7]. Hence, the resulting Huynen fork concept represents a unique example of a fundamental polarimetric radar inverse problem.

#### 4. Acknowledgement

The financial support for this research was provided by the US Office of Naval Research, Contract Nos. N00014-80-C-0773 and N00014-90-J-1405, the US Army Research Office, Contract N. DAAL-03-89-K-0116, and a US Senior Scientist Fellow Award of the Alexander von Humboldt Stiftung, Bonn, FRG.

#### 5. References

- [1] E.M. Kennaugh, "Effects of Type of Polarization on Echo Characteristics", The Ohio State University, Antennas Laboratory, Columbus, OH, Reports 381-1 to 394-24, 1949-1954 and Report 389-12 (M.Sc. Thesis) in particular.
- [2] J.R. Huynen, "Phenomenological Theory of Radar Targets", Ph.D. dissertation, Rotterdam: Drukkerij Bronders-Offset N.V., 1970.
- [3] W.M. Boerner and M.B. El-Arini et.al., "Polarization Dependence in Electromagnetic Inverse Problems", IEEE Trans. A&P, Vol. AP-29, pp. 262-271, 1981.
- [4] M. Davidovitz and W-M. Boerner, "Extension of Kennaugh's Optimal Polarization Concept to the Asymmetric Matrix Case", IEEE Trans. A&P, Vol. AP-34, No. 4, pp. 569-574, Apr. 1986.
- [5] A.B. Kostinski and W-M. Boerner, "On Foundations of Radar Polarimetry", IEEE A&P, Vol. AP-34, No. 12, pp. 1395-1404, also see: comments by H. Mieras, pp. 1470-1471, and author's reply, pp. 1471-1473, Dec. (1986).
- [6] A.P. Agrawal and W-M. Boerner, "Redevelopment of Kennaugh's Target Characteristic Polarization State Theory Using the Polarization Transformation Ratio Formulism for the Coherent Case", IEEE Trans. A&P, Vol. AP-27, No. 1, pp. 2-14, Jan 1989.
- [7a] W-M. Boerner and A-Q. Xi, "The characteristic radar target polarization state theory for the coherent monostatic and reciprocal case using the generalized polarization transformation ratio formulation", Archiv der Elektrischen Übertragung; AEU, Vol. 44, No. 4, 273-281, July 1990
- [7b] A-Q. Xi and W-M. Boerner, "Determination of the characteristic polarization states of the target scattering matrix  $[S(AB)]$  for the coherent, monostatic and reciprocal propagation space using the polarization transformation ratio formulation", J. Opt. Soc. Am. A, Ser. 2, Vol. 8, 1991 (in press).
- [8] W-L. Yan and W-M. Boerner, "Optimal Polarization States Determination of the Stokes Reflection Matrices  $[M_p]$  for the coherent Case, and of the Mueller Matrix  $[M]$  for the Partially Polarized Case", Journal of Electromagnetic Waves and Applications, Vol. 5, No. 10, pp. xx-yy, Oct. 1991
- [9] Y. Yamaguchi, K. Sasagawa, M. Sengoku, T. Abe, W-M. Boerner, W-L. Yan and A-Q. Xi, "Characteristic Polarization States of Coherently Reflected Waves Based on the Stokes Vector Formulation in Radar Polarimetry", Japan Journal for Electronics and Communications Engineering (JIEECE), Vol. AP/90-35, pp. 33-36, 1990 July 19.

- [10] D. Giuli, "Polarization Diversity in Radar", Proc. IEEE, Vol. 74(2), pp. 245-269, Feb. (1986)
- [11] J.J. van Zyl, "On the Importance of Polarization in Radar Scattering Problems", Ph.D. Dissertation, California Institute of Technology, Pasadena, CA, Jan. (1986)
- [12] W-M. Boerner, et. al., eds., Inverse Methods in Electromagnetic Imaging, Proc. NATO Advanced Res. Workshop on IMEI, Bad Windsheim, FR. Germany, Sept. 18-24, 1983, NATO-ASI-Series, Series C, Math. & Phys. Sci., Vol. 143, Dordrecht, Holland: D. Reidel Publ. Co., (1985)
- [13] L.W. Root and Matkin, Chairmen/Editors, Proceedings, (Third) Polarimetric (Technology) Workshop, Redstone Arsenal, AL, 1988 August 16-18, GACIAC IIT-RI, 10 W. 35th St., Chicago, IL 60612, (1989)
- [14] W-M. Boerner, et al, eds., Inverse Methods in Electromagnetic Imaging Polarimetry, Proc. NATO-ARW-DIMRP (W-M. Boerner, Director), 1988 Sept. 18-24, Bad Windsheim FRG, NATO-ASI-Series C, (Math. & Phys. Sci.), Dordrecht/Boston: D. Reidel Publ. Co., (1990)
- [15] G.C. McCormick, The theory of polarization diversity systems, J. Elmag. Waves & Applications, Vol. 4, No. 8, pp. 707-725, Aug 1990
- [16] A.B. Kostinski, B.D. James and W-M. Boerner, "On the Optimal Reception of Partially Polarized Waves", J. Optical Society of America, Part A, Optics & Image Sciences, Series 2, Vol. 5, No. 1, pp. 58-64, Jan. 1988
- [17] S.R. Cloude, Group theory and polarisation algebra, Optik, Vol. 78, No. 1, pp. 26-36, March 1986
- [18] W-M. Boerner, W-L. Yan, A-Q. Xi, Basic Equations of Wideband Radar Polarimetry: The characteristic polarization states for the coherent and partially polarized case (tutorial text: 84 printed pages), in J.W. Battles, editor, Handbook of Radar Polarimetry Chapter 2, GACIAC, IIT-RI, Chicago, IL, October 1990.
- [19] W-M. Boerner, B-Y Foo, H.J. Eom, "Interpretation of the Polarimetric Co-Polarization Phase Term( $\phi_{HH}-\phi_{VV}$ ) in High Resolution SAR Imaging Using the JPL CV-990 Polarimetric L-Band SAR Data", Special IGARSS '85 Issue of the IEEE Trans., GE-25, No. 1, pp. 77-82, January (1987)
- [20] A.B. Kostinski, B.D. James and W-M. Boerner, "Polarimetric Matched Filter for Coherent Imaging", Can J. Phys., Vol. 66, Issue 10, Special Issue on Coherent Imaging in Optics, pp. 871-877, Oct. (1988)
- [21a] A.J. Poelman and J.R.F. Guy, Polarization Information Utilization in Primary Radar, in W-M. Boerner, et al: Inverse Methods in Electromagnetic Imaging, Proc. NATO ASI Series C, Vol. C-143, pp. 521-752, D. Reidel Publ. Co., Dordrecht, NL, 1987 (also see: IEE Proc. (F) Comm. Radar & Signal Process. 1984, Vol 131, No 4 (pp 383-396) & No 5 (pp 451-465)).
- [21b] A.J. Poelman and C.J. Hilgers, The Effectiveness of the MULTI-NOTCH LOGIC-PRODUCT Polarization Filters in Radar for Countering Rain Clutter, IEE Proc. (F) Comm. Radar & Signal Process. 1990, Vol. 137 (in print).
- [22] R.M.A. Azzam and N.M. Bashara, Ellipsometry and Polarized Light, Amsterdam: North Holland, (1977)
- [23] M. Born and E. Wolf, Principles of Optics, 3rd Ed., New York: Pergamon Press, (1964)
- [24] R.E. Collin, Ant and Radio Wave Propagation, New York: McGraw Hill, (1985).
- [25] H. Mott, "Polarization in Antennas and RADAR", New York: John Wiley & Sons, 1986.
- [26] A. Graham, Kronecker Products and Matrix Calculus: with Applications, New York: Ellis Horwood, Ltd., 1981.

## ADAPTIVE COMMUNICATIONS POLARIMETRY:

SENSING OF PROPAGATION PATH CHANGES AND ADAPTATION  
TO OPTIMAL PERFORMANCE IN CELLULAR COMMUNICATIONS

Yoshio Yamaguchi  
Niigata University, Faculty of Electronics  
NIIGATA-SHI, T 950-21 Japan

Hyo Joon Eom  
KOREA INSTITUTE OF TECHNOLOGY  
KIT/KAIST-EE/WSL, 23 Ku Song Dong  
YUSUNG GU, TAE-JON-SHI, T 300-31 South Korea

Wolfgang-Martin Boerner  
UNIVERSITY OF ILLINOIS AT CHICAGO  
UIC-EECS/CSL, M/C 154, 840 W. Taylor Str.  
UIC-607-4210, CHICAGO, IL/USA 60607

**Summary:** Commonly in radio communications fixed antenna polarization states are in use also for dual orthogonal polarization channel frequency-reuse operations. The most commonly used antenna polarizations are fixed "linear horizontal/vertical" or "circular left/right-handed" polarization states. However, the communications signal will, in general, suffer from polarization state transformation and depolarization effects caused by scattering, refraction, diffraction, etc., in a complex propagation medium. The polarization state degradation includes all obstructing objects affecting the propagation space, i.e., topology, man-induced structures, vegetation and atmospheric scatter, e.g., fog, rain, hail, etc. In addition, in a multi-path propagation environment such as in cellular communications, time-delayed multiple vector waves of different polarization states simultaneously arrive at the receiver, completely changing the polarization state of the initially transmitted wave. Therefore, the common use of (any) fixed antenna polarizations is certainly far from optimal. Thus, the aim of this paper is to develop an agile polarization state adaptive communications systems approach. This is achieved by designing the received antenna system with completely free, arbitrarily adaptive polarization state, providing the following advantages:

- 1) Maintain matched polarization state conditions resulting in increased steady systems performance;
- 2) Reject undesired signals by adaptively switching receiver antenna state to a polarization state orthogonal to that of the undesired signal;
- 3) Apply polarimetric matched signal filter techniques with space filtering by use of adaptive polarization array antennas, so that the desired signal can be selected within the "main beam".

In view of the rapid advances currently being made in miniature compact electro-optical signal processing device technology, the relatively large and complex adaptive antenna polarization state control and polarimetric matched signal filter systems will soon become miniaturized and

realized, elevating "radar polarimetry" to an indispensable tool also in cellular communications technology.

## 1. Introduction

This paper introduces the basic principle for a polarization agile communications system which adjusts the polarization state of receiving antenna to that of incoming wave. The basic idea is derived from basic principles of radar polarimetry.

In radio communications, fixed polarization states (one or two, being orthogonal to one other) are used for conventional communications systems. Most commonly used polarizations are fixed "linear horizontal/vertical" or "circular left-handed/right-handed" polarization states. However, if a fixed polarization state, say, vertical polarization, is sent through a transmitting antenna, the polarization state changes and then arrives at a receiving antenna as shown in Fig. 1. This

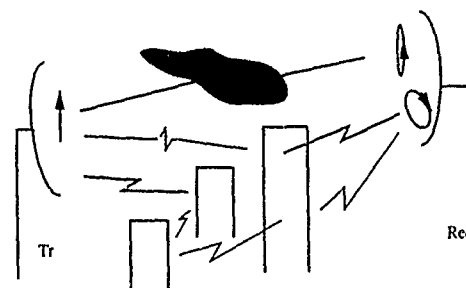


Fig. 1: Polarization degradation in propagation space

change is due to the scattering process in a complex propagation environment. The scatterer includes everything in the propagation space, i.e., buildings, mountains, trees, bushes, or fluctuations in the atmosphere such as rain, fog, hail, etc. In addition, in a multi-path environment

such as a cellular communication, time delayed multiple waves having their own polarization states arrive at the receiving antenna simultaneously. Therefore, the polarization state of the wave incident on a receiving antenna becomes different from that of the transmitted wave as an inevitable consequence, and it will change randomly from one instant to another.

Therefore, the use of a fixed polarization state is not optimal for communications from a view point of polarimetry. The aim of this paper is to develop a polarization state adaptive communications system. Attention is paid to the polarization state of an incoming wave to a receiving antenna. If the polarization of the receiving antenna is matched to it, the received power will be maximized, whereas, if the polarization state is adjusted orthogonal to it, the power will be zero even though there is Poynting power in front of the receiving antenna. In other words, if the polarization state of the receiving antenna could be changed arbitrarily and freely in a controlled feed-back approach, then the following advantages would become available:

- 1) It is possible to maintain the matched polarization state. As a result, the receiver and the system performance will be increased.
- 2) We do not have to take the complex propagation environment into account because we only have to concentrate on the polarization state of incoming wave.
- 3) It is possible to reject the undesired signal by changing the receiving antenna polarization state orthogonal to that of the undesired signal.
- 4) If this polarimetric filtering technique is combined with space filtering (antenna pattern manipulation such as in adaptive array processing), it may be possible to select the desired signal even in the main beam.

The disadvantages are such that:

- 1) This polarimetric system cannot be applied to a non-reciprocal propagation environment.
- 2) The system must measure the polarization state of the incoming wave all the time and adjust the receiving antenna polarization to it which may result in a larger system.

The second advantage may soon be overcome by future advancements and by the rapid development of electro-optic signal processing devices and integrated systems. In the following, we explain the fundamental theory for adaptive communications polarimetry in accordance with basic principles of radar polarimetry.

## 2. Representation of Polarization

The polarization of a wave is defined as the property of the wave describing the

time-varying direction and amplitude of the electric field, specifically, the figure traced as a function of time by the extremity of the field vector at a fixed location in space, as observed along the direction of propagation. In general, the trace is an ellipse. In this section, several parameters and their relations to express elliptically polarized waves are given.

If a single monochromatic plane wave is traveling in the  $z$ -direction, the time dependent electric field vector can be expressed using the two-dimensional column vector description

$$\vec{E}(t) = \begin{bmatrix} E_x(t) \\ E_y(t) \end{bmatrix} = \begin{bmatrix} |E_x| \cos(\omega t + \phi_x) \\ |E_y| \cos(\omega t + \phi_y) \end{bmatrix} \quad (1)$$

where,  $E_x$  and  $E_y$  are the components of the electric field in the  $x$ - and  $y$ -direction, respectively. The tip of the electric field describes an ellipse as shown in Fig. 2. The

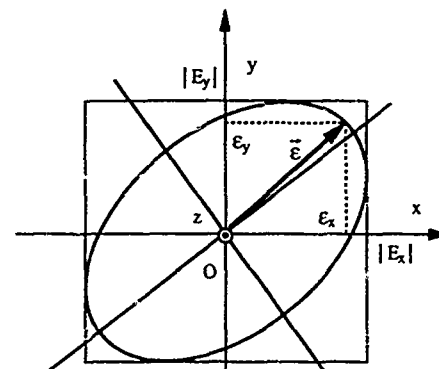


Fig. 2: Trace of electric field vector

sense of rotation is defined by the phase difference  $\phi = \phi_y - \phi_x$  ( $-\pi < \phi < \pi$ ) with  $\phi < 0$  for right handed polarization and  $\phi > 0$  for left handed polarization as shown in Fig. 3.

Now assuming that the  $x$ - and  $y$ -directions coincide with horizontal and vertical directions, respectively, we can define the following parameters,  $\gamma$  and  $\phi$ , after taking a ratio of complex phasors  $E_x$  and  $E_y$ .

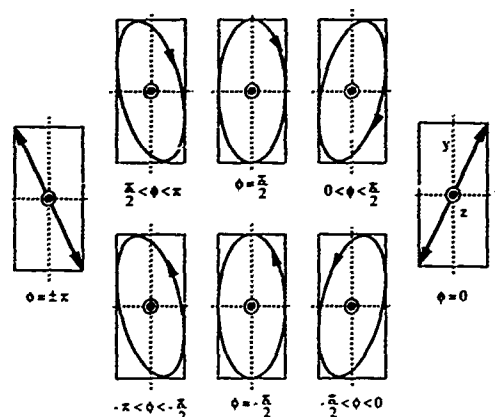
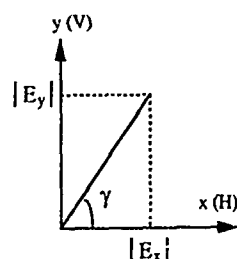
$$p = \frac{E_y(t)}{E_x(t)} = \frac{|E_y|}{|E_x|} \exp(j(\phi_y - \phi_x)) = \tan \gamma e^{j\phi} \quad (2)$$

$$\tan \gamma = \frac{|E_y|}{|E_x|}, \quad 0 \leq \gamma \leq \frac{\pi}{2} \quad (3)$$

$$\phi = \phi_y - \phi_x, \quad -\pi < \phi < \pi \quad (4)$$

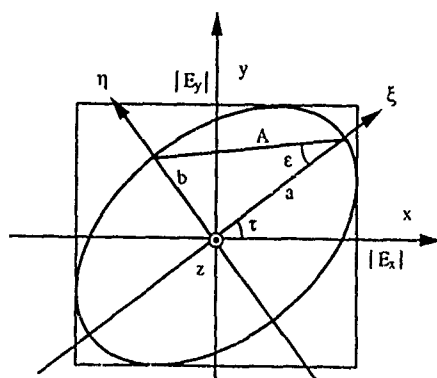
where the angle  $\gamma$  is defined in Fig. 4. Therefore, the expression (1) can be written in terms of  $\gamma$  and  $\phi$  as

$$\vec{E}(A, \gamma, \phi, \phi_x, t) = A \operatorname{Re} \left\{ \begin{bmatrix} \cos \gamma \\ \sin \gamma e^{j\phi} \end{bmatrix} \exp \{ j(\omega t + \phi_x) \} \right\} \quad (5)$$

Fig. 3. Sense of rotation with respect to  $\phi$ Fig. 4: Definition of  $\gamma$ 

$$A^2 = |E_x|^2 + |E_y|^2 \quad (6)$$

Since the trace is of geometric form, it is convenient to employ geometric parameters, tilt angle  $\tau$ , ellipticity  $\epsilon$ , and size  $A$ . The tilt angle represent the angle between the major axis of the ellipse and the x-axis in Fig. 5, while the ellipticity is defined as

Fig. 5: Geometric parameters: ellipticity  $\epsilon$ , tilt angle  $\tau$  and size  $A$ 

$$\epsilon = \tan^{-1}\left(\frac{b}{a}\right), \quad -\frac{\pi}{4} \leq \epsilon \leq \frac{\pi}{4} \quad (7)$$

where  $a$  is the length of the major axis and  $b$  is the length of the minor axis of the ellipse. Hence, eq(1) can be written in terms of these parameters as

$$\vec{E}(A, \epsilon, \tau, \phi, t) = A \begin{bmatrix} \cos \tau & -\sin \tau \\ \sin \tau & \cos \tau \end{bmatrix} \begin{bmatrix} \cos \epsilon \\ \sin \epsilon \end{bmatrix} \cos(\omega t + \phi) \quad (8)$$

The Stokes vector  $\mathbf{g} = (g_0, g_1, g_2, g_3)$  can also represent the polarization state. The components corresponding to the coherent wave expression of eq(1) are defined as

$$\begin{aligned} g_0 &= |E_x|^2 + |E_y|^2 \\ g_1 &= |E_x|^2 - |E_y|^2 \\ g_2 &= 2|E_x||E_y|\cos \phi \\ g_3 &= 2|E_x||E_y|\sin \phi \end{aligned} \quad (9)$$

There exist various sets of basic parameters that can represent a polarization state. There exist strict relations among these parameters. The relations are summarized in Fig. 6.

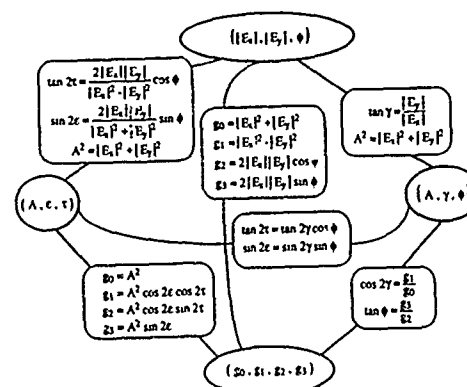


Fig. 6: Relations among parameters representing an elliptic polarization

### The Poincaré Sphere

Next, we introduce the Poincaré sphere to represent a polarization state and the relation among parameters graphically. As is well known any polarization state can be specified as a point on its spherical surface. There exists a one-to-one correspondence between all possible polarization states. Fig. 7 displays the Poincaré sphere and identifies the parameters.

The three axes which constitute a rectangular coordinate of the sphere represent Stokes vector components. The angle  $2\gamma$  is measured from the intersection point of  $+g_1$  axis and the spherical surface to a polarization point  $P$  on the Poincaré sphere. The phase difference  $\phi$  is measured from the equator to the  $2\gamma$  line. It should be noted that the antipodal point on the sphere represents an orthogonal polarization state to a specified polarization state.

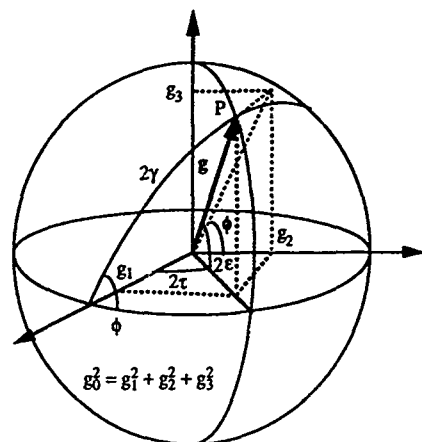


Fig. 7: Poincaré sphere

### 3. Adaptive Communication Polarimetry

Polarimetry utilized the full vector nature of the electromagnetic wave for an intended application. In communications, both transmitting and receiving antennas are separated from each other regardless of the line of sight and/or out of sight propagation environments. Thus, we can model a radio communications system as shown in Fig. 8. The box in Fig. 8

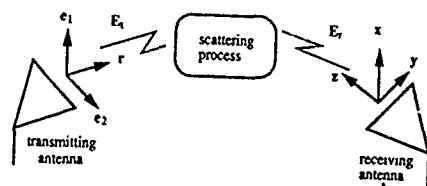


Fig. 8: Radio communications system

represents the scattering process which causes the change of polarization state of the transmitted wave. The scattering process includes reflection, scattering, and diffraction from natural and man-made structures, mountains and hills, or fluctuations within the atmosphere, etc.

Now, in order to examine the polarization state of a wave, we choose a right-handed coordinate system as shown in Fig. 8. In the far field, the transmitted wave and scattered wave can be treated as plane waves. Thus,

$$\begin{aligned} \vec{E}_t &= (E_{t1} \hat{e}_1 + E_{t2} e^{j\phi} \hat{e}_2) \exp j(\omega t + kr + \alpha_t) \\ \vec{E}_r &= (E_{rx} \hat{x} + E_{ry} e^{j\phi} \hat{y}) \exp j(\omega t + kz + \alpha_r) \\ h &= (h_x \hat{x} + h_y e^{j\phi} \hat{y}) \end{aligned} \quad (10)$$

where in all equations,  $\phi$  is the phase difference defined in (4),  $\alpha$  is the absolute phase, subscripts  $t$  and  $r$  denote transmitter and receiver, respectively; and  $h$  is the wave which the receiving antenna would radiate in the  $+z$  direction if it acted as a transmitter. Now, we define the following Jones vector representation, the transmitted electric field component by

$$\vec{E}_t = \begin{bmatrix} \cos \gamma_t \\ \sin \gamma_t e^{j\phi_t} \end{bmatrix} \quad (11)$$

This two-dimensional column vector is called a 'Spinor' representing the wave polarization state and known as the Jones vector in optics. The polarization state determines the polarization ellipse of the wave at a fixed point in space. For example,  $\gamma = 0$  always represents horizontal polarization,  $\gamma = \pi/2$  represents vertical polarization. On the other hand,  $\gamma = \pi/4$  and  $\phi = \pi/2$  represents left handed circular polarization (LHC) if the wave is viewed along the propagation direction and represents right handed circular (RHC) polarization if it is view towards the wave. Therefore, a polarization state given by

$$\frac{1}{\sqrt{2}} \begin{bmatrix} 1 \\ j \end{bmatrix}$$

is LHC for  $h$ , and is RHC for  $E_r$ . The direction of propagation can be recovered from the exponents in (10).

In this paper, we are concerned with the polarimetric information of a scattered wave excluding the amplitude dependence due to path length variations, etc. Since the transmitted polarization state changes due to the scattering process, the scattered wave arriving at the receiving antenna can be written as

$$\vec{E}_r = [S] \vec{E}_t \quad (12)$$

where  $[S]$  represents scattering matrix dependent on propagation environment. This wave induces the antenna terminal voltage

$$V = h^T \vec{E}_r = h^T [S] \vec{E}_t \quad (13)$$

where the notation  $a^T b = a_x b_x + a_y b_y$  is for column vectors, subscript  $T$  denotes the transpose and all quantities are normalized to unity in order to concentrate on polarization properties. The antenna height  $h$  is defined here as a polarization state of the transmitted wave which would result if the receiving antenna were to transmit. Since we cannot control  $E_r$  because it depends on the propagation environment, we can only control the  $h$ . It should be noted that eq(13) is not of an inner product form. The maximum condition for  $V$  is apparently,

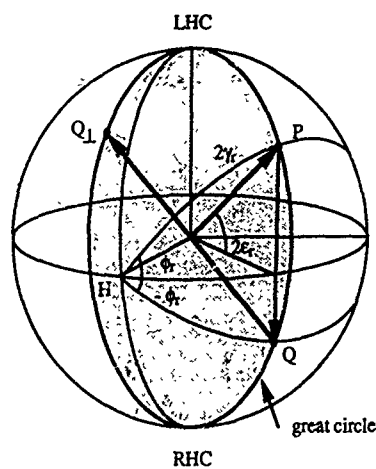
$$h = \vec{E}_r^* \quad (14)$$

where  $*$  denotes complex conjugation. This is the polarization match condition. The complex conjugation to a polarization state reverses the sense of rotation of the corresponding polarization ellipse.

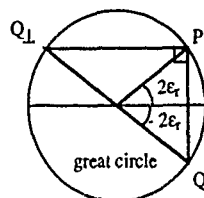
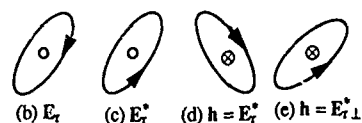
On the other hand, if we do not wish to receive the wave or reject it, it can be achieved by adjusting  $h$  to the orthogonal ( $\perp$ ) polarization state of the incoming wave as

$$h = \vec{E}_{r\perp}^* \quad (15)$$

This important polarization state adaptation theory is explained graphically on the Poincaré sphere in Fig. 9. In the spinor or Stokes vector notations, the scattered wave arriving at the receiving antenna is given by



(a) Poincaré sphere representation



(f) right-angled triangle on great circle

Fig. 9: Graphical interpretation of polarization states

$$E_r = \begin{bmatrix} \cos \gamma_r \\ \sin \gamma_r e^{j\phi_r} \end{bmatrix} \quad \text{or } (g_1, g_2, g_3) \quad (16a)$$

(x - y) plane

the polarization state can be plotted on the Poincaré sphere as a point P as shown in Fig. 9(a). The polarization ellipse as well as the sense of rotation is like Fig. 9(b). Then the complex conjugation is

$$h = E_r^* = \begin{bmatrix} \cos \gamma_r \\ \sin \gamma_r e^{-j\phi_r} \end{bmatrix} \quad \text{or } (g_1, g_2, g_3) \quad (16b)$$

(x - y) plane

by definition. Therefore this point should be located on point Q. The polarization ellipse is the same as (b), however, the sense of rotation is opposite (c). On the other hand, in order to reject the incoming wave, the polarization state of the receiving antenna should be moved to the antipodal point  $Q_1$  in (a) resulting in the polarization ellipse as shown in (e).

The interesting feature is the manner of location of these polarization points. First, one can see that these P, Q, and  $Q_1$  are located on a great circle of the sphere in (a). If the point P is given, the matched condition point Q locates at the symmetric point with respect to the equatorial plane of the sphere, and the mis-matched condition point  $Q_1$  locates at anti-podal point to Q. On the great circle (f), these three points constitute a right-angled triangle with  $Q_1$  being parallel to  $g_2 = 0$  plane. Therefore, if the polarization state of the incoming wave is given, the optimal polarization state is determined on the Poincaré sphere immediately.

#### Example

Let us consider a problem of reflection from an infinite, perfectly conducting flat plate at normal incidence where we have a bistatic antenna communications system. Two experimental facts are known: the returned wave is in the same polarization state as the transmitted one, e.g., changes from RHC to LHC due to a reversal in the direction of propagation, and the fact that the voltage across the receiving antenna is maximal for linear polarizations and zero for circular polarizations. Then if the horizontal polarization is transmitted, we find that

$$E_r = \begin{bmatrix} 1 \\ 0 \end{bmatrix} \quad : \text{Horizontal}$$

$$h = E_r^* = \begin{bmatrix} 1 \\ 0 \end{bmatrix} \quad \Delta \text{ Horizontal} \rightarrow V = [1, 0] \begin{bmatrix} 1 \\ 0 \end{bmatrix} = 1 = \max$$

$$h = E_{r\perp} = \begin{bmatrix} 0 \\ 1 \end{bmatrix} \quad \Delta \text{ Vertical} \rightarrow V = [0, 1] \begin{bmatrix} 1 \\ 0 \end{bmatrix} = 0 = \min$$

On the other hand, if RHC is transmitted, then

$$E_r = [S]E_t = \frac{1}{\sqrt{2}} \begin{bmatrix} 1 & 0 \\ 0 & 1 \end{bmatrix} \begin{bmatrix} 1 \\ j \end{bmatrix} = \frac{1}{\sqrt{2}} \begin{bmatrix} 1 \\ j \end{bmatrix} \quad : \text{LHC}$$

$$h = E_r^* = \frac{1}{\sqrt{2}} \begin{bmatrix} 1 \\ -j \end{bmatrix} \quad \Delta \text{ RHC} \rightarrow V = \frac{1}{2} [1, -j] \begin{bmatrix} 1 \\ j \end{bmatrix} = 1 = \max$$

$$h = E_{r\perp} = \frac{1}{\sqrt{2}} \begin{bmatrix} 1 \\ j \end{bmatrix} \quad \Delta \text{ LHC} \rightarrow V = \frac{1}{2} [1, j] \begin{bmatrix} 1 \\ j \end{bmatrix} = 0 = \min$$

These results satisfy experimental facts

#### Received Power

If the polarization state is not completely matched or mismatched, the received power would not be optimal. We calculated the power variations due to the polarization change, base on the following equation.

$$\text{Power} = V \cdot V^* = |h^T E_r|^2 \quad (17)$$

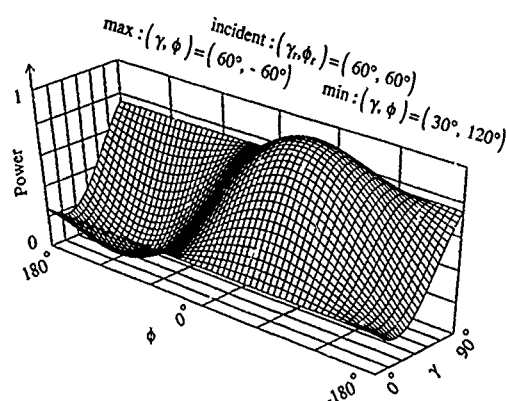


Fig. 10: Received power variation with respect to receiver polarization state  $h$

The parameters  $\gamma$  and  $\phi$ . In the calculated results shown in Fig. 10, the incident wave is assumed to be characterized as  $\gamma = \phi = 60$  degrees. The maximal polarization state is found to be  $(\gamma, \phi) = (60^\circ, -60^\circ)$ , and mismatched point becomes  $(\gamma, \phi) = (30^\circ, 120^\circ)$ .

#### 4. Conclusion

In this paper, we applied basic principles of radar polarimetry to radio communications under the condition that the polarization state of the incoming wave changes according to effects caused by the propagation environment. Since we cannot control the polarization state of an incoming wave, the only possible way to control the receiving power is the polarization state of the receiving antenna. Based on basic principles of radar polarimetry, the matching and mismatching conditions are derived using the Poincaré sphere. We found an interesting relation between the maximal and minimal polarization states with respect to that of the incoming wave, i.e., these points constitute a great circle on the Poincaré sphere and that they form a right-angled triangle on the great circle. Therefore, if the polarization of the incoming wave is given, these maximal and minimal polarization points can be determined graphically on the Poincaré sphere instantaneously. This concept of

adaptive communications polarimetry may be useful not only to cellular radio communication systems, but to fixed-station link radio communication systems suffering from atmospheric fluctuations as well.

#### 5. References

- [1] W-M. Boerner, Wei-Ling Yan and An-Qing Xi, "Basic equations of radar polarimetry and its solutions: the characteristic radar polarization states for the coherent and partially polarized cases", Proc. of the International Society for Optical Engineering, SPIE Vol. 1317 Polarimetry: Radar, Infrared, Visible Ultraviolet, and X-Ray, pp. 16-79, May 15-17, 1990.
- [2] A.B. Kostinski and W-M. Boerner, "On foundations of radar polarimetry", IEEE Trans. Antennas Propag., Vol. AP-34, No. 12, pp. 1359-1403, Dec. 1986.
- [3] IEEE Standard Dictionary of Electrical and Electronics Terms, IEEE, Aug. 1984.
- [4] H. Mott, Polarization in Antennas and Radar, Wiley-Interscience, 1986.
- [5] T. Sekiguchi, Electromagnetic Waves, Asakura-Shoten, 1976.
- [6] J.R. Huynen, "Phenomenological theory of radar targets", Ph.D. Dissertation, Technology University, Delft, the Netherlands, 1970.
- [7] A. Ishimaru, Wave Propagation and Scattering in Random Media, Academic Press, New York, 1978.
- [8] Y-C. Yeh, "The received power of a receiving antenna and the criteria for its design", Proc. of IRE, Vol. 37, pp. 155-158, Feb. 1949.
- [9] R.M.A. Azzam and N.M. Bashara, Ellipsometry and Polarized Light, Amsterdam, North-Holland, 1977.
- [10] Y. Yamaguchi, M. Sengoku, and T. Abe, "Communications Polarimetry", Technical Report of Antennas Propag., IEICE Japan, A-P90-89, pp. \_\_\_\_\_, Dec. 1990.

#### DISCUSSION

##### W. FLOOD (Comment)

There are two papers which will appear shortly. The first will appear in *Antennas and Propagation* showing how for certain classes of diffuse targets, one can approximate the Mueller matrix with measurements of  $\sigma^{HH}$ ,  $\sigma^{VV}$  and  $\sigma^{VH}$ . The second paper, which shows how the phase statistics of the  $S$  matrix can be obtained from the Mueller matrix will appear in *Radio Science*.

## ANALYSIS ALGORITHMS FOR PROCESSING ULTRAVIOLET FLUORESCENCE DATA

J. B. Gillespie, D. L. Rosen, Y. P. Yee, and R. Gonzales  
 Atmospheric Sciences Laboratory  
 U.S. Army Laboratory Command  
 White Sands Missile Range, NM 88002-5501, USA

## SUMMARY

Laser-induced fluorescence (LIF) lidar is a promising technique for remote chemical detection and analysis for both hard targets and extended atmospheric targets dispersed as aerosols or gases. However, the volume sampled in the atmosphere by a lidar may contain mixtures of several fluorescing compounds. The fluorescence spectra of the hard targets and of the aerosols and gases in the troposphere are primarily very broad and devoid of sharp line structure. When several species are present, the resulting overlapped spectrum is difficult to analyze. Interpretation of the multi-component spectra of the lidar signal return is necessary for application of an ultraviolet (UV) lidar in a complex atmospheric environment such as a modern battlefield.

We describe algorithms that we have developed to process UV lidar fluorescence data and to analyze for chemical components. Our analysis algorithms are based on factor-analysis rank-annihilation (FARA) techniques. We apply four methods to lidar systems modeling and simulation analysis that contains both shot noise and sky radiance. We demonstrate the limitations of UV lidar systems in terms of range, daytime/nighttime operation, and lidar system parameters. We find that for situations in which several constituents are fluorescing and have close overlap, sky radiance limits use to nighttime application. Ranges of a kilometer or more are obtainable for easily realizable UV lidars operating at night.

## 1. INTRODUCTION

LIF is sometimes used for lidar because LIF spectra contain information about chemical composition (Ref 1). Fluorescence lidar has been limited because the LIF spectra of most constituents in the troposphere are very broad and devoid of line structure. The LIF spectra of aerosol particles do not have line structure because of inhomogeneous broadening by vibrational states. Sharp fluorescence lines from gases in the troposphere are quenched by collisional de-excitation. The broad LIF spectra from an atmospheric constituent overlap LIF spectra from other constituents and the spectrum of sky radiance. An atmospheric constituent is not easily distinguished from the background spectra because of this overlap.

Rank annihilation-factor analysis (RAFA) is a set of algorithms for interpreting broad fluorescence spectra in complex mixtures. RAFA compares the excitation-emission matrix (EEM) of an unknown to the EEM of a calibrant. An EEM is a matrix containing the spectral intensity as a function of excitation wavelength and emission wavelength. RAFA can only detect the EEM of a calibrant within the EEM of a complex mixture under the following conditions. First, the fluorescence of the various components of the mixture should add up linearly. Second, the EEM can only be analyzed if both the number of excitation and emission wavelengths is greater than the number of fluorescing compounds in the mixture. Many more excitation wavelengths than fluorescing compounds may be necessary because of noise and uniqueness problems. This means that a wavelength tunable excitation source is necessary for RAFA.

This paper describes a computer simulation of an RAFA detection algorithm applied to a hypothetical fluorescence lidar return with noise and sky radiance. Detection algorithms determine whether or not the concentration of the calibrant in an unknown mixture is zero. In previous simulations we analyzed RAFA algorithms that can calculate only nonzero concentrations of the calibrant in the unknown mixture from a fluorescence lidar return (Ref 2). Noise and sky radiance were not included in our previous studies.

If the spectra of the components are both nonoverlapping and free of random noise, RAFA requires a calibrant EEM only from the compound of interest. This suggests that RAFA may be useful in remote sensing where an unknown background may also be fluorescing. However, real lidar measurements often contain large amounts of random noise and overlap. A priori information is necessary to eliminate random noise. We will show that detection by RAFA may require some knowledge of the fluorescence background to set a rejection level. A detailed knowledge of the fluorescence background may not be necessary if one has used the worst possible fluorescence background to set the rejection level.

## 2. THEORY

The theory behind the simulation is described in two parts: the RAFA detection algorithm and the UVTRAN model for lidar.

## 2.1 Detection Algorithm

We used the overlap index method (Ref 3) to determine the presence or absence of the calibrant compound in the mixture. The overlap index method assumes that the calibrant EEM is bilinear; that is, the emission spectrum of the calibrant is independent of excitation wavelength. Pure compounds generally have bilinear EEM because of rapid nonradiative transitions within a molecule. The overlap index method will not work if the EEM of the calibrant is linearly dependent with a set of EEM from other components in the unknown.

We now define the overlap index,  $p$ . In the following discussion, the row vectors of an EEM correspond to emission spectra and the column vectors of an EEM correspond to excitation spectra. The overlap index method requires a bilinear calibrant EEM,  $M$ , and the EEM,  $D$ , from an unknown mixture. Then

$$p = \sum_{i=1}^r |u_i \cdot x|^2 \sum_{j=1}^r |v_j \cdot y|^2 \quad (1)$$

where  $x$  is a normalized excitation spectrum of the calibrant,  $y$  is a normalized emission spectrum from the calibrant,  $i$  and  $j$  are subscripts designating the significant nonzero eigenvalues of  $DD^T$  or  $D^T D$ ,  $u_i$  is an eigenvector of  $DD^T$  associated with a significant eigenvalue,  $v_j$  is an eigenvector of  $D^T D$  associated with a significant eigenvalue, and  $r$  is the number of significant nonzero eigenvalues of  $DD^T$  and  $D^T D$ .

The value of  $r$  is necessary for calculating a precise value of  $p$ . Underestimating  $r$  generates a numerical error in  $p$ , while overestimating  $r$  causes  $p$  to be sensitive to noise and experimental error. Algorithms for finding  $r$  are available (Refs 4 and 5), but were not included in this study. We simulated EEM whose values of  $r$  were known, modified these EEM by using a lidar model, and then used the unmodified values of  $r$  in our calculations of  $p$ .

The overlap index,  $p$ , is used to compare spectra in a similar way to correlation functions. The overlap index algorithm will work under certain conditions even in the presence of unknown fluorescing spectra, where correlation functions cannot work. If  $p$  is 0, the calibrant EEM and the unknown EEM are completely uncorrelated and the calibrant is not part of the unknown mixture. If  $p$  is 1, the calibrant EEM and the unknown EEM are completely correlated and the calibrant may be part of the mixture. A detection criterion is necessary if  $p$  is between 0 and 1. We will propose a possible detection criterion in the discussion section of this paper. However, this criterion requires partial knowledge of the background fluorescence.

## 2.2 Lidar Model

UVTRAN is a UV and visible wavelength atmospheric propagation model recently reported by Patterson and Gillespie (Ref 6). UVTRAN calculates the atmospheric extinction coefficient, optical atmospheric transmission, sky radiance, and the total lidar signal for backscatter and fluorescence. Only calculations for the atmospheric extinction coefficient have been previously described. The other parts of the model are currently being documented and verified.

A modified version of UVTRAN simulated the fluorescence lidar return signals. The new version includes RAFA analysis and photon counting (that is, shot) noise. The calculation of photon noise required the detector integration time and fluorescence lifetime as input parameters. The new model enters the concentration and laboratory EEM of the unknown mixture, the excitation and emission spectrum of the calibrant, the visibility, desired options, and other parameters. The program calculates fluorescence lidar returns. The overlap index is then calculated from the fluorescence lidar return as a function of distance or detection integration time.

The new model has several options concerning sky radiance and noise. The overlap index can be calculated with or without photon noise, and with or without sky radiance. Typical sky radiance can be calculated for night, overcast day, or clear day. The calculations shown are for nighttime sky radiance.

The fluorescence detector is assumed to be a shot noise limited photon counter. The photon detector has a shutter. The detector has a temporal window over which the detector counts photons. With photon noise, the mean collection rate of photons is calculated and multiplied by the detector integration time. The photon count is assumed Poisson distributed about the mean number of photons. Once the random number is generated, the mean sky radiance signal may or may not be subtracted from the noisy signal, depending on the option chosen.

The model uses five approximations. First, the spatial extent of the fluorescing unknown is much less than the distance between the unknown and the detector. For visual clarity, some of the calculations and plots shown in later sections will be extended past the validity of this approximation. Second, the laser pulse is much shorter than either the detector integration time or the fluorescence lifetime. The validity of this assumption will be included in the conclusion. Third, the spatial extent of the fluorescing unknown is  $ct_d$ , where  $c$  is the speed of light and  $t_d$  is the detector integration time.

Fourth, the fluorescence lifetimes of all the components in the unknown mixture are the same as the lifetime of the calibrant. Fifth, neither the excitation pulse nor the fluorescence is significantly attenuated passing through the unknown.

### 3. COMPUTER SIMULATION

The following scenario was chosen for our simulation. The fluorescence lidar was being used in the troposphere to detect the presence or absence of nitrogen dioxide,  $\text{NO}_2$ , in a plume that contained carbon particles. The overlap index for an  $\text{NO}_2$  calibrant was calculated by using simulated lidar returns from aerosol plumes with and without  $\text{NO}_2$  as the unknown EEM. The overlap index for unknowns with and without  $\text{NO}_2$  were compared. The computer simulation will be described in three parts: parameters for the  $\text{NO}_2$  vapor, parameters for the carbon particles, and parameters for the fluorescence lidar apparatus.

We used emission spectra of  $\text{NO}_2$  at 0.1 Torr pressure measured by Sakuria and Broida (Ref 7). The emission spectrum has two components: a broad-band component and a narrow-band component. The narrow-band component is far more easily quenched at higher pressures than the broad-band component. The simulation therefore did not include the sharp lines.

Our simulation used a peak fluorescence cross section of  $9 \times 10^{-24} \text{ cm}^2$  and a fluorescence decay time of 1.65 ns. These values were estimated for atmospheric pressure by multiplying the low pressure values by the quenching factor. The fluorescence cross section without quenching (peak value of  $3 \times 10^{-18} \text{ cm}^2$ ) and the quenching factor ( $3 \times 10^{-4}$ ) at atmospheric pressure of  $\text{NO}_2$  were taken from Measures book (Ref 1). The fluorescence lifetime for  $\text{NO}_2$  of 55 ns was measured without quenching by Keyser et al. (Ref 8).

We chose Kansas City fly ash studied by Tucker et al. (Ref 9) as the background fluorescence source. Fly ash and  $\text{NO}_2$  are often emitted together from smoke stacks. This is only one of several possible fluorescence backgrounds because the fluorescence spectra of fly ash changes with the source.

We used a digitizer to measure emission spectra of  $\text{NO}_2$  and fly ash as shown in journal illustrations (Refs 9 and 10). The excitation spectrum in the literature was incomplete for both  $\text{NO}_2$  and fly ash. We had to interpolate the excitation spectrum from only a few points. The interpolation was done in such a way that the EEM of  $\text{NO}_2$  and the EEM of fly ash were each bilinear (that is,  $r = 1$  for each). The fly ash EEM was definitely not bilinear out to 355 nm in the literature, but the simulation was done over a much narrower range of excitation wavelengths.

The fluorescence lidar EEM was a linear combination of the  $\text{NO}_2$  and the fly ash EEM. Emission spectra of the  $\text{NO}_2$ , the fly ash, and the mixture at one excitation wavelength are shown in Fig. 1. A concentration for  $\text{NO}_2$  of 100 ppb was chosen for the unknown because it was the maximum concentration measured by Gelbachs et al. (Ref 10) in the ambient atmosphere of a city. The concentration of the fly ash was chosen so the peak fluorescence of fly ash was twice the peak fluorescence of  $\text{NO}_2$ , which was also consistent with measurements by Gelbachs et al. (Ref 10). The EEM of the unknown from which the fluorescence lidar returns were generated had two components (that is,  $r = 2$ ). For calculational ease, the fluorescence lifetimes of the  $\text{NO}_2$  and the fly ash were assumed to be the same.

Our hypothetical lidar is now described. The lidar uses three excitation lines: 457.9 nm, 488.0 nm, and 514.5 nm. The energy of each pulse is 0.1 J and each pulse is much shorter than either the fluorescence lifetime or the detector integration times. Other parameters of the detector are given in Table 1. The receiver field of view was assumed perfectly matched with the laser divergence. The emission spectra were collected from 400 nm to 750 nm in 5-nm increments. Elastic scatter was not included as there are methods of filtering it out of the fluorescence lidar return. The receiver was shot noise limited. The lidar path was horizontal through an atmosphere with a 23-km visibility.

We averaged the signal over 6000 pulses per excitation wavelength for each trial. Adequate lidar returns with sky radiance and photon noise could not be gathered with a much smaller number of pulses. This number is far too large for many applications of fluorescence lidar. However fluorescence lidar may be possible for gases whose cross sections are much larger than  $9 \times 10^{-24} \text{ cm}^2$  or whose concentrations are much larger than 100 ppb because fewer pulses would be necessary. The statistical average and standard deviation of the overlap index were calculated from 17 trials. The error bars were defined as plus or minus a standard deviation.

### 4. RESULTS AND DISCUSSION

A threshold (that is, rejection level) for the overlap index is required to determine whether a compound is present or absent. We determined one possible criterion as follows. We assumed that the fly ash background we used was either very typical or worse than the actual background. For example, aerosols can be monitored by independent techniques. The RAFA analysis would then be discarded if the aerosol concentration was too high. A reasonable threshold under these conditions would be between the two curves.

The following numerical definition of threshold was tested. The overlap indices with no sky radiance are clearly separable out to 10 km for the mixture of NO<sub>2</sub> and fly ash ( $p_a$ ) and the fly ash background alone ( $p_b$ ). A slight dependence on distance was observed for both  $p_a$  and  $p_b$ , so a threshold,  $p_t$ , that was also dependent on distance was defined. The threshold,  $p_t$ , was defined as the average of  $p_a$  and  $p_b$ ; that is,

$$p_t = \frac{p_a + p_b}{2} \quad (2)$$

Any  $p$  above  $p_t$  indicates the presence of NO<sub>2</sub>, and any  $p$  below  $p_t$  indicates the absence of NO<sub>2</sub>. This criterion presumes that the user has anticipated the worst fluorescence background interferent possible in a given situation.

The simulation was done with both photon noise and sky radiance. The mean sky radiance was subtracted from the noisy signal. This scenario is the most realistic for applications of fluorescence lidar.

The noise from the sky radiance severely limited the ability of the fluorescence lidar to distinguish between the presence and absence of NO<sub>2</sub>. The functional dependence of the average overlap index on distance is shown in Fig. 2 for nighttime sky radiance for a 2-ms detector integration time.

The effect of detector integration time on the overlap index was studied because the detector integration time often determines the distance resolution of the lidar. The functional dependence of the overlap index on detector integration time is shown in Fig. 3.

The overlap index with NO<sub>2</sub> was clearly distinguishable from the overlap index without NO<sub>2</sub> for detector integration times larger than 1 ms. One could not distinguish between the presence and absence of NO<sub>2</sub> using detector integration times less than 500 ns because the overlap index was too sensitive to the shot noise from nighttime sky radiance.

##### 5. CONCLUSIONS

Photon counting noise with sky radiance severely limits the ability to detect NO<sub>2</sub>. RAFA may be sensitive to random noise because random noise is not the sum of a small number of bilinear matrices. RAFA is based on the fact that EEM from background compounds are bilinear. The photon noise from the sky radiance is a larger problem than photon noise from the lidar return because the sky radiance is stronger than the lidar return.

The noise from sky radiance problems may make the detection of NO<sub>2</sub> impractical. The large number of pulses per excitation wavelength, 6000, required for signal averaging would occupy a large amount of the observer's time. The experimenter would have to wait 60 s per excitation wavelength at a very high repetition rate of 100 Hz. This would not be a real-time measurement for many applications. The required number of pulses could be decreased by increasing the detector integration time at the expense of distance resolution. Fluorescence lidar may be practical for atmospheric constituents with much higher fluorescence cross sections or concentrations than were used in our simulation.

The distance resolution of fluorescence lidar can be seriously limited by noise and sky radiance. Adjusting the detector integration time determines the distance resolution of the lidar. For example, a 1-ms detector integration time limits the distance resolution to 130 m, but provides a greater photon count than a 100-ns detector integration time. An NO<sub>2</sub> signal could not be distinguished from a fly ash signal for integration times less than 500 ns in our simulation, which limited the range resolution to 65 m.

The initial assumption that the transit time is much greater than the detector integration time is not completely valid for the small distances where our lidar model is valid. Our simulation results are therefore very approximate in this region. However, the calculations are sufficient to show how poor RAFA would be for large distances with noise and sky radiance.

The fluorescence lidar apparatus that we simulated is feasible, but would be very marginal. Our fluorescence lidar model is being used to investigate the effectiveness of possible improvements. Narrowing the receiver field of view could reduce the sky radiance noise. However, the 2 mrad used in our simulation is already too narrow to easily achieve. Using an excitation source with a greater number of lines would enable the lidar to discriminate NO<sub>2</sub> from even more complex fluorescence backgrounds than the simulated fly ash.

##### 6. REFERENCES

1. Measures, Raymond, Laser Remote Sensing, New York, Wiley, 1984.
2. Rosen, David L., and Gillespie, James B., "Atmospheric Extinction Effect on Analysis of UV Fluorescence Signatures," Appl. Opt. 28, 4260, 1989.

3. Ho, C. N., Christian, G. D., and Davidson, E. R., "Application of the Method of Rank Annihilation to Quantitative Analyses of Multi-component Fluorescence Data from the Video Fluorimeter," Anal. Chem. 50, 1108, 1978.
4. Malinowski, E. R., and Howerly, D. G., Factor Analysis in Chemistry, New York, Wiley, 1980.
5. Geladi, Paul, and Wold, Svante, "Local Principal Component Models, Rank Maps and Contextuality for Curve Resolution and Multi-way Calibration Analysis," Chemometrics and Intelligent Laboratory Systems 2, 273, 1987.
6. Patterson, Edward M., and Gillespie, James B., "Simplified Ultraviolet and Visible Wavelength Atmospheric Propagation Model," Appl. Opt. 28, 425, 1989.
7. Sakurai, Katsumi, and Broida, H. P., "Spectral Study of NO<sub>2</sub> Fluorescence Excited by 11 Lines of Argon and Krypton Ion Lasers" J. Chem. Phys. 50, 2404, 1969.
8. Keyser, L. F., Levine, S. Z., and Kaufman, F., "Kinetics and Mechanism of NO<sub>2</sub> Fluorescence," J. Chem. Phys. 54, 355, 1971.
9. Tucker, Armin W., Birnbaum, Milton, and Fincher, Curtis L., "Fluorescence of Fly Ash Samples: Implications for In Situ and Remote Detection," J. Luminescence 9, 1, 1974.
10. Gelbwachs, J. A., Birnbaum, M., Tucker, A. W., and Fincher, C. L., "Fluorescence Determination of Atmospheric NO<sub>2</sub>," Opto-electronics 4, 155, 1972.

#### 7. ILLUSTRATIONS

Table 1: Lidar parameters

1. Laser pulse energy -- 0.1 J
2. Number pulses -- 6000
3. Receiver Mirror Diameter -- 0.6 m
4. Receiver field of view -- 2 mrad
5. Spectral Bandwidth of System -- 2.5 nm
6. Transmitter Efficiency -- 0.55
7. Receiver Efficiency -- 0.54

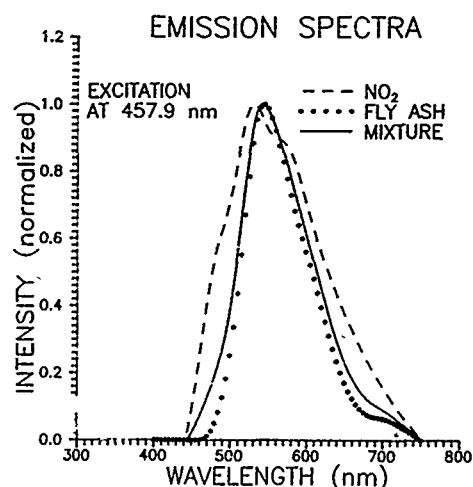


Fig. 1. Normalized emission spectra of NO<sub>2</sub> (---), fly ash alone (\*\*\*\*), and a mixture of fly ash and NO<sub>2</sub> at 457.9 nm excitation (—).

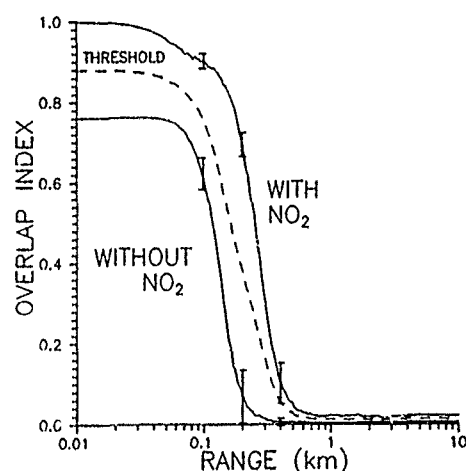


Fig. 2. Functional dependence of the overlap index on range with photon noise and sky radiance for daytime and nighttime conditions with typical error bars. The mean sky radiance has been presubtracted from the lidar return. Error bars are defined as plus or minus a standard deviation.

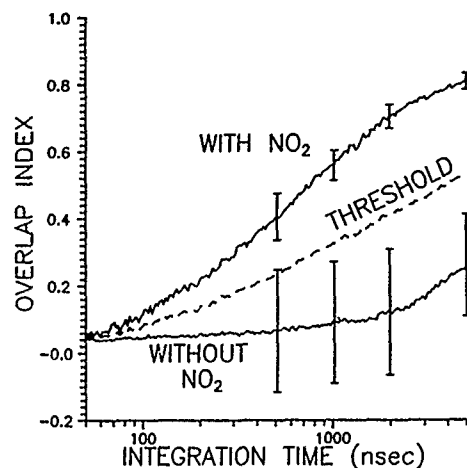


Fig. 3. Functional dependence of the overlap index on detector integration time with photon noise and sky radiance for daytime and nighttime conditions. The mean sky radiance has been presubtracted from the lidar return. Error bars are defined as plus or minus a standard deviation.

## DISCUSSION

### W. FLOOD

*What is the effect of a multi-component background on the detection process?*

### AUTHOR'S REPLY

*Depending on the degree of overlap by the interfering species the multi-component background could, and probably will, mask the target material of interest. This is because most fluorescence is very broad and devoid of line structure. A spectral sorting algorithm such as RAFA can spectrally discriminate and locate the species of interest if there are at least as many unique excitation wavelengths as there are fluorescing species in the target volume.*

### E. TULUNAY

*Do you think that neural net will be useful in making decisions especially in noisy cases?*

### AUTHOR'S REPLY

*The appropriate spectral discrimination methodology must first be developed (RAFA) to solve the problem. Then the software should be packaged as a neural net product with the artificial intelligence aspect used as a prefilter to select candidate target substances. This would greatly improve the speed of the detection process and perhaps make the technique almost real-time.*

# **RECENTLY IMPLEMENTED WEATHER RADAR DATA PROCESSING TECHNIQUE FOR RAIN CELL MODELLING AND GROUND CLUTTER DETECTION**

Y. Korbay  
L. Ligthart  
Delft University of Technology  
Faculty of Electrical Engineering  
P.O. Box 5031  
2600 GA Delft  
The Netherlands

## **SUMMARY**

Throughout the last two decades, dramatic changes have been taking place in the field of radar meteorology. The effects of modern digital signal processing techniques should be especially considered. These new technologies present new opportunities in the weather radar research arena.

Real-time processing is at present the key problem in this field, because, by nature, meteorological targets are distributed in space and occupy a large portion of the spatial resolution cells observed by radar. For this reason, meteorological radars require high-data-rate recording and effective real-time processing.

To solve the data handling and processing problems for weather surveillance radars, a method was initiated by TUDelft. The method makes use of a "Framing-Based Radar Data Analysis" and is under development as part of two contracts for the Dutch PTT.

The method demonstrates great potential in the field of rain cell modelling and ground clutter suppression.

The first verifications were performed using off-line experimental data obtained from the operational Delft radar SOLIDAR.

## **1. INTRODUCTION**

Meteorological radars appear similar to radars used for other purposes. The major distinction between these radars lies in the nature of the targets.

Operational meteorological radars are designed for reliability and simplicity of

operation while providing the performance required for operational applications. There is no universal weather radar system design that can serve all purposes. Most meteorological radars are pulse Doppler radars, like NEXRAD in the United States [2].

An intensive effort has been made in the field of FM-CW weather radar research by the Delft University of Technology, Faculty of Electrical Engineering. In Section 2, a descriptive overview of SOLIDAR, Solid State Delft Atmospheric Radar, is given.

In Section 3, the Delft approach to the radar data handling in using two-dimensional data frames is introduced.

Delft has developed a new approach to ground clutter subtraction and rain cell definition which is explained in Sections 4 and 5.

## **2. SOLIDAR IN GENERAL TERMS**

### **2.1 System Description**

SOLIDAR [1] was developed to perform site-diversity studies at a number of locations and in 1989 the radar system was placed on the roof of the 92m tall building of the Department of Electrical Engineering, Delft. Specifications are summarized in Table 1.

For the site-diversity experiment, various pieces of equipment for making the necessary measurements were installed at two sites located at a distance of about 10 km apart.

Radar type : Linear FM sawtooth		After processing:	
Transmitted power	(dBm) 30	Range $R_{max}$	(km) 15.36
Max. received signal	(dBm) -10	Range resolution	(m) 120
Centre frequency	(GHz) 9.47	Azimuth resolution(degree)	1.875
Frequency excursion	(MHz) 5	Number of range cells	128
Range resolution	(m) 30	Number of sector angles	128
Sweep time	(ms) 5	Total sector	(degree) 240
Beat frequency max.	(kHz) 102.4	Analyzer bandwidth	(Hz) 25
Receiver NF	(dB) 2.5	Minimum detectable rain	
Antenna gain	(dB) 38	intensity at max range and	
Beam width	(degree) 2.8	S/N = 35 dB	(mm/hr) 1
Antenna isolation	(dB) >60	Max detectable rain	
Antenna revolution time(s)	15.36	intensity	(mm/hr) 100
Antenna tilt angle(degree)	0 to 8	Dynamic range ADC	(dB) 96

Table 1: SOLIDAR specifications

The equipment at Delft consists of one 12 GHz and one 30 GHz Olympus Satellite beacon receiver, one 20 GHz radiometer, one 37.5 GHz radio link, the X-Band FM-CW weather surveillance radar SOLIDAR and the S-Band FM-CW Doppler polarimetric radar DARR. The equipment at the second site in Leidschendam consists of one 12 GHz and one 30 GHz Olympus beacon receiver and one 20 GHz radiometer.

Additionally, rain gauges have been installed at four places within the radar range.

All this equipment is connected to a dedicated data-acquisition network, so that all data is available to the experimenters at both sites.

## 2.2 Preliminary Data Processing

The Fourier transform of the beat signal is basic to FM-CW radar for the extraction of reflectivity data as a function of range.

Fast Fourier transforms, power spectra averaging, phase averaging, conversion of reflectivity into rain intensity, displaying, registration of radar data for further off-line processing, ground clutter detection, reflectivity based ground clutter suppression, and rain cell definition are some of the present software functions in SOLIDAR.

In brief, measurements, data collections and data analysis are carried out on an event basis during rain showers to define rain cells. For the ground clutter detection and suppression, the necessary measurements are made and stored on an optical disc during no-rain situations.

## 2.3 Data Types

To understand the basis of the framing-based algorithms, it is necessary to have a close look at the SOLIDAR data.

For a specified area, depending on the analysis purposes, such as ground clutter analysis or stability analysis, high resolution data is available and it is called original power/phase area data. The whole original data cannot be stored because of the huge amount of data 2 Mbyte per antenna revolution.

High resolution data has to be reduced to make the system manageable. A reduction by a factor of 64 is achieved and this modified data is called raw data or low resolution data, which consists of 33152 bytes.

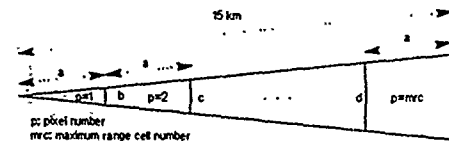
There are four different types of raw data. They carry averaged power, phase information and standard deviations of power and phase.

## 2.4 SOLIDAR Data Visualization

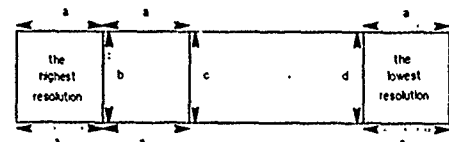
The high and low resolution data can be displayed in the B-scope mode which means horizontal pixels are used as range cells, and vertical pixels are used for sweeps.

Raw data resolutions are of sufficient accuracy to meet our purpose to detect and subtract ground clutter and to define rain cells.

In Fig. 1, pixel resolutions are given for each type of data format.



(a) PPI Scope configuration



(b) B-Scope configuration

	[512x2048]pixel original data	[128x128]pixel raw data
a	29.3m	117m
b	6cm	3.8m
c	12cm	7.7m
d	30.6m	487m
e	30.7m	490m

(c) pixel resolution list

Fig. 1: Pixel resolutions of the original data and raw data

From the framing-based analysis point of view, the B-scope mode is preferred. Related results are also stored as data files in B-scope configuration. If it is necessary for visualization purposes, they all can be transferred into polar coordinates as PPI mode pictures.

## 3. THE BASIS OF DATA HANDLING IN THE FRAMING-BASED ALGORITHMS

### 3.1 Framing

For efficient monitoring, when radar data is visualized on the screen, different windows are used for different types of input or processed data.

Raw data is displayed in the 2-D range-azimuth B-Scope mode and is called the Data Window (DW), and it is divided into equal parts called frames. Rain cells, depending on the chosen rain-intensity thresholds and space-continuity threshold, are defined in window MRW.

There are two types of framing, low/high resolution framing, depending on the accuracy of the rain cell modelling.

### 3.2 Rain Intensity Thresholding

All the analysis is done on a framing-based data handling basis and for specified rain intensities.

The following formulas are used to define rain intensity values in [mm/hr] unit.

$$\begin{aligned} Z[.] &: \text{reflectivity} \\ R[.] &: \text{rainintensity} \end{aligned}$$

$$Z[.] = a * R[.]^b$$

$$dBZ[.] = 10 * \log Z[.]$$

Multi- or monothresholding can be chosen, depending on the analysis purposes.

When DW is displayed, each grey level ( or colour ) corresponds to the different rain intensity threshold levels.

How these thresholds affect, is explained in Sections 4 and 5.

#### 4. CLUTTER ANALYSIS

##### 4.1 Some Properties of Ground Clutter and Precipitation Echoes

Interest in clutter is almost universal in radar research, because most of the echo signals received by radar do not originate from the desired target only, but also from surrounding objects or surfaces which tend to mask the target signal.

In rainfall observations by radar, the interference of ground clutter cannot be always avoided. Therefore it is necessary to use techniques to extract only the precipitation echoes from the received radar signal by rejecting the ground clutter.

Major problems in implementing such techniques are the need for a huge and fast computer memory capacity and for a reliable low rain intensity detection data algorithm.

To solve these problems, framing-based clutter data is analysed and one direct elimination, three different subtraction techniques are proposed.

When we consider radar systems, in which the radar target is defined as a distinct desired object, we may define clutter as any kind of unwanted echo from clouds, precipitation, land areas, sea, birds and chaff which clutter the radar output by making the detection of the target difficult.

In general, the radar echoes from weather sources vary randomly, while the echoes from ground and other ground-based obstacles are relatively stable. Furthermore, radar scattering from land is affected by rain, snow cover, the type of vegetation or crops, the time of the year, the presence of streams and lakes, and man-made objects interspersed among other terrain features.

The choice of an effective detection process is critically dependent upon the statistics of clutter and its variability, as a function of time, location and radar resolution properties, which makes the field of clutter research so complex.

##### 4.2 Several Ground Clutter Elimination Techniques

There are a number of anti-clutter techniques. From our point of view, clutter detection/suppression methods may be grouped into two categories i.e. amplitude-based and phase-based techniques.

The decision process in this class of methods is based on the statistical amplitude properties of radar data.

The amplitude fluctuations of the radar data provide the opportunity to reject ground clutter in order to extract precipitation echo signals. This technique is called non-coherent MTI. In practice, however, the use of the correlation coefficient is better for studying the fluctuation characteristics of the signal amplitude.

However, uniform noise superimposed on the ground clutter signal can never be rejected. On the other hand, amplitude fluctuations coming from low rain intensity levels are not enough to distinguish them from high ground clutter. These are the reasons why we recently started to analyse phase fluctuations together with amplitude fluctuations to detect precipitation echo.

The phase information of the radar data can be used as a decision parameter in target and clutter discrimination methods, such as moving-target indication ( MTI or coherent MTI ).

Problems arise for rain cells moving through the radar beam with a small radial velocity only.

These problems can be eliminated by analysing phase fluctuations based on full scan-to-scan decorrelation for rain and high scan-to-scan correlation for ground clutter.

#### 4.3 Framing-Based Clutter Study [4] [5]

##### 4.3.1 Ground Clutter Detection

In our method, we detect and/or eliminate ground clutter by using its space, time continuity and phase fluctuations. The space continuity threshold value has a strong effect on the clutter study. In no-rain situations, depending on the chosen space-continuity value, frames containing ground clutter echo can be specified and called clutter frames. They are categorized according to their reflectivities and their space continuities.

To decide whether radar data includes precipitation echo or not, calculated raw phase correlations are used. Two successive scans from an antenna revolution at the same azimuth and at the same elevation deliver highly correlated ground clutter observations, while rain is uncorrelated from scan to scan. Further analysis can be done on a scan-to-n scan basis.

Up to now, very high reflectivity clutter frames and non-clutter frames, low space continuity frames, have been analysed. Further research is required to characterize different clutter frames in order to make the decision process simple and more reliable.

##### 4.3.2 Ground Clutter Elimination When There Is Local Rain

If the rain is local, it only comprises a few frames. By detecting the movement of the rain cell ( Section 5 ), the rain frames can be specified. Attention should be given to them because the remaining

small cells include clutter echo as well, and these clutter frames have to be excluded in the definition of the rain cells.

#### 4.3.3. Ground Clutter Elimination by Means of Updated Clutter Map

The basic principle of the Area MTL or Clutter Map is to store representative data in dry weather conditions in order to remove them from the output residue on subsequent scans by either subtraction or gain normalization.

Later, when rainfall observations by radar are carried out, the radar data which may be superimposed by ground clutters are subtracted from the ground data already stored, and then only the precipitation echo will be obtained.

This technique is applicable especially to ground clutter, because returns from land clutter scatterers usually are spatially fixed and therefore appear at the same range and bearing from scan to scan.

There are some hardware problems such as the lack of appropriate memory, registration accuracy, simultaneous read-and-write capability, and stability. The development of high-capacity semiconductor memories is the technological breakthrough that has made the design of a working area MTL a reality. Another disadvantage is that an obstacle moistened by rain produces different reflections that when dry. In addition, the wave propagation and thus the ground clutter is highly variable, especially over flat land.

Framing-based clutter subtraction techniques eliminate these problems to a certain extent by analysing some part of the reduced radar data scan-to-scan.

When rain is detected, the previous radar data is assigned as the *Updated Clutter Map* and subtracted scan-by-scan from the radar data to distinguish the precipitation signal. This method is called the *Directly Updated Clutter Map*.

To define the *Updated Clutter Map*, two other methods based on framing are also worked out. They are called the *Framing-Based Clutter Pixel Averaging* and the *Framing-Based Weighted Clutter Pixel Averaging*.

For framing-based methods, the clutter frames are specified. However, in these two methods, additional clutter pixels (from strong clutter reflections) should also be specified for each clutter frame. The difference between these two methods is the definition of the clutter pixels and the assigned values of the clutter pixels.

The last method may provide an opportunity to eliminate the effect of the weak clutters. However, it should be investigated theoretically and experimentally before their properties and capabilities are given in more quantitative description.

## 5. FRAMING-BASED RAIN CELL MODELLING

### 5.1 Definition of the Rain

In weather radar data processing, many problems arise. As mentioned before, real-time processing becomes very difficult because of the huge amount of radar data. Also, clouds have blurred (noisy) boundaries. The human eye can easily interpret the edge and contour of a cloud configuration, it is easy to follow a contour when a picture presents a few grey levels. It is difficult for a computer to construct the closed contour of such a cloud and, therefore, techniques used in this field are somewhat complicated.

A recently implemented Rain Cell (RC) Modelling technique [4] [5] developed by the TUDelft eliminates most of these problems. Here, it is explained how the RC Algorithm derives the rain cell for a given rain-intensity threshold and space continuity threshold, and how rain cells are modelled.

As has been mentioned before, all analysis is done frame by frame for specified rain intensity thresholds and space continuity threshold.

The distribution of the rain intensity thresholds in frames provides information about the rain cell edges. It is the space continuity properties of rain cells.

There is an important remark to be made at this point, raw power data are used as input data without any clutter elimination technique being applied to it. This study was supported by Dutch PIT under the Contouring Contract and this contract was performed before the clutter study.

When a rain cell is determined for given rain-intensity threshold and space-continuity threshold, this model includes the following parameters;

- \* contour of the rain cell, as a set of rectangles,
- \* cell size,
- \* centre point,
- \* orientation,
- \* distribution,
- \* maximum rain-intensity centre
- \* maximum rain-intensity value

#### 5.1.1 Rain Cell Contour Definition

When the level of noise is low, contours can be detected by using only local criteria by means of thresholding. However, the choice of the proper value for the threshold is very important and it is notoriously difficult to choose a good binarizing threshold.

There are several methods for rain cell contour determination. However, most of them are not applicable to real-time radar data processing. Therefore, when we consider the future prospects, real-time capability of the chosen technique is of interest. For this reason, we proposed rectangular-shaped rain cell contouring.

The RC Algorithm searches only a limited number of neighbourhoods. The reduction rate, obtained in this way, changes between 37.5 % and 50 %, depending on the framing.

The amount of radar data is reduced to the number of frames consisting of rain cells. When thousands of items of radar data have to be processed, the reduced data can also be used for off-line statistical analysis purposes.

## 5.2 Utilization of The Rain Cell Modelling

### 5.2.1 Orientation and Distribution by Means of Multi-Thresholding

One of the most promising features is the multi-thresholding. To show how it can be used for modelling and analysis studies, a brief example is given in Fig. 2.

Fig. 2(a) shows raw power data with three rain-intensity threshold levels,  $R[1]=3$  mm/hr,  $R[2]=6$  mm/hr and  $R[3]=10$  mm/hr. Fig. 2(b) shows the frames filled with rain after thresholding.

An original rain cell can be simply transformed into a circle. To define a circle, the centre point and the radius should be specified. The centre of the circle is the centre point of the rain cell, and the radius is calculated from the cell size. When they are defined for different rain-intensity thresholds, the cell orientation can be specified. After this definition, the rain-intensity distribution in the rain cell can be derived in any direction, depending on the user's interest (Fig. 2(c)).

### 5.2.2 Moving Cell

As mentioned before, it is also possible to predict the trend of the rain cell by using the time series of the rain cell for specified rain-intensity threshold and space-continuity threshold.

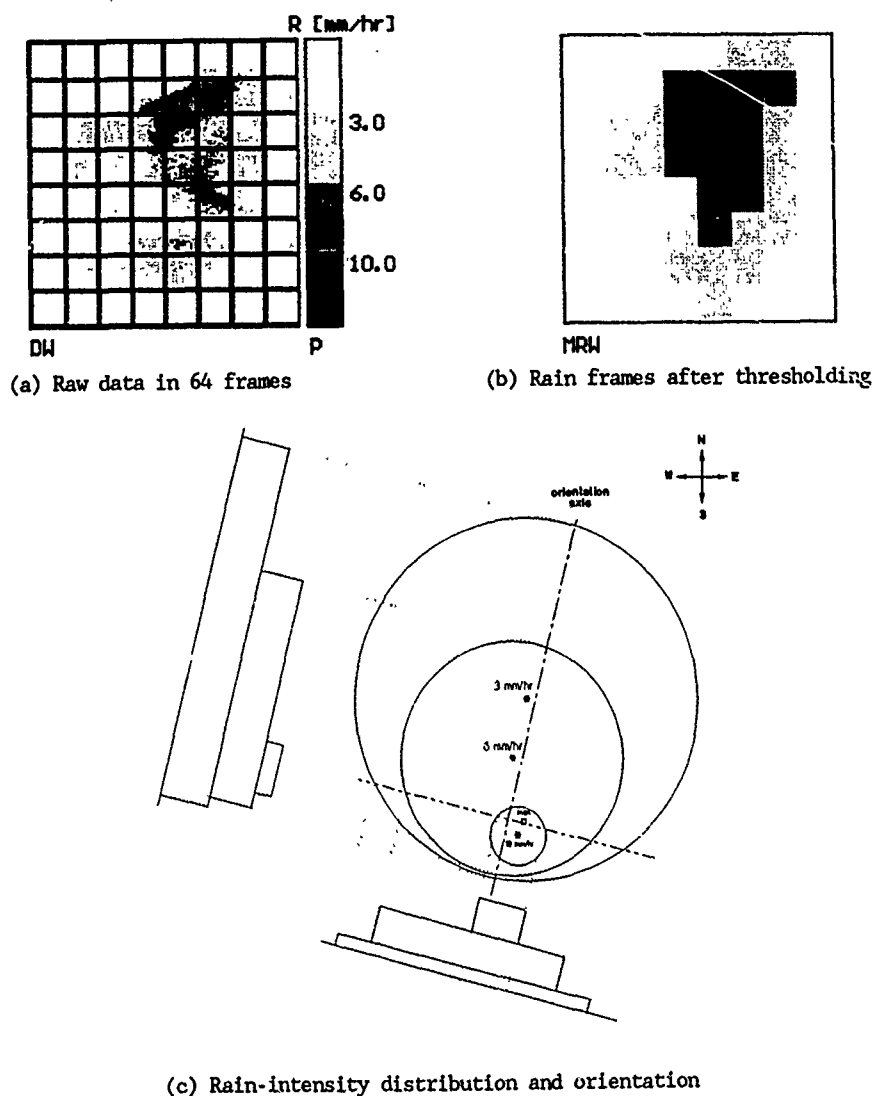


Fig 2: Multi-thresholding effect

### 5.3. Comparison With EXCELL Model

[CAPSONI C., PARABONI A.] [3]

For modelling purposes, basically three methods are used. Empirical models give the results of prediction by using equiprobability rules and relations whose parameters have been optimized over a large number of different experiments. Analytical models describe the physical process analytically. They are based on an easily manageable mathematical description. It is not applicable when the common volume is large. Physical models are more flexible and are widely accepted, for example, to handle propagation data, because measurements are rarely taken in the same circumstances. In the end it either works or it does not.

The potentials and applications still have to be proved based on reliable measurements. Therefore we limit ourselves here to physical models.

The Quasi Physical Rain Cell Model developed by C. Capsoni and A. Paraboni, and described in the literature is substantially based on a distribution of rain cells characterised by the inside distribution of rain,  $R$ , obeying an exponential shape and the conditional average radius  $\langle r_0 \rangle$ . This radius depends on the peak value of rain  $R_M$ . For a given peak rain-fall rate, the radial intensity profile follows an exponential distribution. This means that each rain cell is simply defined by  $R_M$  and  $r_0$ . In the RC Model, introduced by the TUDelft, the same analysis can be derived not only for the peak rain-fall rate, but also for any rain-intensity value which is defined as a rain-intensity threshold. However, there are also additional outputs which give more opportunities for statistical analysis, simple modelling and correlation studies.

The output of the model consists of a set of data files for each rain cell at a certain time, and each one containing a rain cell representation according to the user's interest.

Radar rain-cell measurements and rain-gauge

values can be used for calibration. It is also possible to use them to measure on-line satellite link performance.

In this RC Model, not only the geometrical dependence of the rain cell but also the time dependence can be derived by means of a time series, which carries information to distinguish moving rain cells from fixed targets.

Additionally, the velocity of the rain cell per antenna revolution can be easily calculated from the reduced data set, and the trend of the moving cell can be predicted by using the time series to define how the rain cell passes through the beams.

In brief, the RC Model has not only the capability to define rain cells and to predict the trends of rain cells, but the model has a great potential to be implemented in real-time SOLIDAR processes.

### REFERENCES

#### Periodical Articles

1. Ligthart, L.P., Nieuwkerk, L.R., "An X-Band Solid-State FM-CW Weather Radar", IEE Proc F, Dec. 1990, vol. 137, No. 6, pp. 418-426.

#### Reports

2. "NEXRAD Product Description Document", The NEXRAD Joint System Program Office, December 1989.
3. Capsoni, C., Paraboni, A., "A Quasi Physical Rain Cell Model For Hydrometeor Scatter Interference Prediction", URSI, Prague, 28 August - 5 September 1990.
4. Korbay, Y., Ligthart, L.P., Nieuwkerk, L.R., "SOLIDAR Rain Cell Definition Algorithm Description Report", Delft University of Technology, 3 October 1990.
5. Korbay, Y., Ligthart, L.P., "SOLIDAR Framing-Based Clutter Suppression Description Report", Delft University of Technology, 8 May 1991.

## A CALIBRATION TECHNIQUE FOR THE CNET HF BACKSCATTER RADAR

N. RUELLE\*, F. GAUTHIER\*, J.Y. LE SAOUT\*  
L. BERTEL\*\*, V. BALTAZART\*\*

\* Centre National d'Etudes des Télécommunications  
LAB/PTI/GER, Route de Trégastel  
B.P. 40, 22301 Lannion, France

\*\* Université de Rennes I  
Laboratoire Radiocommunications - URA 834  
Campus de Beaulieu, 35042 Rennes Cedex, France

### 1 SUMMARY

The purpose of this paper is to describe a calibration procedure used in conjunction with the CNET HF backscatter radar at Losquet Island, France. This procedure characterises the capability of the radar to determine angles of arrival of echoes by beam scanning.

### 2 INTRODUCTION

In the area of HF backscatter radar, data analysis techniques are often hampered by the lack of prior knowledge of propagation conditions within the refraction zone of the ionosphere. Determination of the precise location of the backscattering area (coordinate registration) and/or determination of the angles of arrival of the backscattered signal helps to deal with this difficulty.

In order to investigate the possibilities in this area afforded by the CNET HF backscatter radar at Losquet Island, a calibration procedure was used to study the ability of the radar to determine azimuth and elevation angles of arrival of backscatter echoes by beam scanning.

Before giving results from this calibration procedure we describe briefly the CNET radar and the mobile HF transponder which is used for calibration.

### 3 THE LOSQUET ISLAND BACKSCATTER RADAR

This instrument, situated at Losquet Island, in Brittany (48.8N, 3.6W) has been described elsewhere (1) (2). It has the following characteristics, which are of interest in this context: operating frequency is chosen between 6 and 30 MHz. 2 circular concentric antenna arrays are used for transmission and reception.\*

Array directivity patterns are controlled through the use of digital phase shifters on all antennas. Beamforming and scanning of the beam over 360° in azimuth and 0°-90° in elevation are thus possible. 3 dB beamwidth varies approximately between 20° at 6 MHz and 5° at 30 MHz. Further information on directivity patterns is given by Ruelle et al. (3).

\* the transmitting array is 94 m in diameter, with 32 antennas  
\* the receiving array is 140 m in diameter, with 64 antennas.

Group delay analysis of backscattered echoes is possible through the use of a pseudo-random modulation of the transmitted signal (as described by Goutelard et al. (4)). This can be combined with scanning either in frequency  $f$ , in azimuth beam angle  $\alpha_0$  or in elevation beam angle  $\epsilon_0$ , resulting in what we call scan soundings, which are records of backscattered power  $P$  vs. group delay  $T_g$  and scan parameter (either  $f$ ,  $\alpha_0$  or  $\epsilon_0$ ).

The precise effect of beam angle on backscatter data was not well known, however, and an experimental technique was needed to characterise it. For this purpose a mobile HF transponder was used.

### 4 THE TRANSPONDER.

A remote radar transponder produces in effect an artificially intense point-like target in the far field of the radar. Its image, which is distorted by the propagation medium and by the radar itself, is useful in characterising the instrument response because we know the geometry of the propagation, as in our case where we wished to study the effects of azimuth/elevation scan soundings.

The transponder we use functions according to the following principle: the signal transmitted from the radar at  $f = 10.8$  MHz is detected by a receiving antenna. It is then frequency shifted to  $f' = 10.4$  MHz, amplified (200 W amplifier) and retransmitted through a second antenna. This retransmitted signal is then detected by the radar. Since the radar transmits and receives at frequencies that are 400 kHz apart, no natural clutter obscures the transponder image (yet 400 kHz is small enough that ionosphere and radar properties remain essentially the same). This dual frequency technique allows continuous operation of the transponder, which is an advantage for us because the radar itself uses a 50% duty cycle (transmitting and receiving arrays being colocated). However it requires very strong decoupling between transponder transmit and receive antennas. This dictates the 400-kHz frequency separation, and is achieved by placing transmit and receive antennas 20 m apart, and by using a notch filter at the output of the receive antenna, which rejects the retransmitted frequency  $f'$ . Future plans include modifications to the transponder enabling it to operate at frequencies higher than 10 MHz.

Since this transponder is mobile, it has been operated at a variety of remote locations. During these operations, azimuth and elevation scan soundings were recorded over various

lengths of time for further analysis. In order to properly interpret these experimental results, it was necessary to determine ionospheric propagation conditions independently. This was done as described in the following paragraph.

## 5 SIMULATIONS IN SUPPORT OF TRANSPONDER DATA INTERPRETATION

Our objective was to determine the mode structure (time delay and elevation angle for each mode) of the point-to-point link between radar and transponder at frequencies  $f$  and  $f'$ . This would then help us in separating propagation effects from those due to the radar directivity pattern.

From vertical incidence (V.I.) ionosonde data recorded near the radar-transponder midpoint, we could, using standard real height inversion techniques, derive an electronic density profile in the refraction zone. This was then used as an input to propagation modelling by fitting this profile with a multi-quasiparabolic model, as described by Hill (5). This model has been used extensively by several groups recently (6) (7) for propagation simulation because analytical solutions are obtained for group delay and ground distance calculations, and because an arbitrarily good fit to real profiles is possible.

We define the electron density profile:

$$N(r) = \sum_{i=1}^7 N_{mi} \left[ 1 \pm \left( \frac{r - r_{mi}}{y_{mi}} \right)^2 \left( \frac{r_{bi}}{r} \right)^2 \right] \quad (1)$$

where:

$\pm$  sign is linked to quasiparabolic (-) or inverted quasiparabolic (+) nature of  $i$ -th layer

$N_{mi}$ : maximum value of electron density for the  $i$ -th layer

$r = h + r_0$ ;  $h$ : altitude,  $r_0$ : radius of the earth

$r_{mi}$ : value of  $r$  for  $N(r) = N_{mi}$  (peak of the  $i$ -th layer)

$r_{bi}$ : value of  $r$  at the base of the  $i$ -th layer

$y_{mi}$ : semi-thickness of the  $i$ -th layer ( $r_{mi} = r_{bi} + y_{mi}$ )

$i$  runs from 1 to 7 because we assume 4 quasi-parabolic layers to represent the E, F1 and F2 layers, and the valley between E and F1. Between these 4 layers we sandwich 3 quasi-parabolic connecting layers, resulting in a 7 piece profile.

Connecting layer parameters are forced by imposing continuity of the profile and its derivative at junction points. Valley parameters are deduced from the E layer:

$$\begin{aligned} N_{mV} &= N_{mE}/1.04 \\ r_{mV} &= r_{mE} + 20 \text{ km} \\ y_{mV} &= 15 \text{ km} \end{aligned}$$

as usually assumed in real height ionogram analysis.

Thus E, F1 and F2 layer parameters may be adjusted to fit the real-height profile. We are then able to perform fast calculations of group delay  $T_g$  and ground distance  $D$  for raypaths at specific elevation angles and frequencies. In our case the distance  $D_0$  (radar-transponder) and the frequency ( $f$ ,  $f'$ ) being known, we use Newton's method to solve:

$$D \Rightarrow D(e) \quad (2)$$

In e. For the appropriate angles  $T_g$  is then computed, and we have (e,  $T_g$ ) pairs for up to six single hop modes (1E, 1F1, 1F2, with high and low rays) plus multiple hops. Figure 1 shows an example of this result. This simulation can be updated in time to reflect the evolving propagation conditions in the refraction zone.

Since the radar is able to analyse echoes in the group delay-azimuth-elevation space by scanning, we should then be able to see a number of point-like features at a fixed azimuth, lying

along a fixed  $T_g(e)$  curve, as shown in figure 1. This picture, however, is subject to a number of perturbations which are mentioned in the following paragraph.

## 6 PERTURBATING EFFECTS

### 6.1 Low resolution

Radar temporal and angular ambiguity functions will lead to a smearing out of point-like echoes. Time-delay resolution is close to 0.2 ms. Angular resolution is more difficult to characterise, though 3 dB beamwidth is an indication (at 10 MHz it is of the order of  $12^\circ$  in azimuth and  $15^\circ$  in elevation).

### 6.2 Fading

Small scale variability of the ionosphere will lead to rapid amplitude variations of the different modes, thus changing notably the aspect of instantaneous scan results. Time averaging of data can reduce this effect.

### 6.3 Mixed modes

Since measurements are made after a two-way propagation, the radar-transponder path may correspond to one mode, and the transponder-radar path to another. Elevation angle is measured on the return path, whereas time delay is the sum of the forward and return delays. There is then, for a given computed mode characterised by its elevation angle, a number of mixed modes, with  $T_g$  above or below that of the "pure" mode, depending on the forward path. This effect, which is illustrated by figure 1, will combine with low resolution (6.1) to cause a time delay broadening in experimental results.

There will also, in all likelihood, be a change in the apparent slope of the  $T_g(e)$  curve, as shown in figure 1. As we will now see, these effects were indeed detected in the experimental data.

## 7 EXPERIMENTAL RESULTS

We report on results obtained during a campaign conducted from 15 to 19 april 1991. The transponder was operated from a CNET site at La Turbie in Southern France (43.7N, 7.4E). Azimuth from Losquet Island is  $119.3^\circ$  and ground distance is 1014 km.

During this time azimuth scans ( $0^\circ$  to  $360^\circ$ ,  $5^\circ$  step) and elevation scans ( $0^\circ$  to  $60^\circ$ ,  $3^\circ$  step) were recorded, each scan being of about 40 s duration. These were then combined by averaging 30 to 40 scans over 20 minute periods to compensate for fading effects.

Examples of results are given in figure 2, which is an azimuth scan, clearly showing a peak in the correct direction, and in figure 3, an elevation scan. In figure 3 calculated pure and mixed modes have been superimposed on the experimental results, which clearly shows the time delay broadening and smearing, and also the apparent slope of the resulting elongated shape, which is weaker than predicted.

During this campaign, ionograms from the Poitiers VI sounder (situated 145 km from the radar-transponder midpoint) were recorded every 15 minutes. Then, following the procedure of section 5, we simulated propagation conditions during the experiment. Figure 4 shows an example of this from 17 april 1991. These simulations enabled us to interpret the data.

## 8 DATA INTERPRETATION

### 8.1 Azimuthal scans

Our data set shows that azimuth discrimination is efficient; figure 2 gives an idea of azimuth angle resolution (which is rather low compared to other HF radars because of the small overall size-140m-of the array).

## 8.2 Elevation scans

Elevation scans produce the expected (see 6.3) elongated shape, as seen in figure 3, with one or more amplitude maxima. Our objective was to relate the position of these maxima in the (Tg, e) space to predicted propagation modes. An example of this is given for 17 april 1991 in figure 4, where the positions of the maxima recorded at various times during the day are superimposed on simulated propagation conditions. In this example, it can be seen that a good match for the low IF1 mode is always present, while for the IF2 mode this is occasional (though only when this mode is actually predicted to be present). There is usually no match for the IF mode although this is always predicted to exist. Since the predicted elevation for the low IF mode is 10°, it is possible that this mode is affected either at the radar or more probably at the transponder site by bad low elevation propagation, due to ground characteristics.

Reliable mode identification in the (Tg, e) space appears to be restricted to one dominant mode, here IF1. Indeed the analysis of our complete data set confirms this, and it is further illustrated by the example of figure 5 (18 april 1991) where simulations predict a transition from a IF2 to IF1 mode over a period of about one hour. This seems to be confirmed by the position of the maximum in our experimental data.

## 9 CONCLUSION

Our experimental and theoretical work on transponder techniques has given us a clearer idea of angular discrimination capabilities of the CNET radar, particularly in the elevation domain. We show that when, as is usually the case, there exists a dominant propagation mode (in terms of signal amplitude) then this mode can be discriminated in the (Tg, e) space by scanning, while finer structure is usually lost due to broadening and smearing, both in group delay (caused by mixed modes) and in elevation angle (caused by large beamwidth).

This conclusion is of interest for the analysis of backscatter radar data because a similar situation occurs due to amplification of clutter power caused by so-called leading edge focusing. This focusing produces an increase in echo power for raypaths exhibiting minimum time delay (see Croft (8)) so that a sort of natural transponder is created.

This work gives us confidence in using elevation scan techniques to determine the location of the backscatter leading edge in the (Tg, e) space. This data should then prove very useful in the application of backscatter data to ionospheric propagation diagnostics, as proposed by Gauthier et al. (9).

## ACKNOWLEDGEMENTS

The authors wish to express their thanks to R. FLEURY for the processing of VI data, and for many illuminating discussions.

## REFERENCES

1. Le Saout J.Y. and Bertel L., "Les systèmes d'aériens utilisés par le radar HF à rétrodiffusion du CNET". JINA 88 Conf. Proc., pp 509-513, 1988.
2. Le Saout J.Y., Bertrand P. and Poitevin R., "Les caractéristiques expérimentales des systèmes d'aériens du radar HF à rétrodiffusion du CNET", JINA 90 Conf. Proc., pp 572-575, 1990.
3. Ruelle N., Le Saout J.Y. and Bertel L., "New perspectives for the inversion of backscatter ionograms", AGARD Conf. Proc., n° 453, 28, 1988.
4. Goutelard C., Caratori J. and Joisel A., "Technique de sondage électromagnétique par échantillonnage spatio-fréquentiel des signaux de réception, application à l'étude des inhomogénéités du plasma ionosphérique", AGARD Conf. Proc., n° 244, 13, 1977.
5. Hill J.R., "Exact ray paths in a multisegment quasi parabolic ionosphere", Radio Science, vol. 14, n° 5, sept-oct. 1979.
6. Baker D.C., BURDEN J.J., "The multisegmented parabolic model for ionospheric electron density distribution : a convenient model for HF engineering applications", IEE Conf. Publ., n° 339, p. 183, 1991.
7. Dyson P.L., BENNETT J.A., "A model of the vertical distribution of the electron concentration in the ionosphere and its application to oblique propagation studies", JATP, vol. 50, n° 3, pp 251-262, 1988.
8. Croft T.A., "Sky-wave backscatter : a means for observing our environment at great distances", Review of Geophysics and Space Physics, 10-1, pp 73-155, 1972.
9. Gauthier F., Le Saout J.Y. and Ruelle N., "Possible contribution of CNET HF backscatter radar to ionospheric data bases", Adv. Space Res., vol. 11, n° 10, pp 135-136, 1991.

# mode structure 17-april 1991 08:00 UT

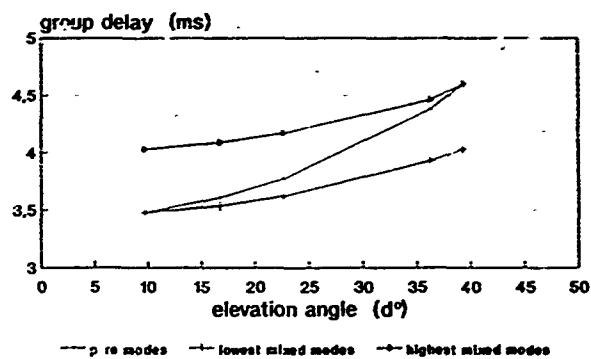


Figure 1 : calculated modes of propagation in the group delay-elevation space, 17 april 1991.

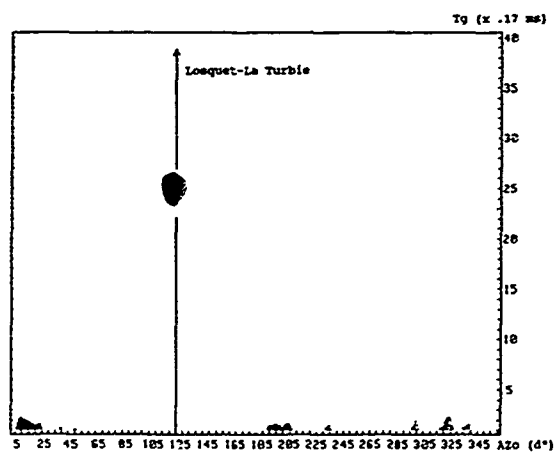


Figure 2 : azimuth scan, 18 april 1991  
09:23TU.

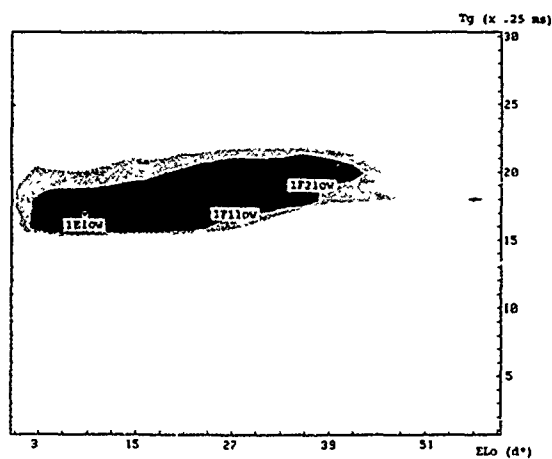
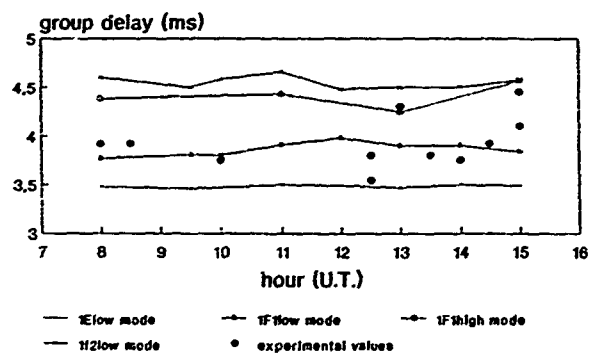


Figure 3 : elevation scan, 17 april 1991  
12:45TU,  
Calculated modes are superimposed.

### group delay vs time 17 april 1991



### elevation angles vs time 17 april 1991

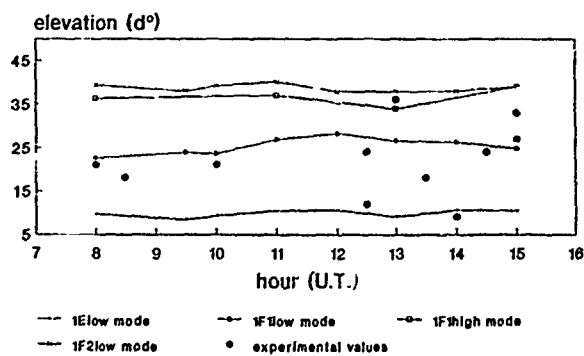
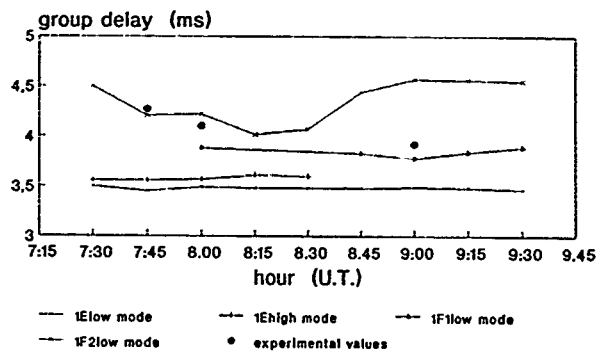


Figure 4 : evolution of time delay and elevation of propagated modes. - : simulation and experimental. 17 april 1991.

### group delay vs time 18 april 1991



### elevation angles vs time 18 april 1991

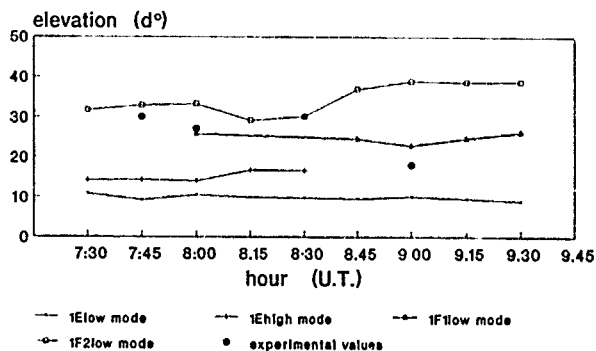


Figure 5 : evolution of time delay and elevation of propagated modes. - : simulation and experimental. 18 april 1991.

#### DISCUSSION

##### C. GOUTELARD

Vous introduisez une vallée dans le profil ionosphérique modélisé que vous utilisez. C'est une excellente chose notamment parce que, comme l'a fait Dudney dans son modèle, la diversité du profil devient continue, ce qui facilite les calculs de rayons. Comment à partir des sondages zénithaux remontez-vous à la vallée? Utilisez-vous une méthode particulière?

*You introduce a valley into the modelled ionospheric profile which you have used. This is excellent, especially since, as in the Dudney model, the diversity of the profile becomes continuous, which facilitates ray calculations. How do you get back to the valley from the zenith soundings? Do you use a special method?*

##### AUTHOR'S REPLY

Les paramètres de la vallée sont obtenus à partir de ceux de la couche E à l'aide des relations qui sont utilisées dans le programme d'inversion POLAN (Thitheridge).

*The parameters of the valley are obtained from those of the E layer using equations used in the POLAN inversion programme (Thitheridge).*

LIST OF PARTICIPANTS

AFONSO Capt A. JORGE AFONSO, Portugal  
Direccao de Electrotecnica - Base de Alfragide - 2700 Amadora -

ALBRECHT Dr H.J. ALBRECHT, Germany  
FGAN - Neuenahrerstrasse 20 - W-5307 Wachtberg-Werthhoven -

ANDERSON Mr K. D. ANDERSON, United States  
Naval Ocean Systems Center - Code 543 - San Diego, CA 92152-5000 -

ARTHUR Mr P.C. ARTHUR, United Kingdom  
FS4C, Flight Systems Dept. - P 161 Building - Defence Research Agency - Farnborough, Hants GU14 6TD -

BAARS Mr E.P. BAARS, Germany  
FGAN-FHP - Neuenahrerstrasse 20 - W-5307 Wachtberg -

BAHAR Prof. E. BAHAR, United States  
Electrical Engineering Dept - 209 N WSEC - University of Nebraska-Lincoln - Lincoln, NE 68588-0511 -

BELROSE Dr J.S. BELROSE, Canada  
Communications Research Center - PO Box 11490 - Station II - Ottawa, ON, K2H 8S2 -

BENSON Dr R F. BENSON, United States  
Code 692 - NASA/Goddard Space Flight Center - Greenbelt, MD 20771 -

BOERNER Prof. Dr W.M. BOERNER, United States  
University of Illinois at Chicago - UIC-EECS/CSL, M/C 154 - Chicago, IL 60680-4348 -

BOLIOLI Mr S. BOLIOLI, France  
ONERA-CERT - BP 4025 - 2, Ave E. Belin - 31055 Toulouse Cedex -

CANBILEN Ustegmen SABIT CANBILEN, Turkey  
Muhabere Okulu - 06264 Mamak/Ankara -

CANNON Dr P.S. CANNON, United Kingdom  
Applied Ionospheric Physics, FS4C - Flight Systems Department, - P161 Building - Defence Research Agency - Farnborough, Hants GU14 6TD -

CASSARA Lt-Col. A. CASSARA\*, Italy  
Aeronautica Militare - DASRS/RASA - I-00040 Pratca di Mare (Roma) -

CLIFFORD Dr S.F. CLIFFORD, United States  
Director, WPL - US Department of Commerce - 325 Broadway - Boulder, CO 80303 -

COOK Mr J. COOK, United States  
Naval Oceanographic and Atmospheric - Research Laboratory - Atmospheric Directorate - Monterey, CA 93943-5006 -

CRAIG Dr K.H. CRAIG, United Kingdom  
Rutherford Appleton Laboratory - Chilton, Didcot - OX9 0X11 -

CRESCIMBENI CDR F. CRESCIMBENI, Italy  
C/o Manteleradar - Viale Italia N°72 - 57126 Livorno -

DARNELL Prof. M. DARNELL, United Kingdom  
Dept. of Electronic Engineering - University of Hull - Hull - HU6 7RX -

DAVARIAN Dr F. DAVARIAN, United States  
JET Propulsion Laboratory - MS 161-228 - 4800 Oak Grove Drive - Pasadena, CA 91109 -

FLOOD Dr W.A. FLOOD, United States  
Director, Geosciences Div. - US Army Research Office - PO Box 12211 - Research Triangle Park - NC, 27709-2211 -

FUERXER Mr P. FUERXER, France  
CNET - 38-40 rue du Général Leclerc - 92131 Issy les Mouleneaux -

GALLAGHER Mr M. GALLAGHER, United Kingdom  
Hull Warwick Comm. - Research Group - Dept. of Electronic Engineering - University of Hull - Hull, Humberside, HU6 7RX -

LP-2

GAUTHIER	Mr N. GAUTHIER, France CNET/LAB/PTI/GER - route de Trégastel - 22301 Lannion -
GEDIK	Mr A. GEDIK, Turkey Instructor - Kara Harp Okulu - Ogretim Baskanligi - Ankara -
GHICOPOULOS	Dr. B. GHICOPOULOS, Greece Hellenic Air Force - Technology Research Center - Terpsithea Post Office - Glyfada 16501 Athens -
GIBSON	Mr A.J. GIBSON, United Kingdom S.E.R.C. - Rutherford Appleton Laboratory - R25, Chilton - Didcot, Oxon OX11 0QX -
GILLESPIE	Dr J. B. GILLESPIE, United States US Army Atmospheric Sciences Lab. - SLCAS-AR-P - White Sands Missile Range, NM 88002 -
GOLDHIRSH	Dr J. GOLDHIRSH, United States The Johns Hopkins University - Applied Physics Laboratory - Johns Hopkins Road - Laurel, Maryland 20723-6099 -
GONCALVES	Mr C.A. GONCALVES, Portugal Instituto Nacional Meteorologica - e Geofisica - Rua C do Aeroporto - 1700 Lisboa -
GOSSARD	Dr F E. GOSSARD, United States CIRES - Campus Box 449 - University of Colorado - Boulder, CO 80309 -
GOUTELARD	Prof. C. GOUTELARD, France Directeur, LETTI - Université Paris-Sud - Bâtiment 214 - 91405 Orsay Cedex -
HITNEY	Mr H. V. HITNEY, United States Naval Ocean Systems Center - Code 543 - San Diego, CA 92152-5000 -
HÖHN	Dr D. HÖHN, apl. Prof., Germany Director, FGAN-FfO - Schloss Kressbach - W-7400 Tübingen -
HURTAUD	Dr Y. HURTAUD, France CELAR - 35998 Rennes Armées -
JENSEN	Dr D. R. JENSEN, United States Ocean and Atmospheric Sciences Div. - Code 543 - Naval Ocean Systems Center - San Diego, CA 92152-5000 -
KAYA	Col. D. KAYA, Turkey Ministry of Defence (MSB) - 06650 Ankara -
KORBAY	Dr Y. KORBAY, Netherlands Technical University Delft - E.T. - PO Box 5031 - 2600 GA Delft -
LORENZ	Dr R. W. LORENZ, Germany Forschungsinstitut der DBP Telekom - Postfach 10 00 03 - W-6100 Darmstadt -
NORBURY	Prof. J.R. NORBURY, United Kingdom Head, Radio Communication Research - Unit - Rutherford Appleton Laboratory - Chilton, Didcot OX11, OQX -
ÖZMEHMET	Prof. Dr K. ÖZMEHMET, Turkey Chairman, Dept. of Electrical and Electronic Engineering - Dokuz Eylül University - Izmir -
PAPAPASCHALIS	Lt-Col. A. PAPAPASCHALIS, Greece Hellenic Air Force General Staff - Branch A' - Directorate A1 - Holargos, TGA 1010 - Athens -
PATRICIO	Ing. J.F. PATRICIO, Portugal R. Alferes Barrilero Ruas - No 1 - 8 Dt - 1800 Lisboa -
RASMUSSEN	Mr J.E. RASMUSSEN, United States Phillips Laboratory / LID - Hanscom AFB, MA 01731 -
RAVARD	Mr O. RAVARD, France Université de Rennes I - Laboratoire Radiocommunications - Campus de Beaulieu - 35042 Rennes Cedex -
RAYMUND	Dr T. D. RAYMUND, United States WPL Room 60, Dept. of ECE - University of Illinois - 1406 W. Green Street - Urbana, IL 61801-2991 -
REINISCH	Prof. B. W. REINISCH, United States University of Lowell - 450 Aiken Street - Lowell, MA 01854 -
RICHTER	Dr J. H. RICHTER, United States Head, Ocean and Atmospheric - Sciences Division - Code 54 - Naval Ocean Systems Center - San Diego, CA 92152-5000 -

**ROGGE** Ir J. ROGGE, Netherlands  
 Royal Military Academy - PO Box 90154 - 4800 RG Breda -

**ROSENTHAL** Mr J. ROSENTHAL, United States  
 Pacific Missile Test Center - Code 3250 - Point Mugu, CA 93042-5000 -

**ROTHER** Dr D. ROTHER, Germany  
 Director, RD & E - Dept. LS/E, - Standard Elektrik Lorenz AG (SEL) - Lorenzstrasse 10 - W-7000 Stuttgart 70 -

**SCHWEICHER** Prof. E. SCHWEICHER, Belgium  
 Ecole Royale Militaire - Chaire OM - 30, Ave de la Renaissance - B-1040 Bruxelles -

**SENGIL** Lt. NEVSAN SENGIL, Turkey  
 Deniz Kuvvetleri Kom - Lojistik Baskanligi - 06100 Bakanliklar - Ankara -

**SPOELSTRA** Dr T.A.Th. SPOELSTRA, Netherlands  
 NFRA Radio Observatory - PO Box 2 - 7990 AA Dwingeloo -

**SÜRÜCÜ** Mr F. SÜRÜCÜ, United States  
 Aeronomy Laboratory - University of Illinois - 1406 W. Green Street - Urbana, IL 61801-2991 -

**TAAGHOLT** Mr J. TAAGHOLT, Denmark  
 Danish Polar Center - Hausergade 3 - DK-1128 Copenhagen K -

**TANSAN** Lt TAYFUN TANSAN, Turkey  
 Deniz Kuvvetleri Kom. Teknik Bsk. - Bakanliklar - Ankara -

**THOMSON** Prof. D. W. THOMSON, United States  
 Dept of Meteorology - 507 Walker Bldg - University Park, PA 16802 -

**TOKER** Prof. Dr C. TOKER, Turkey  
 Dept. of Electrical and Electronic - Engineering - Middle East Technical University - ODTU Ankara -

**TORUN** Capt. E. TORUN, Turkey  
 Ministry of National Defence MSB - Research and Development Dept. ARGE - 06650 Ankara -

**TULUNAY** Prof. Dr E. TULUNAY, Turkey  
 Middle East Technical University - 06531 Ankara -

**TULUNAY** Prof. Dr Y. TULUNAY, Turkey  
 Dept. of Aeronautical Engineering - Middle East Technical University - ODTU-METU - 06531 Ankara -

**TURKYILMAZ** Major M. TURKYILMAZ, Turkey  
 Hava Lojistik K. Ligi - Etimesgut Ankara -

**VISSINGA** Ir H. VISSINGA, Netherlands  
 van Kempenstraat 30 - 2252 VH Voorschoten -

**VLAHAKIS** Capt. G. VLAHAKIS, Greece  
 Hellenic Air Force General Staff - A1 - Holargos, TGA 1010 - Athens -

**WALKER** Dr I. K. WALKER, United Kingdom  
 Physics Department - University College of Wales - Aberystwyth, Dyfed SYR3 3BZ -

**WATKINS** Dr W. R. WATKINS, United States  
 US Army Atmospheric Sciences Lab - SLCAS-AR-1 - White Sands Missile Range - NM 88002-5501 -

**WERNER** Dr C. WERNER, Germany  
 DLR - Institut fuer Optoelektronik - W-8031 Oberpfaffenhofen -

**YAVUZ** Dr D. YAVUZ, STC, The Netherlands  
 Head, Radio Branch - Communications Division - SHAPE Technical Center - PO Box 174 - 2501 CD The Hague -

**YEH** Prof. K C. YEH, United States  
 ECE/UIUC - 1406 W. Green Street - Urbana, IL 61801-2991 -

REPORT DOCUMENTATION PAGE			
1. Recipient's Reference	2. Originator's Reference	3. Further Reference	4. Security Classification of Document
	AGARD-CP-502	ISBN 92-835-0654-5	UNCLASSIFIED
5. Originator	Advisory Group for Aerospace Research and Development North Atlantic Treaty Organization 7 rue Ancelle, 92200 Neuilly sur Seine, France		
6. Title	REMOTE SENSING OF THE PROPAGATION ENVIRONMENT		
7. Presented at	the Electromagnetic Wave Propagation Panel Symposium, held in Çeşme, Turkey, 30th September—4th October 1991.		
8. Author(s)/Editor(s)	Various		9. Date February 1992
10. Author's/Editor's Address	Various		11. Pages 352
12. Distribution Statement	This document is distributed in accordance with AGARD policies and regulations, which are outlined on the back covers of all AGARD publications.		
13. Keywords/Descriptors	<div style="display: flex; justify-content: space-between;"> <div> <del>✗</del> Remote sensing, <del>✗</del> Propagation,  <del>✗</del> Ionospheric propagation,            Light transmission,            Light scattering,            Radar,            Optical radar,            Aerosols,         </div> <div>           Refractivity,            Wave dispersion,            Ionosondes,            Radiometry,            Polarimetry,            Meteorology         </div> </div>		
14. Abstract	<p>Increasing complexity and sophistication of modern military sensor and weapon systems require a more accurate and timely description of the propagation environment for the entire electromagnetic spectrum (from extremely low frequencies through the ultraviolet band). Active and passive remote sensing techniques deployed from the ground, from airborne platforms and, very importantly, from satellites offer the greatest potential for producing the desired information in a timely manner.</p> <p><b>NATO</b></p> <p>The Symposium addressed first the subject of sensing tropospheric refractivity using propagation measurements and various other remote sensing techniques. The second topic focussed on ionospheric sensing techniques and interpretation of remotely sensed signatures. The Symposium then turned to sensing of aerosols and other atmospheric parameters important for the propagation of visible and infrared radiation. Also covered were techniques to measure winds, temperature, liquid water and humidity in the lower atmosphere. Finally, measurement, inversion and processing techniques were presented.</p>		

<p>AGARD Conference Proceedings 502 Advisory Group for Aerospace Research and Development, NATO <b>REMOTE SENSING OF THE PROPAGATION ENVIRONMENT</b> Published February 1992 352 pages</p> <p>Increasing complexity and sophistication of modern military sensor and weapon systems require a more accurate and timely description of the propagation environment for the entire electromagnetic spectrum (from extremely low frequencies through the ultraviolet band). Active and passive remote sensing techniques deployed from the ground, from airborne platforms and, very importantly, from satellites offer the greatest potential for producing the desired information in a timely manner.</p> <p>P.T.O.</p>	<p>AGARD-CP-502</p> <p>Remote sensing Ionospheric propagation Light transmission Light scattering Radar Optical radar Aerosols Refractivity Wave dispersion Ionosondes Radiometry Polarimetry Meteorology</p>	<p>AGARD Conference Proceedings 502 Advisory Group for Aerospace Research and Development, NATO <b>REMOTE SENSING OF THE PROPAGATION ENVIRONMENT</b> Published February 1992 352 pages</p> <p>Increasing complexity and sophistication of modern military sensor and weapon systems require a more accurate and timely description of the propagation environment for the entire electromagnetic spectrum (from extremely low frequencies through the ultraviolet band). Active and passive remote sensing techniques deployed from the ground, from airborne platforms and, very importantly, from satellites offer the greatest potential for producing the desired information in a timely manner.</p> <p>P.T.O.</p>	<p>AGARD-CP-502</p> <p>Remote sensing Ionospheric propagation Light transmission Light scattering Radar Optical radar Aerosols Refractivity Wave dispersion Ionosondes Radiometry Polarimetry Meteorology</p>
<p>AGARD Conference Proceedings 502 Advisory Group for Aerospace Research and Development, NATO <b>REMOTE SENSING OF THE PROPAGATION ENVIRONMENT</b> Published February 1992 352 pages</p> <p>Increasing complexity and sophistication of modern military sensor and weapon systems require a more accurate and timely description of the propagation environment for the entire electromagnetic spectrum (from extremely low frequencies through the ultraviolet band). Active and passive remote sensing techniques deployed from the ground, from airborne platforms and, very importantly, from satellites offer the greatest potential for producing the desired information in a timely manner.</p> <p>P.T.O.</p>	<p>AGARD-CP-502</p> <p>Remote sensing Ionospheric propagation Light transmission Light scattering Radar Optical radar Aerosols Refractivity Wave dispersion Ionosondes Radiometry Polarimetry Meteorology</p>	<p>AGARD Conference Proceedings 502 Advisory Group for Aerospace Research and Development, NATO <b>REMOTE SENSING OF THE PROPAGATION ENVIRONMENT</b> Published February 1992 352 pages</p> <p>Increasing complexity and sophistication of modern military sensor and weapon systems require a more accurate and timely description of the propagation environment for the entire electromagnetic spectrum (from extremely low frequencies through the ultraviolet band). Active and passive remote sensing techniques deployed from the ground, from airborne platforms and, very importantly, from satellites offer the greatest potential for producing the desired information in a timely manner.</p> <p>P.T.O.</p>	<p>AGARD-CP-502</p> <p>Remote sensing Ionospheric propagation Light transmission Light scattering Radar Optical radar Aerosols Refractivity Wave dispersion Ionosondes Radiometry Polarimetry Meteorology</p>

<p>The Symposium addressed first the subject of sensing tropospheric refractivity using propagation measurements and various other remote sensing techniques. The second topic focussed on ionospheric sensing techniques and interpretation of remotely sensed signatures. The Symposium then turned to sensing of aerosols and other atmospheric parameters important for the propagation of visible and infrared radiation. Also covered were techniques to measure winds, temperature, liquid water and humidity in the lower atmosphere. Finally, measurement, inversion and processing techniques were presented.</p> <p>Papers presented at the Electromagnetic Wave Propagation Panel Symposium, held in Çeşme, Turkey, 30th September—4th October 1991.</p> <p>ISBN 92-835-0654-5</p>	<p>The Symposium addressed first the subject of sensing tropospheric refractivity using propagation measurements and various other remote sensing techniques. The second topic focussed on ionospheric sensing techniques and interpretation of remotely sensed signatures. The Symposium then turned to sensing of aerosols and other atmospheric parameters important for the propagation of visible and infrared radiation. Also covered were techniques to measure winds, temperature, liquid water and humidity in the lower atmosphere. Finally, measurement, inversion and processing techniques were presented.</p> <p>Papers presented at the Electromagnetic Wave Propagation Panel Symposium, held in Çeşme, Turkey, 30th September—4th October 1991.</p> <p>ISBN 92-835-0654-5</p>
<p>The Symposium addressed first the subject of sensing tropospheric refractivity using propagation measurements and various other remote sensing techniques. The second topic focussed on ionospheric sensing techniques and interpretation of remotely sensed signatures. The Symposium then turned to sensing of aerosols and other atmospheric parameters important for the propagation of visible and infrared radiation. Also covered were techniques to measure winds, temperature, liquid water and humidity in the lower atmosphere. Finally, measurement, inversion and processing techniques were presented.</p> <p>Papers presented at the Electromagnetic Wave Propagation Panel Symposium, held in Çeşme, Turkey, 30th September—4th October 1991.</p> <p>ISBN 92-835-0654-5</p>	<p>The Symposium addressed first the subject of sensing tropospheric refractivity using propagation measurements and various other remote sensing techniques. The second topic focussed on ionospheric sensing techniques and interpretation of remotely sensed signatures. The Symposium then turned to sensing of aerosols and other atmospheric parameters important for the propagation of visible and infrared radiation. Also covered were techniques to measure winds, temperature, liquid water and humidity in the lower atmosphere. Finally, measurement, inversion and processing techniques were presented.</p> <p>Papers presented at the Electromagnetic Wave Propagation Panel Symposium, held in Çeşme, Turkey, 30th September—4th October 1991.</p> <p>ISBN 92-835-0654-5</p>

AGARD

NATO OTAN

7 RUE ANCELLE - 92200 NEUILLY-SUR-SEINE  
FRANCE

Telephone (1) 47.38.57.00 - Télex 610 176  
Télécopie (1) 47.38.57.99

DIFFUSION DES PUBLICATIONS  
AGARD NON CLASSIFIEES

L'AGARD ne détient pas de stocks de ses publications; dans un but de distribution générale à l'adresse ci-dessus. La diffusion initiale des publications de l'AGARD est effectuée auprès des pays membres de cette organisation par l'intermédiaire des Centres Nationaux de Distribution suivants. A l'exception des Etats-Unis, ces centres disposent parfois d'exemplaires additionnels; dans les cas contraire, on peut se procurer ces exemplaires sous forme de microfiches ou de microcopies auprès des Agences de Vente dont la liste suit.

CENTRES DE DIFFUSION NATIONAUX

ALLEMAGNE

Fachinformationszentrum,  
Karlsruhe  
D-7514 Eggenstein-Leopoldshafen 2

BELGIQUE

Coordonnateur AGARD-VSL  
Etat-Major de la Force Aérienne  
Quartier Reine Elisabeth  
Rue d'Evere, 1140 Bruxelles

CANADA

Directeur du Service des Renseignements Scientifiques  
Ministère de la Défense Nationale  
Ottawa, Ontario K1A 0K2

DANEMARK

Danish Defence Research Board  
Ved Idraetsparken 4  
2100 Copenhagen Ø

ESPAGNE

INTA (AGARD Publications)  
Pintor Rosales 34  
28008 Madrid

ETATS-UNIS

National Aeronautics and Space Administration  
Langley Research Center  
M/S 180  
Hampton, Virginia 23665

FRANCE

O.N.E.R.A. (Direction)  
29, Avenue de la Division Leclerc  
92320, Châtillon sous Bagneux

GRECE

Hellenic Air Force  
Air War College  
Scientific and Technical Library  
Dekelia Air Force Base  
Dekelia, Athens TGA 1010

ISLANDE

Director of Aviation  
c/o Flugrad  
Reykjavik

ITALIE

Aeronautica Militare  
Ufficio del Delegato Nazionale all'AGARD  
Aeroporto Pratica di Mare  
00040 Pomezia (Roma)

LUXEMBOURG

Voir Belgique

NORVEGE

Norwegian Defence Research Establishment  
Attn: Biblioteket  
P.O. Box 25  
N-2007 Kjeller

PAYS-BAS

Netherlands Delegation to AGARD  
National Aerospace Laboratory NLR  
Kluyverweg 1  
2629 HS Delft

PORTUGAL

Portuguese National Coordinator to AGARD  
Gabinete de Estudos e Programas  
CLAFIA  
Base de Alfragide  
Alfragide  
2700 Amadora

ROYAUME UNI

Defence Research Information Centre  
Kentigern House  
65 Brown Street  
Glasgow G2 8EX

TURQUIE

Milli Savunma Başkanlığı (MSB)  
ARGE Daire Başkanlığı (ARGE)  
Ankara

LE CENTRE NATIONAL DE DISTRIBUTION DES ETATS-UNIS (NASA) NE DETIENT PAS DE STOCKS  
DES PUBLICATIONS AGARD ET LES DEMANDES D'EXEMPLAIRES DOIVENT ETRE ADRESSEES DIRECTEMENT  
AU SERVICE NATIONAL TECHNIQUE DE L'INFORMATION (NTIS) DONT L'ADRESSE SUIT.

AGENCES DE VENTE

National Technical Information Service  
(NTIS)  
5285 Port Royal Road  
Springfield, Virginia 22161  
Etats-Unis

ESA/Information Retrieval Service  
European Space Agency  
10, rue Mario Nikis  
75015 Paris  
France

The British Library  
Document Supply Division  
Boston Spa, Wetherby  
West Yorkshire LS23 7BQ  
Royaume Uni

Les demandes de microfiches ou de photocopies de documents AGARD (y compris les demandes faites auprès du NTIS) doivent comporter la dénomination AGARD, ainsi que le numéro de série de l'AGARD (par exemple AGARD-AG-315). Des informations analogues, telles que le titre et la date de publication sont souhaitables. Veuillez noter qu'il y a lieu de spécifier AGARD-R-nnn et AGARD-AR-nnn lors de la commande de rapports AGARD et des rapports consultatifs AGARD respectivement. Des références bibliographiques complètes ainsi que des résumés des publications AGARD figurent dans les journaux suivants:

Scientific and Technical Aerospace Reports (STAR)  
publié par la NASA Scientific and Technical  
Information Division  
NASA Headquarters (NTT)  
Washington D.C. 20546  
Etats-Unis

Government Reports Announcements and Index (GRA&I)  
publié par le National Technical Information Service  
Springfield  
Virginia 22161  
Etats-Unis  
(accessible également en mode interactif dans la base de  
données bibliographiques en ligne du NTIS, et sur CD-ROM)



Imprimé par Specialised Printing Services Limited  
40 Chigwell Lane, Loughton, Essex IG10 3TZ

AGARD

NATO OTAN

7 RUE ANCELLE 92200 NEUILLY-SUR-SEINE  
FRANCE

Telephone (1) 47 38 57 00 - Telex 510 176  
Telefax (1) 47 38 57 99

DISTRIBUTION OF UNCLASSIFIED  
AGARD PUBLICATIONS

AGARD does NOT hold stocks of AGARD publications at the above address for general distribution. Initial distribution of AGARD publications is made to AGARD Member Nations through the following National Distribution Centres. Further copies are sometimes available from these Centres (except in the United States), but it may be purchased in microfiche or photocopy form from the Sales Agencies listed below.

NATIONAL DISTRIBUTION CENTRES

BELGIUM

Coordonnateur AG  
Etat-Major de la Fg  
Quartier Reine Elis  
Rue d'Evere, 1140

CANADA

Director Scientific  
Dept of National D  
Ottawa, Ontario K1

DENMARK

Danish Defence Re  
Ved Idraetsparken  
2100 Copenhagen

FRANCE

O.N.E.R.A. (Direct  
29 Avenue de la Di  
92320 Châtillon

GERMANY

Fachinformationsze  
Karlsruhe  
D-7514 Eggenstein

GREECE

Hellenic Air Force  
Air War College  
Scientific and Technical Library  
Dekelia Air Force Base  
Dekelia, Athens TGA 1010

ICELAND

Director of Aviation  
c/o Flugrad  
Reykjavik

ITALY

Aeronautica Militare  
Ufficio del Delegato Nazionale all'AGARD  
Aeroporto Pratica di Mare  
00040 Pomezia (Roma)



National Aeronautics and  
Space Administration

Washington, D.C. SPECIAL FOURTH CLASS MAIL  
20546 BOOK

Postage and Fees Paid  
National Aeronautics and  
Space Administration  
NASA-451

Official Business  
Penalty for Private Use \$300



L3 001 AG-CF-502 9203105002672D  
DEPT OF DEFENSE  
DEFENSE TECHNICAL INFORMATION CENTER  
ATTN : DTIC-FDAB/JOYCE CHIRAS  
CAMERON STATION BLDG 5  
ALEXANDRIA VA 223046145

28008 Madrid

TURKEY

Milli Savunma Bakanligi (MSB)  
ARGE Daire Bakanligi (ARGE)  
Ankara

UNITED KINGDOM

Defence Research Information Centre  
Kentigern House  
65 Brown Street  
Glasgow G2 8EX

UNITED STATES

National Aeronautics and Space Administration (NASA)  
Langley Research Center  
M/S-180  
Hampton, Virginia 23665

THE UNITED STATES NATIONAL DISTRIBUTION CENTRE (NASA) DOES NOT HOLD  
STOCKS OF AGARD PUBLICATIONS AND APPLICATIONS FOR COPIES SHOULD BE MADE  
DIRECT TO THE NATIONAL TECHNICAL INFORMATION SERVICE (NTIS) AT THE ADDRESS BELOW.

SALES AGENCIES

National Technical  
Information Service (NTIS)  
5285 Port Royal Road  
Springfield, Virginia 22161  
United States

ESA/Information Retrieval Service  
European Space Agency  
10, rue Mario Nikis  
75015 Paris  
France

The British Library  
Document Supply Centre  
Boston Spa, Wetherby  
West Yorkshire LS23 7BQ  
United Kingdom

Requests for microfiches or photocopies of AGARD documents (including requests to NTIS) should include the word 'AGARD' and the AGARD serial number (for example AGARD-AG-315). Collateral information such as title and publication date is desirable. Note that AGARD Reports and Advisory Reports should be specified as AGARD-R-*nnn* and AGARD-AR-*nnn*, respectively. Full bibliographical references and abstracts of AGARD publications are given in the following journals:

Scientific and Technical Aerospace Reports (STAR)  
published by NASA Scientific and Technical  
Information Division  
NASA Headquarters (NTI)  
Washington D.C. 20546  
United States

Government Reports Announcements and Index (GRA&I)  
published by the National Technical Information Service  
Springfield  
Virginia 22161  
United States  
(also available online in the NTIS Bibliographic  
Database or on CD-ROM)



Printed by Specialised Printing Services Limited  
40 Chigwell Lane, Loughborough, Essex IG10 3TZ

ISBN 92-835-0654-5